

**Tracing fluids during medium to ultra-high pressure metamorphism: insights by combined in situ oxygen isotopes and trace element analysis.**

Laure Gauthiez Putallaz

November 2017

A thesis submitted for the degree of Doctor of Philosophy of  
The Australian National University

© Copyright by GAUTHIEZ PUTALLAZ 2017

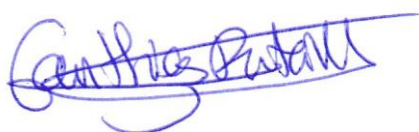
All Rights Reserved



## Declaration

This thesis contains no material which has been accepted for the award of any other degree or diploma in any university. To the best of the author's knowledge, it contains no material previously published or written by another person, except where due reference is made in the text.

*Word count: 84 312*

A handwritten signature in blue ink, reading "Laure Gauthiez Putallaz". The signature is written in a cursive style with a long horizontal stroke at the end.

Laure Gauthiez Putallaz

November 2017



## Acknowledgments

I dedicate this thesis to my mother, Britta Hagemann, who always encouraged me to go forward and aim high. I was fortunate to spend her last months at her side as she was battling cancer that led to her passing in 2016. She would have enjoyed to see the completion of this PhD work.

I would like to thank my supervisor Daniela Rubatto for accompanying me through this journey of growth as a scientist but also as a person, for her energy, her guidance and her support. Jörg Hermann also offered invaluable support by his enthusiasm and attention to detail. Warm thanks to Laure Martin who offered rich discussions and showed me the ropes both at RSES and for a short stay in Perth. I am grateful for the help provided by Donna Whitney by providing samples, guiding us on the field and welcoming me in Minneapolis for a stay with her student Katherine Fornash. I owe my thanks to Allen Nutman and Vickie Bennett for introducing me to the Eoarchaeon and trusting me to come to the field in Greenland. Thank you to all six members of my panel for your review of parts or the entirety (Daniela Rubatto) of this manuscript, which made writing a successful and rewarding experience.

This work would not have been possible without great discussions and technical support by Shane Paxton (mineral separation and sample preparation), Iam Williams, Peter Lanc, Peter Holden, Mark Fanning and Trevor Ireland (SHRIMP), Robert Rapp (EMPA), Charlotte Allen, Jung Woo Park, Peter Tollan and Michael Jollands (LA-ICP-MS), Amber Jarrett (carbonate chemistry), Joe Cali (carbonate analysis), Annette Von Der Handt (EMPA, University of Minneapolis).

I was lucky to share my time at the Research School of Earth Sciences with an outstanding community of students and staff, some of which have already been named above. Many thanks to my fellow students in no particular order: Kate, Mari, Tanya, Morgan, Lizzie, Malte, Magda, Nur, Bianca, Kate, Tanja, Nick, Jo, Frauke, Alex, Piers, and many more I forgot in this list. Thank you to the SHRIMP group for morning coffee and Friday night drinks. Thanks for the ANU Mountaineering Club and the ACT Rogaining Association for the opportunity to explore the wilds surrounding Canberra, which rounded up an awesome experience at ANU.

Finally, I would like to thank my family, firstly my husband Pierre-Dominique for his courage to follow me on the other side of the planet pursuing geochemical dreams and his unwavering support of my work. My father Bernard and sister Jeanne are the roots that keep me strong every day, thank you for being there for me.

## Abstract

Fluids are an essential component of tectonic and metamorphic processes such as subduction and crustal anatexis. Fluids are elusive to trace as they commonly escape high-pressure rocks. This study uses oxygen isotopes to identify fluid influxes in metamorphic rocks and tie them to geologic events, measuring  $\delta^{18}\text{O}$  in situ by ion microprobe in garnet, zircon, apatite, monazite and lawsonite.

New method developments are presented for  $\delta^{18}\text{O}$  analyses by Sensitive High Resolution Ion MicroProbe: (i) in apatite, a precision of 0.2‰ (1 $\sigma$ ) is achieved; diffusion modelling shows that apatite is expected to preserve oxygen isotope signatures from 400-450°C and below; (ii) a matrix correction scheme is derived for monazite oxygen isotope measurement, allowing a precision of 0.35‰ (1 $\sigma$ ); (iii) rutile oxygen isotope measurements yield major orientation effects.

Fluid pulses generated by prograde dehydration reactions are investigated in the ultra-high-pressure Dora Maira whiteschists, Italy. Rare-earth-element abundances indicate prograde monazite and zircon growth (pre-garnet  $34.5\pm 0.7$  Ma, 6.4‰ and syn-garnet at  $34.9\pm 0.4$  Ma, 6.2 to 6.7‰), which are linked to dehydration reactions using thermodynamic modelling. This allows drawing a P-T-time-fluid path that implies that (i) prograde subduction from 25 to 45 kbar occurred within a couple of My (minimum burial rate of 2 cm/yr); (ii) high-pressure fluids were of internal origin and metasomatism likely have occurred at a rifting phase before subduction.

Four phases of fluid circulations are identified in the high-pressure low-temperature lawsonite eclogites and blueschists of the Tavşanlı zone, Turkey. The Halilbağı unit is an oceanic complex containing various sediments and serpentinite together with  $222\pm 5$  Ma MORB and  $123\pm 3$  Ma OIB lithologies (zircon U-Pb, whole-rock major and trace elements). The sequence was thoroughly altered and mechanically mixed at the seafloor and in the accretionary prism, leading to overall high whole-rock  $\delta^{18}\text{O}$  of 11.0-17.0‰ for metabasites. Garnet, apatite and lawsonite are zoned in  $\delta^{18}\text{O}$  in samples across the unit, with contrasts of 7‰ in a MORB eclogite (garnet core: 6.3‰, rim: 13‰) and 3‰ in an impure quartzite (apatite core: 19.5‰, rim: 17‰). Petrographic and trace element evidence allow identifying localised prograde-peak fluid influx, and homogenisation of oxygen isotopes and Sr/Pb at the start of retrogression by pervasive fluid circulation across the unit.

Heavy  $\delta^{18}\text{O}$  signatures (WR: 11.8 to 13.6‰) were measured in Eoarchaeon metasediments from the Isua supracrustal belt, Greenland. The sources of the sediments were mantle-derived boninites (mafic component) and andesites (felsic component, detrital/volcanic zircons dated at 3709 Ma,

$\delta^{18}\text{O}$  5.3‰). Three garnet growth zones record high  $\delta^{18}\text{O}$  (9 to 10‰), in equilibrium with the whole-rock. Rare-earth-element and petrographic evidence allow identifying a higher-pressure signature in the high-  $\delta^{18}\text{O}$  garnet, which can be linked to a 3690-3660 Ma tectonic event. The elevated  $\delta^{18}\text{O}$  signature in the metasediments thus originated from surficial processes (e.g. weathering) before 3690Ma. Melting of such heavy- $\delta^{18}\text{O}$  amphibolite-facies sediments could represent a source for early Archean high- $\delta^{18}\text{O}$  magmas and zircons.

The combination of oxygen isotope and trace element microanalysis in zoned minerals proves a powerful tool for uncovering multistage minor and major fluid infiltration events in metamorphic rocks.



# Table of Contents

Declaration .....	iii
Acknowledgments .....	v
Abstract.....	vii
Table of Contents .....	ix
Introduction .....	1
<b>Chapter 1</b>	
<b>Preliminary study of <i>in situ</i> <math>\delta^{18}\text{O}</math> analysis of rutile, apatite and monazite by SHRIMP ion microprobe .....</b>	<b>5</b>
1 Introduction.....	5
1.1 Target minerals .....	5
1.2 Challenges in the <i>in situ</i> analysis of oxygen isotopes .....	6
1.3 Origin of samples .....	7
2 Methods.....	8
2.1 Sample preparation .....	8
2.2 Imaging .....	9
2.3 Major elements.....	10
2.4 Trace elements .....	11
2.5 SHRIMP oxygen isotopes.....	11
3 Apatite.....	12
3.1 Sample composition and zoning .....	12
3.2 Results.....	15
3.3 Discussion .....	17
3.3.1 Oxygen diffusion.....	18
4 Monazite .....	24
4.1 Sample and standards.....	24
4.2 Results.....	26
4.3 Discussion .....	27
4.3.1 Compositional matrix effect.....	27
4.3.2 Monazite-zircon fractionation.....	32
5 Rutile.....	32
5.1 Samples and standards .....	32
5.2 Results.....	34
5.3 Discussion .....	37

5.3.1	Orientation effects .....	37
5.3.2	Accuracy .....	40
6	Conclusions and outlook .....	40

## Chapter 2

### **Dating prograde fluid pulses during subduction by in situ U-Pb and oxygen isotope analysis..... 43**

1	Introduction .....	43
1.1	Geological background.....	44
2	Analytical methods .....	45
3	Results .....	47
3.1	Sample description .....	47
3.2	Zircon textures, inclusions and composition .....	49
3.3	Monazite textures and composition.....	52
3.4	Thermodynamic modelling of Si-poor whiteschists.....	53
3.5	U-Pb dating.....	55
3.6	SHRIMP Oxygen Isotopes .....	58
4	Discussion.....	60
4.1	Metamorphic conditions of zircon and monazite growth .....	60
4.2	Fluid-induced prograde zircon formation.....	63
4.3	Subduction rate.....	64
4.4	Equilibrium oxygen isotopic fractionation between peak metamorphic phases.....	65
4.5	Evolution of the oxygen isotope composition of the whiteschists from protolith to subduction.....	66
4.6	Metasomatic event.....	69
5	Conclusions .....	70

## Chapter 3

### **Geodynamic setting of the Halilbağı unit, Tavşanlı zone, Turkey ..... 73**

1	Introduction .....	73
1.1	Geodynamic setting .....	73
1.2	Cretaceous subduction.....	78
2	Methods .....	80
2.1	Whole-rock geochemistry.....	80
2.2	SHRIMP U-Th-Pb zircon dating .....	81
2.3	SHRIMP U-Th-Pb allanite and florencite dating .....	82
2.4	Zircon trace elements.....	82
3	Sampling and field-relations.....	83
3.1	Halilbağı.....	84
3.2	South Halilbağı.....	87

3.3	Neighbouring units.....	88
4	Geochemistry of Halilbağı lithologies .....	91
4.1	Metasediments .....	91
4.2	Metabasites and serpentinite .....	92
5	U-Pb and Th-Pb dating .....	98
5.1	Zircon U-Pb .....	98
5.1.1	Lws-phen-grt layer SHS44A.....	98
5.1.2	Blueschist SHB45 .....	102
5.1.3	Calcschist SHM23B.....	104
5.2	Florencite and Allanite U-Th-Pb.....	105
6	Discussion.....	107
6.1	Origin of the detrital component.....	107
6.2	Affinity of magmatic rocks in the Halilbağı Formation.....	109
6.2.1	Group 2 metabasites: MORB and Leucogabbro SHS44A.....	110
6.2.2	Group 3 - OIB basalt.....	110
6.2.3	Serpentinite pod .....	111
6.2.4	Origin of the sediment signature in group 1 metabasites .....	112
6.3	Lithostratigraphic correlation and tectonic setting.....	112
6.4	Timing of subduction.....	115
6.5	Place of Halilbağı unit in subducting structure .....	117
7	Conclusions.....	118

#### Chapter 4

	<b>Fluid circulation in subducted crust investigated by in situ O isotopes and trace elements in zircon, garnet, apatite and lawsonite (HP-LT Halilbağı unit, Turkey).</b> .....	<b>119</b>
1	Introduction.....	119
2	Methods.....	123
2.1	Mineral chemistry .....	123
2.2	Oxygen isotope analysis.....	124
3	Sample description and mineral composition .....	126
3.1	Metabasites (group 2 and 3) and serpentinite .....	128
3.2	Mixed metabasites (group 1).....	131
3.3	Metasediments .....	136
4	Oxygen isotopes.....	138
4.1	WR silicates and carbonates .....	139
4.2	Mineral data .....	139
4.2.1	Zircon.....	142
4.2.2	Garnet.....	144
4.2.3	Apatite.....	147

4.2.4	Lawsonite .....	151
4.3	Fractionation modelling.....	154
5	Discussion.....	157
5.1	Evidence of fluid-rock interaction in zoned minerals.....	157
5.1.1	Zircon zoning.....	157
5.1.2	Garnet zoning .....	158
5.1.3	Apatite zoning.....	161
5.1.4	Lawsonite zoning.....	164
5.2	Protolith $\delta^{18}\text{O}$ and early metasomatism .....	165
5.3	High-pressure fluid events.....	169
5.4	Chemical WR changes and hybridisation.....	175
5.4.1	Mechanism for WR metasomatism .....	175
5.4.2	Influence of metasomatism on WR trace-element signatures .....	176
6	Conclusions .....	180

## Chapter 5

### **Tracking heavy $\delta^{18}\text{O}$ signatures in the Archaean crust, a combined *in situ* and WR oxygen isotope study in Archaean metasedimentary rocks from the Itsaq complex, West Greenland. .... 183**

1	Introduction .....	183
1.1	General context.....	184
1.2	Tectonics and metamorphic events.....	186
2	Methods .....	189
2.1	WR geochemistry .....	189
2.2	Mineral chemistry.....	190
2.3	SHRIMP oxygen isotopes .....	191
2.4	SHRIMP U-Pb dating.....	191
3	Results .....	192
3.1	Sample petrology and garnet zoning .....	192
3.1.1	Mafic schists G12-101 and G12-113 .....	192
3.1.2	Sample G04-46.....	196
3.1.3	Tikeraq.....	198
3.2	WR Geochemistry .....	201
3.3	U-Pb dating.....	203
3.4	Oxygen isotopes .....	204
3.4.1	Whole-rock .....	204
3.4.2	Garnet ion microprobe measurements .....	204
3.4.3	Zircon .....	206
3.4.4	Fractionation modelling.....	208
4	Discussion.....	209

4.1	WR $\delta^{18}\text{O}$ records 3.7 Ga signatures in the B2 schists .....	209
4.1.1	Garnet growth in Isua B2 schists .....	209
4.1.2	Tracking WR $\delta^{18}\text{O}$ through geologic time .....	212
4.2	Isua B2 schists are the results of weathering on the Eoarchaeon surface. ....	215
4.2.1	Magmatic source-material of the B2 schists .....	215
4.2.2	Mechanism of weathering /diagenesis .....	216
4.3	Tikeraq .....	219
4.4	Heavy $\delta^{18}\text{O}$ mid-crustal lithologies in the Archaean.....	221
5	Conclusion .....	222
	<b>Conclusion.....</b>	<b>183</b>
	<b>References .....</b>	<b>227</b>
	<b>Electronic appendix contents .....</b>	<b>249</b>
	A1 – Appendix to chapter 1 .....	249
	A2 – Appendix to chapter 2 .....	249
	A3 – Appendix to chapter 3 .....	249
	A4 – Appendix to chapter 4 .....	250
	A5 – Appendix to chapter 5 .....	250



## Introduction

The circulation of aqueous fluids plays an important role in geological processes, particularly at subsolidus conditions. Fluid-rock interaction is linked to reaction catalysis, deformation including seismic activity, advection of heat and mass. The main locus of aqueous fluid-rock interaction is the seafloor, where the water volume of the oceans is cycled through the cooling oceanic crust every 4-8 ky (e.g. Elderfield and Schultz 1996). Fluid-rock interactions are also particularly critical in crust-building systems such as the dehydrating subducting crust (e.g. Peacock 1990; Hacker et al. 2003), and the creation of the subduction component in arc magmas (e.g. Pearce and Peate 1995; Spandler and Pirard 2013), as well as mid-crustal partial melting initiated by mica dehydration (e.g. Breton and Thompson 1988; Harrison and Wielicki 2016). Understanding the chemical transfers happening with aqueous fluids of different sources interacting with crustal rocks is thus critical to determining how the Earth differentiates and elements cycle from mantle to crust. Moreover, in low to moderate temperature systems, the presence of an aqueous fluid is necessary to the kinetics of metamorphic reactions, and is thus one of the main players in crustal metamorphism.

However, fluid-rock interaction is often an instantaneous process in geologic time, and fluids can be elusive to trace. Undoubtedly, the investigation of veins and fluid inclusions in minerals can provide direct constraints on fluid composition and dynamics (e.g. Etheridge et al. 1984; Touret 2001). However, veins are often not in equilibrium with their surroundings (e.g. Oliver and Bons 2001), consequentially what is observed in a vein is the result of kinetics and disequilibrium. Fluid inclusions can present the same challenge, and are commonly too small to be targeted for trace element or isotopic analysis in order to constrain the fluid chemistry better. Fluid inclusions can also exchange with the encasing minerals or become open by fracturation, which complicates the retrieval of the primary signal. The aim of this study is to track fluids using the unique major element that is common to fluids and rock: oxygen. Oxygen atoms incorporated into a mineral at the time of fluid-rock interaction yield an isotopic signature that is influenced by the fluid. Indeed, oxygen yields a major isotope:  $^{16}\text{O}$ , as well as a minor isotope present at the permil level:  $^{18}\text{O}$ .  $^{16}\text{O}/^{18}\text{O}$ , relative to a reference material (Vienna Standard Mean Oceanic Water -VSMOW) and expressed in permil ( $\delta^{18}\text{O}$ ), has been used extensively as a tracer for fluid-rock interaction, as different reservoirs (mantle, ocean, surficial water) yield contrasted  $\delta^{18}\text{O}$  values. In ophiolites for instance, fluid-rock interaction along the geotherm creates  $\delta^{18}\text{O}$  profiles that yield enrichment of  $^{18}\text{O}$  progressing into depletion at depth (e.g. Gregory and Taylor 1981). At low temperatures, silicates are enriched in  $\delta^{18}\text{O}$  compared to the fluid; at high temperature on the contrary, the fractionation is much smaller, and some minerals even take in less  $^{18}\text{O}$  than the fluid they are in equilibrium with. This allows distinguishing surface lithologies (detrital sediments, top of the

seafloor) that yield high  $\delta^{18}\text{O}$  from deep lithologies (mantle, mantle-derived crust) that yield mantle-like lower  $\delta^{18}\text{O}$ .

When studying metamorphic lithologies, it is often challenging to establish if the main episode of fluid-rock interaction occurred during the formation of the protolith and its alteration on the seafloor, or later during a metamorphic stage. In order to better resolve the conditions of fluid-rock interaction and unravel multi-stage processes, this study uses in-situ measurement methods for oxygen isotopes. The approach is to investigate samples that yield a snapshot of fluid-rock interaction: where the reaction was not complete and both the starting material and the end-result coexist, for example in the form of zoned minerals. Such textures have been documented by dissolution-precipitation, or the presence of reaction fronts in minerals (e.g. Putnis and John 2010). Measuring  $\delta^{18}\text{O}$  within the rock-forming minerals in their metamorphic texture allows deriving pressure-temperature-fluid (P-T-fluid) paths for metamorphic rocks. Oxygen isotope changes can be correlated to textures, in turn to petrological evolution and, when present, absolute time constraints from geochronology to pinpoint the time and relative place in the crust at which the fluid circulation occurred. Moreover, these measurements can be combined to trace element analysis that yields information on the composition of the fluid (e.g. Sr and Pb in apatite) or the growth evolution of the mineral phase (e.g. REE in zircon and garnet). These methods have been successfully applied to metamorphic rocks in recent years (Page et al. 2007; Martin et al. 2008; Andrews et al. 2010; Russell et al. 2013; Errico et al. 2013; Martin et al. 2014b; Page et al. 2014; Rubatto and Angiboust 2015).

Here, the minerals are prepared either in thin section or in grain mounts, and mineral zones are measured for oxygen isotopes using Secondary Ion Mass Spectrometers (SIMS), the Sensitive High Resolution Ion Micro Probe (SHRIMP) instruments at the Research School of Earth Sciences (RSES, Canberra). This method has been established for zircon and garnet at RSES (Ickert et al. 2008; Martin et al. 2014b) as well as in other SIMS labs (Valley 2003; Vielzeuf et al. 2005a; Page et al. 2010), and has been used for about 10 years. My PhD aims at extending the method to other minerals, and apply it to case studies to investigate fluid-rock interactions in a variety of crustal rocks, with an emphasis on subduction processes.

**The first chapter** explores the in situ analysis of oxygen isotopes in apatite, monazite and rutile using SHRIMP. Indeed, zircon, although a great chronometer, is not very reactive in low to moderate temperatures, as seen in high pressure low temperature (HP-LT) settings. Garnet is a great tool in investigating peak-pressure events in subducted rocks, but grows only during part of the prograde path of subducted rocks. Moreover, these two minerals do not incorporate many



---

fluid-mobile elements. New targets for in situ oxygen isotope analysis are explored. Apatite was chosen as a mineral growing in most subducted slab crustal lithologies at relatively early stages, and yields numerous fluid-mobile elements in its structure. Monazite is a geochronometer that is more reactive than zircon, and is present in the higher-temperature lithologies studied here. Rutile is frequent in HP rocks and is a geothermometer and potentially even a chronometer, measuring  $\delta^{18}\text{O}$  in rutile is thus a great potential tool in the building of P-T-time-fluid paths. The feasibility of measuring these three minerals is explored through datasets acquired for the Dora Maira and Tavşanlı case studies.

Fluid-rock interactions are explored in three case studies from weathering and sea-floor alteration at low temperature to metamorphism in the middle crust to sub-arc depths, from the point of view of the  $\delta^{18}\text{O}$  record in key minerals. The studies on Dora Maira whiteschists (**Chapter 2**) and the Tavşanlı blueschists (**Chapters 3 and 4**) aim at characterising the fluid exchanges in subduction rocks, at sub-arc depth and during their prograde evolution. The study of Isua and Tikeraq high-pressure metasediments (**Chapter 5**) explore surficial alteration and crustal melting processes in the Early Archaean.

**Chapter 2** presents the investigation of the Dora Maira ultra-high-pressure (UHP) whiteschists. Such unique rocks represent a well-known setting (a type locality for UHP metamorphism that have been extensively studied), contain four of the target minerals for oxygen and provide an excellent test case to the method. P-T path and timing of exhumation have been established for the UHP, and the petrology is well constrained. Moreover, these whiteschists are the result of metasomatism of a granitic protolith, but the tectonic setting of the metasomatism is debated. In this case study, the emphasis was put on garnet, zircon and monazite  $\delta^{18}\text{O}$ , and geochronology of these two accessory phases. Thermodynamic modelling, facilitated by the relatively simple chemistry of the whiteschists, is used to constrain the P-T of garnet-forming reactions and the dehydration reactions. This allows linking the growth of zircon, monazite and garnet (using REE indicators) to prograde P-T conditions. A P-T-time-fluid prograde path for the Dora-Maira whiteschists is obtained. The origin of metasomatic fluids is then investigated using the O isotope results. This study was published in *Contributions to Mineralogy and Petrology* (Gauthiez-Putallaz et al. 2016).

The main case study of this PhD work investigates fluid circulation during subduction at the unit scale (23 samples) in the Tavşanlı zone in Turkey. This work benefited from collaboration with Donna Whitney (University of Minnesota) and Laure Martin (University of Western Australia). The Tavşanlı zone was chosen because it is one of the best preserved terranes in lawsonite-

blueschist facies. The main focus is on the Halilbağı unit, which yields lawsonite eclogite, the highest grade recorded in the Tavşanlı zone. These rocks have seen minimal overprinting and deformation during exhumation, they represent a unique window into mid-depth subduction processes (ca. 23 kbar). In **Chapter 3**, the origin of the Halilbağı unit is explored using U-Pb in detrital and magmatic zircons, as well as WR geochemistry. Indeed, in contrast to the western part of the Tavşanlı zone, such information was missing for the Halilbağı unit itself. The Halilbağı unit is composed of metabasites of MORB and OIB origin, as well as metasediments such as metacherts, marbles, calcsilicates and mica-rich quartzites, providing great  $\delta^{18}\text{O}$  contrasts to be explored. In **Chapter 4**, 23 samples are investigated for fluid circulations using bulk-rock  $\delta^{18}\text{O}$  determination as well as in situ mineral data for garnet, zircon, apatite and lawsonite. In this chapter, the persistence of mantle-like  $\delta^{18}\text{O}$  signatures in metabasite is explored as they interact with the metasediments. Additionally, trace element indicators in both metasediments and metabasites are used to determine if the trace elements homogenised during metamorphism, and what elements are mobile.

The last case study in **Chapter 5** deals with metasediments from the Early-Archaean Isua supracrustal belt (West Greenland), a work in collaboration with Vickie Bennett (Australian National University) and Allen Nutman (University of Wollongong). The aim of this study is to identify and track surficial heavy  $\delta^{18}\text{O}$  signatures and their introduction in the deforming middle crust in the early stage of crustal formation. The Early Archaean metasediments from Isua are the earliest equivalent to detrital lithologies, although their chemistry is less evolved and more mafic than their modern equivalent. Zircon, garnet and bulk-rock were analysed to track their  $\delta^{18}\text{O}$  signature from the crystallisation of their magmatic source, to the creation of the sediment and its metamorphic evolution during Early Archaean crust stacking. Garnet major and trace element zoning is used to link the  $\delta^{18}\text{O}$  results to the successive tectonic episodes experienced by this unit of the Isua supracrustal belt. The results are investigated for their significance in the creation of high-  $\delta^{18}\text{O}$  zircons in the Early Archaean.

In summary, this thesis explores the use of in situ analysis of oxygen isotopes in metamorphic minerals to uncover fluid-circulation events in the context of P-T-time evolution in metamorphic rocks. The chapters are presented as stand-alone studies. The first case study looks at the prograde evolution of continental rocks brought to UHP, the second case study investigates the fluid and trace element exchanges in a heterogeneous low-temperature subducted unit, and the third aims at understanding  $\delta^{18}\text{O}$  signatures in proto-subduction processes in the Early Archaean crust.

# Chapter 1

## Preliminary study of *in situ* $\delta^{18}\text{O}$ analysis of rutile, apatite and monazite by SHRIMP ion microprobe

### 1 Introduction

Measuring oxygen isotopes *in situ* is a powerful tool to investigate fluid circulations and exchanges in metamorphic rocks. In order to get the most complete record of potential oxygen isotope changes in a rock, minerals that preserve compositional zoning and grow over different P-T stages have to be considered. In subduction rocks, a few recent papers have investigated oxygen isotope zoning in zircon and garnet, more rarely in other minerals. This chapter presents the application of ion microprobe oxygen isotopes measurements to other oxide and phosphate minerals: rutile, apatite, and monazite.

#### 1.1 Target minerals

Rutile ( $\text{TiO}_2$ ) is together with titanite the main Ti mineral present in subduction lithologies. Rutile is stable at higher pressures and lower Si and Ca contents than titanite (e.g. Tropper and Manning, 2008). It is widely used as a geothermometer in metamorphic rocks, by measuring the amount of Zr it incorporates (Zack et al. 2004; Tomkins et al. 2007). Rutile can also be used as an oxygen isotope thermometer coupled to quartz as these two minerals are respectively the most and least  $^{18}\text{O}$  enriched (e.g. Li et al., 2011). Rutile is a minor phase, which makes separating large enough quantities for laser fluorination difficult (or impossible when riddled with inclusions). Measuring  $\delta^{18}\text{O}$  *in situ* in rutile has great prospects for obtaining both a temperature and a tracer signature for oxygen isotopes in the same mineral, as well as for cross-checking geochemical thermometers.

Apatite ( $\text{Ca}_5(\text{PO}_4)_3(\text{OH},\text{F},\text{Cl})$ ) is the ubiquitous phosphate phase in low to medium temperature rocks. Apatite is a robust mineral throughout the metamorphic cycle and commonly preserves some prograde zoning and even potentially magmatic cores (e.g. Hammerli et al., 2014). It contains volatiles as structural components: Li and Hermann (2015) have shown that Cl and F proportion in apatite can be used to determine fluid salinity, although more fluid parameters can influence this concentration (Kusenbauch et al. 2015). As such, it is a valuable tracer for fluid influx across lithologies in the subducting slab. Apatite is also a major host for trace elements such as REE, Sr and Pb at low to medium temperatures (e.g. Spandler et al., 2003), which allows linking its crystallisation to the presence of other REE-bearing phases such as lawsonite and garnet, which are in turn P-T indicators. Oxygen isotopes are regularly measured in biogenic apatite such as teeth and conodonts (e.g. Trotter et al., 2008 as tracers for seawater evolution). At

present, no published study has investigated the same isotopic indicators in metamorphic apatite, although a study of standard materials has been recently published (Sun et al. 2016).

Monazite (LREE PO<sub>4</sub>) is a common accessory mineral in middle to high temperature metamorphic rocks. Because of its enrichment in Th and U and rather low initial Pb contents, it has been used as a U-Pb chronometer for magmatic and metamorphic rocks, only second to zircon. Its stability in HP rocks is limited to some compositions (e.g. Janots et al. 2006), whereas commonly is replaced by allanite in HT rocks. Monazite has been shown to be reactive to fluid flow in rocks as it readily recrystallizes or forms overgrowth (e.g. Ayers et al., 2006). Although its zoning is often more patchy than zircon, it can be imaged in BSE and monazite can provide a protracted record of event history in a metamorphic rock (e.g. Massonne et al., 2007). Monazite is also one of the main hosts of REE, U and Th in metamorphic rocks (e.g. Hermann and Rubatto, 2009). Its REE composition can be used to link its crystallization to garnet and zircon (Rubatto 2002; Hermann and Rubatto 2003). With the ability for providing both timing and link to P-T conditions, it is a prime target for recording fluid influxes using oxygen isotopes. A few studies have investigated measurement of oxygen isotopes in monazite by ion microprobe (Ayers et al., 2006; Breecker and Sharp, 2007, Didier et al., 2017) with variable success.

## 1.2 Challenges in the in situ analysis of oxygen isotopes

Establishing the measurement of a new mineral by SIMS includes finding suitable standards and defining potential matrix effects during ion microprobe analysis. The main hurdles can be summed up in 4 points:

- a) Standard  $\delta^{18}\text{O}$  heterogeneity, and robust bulk reference values (particularly for phosphates)
- b) Matrix effects induced by compositional differences
- c) Matrix effects induced by crystal orientation
- d) Preservation of primary oxygen signatures: influence of diffusion

Apatite and rutile are favourable minerals for point b) as their composition does not vary in major elements, and minor and trace element zoning spans a maximum of a couple of wt%. On the other hand, apatite is commonly zoned and inclusion-rich in low to mid temperature rocks. Zoning is a desirable feature for the in situ analysis of unknowns, but induces heterogeneity that is not favourable in standards, which makes point a) critical. Also, the presence of water in the crystal structure seems to pose analytical problems such as the roughness of the sputtering pit, as observed in apatite (L. Martin, pers. comm.), which could induce more variability and orientation effects.

This chapter summarises the results obtained for each mineral, to identify which of these issues are significant and which accuracy can be reported for the unknown analyses. The results will be assessed in geological context, to get indications on how the  $\delta^{18}\text{O}$  signatures are preserved in terms of diffusion.

### 1.3 Origin of samples

Samples are taken from the two case studies discussed in **Chapter 2** – Dora Maira whiteschists, and **Chapters 3&4** – Halilbağı blueschists respectively. More context and information about the samples can be found in the respective chapters. Here, a short summary of rock characteristics and mineral zoning and chemistry is provided (Table 1 - 1).

In the LT-HP Tavşanlı belt of central Turkey, the Halilbağı unit is made of interlayered metasediments (marbles: bulk  $\delta^{18}\text{O}$  19.9-26.5‰, quartzites: 18.5-22.5‰) and metabasites (11.0‰ to 17.0‰, see **Chapter 4**, Table 4 - 2). Fluid exchanges between these lithologies should thus induce variations in  $\delta^{18}\text{O}$ . The Tavşanlı zone is characterised by low temperatures (450-550°C) during both subduction and exhumation metamorphism. This cold evolution allows early assemblages to be preserved in the cores of zoned minerals such as garnet, lawsonite and apatite. Measurements of in situ oxygen isotopes by SHRIMP in an array of lithologies show  $\delta^{18}\text{O}$  variations of up to 6‰ between garnet core and rim, which indicates the influx of external fluids at high pressure.

The Dora Maira whiteschists are ultra-high pressure lithologies that derive from a Permian granite that underwent intense metasomatism. These rocks are particularly Ca-poor (0.5-2 wt%) and thus contain monazite as the UHP phosphate.

**Table 1 - 1. Sample description and minerals analysed, mineral abbreviations according to (Whitney and Evans 2010), WM: white mica.**

Sample	Rock type	Mineralogy	$\delta^{18}\text{O}$ analysis					
			ap	lws	rt	mon	grt	zrn
Halilbađı	- see <b>Chapter 3</b>		ap	lws	rt	mon	grt	zrn
SHS03	Impure quartzite layer	Qz, lws, WM, grt, ep, flo, aln, opq, tur	x	x			x	
SHB05	Eclogite pod	Omp, gln, grt, lws, amp, rt, ttn, ap	x	x			x	
SHB08	Blueschist layer	Gln, lws, omp, WM	x					
SHB12	Eclogite pod	Omp, WM, grt, chl, ep, rt, ttn, ap	x	x	x		x	
SHB53	Eclogite pod	Omp, gln, WM, lws, grt, ep, rt, ttn, aln	x				x	
SHS27	Calcsilicate layer	Cal, opq, chl, WM, ep, qz, lws	x					
SHB45	Eclogite layer	Omp, Gln, grt, WM, lws rel., rt, ttn	x		x		x	x
SHS44A	Lws-phen-grt layer	Qz, grt, WM, ep, all, lws rel., ap, zrn	x				x	x
SIB32A	Lws-chl pod	Lws, chl, opq, ttn, $\pm$ ep	x	x				
SIB50B	Gln micaschist layer	Gln, lws, omp, grt, WM, qz, opq, rt, ttn, ep-aln, chl, amp	x	x			x	
Dora Maira	- see <b>Chapter 2</b>		ap	lws	rt	mon	grt	zrn
DM1C	Quartz-rich whiteschist	Qz, ph, grt, rt, ap, flo, zrn			x	x	x	x
DM51	Whiteschist 2mm garnets	Grt, ph, ky, rt, zrn, mon				x	x	x
DM52	Whiteschist 2cm garnets	Grt, ph, ky, rt, zrn, mon			x	x	x	x
DM53	Whiteschist 10cm garnets	Grt, ph, ky, rt, zrn, mon				x		x

## 2 Methods

### 2.1 Sample preparation

For mineral separation, aliquots of the rock samples (50 to 500 g) were crushed using a guillotine, hydraulic press and a tungsten carbide mill in a succession of 10 second runs to a grain size smaller than 250  $\mu\text{m}$  (using single-use plastic mesh sieve). The powders were then deslimed (small grains of light minerals were washed away with tap water in a tall beaker).

Mineral separation was achieved by a combination of density (heavy liquids, panning) and magnetic (hand magnet, Carpco, Frantz) methods. The Dora Maira whiteschists, being virtually Fe-free UHP lithologies, contain a great proportion of heavier than 3.3g/cm<sup>3</sup> and non-magnetic

minerals. This hinders the conventional separation technique that is not able to separate zircon, monazite and rutile from kyanite or pure pyrope. Zircon, monazite and rutile separation was achieved by panning.

Apatite has a density of  $3.19 \text{ g/cm}^3$  and is thus in the heavy fraction of the  $2.9 \text{ g/cm}^3$  heavy liquid separation, but in the light fraction after separation at  $3.3 \text{ g/cm}^3$ . Inclusion-free apatite is non magnetic. Two approaches have been taken for separating apatite grains from the Tavşanlı zone rocks. In mafic rocks: the Frantz magnetic separator is used at a current of 0.5 A. This eliminates amphiboles, epidote, pyroxene and garnet. The sample is then run through the  $2.9 \text{ g/cm}^3$  heavy liquid. Finally, most lawsonite is eliminated by running the powder through the Frantz at 1A. If a lot of rutile is present in the sample,  $3.3 \text{ g/cm}^3$  density separation might be needed as a last step. In metasedimentary rocks, the sample is first run through the  $2.9 \text{ g/cm}^3$  liquid which floats quartz and micas. The heavies are then run through the Frantz at 0.5 A, then 1 A. If abundant rutile is present in the sample,  $3.3 \text{ g/cm}^3$  liquid is needed as a last step. Apatite and clear lawsonite can be separated by either very high current Frantz (1.5 A,  $10^\circ\text{C}$  inclination) or by an intermediate-density liquid ( $3.15 \text{ g/cm}^3$ ) obtained by mixing 2.96 and 3.3 liquids. Because magnetic separation discriminates inclusion-bearing apatite from clear apatite, the latter method was favoured not to bias the apatite population.

Single grains, thin section fragments and rock fragments were mounted along with standard grains on sticky tape and cast in epoxy. For composite mounts, a two-step method is favoured: single grains are mounted in a precursor epoxy mount, then polished and cut into blocks. Pieces of polished thin section and polished rock fragments are then embedded in a new epoxy mount that is not further polished. With that method, both single grains, pieces of rock and standards can be at the same topographic level and with a good polish level in the same mount. An impregnator should not be used on composite mounts because it forces epoxy to reach between the sticky tape and the polished surfaces. Pieces of rock should be impregnated before polishing and remounting, in order to eliminate potential gas-trapping cavities that would be detrimental to achieving good vacuum in the ion microprobe.

The measured grains were placed within 5 mm of the centre of SHRIMP mounts, thus minimising the influence of sample position on the measured  $\delta^{18}\text{O}$  (see Ickert et al. 2008).

## 2.2 Imaging

Back-scattered electron (BSE) as well as cathodoluminescence (CL) images were produced with a JEOL-JSM\_6610A SEM at the Research School of Earth Sciences – RSES – at ANU, using an

acceleration voltage of 15 kV and a working distance around 11 mm and 25 mm respectively. Different “spot sizes” corresponding to different internal apertures in the column were used in order to vary the amount of electrons sent to the sample, and thus the intensity of the secondary signal (seen as SE brightness for instance). The RSES JEOL SEM fitted with a Robinson detector for panchromatic CL. CL imaging of apatite grains was attempted for all the samples but most of the time could not be used: some apatite grains have a photo luminescent effect: a beam excited area emits light for a period of time after the beam is switched off or leaves the area, making sharp scanned images impossible. The best setting to mitigate this effect is fast, low-resolution scanning used for preview, averaging a high number of frames to increase the signal to noise ratio. The apatite present in the calcite-rich samples presented no photoluminescent effect and a very complex zoning (Figure 1 - 2).

EBSD rutile orientation determinations were performed after SHRIMP analysis at the Centre for Advanced Microscopy at ANU on a Zeiss UltraPlus SEM equipped with an Oxford Instruments EBSD detector, following an alumina powder and colloidal silica re-polishing step, as per the method described in Carr et al. (2017).

## 2.3 Major elements

EMPA analyses of monazites were performed at RSES using a Cameca SX100 with a current of 100 nA, acceleration voltage of 15 kV and a spot size of 1.5  $\mu\text{m}$ . For REE analyses,  $L\alpha$  or  $L\beta$  peaks and background were carefully selected to minimise interferences. Al and Si were measured for 10 s on the first spectrometer (Sp1, TAP), and Y was measured for 30s. On Sp2 (PET), Ca was measured for 10s, P (20 s) and Y (30 s). On Sp3 (LPET), La was measured for 10 s on  $L\alpha$ , as well as U (60 s) and Th (30 s). On Sp4 (LLIF), Ce was measured for 10 s on  $L\alpha$  and the heavier REE for 30 s: Nd, Sm, Pr and Gd on  $L\beta$ ; Dy, Er and Yb on  $L\alpha$ . Synthetic phosphates were used for the calibration of REE, synthetic oxides for Th and U, wollastonite for Ca, corundum for Al, apatite for P and quartz for Si. Trebilcock (J. Pyle) and 8153 (R. Stern) monazites were used as secondary standards and our data agreed within error with the published values.

F, Cl and minor elements were measured in apatite using a Cameca SX100 with a current of 10nA, acceleration voltage of 15 kV and a spot size of 20  $\mu\text{m}$  in order to minimize the loss of volatile elements, following the method by Li and Hermann (2015). P was standardized on apatite, Ca on wollastonite and F on phlogopite standards. Durango apatite was used as a secondary standard in two mounts: a grain cut perpendicularly to C-axis (H. Li) was measured throughout the session to monitor how we were measuring F and Cl. The results for the oriented Durango crystal axis were compared to randomly oriented Durango crystal fragments used as SHRIMP standard in the



unknown mounts. A correction factor of +10% was used, as proposed by Li and Hermann (2015) for F contents in randomly oriented samples. The accuracy of the results is discussed in the apatite section.

## 2.4 Trace elements

Trace elements were measured on an ArF excimer laser coupled to a quadrupole Inductively Coupled Plasma Mass Spectrometer (ICP-MS) Agilent 7700 at RSES, using the setup described in Eggins et al. (1998). The laser was tuned to a frequency of 5 Hz and energy of 50 mJ (corresponding to a HV of around 26-27 kV). Spot sizes of 22  $\mu\text{m}$  for monazite and apatite cores, 28  $\mu\text{m}$  for apatite rims and 62  $\mu\text{m}$  for rutile were used. Data were acquired over a 65 seconds analysis that included a 20 s background and the reference materials were measured after every eight unknowns.

Three international standards were measured in every run: NIST 610 and 612 glasses, as well as the rhyolite BCR. NIST 610 was preferred as primary external standard for trace element rich minerals such as monazite. NIST 612 was used in other cases to better match standard to unknown concentrations. BCR is a natural material that was used as a secondary standard to check for accuracy in the results. Recent data for the NIST glasses (Jochum et al. 2011; Spandler et al. 2011) differ from previous estimations (Pearce et al. 1997) by as much as 5 to 10% for certain elements (Cl, Nb, P, Sc, Sn, Ta) in NIST 610 and NIST 612 (As, F, P, Ti). Values of Spandler et al. (2011) have been used for data reduction.

For most minerals, a major element such as Si is used as an internal standard. A stoichiometric value is used. However, for monazite this method is very inaccurate since P is poorly measured by ICP-MS: Th is used (determined by EMPA) since La and Ce were particularly variable in the studied samples.

## 2.5 SHRIMP oxygen isotopes

The setup used for rutile is similar to what is described for zircon in Ickert et al. (2008). The main difference is that for rutile, being a semi-conductor, we used a smaller primary beam to obtain a secondary intensity comparable to the signal obtained for zircon and garnet ( $8 \times 10^7$  counts on  $^{18}\text{O}$  for a primary voltage of 7 V on garnet in the same session on the same mount). This was done by decreasing the voltage of the Kohler lens in the primary column from 15000 to 14000 V. This resulted in  $8.9 \times 10^7$  counts on  $^{18}\text{O}$  on the rutile standard WOD for a primary voltage of 7.54V. Rutiles were measured with SHRIMP SI, using 4 scans of 20 s, a raster was done before analysis

to clean the surface of the grains. The standard WOD (for Wodgina rutile) was measured 4 times every 10 unknowns. Dora Maira whiteschists rutiles (DM52, DM1C) were measured during this session as a potential secondary standard. Sharp et al. (1993) reported 3 laser fluorination analyses of Dora Maira rutile of a similar sample giving an average of  $3.47 \pm 0.14$  %.

Apatite grains were analysed on SHRIMP II and SHRIMP SI during several sessions following the method of Trotter et al. (2008) for biogenic apatite. The 13/03/2013 and 17/03/2013, two sets of 6 scans of 8s were measured (the standard UWG2 measured every 5 unknowns), no raster was used prior to analysis. On the 04/04/2013 on SHRIMP SI, 4 scans of 20 s were measured, a raster was used prior to analysis. The standard DUR (for Durango apatite chip #3, absolute value by Rigo and Joachimski, 2010: 9.82 %; NB: the standard material used comes from one particular chip, and is thus not likely subject as the heterogeneity shown by Sun et al. 2016 for different grains of Durango apatite) was measured 4 times every 10 unknowns. Monazites were analysed using SHRIMP II at RSES, the method was described in Rubatto et al. (2014).

### **3 Apatite**

#### **3.1 Sample composition and zoning**

Apatite grains were separated from 16 samples covering all lithological types in the Halilbağı area. In thin section, apatite crystals are present in the matrix as clear round grains. The sample SHS44A is particularly apatite-rich (modal abundance 5%), whereas apatite is an accessory phase in all other lithologies except from the pure marble SHM04. Regardless of lithology, most apatite grains show inclusion-rich cores and clear rims, forming an overall rounded shape. A few grains were homogeneously clear; other grains were very porous and milky. The grain size of recovered apatite grains spans from 20  $\mu\text{m}$  to over 250  $\mu\text{m}$  in most samples. When possible to image, the CL zoning showed bright cores and darker rims on some samples (Figure 1 - 2). The marble samples SGM21 and SHM23B had particularly complex CL zoning. Optical CL (not shown here) showed mostly yellow luminescence, attributed to Mn (Barbarand and Pagel 2001). The resolution of the RSES optical CL setup did not provide more information than the SEM-based imaging. In several samples such as SHB05, apatite grains yield BSE-bright cores that contain LREE (from EDS analysis). In most samples, apatite grains were not zoned in either BSE or CL.

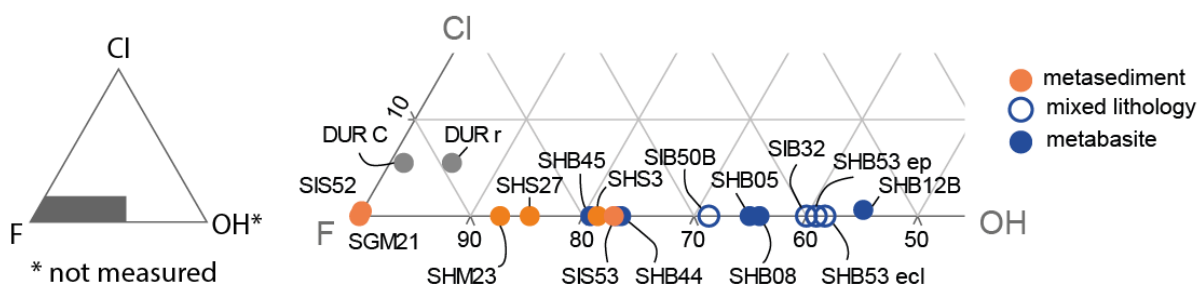


**Figure 1 - 1** Triangular diagram showing occupancy on the apatite A site for Durango and Halilbağı samples. F and Cl are measured by EPMA. The remaining of the A site is filled with OH.

The measured apatites lie on a range between pure fluorapatites and 50% hydroxyapatites (Figure 1 - 1, Table 1 - 2, *Appendix Table A1 - 1*). Durango-C (EMPA standard aligned on C axis) and Durango-R (randomly oriented Durango, SHRIMP standard material) return Cl values of 0.38 wt%, which is within the range reported for Durango apatites (0.36 - 0.46 wt%, Sun et al., 2016). In all measured apatite samples from Halilbağı but a few analyses in SHB12B and one analysis in SIS52 at ca. 400 ppm, Cl content is below EMPA detection limit of 346 ppm. The F amount is variable from one sample to another, and in the highest concentrations in SIS52 and SGM21 represents 101% of A axis capacity which shows that the method used, developed by Li and Hermann (2015), provides a good correction to the problem of high F counts reported by numerous previous studies (Spear and Pyle, 2002; Sun et al., 2016). C-prism oriented Durango yields a value of  $3.51 \pm 0.06$  wt% (1 s.d., n= 12) and random Durango a corrected  $3.35 \pm 0.14$  wt% (1 s.d., n= 10) which is within the range of values obtained by other authors on Durango crystals (3.40 to 3.70 wt%, Sun et al., 2016). Intra-sample zoning was not detected past the high uncertainty for F and the low contents in Cl. Indeed, the samples show F compositional variability similar to the reproducibility on the randomly oriented Durango ( $\pm 0.14$  wt%, 1 s.d. n= 10), and thus they are considered homogenous for F within our analytical capabilities. Samples SIS52 and SHB05 show significantly larger variability with 0.26 and 0.34 s.d., which could be the sign of intra sample heterogeneities. In absence of other measurements, it is assumed that the A site is filled by OH<sup>-</sup> (Figure 1 - 1).

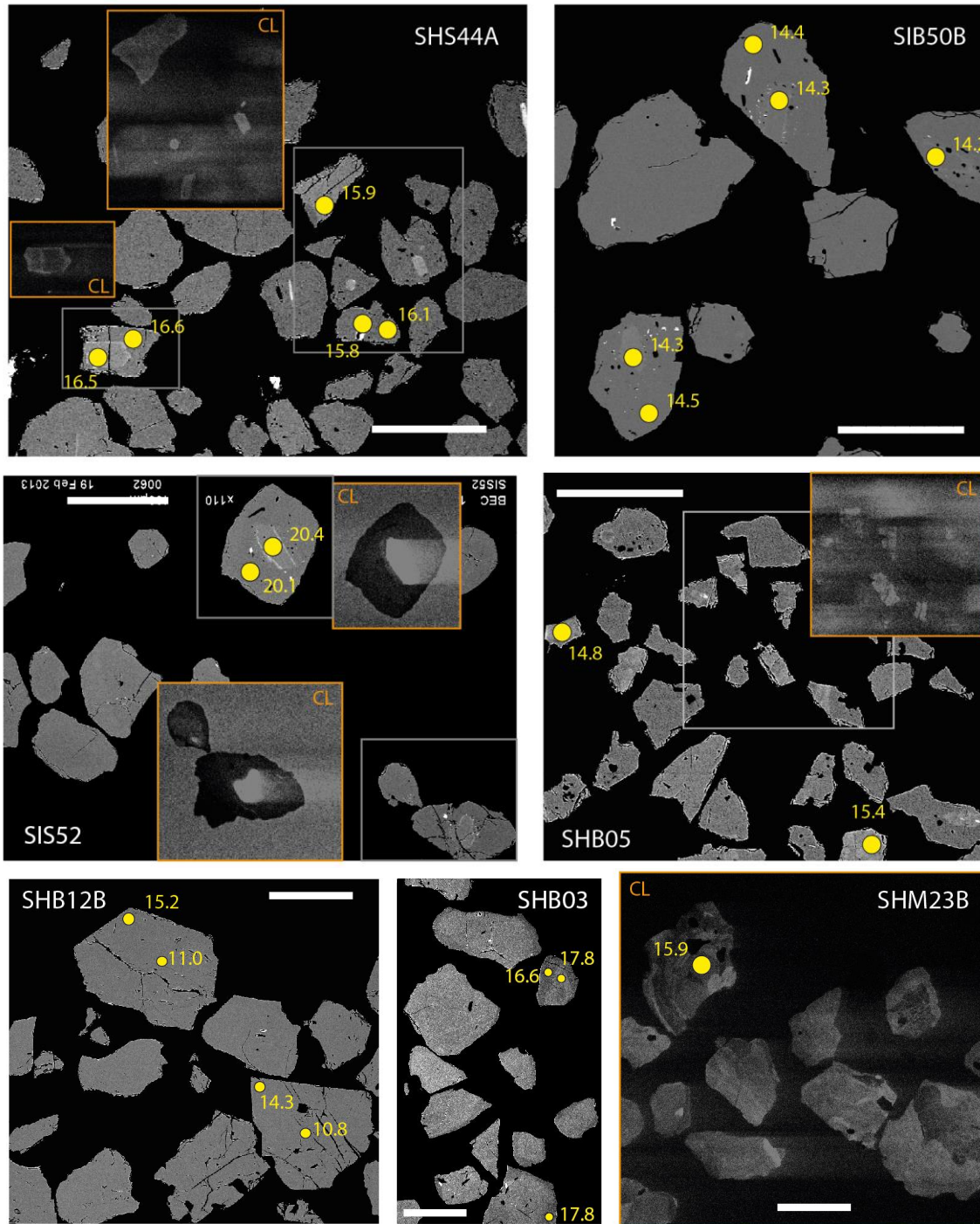


Figure 1 - 2. High-contrast BSE images of Halilbaği apatite grains. CL images as insets show persistent luminescence in the cores. Scale bars are 200  $\mu\text{m}$ . Yellow circles indicate SHRIMP spots with measured  $\delta^{18}\text{O}$  in ‰, the spots are 25  $\mu\text{m}$  in size.

The most common minor elements (LA-ICPMS data presented in **Chapter 4, Appendix Table A4 - I**) in Tavşanlı apatite are Si (570-1460 ppm), Sr (64-4801 ppm), Fe (196-584 ppm), Mn (9-1550 ppm), Mg (271-506 ppm), Zn (267-498) and Y (7-1887 ppm) on average across the 17 samples.

**Table 1 - 2. EMPA analyses of apatite. Sample averages of values above detection limit. Individual measurements are provided in *Appendix table A1 - 1*. LAICPMS minor and trace element analyses are provided in *Appendix table A4 - 1*.**

Sample	DUR-C	DUR-R	SGM21	SHB05	SHB08	SHB12B	SHB44A	SHB44B	SHB45
F	3.5	3.4	3.8	2.5	2.4	2.1	2.9	2.9	3.0
Cl	0.38	0.38	<0.03	<0.03	<0.03	0.04	<0.03	<0.03	<0.03
CaO	53.1	51.5	53.9	53.1	53.6	52.8	53.1	53.5	53.4
P <sub>2</sub> O <sub>5</sub>	40.6	38.8	41.8	41.0	41.3	40.6	40.9	41.5	41.1
FeO	<0.09	<0.09	<0.09	0.26	<0.09	<0.09	0.09	<0.09	<0.09
SrO	0.12	<0.10	<0.10	<0.10	<0.10	0.13	0.15	0.14	0.34
MnO	<0.07	<0.07	<0.07	0.09	0.11	0.08	0.09	<0.07	<0.07
Ce <sub>2</sub> O <sub>3</sub>	0.54	0.57	<0.08	0.32	<0.08	<0.08	<0.08	<0.08	0.13
Total	98.2	94.6	99.6	96.6	97.4	95.5	97.0	98.1	97.8
n	14	10	7	11	5	20	7	4	8

**Table 1 – 2 continued.**

Sample	SHB53 ecl	SHB53 ep	SHM23	SHS27	SHS3	SIB32	SIB50B	SIS52	SIS53
F	2.2	2.2	3.3	3.2	3.0	2.3	2.6	3.8	2.9
Cl	<0.03	<0.03	<0.03	<0.03	<0.03	<0.03	<0.03	0.04	<0.03
CaO	53.3	53.4	53.2	52.8	52.7	53.9	52.9	53.8	53.3
P <sub>2</sub> O <sub>5</sub>	40.8	41.2	40.5	40.2	40.4	42.1	40.7	42.3	41.1
FeO	<0.09	<0.09	<0.09	<0.09	<0.09	<0.09	0.16	0.28	0.15
SrO	0.14	0.18	0.16	<0.10	0.14	<0.10	0.20	0.14	0.13
MnO	<0.07	<0.07	<0.07	0.08	0.16	0.08	0.16	0.06	0.11
Ce <sub>2</sub> O <sub>3</sub>	<0.08	<0.08	<0.08	<0.08	<0.08	<0.08	0.16	0.45	0.14
Total	96.3	96.9	97.1	96.2	96.3	98.2	96.4	100.2	97.6
n	4	6	8	8	10	5	7	10	6

## 3.2 Results

Apatite oxygen isotopes were measured on SHRIMP II and SHRIMP SI on 3 grain mounts (*Appendix Table A1 – 2*). The quality of the data varied across sessions, producing a repeatability between 0.4 ‰ (1 $\sigma$ ) and 0.14 ‰ (1 $\sigma$ ) on the Durango apatite standard (Figure 1 - 3, Table 1 - 3). Apatite samples analysed have a relatively constant chemical composition (apart from A site variations, the content in minor elements is <1 wt%): in a first approximation, no matrix correction was applied.

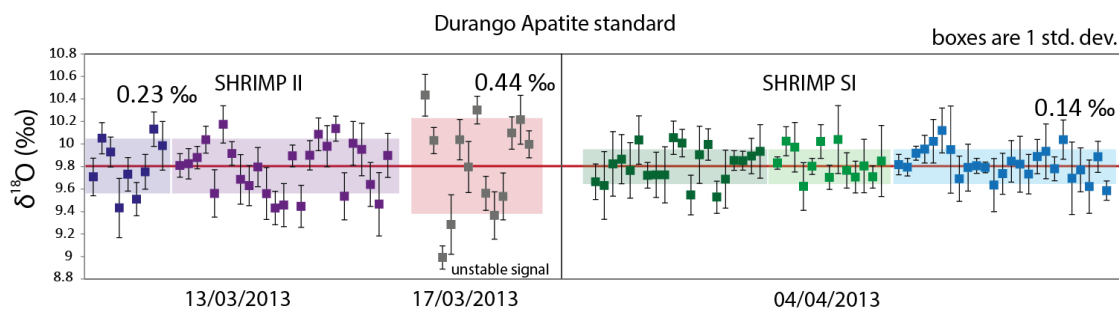


**Figure 1 - 3. Stability of  $\delta^{18}\text{O}$  in ‰ for individual measurement of the Durango apatite standard over 3 analytical sessions with 1 SE error bars, each session standardised to an average of 9.82 ‰. Colour rectangles represent sub-sessions on single mounts, their height is 1 standard deviation**

The average  $\delta^{18}\text{O}$  values range from 26.3 ‰ for the impure marble SGM21 apatite to 13.5‰ for apatite in eclogite SHB12B (Table 1 - 3, Figure 1 - 4).

**Table 1 - 3 Summary of  $\delta^{18}\text{O}$  results on Halilbağı apatite samples**

Sample	Average $\delta^{18}\text{O}$ (‰)	std dev (‰)	session	SHRIMP
SHM23B	15.88	0.24	04.04.13	SI
SHS27	20.63	0.94	04.04.13	SI
SHS3	18.42	1.10	04.04.13	SI
SHB08	15.65	0.20	04.04.13	SI
SHB05	15.27	0.25	13.03.13	II
SHB45	15.96	0.31	13.03.13	II
SHB53ec	13.23	0.59	04.04.13	SI
SHB53ep	13.56	0.34	04.04.13	SI
SHB12B	13.05	2.12	13.03.13	II
SHS44B	16.57	0.24	13.03.13	II
SHS44A	16.21	0.46	13.03.13	II
SIB32	14.11	0.14	04.04.13	SI
SIB50B	14.20	0.37	13.03.13	II
SIS52	20.21	0.52	17.03.13	II
SIS53	16.31	0.43	17.03.13	II
SGM21	26.27	0.57	13.03.13	II
Durango	9.79	0.23	13.03.13	II
Durango	9.82	0.44	17.03.13	II
Durango	9.82	0.14	04.04.13	SI

In sessions where the variability in the samples exceeds the repeatability of the standard analyses, it is attributed to sample heterogeneity. Samples SHS27, SHS3 and SHB12B show a significant variability, bigger than 3 times the standard repeatability. In SHS3 and SHB12B, differences in  $\delta^{18}\text{O}$  were observed in single grains. SHB12B apatite yields a bimodal distribution (Figure 1 - 4) whereas SHS3 apatite has an even large range of values between 16.5 ‰ and 20.0 ‰. Other samples (SGM21, SHS44A, SHB45) yield a small spread of values but asymmetrical peaks with a tail towards lower values.

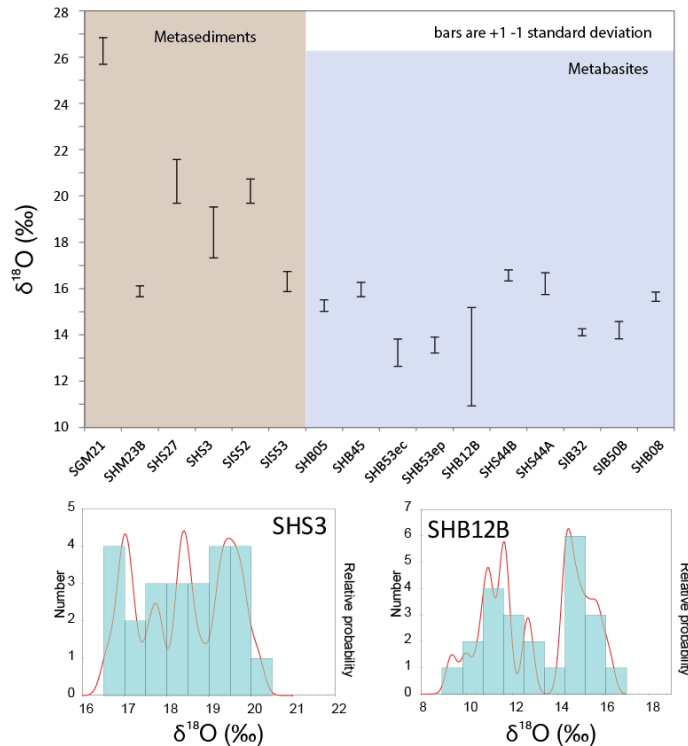


**Figure 1 - 4 Summary of apatite  $\delta^{18}\text{O}$  data, showing sample averages with 1 standard deviation error bars in top panel, and probability density plots (Isoplot, Ludwig 2012) of individual analyses from the two samples showing the highest variability: quartzite SHS03 and eclogite SHB12B.**

### 3.3 Discussion

For minerals, two main issues may be relevant for accuracy of oxygen isotopes by SIMS measurements: 1) orientation effects and 2) matrix effects due to compositional variations. The reproducibility obtained during this study 0.15 - 0.20 ‰ ( $1\sigma$ , excluding the anomalous session of the 17/03/13) is similar to the SHRIMP bioapatite work done previously (e.g. Trotter et al., 2008), and on par with the precision of zircon analysis (Ickert et al. 2008). During this study, apatite grains were rounded and thus it is probable that the grains spread on the mounting tape with a random orientation. The reproducibility obtained on both the randomly oriented Durango fragments and homogenous samples is within the range of what is obtained for isotropic minerals such as garnet. This limited dataset indicates that any orientation effect in SHRIMP measurement of oxygen isotopes in apatite is smaller than the internal repeatability of 0.2‰.

In terms of composition, the main chemical variation in apatite is the A site anions. Most biogenic apatites are hydroxyapatites, with some carbonate. Conodonts analysed with Durango standard return 0.5 ‰ lower values than conventional analyses of the same sedimentary beds (Trotter et al. 2008), which might be an indication of the magnitude of the matrix effect related to 100% OH in A site compared to the composition of Durango (predominantly F with some Cl in the A site, Table 1 - 2). Carbonate content might have an influence, as mentioned by Trotter et al. (2008)

and Sun et al. (2016), and could also be the source of the 0.5 ‰ quoted in Trotter et al. (2008) but should not be a problem for inorganic apatite since it usually does not contain any C (e.g. Spear and Pyle, 2002). Cl content is ca. 0.4 wt% in Durango, and much smaller in the other analysed samples. As this is a very minor component, it is expected that no significant matrix effect is related to Cl within the investigated samples. Matrix effects related to Cl, however, need to be further investigated if applying this method to more Cl-rich apatite. Minor elements, always under 1.5 wt%, should not be causing major matrix effects in SHRIMP measurement of oxygen isotopes in apatite.

Sun et al. (2016) report a co-variation of  $\delta^{18}\text{O}$  and Ca content across one Durango crystal. It is not clear if this relationship can be explained with a matrix effect. Variation of Ca content in the apatite reported here is small (EMPA values between 52 and 53 wt% Ca for all samples), and it likely not the source of major matrix effects.

### 3.3.1 Oxygen diffusion

Experimental studies on oxygen diffusion in apatite are scarce. Farver and Giletti (1989) predicted oxygen to diffuse faster than REE (Nd, Sm). They studied oxygen self-diffusion at hydrothermal conditions from 550 to 1200°C and oxygen isotopes were measured by depth profiling using a Cameca ion microprobe. Diffusion of oxygen along the c axis of apatite was found to be 3 orders of magnitude faster than perpendicular to the c axis.

No published study has investigated oxygen diffusion in apatite in a geological setting. In a study on the resetting of various isotopic systems in a prograde metamorphic sequence (Hammerli et al. 2014), oxygen data were acquired (Hammerli, pers comm.). The results showed that for rocks experiencing a maximum of 350°C, the detrital  $\delta^{18}\text{O}$  signature in apatite was preserved, whereas at ~420°C, apatite that retained its detrital Sm-Nd isotopic signature had a homogenised oxygen isotope composition. The conservation of Sm-Nd isotopic signature shows that this homogenisation was likely not due to recrystallization, but to solid-state diffusion of oxygen.

Closure temperature modelling following the diffusion coefficient from Farver and Giletti (1989) for the C-axis (activation energy = 205 kJmol<sup>-1</sup>, pre-exponential factor = 9x10<sup>-9</sup> m<sup>2</sup>s<sup>-1</sup>) using the formulations of Ganguly and Tirone (1999; 2001) was done in collaboration with Michael Jollands. The model produced for spherical grains of 40 µm diameter (Figure 1 - 5) yields bulk closure temperatures between 340 and 440°C for most geologically relevant cooling rates, which is consistent with the data provided by J. Hammerli (pers. comm.).



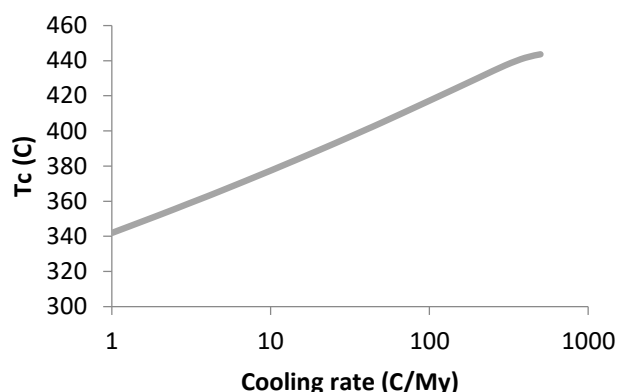


**Figure 1 - 5 Model of Temperature of Closure of apatites for self-diffusion of oxygen, for a grain diameter of 40  $\mu\text{m}$  according to geologically relevant cooling rates, calculated using data by Farver and Gilletti (1989).**

Given that closure temperature is an estimate of the bulk closure of a crystal, and we measured  $\delta^{18}\text{O}$  in situ observing microscale contrasts within a grain, a 1D finite difference approximation to Fick's second law was also modelled, following, e.g. Crank (1975) and Costa et al. (2008). Initial conditions were assumed to be a step function, the boundary kept constant throughout the model duration (assuming an infinite external reservoir), and with constant diffusion coefficients (isothermal model). This model is created with the assumption that the homogenisation of  $\delta^{18}\text{O}$  signatures is akin to the diffusion of a trace element into the crystal: the change in lattice created by the introduction of the new atomic species is negligible (here change in permil concentration of a nearly identical atom) and does not cause the diffusivity to change with concentration.

The time taken to homogenise a 1D transect along the c axis of a 40  $\mu\text{m}$  grain, is <1Myr at 500°C (Figure 1 - 6, Table 1 - 4) in both the case where it is standing in a matrix, and if it is surrounded by an overgrowth. In contrast, at 400°C (Table 1 - 4), a >10% zoning can persist for >10 Myr.

**Table 1 - 4 Time of  $\delta^{18}\text{O}$  homogenisation for a small apatite crystal . Homogenisation is defined as the time when the central cell reaches 90% of the boundary value.**

T (°C)	core (40 $\mu\text{m}$ )	core + overgrowth (40 $\mu\text{m}$ +40 $\mu\text{m}$ )
550	15 kyr	104 kyr
500	105 kyr	724 kyr
450	949 kyr	6 559 kyr
400	11 943 kyr	82 872 kyr
350	227 000 kyr	1 570 570 kyr

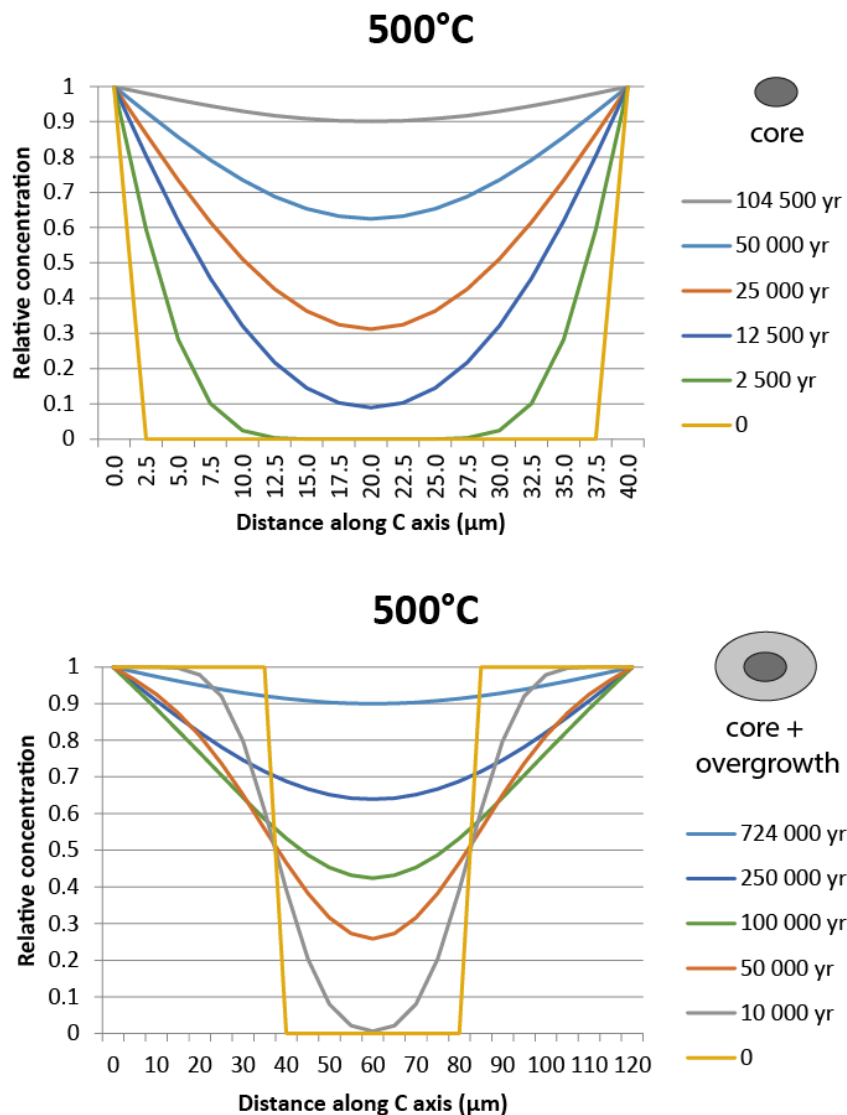


**Figure 1 - 6. Relative concentration profiles along the C axis of modelled apatites, showing the evolution of relative concentration contrasts in the crystal at 500°C. The final time step represent the time required for a 10‰ contrast to be preserved. This corresponds to the minimal difference analysable by SHRIMP (ca. 1 ‰), in the case of the maximal initial  $\delta^{18}\text{O}$  contrast expected in the Halilbağı unit: ca. 10 ‰, it thus represents a maximum homogenisation time.**

Based on these two diffusion models and the preliminary data of Hammerli (pers. comm.), it is expected that small prograde or magmatic apatite cores in the Halilbağı samples (20  $\mu\text{m}$  size) were reset during the time apatite resided at 500°C and above (up to 580°C, see details in **Chapters 3&4**) during prograde evolution to exhumation of the Halilbağı unit. This result is quite robust since this evolution happens on a heating trajectory so that the maximum temperature controls the diffusion evolution, without much influence of the heating rate.

In contrast to the homogenised small cores, a ca. 5 ‰ core-rim zoning in oxygen isotopic composition is observed in apatite grains from sample SHB12B, which have a diameter of 200-250  $\mu\text{m}$ . In this sample, the minimum  $\delta^{18}\text{O}$  contrast as sampled by garnet is 6 ‰ (see **Chapter 4**),

which indicates that single apatite crystals preserve at least 80% of the  $\delta^{18}\text{O}$  heterogeneity. The working hypothesis for the creation of such contrasts (see **Chapter 4**) is a metasomatic event occurring at the start of exhumation, altering the initial WR of ca +8 ‰. This fluid event created recrystallization rims in all major rock-forming minerals (garnet, omphacite and phengite) that yield a reactive WR  $\delta^{18}\text{O}$  of ca. 14 ‰, and then the sample reequilibrated during cooling. This scenario is different from cooling-only, where  $\delta^{18}\text{O}$  contrast is only created by changes in fractionation behaviour according to T decrease (e.g. Eiler et al., 1992).  $\delta^{18}\text{O}$ -zoned apatites might be created by crystallisation of a high  $\delta^{18}\text{O}$  rim around low  $\delta^{18}\text{O}$  cores similarly to garnet, or by diffusion of surrounding  $^{18}\text{O}$  into unzoned low  $\delta^{18}\text{O}$  apatites.

In order to explore conditions that would allow the preservation of 80% of the initial  $\delta^{18}\text{O}$  contrast in single apatite crystals, oxygen diffusion was also modelled in a cooling system, starting at the T of metasomatism (450-500°C, see **Chapter 4** for more details) and cooling assuming the relationship between 1/T as time is linear (Figure 1 - 7c, as commonly done in conductively cooling systems, e.g. Ito and Ganguly, 2006). This assumption is likely only crudely modelling the cooling rate, as the dynamics of the top of the subduction plate would allow more complicated temperature trajectories by juxtaposition of cooler or warmer units (e.g. Whitney et al., 2014). One-dimensional profiles along the C axis were again modelled using the finite difference approximation for an initially homogenous grain of 240  $\mu\text{m}$  across with constant boundary conditions, with T and thus diffusion coefficients changing at each time step. A typical diffusion profile is shown in Figure 1 - 7b, and the core concentration x is tracked through time following different cooling rates in Figure 1 - 7a, showing much more homogenisation at lower cooling rates (cooling parameter:  $\log \eta = -17.8$ ), and virtually no homogenisation at high cooling rates ( $\log \eta = -16.5$ ). Tables showing how residence times above a certain temperature and maximum x change according to cooling rate ( $T_{\text{max}}$  is constant, x max changes) and  $T_{\text{max}}$  (x max is kept constant and the cooling rate changes) are also presented in Figure 1 - 7.

In order to retain isotopic heterogeneities of the order of 80% of the initial step, the apatites need to have cooled to 400°C within ca 3.3 My for a starting temperature of 500°C ( $\log \eta = -17.3$ ). The time increases for lower  $T_{\text{max}}$ : if metasomatism happened at 475°C, a contrast of 80% can be retained for 7.4 My on a conductive cooling trajectory ( $\log \eta = -17.7$ ).

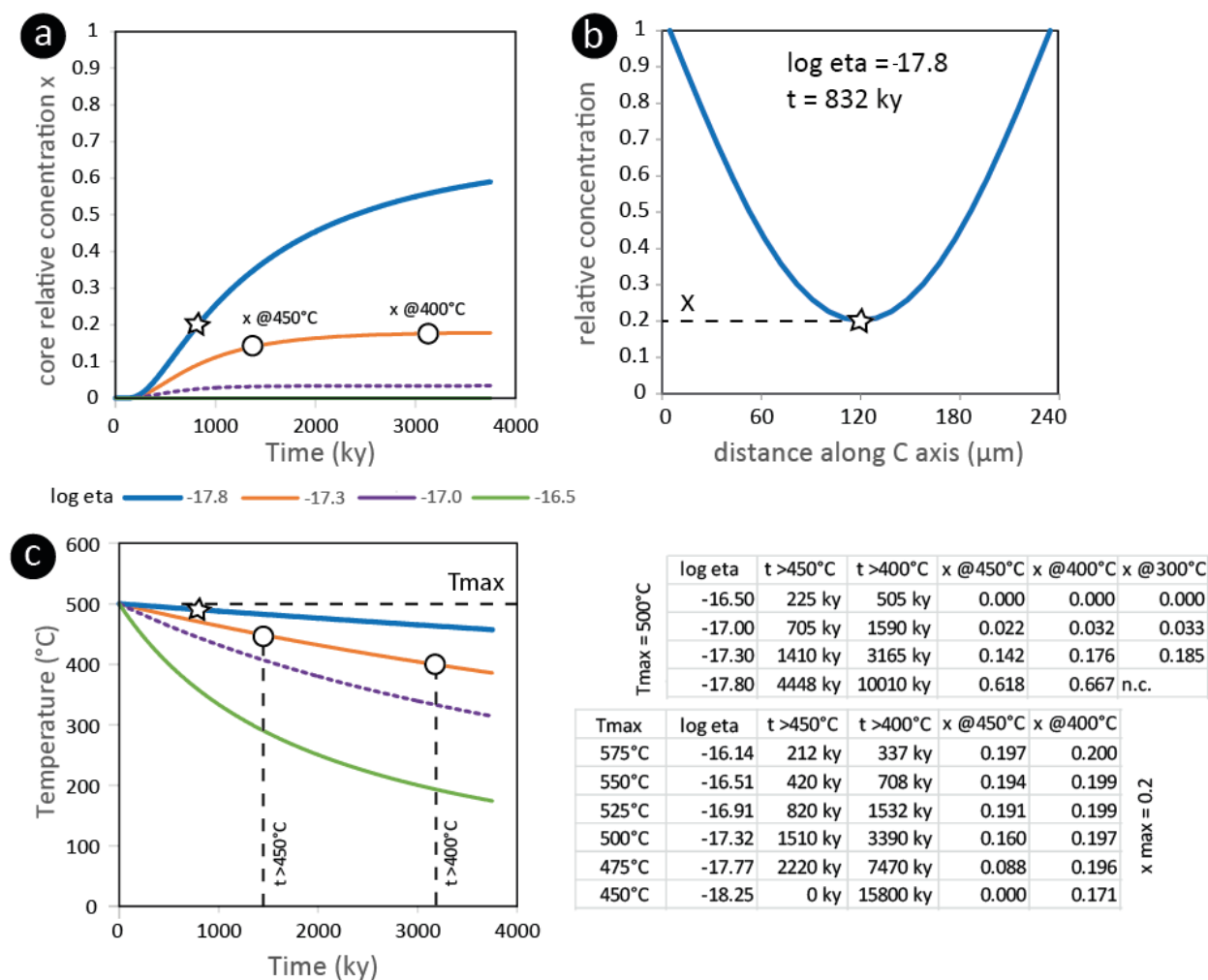


**Figure 1 - 7. a.** Evolution of the apatite core concentration ( $x$ ) according to time. **b.** Example of a relative concentration profile along the C axis corresponding to the conditions symbolised by the star ( $\log \eta = -17.8$ ,  $t = 832$  kyr). **c.** Evolution of temperature according to time for different  $\log \eta$  values. The tables correspond to the set of time and concentration values corresponding to different models (one line per model), first for a constant  $T_{\text{max}}$  and different cooling rates, then for varying  $T_{\text{max}}$ , with  $x_{\text{max}}$  set to 0.2.

However, at temperatures above  $500^{\circ}\text{C}$ , this time is greatly reduced, e.g. 708 ky for a  $T_{\text{max}}$  of  $550^{\circ}\text{C}$  ( $\log \eta = -16.15$ ). This is also the case if the apatite stays at  $500^{\circ}\text{C}$  on a slow cooling trajectory (e.g.  $\log \eta = -17.8$ ), in which case 80% contrast is lost within 832 ky and with further cooling results in an end contrast of 40% only. It is thus likely that the WR change in  $\delta^{18}\text{O}$  occurred shortly before the apatites were cooled and exhumed quickly, or during a slower exhumation but at temperatures lower than  $500^{\circ}\text{C}$  (more details given in **Chapter 4**). The cooling rate modelled here for a starting temperature of  $500^{\circ}\text{C}$  is compatible with a plate-motion speed of exhumation or faster, as proposed by previous authors for the Halilbağı unit (Whitney and Davis 2006; Whitney et al. 2014; Fornash et al. 2016).

It is to note that the hypothesis of an infinite exchanging reservoir providing constant boundary conditions could not apply to these minerals, similarly to a cooling only scenario explored by Eiler et al., (1992). Indeed, at ca. 450°C or even 500°C, most rock-forming minerals are closed for diffusion (e.g. garnet, omphacite), which would restrict the exchanging reservoir for the equilibrating apatites, if a fluid phase is absent. Moreover, the studied apatites are small (200-250  $\mu\text{m}$ ) compared to rock-forming minerals and thus might have been included in closed phases. This could explain some of the grain-to-grain variability observed in SHB12B: small grains can preserve core-like signatures (inclusion in the core of closed phases), and large grains can preserve rim-like signatures (new growth only). This shows that the interpretation of  $\delta^{18}\text{O}$  signatures on the exhumation path is much less robust than on the prograde path, especially when T is nearing the closure temperature of the investigated minerals. As such, the population of measured apatites may or may not record metasomatic oxygen contrasts, according to their textural position. Nevertheless, the models yield more robust information about the homogenisation within single apatite crystals, which indicates that the temperature of metasomatism is likely lower than 500°C, and/or the exhumation relatively quick (less than 1.5 Ma spent >450°C) in order to preserve the observed contrasts.

The oxygen isotopic composition of apatite and garnet was measured together in 8 samples: SHS3, SIB50B, SHB53, SHB45, SHS44A, SHB12B and SHB05. In samples that yield homogenous garnet and apatite  $\delta^{18}\text{O}$  (SHS44A, SHS44B, SHB05),  $\Delta^{18}\text{O}_{\text{garnet-apatite}}$  is around 2 ‰, a bit higher for SIB50B (3 ‰), where garnets are tiny, Mn-rich and likely crystallised earlier on the prograde path at lower temperature. According to the increment method calculations of Zheng (1991, 1993), this would correspond to apparent equilibrium temperatures of 500 and 300°C respectively (Figure 1 - 8). SHS44A and SHS44B record temperatures  $\geq 500^\circ\text{C}$ , which indicates that diffusion played a limited role on the retrograde path for these samples, as significant re-equilibration would lead to a higher  $\delta^{18}\text{O}$  in apatite, a higher  $\Delta^{18}\text{O}_{\text{garnet-apatite}}$  and thus lower apparent equilibration temperatures.

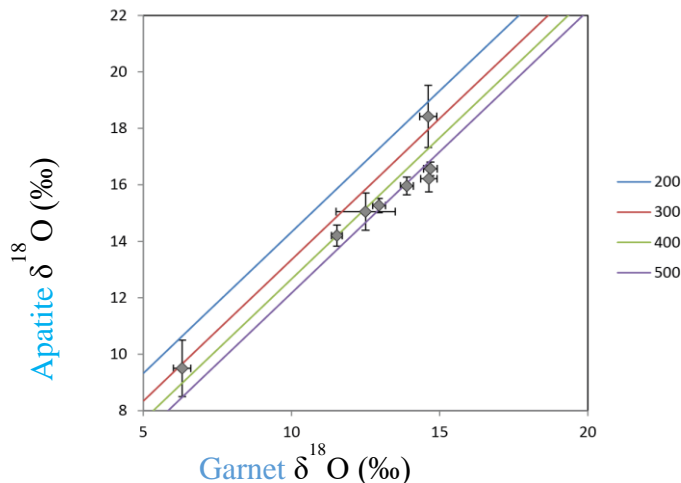


**Figure 1 - 8. Relation between apatite and garnet  $\delta^{18}\text{O}$  measured in the same sample, where apatite shows REE depletion indicating garnet presence. Lines indicate fractionation behaviour at varying temperatures as modelled by (Zheng 1993a; Zheng 1996).**

The results of diffusion modelling and comparison with garnet thus indicate that prograde  $\delta^{18}\text{O}$  zoning of apatites is lost during a short residence at peak temperature (550-580°C), but that  $\delta^{18}\text{O}$  zoning created on the retrograde path from ca. 500°C can be preserved in the Halilbağı apatites.

## 4 Monazite

Oxygen isotopes in monazite were explored for the study of the timing of fluid circulation in the Dora Maira whiteschists. The results of this work were published in *Chemical Geology* (Rubatto et al. 2014, *Appendix A1*) as part of the development of matrix effect calibration, the context of the case study is found in **Chapter 2** (Gauthiez-Putallaz et al. 2016, *Appendix A2*). Here, the main results are summarized and discussed in light of a recent study proposing a new correction scheme for oxygen isotope analysis in monazite (Didier et al. 2017).

### 4.1 Sample and standards

Monazites were separated from four samples of the Dora Maira whiteschists (see **Chapter 2** for geological background and sample description), using panning as a refined density separation method. Whiteschists DM51 to DM53 yield abundant honey-coloured monazites of 50 to 250  $\mu\text{m}$  in size. DM51-53 monazites are zoned in a combination of overgrowths and patches with rare systematic core-rim zoning (Figure 1 - 9). In these monazites, Th is incorporated both in the huttonite substitution ( $\text{ThSiO}_4$ ) and the cheralite substitution ( $\text{CaTh}(\text{PO}_4)_2$ ) (Figure 1 - 11). Their overall Th content is high, up to 10 wt% (*Appendix table A2 – ESM3*).

Sample DM1C yields rare, light green monazites of 50 to 200  $\mu\text{m}$  in size. DM1C monazites yield a Y and HREE richer core that is surrounded by several rims of high Th and lesser HREE enrichment (Figure 1 - 9). Th contents are as high as 30 wt%. Th is incorporated together with Ca in the cheralite substitution ( $\text{CaTh}(\text{PO}_4)_2$ ) (Figure 1 - 11).

The standard used is USGS44069 (Aleinikoff et al. 2006), proposed as oxygen isotope standard in Rubatto et al. (2014) and named here S440. S440 yields a relatively pure monazite composition, with minor amounts of Cheralite (up to 10%) and variation in Th composition between 2.1 and 3.6 wt%; bright BSE patches were avoided during  $\delta^{18}\text{O}$  analysis to ensure a more homogenous dataset. More details in Rubatto et al. (2014).

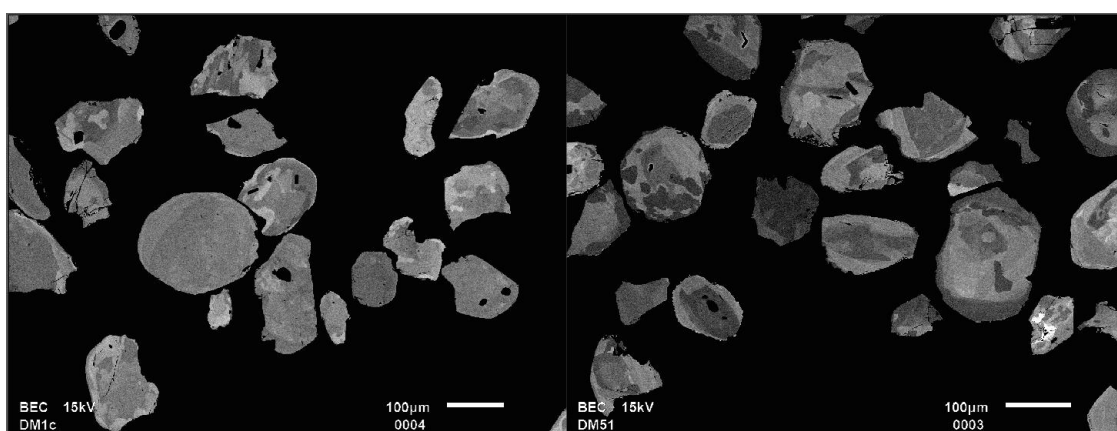


Figure 1 - 9. High-contrast BSE images of Dora Maira monazites.

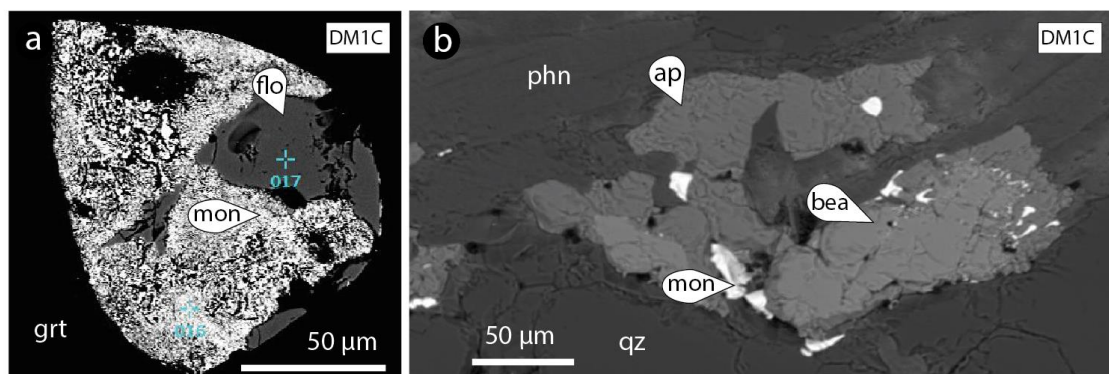


Figure 1 - 10. BSE images of DM1C whiteschist thin section. a. composite inclusion in garnet showing florencite being destabilised into a symplectite of monazite and a silicate phase. b. Bearthite destabilised into monazite and apatite in the matrix.

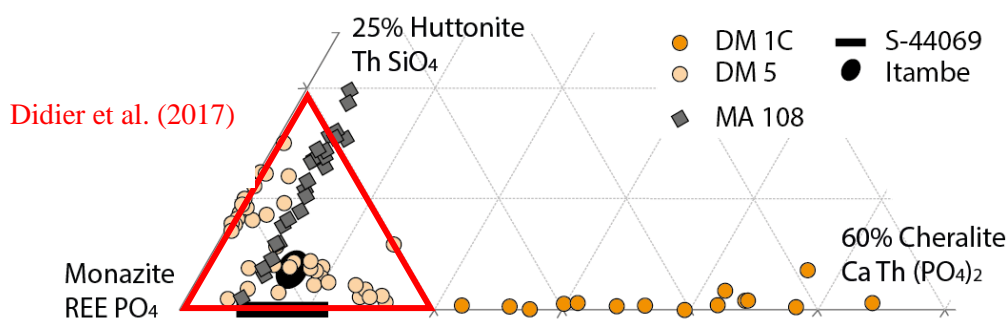


Figure 1 - 11. Cut-off of monazite-huttonite-cheralite triangular diagram showing the composition of the Dora-Maira monazites as well as other samples used in Rubatto et al. (2014).

In DM1C, prograde phosphates have been identified in addition to monazite. Garnet in thin section contains inclusions apatite and of monazite replacing florencite in symplectites (Figure 1 - 10a). In the matrix, one occurrence of monazite and apatite overgrowing bearthite has been found (Figure 1 - 10b).

## 4.2 Results

Oxygen isotopes were measured in the one session for the four Dora Maira samples. The standard S440 yields a repeatability of  $\pm 0.35$  ‰ ( $2\sigma$ ), which is in line with measurements on zircon and garnet on the same instrument. Samples DM51, DM52 and DM53 return slightly higher standard deviations in S440-standardised data (ca. 0.5 ‰) with similar values around 6 ‰, and sample DM1C yields lower values and a larger variation (2.5- 5 ‰, 2sd: 1.5 ‰) see data in *Appendix table A2 – ESM9*.

The measured variations in  $\delta^{18}\text{O}$  correlate with chemistry, with the more BSE-bright (Th-rich) zones yielding lower S440-standardised  $\delta^{18}\text{O}$  values. This correlation is an indication for a matrix effect as proposed by Breecker and Sharp (2007), by Rubatto et al. (2014) in sample MA108, and more recently by Didier et al. (2017).

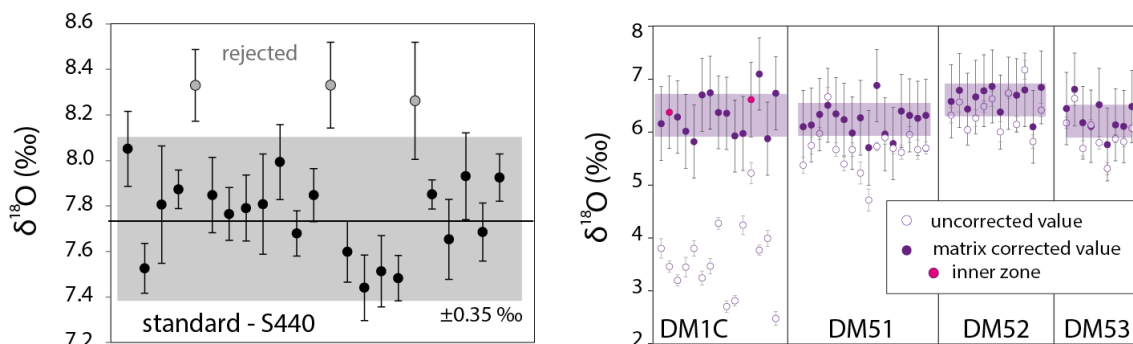


Figure 1 - 12. Results of SHRIMP  $\delta^{18}\text{O}$  analyses in Dora Maira monazites. Matrix correction is done from the coefficients obtained on the Dora- Maira samples themselves, using equation 3a, below.



## 4.3 Discussion

UHP monazite from the DM samples is chemically zoned at the microscale. REE in monazite show HREE depletion similar to zircon and garnet, which indicates that monazite crystallised before and during garnet growth (see **Chapter 2**). Garnet growth is prograde in these samples, and the growth of accessory minerals is related to prograde dehydrating reactions (see **Chapter 2**). During garnet and zircon formation/recrystallization the REE are redistributed amongst host phases. The mass balance for Th and LREE was not investigated specifically, but likely they are controlled by the HP phosphate phases such as bearthite and florencite (Scherrer et al. 2001; Janots et al. 2008). Inclusions of apatite, bearthite and florencite are found in zircon (see **Chapter 2**). In DM1C, florencite might be an important precursor to monazite – in addition to apatite and bearthite, which might be a reason for the Th enrichment in monazite. The florencite and bearthite precursor might also explain why some of DM monazites (and all of DM1C) yield large amounts of radiogenic initial lead (see **Chapter 2**).

Oxygen isotopes have also been measured in garnet and zircon in the DM whiteschists (see **Chapter 2**). All three phases grew in the same range of P-T conditions as shown by REE and age data. Zircon analyses yield averages of  $6.4 \pm 0.3\text{‰}$  in DM1C,  $6.4 \pm 0.3\text{‰}$  in DM51,  $6.7 \pm 0.3\text{‰}$  in DM52,  $6.3 \pm 0.3\text{‰}$  in DM53, all values identical within uncertainty (see **Chapter 2**). It is thus expected that monazite in the four samples yield the same  $\delta^{18}\text{O}$ , as the fractionation between monazite and zircon is small. However, large inter- and intra-sample variations are observed in the raw data, notably with sample DM1C that yields lower and scattered  $\delta^{18}\text{O}$  values. Previous studies have identified chemical variations as a source for matrix effects in monazites (Breecker and Sharp, 2007; Rubatto et al., 2014; Didier et al., 2017). The present data is compared to what is known about matrix effects in monazites.

### 4.3.1 Compositional matrix effect

Breecker and Sharp (2007) measured a series of standards of varied composition by laser fluorination (LF). In their work they admit that LF of monazite is challenging and the partial fluorination (low yield) of phosphates produces inaccurate results. This issue was further discussed in Rubatto et al. (2014). By comparing laser fluorination values to ion microprobe measured values for every standard Breecker and Sharp (2007) determine a matrix-bias correction factor for SIMS analyses of oxygen in monazite according to Th content of monazite. Unfortunately, Breecker and Sharp (2007) do not describe the detail of their calculation. Didier et al. (2017) follow the same approach with a more precise dataset, comparing SIMS sample averages with LF values. Their conclusion is that the best indicator for bias in the measurement of oxygen isotopes by SIMS (Cameca 1280 HR) is the YREE endmember component in monazite.

Rubatto et al. (2014) took a slightly different approach in measuring an array of monazites from the same syenite magma that showed varying Th contents (sample MA 108). The assumption was made that different grains in the same sample had the same oxygen isotope composition because oxygen isotope fractionation during fractional crystallization is very small. Additionally, oxygen isotopes have been shown to diffuse quickly through monazite at magmatic temperature (e.g. Cherniak et al., 2004) so the magmatic monazites are expected to have equilibrated to the same value. In the MA108 sample investigated in Rubatto et al. (2014), Th in monazite is solely incorporated through the huttonite substitution ( $\text{ThSiO}_4$ ). A linear regression through the dataset is used to calculate a correction factor for measured oxygen composition based on the Th content of the measured monazite domain. In this case, no assumption is made on the absolute oxygen isotope composition of the individual monazites, but their relative variation provides the basis for the correction.

The Dora Maira dataset provides an opportunity to use the same approach as for MA108 in Rubatto et al. 2014. This approach assumes that the variation in the measured  $\delta^{18}\text{O}$  is solely analytical and that no geological variation is present outside of the reported analytical uncertainty. This is a working hypothesis that is clearly imperfect as the variation in natural grains is typically larger than the analytical uncertainty (Ferry, 2010), the reasons for this choice are explained below. It is unlikely that the oxygen isotope composition might co-vary with Th incorporated with Ca or Si along the P-T path. In sample DM1C all intermediate and external zones in monazite crystallise with garnet at peak P-T, and garnet in DM1C shows a maximum 1 ‰ difference between core and rim (between 7.4 and 6.4 ‰, see **Chapter 2**), which is attributed to matrix-related effects and not actual zoning in  $\delta^{18}\text{O}$ . The direction of oxygen isotope variation in garnet is opposite to the lower  $\delta^{18}\text{O}$  recorded by the inner Th-rich monazite zones, supporting that this is not a bulk, correlated variation recorded by the two minerals. In DM51, DM52 and DM53, monazite also grew together with garnet, no  $\delta^{18}\text{O}$  zoning can be observed in garnet. Moreover, in the monazite in these samples there is only a weak correlation between Y and REE (decreasing with increasing mode of garnet on the prograde path) and the Ca, Si and Th content of the monazites (Figure 1 - 11); this makes a geological variation in  $\delta^{18}\text{O}$  unlikely. Differential fractionation could occur between cheralite, huttonite and monazite compared to quartz in natural systems. This can be estimated using the increment method: according to the calculations in Rubatto et al. (2014), a pure cheralite monazite in a quartz-dominated system is expected to yield a value that is 0.25 ‰ lower than a pure monazite at 700°C. As the chemical variation observed in DM1C is between 20 and 60% cheralite, the effect would scale down to about 0.1 ‰. This effect is well within the uncertainty quoted for the analytical method and thus cannot be responsible for the relatively large variations in measured oxygen isotope composition on the DM monazite. Therefore it can be

concluded that the up to 5‰  $\delta^{18}\text{O}$  variation measured in Dora Maira monazites cannot be ascribed to geological co-variations with Si, Ca and Th contents, and are likely the result of a matrix effect.

The variation in the measured oxygen isotope composition (expressed in  $\delta^{18}\text{O}$ ) of DM samples standardized to S440-monazite is explored using different vectors of chemical composition (Figure 1 - 13). As proposed by Breecker and Sharp (2007), the matrix effect can be related to Th and U content (Figure 1 - 13a, here calculated with LA-ICPMS data available in **Chapter 2**, *Appendix table A2 – ESM3*). Th and U are added in wt% as their atomic mass is not significantly different within the error of measurement. The obtained regression is:

$$\text{measured } \delta^{18}\text{O} = 7.62 - 0.192 * (\text{Th} + \text{U wt}\%) \quad (1a)$$

The same regression using EMPA data (in **Chapter 2**) for Th and U yields a slightly better fit, with an  $R^2$  of 0.88:

$$\text{measured } \delta^{18}\text{O} = 7.59 - 0.207 * (\text{Th} + \text{U wt}\%) \quad (1b)$$

The same  $\delta^{18}\text{O}$  – Th+U correlation was investigated by Didier et al. (2017) who obtained similar slopes of -0.210 ( $\pm 0.050$ ), -0.161 ( $\pm 0.047$ ) and -0.216 ( $\pm 0.042$ ) ‰/wt%. It has to be noted that Didier et al. (2017) plotted unstandardised  $\delta^{18}\text{O}$  values. A slope of 0.085 was instead calculated by Rubatto et al. (2014) for the MA108 sample. However, Th and U do not describe the variation in DM1C composition very well, and if this correction is applied the average corrected value of DM1C is still lower than the zircon value in the same sample.

An alternative correlation is calculated for the YREE monazite component (Figure 1 - 13b, again with LA-ICPMS data, formula calculated using method from Pyle et al., 2001):

$$\text{measured } \delta^{18}\text{O} = -1.98 + 9.14 * X_{\text{REEY}} \quad (2)$$

This relation is comparable to the variation observed by Didier et al. (2017), although the slopes cannot be numerically compared since expressed in different units.

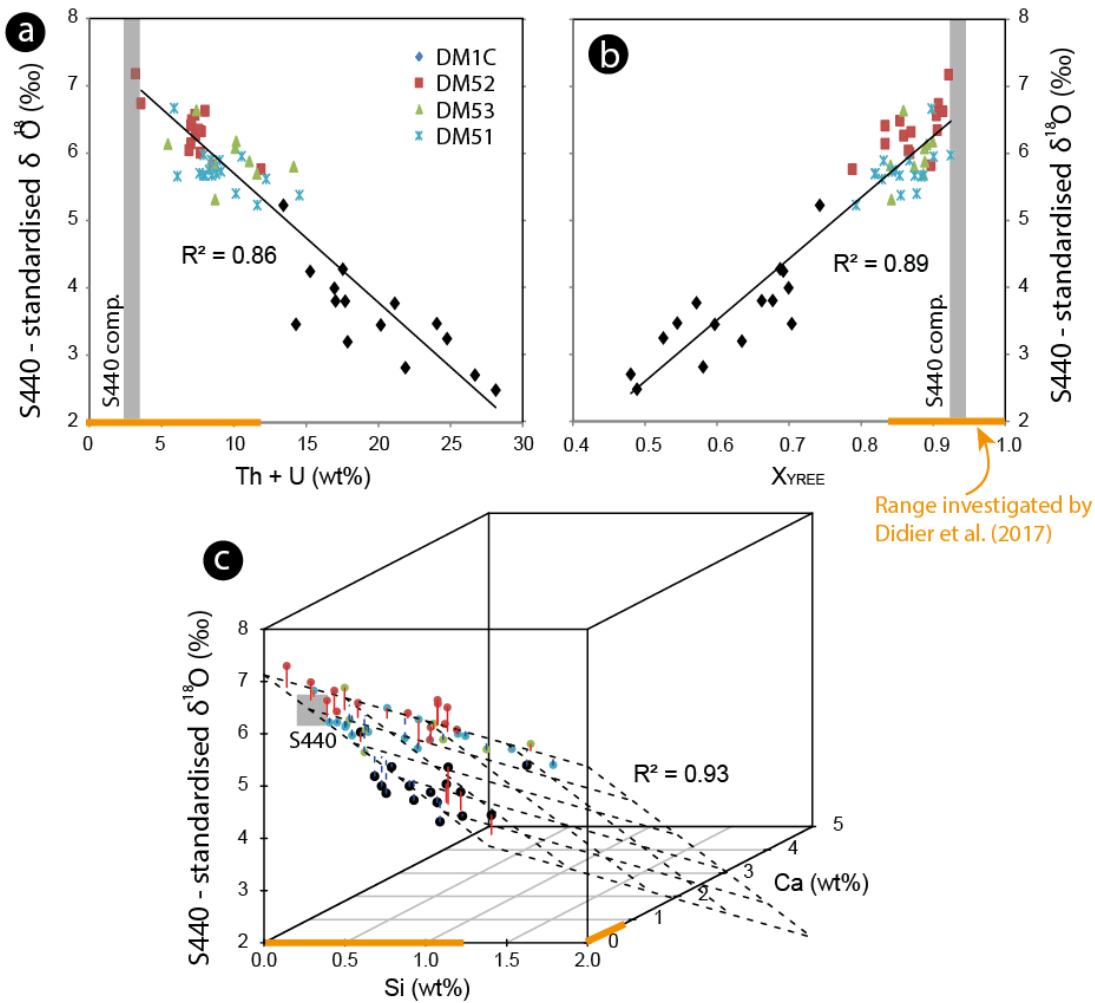


Figure 1 - 13. a.  $\delta^{18}\text{O}$  variation according to Th+ U content (wt%). b.  $\delta^{18}\text{O}$  variation according to X YREE as proposed by Didier et al. (2017). c.  $\delta^{18}\text{O}$  variation according to chemical vectors corresponding to the two substitutions: Ca and Si. In all three diagrams, the apparent  $\delta^{18}\text{O}$  is not the IMF as we have no LF data for the individual monazite zones, but the individual analyses standardized to S440, showing relative variations. The 'true' value for the samples is found at the intersection of the calibration line or plane, and the coordinates corresponding to the composition of S440.

Since DM51, DM52 and DM53 yield primarily a huttonite substitution and DM1C a cheralite substitution, it is possible and more suitable to define a correlation between measured  $\delta^{18}\text{O}$  and composition in terms of Ca and Si (EMPA measurements, available in **Chapter 2, Appendix table A2 – ESM9**), indicators of the two substitutions that incorporate Th (Figure 1 - 13c):

$$\begin{aligned}
 \text{measured } \delta^{18}\text{O} &= 7.12 \text{ (‰, se 0.12, [6.88; 7.37])} \\
 &\quad - 0.88 * \text{Si (wt\%, se 0.12, [-1.12; -0.63])} \\
 &\quad - 1.09 \text{Ca (wt\%, se 0.05, [-1.19; -1.00])}
 \end{aligned} \tag{3a}$$

with a  $R^2$  of 0.93 and a residual standard deviation is 0.33 ‰. This can be translated into:

$$\begin{aligned} \text{measured } \delta^{18}\text{O} &= 7.12 \text{ (‰, se 0.12)} \\ &- 0.106 * \text{Th (Hutt, wt\%, se 0.20)} - 1.90 \text{Th (Cher, wt\%, se 0.08)} \end{aligned} \quad (3b)$$

This linear regression diverges slightly from the slopes of -0.192/-0.206 obtained by regression in the Th +U system, the latter appearing dominated by the cheralite-related matrix effect. The slopes for Si is identical to that found by Didier et al. (2017), using the R script developed above, in more monazite-rich samples -0.87\*Si (wt%). However, the slope in Didier et al. (2017) was much larger for Ca at -3.02\*Ca (wt%), although they don't report its uncertainty which is likely large as it is calculated over a small variation of 0.7 wt% Ca vs. 4.5 wt% Ca in our study. The fact that the slope for Th included by cheralite substitution is statistically different from the slope of Th included by huttonite substitution at the 95% confidence level indicates that it is better to perform a two-step correction compared to a Th-based correction when correcting our dataset. The residual of 0.33 ‰ on the 3D correlation is of the same order as the repeatability in the standard measurements, which is a good indication that the two-step correction successfully eliminates matrix-related variations.

The approach by Didier et al. (2017) looking at  $X_{\text{YREE}}$  (in a way the left-over from cheralite and huttonite substitution in monazite) introduces an artificial constraint which is that the matrix bias induced by 1 mol of huttonite is the same as by 1 mol of cheralite. While this assumption seems plausible within error of our dataset, the two-step approach allows for a truly independent regression (as far as possible when dealing with compositional data).

In summary, in contrast to other studies, the DM dataset covers a large range in composition, especially along the monazite-cheralite solid solution. This allows calculating matrix correction coefficients despite the noise in the single-measurement data. This is done with trace element zoned monazites, with the assumption that the grains and zones are in isotopic equilibrium as indicated by zircon and garnet in the same samples. Here, to calculate the matrix correction coefficients, the data is not anchored in absolute  $\delta^{18}\text{O}$  but examined on a relative basis. While this cannot replace studies such as Didier et al. (2017) in developing high precision standards using LF, this approach allows mapping a much larger chemical space, and can thus enlighten non-linearity in the behaviour of the matrix bias according to composition (not seen here). In addition, the two-component matrix correction approach uses only two chemical measurements (Si and Ca) that can easily be done by EMPA.

### 4.3.2 Monazite-zircon fractionation

An important point is that in the previous calculation of matrix correction factor for the Dora Maira monazite, no assumption was made on the absolute composition of the monazites. This absolute composition can be retrieved from the intersection of the regression plane with the line of Ca and Si content of the S440 standard. This yields a value of 6.38 ‰ that can be compared with the zircon average value of 6.4 ‰ to calculate the zircon-monazite fractionation coefficient, which yields an average  $\Delta^{18}\text{O}_{\text{zircon-monazite}}$  of  $0.1 \pm 0.7$  ‰ ( $2\sigma$ ). The value obtained is coherent with previous estimations of quartz-monazite and zircon-monazite fractionation (Figure 1 - 14, see details in **Chapter 2**).

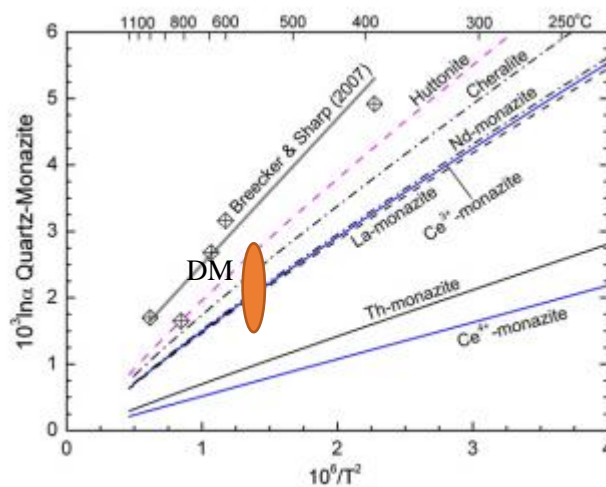
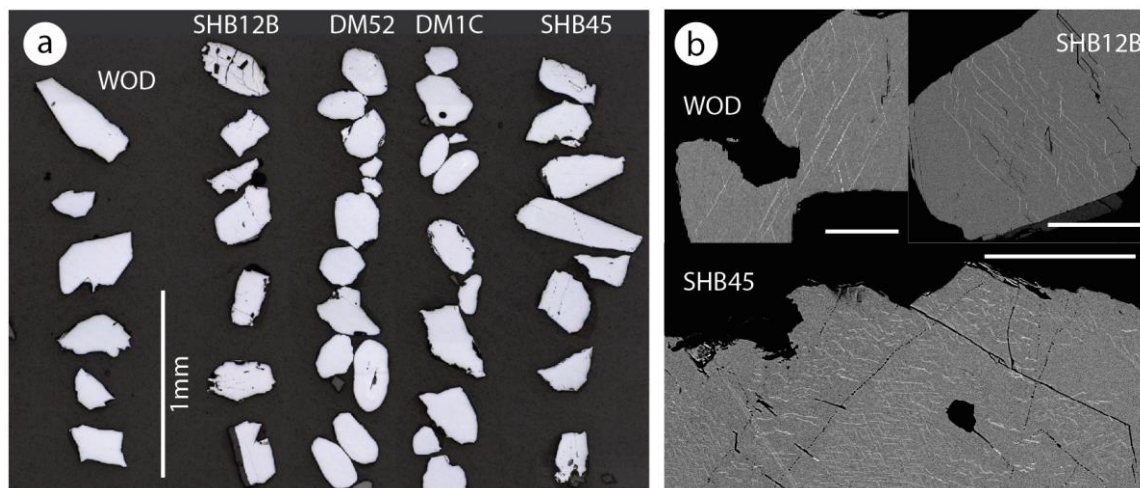


Figure 1 - 14. From Rubatto et al. (2014), equilibrium fractionation between quartz and monazite endmembers calculated using the increment method. The data point regarding Dora-Maira monazite is set at 720°C, 2.1 ‰ (see details in Chapter 2).

## 5 Rutile

### 5.1 Samples and standards

Rutiles for oxygen isotope analysis were separated from four samples: two mafic rocks from the Tavşanlı zone in Turkey (SHB12B and SHB45) and two whiteschists from the Dora Maira, Western Alps (DM1C and DM52). DM1C and DM52 rutiles are brown rounded grains between 50 and 500  $\mu\text{m}$  in diameter. SHB12B and SHB45 rutiles are orange, tabular in shape and contain multiple inclusions. In all samples, ilmenite exsolutions are present in some grains, but were avoided during  $\delta^{18}\text{O}$  in situ analysis.



**Figure 1 - 15. a. Reflected light image of rutile grain mount. b. BSE images of ilmenite exsolutions in rutile. These areas were avoided during SHRIMP analysis. The scale bar is 100  $\mu\text{m}$ .**

The standard Wodgina was characterized by Tanya Ewing for chemistry and U-Pb isotopes (Ewing et al. 2011). Four laser fluorination oxygen isotopes analyses were performed by Benita Putlitz at the University of Lausanne (Rubatto, pers. comm.) and provide an average value of  $-0.5 \pm 0.12 \text{ ‰}$ . WOD grains were extracted from a single chip that is homogeneous for chemistry (Ewing et al. 2009). The main minor elements in the analysed rutile samples are Cr and W (ca. 1 wt% in WOD) as well as Fe (ca. 1 wt% in the Halilbağı and Dora-Maira samples). All other elements are present in much smaller concentrations. For indication, Zr-in-rutile temperatures are calculated (Table 1 - 5, *Appendix tables A1 - 3, A1 - 4*) at ca.  $550^\circ\text{C}$  for SHB12B,  $570^\circ\text{C}$  for SHB45,  $590^\circ\text{C}$  for DM1C and  $710^\circ\text{C}$  for WOD. In samples SHB12B and SHB45, zircon and quartz were not shown to be present or reactive at the time of rutile crystallization, and the temperatures calculated are indicative only.

**Table 1 - 5. Typical LA-ICPMS composition of Halilbağı, DM and WOD rutiles. Zr-in-rutile temperatures in °C are calculated using the pressure dependent calibration of Tomkins et al., 2007).**

(ppm)	Rutile_3 SHB12B	Rutile_21 SHB45	WOD_1 WOD	Rutile_17 DM1C
Al	136.4	94.2	8.19	1433
Si	3040	2638	3107	1158
P	20.5	24.5	22.9	-
Ca	23	bdl	16	Bdl
Sc	2.27	1.93	19.8	1.54
V	791.8	685.4	2354	710
Cr	710	871	11630	117
Mn	0.18	2.03	bdl	Bdl
Fe	9388	10330	2152	349
Co	0.158	0.165	bdl	-
Ni	0.71	0.55	1.45	-
Cu	22.36	20	21.98	-
Zn	8.63	7.54	8.74	-
Zr	69.26	103	602.8	146
Nb	3485	439.5	1903	5134
Mo	1.08	3.3	50.3	0.73
Sn	17.9	17.1	576	-
Sb	2.11	1.74	5.6	-
Hf	3.37	4.65	32.6	7.61
Ta	112.49	22.99	204.6	511
W	60.59	3.42	13936	217
Pb	bdl	0.49	342	0.34
U	0.0478	0.128	164.3	1.88
T 20 kbar	583	610	755	636
T 10 kbar	545	571	709	595
Nb/Ta	30.98	19.12	9.30	10.05

## 5.2 Results

Analyses of the rutile standard WOD are presented in Figure 1 – 16, all rutile oxygen data is in *Appendix table A1 – 5*. The measured  $\delta^{18}\text{O}$  spread from -2.6 ‰ to 1.4 ‰, well outside of the LF normalising value of -0.5 ‰ within  $2\sigma$  of individual measurements (from 0.06 to 0.16 ‰). Two standard deviations of WOD analyses representing the repeatability of the standard at 95% confidence yield 3.8 ‰, compared to the 0.4 ‰ obtained on UWG2 garnet of the same mount in the 10h prior to the start of the rutile session. Notably, if the analyses are grouped by grain on which they were measured (right panel on Figure 1 - 16), this spread is reduced to 0.8 ‰ or less for each individual grain.



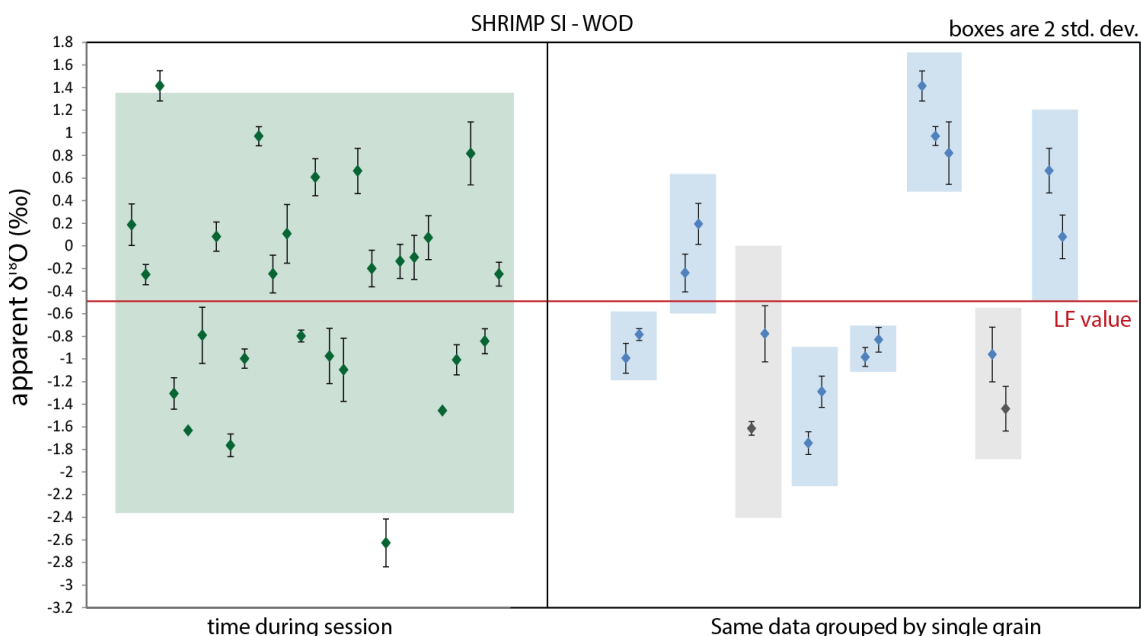


**Figure 1 - 16. SHRIMP  $\delta^{18}\text{O}$  analyses on WOD rutiles, ordered by time in the session and then by individual fragment. Error bars are internal error on the measurement,  $1\sigma$ . Analyses performed on parts of grains with rutile exsolutions are shown in grey symbols.**

Two WOD analyses were performed on rutile domains that had ilmenite exsolutions and they return lower values than the other measurement in the same grain by 1 ‰ and 0.6 ‰ (Figure 1 - 16), which is not statistically distinguishable from the variation observed in other grains. On unknowns, the same grain was rarely analysed twice and comparable spreads as unordered WOD can be observed (Figure 1 - 17).

DM1C yields results between -0.2 and 2.8 ‰, with an average of 1.2‰ (n=16) (Figure 1 - 17, Table 1 - 6). DM52 yields similar values, between 0.0 and 3.3 ‰, with an average of 2.0‰ (n=14). In the case of these two samples, the range represented by values is similar within 0.2 ‰, the change in average of 0.8 ‰ is due to more representation of low values in DM1C and more high values in DM52, hinting at a non-Gaussian distribution of values. In DM52, three grains were measured twice, and yield a spread of 0.3 to 1.0 ‰ between analyses (Figure 1 - 17).

SHB12B yields values between 0.0 and 4 ‰, for an average of 2.3 ‰ (n=14). Two analyses in the same grain are distant by 0.8 ‰. SHB45 yields values between 5.6 ‰ and 8.8 ‰, with an average of 7.5 ‰ (n=16). Two analyses in the same grain yield 0.2 ‰ difference.

For all samples, the SE associated to the individual mean is ca. 0.3 ‰ (Table 1 - 6), but might not be indicative if the analyses are not normally distributed.

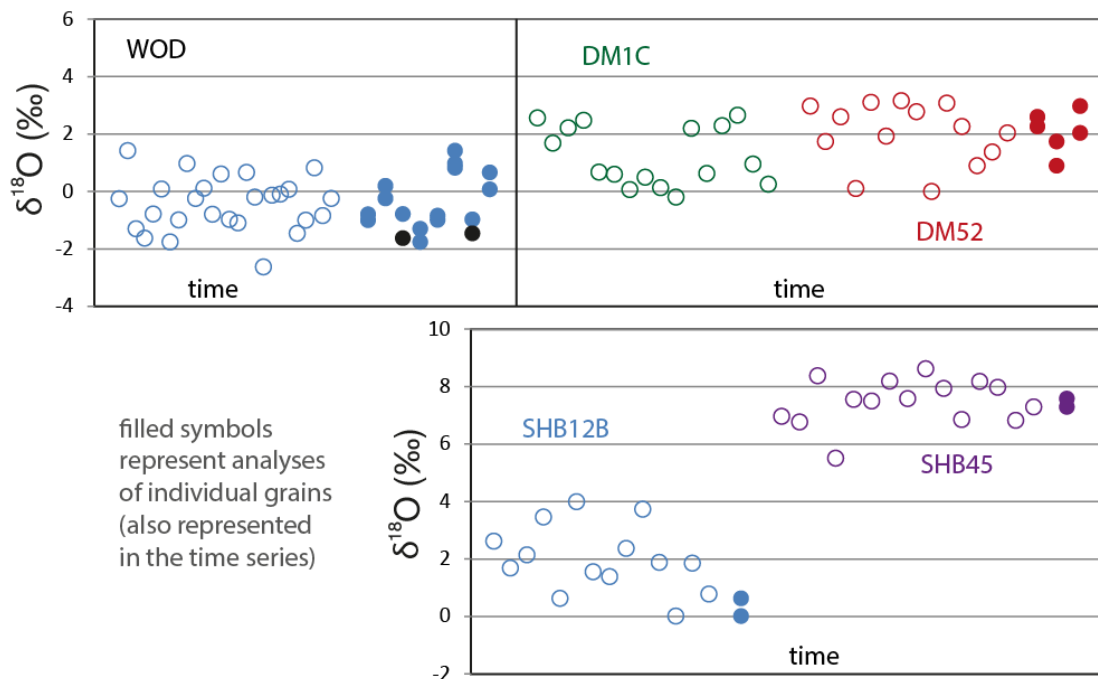
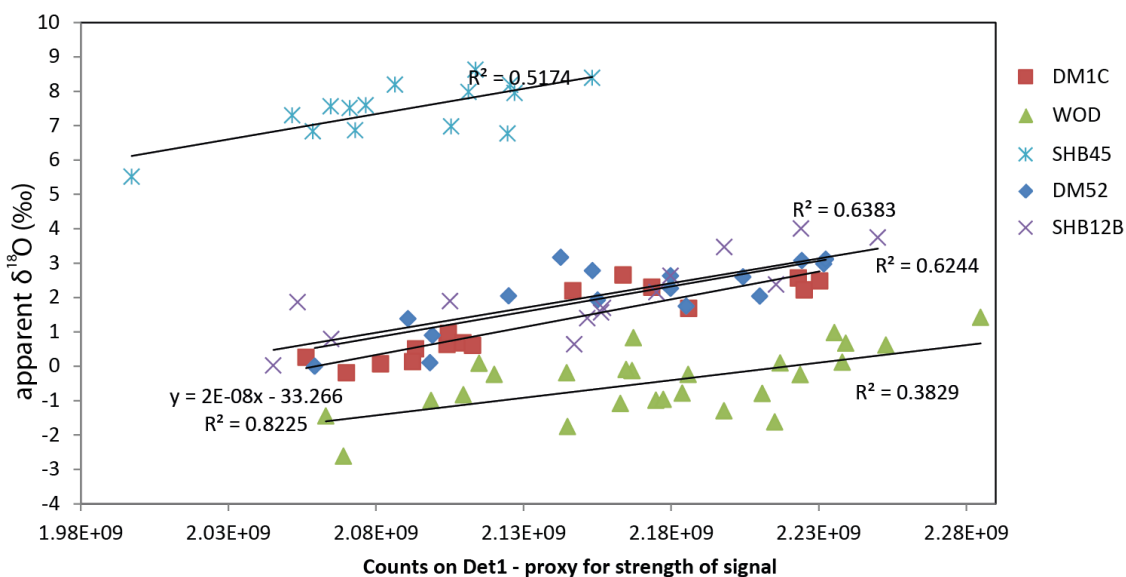


Figure 1 - 17. SHRIMP  $\delta^{18}\text{O}$  analyses on rutile, individual measurement error is smaller than the symbols. Analyses performed on parts of grains with rutile exsolutions are shown in grey symbols.

Table 1 - 6. Summary of sample averages for SHRIMP  $\delta^{18}\text{O}$  analyses on rutile samples, all values are in ‰.

	average	SD	SE	garnet
WOD	-0.43	0.93	0.18	
DM1C	1.23	1.03	0.28	6.3
DM52	2.00	1.07	0.29	6.9
SHB12B	2.29	0.99	0.29	6.3-12.5
SHB45	7.48	0.87	0.24	12.1-13.8

Some of the intra-sample variation correlates with signal intensity (Figure 1 - 18). A similar range of intensity on Detector 1 measuring  $^{16}\text{O}$  (from  $2.05 \times 10^9$  to  $2.25 \times 10^9$  except for one analysis of SHB45 and one analysis of WOD) is observed across samples. A positive slope is observed between measured  $\delta^{18}\text{O}$  and the counts on Detector 1 in all samples, with a  $R^2$  between 0.38 (WOD) and 0.82 (DM1C). The observed slopes are similar across samples, which would indicate that a common mechanism is responsible for this trend.



**Figure 1 - 18. Variation of  $\delta^{18}\text{O}$  according to intensity of the secondary signal (Counts on Detector 1).  $R^2$  are quoted for linear regression through every sample population.**

### 5.3 Discussion

It is not known if the samples are homogeneous, but the standard WOD grains are shards taken from the same large grain of rutile. This large crystal has been reported homogenous by Ewing (2009; 2015) for U-Pb and trace elements, it is thus unlikely that it is heterogeneous for oxygen isotopes. Moreover, the 4 batches for laser fluorination gave values that were identical within error (D. Rubatto, pers. comm).

Rutile does not have major elements substituting in its structure. Trace components are Fe, Cr and W at a maximum of 1.5 wt% each (Table 1 - 5). By analogy to highly variable solid solutions such as garnet, it is thus improbable that chemical variations so small would induce significant matrix effects during ion microprobe oxygen isotope measurements. Moreover, the  $\delta^{18}\text{O}$  variability is also observed in the standard that has been shown to be homogenous for trace element concentrations. In WOD measurements, ilmenite exsolutions don't induce an effect that is distinguishable from the intra-grain variability observed in clean grains. As analyses performed in the same grain were similar, it is thus possible that the spread observed is the result of orientation effects.

#### 5.3.1 Orientation effects

A few studies have investigated orientation effects in the analysis of isotopes in oxides ion microprobe. Orientation effects during analysis have been previously described for U-Pb analysis of rutile (Taylor et al. 2012) and baddeleyite (Wingate and Compston 2000), and for oxygen isotope analysis of the Fe oxide magnetite (Huberty et al. 2010; Kita et al. 2011). In the study of

orientation effect during U-Pb analyses of baddeleyite by SHRIMP (Wingate and Compston 2000), 100 grains of baddeleyite were mounted on their (100) surface in a radial array to measure the influence of the angle of the C axis to the incoming beam. The results yield higher apparent ages (more Pb vs U) when the C axis was laid flat on the mount surface. In a similar experiment, Lyon et al. (1994) rotated the same crystal of magnetite in the sample holder and measured periodic increases in apparent  $\delta^{18}\text{O}$  at  $120^\circ$  angles. In both of these experiments, the angle of the crystal compared to the mount surface was kept constant, but the angle to the incoming beam was changed by rotating the sample. The fact that the whole amplitude of  $\delta^{18}\text{O}$  and age range is explained by this experiments suggests that most of the orientation effect is caused by the channelling of primary ions, as the extraction angle was kept constant. Kita et al. (2011) reduced the impact energy from 20 to 10 keV of the incoming ions, and saw a decrease in the range observed for  $\delta^{18}\text{O}$  from 5 to 2.5 ‰, which is another indication that the channelling of incoming ions, more important at higher energies, is the problem in oxides.

To test if orientation effects are the cause for the observed heterogeneity in measured oxygen isotope analysis in the investigated samples (WOD, DM1C, DM52, SHB12B and SHB45), the orientation of the rutile grains mounted in the epoxy measured by SHRIMP was determined using EBSD in collaboration with Patrick Carr. The EBSD results (*Appendix table A1 – 6*) are shown in Figure 1 - 19 that represents the orientation of all measured rutiles compared to the surface of the mount. It can be observed that most points cluster around the outer edge of the diagram. This indicates that most grains were laid with their c axis parallel to the mounting tape. The c-axis is the elongation axis in well-developed rutile so this is not surprising, even if the metamorphic rutile grains studied here are roughly rounded. The colour of the symbols represents the individual measurement deviation from the sample average, with positive deviations in red and negative deviation in blue. Two main clusters can be identified: the points measured on rutile grains laid on their (100) face yield high  $\delta^{18}\text{O}$  values, whereas the rutile grains that lay on their (110) face yield low values.

These results mirror what is described in Taylor et al. (2012) in their investigation of the effect of orientation on rutile U-Pb SHRIMP measurements. They observed highest count rates and more  $\text{UO}^+$  vs Pb when the face of the rutile grains (100) is parallel to the mount surface, in which case they measured more  $\text{UO}^+$  than  $\text{UO}_2^+$ . The structure of the rutile facing the extraction line is described in Taylor et al. (2012) as more packed in the direction (110), and more open in the direction (100) (see crystal structure diagrams in Figure 1 - 19), which causes some ion channelling and subsequently the fractionation of  $\text{UO}^+$  vs  $\text{UO}_2^+$ . In the case of oxygen, it seems like a tighter structure (110) yields a lower  $\delta^{18}\text{O}$  compared to a more open structure (100) that

yields more O counts and a higher  $\delta^{18}\text{O}$ . The process invoked by Taylor et al. (2012) to explain these differences is ion channelling and subsequently differences in sputtering rates, similarly to what is proposed for other oxides.

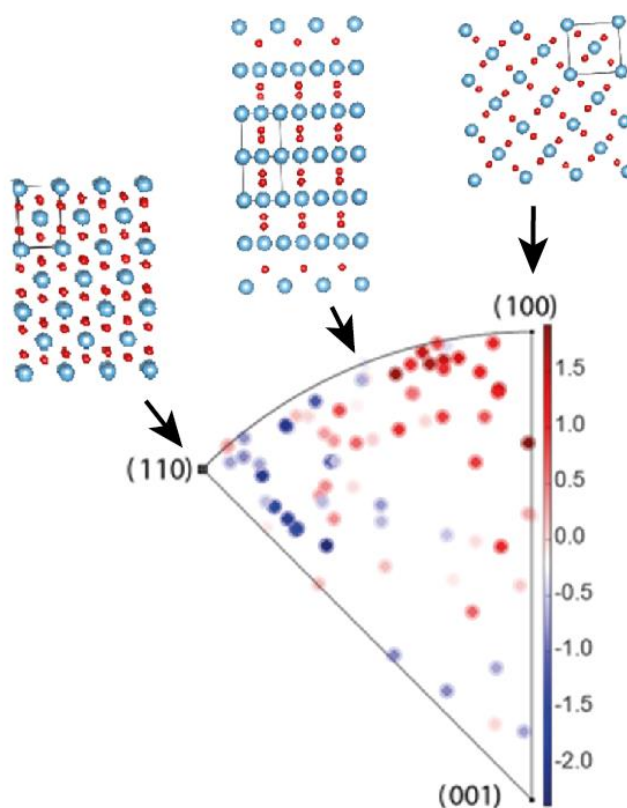


**Figure 1 - 19. Inverse pole figure showing orientation measured by EBSD of the rutile grains analysed for oxygen isotopes. Colours indicate the deviation in  $\delta^{18}\text{O}$  from sample average in %. Above, crystal structure point of view perpendicular to mount surface, at different angles when rutile laid on c-axis, perpendicular to (001).**

Cassiterite ( $\text{SnO}$ ), that shares its crystallographic structure with rutile, has been investigated by Carr et al. (2017) using the same instrument and methods. Their results show that no significant SHRIMP oxygen isotope bias can be observed when measuring cassiterite at different orientations. This shows that orientation effects cannot be predicted by the type of mineral or its structure, as noted by Kita et al. (2011) for S isotopes in sulphides, and that orientation effects depend on complex chemical characteristics of the element involved. Carr et al. (2017) propose that the crystallographic orientation-dependent dielectric constant of rutile is an important parameter in the emergence of orientation effects by SHRIMP analysis, as this constant is lower and less variable in cassiterite. Following this hypothesis by Carr et al. (2017), the dielectric constant of rutile would result in local alteration of the extraction field gradient, and impact the secondary ion energy distribution differently in different crystal orientations in rutile and not in cassiterite.

### 5.3.2 Accuracy

Taylor et al. (2012) recommend measuring a sufficient number of standards of random orientation to produce reliable measurements of U-Pb ages in rutile. For oxygen measurements, this approach may not be effective in alleviating the problem. Metamorphic rutile crystallizes with some habit characteristics such as elongation along the C axis (c.f. density of analyses in Figure 1 - 19). Therefore it is likely that the orientation distribution in metamorphic rutile mounted on tape would not be random, and thus the measured  $\delta^{18}\text{O}$  not normally distributed, leading to skewed averages (instead of populating the extent of a calibration curve as for U-Pb dating). In our dataset, DM1C and DM52 show some of this effect: the garnet  $\delta^{18}\text{O}$  value measured in these samples is 6.3 and 6.9 ‰ respectively (see **Chapter 2**, Gauthiez Putallaz et al. 2016), but the average rutile values show more spread at 1.2 and 2.0 ‰, which is due to non-normal distributions. Moreover,  $\Delta^{18}\text{O}_{\text{rutile-garnet}}$  at 650°C is estimated to ca. +2.5 ‰ by the increment method (Zheng, 1991; Zheng, 1993) and similar to  $\Delta^{18}\text{O}_{\text{rutile-garnet}}$  of ca. +2.2‰ measured in Dora Maira whiteschists by Sharp et al. (1993). This fractionation would predict rutile values of ca. 3.8 and 4.4 ‰ for DM1C and DM52 respectively. The measured values estimated from sample averages in this study are thus too low by over 2 ‰ assuming that rutile grew together with the first garnet, at the temperature recorded by Zr-in-rutile thermometry (ca. 146 ppm Zr, sd=6, n=24, for DM1C, that yield 636 °C at 20 kbar and 682°C at 30 kbar using the calibration of Tomkins et al., 2007). This indicates that the measurement of oxygen isotopes in randomly oriented rutile using SHRIMP yields inaccuracies due to the orientation effects of at least 2 ‰, and it cannot be mitigated by increasing measurement numbers. Further strategies will have to be designed to allow precise oxygen measurement of rutile by ion microprobe.

## 6 Conclusions and outlook

Oxygen isotopes can be measured in inorganic apatite in situ with a similar precision as for zircon analysis (ca. 0.2 ‰  $1\sigma$ ), and do not suffer from significant matrix composition or orientation effects. Coupled to volatile and trace element analysis, micro analysis oxygen isotopes in apatite may be a very powerful tool to unravel fluid history in subducted rocks, especially because apatite is an important mineral for trace element budget in low temperature metasediments. Unfortunately, oxygen diffusion in apatite is fast enough to reset prograde zoning in the Tavşanlı apatites. Only large apatite grains in a sample that underwent peak metasomatism followed by a quick exhumation preserve an earlier oxygen signature. This opens avenues for measuring the timeframe of exhumation for this unit. Speedometry based on oxygen diffusion has to be further investigated and compared to other elements, for instance by measuring Sr profiles in apatite using EMPA.

The protocol for accurate analysis and matrix-correction of oxygen isotopes in monazite by ion microprobe has now been established for both Cameca and SHRIMP instruments. It requires the additional measurement of Th, Si and Ca by EMPA, similarly to garnet, to correct measured ratios according to the proposed matrix-related bias calibration. The achievable precision (ca. 0.3-0.4‰ 1 $\sigma$ ) is not as good as can be obtained on a constant matrix mineral such as zircon, but approaches what can be done for garnet. The matrix-bias correction scheme developed using the Dora Maira monazites covers a wide range of chemical compositions for monazite. This should encompass most of the wt% level chemical variation observed in natural monazite. Additional work should be directed to describe the Y-related variation compared to the xenotime endmember. The monazite-huttonite calibration is in agreement with what is calculated for monazite-huttonite sample Ma108 (Rubatto et al. 2014) in an entirely different geological setting.

The analysis of oxygen isotopes in rutile is hampered by strong orientation effects leading to a variation of 3 to 4 ‰ (1 ‰ sd.) in the  $\delta^{18}\text{O}$  obtained for standard grains. This is not related to how perpendicular to the c-axis the grains are, but to which prism they are laid on. Placing grains randomly and calculating an average is a possible method, but it is shown that for natural grains, mounting random orientations is challenging. Unknowns measured against randomly oriented standards deviate from their predicted values by up to 2 ‰ (from mineral equilibration and WR modelling). It might be possible to minimize the effect by standing all the grains on their elongation axis. In conclusion, although the SHRIMP ion microprobe offers good conditions for measuring oxygen isotopes in rutile, it is not possible to do so within acceptable precision.

**Table 1 - 7. Summary of preliminary results of  $\delta^{18}\text{O}$  SHRIMP analysis in rutile, apatite and monazite. The repeatability of the standard is reported.**

Mineral	Instrument	1 SD on best session	Main challenge
Rutile	SHRIMP II (ANU)	0.93 ‰	Orientation effects
Apatite	SHRIMP II, SHRIMP SI (ANU)	0.23; 0.14 ‰	Diffusion from 400°C
Monazite	SHRIMP II (ANU)	0.18 ‰	Compositional matrix effects





## **Chapter 2**

# **Dating prograde fluid pulses during subduction by in situ U-Pb and oxygen isotope analysis**

*This chapter was published in Contributions to Mineralogy and Petrology in January 2016 and is available in Journal format in the Appendix A2:*

Gauthiez-Putallaz L, Rubatto D, Hermann J (2016) Dating prograde fluid pulses during subduction by in situ U-Pb and oxygen isotope analysis. *Contrib to Mineral Petrol* 171:1–20.

## **1 Introduction**

The subduction of crustal material to mantle depths and its chemical modification during burial and exhumation contribute to element recycling in the mantle and the formation of new crust through arc magmatism. Crustal rocks that are subducted to ultra-high-pressure conditions (UHP, > ~30 kbar) and are exhumed back to the surface provide a rare window into such deep Earth processes. Exhumed UHP rocks offer the unique opportunity to study fluids at sub-arc depths, where such fluids facilitate significant crust–mantle mass transfer of major and trace elements (Hermann and Rubatto 2014; Manning 2004; Tatsumi and Eggins 1995). UHP fluids have been mostly investigated through fluid inclusions (e.g. Ferrando et al. 2009; Frezzotti et al. 2011; Zhang et al. 2008) or metamorphic veins (John et al. 2012; Zheng 2009). In samples that underwent extensive metasomatism, oxygen isotopes can assist in defining the source of the fluids. With the capability to analyse oxygen isotopes in-situ, it is now possible to retrieve information regarding the oxygen isotopic composition of the mineral zones at the same scale as U-Pb dating and trace element analysis. This allows reconstructing P-T-time-fluid evolutions in complex metamorphic rocks (Martin et al. 2014b; Martin et al. 2011; Page et al. 2010; Page et al. 2014).

Dating of prograde fluid pulses that are related to the breakdown of hydrous phases is a difficult task. Pollington and Baxter (2010) and Dragovic et al. (2012) showed that prograde fluid release in subducted rocks can be dated with the Sm-Nd and Lu-Hf method by carefully selecting garnet domains that result from dehydration reactions. However the likely resetting of the Sm-Nd or Lu-Hf system above 700°C (Philippot et al. 2001) hamper its use in many UHP terranes. Zircon and monazite also have the potential to preserve prograde stages of metamorphism and particularly its timing as they are readily datable using micro-analytical techniques. The age of different monazite/zircon growth zones can potentially be linked to different stages of metamorphism using inclusions and trace elements thus allowing the reconstruction of P-T-time paths for UHP rocks (e.g. Gillotti et al. 2013; Hermann et al. 2001; Liu and Liou 2011; Rubatto 2002). With the

addition of in-situ oxygen isotope analyses of zircon and monazite domains, it is thus possible to additionally constrain the composition of fluids that were present during metamorphic stages.

One key question regarding the dynamics of UHP rocks is related to rates of subduction. The timing of exhumation of UHP units is relatively well known, as decreasing temperature during exhumation leads to the sequential closure of multiple radiogenic systems. Exhumation rates of UHP terranes is variable (Hermann and Rubatto 2014; Kylander-Clark et al. 2012): it has been proposed that smaller units as those found within the Western Alps (e.g. Lago di Cignana and Dora Maira) undergo a fast exhumation cycle (of a few to ~10 Ma, Lapen et al. 2003, Amato et al. 1999, Rubatto and Hermann 2001), whereas larger UHP terranes record a more protracted history spanning over tens of million years (e.g. Dabie Sulu or Western Gneiss Region Liu and Liou, 2011, Schmidt et al., 2011). The rates at which such units are brought to depth are harder to constrain and rely on formation of prograde datable minerals, such as zircon and monazite, that can survive peak and retrograde equilibration. However, it has been recently proposed, based on Zr mass balance of rock forming minerals, that new growth of zircon in UHP rocks is far more often related to retrograde than prograde metamorphism (Kohn et al. 2015). On the other hand, in fluid-rich systems zircon dissolution and precipitation might be the dominant process, resulting in formation of metamorphic zircon during prograde fluid release (Geisler et al. 2007; Rubatto and Hermann 2003).

In this paper we perform a detailed investigation of zircon and monazite formation during prograde dehydration reactions in the classical Dora Maira UHP whiteschists, Western Alps. By combining U-Pb, oxygen isotopes and trace element micro-analysis of distinct mineral zones, together with thermodynamic modelling, we aim at reconstructing the prograde P-T-time-fluid path of the UHP Dora Maira whiteschists. This information is used to constrain subduction rates of the UHP unit and to gain information on the sources and timing of fluid-rock interaction.

## **1.1 Geological background**

The Dora-Maira whiteschists outcrop in the Brossasco-Isasca unit of the Western Alps, Italy. This unit is composed of a basement that underwent amphibolite-facies metamorphism during the Variscan orogeny and was later intruded by Permian granites (Gebauer et al. 1997) that constitute a monometamorphic complex (Compagnoni and Hirajima 2001; Compagnoni et al. 2012). The unit underwent Alpine metamorphism in the Late Eocene to Early Oligocene (Gebauer et al. 1997; Rubatto and Hermann 2001).

The Dora-Maira whiteschists are key samples to understanding UHP metamorphism as 50 years of previous studies covering mineralogy, petrology, thermobarometry and fluid inclusions allow an extraordinary level of depth in interpretations of new data. The Dora Maira whiteschists are the type locality for UHP metamorphism (Chopin 1984) and preserve extreme metamorphic grade up to diamond stability field (Hermann, 2003). The whiteschists (Schreyer 1973) are also referred to as pyrope-quartzite (Chopin and Monie 1984) and form lenses and layers of talc-phengite-kyanite-pyrope-quartz/coesite schists within the metagranite. The whiteschists have a peculiar chemistry characterised by average SiO<sub>2</sub> of 65-75 wt%, are strongly enriched in Mg, and depleted in Na, Ca, and K to a lesser extent (their chemistry is close to the KMASH system e.g. Chopin and Schertl 1999). For most elements, the trace element signature of the whiteschists is similar to that of the surrounding metagranite (Schertl and Schreyer 2008); but they are depleted in Zn, Rb, Ba, Sr and P. Previous authors (Compagnoni and Hirajima 2001; Ferrando et al. 2009) proposed that the whiteschists' composition resulted from pervasive metasomatism during subduction, with important implications for fluid migration and depth in the subduction zone.

The relatively simple composition of the whiteschists provides an excellent basis to compare observed mineral assemblages and compositions to experimentally determined phase relations. Schertl et al. (1991) proposed peak metamorphic conditions of 750°C and 37 kbar. Later, slightly higher peak pressures of ~43 kbar were postulated (Simon et al. 1997; Hermann 2003). Main retrograde decompression stages through 700-670°C and 30-25 kbar and 600°C and 11 kbar are associated with the influx of minor amounts of fluid.

Gebauer et al. (1997) pioneered ion-microprobe U-Pb dating in high-pressure samples and showed that zircons in the whiteschists have cores of Permian age that are identical to the zircons in the surrounding metagranite. Rare zircon rims yield an age of  $35.4 \pm 1.0$  Ma (Gebauer et al. 1997) dating UHP metamorphism, confirming earlier results by Tilton et al. (1991). Other minerals have been dated previously such as monazite that from the also yield Alpine ages around 35 Ma, Ellenbergerite (30-34 Ma), as well as pyropes that yield Sm/Nd ages of 34-38 Ma (Tilton et al. 1991). UHP titanite from a calcsilicate within the same unit also returned U-Pb ages  $35.1 \pm 0.9$  Ma, whereas low pressure titanite constrained the exhumation to mid crustal levels at  $31.8 \pm 0.5$  Ma (Rubatto and Hermann 2001). These geochronological constrains allowed calculation of an initial fast exhumation rates of ~3.6 cm/year for the UHP unit (Rubatto and Hermann 2001).

## 2 Analytical methods

Trace elements were measured on an ArF excimer laser coupled to a quadrupole Inductively Coupled Plasma Mass Spectrometer (ICP-MS) Agilent 7700 at the Research School of Earth

Sciences – RSES – at ANU), using the setup described in Eggins et al. (1998). The laser was tuned to a frequency of 5 Hz and energy of 50 mJ (corresponding to a HV of around 26-27kV). Spot sizes of 22  $\mu\text{m}$  for zircon and monazite and of 62  $\mu\text{m}$  for garnet were used. The counts were standardised to NIST 610 (zircon and monazite) and NIST 612 (garnet) glasses and accuracy was monitored by analysing BCR-2G glass. Data were acquired over a 65 seconds analysis that included a 20s background and the reference materials were measured after every eight unknowns. Stoichiometric Si was employed as internal standard for zircon ( $\text{SiO}_2$ : 31.6 wt%) and garnet ( $\text{SiO}_2$ : 42wt%), whereas Th concentrations measured by electron microprobe (EMPA) were used for monazite. Reproducibility and accuracy as assessed on the BCR-2G glass were within 10% or less across all analysed elements. The data was reduced with the freeware Iolite (Paton et al. 2011) and its data-reduction scheme for trace elements (Woodhead et al. 2007). Accuracy and reproducibility of the secondary standard were generally within 10% of the reference value.

EMPA analyses of monazites were performed at RSES using a Cameca SX100 with a current of 100nA, acceleration voltage of 15kV and a spot size of 1.5 $\mu\text{m}$ . For REE analyses,  $L\alpha$  or  $L\beta$  peaks and background were carefully selected to minimise interferences. Al and Si were measured for 10s on the first spectrometer (Sp1, TAP), and Y was measured for 30s. On Sp2 (PET), Ca was measured for 10s, P (20s) and Y (30s). On Sp3 (LPET), La was measured for 10s on  $L\alpha$ , as well as U (60s) on  $M\beta$  and Th (30s) on  $M\alpha$ . On Sp4 (LLIF), Ce was measured for 10s on  $L\alpha$  and the heavier REE for 30s: Nd, Sm, Pr and Gd on  $L\beta$ ; Dy, Er and Yb on  $L\alpha$ . Synthetic phosphates were used for the calibration of REE, synthetic oxides for Th and U, wollastonite for Ca, corundum for Al, apatite for P and quartz for Si. Trebilcock (J. Pyle) and 8153 (R. Stern) monazites were used as secondary standards and our data agreed within error with the published values.

Back-scattered electron (BSE) as well as cathodoluminescence (CL) images were produced with a JEOL-JSM\_6610A SEM, using an acceleration voltage of 15kV and a working distance around 11mm and 25mm respectively.

Zircon U-Pb dating was performed on the Sensitive High Resolution Ion Microprobe SHRIMP II at RSES, according to the method described in Williams (1998). Standards and unknown were analysed with a spot size of around 20x25 $\mu\text{m}$ . Temora zircon (417 Ma, Black et al. 2003) was used as standard for internal mass fractionation and U concentration (160 ppm). Monazites were analysed using a similar method as for zircon and standardised to USGS44069 monazite (424.9  $\pm$ 0.4 Ma, Aleinikoff et al. 2006). Energy filtering was used in order to exclude LREE-Hf molecule interferences on the Pb peaks and reduce ThO counts as described in Rubatto et al. (2001). The typical calibration errors were 1.5% for the zircon and 1% for the monazite sessions. Ratios were

corrected for common Pb according to the measured  $^{207}\text{Pb}/^{206}\text{Pb}$  ( $^{7/6}\text{R}_m$ ) and the non-radiogenic  $^{207}\text{Pb}/^{206}\text{Pb}$  ( $^{7/6}\text{R}_c$ ) following the method described in Williams (1998), i.e.  $f_{206} = (^{7/6}\text{R}_m - ^{7/6}\text{R}^*) / (^{7/6}\text{R}_c - ^{7/6}\text{R}^*)$ , where  $^{7/6}\text{R}^*$  is the expected radiogenic  $^{207}\text{Pb}/^{206}\text{Pb}$  assuming concordance at the approximate age of the sample. For zircon, the  $^{7/6}\text{R}_c$  composition was assumed to be that predicted by Stacey and Kramers (1975) model, but in the case of monazite with high  $f_{206}$  the common Pb composition was regressed from the analyses (see details in result section). Data reduction was performed using MS Excel extensions SQUID 2.5 (Ludwig 2009) and Isoplot 4 (Ludwig 2012).

Zircon and monazite oxygen isotopes were analysed on the same mounts as U-Pb dating with the SHRIMP II instrument following the procedure described in Ickert et al. (2008) and Rubatto et al (2014), respectively. Standards Temora (8.2‰, Black et al. 2004) and USGS44069 (7.7‰, Rubatto et al. 2014) were used for zircon and monazite respectively. The reproducibility of TEM zircons and USGS44069 monazite was within 0.5‰ ( $2\sigma$ ) during each analytical session. Raw data were processed with the in-house software POXI. The monazite analyses were corrected for matrix effect according to the cheralite and huttonite substitutions, as proposed in Rubatto et al. (2014) using Si and Ca measured by EMPA near the SHRIMP spots.

Garnet oxygen isotopes have been measured on SHRIMP SI following the method of Martin et al. (2014b). Two half garnets were cut out of the thin sections used for trace element analyses and were mounted alongside grain separates from the same samples and garnet standards UWG2 and PrPDM. Analyses consisted of 5 scans of 20s for a total counting time of 100s and the standards were measured every 5 unknowns. The reproducibility of UWG2 and PrPDM was within 0.5‰ ( $2\sigma$ ) for the analytical session. Error propagation for oxygen isotope analyses follows Martin et al. (2014b). For sample averages, the uncertainty is calculated as the quadratic sum of the standard error of the mean of the standard measurements within that analytical session, the standard error on the Laser Fluorination value of the standard and the average uncertainty on individual analyses.

## 3 Results

### 3.1 Sample description

We investigated four samples of whiteschists and pyrope quartzite from the whiteschist lens that outcrops at the Case Parigi locality (Chopin 1984; Schertl and Schreyer 2008) and that were previously used for P-T calculations by Hermann (2003). DM1C has been sampled close to the border of the whiteschist lens and is of the quartz-rich type of Hermann (2003). It contains 50% of quartz (retrogressed from peak coesite), small garnets (up to 1cm in size) as well as phengite and kyanite (Figure 2 - 1). Peak phengite is aligned along a weak foliation and is characterised by

a high Si content per formula unit (pfu) of 3.6 (Hermann, 2003). Accessory phases are abundant rutile, rare monazite and zircon, as well as inclusions of apatite and florencite in garnet. DM1C displays a small degree of retrogression with talc, kyanite and minor biotite forming at the rims of garnet.

Garnets from sample DM1C (5 mm in diameter) display a regular bell-shaped decrease in Fe and Mn from core to rim resulting in an increase of the pyrope content from 85 to 99%. Grossular contents are below 3% (*Appendix table A2 - 1*). Chondrite normalised patterns (Figure 2) show strong core–rim variations within garnet, from a LREE-depleted and flat HREE to a pattern characterised by a steep decrease in HREE after a peak at Gd-Tb. A small negative Eu-anomaly is present throughout the garnets and HREE and Y are gradually depleted from core to rim in both samples. The strong variation in HREE and the presence of high Y and HREE cores indicate that equatorial sections through the garnets were likely analysed.

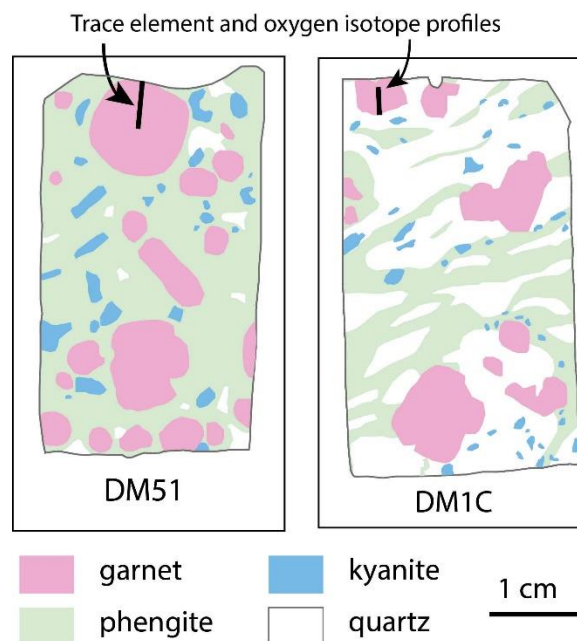


**Figure 2 - 1. Schematic drawing of major phases in DM1C and DM51 thin sections. Retrogression coronas have been integrated into the area allocated to garnet in order to reconstruct the peak metamorphic modal composition**

Samples DM51–53 have been collected in the inner part of the whiteschist lens in horizons that are characterised by abundant garnet (up to 10 cm in size). Garnet is embedded in a kyanite bearing phengite matrix, where quartz is a minor phase (Figure 2 - 1). Rutile occurs as inclusions in garnet as well as in the matrix. Bearthite can be found as inclusions in garnets. Many of the large garnets contain inclusions of quartz after coesite that are surrounded by radial cracks. On mineral separation, abundant zircon and monazite were retrieved. These samples display a higher degree of retrogression with talc+kyanite replacing pyrope garnet.

Garnets in DM51 are up to 1 cm in diameter and display a less pronounced variation in pyrope content from Py96 in the centre to Py99 in the rim. Trace elements in garnets have been analysed as spot analyses along a traverse from core to rim (Figure 2 - 2, *Appendix table A2 - 1*). The HREE patterns in the cores are flat at about 10 times chondrite and their abundance decreases towards the rims, whereas the MREE contents increase slightly. The relatively high pyrope content and the lack of a pronounced enrichment in Y and HREE suggest that the section did not go through the exact core of the garnet.

### 3.2 Zircon textures, inclusions and composition

Zircons in all samples are either rounded and translucent or more elongated and slightly pink in colour. Their size ranges from 20 to 300  $\mu\text{m}$  in length. In CL, they show oscillatory-zoned cores and 1 or 2 unzoned rims that have distinct CL emission (Figure 2 - 3a). The cores are dusted with fluid and mineral inclusions and show embayments and resorption features. In the quartz-poor samples DM51–53, the core is directly overgrown by a CL-bright inner-rim that rarely exceeds a few microns in thickness. In these samples an outer zircon rim, which is darker in CL and shows weak zoning, is present in most crystals. In sample DM1C the oscillatory-zoned zircon cores are overgrown by a single rim that is free of inclusions.

In all samples, oscillatory-zoned cores have a steep HREE pattern, with a pronounced negative Eu-anomaly ( $\text{Eu}/\text{Eu}^*$  0.02-0.06, Figure 2 - 2, *Appendix table A2 - 2*). The inner zircon rims in sample DM52 yield steeper patterns that are HREE-rich and slightly MREE-depleted with respect to the cores. The outer rims in all samples are gradually depleted in HREE compared to the oscillatory-zoned cores and DM52 inner rims. All rims display a weak negative Eu anomaly ( $\text{Eu}/\text{Eu}^*$  0.15-0.30) and a positive Ce anomaly. DM52 outer zircon rims are depleted in MREE compared to the cores, a depletion that is not observed in DM1C zircons.

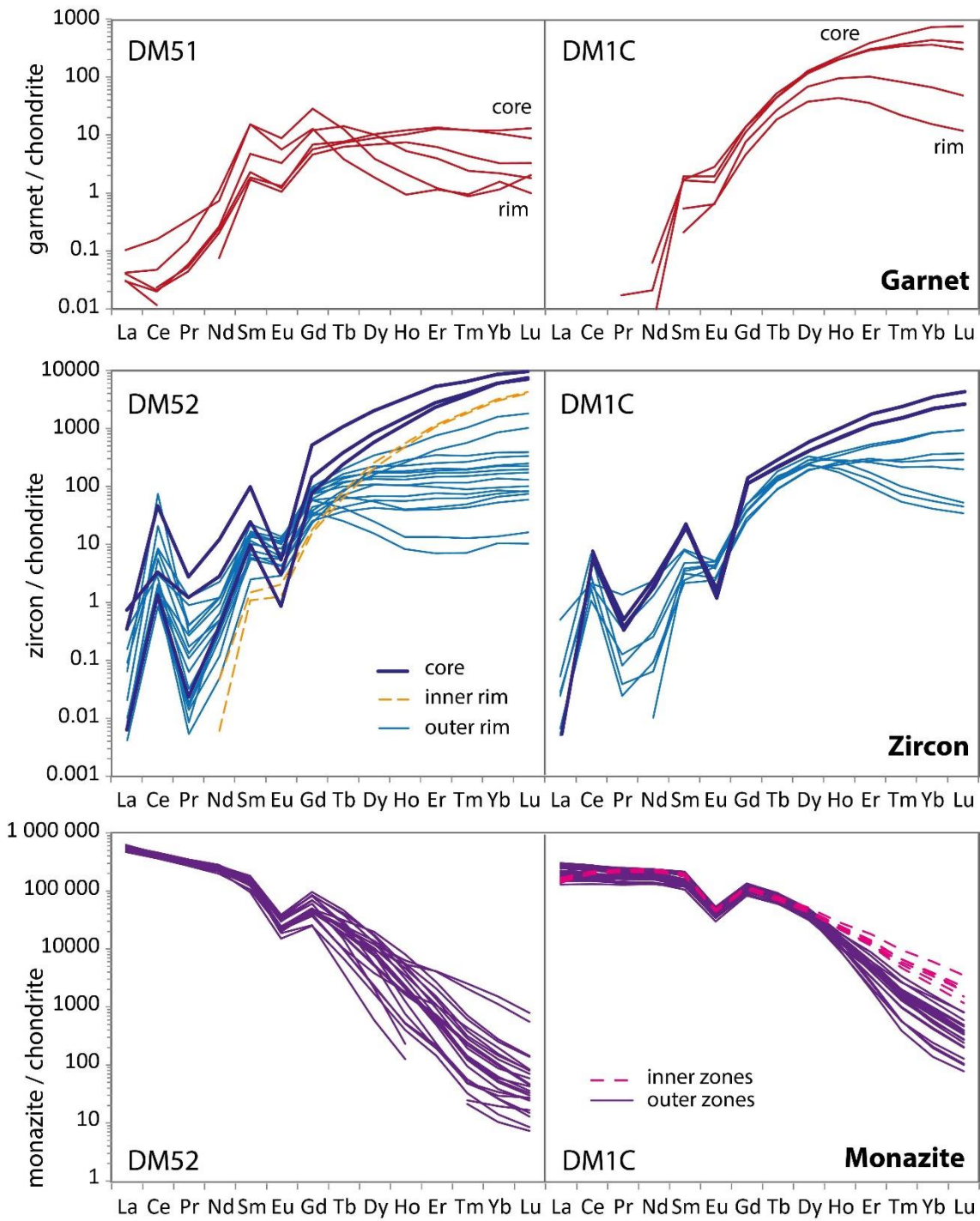
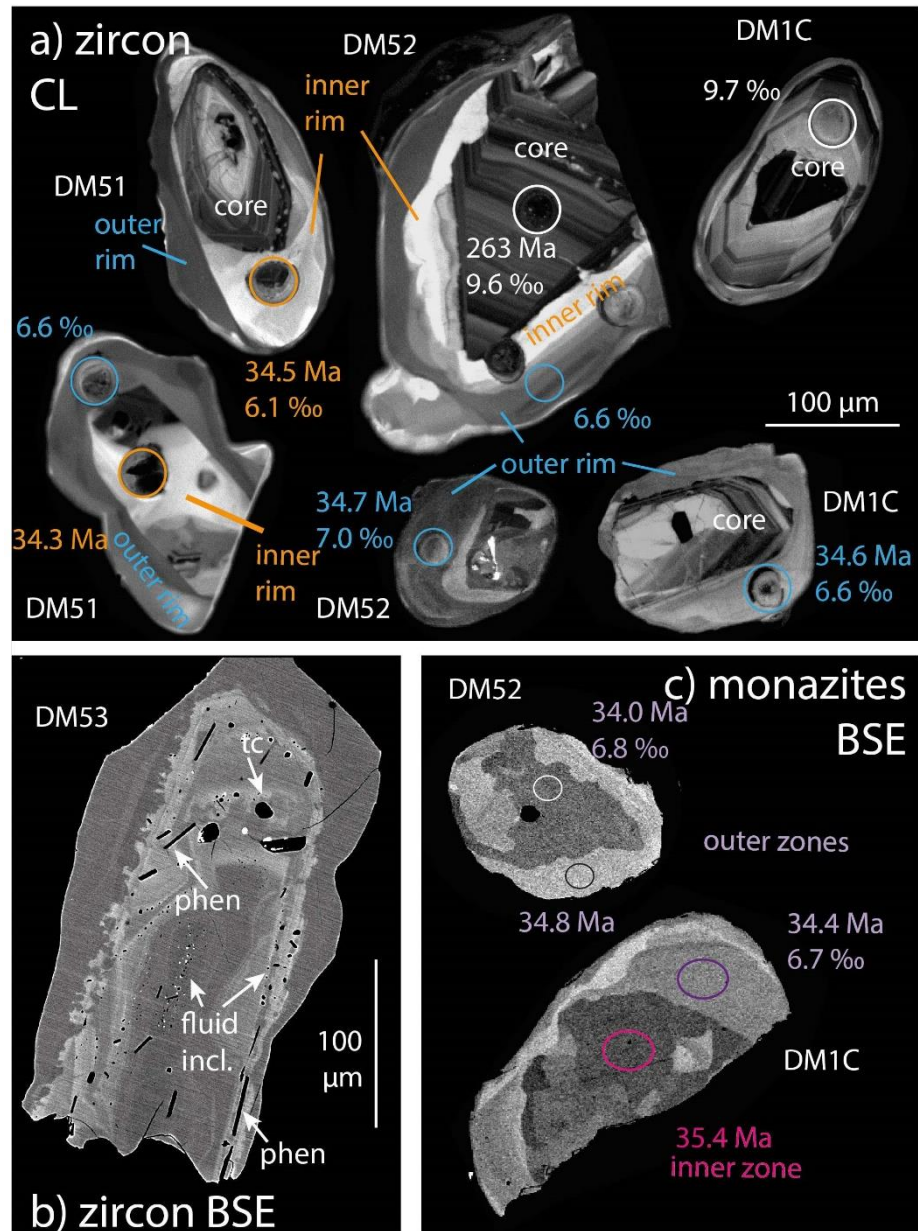


Figure 2 - 2. REE patterns normalised to chondrite (Sun and McDonough 1989) for representative garnets, zircon and monazite from SiO<sub>2</sub>-rich (DM1C) and SiO<sub>2</sub>-poor samples (DM51-53)





**Figure 2 - 3. CL and BSE images of zircons and monazites. Ages and  $\delta^{18}\text{O}$  values were obtained by SHRIMP analyses on two successive polished surfaces**

DM1C zircons contain inclusions of phengite, talc, florencite, monazite, biotite and apatite. In sample DM52–53, zircons contain biotite, chlorite, phengite, monazite, bearthite and apatite. Inclusions are only present within the oscillatory-zoned cores of the investigated grains, most concentrated in oscillatory bands that are lighter in BSE (U-rich domains), as well as the interface between core and inner rim (Fig. 3b). Phengite and biotite inclusions away from cracks yield high Si content per formula unit (between 3.5 and 3.6 Si pfu in phengite; 3.0 and 3.2 Si pfu in biotite, Table 1). Micron-sized, round fluid inclusions are present together with the mineral inclusions (Fig. 3b). On polished surfaces, these inclusions appear only partly filled and EDS analyses show

variable amounts of Na, Al, Cl, K Ca and likely Si (which is more difficult to detect due to overlap with zircon).

**Table 2 - 1. EDS chemical composition of mineral inclusions in DM52 zircons**

Mineral	Bt	Bt	Phe
wt%			
SiO <sub>2</sub>	45.7	42.4	53.7
TiO <sub>2</sub>	0.4	0.3	0.3
Al <sub>2</sub> O <sub>3</sub>	13.0	16.1	23.1
FeO	0.3	0.5	0.1
MgO	24.7	23.8	6.2
Na <sub>2</sub> O	0.1	0.2	0.2
K <sub>2</sub> O	8.6	9.3	9.9
Total	92.8	92.5	93.5
Si	3.19	3.00	3.59
Ti	0.02	0.02	0.02
Al	1.07	1.34	1.82
Fe <sup>2+</sup>	0.02	0.03	0.00
Mg	2.57	2.51	0.62
Na	0.02	0.03	0.02
K	0.76	0.84	0.85
X <sub>Mg</sub>	0.99	0.99	1.00

Cation proportions are calculated for 11 oxygens (phengite) and 12 oxygens (biotite)

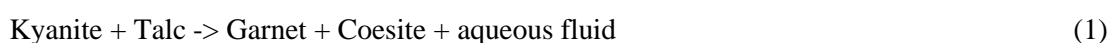
### 3.3 Monazite textures and composition

Samples DM51–53 contain abundant monazite grains that are yellow to green in colour and range in size from 100 to 200  $\mu\text{m}$ . In these samples monazite contains moderate amounts of Th (up to 12 wt%, *Appendix table A2 - 3*). In quartz-rich sample DM1C monazite grains are rare, green in colour and with higher U and Th contents (up to 5 and 30 wt%, respectively) incorporated mainly by cheralite  $[\text{CaTh}(\text{PO}_4)_2]$  substitution. Monazite zoning in BSE images (Figure 2 - 3c) displays both banded and patchy zoning, but these domains are not organised in a systematic core-rim structure. Microprobe analysis shows that BSE brightness is correlated to Th content. Monazites yield a steep LREE-rich REE pattern with a gradual HREE depletion in the outer rims (Figure 2 - 2). In sample DM52, MREE are depleted in the rims compared to the cores, whereas enrichment

in MREE is observed from core to rim in DM1C. A weak negative anomaly in Eu is observed in all analyses.

### 3.4 Thermodynamic modelling of Si-poor whiteschists

The metamorphic reactions resulting in fluid liberation during prograde subduction are different for Si-rich and Si-poor (chlorite-rich) whiteschists (Hermann 2003). Experiments have shown that in Si-rich whiteschists similar to DM1C, chlorite is completely consumed when it reacts with quartz to produce kyanite and talc early on the prograde path. Garnet formation in the pure MASH system is restricted to UHP conditions and forms at ~40kbar, 720°C through the reaction



DM51–53 belong to the Si-poor type of Hermann (2003) and in these rocks, chlorite is in excess and quartz reacts out during prograde metamorphism. With chlorite persisting to higher pressures, there is the possibility for additional dehydration reactions during the prograde path. In order to investigate the fluid release in these Si-poor whiteschists, we have calculated a pseudosection for sample DM51 in KFMASH. The bulk rock composition was calculated from mineral modes observed in thin section (phengite 56%, garnet 34%, kyanite 7% and coesite 3%, Figure 2 - 1). A pure pyrope garnet and the phengite composition measured in DM1C by Hermann (2003) were used. Fe content was not directly measured but estimated using the whole-rock Mg# measured in DM whiteschists by Ferrando (2009), which is very similar in both samples reported in the study. The resulting bulk rock is 53 wt.% SiO<sub>2</sub>, 26 wt.% Al<sub>2</sub>O<sub>3</sub>, 3.5 wt.% FeO, 14 wt.% MgO and 6.6 wt.% K<sub>2</sub>O. This translates to an atomic relative abundance of Si(40) Al(23) Mg(16) Fe(2.2) K(5.9). H<sub>2</sub>O was assumed in excess and all Fe was considered Fe<sup>2+</sup>. The thermodynamic calculations are done using the programs Theriak and Domino (de Capitani and Petrakakis 2010), using the tcdb55c2d database (Holland and Powell 1998) with default solution models (white mica: updated tc325, Coggon and Holland 2002, garnet and biotite: tc330 based on White et al. 2007, orthopyroxene: tc330 based on White et al. 2002 and White et al. 2007).

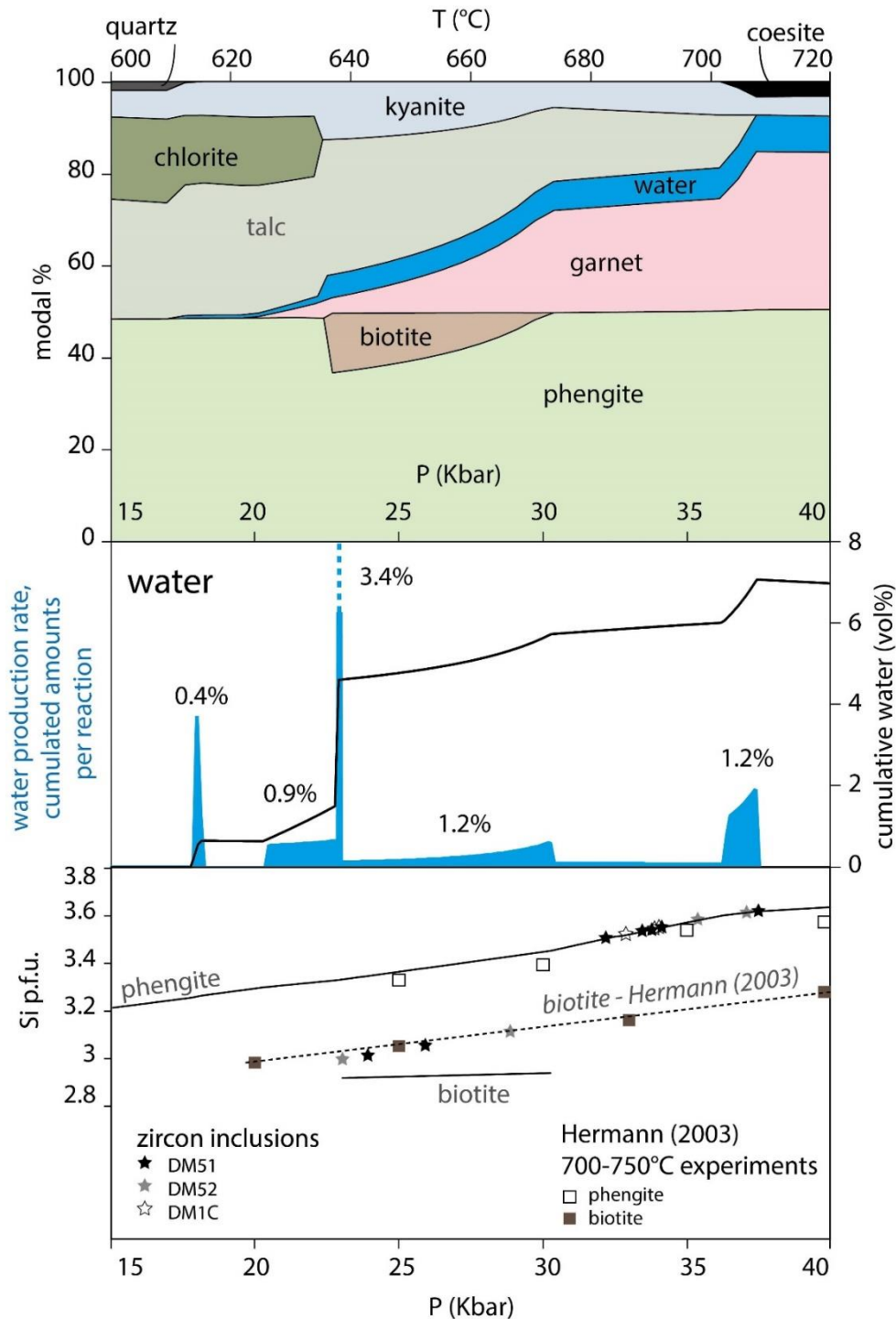


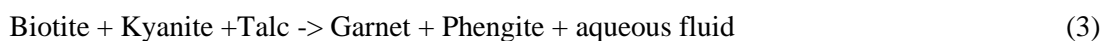
Figure 2 - 4. Theriak modelling results along a P-T path from 15kbar-600°C to 40kbar-720°C. Upper panel: Volume % of mineral phases. Middle panel: Cumulative water release and rates of release (qualitative only) with total volume % of water released per reaction. Lower panel: Si per formula unit in phengite and biotite as predicted by the Theriak model (Holland and Powell database, continuous lines), and from Hermann (2003) experiments (dotted line and squares) and measured values in zircon inclusions (stars). The pressure for each analysed inclusion has been fitted to the corresponding model curve for that mineral according to their Si pfu

The calculated pseudosection for the Si-poor whiteschist DM51 is given in the *Appendix table A2 - 4*. As we are most interested in the release of fluid during prograde metamorphism, we have

calculated the relative phase abundances along a path from 600°C, 15 kbar to 720°C, 42 kbar in 200 steps using the program Theriak (Figure 2 - 4). The modelling shows that a first pulse of fluid production (0.4% of rock volume) occurs at around 17 kbar when quartz disappears in reaction with chlorite to produce kyanite and talc. Shortly after, a small amount of garnet starts growing at the expense of chlorite, resulting in a gradual release of water. The most significant fluid pulse with 3.4 vol% water released is when chlorite disappears along the reaction at 22 kbar and biotite is produced:



It is worth noting that in Si-rich whiteschists, no biotite appears on the prograde path. Biotite then is consumed along the continuous reaction to form more garnet and liberating additional aqueous fluid



A third pulse of fluid liberation occurs at the final consumption of talc at the same reaction that also produces garnet in the Si-rich whiteschists (1).

### 3.5 U-Pb dating

Most analysed oscillatory-zoned zircon cores have small amounts of common Pb (common  $^{206}\text{Pb}$  up to 1.7%); they are discordant and scatter in apparent age from ca. 270 to ca. 100 Ma. The four oldest dates in DM52 are concordant with an average  $^{206}\text{Pb}/^{238}\text{U}$  age of  $261 \pm 9$  Ma (Figure 2 - 5, *Appendix table A2 - 5*). The zircon cores contain between 800 and 2000 ppm U, and have a relatively high Th/U of 0.2–0.5. Inner zircon rims in DM52 are moderately U-rich (300-700 ppm) and are Th-poor with a Th/U of 0.01. Only a few analyses could be placed on this thin inner rim and their average age is  $35.1 \pm 0.5$  Ma (n=3, Figures 2 - 5 and 2 - 6). In DM51, inner zircon rims are broader and more could be analysed; they yield a similar age of  $34.5 \pm 0.7$  Ma (n=6). U content of the inner zircon rim is between 200 and 300 ppm and Th/U is low at 0.13–0.05. Outer zircon rims are abundant in sample DM52, are rich in U (300–1700 ppm, Th/U of 0.01–0.05) and yield an age of  $34.9 \pm 0.2$  Ma (n=13). A rim age of  $35.1 \pm 0.8$  Ma (n=5) is obtained for DM1C zircons, which are relatively poor in U (56–580 ppm, Th/U 0.10-0.01).

Most of the monazite analyses in the qtz-poor samples DM51 and DM52 yield an unusually high proportion of initial lead (from 11% to 80%  $^{206}\text{Pb}$ , *Appendix table A2 - 6*), for U contents between 50 ppm and 1 wt%. DM1C monazites are particularly Th and U-rich up to 30 and 5 wt%

respectively, and contain significant amounts of initial  $^{206}\text{Pb}$  (1-10%). In either samples, defining the composition of the initial lead is crucial to accurately determine the age of the monazites. Uncorrected data plotted in Tera-Wasserburg diagrams (Figure 2 - 5) define a linear regression which upper intercept indicates a  $^{207}\text{Pb}/^{206}\text{Pb}$  composition of initial Pb that is best determined in DM52 at  $0.7154 \pm 0.017$  (MSWD=1.5). In the two other samples, the regression is poor and the obtained initial lead composition is not robust ( $0.750 \pm 0.039$ , MSWD=4.5 for DM51 and  $0.652 \pm 0.063$ , MSWD=2.3, for DM1C). The values for all three samples are lower than the model common  $^{207}\text{Pb}/^{206}\text{Pb}$  ratio of 0.838 expected at 35 Ma according to Stacey and Kramers (1975). This indicates that the initial lead present in the monazites has a radiogenic component. Identical free intercept ages are calculated for the two samples where the regression is better defined: DM52 yields an age of  $33.8 \pm 0.9$  Ma (MSWD=1.5) and DM1C an age of  $33.8 \pm 0.7$  Ma (MSWD=2.3). Monazite analyses in sample DM51 are more scattered and contain the largest initial lead contribution. A poorly defined regression gives an age of  $36.8 \pm 3.5$  Ma with a high MSWD of 4.5. Seventeen analyses of DM1C monazite contain less than 10% initial Pb and when the intercept is forced to the model common-Pb composition (Stacey and Kramers 1975), they yield a weighted average  $^{206}\text{Pb}/^{238}\text{U}$  age of  $34.7 \pm 0.4$  Ma which is within the error of the intercept age for the same sample.

It has been previously reported that the preferential incorporation of Th relative to U in minerals such as monazite from a short-lived melt or fluid can induce a disequilibrium in the Th-U series: namely, excess  $^{230}\text{Th}$  incorporated at the time of monazite crystallisation can lead to the production of excess  $^{206}\text{Pb}$ . This effect can be estimated in magmatic systems (Schärer 1984), but it is hard to assess if monazite crystallises from an aqueous fluid as the fluid Th/U is unknown. If corrected on the basis of the measured  $^{204}\text{Pb}$  and a Stacey and Kramers (1975) common Pb composition, all but three Pb-rich analyses in DM1C are concordant in the conventional Wetherill diagram and give a weighted average of  $34.6 \pm 0.3$  Ma. As excess  $^{206}\text{Pb}$  would affect only one of the two decay systems, concordance is taken as evidence that any potential  $^{206}\text{Pb}$  excess is within the analytical error of the analyses in these monazites. In other samples, excess  $^{206}\text{Pb}$  is also expected to be within analytical uncertainty even though the amount of initial Pb prevents performing the same test.

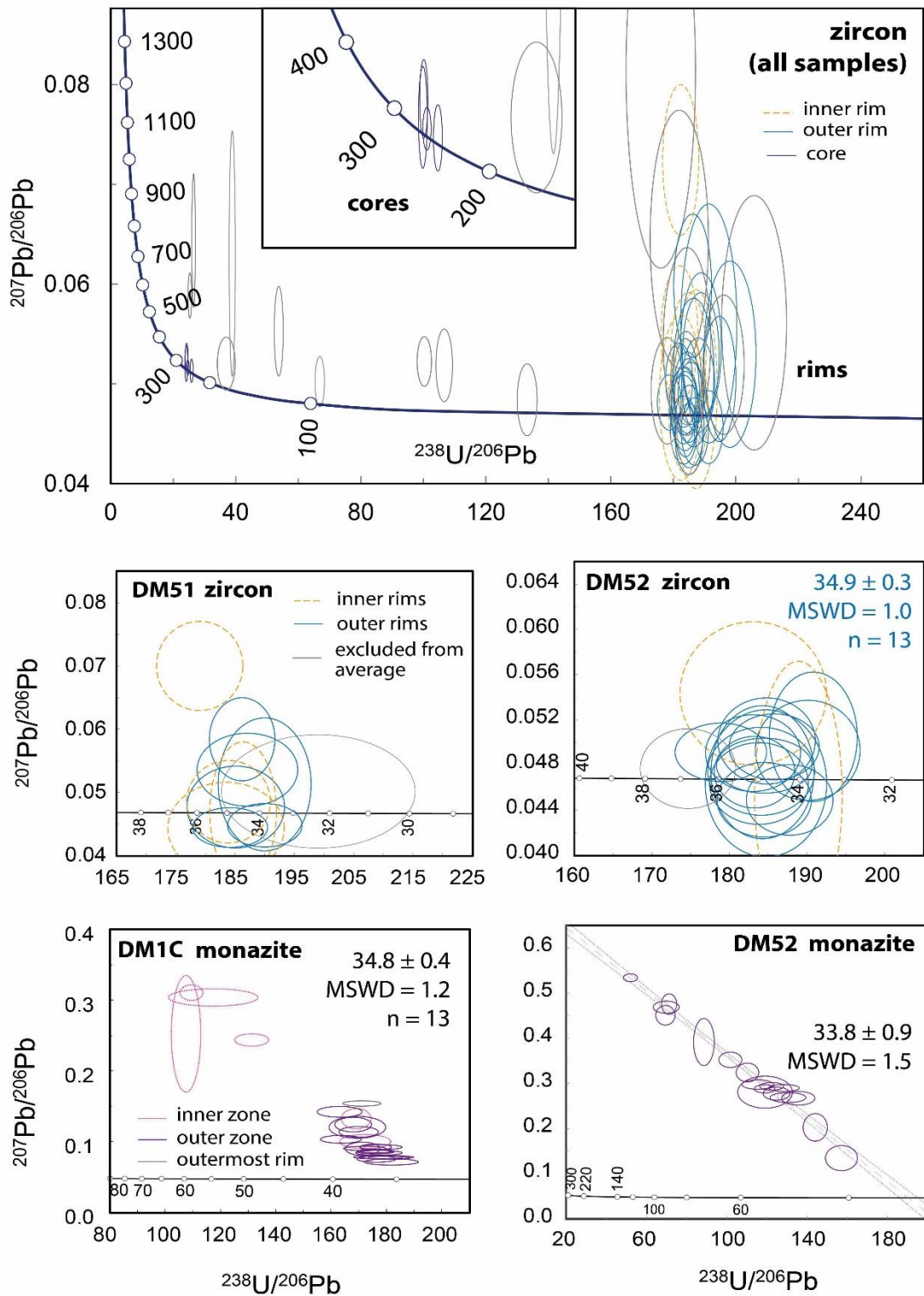


Figure 2 - 5. Tera-Wasserburg diagrams for U-Pb analyses of zircon and monazite, uncorrected for initial Pb

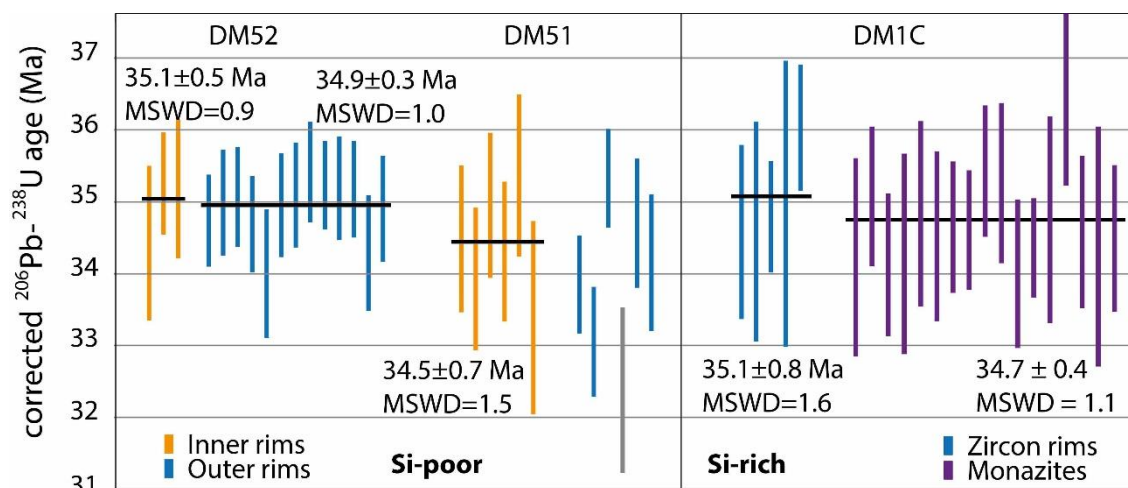


Figure 2 - 6. Summary of  $^{206}\text{Pb}$ - $^{238}\text{U}$  ages for zircon and monazite corrected for initial Pb

### 3.6 SHRIMP Oxygen Isotopes

Oxygen isotopes in zircon were measured on the same domains as U-Pb ages. In each sample, oscillatory-zoned zircon cores yield  $\delta^{18}\text{O}$  average values between  $9.9 \pm 0.4$  ‰ and  $10.2 \pm 0.4$  ‰, 2 sigma (Figure 2 - 7, Appendix table A2 - 7). The scatter observed in sample DM53 is slightly larger than what measured for Temora standard and it is speculated that this may be the effect of the micro-inclusions visible in this domain. This is supported by the metamict aspect of the zircons cores and their discordant U-Pb dates.

Zircon rims yield  $\delta^{18}\text{O}$  average values between  $6.2 \pm 0.4$  ‰ in DM53 and  $6.7 \pm 0.4$  ‰ in DM52 for about 10 analyses in each sample (Figure 2 - 6). A few inner rims were analysed in sample DM51–53 and yield the same  $\delta^{18}\text{O}$  value of around 6.4 ‰. Some scatter is present in zircon analyses from DM1C and DM51 and this is attributed to small amounts of mixing between core and rim, given the small size and irregular geometry of the analysed domains.

Core-rim profiles for  $\delta^{18}\text{O}$  have been measured in one DM1C and one DM51 garnet along the same direction of the trace element profiles, and in DM52 garnet fragments. Using pyrope PrPDM (Vielzeuf et al. 2005a; Page et al. 2010) as a matrix-matched primary standard, the averages  $\delta^{18}\text{O}$  values measured for pyropes ( $X_{\text{Pyr}}$  0.95–0.99) are between  $6.3 \pm 0.2$  ‰ and  $6.8 \pm 0.3$  ‰ (Figure 2 - 7, Appendix table A2 - 8). For these compositions, the value obtained in the garnet core is indistinguishable from the rim. DM1C garnet core lies outside of the compositional range matched by PrPDM, with  $X_{\text{Alm}}$  as high as 0.11. This results in higher measured apparent values (up to 7.4‰) against PrPDM. This is believed to be the effect of a Mg# related matrix effect at high  $X_{\text{Prp}}$  that has not been previously described, as these compositions were not covered by Martin (2014). Indeed, analysing pyrope garnet PrPDM using UWG2 (Valley et al. 1995,  $X_{\text{Grs}}$



0.14,  $X_{\text{Pyr}} = 0.40$ ,  $X_{\text{Alm}} = 0.45$ ) as primary standard and applying the Martin et al. (2014) correction for the grossular component of the garnet, the  $\delta^{18}\text{O}$  value obtained for PrPDM ( $0.95 < X_{\text{Pyr}} < 0.99$ ) is 4.2 ‰, instead of the published value of 5.6 ‰ (Vielzeuf et al. 2005a). This test implies an additional matrix bias of -1.4 ‰ for near-endmember pyropes compared to the calibration of Martin et al. (2014). Therefore, in order to get a lower bracketing value, DM1C cores with  $X_{\text{Pyr}} < 0.90$  were standardised to UWG2 and corrected for their grossular component according to Martin et al. (2014); this yielded a  $\delta^{18}\text{O}$  value of around 5.6 ‰. The true value of these cores is believed to lie between 7.4‰ and 5.6‰ (standardised to PrPDM and UWG2 with correction, respectively).

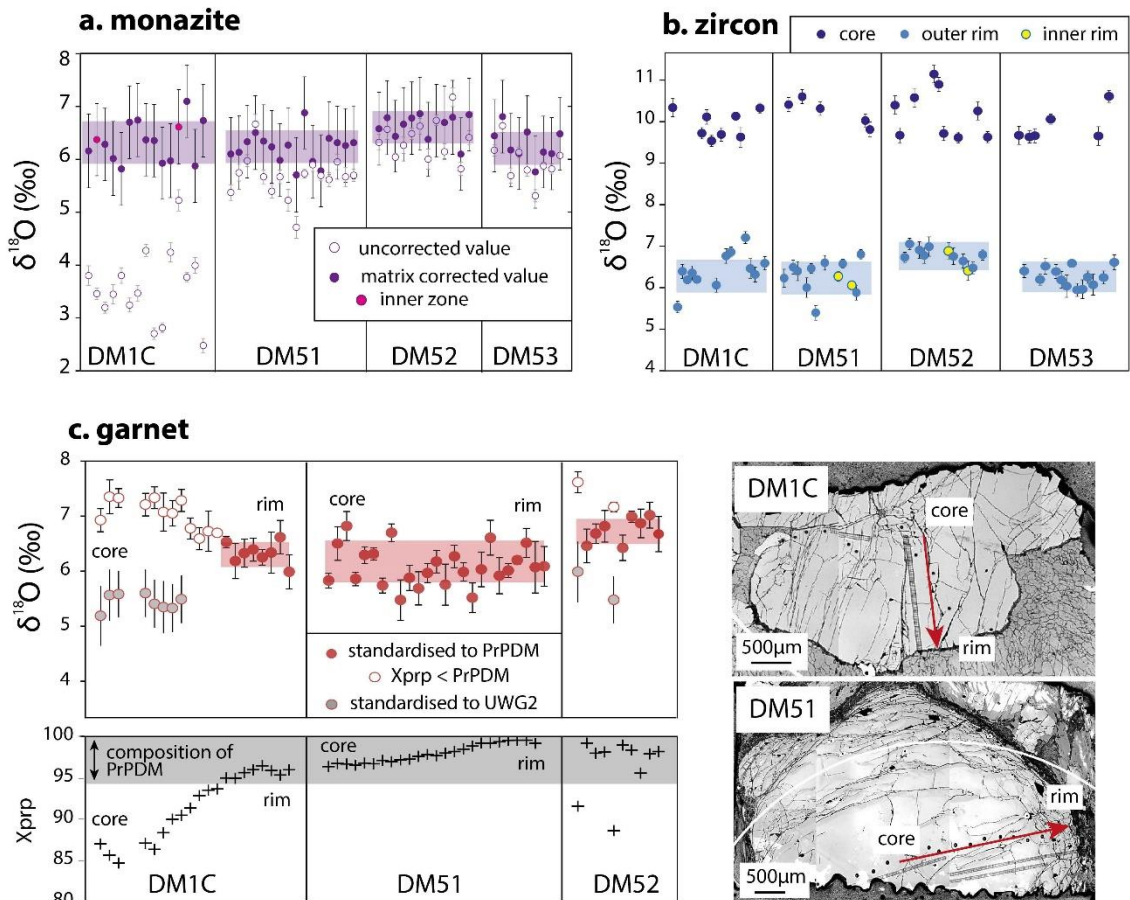


**Figure 2 - 7. Oxygen isotope analyses in a. monazite, b. zircon and c. garnet with reflected light images of the analysed garnet grains on the right. Individual error bars represent 2SE for uncorrected measurements only; for corrected measurements the uncertainty include SE on the measurement SE, matrix correction residual SE and standard value SE (as per Martin et al. 2014 and Rubatto et al. 2014). In a. the values corrected for matrix effect (see text for details) are plotted together with the uncorrected values. Garnet measurements in c. were generally standardised to PrPDM pyrope standard, but for garnet with pyrope content below 95% standardisation to UWG2 garnet was preferred (see text for details)**

In monazites, analysis corrected for the huttonite and cheralite component (see details in Rubatto et al. 2014) for DM51, DM52 and DM53 yield homogenous populations with  $\delta^{18}\text{O}$  of  $6.4 \pm 0.7$  ‰,  $6.8 \pm 0.7$  ‰ and  $6.6 \pm 0.7$  ‰, respectively (Figure 2 - 7, Appendix table A2 - 9). For the cheralite-

rich DM1C monazites the average  $\delta^{18}\text{O}$  is  $6.3 \pm 0.8$  ‰. Monazites in all samples are homogenous and identical within uncertainty in their oxygen isotopic composition.

## 4 Discussion

We will first assess the conditions of when metamorphic zircon and monazite grew and link this to fluid release in the whiteschists to constrain the mechanisms of formation/recrystallisation of these accessory phases. This provides the basis for the interpretation of the dating results that are used to estimate subduction rates. The addition of in-situ oxygen isotope measurements in garnet, monazite and zircon provides a framework to trace fluid-rock interactions from the intrusion of Permian granites to Alpine UHP metamorphism.

### 4.1 Metamorphic conditions of zircon and monazite growth

The first step for the interpretation of the obtained ages and in-situ oxygen isotope data is the correlation of zircon and monazite domains to metamorphic conditions. The garnet forming reactions in Si-rich and Si-poor whiteschists are well constrained by experimental results and the thermodynamic modelling (Figures 2 - 4 and 2 - 8, *Appendix figure A2 - 4*). The relative growth of zircon and monazite domains with respect to garnet can be assessed based on REE patterns (eg. Rubatto 2002). Garnets from samples DM1C and DM51 show a gradual depletion in Y and HREE from core to rim. Preserved small-scale variations indicate that diffusion is not significant for trace elements at these temperatures as shown by previous studies (eg. Hermann and Rubatto 2003). With enrichments up to 1000/chondrite in Lu and modal abundance between 20 and 40 %, garnet is the main host for HREE in all analysed whiteschists. The HREE depletion is thus interpreted as growth zoning, reflecting Raleigh fractionation (Otamendi et al. 2002) of REE and Y. This effect is much more pronounced in whiteschist DM51 where the garnets are larger and more abundant. It is worth noting that core compositions on the large garnets of DM51 are absent. Garnet REE patterns also show a small negative Eu anomaly that is unchanged from core to rim and is comparable in magnitude to that of the bulk-rock (Grevel et al. 2009). This suggests that no other phase capable of fractionating Eu, such as plagioclase, was present in the metamorphic assemblage throughout garnet growth.

The second zircon rim in samples DM51–53 and the rim overgrowing the cores in DM1C zircons yield variable depletion in HREE and Y of the same magnitude as observed in garnet, as well as a weak negative Eu-anomaly. Using analyses from sample DM1C, calculated zircon-garnet HREE partitioning between garnet and zircon rims are between 17–20 for Lu, down to 4–7 for Er. This is comparable to previous coefficients determined in experimental and natural samples

at similar temperatures (600-800°C; Rubatto 2002; Rubatto and Hermann 2007), and might be taken as an indication for equilibrium between zircon and garnet. Because these garnets have a different composition to the experiments and natural samples considered by previous studies the comparison of partitioning values is indicative only. On the basis of their trace element composition relative to garnet, the outer zircon rims are interpreted as crystallising during the growth of HREE-depleted garnet. These rims yield an average age of  $34.5 \pm 0.4$  Ma in quartz-poor, garnet-rich samples DM51 and DM52, which is interpreted as the average age of peak garnet growth along reaction (1). In the quartz-rich sample DM1C where garnet grew only at peak conditions (Hermann 2003), zircon outer rims yields scattered analyses around the same age (Figure 2 - 5).

In samples DM51–53, the inner zircon rim directly overgrowing the cores is distinct in chemistry with a low U content, steep HREE patterns (similar to the cores, but distinct from the other rims), and small negative Eu-anomaly that is of the same magnitude as the bulk-rock, but weaker than the zircon cores. These features suggest that the inner zircon rim grew in the absence of significant modal garnet and plagioclase (Rubatto 2002). We interpret these observations as first growth of zircon during prograde metamorphism, before significant garnet growth. According to our thermodynamic modelling, garnet growth in these Si-poor whiteschists starts already at ~22 kbar and thus the inner zircon rim likely formed close to this pressure.

Mineral inclusions provide additional information on the growth of the metamorphic zircon domains. The interpretation of these inclusions is complicated by the fact that most inclusions occur in the zircon cores (see next section), but some important inferences can be made nevertheless. Zircons from Si-rich and Si-poor whiteschists contain abundant talc and phengite inclusions, indicating that these inclusions were captured when talc was still a stable phase. The Si pfu of most of the included phengites is around 3.5 and only few phengites show a Si pfu of 3.6 that is comparable to the peak phengite in the matrix. According to the experiments and thermodynamic calculations (Figure 2 - 4), phengite with 3.5 Si pfu and talc coexist just before the final breakdown of talc. Combined with the REE characteristics, the inclusions thus provides evidence that the outer zircon rims formed at the talc-out and garnet forming reaction (1) on the prograde path at 700°C, 35 kbar. In the Si-poor whiteschists, zircon hosts phengite with a lower Si content and biotite. The presence of biotite is very important as it occurs only in a restricted P-T interval on the prograde path. The thermodynamic model does not include a biotite solid-solution that permits  $\text{Si} > 3$  pfu. However, in the experiments of Hermann (2003) changing biotite compositions with pressure are reported that can be used to constrain the pressure of trapping of the biotites to 22-25 kbar. This pressure estimates coincides with the calculated stability field of

biotite (Figure 2 - 4, Appendix figure A2 - 4). Together with the HREE enriched characteristics of the inner zircon rim, these inclusions suggest that the inner metamorphic rim found in the zircons of Si-poor whiteschists formed at ~22 kbar, 640°C.

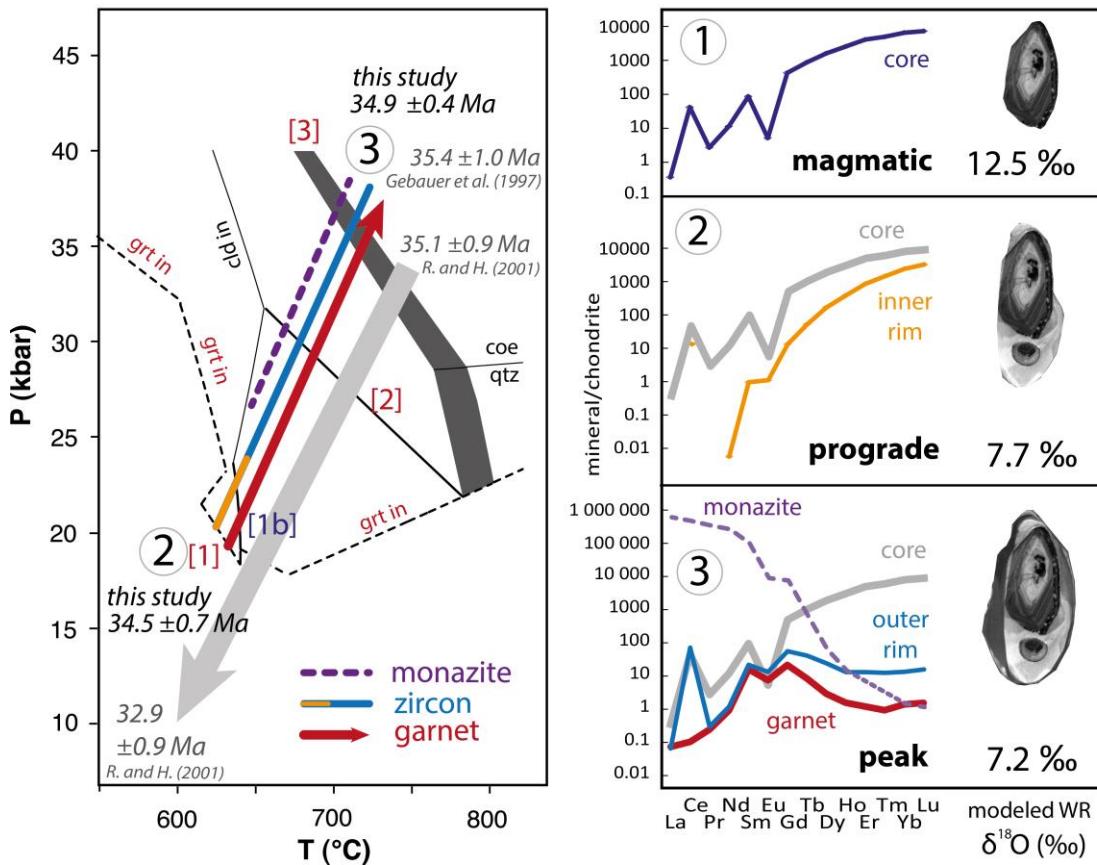


**Figure 2 - 8. Summary of P-T-time path (left) and zircon record (right). Garnet-forming reactions reported in the P-T path are from our modeling (Appendix figure A2 - 4) [1]: chl+ky+tc → grt+liq, [2]: bt+ky+tc → grt+phe+liq, [3]: ky+tc → grt+coe+liq. Main dehydration reaction [1b]: chl+phe → bt+ky+liq. Exhumation path (thick grey arrow) is from Rubatto and Hermann (2001). Ages are from DM51 zircon inner rims (2) and DM1C zircons rims (3). For the three major stages, magmatic, prograde and peak we report on the right a representative zircon from DM51 from a modified CL image, and the REE patterns from DM52 zircon and monazite, and DM51 garnet. The modelled bulk rock (WR) oxygen estimates are based on the average zircon core δ<sup>18</sup>O (magmatic stage) and the DM51, 52, 53 inner and outer zircon rim averages (prograde and peak stage, respectively)**

In all samples, prograde phosphate phases such as bearthite, florencite or apatite, as well as monazite are found as inclusions in zircon. This indicates that the transition of prograde phosphates to monazite occurred within the P-T range at which zircons recrystallized, potentially at the time of first pyrope growth in DM51 or the main garnet growth event in DM1C. Monazite records a similar chemical evolution as observed in garnet and zircon (Figure 2 - 2). In SiO<sub>2</sub>-poor samples DM51–53 as well as the outer growth zones in DM1C, monazite shows HREE and Y depletion and a weak negative Eu-anomaly. Based on the REE record, monazite is interpreted to recrystallize during the main prograde episode of garnet growth (22–40 kbar). Monazite yield

Alpine ages that are best determined for sample DM1C ( $34.7 \pm 0.5$  Ma). We conclude that monazite grew during prograde to peak Alpine metamorphism together with garnet and zircon outer rims.

## 4.2 Fluid-induced prograde zircon formation

The correlation of zircon formation to metamorphic conditions revealed that two distinct episodes of zircon recrystallization coincide with the major dehydration reactions. In Si-rich whiteschists, the main fluid-producing reaction is close to peak pressure where talc breaks down and garnet appears. Zircons retrieved from such a sample displays only one metamorphic overgrowth and inclusion compositions suggest rim formation close to peak metamorphic conditions. Zircons from Si-poor whiteschists present an additional inner rim that likely formed during the complete consumption of chlorite, representing the main fluid pulse in these rock types (Figure 2 - 4). The first fluid liberation event from the destabilisation of chlorite at  $640^{\circ}\text{C}$  and 22 kbar could correspond to the first generation of fluid inclusions (a NaCl-MgCl<sub>2</sub>-rich brine) described by Ferrando et al. (2009) during the initial growth of pyrope. The later fluid liberation events by destabilisation of biotite and talc at 29–37 kbar would correspond to a more solute-rich fluid of potentially supercritical character, containing Al, Si, Mg and a range of trace elements (Ferrando et al. 2009).

The distribution of inclusions in the zircons provides additional clues on the mechanisms of zircon formation during prograde fluid liberation. The great majority of inclusions are hosted within the inherited zircon cores. The magmatic zircon cores show signs of partial dissolution: the oscillatory zones are truncated and show embayments and are peppered with mineral and fluid inclusions. In DM51 and DM52, these inclusions contain talc, phengite and biotite whose chemistry is similar to what was experimentally obtained by Hermann (2003) for prograde to peak phengite and prograde biotite (Figure 2 - 4). These results complement a study by Schertl and Scheryer (1996) where they found prograde phases such as talc and chlorite in crushed zircon separates along with coesite and phengite with 3.50 to 3.55 Si pfu. These authors also found a single inclusion of pyrope that yielded the same composition as the core of the groundmass pyropes in the same sample. Schertl and Scheryer (1996) noted that most inclusions occurred in the central part of the zircon grains, and in the absence of in-situ dating work concluded that they were primary inclusions, and the whole zircon crystals metamorphic. By imaging, dating and measuring the composition of the inclusions in situ, we are able to determine that they are in fact secondary inclusions (as mentioned in Gebauer et al. 1997 on the basis of CL images), crystallising during partial dissolution of the magmatic cores during Alpine HP to UHP metamorphism. This is in agreement with a detailed study of zircon within a UHP gneiss recovered from the deep Chinese

Continental Scientific Drilling project, where coesite and jadeite were found within partially altered inherited cores (Zhang et al. 2009). Interestingly the metamorphic inclusions in zircons from the whiteschists are more abundant in the BSE-light, U-rich oscillatory zones (Figure 2 - 3b) which may have been selectively dissolved due to radiation damage and metamictisation. All these observations suggest that the main process for new zircon growth in the Dora-Maira whiteschists is related to fluid-induced dissolution-precipitation during metamorphism as previously suggested in other studies (Geisler et al. 2007; Rubatto et al. 2008; Tomaschek et al. 2003). The type of fluids rich in NaCl and MgCl<sub>2</sub> (Ferrando 2009) documented in the whiteschist have indeed been shown to enhance zircon dissolution (e.g. Rizvanova et al. 2000). Based on Zr mass balance in metamorphic minerals Kohn et al. (2015) have suggested that in UHP eclogites, metamorphic zircon should form during the retrograde path rather than during prograde metamorphism. Our study shows that partial dissolution of metamict inherited zircon and precipitation of newly formed zircon rims provides an alternative mechanism to form metamorphic zircon on the prograde path, mainly during episodes of intense dehydration or fluid-rock interactions.

### 4.3 Subduction rate

In the previous sections we have shown that the age of the outer zircon rim ( $34.4 \pm 0.4$  and  $34.6 \pm 0.4$  Ma) and that of monazite ( $34.5 \pm 0.5$  Ma) date the breakdown of talc at 35 kbar, 700°C. These ages are identical within uncertainty to the titanite age of  $35.1 \pm 0.9$  Ma obtained by Rubatto and Hermann (2001) for peak metamorphism in calc-silicate nodules within the coesite-bearing unit. The ages obtained for the inner zircon rim that likely grew during chlorite breakdown in sample DM51 and DM52 at ~22 kbar, 640°C are undistinguishable from that of the outer zones. Given that the uncertainty of single analyses is smaller than 0.5 Ma, we can assume that the subduction of the Dora-Maira whiteschists occurred within less than 1-2 million years, for a pressure difference of 13 kbar that correspond to a difference in depth of about 40 km. These values translate into a minimal burial rate of 2 cm/yr, which is comparable to exhumation rates calculated for the same unit by Rubatto and Hermann (2001). Our minimum burial rate is close to the Eocene convergence rate of 1.3 cm/yr (Ford et al. 2006) along a steep dipping slab as proposed by Carry et al. (2011), although our new data suggest it might have been even faster. Combining the prograde to peak (this study, Gebauer et al. 1997) and the retrograde ages (Rubatto and Hermann 2001) an exceptionally complete P-T-time path for the subduction and exhumation of this iconic UHP unit can be defined (Figure 2 - 8). Such detail in rates, particularly subduction/burial rates are hard to obtain because commonly prograde minerals readily recrystallize at the peak or during decompression.

#### 4.4 Equilibrium oxygen isotopic fractionation between peak metamorphic phases

Garnet, zircon outer rims and monazites have been shown to crystallise contemporaneously just before peak metamorphic conditions in each individual sample. Their oxygen isotope composition (Table 2) can thus be combined to produce a set of mineral-mineral fractionation values for oxygen. On average  $\Delta^{18}\text{O}$  (zircon-monazite) obtained from our data is  $0.1 \pm 0.7\text{‰}$  and  $\Delta^{18}\text{O}$  (zircon-garnet) is  $0.1 \pm 0.5\text{‰}$  (Table 2 - 2). The temperature at which these minerals formed is estimated to be 680–720°C (Hermann 2003; this work). The zircon-pyrope results are equal within error to values predicted at 700°C by previous empirical studies of  $\Delta^{18}\text{O}$  (zircon-almandine) =  $-0.07\text{‰}$  (Valley et al. 2003 and references therein) as well as using the increment method (0.0 ‰, Zheng 1993a).

**Table 2 - 2. Sample average  $\delta^{18}\text{O}$  and calculated fractionation values between zircon, monazite and garnet**

Sample	Zircon rims		Monazites		Garnet		Zirc.-monazite		Zircon-garnet	
	$\delta^{18}\text{O}\text{‰}$	2se	$\delta^{18}\text{O}\text{‰}$	2se	$\delta^{18}\text{O}\text{‰}$	2se	$\Delta^{18}\text{O}\text{‰}$	2se	$\Delta^{18}\text{O}\text{‰}$	2se
DM1C	6.37	0.28	6.34	0.69	6.29	0.29	0.03	0.74	0.08	0.40
DM51	6.35	0.28	6.22	0.69	6.20	0.29	0.13	0.74	0.15	0.40
DM52	6.74	0.29	6.64	0.69	6.86	0.28	0.10	0.75	-0.12	0.40
DM53	6.26	0.29	6.28	0.68	na		-0.02	0.74	na	
					Average		0.06		0.04	

This is the first study looking at zircon-monazite fractionation directly. From previous works, similar values can be calculated at 700°C for  $\Delta^{18}\text{O}$  quartz-zircon (2.41 ‰, Valley et al. 2003; 2.46 ‰, Trail et al. 2009) and quartz-monazite (2.32 ‰, Breecker and Sharp 2007, 1.58 ‰ for Ce-monazite to 2.07‰ for huttonite, Rubatto et al. 2014). This set of previous values predicts a  $\Delta^{18}\text{O}$  (zircon-monazite) at 700°C from  $-0.9\text{‰}$  to  $-0.1\text{‰}$ : our value of  $0.1 \pm 0.7\text{‰}$  is consistent with both within error, but agrees best with the quartz-monazite fractionation reported by Breecker and Sharp (2007).

In addition to previous studies, these fractionation values can be used as an additional tool to assess if accessory phases crystallised in equilibrium with major minerals such as garnet, especially in cases where external fluid influx might lead to a significant change in oxygen isotope values of mineral domains. Any deviation from the described fractionation would indicate

disequilibrium due to external fluid influx or temperature changes. Together with trace elements and geochronology at the mineral scale, oxygen isotopic equilibrium between mineral zones can thus be a valid tool to investigate the P-T-time-fluid path of metamorphic rocks.

#### **4.5 Evolution of the oxygen isotope composition of the whiteschists from protolith to subduction**

The oldest remnants of the evolution of the Dora Maira whiteschists are preserved in the inherited zircon cores. The least-altered zircon cores display steep REE patterns with enrichment in HREE (Figure 2 - 2), and have a marked negative Eu-anomaly ( $\text{Eu}/\text{Eu}^* = 0.02\text{-}0.06$ ); this signature is typical of granitic zircons (Hoskin and Schaltegger 2003). The best preserved zircon cores yield Permian ages that are comparable to the ages measured in zircons from the surrounding orthogneiss and other zircon cores in whiteschist analysed by Gebauer et al. (1997). This provides strong evidence that the orthogneiss and whiteschists derived from the same granitic protolith (e.g. Chopin and Schertl 1999). Zircon magmatic cores across the samples yield an average  $\delta^{18}\text{O}$  of  $10 \pm 1 \text{‰}$ . This contrasts with metamorphic zircon domains that yield  $\delta^{18}\text{O}$  values of  $6.4 \text{‰}$ .

In order to quantify the bulk-rock  $\delta^{18}\text{O}$  change in regard to contributions from temperature, co-crystallising assemblage evolution or metasomatic fluid infiltration, we modelled the  $\delta^{18}\text{O}$  composition of rock-forming minerals at given temperatures, in equilibrium with the measured zircon values. This is done in a similar way as in Martin (2014b): the bulk rock-oxygen is calculated as the sum of the modal contribution of equilibrium fractionation values for minerals. Zircon is present in the model as a spectator phase for which an oxygen value is fixed or calculated but does not participate in the redistribution of oxygen isotopes (its mode is set to 0). The fractionation coefficients between minerals are taken from Zheng (1993a and b) for consistency. Using that set of fractionation coefficients, quartz-water calculations are similar to what is obtained using the most recent Hu and Clayton (2003) experimental coefficients, albeit  $0.2 \text{‰}$  lower at  $600^\circ\text{C}$ . For other phases, as shown in Kohn (1993), the overall trends obtained for each mineral should not be influenced significantly by the uncertainty related to fractionation coefficients nor small changes in mineral modes.

For the granitic protolith of the whiteschists, the main phases and their modal abundance are calculated from a CIPW norm using the DM989 whole rock (WR) major element analysis from Ferrando et al. (2009). The three major phases quartz, albite and orthoclase are used in the calculation (Table 3). Using the average oxygen value measured in zircon cores ( $10\text{‰}$ ) the modelled WR  $\delta^{18}\text{O}$  of the metagranite is  $12.5\text{‰}$  for an estimated magmatic temperature of  $750^\circ\text{C}$  (a higher temperature of  $850^\circ\text{C}$  would shift the value to  $12.1\text{‰}$ ). A calculation based on  $73\text{wt}\%$



SiO<sub>2</sub> content following the equation of Lackey et al. (2008) returns a value of 12.0‰. This agrees with quartz measurements in the orthogneiss that gave a δ<sup>18</sup>O of 11.5 to 11.9‰ (Sharp et al. 1993). Such high values are characteristic of S-type granites that inherit this signature from surface-altered sediments (e.g. Jeon et al. 2012; Lackey et al. 2008).

The peak metamorphic assemblage for the two types of whiteschist DM1C and DM51 is reconstructed using mineral modes from thin section observations (Figure 2 - 1). Using the zircon outer rims values of 6.4‰ in both samples, the modelled WR oxygen isotope composition is 8.4 ‰ for DM1C, and 7.4‰ for DM51 at a peak temperature of 720°C (Hermann 2003). This model demonstrates that the measured zircon core-rim and garnet δ<sup>18</sup>O values reflect a change in the bulk rock of -5.1 (maximum value for DM51) to -3.7 ‰ (minimum value for DM1C), which was necessarily produced by external fluids.

**Table 2 - 3. Whole-rock (WR) oxygen isotope modelling from zircon values for Ferrando (2009) DM989, peak conditions DM1C and DM51**

Granite DM 989 CIPW norm (T=750°C)			Whiteschist DM1C Thin section (T=720°C)			Whiteschist DM51 Thin section (T=720°C)		
mineral	mode	δ <sup>18</sup> O‰	mineral	mode	δ <sup>18</sup> O‰	mineral	mode	δ <sup>18</sup> O‰
Quartz	35	13.1	Quartz	49	9.7	Quartz	3	9.7
Orthoclase	31	12.1	Garnet	18	6.4	Garnet	34	6.4
Albite	23	12.1	Kyanite	3	7.9	Kyanite	7	7.9
			Phengite	30	7.8	Phengite	56	7.8
<i>Zircon</i>	<i>0</i>	<i>10.0</i>	<i>Zircon</i>	<i>0</i>	<i>6.4</i>	<i>Zircon</i>	<i>0</i>	<i>6.4</i>
WR		12.5	WR		8.4	WR		7.4

In the case that DM1C and DM51 evolved in a closed system from 15kbar, 600°C to 40kbar, 720°C, the prograde variation of equilibrium δ<sup>18</sup>O for the metamorphic minerals can be calculated using the modal information extracted from the Theriak data. In this way, δ<sup>18</sup>O values obtained in the different zircon zones can be interpreted in terms of the evolution of the whole rock (Figure 2 - 9).

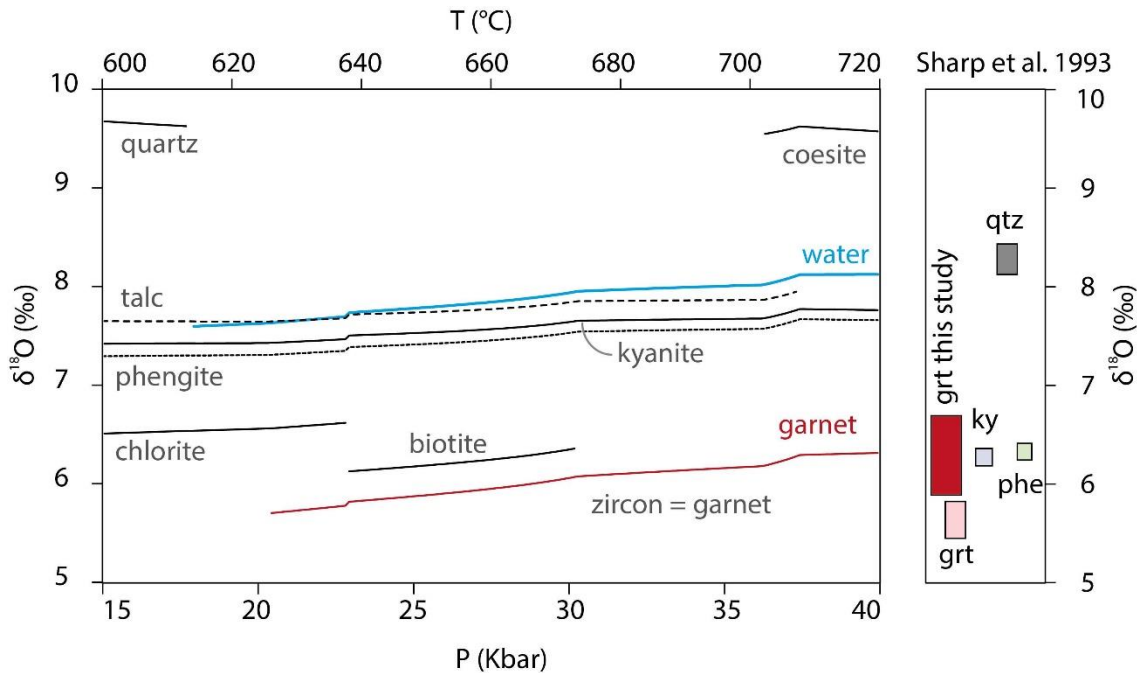


**Figure 2 - 9. Modelled oxygen isotope values for different minerals during prograde metamorphism of DM51, at a constant bulk rock  $\delta^{18}\text{O}$ . The right panel shows the measured values for mineral composition from Sharp et al. (1993) and this study (garnet)**

The DM51 modelling results differ significantly from the measured values of Sharp et al. 1993. For instance, the modelled  $\delta^{18}\text{O}$  of quartz is 1.2‰ higher than the quartz measured by Sharp et al. (1993). The fractionation coefficient used for garnet-quartz in Zheng (1993) predicts a bigger  $\Delta^{18}\text{O}$  quartz-garnet than admitted in most recent studies (eg. Lackey et al. 2006; Valley et al. 2003). This will not change the behaviour of other phases much, given the low modal abundance of quartz but may generate an offset in the values for other phases as they are calculated from the measured garnet. Given that the  $\delta^{18}\text{O}$  of garnet measured by Sharp et al. (1993) is 0.8‰ lower than the garnet we measured in this study, part of the observed offset could also be due to a difference in the bulk rock  $\delta^{18}\text{O}$  between the two samples. As other fractionation coefficients, such as garnet-kyanite and garnet-phengite, seem to be overestimated by the increment method calculations of Zheng (1993a,b) compared to what is measured by Sharp et al. (1993), the prograde zoning modelled in minerals is likely to be of the maximum amplitude expected for this sample. Our results for DM51 (Figure 2 - 9) show that along the prograde path, the variation in  $\delta^{18}\text{O}$  expected in zircon and garnet is small, of the order of +0.6 ‰ between core and rim. 0.6 ‰ is within the analytical precision of single measurements for our analyses, so the presence of such zoning in DM51 garnet cannot be tested. Nevertheless, we observe no variation from garnet core to rim in DM51 outside analytical precision, nor in between zircon inner and outer rims. This is consistent with the constant whole rock hypothesis used to produce the model. In the other sample DM1C, garnet and zircon most likely crystallised close to peak pressure and temperature in a single event, and are thus expected to yield homogeneous  $\delta^{18}\text{O}$  signatures. Therefore we can

conclude that the oxygen isotopic composition of the UHP metamorphic minerals is the product of internal fractionation within a bulk rock with a  $\delta^{18}\text{O}$  of 7.4–8.4‰. This  $\delta^{18}\text{O}$  value is well below the protolith value of 12‰ and was acquired before UHP conditions. The timing and conditions of the process that led to this isotopic signature are discussed below.

#### 4.6 Metasomatic event

Our new oxygen isotope, trace element and age data of inherited zircon combined with bulk rock compositions (Schertl and Schreyer 2008; Ferrando et al. 2009) convincingly show that the whiteschists represent a metasomatised granite. Additionally, ages of the zircon cores analysed by Gebauer (1997) yield a Permian age that is identical to what is measured in the surrounding metagranite (Paquette et al. 1999), suggesting that the whiteschists have evolved from the metagranite by a metasomatic process after the crystallisation of the magmatic zircons. The context in which this fluid circulation occurred is debated (e.g. discussion in Schertl and Schreyer, 2008), but a number of studies have attributed metasomatism to prograde Alpine metamorphism (Compagnoni and Hirajima 2001; Ferrando et al. 2009; Sharp and Barnes 2004).

Peak zircon, monazite and garnet (this study) as well as other metamorphic phases analysed by Sharp et al. (1993) are homogenous in  $\delta^{18}\text{O}$  and have equilibrium compositions. The S-type metagranite and metasedimentary sequence that outcrop in the same unit are expected to have significantly different  $\delta^{18}\text{O}$  values (metagranite ~ 12‰, Sharp et al. 1993) than the 7.4–8.4 ‰ of the whiteschists. The absence of measurable zoning in garnet and metamorphic zircon within the whiteschists, as predicted by constant whole rock modelling (Figure 2 - 9), indicates that there was no significant fluid influx into the whiteschist from either the metagranite or metasediments at conditions where garnet was stable, i.e. HP to UHP. On the other hand, Vielzeuf et al. (2005a) documented oxygen isotope zoning in a garnet within the paragneiss surrounding the whiteschists which is similar to the superzoned garnet of Compagnoni and Hirajima (2001). They measure an almandine core at 7.5–8.0‰ and a thin pyrope rim at 5.0–5.5‰ and attributed this to high-pressure overgrowth. This result can be interpreted as the late HP-UHP influx of a fluid derived from the neighbouring whiteschists layers into the gneiss.

The oxygen results, together with the thermodynamic modelling indicate that during high pressure metamorphism fluids in the whiteschists were internally derived, and that they already had acquired their Mg-rich and low  $\delta^{18}\text{O}$  signature. Therefore we conclude that the main metasomatic event that caused the granite to whiteschist transformation occurred prior to HP –UHP metamorphism, that is before a significant dehydration reaction modelled in the whiteschists at ~22kbar, 640°C which produced the first garnet. This is consistent with what was previously

established on the basis of fluid inclusions in the main whiteschist lens (Compagnoni and Hirajima 2001; Ferrando et al. 2009). It has been suggested that metasomatism of the whiteschists occurred early in the metamorphic path and was the result of serpentinite dehydration in the lower levels of the slab during initial subduction (Compagnoni and Hirajima 2001; Ferrando 2012). This scenario is difficult to reconcile with the observation that the gneisses surrounding the whiteschist appear unaffected by such external fluid influx. Instead, the available data suggest that the gneisses were locally infiltrated by fluids that derive from the whiteschists. Therefore it seems more feasible that the alteration of the S-type granite occurred prior to subduction. Franz et al. (2013) compiled worldwide occurrences of whiteschists and looked at potential protolith formation. They concluded that the best explanation for the Dora-Maira whiteschists is a chemical weathering to produce a kaolinite-chlorite rich protolith. In context of the tectonic evolution between Permian intrusion and Alpine high-pressure metamorphism, the simplest explanation is that the S-type granites were metasomatised in an oceanic environment, where large fluid-rock ratios can achieve significant shifts in  $\delta^{18}\text{O}$ . We speculate that the continental sequence and S-type granite of the Dora-Maira was a continental sliver that was part of a hyper-extended margin during the well-documented Jurassic rifting episode, as reconstructed by Beltrando et al. (2010). Focussed circulation of seawater along shear zones is common in submerged extensional settings, such as rifting or oceanic spreading when a high thermal gradient is present (e.g. McCaig et al. 2007). Such localised fluid-rock interaction could lead to a kaolinite/muscovite-chlorite alteration. From the modelled chlorite ( $\delta^{18}\text{O}\sim 6.5$ ) and phengite ( $\delta^{18}\text{O}\sim 7.3$ ) oxygen isotopes at 15 kbar, 600°C, we can infer that the hydrothermal fluid acting at  $T\leq 350^\circ\text{C}$  had a  $\delta^{18}\text{O}$  of maximum 7 ‰ (more likely  $< 7$  ‰). This scenario is also supported by the occurrence of similar whiteschists lithologies in the same tectonic setting along the Alpine orogeny (review in Ferrando 2012).

## 5 Conclusions

The systematic study at the microscale of garnet, zircon and monazite composition and oxygen isotopes together with age constraints from the accessory minerals allows reconstruction of a detailed P-T-time-fluid path for the Dora Maira UHP whiteschists. Zircon growth during prograde metamorphism is related to fluid pulses in the whiteschists due to the breakdown of chlorite and talc. Fluid circulation led to the partial dissolution of inherited, U-rich, metamict zircon cores and the precipitation of metamorphic rims. The cavities resulting from zircon dissolution were filled with metamorphic phases and fluids. The tight link between metamorphic reactions and zircon recrystallization allows constraining subduction rates of the Dora-Maira Massif. Pre-garnet and syn-garnet zircon rims, as well as syn-garnet monazite give the same age of  $34.5\pm 0.7$  to  $35.1\pm 0.5$  Ma, implying a prograde subduction rate of a few cm/yr between  $\sim 22$  and 35 kbar.

Garnet, zircon and monazite yield  $\delta^{18}\text{O}$  values of 6-7 ‰, within error identical for temperatures of 700°C - implying close to 0 ‰ fractionation at this temperature between these minerals. To produce these values, it is concluded that an external fluid with a low  $\delta^{18}\text{O}$  of at most 7 ‰ was responsible for the metasomatism that transformed the original S-type granite into the Mg-rich whiteschists. Moreover, there is no evidence for external fluid input during HP to UHP metamorphism of the whiteschists. We conclude that the significant metasomatic event that affected the original granite occurred by seafloor alteration during Permian extension.



# Chapter 3

## Geodynamic setting of the Halilbağı unit, Tavşanlı zone, Turkey

### 1 Introduction

The HP-LT Tavşanlı zone of central Turkey hosts lawsonite-bearing eclogites, which are of rare occurrence worldwide (Clarke et al. 2006; Tsujimori et al. 2006), attesting to its cold exhumation (Whitney and Davis 2006). The Halilbağı unit is the tectonic unit that records the highest P-T conditions within the Tavşanlı zone. It is thus an ideal area to study prograde subduction processes, such as fluid circulations that are the main aim of this PhD thesis, and will be in the object of the next chapter. This chapter aims at reviewing literature and new geochemical data on the Halilbağı unit in order to draw a picture of the geodynamic setting of emplacement of its different lithologies and the chronology of events. This data is provided to support the interpretation of the protoliths and early evolution of these rocks in Chapter 4. Indeed, Chapter 4 will show that most oxygen isotope exchanges happen in the pre-subduction stages for the Halilbağı rocks.

In this chapter, I present new U-Pb zircon data as well as whole-rock major and trace element data that complement the work done in the western Tavşanlı zone by Özbey et al. (2013) and Okay et al. (2008) to constrain the geodynamic setting of the Halilbağı unit, and the age of its formation and subduction. This provides the context for the study of trace element and fluid migration during the subduction of this unit that is developed in **Chapter 4**.

I will refer to the Halilbağı Formation (Okay and Whitney 2010) as the Halilbağı ‘unit’ in this chapter as it carries less of an *a priori* genetic meaning.

#### 1.1 Geodynamic setting

The Tavşanlı zone is part of the Izmir-Ankara suture, one of the main suture belts in Turkey. It formed during the Cretaceous subduction of the northern Tauride-Anatolide micro continent under the Eurasian continent (Okay 1984; Okay and Kelley 1994). This geodynamic system obducted the large Anatolian ophiolite, and the long-lived subduction of continental material now forming the Tavşanlı zone, the Afyon zone and in part the Menderes Massif (Plunder et al., 2013, **Figure 3 - 1**). This work deals with the Tavşanlı zone, which represents the distal continental margin (Çetinkaplan et al. 2008) or the northernmost micro-continent (Özbey et al. 2013), subducted to the depth of 80 km (Okay 2002).

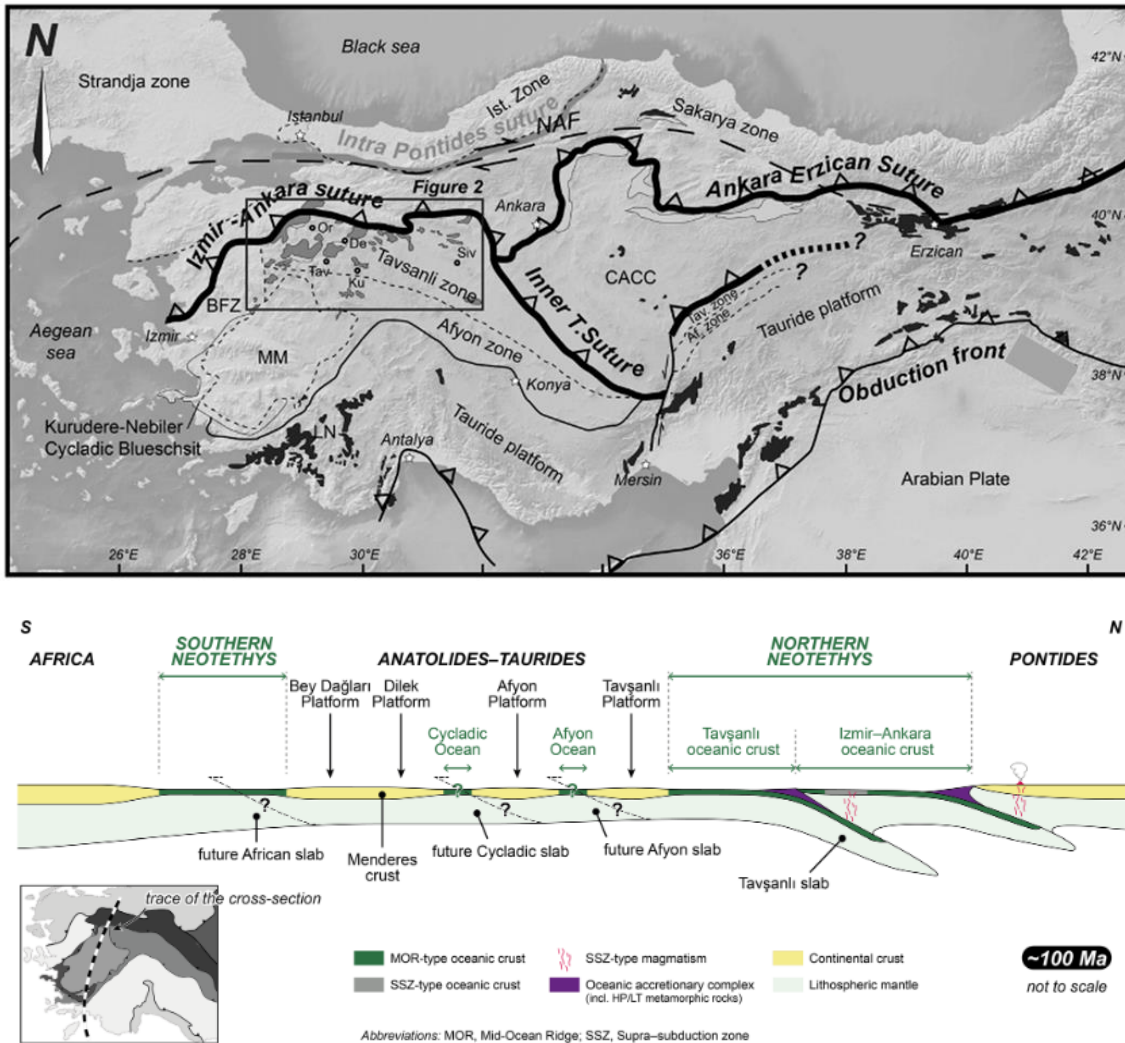


**Figure 3 - 1** Position of the Tavşanlı zone in Anatolia. a. main suture zones, from Plunder et al. (2013) b. geodynamic structure of the Pontides-Anatolides in the early Cretaceous, Pourteau et al. (2015).

Following work summed up in Okay (Okay 1986; Okay 2002), the Tavşanlı zone is divided into an Ovacık unit made of tectonically imbricated oceanic lithologies in incipient blueschist metamorphism, overlaying a metasedimentary pile dominated by graphitic schists and marbles named the Orhaneli unit. The latter shows HP-LT assemblages. Both units are capped by an ophiolitic slice, and intruded by Eocene granitoids (Figure 3 - 2). Finer subdivisions are proposed by Plunder et al. (2013, 2015) and will be discussed below. The HP-LT lithologies crop out mainly along the Izmir-Ankara-Erzincan oceanic suture north of the cities of Tavşanlı and Mihaliçcik. Another HP-LT massif is situated south of the suture, to the west of the town of Sivrihisar. Lawsonite eclogite pods can be found amongst the blueschists in the latter locality, and are the higher-pressure assemblage recorded in the Tavşanlı zone.



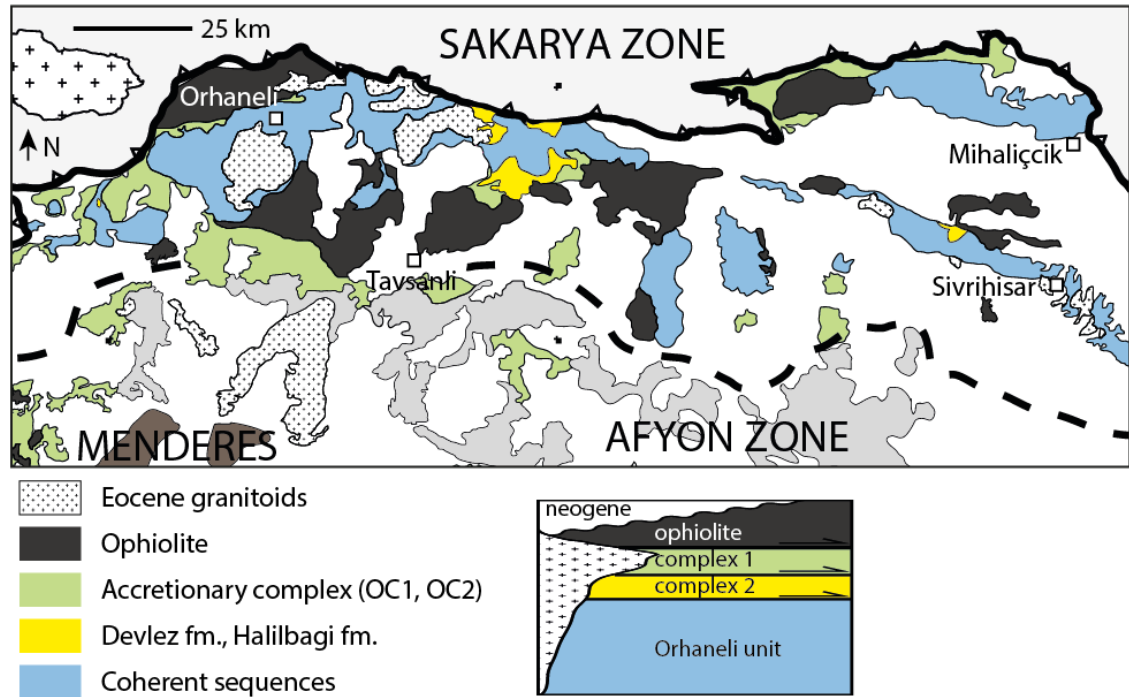


**Figure 3 - 2** Tectonic units in the Tavşanlı zone, figure modified from Plunder et al. (2013), with the addition of the Devlez fm. and the Halilbağ fm. as oceanic complexes (see discussion).

Most geodynamic studies have focused on the western part of the Tavşanlı zone, where the continental margin sequence is more extensive and less deformed (e.g. Özbey et al., 2013). In this area, three units have been distinguished in the Orhaneli group: the Kocasu Formation (graphite-rich quartz micaschists with metabasic intercalations containing mainly Ordovician and Permian-Carboniferous detrital zircons -youngest ages around 310 Ma, Okay et al., 2008) the Inonü marble (pure marble containing Late Triassic conodonts, Kaya et al., 2001), and the Devlez Formation (composite metavolcanic and metasedimentary sequence containing mainly metabasalts). This succession is considered coherent in most previous studies (Okay 1980; Okay and Whitney 2010; Özbey et al. 2013; Plunder et al. 2013), as part of a passive margin. This has been challenged by Çetinkaplan et al. (2008), Plunder et al. (2015) and Pourteau et al. (2016): contrasting metamorphic grades are identified in the Devlez fm. compared to the underlying Kocasu fm. (Plunder et al. 2015), and there is no evidence for widespread volcanism in the Cretaceous in this area (Çetinkaplan et al. 2008; Pourteau et al. 2016) that could explain the presence of metabasites. These authors interpret the Devlez fm. as tectonic imbrication of oceanic slices. The Orhaneli group is tectonically overlain by oceanic complexes made of metabasites, radiolarian cherts and shales previously known as the Ovacık complex (e.g. Okay and Whitney, 2010). On the basis of structural position and P-T determinations, Plunder et al. (2013) distinguish slices OC1 at 4-8 kbar, 250-300°C and OC2 at 10.15 kbar and 350°C. The Devlez fm. is interpreted as the lowest-level, highest-PT, oceanic complex : OC3 at 22 kbar, 480°C (Plunder et al. 2015).

In the Sivrihisar massif in the East of the Tavşanlı belt, two main tectonic slices appear in the structural position of the Orhaneli group and the oceanic complexes present in the West: the Sivrihisar fm. (Gautier 1984; Okay and Whitney 2010) and the Halilbağı unit. The Sivrihisar fm yields a coherent succession of micaschists with metabasite lenses overlain by marbles (Davis and Whitney, 2006; Çetinkaplan et al., 2008; Gautier 1984, Figure 3 - 3), similar to the Kocasu formation and Inonü marble sequence. This Sivrihisar fm. is potentially divided by internal faults, as suggested by Davis and Whitney (2006).

The Halilbağı unit, the unit of interest in this study, differs in some ways from units that can be observed in the western parts of the Tavşanlı Zone. It is made of metabasites, schists, metachert, metagabbros, serpentinite lenses and marble in a disturbed and folded succession, overlying the Sivrihisar Formation by a contact that could be tectonic (Davis and Whitney 2006; Çetinkaplan et al. 2008), see Figures 3 -3 and 3 - 6. While the main structure and lithological similarities indicate that it could be part of the Orhaneli group, its exact stratigraphic correspondence to the western section is more difficult to establish. Okay and Whitney (2010) assumed the Halilbağı unit to be an equivalent to the western Devlez Formation. On the other hand, Cetinkaplan et al. (2008) and Pourceau et al. (2016) have postulated that both the Devlez fm. and the Halilbağı unit are an equivalent of the oceanic complexes which overlie the Orhaneli group in the west (Ovacık complex, more precisely the Devlez fm. as Oceanic complex 3 in Plunder et al., 2015).

This study aims at providing new geochemical and age data to further assess the position of the Halilbağı unit in the Tavşanlı zone, and the geodynamic conditions in which its protoliths were formed.

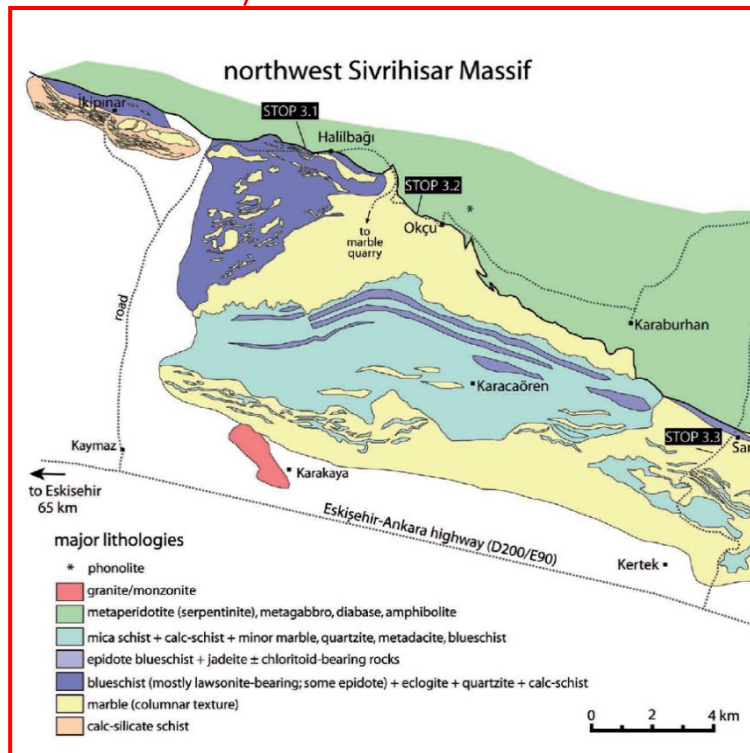
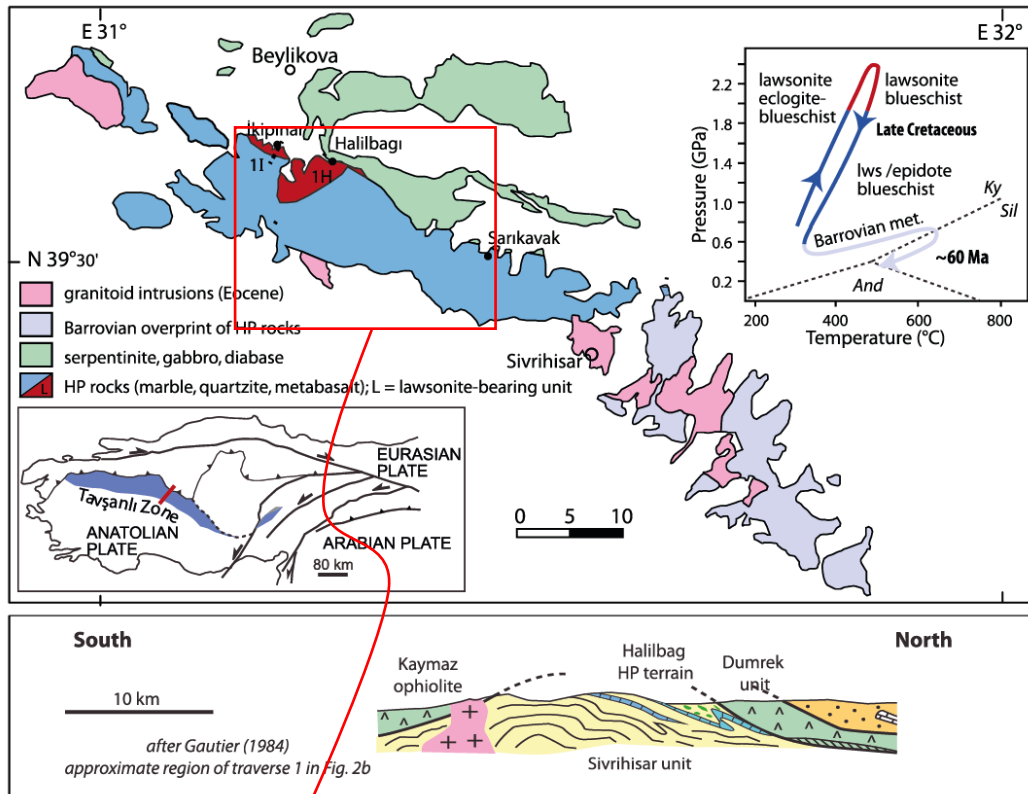


Figure 3 - 3 Location of the study area, after Whitney et al. (2014) and Okay and Whitney (2010). The lower panel shows dominating lithologies and lithological discontinuities, the thick black line indicates the contact separating the Halilbaği unit (south) and the Dumrek metaperidotite unit (north).

## 1.2 Cretaceous subduction

The overall abundance of lawsonite in the Tavşanlı zone and its preservation shows that these are HP lithologies that have gone through exhumation following an unusually low thermal gradient that did not allow the lawsonite to transition to clinozoisite (Tsujimori et al. 2006; Whitney and Davis 2006). Several studies have been conducted on the petrography and the metamorphic assemblages present along the Tavşanlı zone (most recent P-T estimates in **Table 3 - 1**).

**Table 3 - 1 Literature P-T estimates in the Tavşanlı zone. Colour coding refers to Figure 3 - 2.**

Unit	Reference	Lithology	Method	P estimate (kbar)	T estimate (°C)
Halilbağı unit	Cetinkaplan et al. (2008)	Lawsonite eclogite (peak assemblage)	Grt-cpx (T) and grt-cpx-phen-ky-qz (P)	24 ±1	460 ±25
			DOMINO pseudosection	21-25	430 - 470
		associated metabasite (peak assemblage)	Grt-cpx (T) and grt-cpx-phen-ky-qz (P)	24 ±1	435 - 472
			DOMINO pseudosection	23 - 26	453 - 480
	Davis and Whitney (2006)	Lawsonite eclogite	PerpleX pseudosection	26	500
	Davis and Whitney (2008)	Lawsonite eclogite	PerpleX pseudosection	22 - 24 (peak)	520
18 - 20 (blueschist facies transition)				480-520	
Sivrihisar fm.	Cetinkaplan et al. (2008)	Jd-gl-ctd schists	Mineral assemblage	ca. 24	ca. 430
Orhaneli – OC1	Okay (1982)	Basic volcanics	Mineral assemblage	5 - 8	150 - 200
	Topuz et al. (2006)	metabasite	Mineral assemblage	4.6 - 6.5	200 ±50
	Plunder (2013)	metabasites	Mineral assemblage	4 - 8	250 – 300
Orhaneli – OC2	Plunder (2013)	Carpholite-bearing rock	DOMINO pseudosection	10 - 15	300 - 400
	Plunder et al. (2015)	Carpholite-bearing rock	DOMINO pseudosection	11.5 ±3.5	350 ±50
Orhaneli – OC3 Devlez fm.	Plunder et al. (2015)	metabasite	DOMINO pseudosection	13.5 - 20.0	460 ±30
Orhaneli – Kocasu fm.	Okay et al. (2002)	greyschist	Thermocalc	24 ±3	430 ±30
	Plunder (2013)	greyschists	RSCM Tmax		470 - 550
	Plunder et al. (2015)	greyschists	DOMINO pseudosection	23 - 25	470 - 510
		greyschists	RSCM Tmax		480 - 550

In the entire Tavşanlı belt, both the Orhaneli group and the overlying accretionary complexes have undergone HP-LT metamorphism (Okay and Whitney 2010; Plunder et al. 2015). In the western part of the belt, coarse-grained lawsonite blueschist assemblages can be observed in the Devlez fm (Okay 1980). The estimated P-T is 24 kbar, 430°C (Okay 2002). In the Halilbağı unit, blueschists contain lawsonite-eclogite pods showing a slightly higher grade of metamorphism (22-24 kbar, 520°C, Davis and Whitney, 2006). The Orhaneli group and accretionary complexes can be considered as mono-metamorphic in most areas. A barrovian metamorphic imprint is observed east from the town of Sivrihisar (

Figure 3 - 3). It postdate the exhumation of the blueschist and eclogites (Seaton et al., 2009, 2014; Whitney et al., 2011).

In the Halilbağı unit, the lithologies show a slightly higher grade metamorphism: some metabasites are preserved as lawsonite-eclogites (lws-grt-omp-phen(-gln), see Davis and Whitney, 2006; Çetinkaplan et al., 2008). The calculated pressures are similar in the eastern and the western part of the belt: a slightly higher temperature in the Halilbağı unit compared to similar lithologies (e.g. Devlez fm.) is the reason for these differences (e.g. 520°C, Davis and Whitney, 2008).

Dating the HP event in the Tavşanlı zone has proved difficult. Early attempts by K-Ar (Cogolu and Krummenacher 1967) and Ar-Ar on glaucophane and white mica (Okay and Kelley 1994) gave ages ranging from 65 Ma to 108 Ma. A comprehensive list of ages obtained in the Tavşanlı zone can be found in Fornash et al. (2016).

The chronology established by recent studies in the Tavşanlı zone yields a range between ca. 100 Ma (subduction initiation) and ca. 50 Ma (collision). The main events identified in the literature are:

- The obduction of the ophiolitic units at 101– 93 Ma (Ar-Ar on amphibole, Harris et al. 1994; Önen 2003)
- High-pressure metamorphism between 91 Ma (peak) and 83 Ma (retrograde blueschist) (Lu-Hf on lawsonite and garnet, Mulcahy et al. 2014), similar ages are obtained by UV-LAMP Ar-Ar on phengite by Fornash et al. (2016).
- Barrovian metamorphism at 69-59 Ma (Ar-Ar on muscovite, Seaton et al. 2009, 2014)
- Intrusion of granitoids around 60-40 Ma (many methods, e.g. Delaloye & Bingöl 2000)

Ar-Ar dates on phengite and glaucophane related to the high-pressure event yield a big span in ages from 200 Ma to 60 Ma, and much care is needed in their interpretation given the possibility of excess argon highlighted in Sherlock and Kelley (1999), Sherlock and Arnaud (1999).

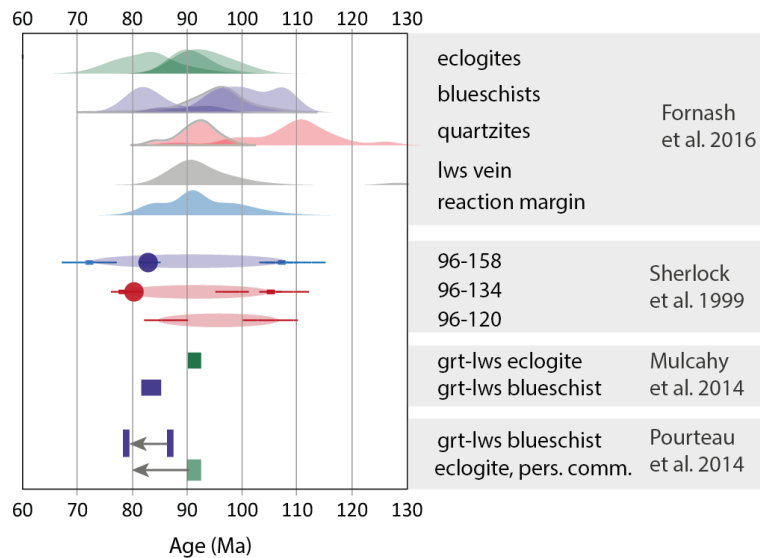


**Figure 3 - 4 Summary of ages in the Halilbağı unit. Ages from Fornash et al. (2016) are UVLAMP Ar-Ar on phengite represented as probability density plots grouped by lithological type, ages from Sherlock et al. (1999) UVLAMP Ar-Ar on phengite; the two extreme dates are represented by a  $2\sigma$  bar and an ellipse represents the spread between the youngest and oldest date in the same sample. Circles represent Rb-Sr ages on phengite. Isochron ages from Mulcahy et al. (2014) and Pourteau et al. (2014) are represented by boxes of  $2\sigma$  width. Arrows represent prograde/peak and retrograde ages in the same sample.**

In the Halilbağı unit itself, only metamorphic ages have been reported and Ar-Ar ages span a large range. Fornash et al. (2016), using the UV-LAMP method, find ages of 90-93 Ma for phengite in textural equilibrium with eclogite-facies minerals, which are attributed to peak metamorphism, and ages of 81 Ma for epidote-eclogites ascribed to the retrograde path. The variety of other dates they measured (75 to 127 Ma, **Figure 3 - 4**) are attributed to different grades of recrystallization linked to deformation and fluid availability. A much more restricted range is obtained from blueschists where Rb-Sr on phengite and Lu-Hf on mineral-rock isochrons agree in the 79-85 Ma range. In an eclogite, an older age of 91 Ma is obtained by Mulcahy et al. (2014), suggesting peak metamorphism was reached earlier in this rocktype.

U-Pb analysis in this study aims at providing complementary information towards dating the metamorphic event.

## 2 Methods

### 2.1 Whole-rock geochemistry

Major elements were measured on fused tabs at Geoscience Australia (GA) with Liz Webber and Bill Pappas. Fused tabs were produced using an Initiative Scientific Products Fusilux 4X4 Fusion Machine using a proportion of 6.000 g of flux for 1.000 g of sample, fusing at 1100°C for 10 min (13 min for carbonates) in platinum crucibles. Some iodine vapor is used to get the fused tabs to

separate better from the platinum mouldables. Two fluxes were used: X-ray flux 12:22 (35.3%  $\text{Li}_2\text{B}_4\text{O}_7$  - tetraborate, 64.7%  $\text{LiBO}_2$  – metaborate) for silicates and X-ray flux 57:43 (57% tetraborate, 43% metaborate) for samples that contained more than 30%  $\text{CaCO}_3$ . The fluxes are certified for containing 0-1 ppm of Pb, Ni, Mn, Cd, Zn, Co, Ag; 1-5 ppm K, Cu, Se, As, Al, Sn, Na, Fe; 2-10 ppm Si, S, Ca and Mg. Powder aliquots were measured on a C/H/moisture analyser Leco RC-612 at GA. Some Leco measures giving inaccurate results had to be repeated.

Fused tabs were recovered from XRF analysis and mounted in epoxy. They were cut in their centre and polished using 3 and 1  $\mu\text{m}$  diamond paste. WR trace elements were measured at the RSES with an ArF excimer laser coupled to a quadrupole Inductively Coupled Plasma Mass Spectrometer (ICP-MS) Agilent 7700 at the Research School of Earth Sciences – RSES – at ANU, using the setup described in Eggins et al. (1998). The laser was tuned to a frequency of 5 Hz and energy of 50 mJ (corresponding to a HV of around 26-27 kV). The spot size was set to 103  $\mu\text{m}$ . 20 s were measured on the background before analysis and 45 s for the signal. The reported value is the average of 3 spots in the same tab. NIST 610 and 612 were used for high (>100 ppm) and low-concentration elements respectively and BCR-2G was used as a secondary standard. Reproducibility and accuracy as assessed on the BCR-2G glass were within 10% or less across all analysed elements. The data was reduced with the freeware Iolite (Paton et al. 2011) and its data-reduction scheme for trace-elements (Woodhead et al. 2007).

## 2.2 SHRIMP U-Th-Pb zircon dating

Zircons were separated from crushed samples using a combination of magnetic and heavy liquid separation. They were mounted in 1 inch epoxy mounts and imaged in reflected light, secondary electrons (SE) and cathodoluminescence (CL) using a JEOL-JSM\_6610A SEM at RSES, using an acceleration voltage of 15 kV and a working distance around 25 mm.

Magmatic and metamorphic zircons were dated using the SHRIMP II following the method outlined in Gauthiez-Putallaz (2016) during two sessions. Zircon U-Pb dating was performed on the SHRIMP II and SHRIMP RG at RSES, according to the method described in Williams (1998). Standards and unknown were analysed with a spot size of around 20x25  $\mu\text{m}$ . Temora zircon (417 Ma, Black et al., 2003) was used as standard for internal mass fractionation and U concentration (160 ppm). Data reduction was performed using MS Excel extensions SQUID 2.5 (Ludwig 2009) and Isoplot 4 (Ludwig 2012). The  $1\sigma$  external spot to spot error on was 0.78% on the first session (04/12/2013) and 0.73% on the second session (12/03/2014). Detrital zircons were measured on SHRIMP RG. In this instance, Temora mounted together with the unknowns was used as standard

for age, and SL13 in a separate standard mount was used for U concentration (U=238 ppm). The calibration error was 1%.

## 2.3 SHRIMP U-Th-Pb allanite and florencite dating

Allanite and florencite aggregates were separated using heavy liquids and magnetic separation using typical settings for allanites (density >3.3, relatively magnetic). They were mounted in a 1 inch epoxy mount together with the allanite standard TARA. Both minerals were imaged using the RSES SEM using SE and back scattered electrons (BSE). Qualitative chemical analyses were performed with the energy dispersive spectrometer (EDS) on the same instrument.

Allanites were dated using SHRIMP RG at RSES following the method of Gregory et al. (2007). Standards and unknown were analysed with a spot size of around 25x25  $\mu\text{m}$ . TARA allanite (412 Ma, Williams et al., 1983) was used as standard for internal mass fractionation and U concentration. BONA allanite (30.1 Ma, von Blackenburg, 1992) was used as a secondary standard. Age repeatability of the primary standard TARA was 2% for the U system and 1.5 % for the Th system. Reproducibility of the secondary standard BONA was within 1% for the U system and 2% for the Th system. Data reduction was performed using MS Excel extensions SQUID 2.5 (Ludwig 2009), and Isoplot 4 (Ludwig 2012).

In this exploratory study, florencites were treated like allanites, with the assumption that the matrix difference between allanite and florencite is <10%. Indeed, Gregory et al. (2007) report negligible matrix effect over a wide range of allanite compositions, however, the bias related to phosphate nature of florencite has not been assessed. Data was analysed with a custom spreadsheet following initial calibration using SQUID. Following Gregory et al. (2007), the proportion of common  $^{206}\text{Pb}$  ( $f_{206}$ ) is calculated as the deviation of  $^{207}\text{Pb}/^{206}\text{Pb}$  from the ratio calculated on the basis of  $^{207}\text{Pb}$  assuming concordance. Unlike Gregory et al. (2007), in these common-Pb-rich samples, the common Pb composition is not assumed but derived from the Tera-Wasserburg intercept established in the U-Pb system from the same set of analyses. This allows the calculation of  $^{208}\text{Pb}/^{206}\text{Pb}_C$  and  $^{232}\text{Th}/^{206}\text{Pb}_C$ , where  $^{206}\text{Pb}_C$  is the common  $^{206}\text{Pb}$ . These two ratios are used to produce a Th-Pb isochron.

## 2.4 Zircon trace elements

Trace elements were measured on an ArF excimer laser coupled to a quadrupole Inductively Coupled Plasma Mass Spectrometer (ICP-MS) Agilent 7700 using the setup described in Eggins et al. (1998). The laser was tuned to a frequency of 5 Hz and energy of 50 mJ (corresponding to



a HV of around 26-27 kV). Spot sizes of 22 and 28  $\mu\text{m}$  were used. Data were acquired over a 65 seconds analysis that included a 20 s background and the reference materials were measured after every eight unknowns. The counts were standardised to NIST 610 (zircon) glasses and accuracy was monitored by analysing BCR-2G glass. Recent data for the NIST glasses (Jochum et al. 2011; Spandler et al. 2011) differ from previous estimations (Pearce et al. 1997) by as much as 5 to 10% for certain elements (Cl, Nb, P, Sc, Sn, Ta) in NIST 610 and NIST 612 (As, F, P, Ti). Values of Spandler et al. (2011) have been used for data reduction. Stoichiometric Si was employed as internal standard for zircon ( $\text{SiO}_2$ : 31.6 wt%). Reproducibility and accuracy as assessed on the BCR-2G glass were within 10% or less across all analysed elements. The data was reduced with the freeware Iolite (Paton et al. 2011) and its data-reduction scheme for trace-elements (Woodhead et al. 2007).

### 3 Sampling and field-relations

A wide array of lithologies was sampled in the Halilbağı unit based on the maps by Davis and Whitney (2006, 2008). The relevant sample locations are plotted on the map from Whitney et al., 2014, **Figure 3 - 5**).

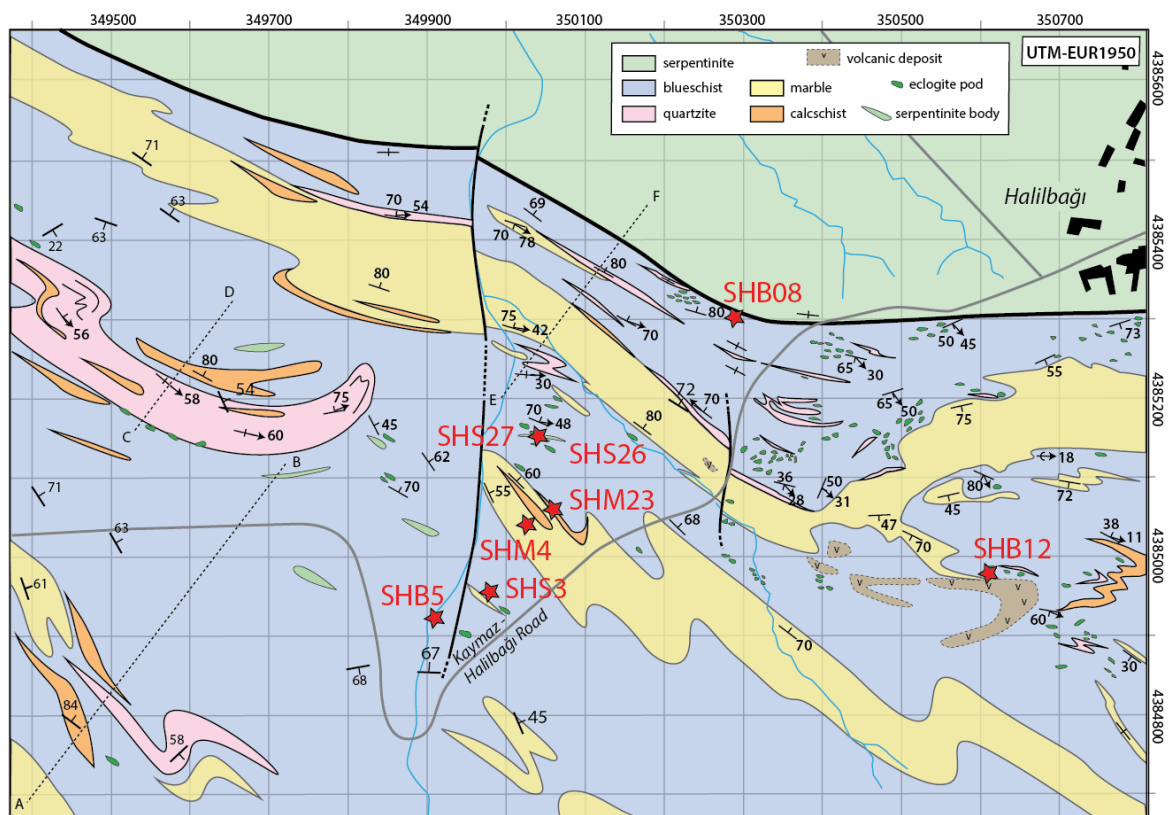


**Figure 3 - 5. Geologic map of the Halilbağı area from Whitney et al. (2014).**

In the following, we give an overview of the outcrops that were sampled. Generally, only the more competent lithologies crop out whereas the encasing schists are covered in soil and grass (**Figure 3 - 6**).



**Figure 3 - 6** Panorama of Halilbağı creek towards northwest showing quartzite interlayered with meta-volcanoclastic sediments. Donna Whitney for scale

### 3.1 Halilbağı

The Halilbağı unit provides outcrops of fresh high-grade lithologies. A diverse range of rock types can be sampled in the creeks near the village of Halilbağı. Out of creek beds, marble and quartzite beds and eclogite pods crop out better than other lithologies.

A first creek (panorama, **Figure 3 - 6**) offers a section through blueschist facies metasediments containing mafic material as well as quartzite and calcsilicate bands. SHB02 is a 20 cm thick layer made of omphacite, lawsonite and chlorite that was sampled close to a quartzite lens. SHB05 is a boulder found in Halilbağı creek next to SHB02. It is a lawsonite eclogite with lawsonite, omphacite, garnet and rutile, showing retrogression of omphacite in glaucophane coronas, as well as titanite aureoles around rutile; dark minerals and lawsonite form respective aggregates evocative of a gabbroic texture. A fresh quartz-micaschist outcrop can be observed downstream where SHS03 (ph, lws, grt) and SHS46 (ph, lws, ep) were sampled. Further down, eclogite pods are present in a blueschist matrix. A peculiar 3-5 m ultramafic pod is present in the blueschist-micaschist sequence, surrounded by a talc-rich contact zone. 6 samples were taken around the ultramafic pod in order to determine its relationship to the surrounding sequence (**Figure 3 - 8**). In thin section, SHS26 is made of antigorite and magnetite, with minor carbonate along fractures and in rounded aggregates (see context in **Figure 3 - 8**). It is composed of fine-grained magnetite zones and coarse-grained magnetite zones. In the coarse-grained magnetite zones, antigorite textures are more complex and maybe contain pseudomorphs of a precursor phase (**Figure 3 - 8**). SHS27, taken 2 m away from the ultramafic pod, is a calc-silicate rock containing abundant lawsonite, phengite and epidote. Continuing downstream towards the north, pure marble lenses are encountered, including a thicker marble unit (20 to 50 m thick). SHM04 is a pure marble from

the main lens, and SHM23B is a calcsilicate layer made of quartz grains in a matrix of Fe-rich carbonates found 20 m downstream.



**Figure 3 - 7. Metabasic lithologies in Halilbaği creek showing different pod structures.**

The lithologies are progressively more and more foliated toward the contact with altered peridotites from the nearby unit (see sample SHB09, **Figure 3 - 7**). The contact between the two units is not outcropping very well; SHB08 is the closest sample to the contact, it is a lawsonite-glaucophane fels with lawsonite veins. Away from the creek in the grassy slopes, more eclogitic pods can be found. The outcrops in this area are characterized by fresh lawsonite, omphacite and garnet in most metabasites, recording the lawsonite-eclogite facies. SHB12A and B were taken in two layers of a massive pod and are dominated by omphacite and phengite, with garnet, chlorite and occasional lawsonite, mostly in veins.

Softer lithologies do not crop out well in the area and it is difficult to place the eclogite pods in their context. It appears that eclogite pods or bands are almost always surrounded by blueschist layers (e.g. ‘micropods’ in SHB10, **Figure 3 - 7**). The eclogite bodies form boudins with complicated structural relationship to the blueschists and metasediments surrounding them (see proposed pod-forming mechanism in Davis and Whitney, 2008). The concordance of metabasites to the surrounding schists is hard to assess. At a larger scale, marbles, micaschists and blueschist

layers seem to form a consistent folded package, with fold limbs being continuous on a kilometric scale (Davis and Whitney 2006). Lithologies are layered at hectometre to centimetre scale, forming a heterogeneous sequence.

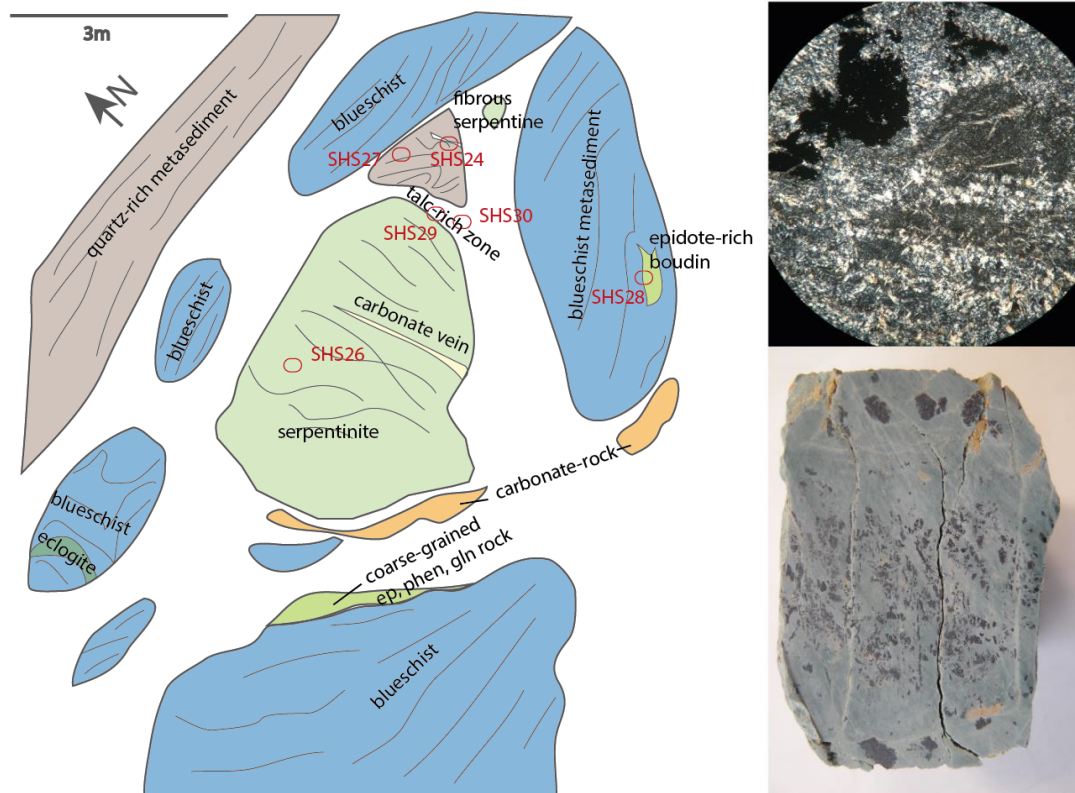


**Figure 3 - 8. Field sketch of the serpentinite pod SHS26. White areas represent grassy zones. b. sample SHS26 (hand sample, 8cm across, thin section view, 4mm across).**

South of the village of Halilbağı, a composite eclogite pod that showed internal heterogeneity and veining was described in detail by Davis and Whitney (2008). Strongly foliated schists and blueschists crop out among the grass around it. Epidote is more present than in the Halilbağı creek area and appears texturally late compared to lawsonite. Only the centre of the pod showed a fresh eclogite assemblage. The outermost part of it shows a blueschist-eclogite layering (where sample SV03-103 was taken), including some lawsonite-rich layers. SHB53 is taken at the rim of SV03-103 pod from Davis and Whitney (2008); it is a lawsonite-eclogite with a partly layered structure (**Figure 3 - 9**). The inner zone of the pod is dominated by omphacite and phengite in varying proportion. Several vein generations can be identified in the main body of the pod. Some patches are dominated by epidote and big lawsonite crystals associated with chlorite. A nearby layered lws-ep-gln-omph pod was sampled. Marbles and metasediments of the vicinity of this pod were sampled in an attempt of documenting its context, but they were not further studied as they were more altered than the Halilbağı creek samples.

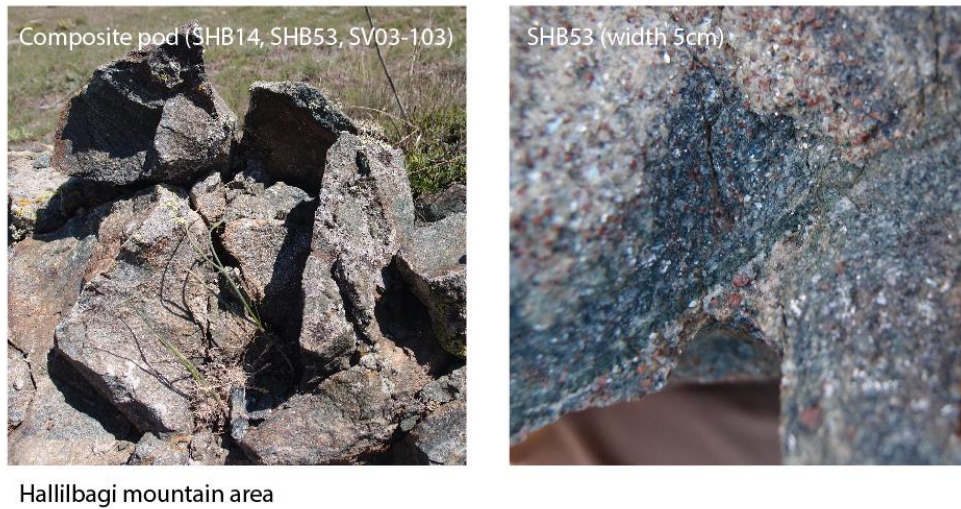


**Figure 3 - 9. SV03-103 composite pod. It has a complex structure including interlayered blueschist and eclogite at the rim. It is cross-cut by veins containing omphacite, epidote and/or lawsonite.**

### 3.2 South Halilbağı

The southern side of the Sivrihisar massif, South of Halilbağı, is dominated by marbles and micaschists. A blueschist band where eclogite pods can be found crops out upslope, within the blueschist unit. A few pods yield complex textures: some are coarse-grained like the SV03-103 pod, others are very finely interlayered (e.g. SHB43, **Figure 3 - 10**). SHB45 is a massive layer of phengite-rich lawsonite eclogite (gln, omph, grt, lws) in which lawsonite is thoroughly retrogressed. In SHB45, glaucophane and omphacite are present in the same foliation, indicating textural equilibrium. Another pod is made of fine grained and retrogressed ground mass where small garnets and 2-3 mm lawsonite pseudomorphs are present (SHB42 samples, **Figure 3 - 10**).

SHB42C was taken at the margin of a chlorite-rimmed fine-grained pod in the southern Halilbağı area. The sample was cut in two sections: a coarse lawsonite layer (A) closest to the chlorite rim and a more epidote-rich section with minor garnet (B). Samples SHS44 are from a blueschist outcrop that showed extensive lws-ph-grt bands and lenses. SHS44A is a lawsonite-phengite-garnet-quartz layer in blueschist SHS44B, dominated by glaucophane, lawsonite, epidote and garnet. After thin section study, it appears that lawsonite is retrogressed to epidote in most of the samples of this area.

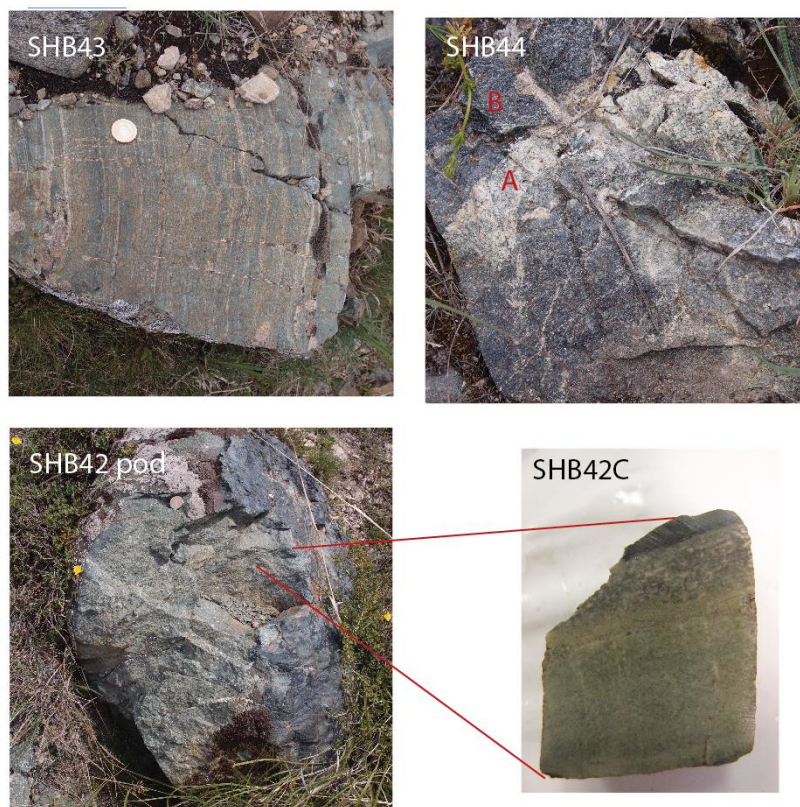
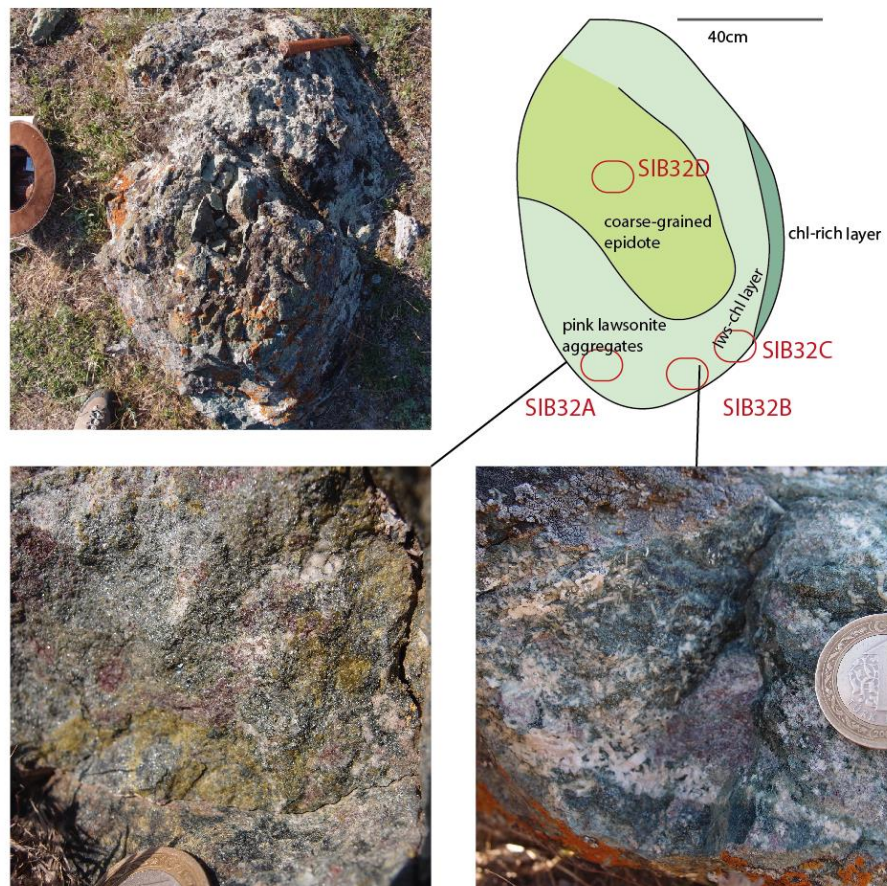


Figure 3 - 10. Pods and layering in Halilbağı southern area. Lawsonite is retrogressed in epidote patches.

### 3.3 Neighbouring units

East of the village of Ikipinar, the calc silicates and marbles forming the hill transition to the North to cultivated areas where eclogite pods crop out of a grassy zone of blueschists, micaschists and quartzite. This suite is best exposed in the creek bed next to the village. One of the pods presents big crystals of lawsonite in a matrix of chlorite (SIB32, **Figure 3 - 11**). Some lawsonite crystals yield deep red colour produced by fine-grained oxide inclusions (SIB32B, **Figure 3 - 11**). Epidote is abundant in the outer parts of the pod, where it appears to replace lawsonite. A chlorite-rich layer forms the outermost shell of the pod. Not very far from this pod, a coarse-grained phengite-glaucophane schist layer is present among more classical-looking micaschist (SIB50B). It contains 20-50  $\mu\text{m}$  Mn-rich garnets. A purple quartzite was sampled a meter away from the micaschist that contains Mn-rich epidotes (SIS52). Some marbles and micaschists layers are found as well. An impure quartzite (SIS53) was sampled close to SIS52.

This succession has similarities with the lithologies outcropping in the Halilbağı creek, but while lawsonite is abundant, garnet can be seen only in thin section in sample SIB50B. Grainsize is also generally larger than in the creek area of Halilbağı.



**Figure 3 - 11. Ikipinar coarse-grained pod with interpretative drawing. Pink minerals are inclusion-rich lawsonite.**

Samples were taken from two marble units near the Halilbağı unit. First, a pure marble sample was taken in the Okçu quarry, SE of Halilbağı. Okçu marble is very pure, of white to light-gray color. The samples taken in this study have a sugary texture, which contrasts with rod-shaped calcite common in this unit (e.g. Seaton et al., 2014). East of the village of Sivrihisar, an impure marble was sampled in the Günyüzü unit. Günyüzü marble contains needle calcite after aragonite (Seaton et al. 2009), and yields some very impure layers containing glaucophane and phengite (SGM21).

**Table 3 - 2 Sample list with information on dating and determined geochemical affinity (see discussion). sed. stands for sedimentary, mag: magmatic, met: metamorphic. Mineral abbreviations are from Whitney and Evans (2010) except for WM: white mica, Flo: florencite, rel.:relict. (1) (2) (3) refer to the groups defined by REE chemistry, see further in text.**

Sample	Rock type	Mineralogy	Dating	Affinity	
Halilbağı					
SHB02	Omph-lws layer	Lws, omp, qz, opq		Mafic sed. (1)	
SHS03	Impure quartzite layer	Qz, lws, WM, grt, ep, flo, aln, opq, tur	U-Th-Pb Flo, Aln	98 ±8 Ma 88±10 Ma	Sed.
SHM04	Marble layer	Cal, opq		Sed.	
SHB05	Eclogite pod	Omp, gln, grt, lws, amp, rt, ttn, ap		MORB (2)	
SHB08	Blueschist layer	Gln, lws, omp, WM		MORB (2)	
SHB12	Eclogite pod	Omp, WM, grt, chl, ep, rt, ttn, ap		MORB (2)	
SHM23B	Calcsilicate layer	Qz, cal, WM, opq	U-Pb Zrn <i>detrital</i>	3.5 Ga – 280 Ma	Sed.
SHS26	Serpentinite pod	Atg, opq, cal		MORB (2)	
SHS27	Calcsilicate layer	Cal, opq, chl, WM, ep, qz, lws		Sed.	
SHS46	Impure quartzite layer	Qz, lws, WM, ep, flo, all, opq, tur		Sed.	
SHB53	Eclogite pod	Omp, gln, WM, lws, grt, ep, rt, ttn, aln		Mafic sed. (1)	
South Halilbağı					
SHB42C	Chl-lws-grt pod	Chl, grt, ep, lws rel., cal, WM, qz, opq		Mafic sed. (1)	
SHB45	Eclogite layer	Omp, Gln, grt, WM, lws rel., rt, ttn	Th-Pb Zrn mag.	123 ±3 Ma	OIB (3)
SHS44A	Lws-phen-grt layer	Qz, grt, WM, ep, all, lws rel., ap, zrn	U-Pb Zrn mag. met.	222 ±5 Ma 89.5 ±2 Ma	MORB (2)
SHS44B	Blueschist layer	Grt, gln, qz, ep, amp, WM, lws rel., omp rel., ap, rt, zrn		MORB (2)	
Ikipinar					
SIB32A	Lws-chl pod	Lws, Chl, opq, ttn, some ep		Mafic sed. (1)	
SIB32B (ep)	Ep-chl-lws pod	Ep, chl, lws, opq, ttn, qz		Mafic sed. (1)	
SIB50B	Gln micaschist layer	Gln, lws, omp, grt, WM, qz, opq, rt, ttn, ep-aln, chl, amp		Mafic sed. (1)	
SIS53	Impure quartzite layer	Qz, WM, lws, gln, opq		Sed.	
SIS52	Piemontite quartzite layer	Qz, opq, ep, cal, WM, tur		Sed.	
SGM21	Impure marble layer	Cal, qz, WM, ep, opq		Sed.	



## 4 Geochemistry of Halilbağı lithologies

23 samples from the Halilbağı unit and the Ikipinar unit were analysed for major and trace elements. They are grouped by mineralogy (metasediments vs. metabasites) and then by geochemical characteristics (grouping in metabasites). In this chapter, the emphasis is put on the implication of chemical signatures for protolith determination. Any chemical and isotopic modifications subsequent to deposition and emplacement will be discussed in **Chapter 4**, together with data for mineral chemistry.

### 4.1 Metasediments

A first group of samples yield a mineralogy of unambiguously metasedimentary origin, with a high quartz or carbonate content. This is reflected in high contents in SiO<sub>2</sub> (up to 93 wt% in SIS53, Table 3 - 3), and CO<sub>2</sub>. Several rocks contain both carbonate and high quartz content (SHM23B, SGM21, SHS27). They yield a detrital/volcanoclastic component with variable contents of Al, K, Fe, Mg.

**Table 3 - 3 Major element composition of Halilbağı metasedimentary lithologies**

XRF	SHS03	SHS46	SIS52	SIS53	SHM23B	SGM21	SHS27	SHM04
SiO <sub>2</sub> (%)	83.3	82.5	92.1	88.8	82.2	67.8	46.3	0.4
Al <sub>2</sub> O <sub>3</sub> (%)	7.7	8.0	2.6	3.8	1.4	5.1	6.5	bdl
Fe <sub>2</sub> O <sub>3</sub> (%)	3.2	3.7	1.8	2.1	0.7	2.2	2.7	0.1
MnO (%)	0.1	bdl	0.7	0.1	bdl	0.1	0.3	bdl
MgO (%)	1.3	1.2	0.9	0.8	0.8	0.6	1.3	1.6
CaO (%)	0.5	0.7	1.2	2.5	10.5	14.3	23.3	54.3
Na <sub>2</sub> O (%)	0.4	0.4	bdl	0.1	0.1	0.2	0.8	bdl
K <sub>2</sub> O (%)	2.9	2.8	0.6	1.6	0.3	1.1	1.4	bdl
P <sub>2</sub> O <sub>5</sub> (%)	0.1	0.1	bdl	0.1	bdl	0.1	0.1	bdl
TiO <sub>2</sub> (%)	0.4	0.4	0.1	0.3	0.1	0.3	0.3	bdl
XRF sum	99.8	99.9	100.1	100*	96.3	91.7	82.9	56.4
LECO LOI								
H <sub>2</sub> O+	1.6	1.6	0.6	1.0	0.5	1.2	2.0	0.1
CO <sub>2</sub>	bdl	0.1	0.2	bdl	6.9	8.8	13.6	33.6
Sum	101.4	101.5	101.0	101	103.7	101.7	98.5	90.1
Mg#	0.45	0.40	0.50	0.42	0.70	0.34	0.48	0.97

\* SIS53 was normalised to 100% as the XRF disc was produced using the carbonate flux and thus yielded an artificially high total of 105%.

Trace element composition (*Appendix table A3 – 1*) show an enrichment in REE and Pb, as well as a depletion in Nb-Ta, Ti, and sometimes Sr compared to chondrite (Sun and McDonough 1989), see Figure 3 – 15. These anomalies are similar to the global subducting sediment estimate of Plank & Langmuir (1998). The patterns from different samples are parallel, but show different degrees

of enrichment: the marble SHS04 yielding the lowest amounts, between 0.1 and 1 times the Primitive Mantle (PM) composition (Sun and McDonough 1989), and the quartzite SHS53 the most enrichment at 10-100 times PM. It is notable that samples SHS03 and SHS46 taken from different layers of the same outcrop yield only slight variations in both major cations content (difference <0.3 wt%) and in trace elements.

## 4.2 Metabasites and serpentinite

The dominant lithologies in the Halilbağı area are of mafic affinity, with a mineralogy dominated by glaucophane, omphacite, lawsonite, garnet, chlorite and/or epidote. They outcrop in pods and layers and are often layered at a finer scale (down to mm scale). For most mafic samples, two sub-samples (named A and B) were analysed for WR composition, in order to investigate potential effects of sampling size and metamorphic mineral modes. Usually, these consist of cm-sized layers within the hand sample. As such, they are not duplicates but rather an indication of local compositional variability. In most cases, the doublets yield identical compositions, which is a good indication that the aliquot of crushed rock (about 200-400 g of sample), represents the WR composition and that immobile elements can be used for protolith determination. Data obtained previously on Halilbağı samples by Davis and Whitney (2008) was produced using smaller sample sizes, in order to describe smaller scale phase equilibria.

Here, the geochemical information is used to determine the geodynamic environment of the protolith. Metasomatism such as seafloor alteration or subduction-related metamorphic fluid flow will be discussed in depth in **Chapter 4**. The emphasis is thus put on “immobile elements”, for comparison with- and as used commonly in geodynamic studies.

The samples are mafic to ultramafic in major elements (SiO<sub>2</sub> 58-35 wt%, Table 3 – 4). Figure 3 – 12 presents a TAS diagram for comparison only, as alkali elements are potentially mobile during metamorphism (e.g. John et al. 2004, see further at Figure 3 – 14).

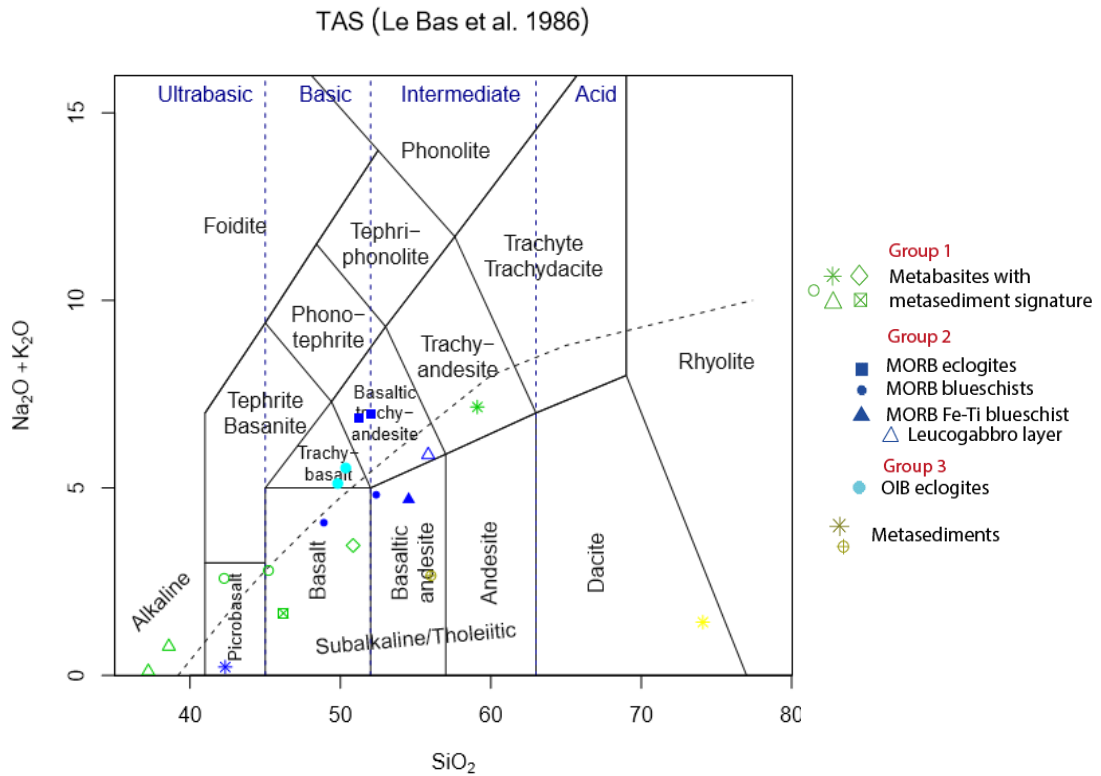


**Figure 3 - 12. Classification of metabasites (blue, light blue and green symbols represent different REE-defined groups, see below for description) according to Le Bas et al. (1986) The major element composition is plotted as anhydrous using the software GCDkit 4.1.**

**Table 3 - 4 Major element composition of Halilbağı metabasites**

Sample	SHB02	SHB05	SHB08	SHB12A	SHB12B	SHB42CA	SHB42CB	SHS44A	SHS44B
Group	1	2	2	2	2	1	1	2	2
SiO <sub>2</sub> (%)	48.4	50.0	45.6	49.3	50.0	43.6	40.8	54.1	51.1
Al <sub>2</sub> O <sub>3</sub> (%)	12.1	13.6	19.1	15.1	13.9	19.5	20.3	22.1	12.9
Fe <sub>2</sub> O <sub>3</sub> (%)	7.2	12.1	8.5	8.7	8.1	7.4	7.8	6.9	14.9
MnO (%)	0.3	0.2	0.1	0.3	0.2	0.7	0.9	0.3	0.2
MgO (%)	6.4	6.3	3.7	8.2	8.5	5.1	5.3	1.5	5.1
CaO (%)	16.9	8.5	12.4	8.0	8.5	17.5	17.8	6.2	4.8
Na <sub>2</sub> O (%)	3.3	4.5	3.0	3.9	4.2	1.1	0.9	0.8	3.7
K <sub>2</sub> O (%)	bdl	0.1	0.8	2.7	2.5	1.6	1.6	4.9	0.7
P <sub>2</sub> O <sub>5</sub> (%)	0.6	0.2	0.1	0.1	0.2	bdl	1.2	0.1	0.3
TiO <sub>2</sub> (%)	0.7	1.4	0.8	1.1	1.1	0.8	0.8	0.7	3.2
XRF sum	95.9	96.9	94.1	97.4	97.2	97.3	97.4	97.6	96.9
LECO LOI									
H <sub>2</sub> O+	3.8	4.0	6.1	2.7	2.6	1.6	2.4	2.6	2.3
CO <sub>2</sub>	1.9	0.1	0.9	0.1	0.1	0.5	0.7	0.2	0.1
Sum	101.5	100.9	101.0	100.2	99.8	99.5	100.5	100.3	99.2
Mg #	0.64	0.51	0.46	0.65	0.67	0.58	0.57	0.31	0.40

**Table 3 - 4 Continued**

Sample	SHB45A	SHB45B	SHB53	SIB32	SIB32ep	SIB50B	SHS26
Group	3	3	1	1 (3)	1 (3)	1	(2)
SiO <sub>2</sub> (%)	46.7	47.3	44.5	35.0	35.1	57.8	37.6
Al <sub>2</sub> O <sub>3</sub> (%)	11.6	12.9	18.0	22.0	21.9	10.8	1.1
Fe <sub>2</sub> O <sub>3</sub> (%)	12.4	11.6	10.2	11.3	12.7	10.6	15.8
MnO (%)	0.2	0.2	0.4	0.2	0.3	0.8	0.1
MgO (%)	8.9	8.4	5.9	10.5	7.8	8.1	33.9
CaO (%)	8.7	8.0	15.7	10.9	16.1	2.6	0.1
Na <sub>2</sub> O (%)	3.7	3.7	1.3	0.7	0.1	4.4	0.2
K <sub>2</sub> O (%)	1.1	1.5	0.3	bdl	bdl	2.6	bdl
P <sub>2</sub> O <sub>5</sub> (%)	0.5	0.4	bdl	0.1	0.3	0.1	bdl
TiO <sub>2</sub> (%)	3.2	2.6	1.3	1.5	1.3	1.1	1.0
XRF sum	96.9	96.6	97.7	92.1	95.6	99.0	89.7
LECO LOI							
H <sub>2</sub> O+	2.6	2.6	2.8	9.3	5.5	2.4	9.8
CO <sub>2</sub>	0.1	0.1	0.1	0.1	0.1	0.1	0.1
Sum	99.6	99.9	100.5	101.5	101.2	101.5	99.6
Mg #	0.59	0.59	0.54	0.65	0.55	0.60	0.81

In REE composition, a reliable mean of protolith determination (*Appendix table A3 – 1*), 3 groups of metabasites can be distinguished on the basis of the slope of the pattern (**Figure 3 - 13**). Group 1 metabasites are LREE enriched to ~100 chondrite, with a small negative Eu anomaly. They mostly look like diluted or enriched GLOSS (Plank and Langmuir 1998) or arc basalts. Group 2 metabasites yield mostly flat patterns at 10-80x chondrite, with sometimes a weak HREE enrichment. Their LREE patterns are parallel to E-MORB from Sun & McDonough (1989). Group 3 metabasites (represented by sample SHB45) have a steeply dipping REE pattern, identical to the OIB from Sun & McDonough (1989). Nb, Y, Zr, Ti plot modified by Pearce (1996) allows discriminating both magmatic type and differentiation. On this diagram, group 1 metabasites plot similarly to metasediments, with the exception of SIB32 samples that fall in the alkali basalt field. Group 2 metabasites are basalts, except for the ultramafic SHS26, unusually enriched in Nb. SHS44A is identified as a more differentiated lithology, plotting in the rhyolite/dacite field. Group 3 metabasites plot in the alkali basalt field.

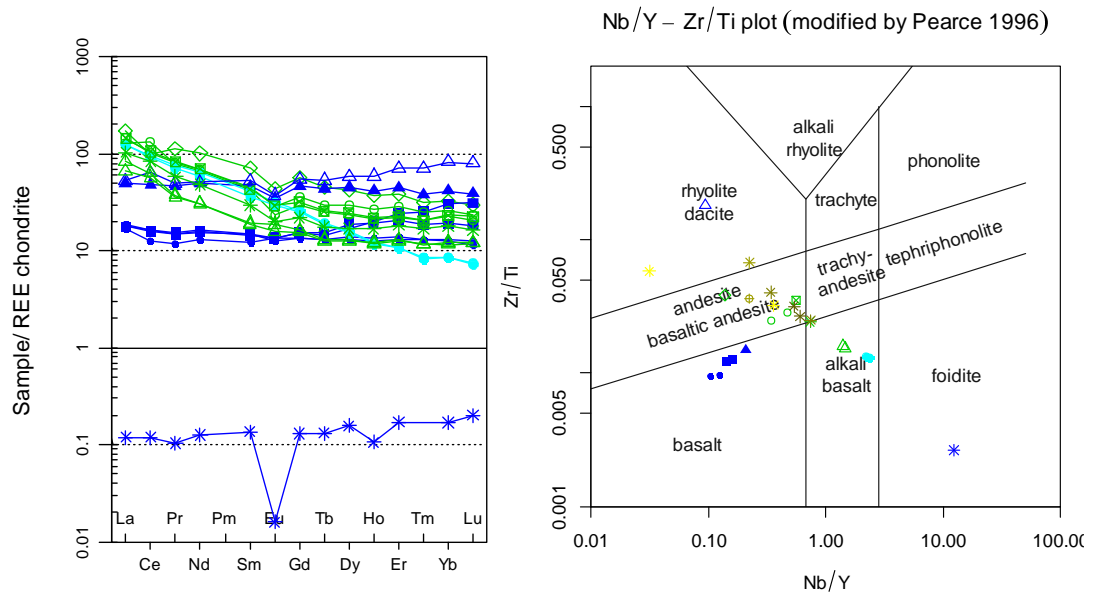


**Figure 3 - 13 Grouping of metabasites: group 1 (green), group 2 (dark blue), group 3 (light blue). a. REE composition normalised to chondrite b. geochemical affinity, with metasediments (brown-yellow). For legend of symbols see Figure 3 - 14.**

Although this study is based mainly on immobile elements, the major elements chemistry of all analysed rocks is compared to seafloor basalts in **Figure 3 - 14** modified from Spandler et al. (2004). It is to note that group 2 and 3 metabasites generally approximate the composition that is to be expected of MORB and OIB, respectively, in  $\text{Al}_2\text{O}_3$  (**Figure 3 - 14a**), CaO and MgO compared to  $\text{Na}_2\text{O}$  (Figure 3 – 14b). Group 1 metabasites yield scattered  $\text{Al}_2\text{O}_3$  compositions that are either lower (SIB50B, SHB02) or higher (SHB42, SIB32) than the field of magmatic seafloor lithologies. Similarly, group 2 metabasites yield higher CaO (SHB53, SHB02, SHB42, SIB32) or lower CaO (SIB50B) than the fresh tholeiites in Figure 3-2b. This is an indication that the group-3 metabasites are either thoroughly metasomatised or the result of diverse mechanical mixing with sediments that can provide high CaO and low  $\text{Al}_2\text{O}_3$  (Figure 3 - 14). As a result, group 2 and group 3 metabasites will be the focus of most of the geodynamic discussion.

All Group 1 metabasites but SIB32 also yield a negative Ti and Nb-Ta anomaly, similar to GLOSS (**Figure 3 - 15**). Among fluid mobile elements, most samples are enriched in Pb, and some in Sr. All group 1 samples show a marked depletion in Rb and Ba, and Cs to a lesser extent. These features showing a sediment component (notably the LREE enrichment) are characteristic both of the global subducting sediment, and of arc basalts (inheriting the sediment signatures through the subduction process).

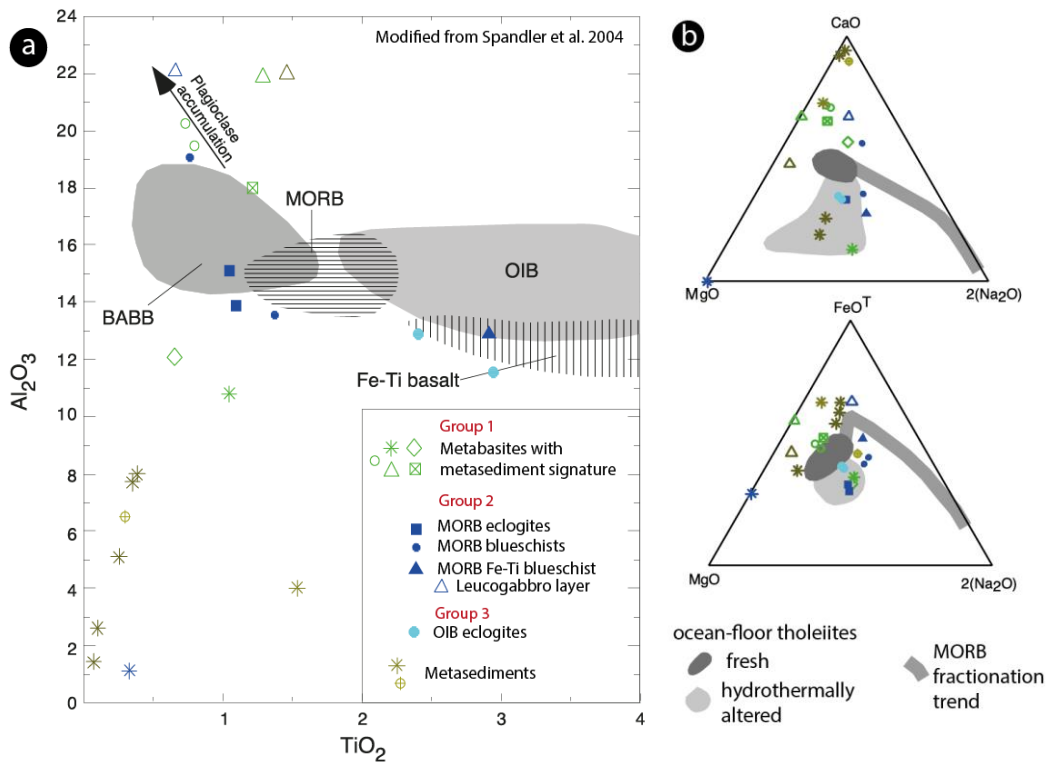


**Figure 3 - 14. Major element composition of investigated lithologies compared to typical seafloor basalts from Spandler et al. (2004).**

Group 2 metabasites yield flatter REE patterns; SHB05 and SHB08 are almost identical to Sun and McDonough (1989) EMORB. SHB12B shows an enrichment in HREE, which is more pronounced in subsample B than in subsample A. SHB44A and B are more enriched in REE, indicative of more fractionated lithologies, which is consistent with their small negative Eu anomaly (indicating the fractionation of small amounts of plagioclase). Similar to SHB12B, SHS44A yielded more HREE than its doublet. This could be a. a sampling artefact due to garnet grain size, b. the result of metamorphic fractionation where garnet-bearing cm-sized layers created diffusion gradients for HREE leading to their enrichment in HREE at the expense of surrounding garnet-poor layers (e.g. Otamendi et al., 2002; Skora et al., 2006), c. the reflection of magmatic fractionation processes.

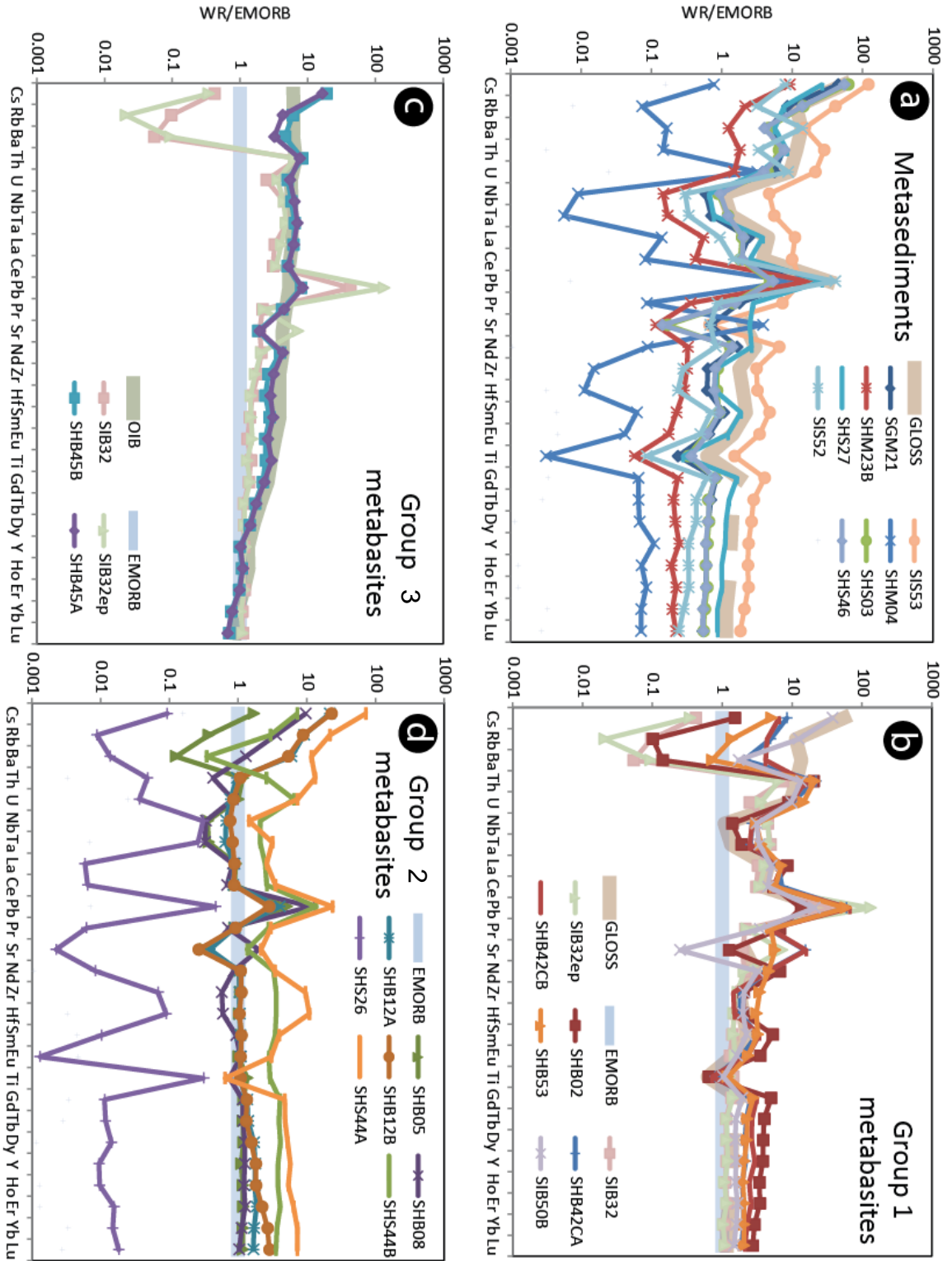


**Figure 3 - 15. Multi-element diagrams normalised to EMORB (Sun and McDonough 1989). Reference values for GLOSS (Plank and Langmuir 1998), OIB (Sun and McDonough 1989). MORB was chosen as the baseline, as it is the least-enriched magmatic component analysed in this unit.**

SHS26, the serpentinite sample, yields overall low REE contents (around 0.1 chondrite) with a flat MORB-like pattern, and a large negative Eu anomaly. SHB05 and SHB08 yield trace elements remarkably similar to EMORB, but with a slight depletion in Nb-Ta, and an enrichment in Pb. SHB08 is enriched in Sr and depleted in Ti, where most other samples are depleted in Sr. Most samples are enriched in Cs, Rb and to a lesser extent Ba, except for SHB05 and SHB44B. SHS44A yields an enrichment in Zr-Hf, and a depletion in Ti and Nb. SHS26 has a pattern that is parallel to EMORB, except for positive anomalies in HFSE elements: Zr-Hf, Ti and Nb-Ta.

Group 3 metabasites SHB45 have a trace element composition remarkably close to OIB, but for small positive anomalies in Cs and Pb, and a small negative anomaly in Sr. Sample SIB32 yields intermediate characteristics with both GLOSS and OIB features. Its trace-element contents are similar to OIB, except for a CS-Ba depletion and Pb and Sr enrichment. The Sr enrichment is limited to the subsample that is dominated by epidote.

## 5 U-Pb and Th-Pb dating

### 5.1 Zircon U-Pb

Zircons were separated from three samples: SHS44A, SHB45 and SHM23B. They were dated using SHRIMP ion microprobes on grain separates. Zircon was investigated as a chronometer for the protolith and of metamorphism, and a tracker of fluid circulations (see **Chapter 4**), as such, samples with high Zr content were targeted: leucocratic layer SHS44A and eclogite SHB45. Both of these rocktypes are interpreted as magmatic. Calc-silicate SHM23B was selected for detrital zircon analysis due to the abundance of zircons (some rounded) in the rutile separate.

#### 5.1.1 Lws-phen-grt layer SHS44A

SHS44A contains numerous small zircons (10 to 50  $\mu\text{m}$ ) disseminated in the thin section, sometimes included in garnet. Micro-zircon aggregates can also be observed. In the separate, some zircon grains are euhedral small prisms, while others displayed a pinker colour, are less translucent and have embayment features. In CL, oscillatory zoned-domains are cross-cut and replaced by lighter patchy zones (**Figure 3 - 16**).



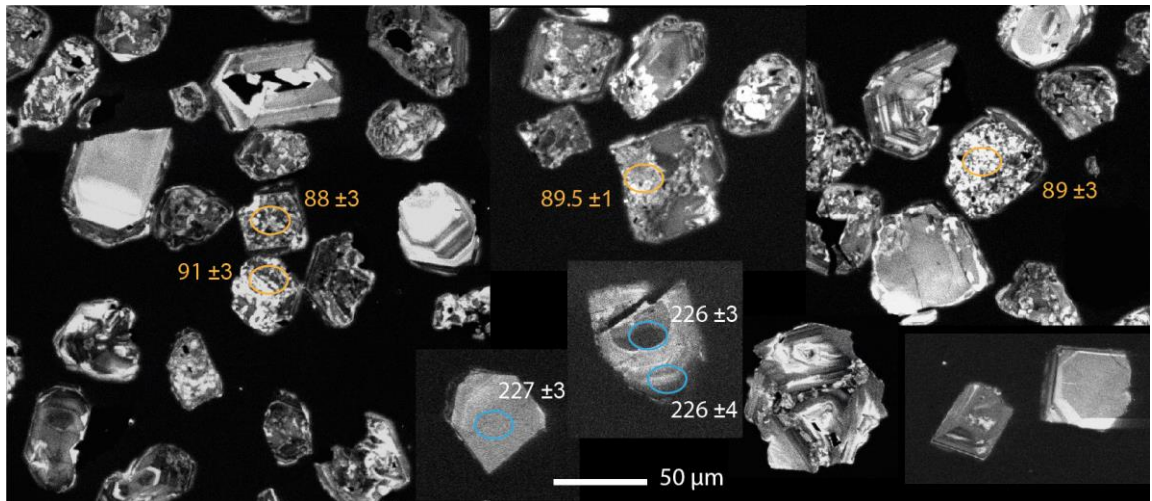


**Figure 3 - 16. Composite CL image of SHS44A zircons showing SHRIMP spots with  $^{238}\text{U}$ - $^{206}\text{Pb}$  ages, spot size is 25 microns. Colour coding refers to Figure 3 - 13.**

The zircon analyses (*Appendix table A3 – 2*) are plotted in an uncorrected Tera-Wasserburg diagram (Figure 3 – 17a). Most zircons contain inclusions that cannot be avoided using a 25  $\mu\text{m}$  beam, which results in high common Pb content in the measured ages.  $\text{Pb}_\text{C}$  is corrected for by using the method by Stacey and Kramers (1975) based on the  $^{207}\text{Pb}$  content of the analysis according to Williams (1998). If corrected according to their  $^{204}\text{Pb}$  content and plotted on a Concordia diagram, all analyses are concordant over an interval that spans from 230 Ma to 85 Ma. Part of this range is interpreted as mixing between different zircon domains, but also by the contribution of inclusions to the Pb content. High common Pb contents analyses yield scattered  $^{206}\text{Pb}$ - $^{238}\text{U}$  ages, but lower common Pb analyses cluster around 3 ages at ca. 223 Ma and ca. 90 Ma. The correlation between common Pb content and age indicates that clean zircon analyses are less-likely to sample mixed age domains. In order to filter out meaningless mixed analyses, only data points that yield less than 2% of common  $^{206}\text{Pb}$  were used for the calculation of ages. This reduces the dataset from 32 to 16 data points. Furthermore, using low common Pb analyses ensures that assuming a Stacey and Kramers (1975)  $\text{Pb}_\text{C}$  composition has no bearing on the age within uncertainty.

In the low-common Pb analyses, 2 populations emerge (**Figure 3 - 17**): oscillatory-zoned cores yield an average age of  $222 \pm 5$  Ma ( $n=5$ ,  $\text{MSWD}=2.1$ ). Amongst patchy rims, dates scatter from 130 Ma toward 90 Ma; the 4 youngest analyses yield an average of  $89.5 \pm 2.2$  Ma ( $n=4$ ,  $\text{MSWD}=0.15$ ). An average of the 5 youngest grains is not significantly different:  $93 \pm 5$  Ma but its associated  $\text{MSWD}$  of 4.2 suggest they do not form a statistically probable population.

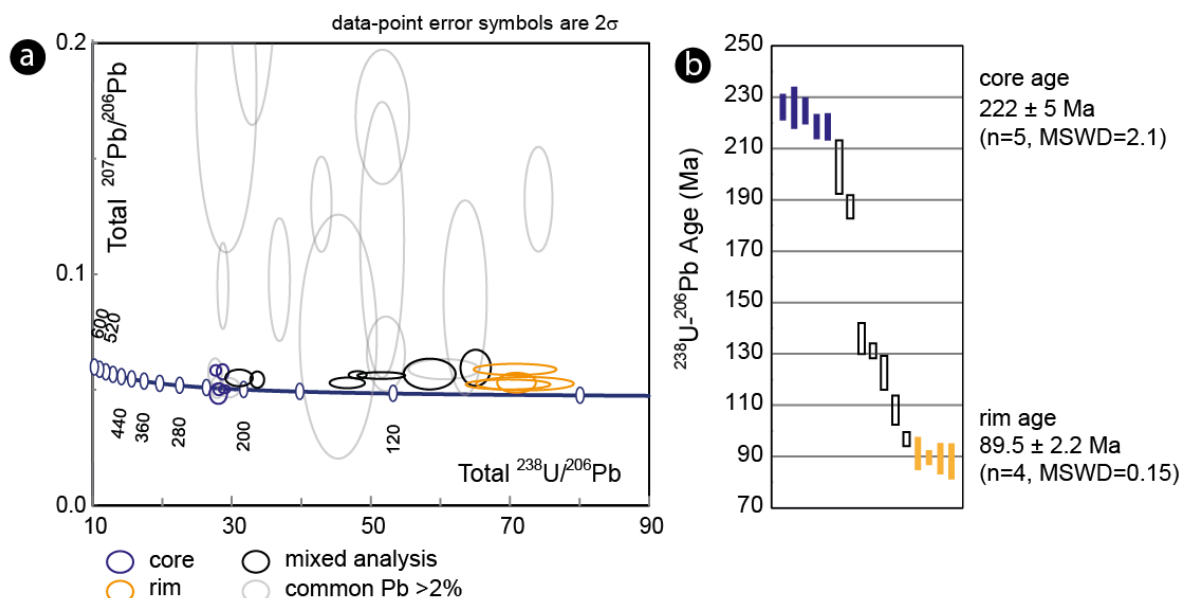


**Figure 3 - 17. Uncorrected Tera-Wasserburg diagram for SHS44A zircons transparent ellipses are analyses containing more than 2 % common  $^{206}\text{Pb}$ ,  $^{238}\text{U}-^{206}\text{Pb}$  corrected ages for analyses with less than 2 % common  $^{206}\text{Pb}$ .**

REE allow distinguishing two types of rims, all of them with similar patchy zoning in CL. One has enriched REE, similar to the cores (rim A, **Figure 3 - 18**, Table 3 – 6, *Appendix table A3 – 3*). The other zircon rim has depleted MREE and enriched HREE (rim B). The two types of rims are hard to distinguish in CL. Generally, rim A corresponds to CL brighter mosaic zones whereas rim B yields smaller sub-domains ( $<1 \mu\text{m}$ ) of contrasted CL brightness. Rim A REE patterns are parallel to core patterns except for the HREE, which are slightly enriched in rim A compared to the cores. This would indicate that rim A are patterns that are dominated by core signature, with the mixing of rim B composition. Such mixing could be the result of either physical mixing by drilling into core compositions downwards, or more likely, the tight spatial relationships between the ‘rim’ and ‘core’ domains at the micrometre scale reflected by the mixing obtained in ages. Generally, the complexity of the mosaic zones geometry makes a direct correlation between SHRIMP and laser spots uncertain, due to differences in sampling volumes compounded by micron-sized heterogeneities in the zircons.

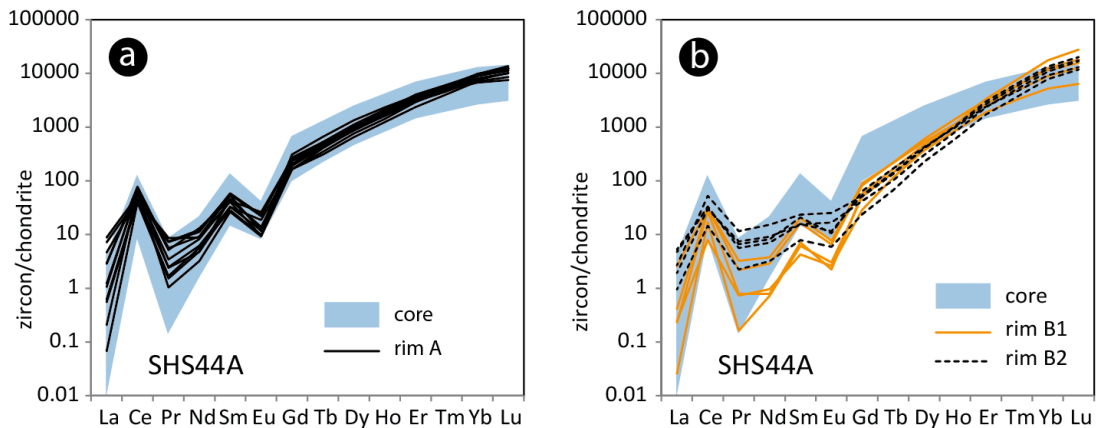


**Figure 3 - 18. REE normalized to chondrite for SHS44A zircons. Normalising values from Sun and McDonough (1989). 12 core analyses are represented as range, for clarity.**

Zircon oscillatory cores yield a REE signature that is typical for magmatic zircons with a generally steep pattern with a negative Eu anomaly and a positive Ce anomaly (Hoskin and Schaltegger 2003). They yield high Th/U around 1.

Four rim B analyses yield smaller Nb/Ta ratios due to an enrichment in Ta (100 ppm, **Table 3 - 5**), low Zr/Hf ratios with 1.8 wt% Hf, have lesser negative Eu anomalies ( $\text{Eu}/\text{Eu}^* = 0.1$ ). The enrichment in Hf is unusual for zircon and rather suggests the incorporation of another secondary phase. These grains yield scattered dates. Other rim B analyses have closer to magmatic Zr/Hf, Nb/Ta, and  $\text{Eu}/\text{Eu}^*$ . They lie on a mixing spectrum between their more MREE depleted equivalent and magmatic REE. These yield the youngest dates around 87 Ma, and could be representative of the metamorphic age (the MREE being incorporated into a metamorphic phase such as the plentiful apatite present in the sample, similarly, preferential incorporation of LREE and MREE by lawsonite could produce a steep pattern in zircon).

Rim A analyses yield magmatic Y/Ho and Zr/Hf. They are enriched in Nb, potentially significant of impurities. They have the largest Eu anomaly of all zones with  $\text{Eu}/\text{Eu}^* = 0.02$ . They generally yield mixed dates.

**Table 3 - 5. LA-ICP-MS Trace-element composition of typical zircon zones**

Source file	zirc28-17.d	zirc22-49.d	zirc22-41.d	zirc22-45.d	zirc22-36.d	zirc22-35.d
Sample zone	SHS44A core	SHS44A Rim A	SHS44A Rim B1	SHS44A Rim B2	SHB45 core	SHB45 Light rim
ppm						
P	781	560	427	409	57.4	45
Ca	bdl	850	bdl	174	86	160
Sc	426	358	389	353	371	362
Ti	8.62	13.8	1.61	8.68	2.8	9.1
Fe	27.4	502	24	2800	710	1243
Y	4718	3500	1510	1938	3090	303
Nb	14	48	15	59	49.8	7.84
La	0.002	0.249	0.006	0.631	0.022	0.101
Ce	32	42	10	32	29.4	4.27
Pr	0.16	0.22	0.02	1.1	0.755	0.091
Nd	3.7	2.2	0.33	7.0	14.4	1.08
Sm	12.3	4.9	0.91	3.5	27.1	1.54
Eu	2.14	0.67	0.17	1.42	19.5	0.99
Gd	95.7	37.3	10.1	10.1	131	6.42
Tb	35.3	16.3	5.13	4.85	40.3	2.42
Dy	457	252	89.9	98.2	424	30.8
Ho	165	110	46.5	56.9	123	10.5
Er	780	631	301	478	482	49.4
Tm	151	147	79.6	159	82.8	9.2
Yb	1305	1452	838	2153	606	86.3
Lu	212	275	156	491	84	14.5
Hf	8240	8490	8770	18280	3455	3860
Ta	4.21	16.8	11.7	101	3.29	0.454
Pb	4.81	6.97	4.22	9.63	16.3	3.92
Th	222	307	193.5	587	1407	241
U	168	492	355	1122	28.7	154
Th/U	1.32	0.62	0.54	0.52	49.0	1.6
Nb/Ta	3.3	2.9	1.3	0.6	15	17
Zr/Hf	52	47	52	21	123	104
Eu/Eu*	0.04	0.03	0.03	0.21	0.82	0.82
Lu <sub>N</sub> /Gd <sub>N</sub>	18	60	125	393	5	18

### 5.1.2 Blueschist SHB45

Two zircon grains yield large enough zones to be analysed for U-Pb in sample SHB45. They yield CL dark oscillatory-zoned cores cut and surrounded by a CL lighter rim (Figure 3 – 19a). A spongy outer rim is present in a couple of grains that were not analysed for U-Pb. These two grains have high trace element contents (**Figure 3 - 19b**) including no distinguishable Eu anomaly and high Th/U ratios, similar to gabbroic zircons (e.g. Kaczmarek et al., 2008). Core and rim yield

parallel REE patterns. This indicates no difference in the co-crystallising assemblage (e.g. appearance of metamorphic apatite or garnet). Both core and rim are thus interpreted as magmatic.

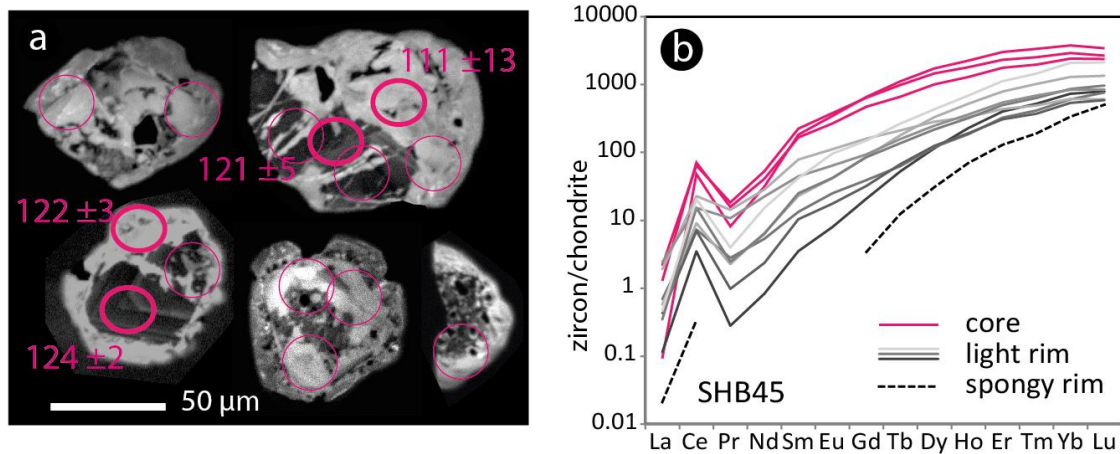


Figure 3 - 19 a. Composite CL image of SHB45 zircons showing SHRIMP spots with  $^{232}\text{Th}$ - $^{208}\text{Pb}$  ages and LA-ICP-MS spots (thin circles). b. Chondrite-normalised REE composition of SHB45 zircons. Normalising values from Sun and McDonough (1989).

One of the two grains yielded high Th and U contents in both core and rim. The second grain was much more depleted and yielded only marginal amounts of radiogenic Pb. The uncorrected analyses are plotted in a Tera-Wasserburg diagram (Figure 3 - 20a, Appendix table A3 – 2). Grain 2 analyses do not yield very useful information in the U-Pb system because of their low U content (4 and 1 ppm). The 4 analyses yield an intercept age of  $128 \pm 3$  Ma. Both zones contain more Th than U and thus Th-Pb dates can be calculated and yield an average of  $123 \pm 3$  Ma ( $n = 4$ , MSWD = 0.56, Appendix table A3 – 4). U-Pb and Th-Pb ages are identical within uncertainty. The Th-Pb age is preferred because of the better precision of individual dates and a better MSWD indicative of less scatter (Figure 3 - 20b).

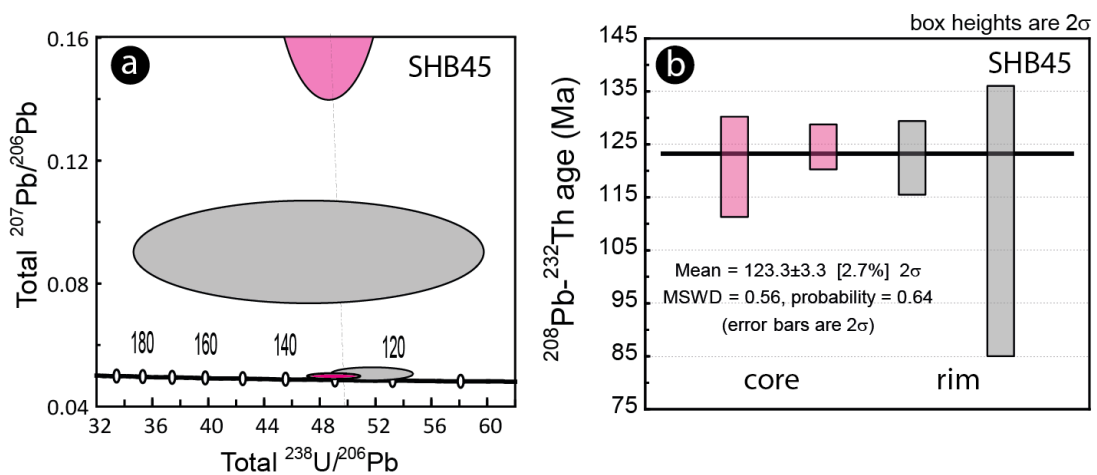
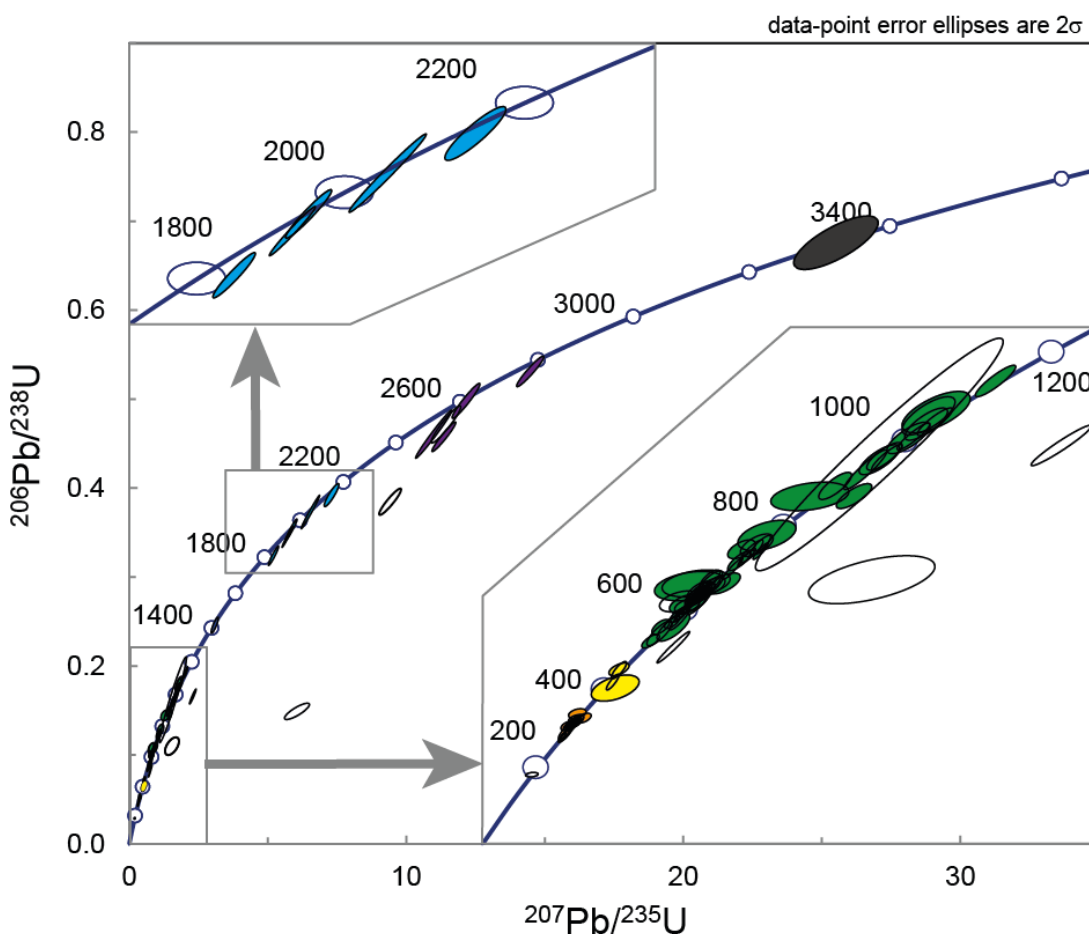


Figure 3 - 20. a. Uncorrected Tera-Wasserburg diagram showing SHB45 zircon analyses (cores in pink, rim in grey). Ellipse size is  $2\sigma$ . b. Individual  $^{232}\text{Th}$ - $^{208}\text{Pb}$  ages of SHB45 zircon cores and rims.

### 5.1.3 Calcschist SHM23B

The calcsilicate SHM23B contains numerous rounded zircons of varying colour and shape. Most of them are oscillatory zoned. Some have thick overgrowths that have been dated with SHRIMP II. A detrital age spectrum was obtained on 102 grains on SHRIMP RG. Analyses that were <95% concordant were discarded, as well as one zircon grain at 186 Ma due to its high U content (1710 ppm), the data table is presented in *Appendix table A3 – 2*.

The zircons yield Th/U ratios between 0.11 and 1.78. Common Pb content was below 0.6% for all but two analyses and most analyses are concordant (**Figure 3 - 21**).



**Figure 3 - 21. Concordia plot of  $^{204}\text{Pb}$ -corrected analyses of SHM23B zircons.**

The detrital zircon population is plotted in a probability density diagram using the program Isoplot (Ludwig 2012). The youngest detrital population defines a peak at  $314 \pm 2$  Ma ( $n=11$ ,  $\text{MSWD}=1.15$ ), and two younger analyses yield 286 Ma and are interpreted as geologically meaningful. A second composite peak is present at around 650 Ma. Older zircons yield scattered Proterozoic and Archaean age, the oldest being 3.35 Ga.

8 grains were analysed for core and rim (**Figure 3 - 22**). In 5 of the grains analysed twice, the two analyses the same age within error. The three remaining grains yield core 1988 ±31 Ma, rim 875 ±14 Ma; core 742 ±8 Ma, rim 405 ±13 Ma; and core 571 ±7 Ma, rim 328 ±7 Ma respectively.

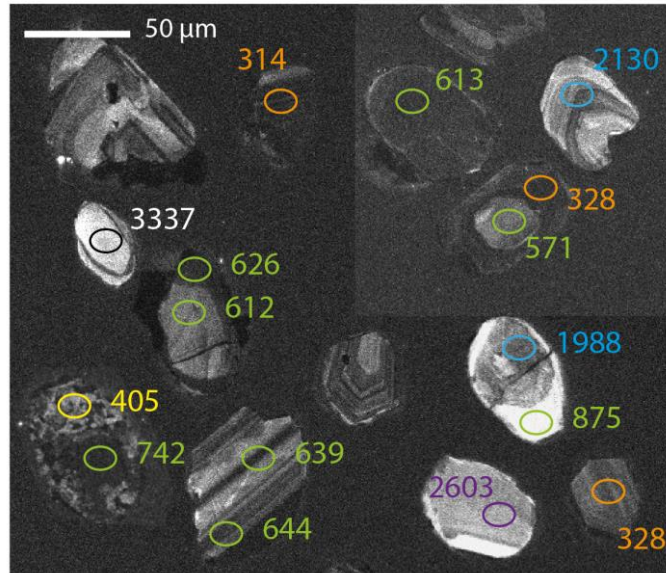


**Figure 3 - 22.** Composite CL image of SHM23B zircons showing SHRIMP spots with  $^{238}\text{U}$ - $^{206}\text{Pb}$  ages. Colour coding refers to age range as shown in Figures 3 - 21 and 3 - 25.

## 5.2 Florencite and Allanite U-Th-Pb

Florencite forms grains of 200-500  $\mu\text{m}$  in size in impure quartzite SHS03 (Figure 3 - 23), with an approximate formula by EDS on 6 cations of  $(\text{Ce}_{0.53}\text{La}_{0.29}\text{X}_{0.18})\text{Al}_{2.98}(\text{P}_{2.15}\text{O}_4)_2\text{OH}_6$ . Allanite is found as overgrowths around florencite grains. Their approximate EDS formula (for  $\text{Al}+\text{Fe}=3$  to estimate minimum cation amounts of REE in structure) is  $(\text{Ca}_{0.10}\text{Ce}_{0.27}\text{La}_{0.13}\text{X}_{0.50})\text{Ca}_{1.0}(\text{Al}_{2.09}\text{Fe}_{0.91})(\text{SiO}_4)_3(\text{OH})$ . The most allanitic (brightest in BSE) domains have been targeted for SHRIMP measurements.

The Halilbağı allanites contain a high proportion of common  $^{206}\text{Pb}$ : >90% in all samples, from 96 to 99 % in SHS03 (*Appendix table A3 – 5*). Allanites in sample SHB03 yield Th/U ratio ranges from 2.0 to 17.3. In this type of mineral, both the age and the common Pb composition need being determined, and the Th content is not high enough for Th-Pb ages to be superior to U-Pb ages (common  $^{208}\text{Pb}$  is also between 96 and 100%). In the U-Pb system, analyses are plotted in a total Tera-Wasserburg diagram (**Figure 3 - 24a**). A regression through the analyses yields an age of 88 ±11-9.9 Ma and a common  $^{206}\text{Pb}/^{207}\text{Pb}$  ratio of  $0.841 \pm 0.002$  (identical to Stacey and Kramers, 1975 for 90 Ma, indicating this initial Pb has negligible radiogenic component).

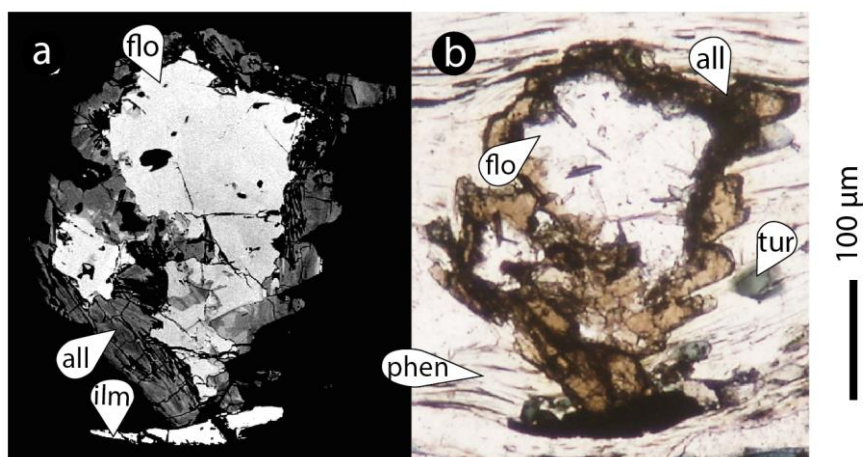


Figure 3 - 23 a. BSE and b. transmitted light image of a florencite-allanite aggregate in SHS03 thin section.

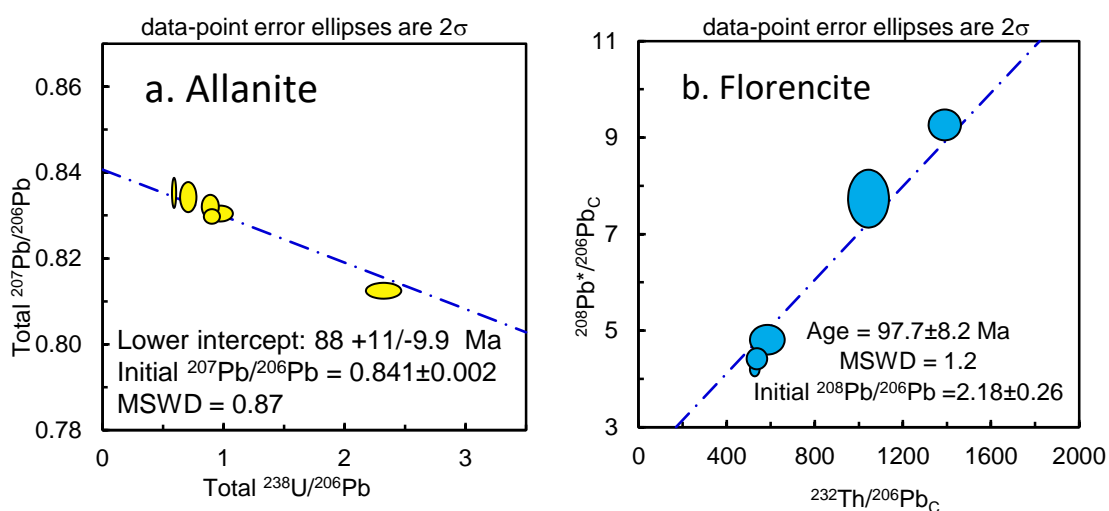


Figure 3 - 24 a. Uncorrected Tera-Wasserburg diagram for SHS03 Allanites. b. Th-Pb isochron for SHS03 Florencites.

Florencites from the same sample were analysed (*Appendix table A3 – 6*). They have been standardised to the TARA allanite (417 Ma, Gregory et al. 2007), these results are thus indicative only as there might be a matrix effect between the phosphate florencite and the silicate allanite. They yield higher Th/U ratios of 132-335. In the U-Pb system, the initial Pb composition can be extracted from the Tera-Wasserburg upper intercept (not shown):  $^{206}\text{Pb}/^{207}\text{Pb}$  ratio of  $0.827 \pm 0.021$ . This ratio deviates from what is obtained by the method of Stacey and Kramers (1975) for an age of 90 Ma (0.841), which indicates that the initial Pb present in florencite has a slight radiogenic component. Florencite is rich in Th (common  $^{208}\text{Pb}$  from 28 to 51%) and an age is calculated in the Th/Pb system by using a Th-Pb isochron (**Figure 3 - 24b**) as described in Gregory et al (2007) where  $^{206}\text{Pb}$  is corrected for the radiogenic component. This yields an age of  $98 \pm 8$  Ma and an initial  $^{208}\text{Pb}/^{206}\text{Pb}_C$  ratio of  $2.18 \pm 0.26$ .



## 6 Discussion

The Halilbağı unit is formed of marbles, quartzites and more micaceous metasediments, intercalated with mafic layers and eclogite boudins. Sample SHS27 is a good example of a quartz and calcite-rich rock (SiO<sub>2</sub>: 42 wt%, CO<sub>2</sub>: 13 wt%) that contains mafic minerals (glaucophane, lawsonite) that are suggesting a volcanoclastic component. The Halilbağı unit, with plenty of mafic material, is very similar to the Devlez formation that crops out in the western Tavşanlı area (Okay and Whitney 2010), and could represent a deformed but coherent sedimentary pile.

On the other hand, other authors (Cetinkaplan et al., 2008, Plunder et al., 2015) interpret this unit as a tectonic melange. The Halilbağı unit would then be the equivalent of the Ovacık accretionary prism unit in the Tavşanlı area (e.g. Plunder et al. 2015). The extent of deformation and reworking that these rocks underwent during subduction is hard to assess because of the fragmental nature of outcrops. The new geochemical data are discussed in light of this controversy on protolith and regional correlations

### 6.1 Origin of the detrital component

Metasedimentary rocks vary from marbles to quartzites to mafic-dominated lithologies and yield a more or less diluted GLOSS-like (Plank and Langmuir 1998) trace element signature (**Figure 3 - 15**). This shows dilution of the main trace element source by carbonates, quartz and mafic volcanic material, respectively. The presence of thick carbonate layers is indicative of relative proximity to the continent, as interpreted in Çetinkaplan et al., (2008) and Özbey et al. (2013). Metacherts such as piemontite quartzite SHS52 are more indicative of a seafloor origin. Zircons extracted from metasediment SHM23B give us information into the source(s) of the detrital component present in the Halilbağı unit. The zircon ages span a wide array between 300 Ma and 3.3 Ga.

In the ages older than 500 Ma, four main groups are observed (**Figure 3 - 25**): Pan-African zircons at 500- 800 Ma, slightly older 800-1100, and two older components from 1800-2200 and 2500-2800 Ma (one grain at 3.3 Ga). These age ranges are similar to data from the western Tavşanlı zone (Okay et al. 2008), and from nearby tectonic units such as the Sakarya basement (Ustaömer et al. 2012), Jordan sandstones or Israel Cambrian siliciclastics (e.g. Kolodner et al. 2006). This confirms the homogeneity of the Northern African margin, close to the Arabian Nubian shield that collects detritus from the African continent (e.g. Condie et al. 2009), up to the Ordovician. Here, one 875 Ma zircon yields a core of 1988 Ma, which indicates crustal recycling in the 875 Ma magmatic source.

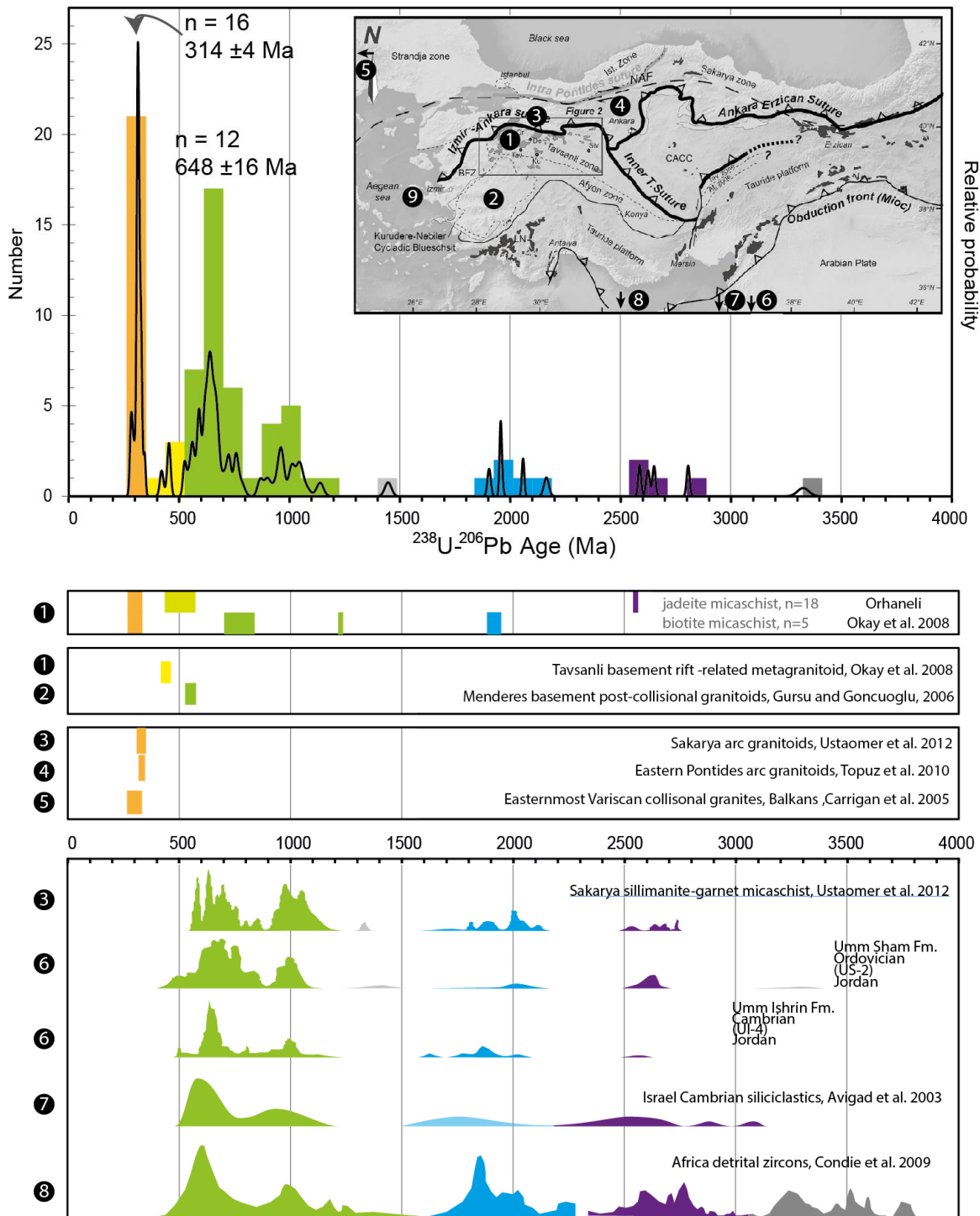


Figure 3 - 25 Comparison of regional detrital rocks and plutonic rocks to the ages detrital zircon from SHM23B. Top panel: probability density plot of concordant  $^{238}\text{U}$ - $^{206}\text{Pb}$  ages in SHM23B zircon cores. Map inset from Plunder et al. (2015). Bottom panels: literature data on detrital and magmatic zircons in the Tavşanlı zone, potential Variscan magmatic sources and detrital zircons in the geographic area. Vertical scale is arbitrary and inherited from probability density plots in the cited papers.

The Carboniferous component can be of two different origins: either the Variscan collisional belt to the West, as suggested by Okay et al. (2008), or the arc to the immediate north. The eastern

end of the Variscan orogen is represented by the Balkans (Carrigan et al. 2005), where 315-285 Ma granitoids are present. Alluvial fans sampling detritus from that arc have been identified in the Greek island of Chios (Zanchi et al. 2003), just to the West of our Tavşanlı unit (#9 in **Figure 3 - 25**). On the other hand, in the vicinity of the Halilbağı unit to the north, the Sakarya zone yields Carboniferous arc granitoids of age 319-327 Ma that could be a more direct source to the detrital component found in the Halilbağı unit (Ustaömer et al. 2012). In the absence of Hf isotopes or precise trace-element measurements on the detrital zircons, both sources are possible or a combination of the two. One grain of 328 Ma yields a core of 571 Ma, which indicates that its source included recycled crustal components, which has been reported for the Variscan orogen (e.g. Carrigan et al., 2005), but also in the Sakarya granitoids (Ustaömer et al. 2012).

## 6.2 Affinity of magmatic rocks in the Halilbağı unit

The composition of mafic pods and layers in the Halilbağı unit is used to provide information about the geodynamic context of their crystallisation. The extent of seafloor alteration and subsequent metasomatism is not discussed here as it is the focus of **Chapter 4**. To provide an indication of the geodynamics, the discussion is based on the least mobile trace-elements at the P-T experienced by these rocks, such as Zr, Nb, Y, but mainly on the REE systematics.

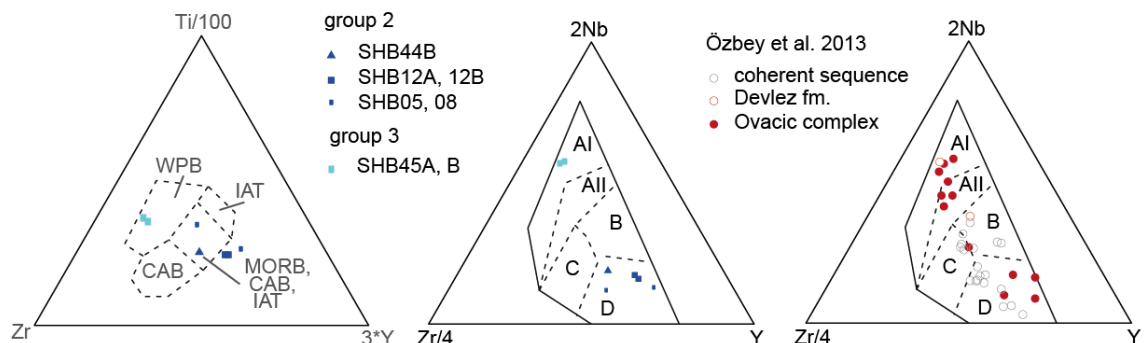


**Figure 3 - 26 Geotectonic classification of Halilbağı unit group 2 and 3 metabasites. Left diagram by Pierce and Cann (1973), rightmost diagrams by Meschede (1986). AI: within plate alkali basalts; All: within plate basalts and within plate tholeiites; B: E-MORB; C: within plate tholeiites and volcanic arc basalts; D: N-MORB and volcanic arc basalts. The rightmost diagram features data by Özbey et al. 2013 from the western Tavşanlı zone.**

Classification diagrams are presented in Figure 3 – 26 in order to compare the dataset obtained here to previous data for the same unit. These results have to be taken with care as it cannot be excluded that these elements have been mobilised during metasomatism (in Chapter 4, the main mobile elements identified are Sr, Pb, potentially Ca and Fe so the HFSE are here considered immobile). Mafic rocks in the Halilbağı unit that don't yield a sedimentary component (group 2 and 3) plot in two distinct field of geotectonic classification diagrams: group 2 metabasites plot in the MORB, CAB, IAT field of the Ti, Zr, Y diagram of Pierce and Cann (1973), Figure 3 - 26,

and the field N-MORB and volcanic arc basalts of the Nb, Zr, Y diagram of Meschede (1986). Whereas, group 3 metabasites plot in the Within-plate basalts field of the Pierce and Cann (1973) diagram, and the within plate alkali basalts field of the Meschede (1986) diagram. The pattern observed in the Halilbağı unit is similar to what Özbey et al. 2013 found in the Ovacic complex, with both the MORB seen in the coherent sequence and the alkali basalts found in the Devlez fm. These two groups are indicative of two different magmatic regimes, similarly to other high-pressure low-temperature terranes (e.g. John et al. 2010). The geodynamic setting for these two magmatic types is discussed below.

### 6.2.1 Group 2 metabasites: MORB and Leucogabbro SHS44A

Among the measured metabasites, 4 samples show a flat LREE pattern compared to chondrites (**Figure 3 - 13**); a pattern that is indicative of a MORB signature. SHB05 and SHB08 are closest to the EMORB endmember, whereas SHB12 and SHS44 yield parallel patterns more enriched, indicative of further differentiation. MORB have been described in the Orhaneli group by Özbey et al. (2013), both in the Kocasu fm., the Inonü marble and the Ovacık complex. MORB have also been found in the Ankara melange, albeit more frequently to the East of Ankara (Gökten and Floyd 2007).

The pair SHS44B-SHS44A has similarities with dolerite – plagiogranite associations found in the Ankara melange (Dilek and Thy 2006), both in their outcrop structure (plagiogranite dykes through gabbro) and trace element composition. They are more enriched in REE, but with a similar pattern: the leucogabbro shows the same trace element concentrations except for a depletion in Ti and an enrichment in Zr and Hf, indicative of further differentiation. It is thus likely that SHS44A is the product of differentiation of SHS44B metagabbro. The spongy zircon alteration textures found in SHS44A are similar to seafloor plagiogranite (Grimes et al. 2013) and support the scenario of oceanic basalts.

The age obtained in SHS44A zircon cores (223 Ma, **Figure 3 - 29**) is similar to radiolarian ages found in the Inonü marble (Late Norian, Kaya et al., 2001), which also feature MORB metabasites (Özbey et al. 2013). Such ages have also been found in radiolarites of the Izmir-Ankara ophiolites (Carnian ages) where the MORB lithologies are interpreted as representing seafloor magmatism, shortly following the rifting of the Tavşanlı ocean (Göncüoğlu et al., 2006 and references therein).

### 6.2.2 Group 3 - OIB basalt

Metabasite SHB45 presents a very LREE-enriched and HREE-depleted REE profile that is different from every other rock-type measured in this study, SHB45 yields very sparse zircons that have oscillatory zoned cores that are potentially a relic from the magmatic assemblage. They

have no Eu negative anomaly, which is indicative of very little (if any) plagioclase fractionation from the magma, and absence of plagioclase in the co-precipitating minerals. Similar signatures are found in ophiolitic gabbros (Kaczmarek et al. 2008).

The trace-element signature of SHB45 is similar to OIB metabasites sampled by Özbey et al. (2013) in the Inonü marble and the Devlez fm. OIB have also been widely recognised in the Ankara melange (Gökten and Floyd 2007) to the NE of the study area. Similarly to the Ankara melange OIBs, SHB45 is interpreted as related to seamount magmatism. The zircon age recorded by SHB45 (123 Ma, **Figure 3 - 29**) is consistent with some of the youngest radiolarian found associated OIB pillow lavas (Rojay et al. 2004; Göncüoğlu et al. 2006; Gökten and Floyd 2007) in the Ankara melange. It also corresponds to the age attributed to the Devlez fm. on the base of regional comparisons by Özbey et al. (2013).

### 6.2.3 Serpentinite pod

Sample SHS26 is a serpentinite, with a mineralogy of antigorite (here determined by optical characteristics, antigorite was identified by Çetinkaplan et al., 2008 in a similar serpentinite lens) and magnetite, from a lens in the Halilbağı unit. It is embedded within blueschists and metasediments, with a reaction halo of talc and carbonate. These lenses are present throughout the Halilbağı unit, more frequent when moving closer to the northern tectonic boundary (Davis and Whitney 2006). Note that these are also described briefly in Whitney et al. (2014), with reaction rims of lawsonite-chlorite±garnet.

This serpentinite's Si, Mg, and Fe contents correspond to a model 92 wt% antigorite with Mg# 0.90, and 8 wt% magnetite. The Mg # of this rock is 0.81, which is lower than expected from a mantle protolith. Moreover, the texture does not show mesh or pseudomorphosis of mantle minerals. Indeed, antigorite and magnetite are very fine grained and randomly oriented, they seem to overprint a precursor serpentinite texture. This is different to the mesh texture described by Çetinkaplan et al. (2008) in a serpentinite lens, which might be the consequence of the smaller size of the SHS26 lens. SHS26 is interpreted as the result of a step of serpentinisation followed by recrystallization: one producing lizardite or chrysotile at low P-T, the second recrystallising the precursor serpentinite into fine grained antigorite. The magnetite is fine-grained and agglomerates in shapes that could be previous opx. Some magnetite is found along fractures, which would imply a redistribution during the later stage of recrystallisation. The indication of a precursor low-grade serpentine mineral favours the hypothesis that this pod was initially serpentinised in an oceanic or accretionary-prism setting and not the mantle wedge: hydration in the mantle wedge would produce antigorite directly (e.g. Schwartz et al., 2013).

In terms of trace elements, this rock has a significant negative Eu anomaly. This implies a cumulate process where plagioclase was present and removed at some stage. The rock is enriched in HFSE elements, which could also be explained by the accumulation of a phase such as chromite or spinel. Specifically, the high TiO<sub>2</sub> content could be explained by a protolith rich in spinel, such as a cumulate. An alternative hypothesis would be preferential leaching of plagioclase during a first stage of fluid-rock interaction, this could be coherent with a high fluid/rock ratio alteration significant of abyssal serpentinites described Hattori and Guillot (2007). The presence of a negative Eu anomaly is interpreted as further evidence that SHS26 is of oceanic crust origin, emplaced for instance as an olivine - orthopyroxene - spinel cumulate gabbro (with an olivine Mg # of e.g. 0.82-0.84). This contrasts with previous interpretations by Zack et al. (2013) and Whitney et al. (2014) stating that these lenses were stripped from the mantle wedge during subduction or exhumation. However, it converges with the interpretation of Çetinkaplan et al. (2008) that the serpentinite lenses are oceanic in nature, incorporated into the Halilbağı by intercalation of oceanic tectonic slices.

#### **6.2.4 Origin of the sediment signature in group 1 metabasites**

The protolith of group 1 metabasites is harder to constrain. Their trace element chemistry is very close to the most enriched metasediments in the Halilbağı unit. This could be the result of either mechanical mixing during sedimentation, accretion or subduction with those metasediments, or by the presence of a subduction component in their source magma. Indeed, immobile trace-element composition of sediment-mixed lithologies are similar to the sediment component in supra-subduction lithologies (e.g. Tatsumi and Eggins, 1995). Group 1 metabasites could thus be the equivalent of metabasites with a subduction component described by Özbey et al. (2013), Göncüoğlu et al. (2006) in the western Tavşanlı zone and the Ankara ophiolites. However, in the Halilbağı unit, there is ample evidence for interlayering and boudinage of mafic rocks into metasediments. Moreover, group 1 metabasites show large deviations from typical major element composition for basalts. This is another evidence for their mixed origin.

In absence of further constraints as to the origin of this signature, these rocks are here interpreted as mixed lithologies such as basaltic pyroclastics previously described in the Tavşanlı zone (Ovacık complex, Plunder et al. 2015; Plunder et al. 2013).

### **6.3 Lithostratigraphic correlation and tectonic setting**

In the stratigraphy established in the western Tavşanlı zone, the coherent Orhaneli group corresponds to a continuous record from rifting to pre-subduction subsidence on the Tavşanlı passive margin, from the Triassic to the Cretaceous (eg. Özbey et al., 2013; Pourteau et al., 2016).

The Kocasu Formation being the record of the rifting creating the Tavşanlı ocean, with bimodal volcanics and detrital infill. The Inonü marble represents a thick carbonate platform due to post-rift passive margin subsidence. The Devlez Formation is interpreted as being a result of a platform collapse. The latter two units contain metabasites that classify as OIB (the intrusive or extrusive nature of these metabasites could not be determined by Özbey et al. 2013).

The accretionary prism complexes (Ovacık unit, OC1-3, Okay, 1986; Plunder et al., 2015) sample the same succession of events, but by stacking of distal oceanic floor lithologies. In these complexes, a variety of basalt chemistries have been reported, with notably MORB and OIB signatures (Özbey et al. 2013).

In the Halilbağı unit, hydrated harzburgites, MOR basalts and more evolved Ti-gabbro and leucogabbro that yield an age of 223 Ma are present, as well as OIB yielding an age of 123 Ma. These rock types are embedded in a succession of basaltic metasediments, marbles, and metacherts, where the GLOSS signature is ubiquitous. This shows the detrital input from the continent, a combination of the northern and southern margin of the Tavşanlı ocean (similar to the detrital zircons reported by Okay et al., 2008 in the Devlez formation). The lithological succession is both close to the Devlez fm. and to the Ovacık complex (e.g. Okay, 1980, Özbey et al. 2013).

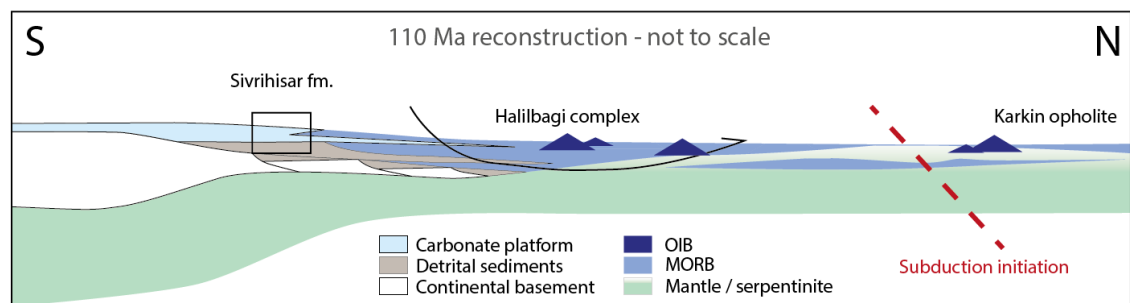


**Figure 3 - 27 Schematic geodynamic reconstruction for Halilbağı at ca. 110 Ma during subduction initiation.**

However, the presence of both a Triassic age and a Jurassic age corresponds to the range of radiolarian ages present in the accretionary complexes such as the Ovacık complex and the İzmir-Ankara ophiolites, that spans the full duration of the Tavşanlı ocean (Figure 3 - 29). Specifically, the presence of Triassic MORB in the Halilbağı unit implies that it cannot be stratigraphically overlaying the coherent sequence (Sivrihisar fm.) as it is synchronous with its base. The presence of these Triassic MORB implies tectonic reworking of Triassic components (such as incorporation as an olistolith in accretionary prism dynamics or later intercalation).

Moreover, the geochemistry of Halilbağı unit metabasites is a good match for the Ovacık unit, with the notable presence of OIB rocks, unknown in the older part of the coherent sequences (Özbey et al. 2013), but common in the Ovacık complex and other similar melanges such as the Ankara melange (Götken and Floyd, 2007). The Halilbağı unit would thus represent a more or less composite assemblage of the distal equivalent of the Sivrihisar fm., sampling Triassic seafloor and Jurassic OIB volcanism, confirming the interpretation of Çetinkaplan et al. (2008), **Figure 3 - 27**. The repartition of the different geochemical types of metabasites does not follow any clear systematics that could help distinguish tectonic slices (**Figure 3 - 28**). If the GLOSS-like metabasites are indeed pyroclastites it is logical to see them closely associated with their lava MORB equivalent. More metabasitic pods should be analysed for trace-elements in order to see if the OIB signature is more widespread. A few analyses are presented in Davis and Whitney (2008) for the pod corresponding to sample SHB53/SV12-13F, but they yield REE patterns indicative of the dominance of mineral signals over WR composition, probably due to the small sample size and thus cannot be used for geodynamics.

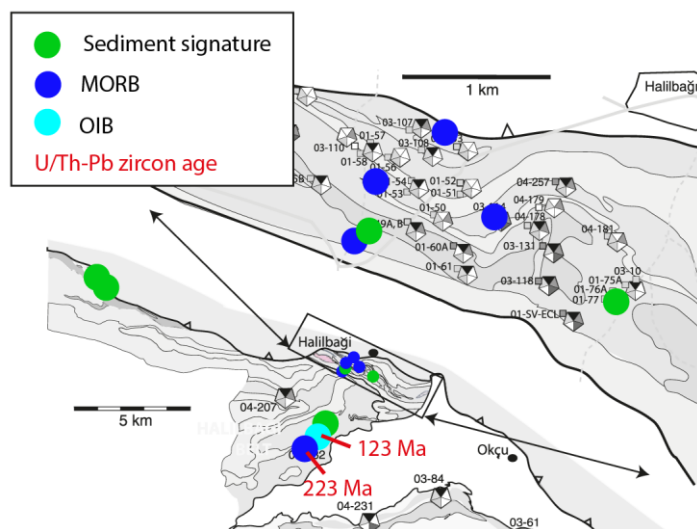


**Figure 3 - 28 Localisation of metabasites and their geochemical signature (superimposed on map from Davis and Whitney (2006). Group 1: sediment signature; Group 2: MORB, Group 3: OIB.**

These geochemical findings are in good agreement with recent interpretations of the Devlez fm. as an oceanic complex (Çetinkaplan et al. 2008; Plunder et al. 2015; Pourteau et al. 2016), on the basis of P-T estimates showing a different tectonic history compared to the Kocasu fm., but also as a reflexion of the geodynamic evolution of the platform, incompatible with OIB volcanism on the continental margin during the Jurassic.



## 6.4 Timing of subduction

The Halilbağı unit has seen a number of recent studies looking at the timing of subduction. Fornash et al. (2016) revisited the Ar-Ar systematics using the UV-LAMP method. This was also addressed by Mulcahy et al. (2014), and Pourteau et al. (2014) using Lu-Hf systematics in WR, garnet and lawsonite. In this study, we look at the U-Pb record in minerals zircon, allanite and florencite.

Zircon is the U mineral providing the most precise ages, given its low content in common Pb and its robustness. It has been shown to be reactive at low temperature conditions in a variety of settings where adequate fluids are present, usually within plagiogranite dikelets into more mafic rocks (Tomaschek et al. 2003; Spandler et al. 2004; Rubatto et al. 2008; Grimes et al. 2013). At these temperatures - in settings varying from seafloor hydrothermalism to blueschist-facies metamorphism, zircons undergo fluid-assisted dissolution-reprecipitation to form skeletal zones, sometimes mixed with the precursor magmatic zircon; instead of forming solid rims as seen in temperatures > 600-700°C in eclogites or granulites.

In the Halilbağı unit, only sample SHS44A, which is a leucogabbro dikelet into a meta-Fe-gabbro, shows patchy zoning and resorption features in zircons. The patchy zones yield mixed dates as young as 87 Ma, contrasting with the 223 Ma magmatic crystallisation age. The dissolution-reprecipitation textures are interpreted to be the result of a fluid reaction event, that could have taken place at any stage of the P-T path of these rocks, as these textures have been documented in seafloor (Grimes et al. 2013) as well as high-pressure rocks (Tomaschek et al. 2003). The trace-element composition of the zircon domains is used to constrain the setting at which the recrystallization happened. Three types of mosaic zone trace-element compositions were found due to the scale in trace element variations, despite the potential for a lot of mixing. The first type yields magmatic-like REE patterns that are slightly enriched in the heaviest REE (rim A), they yield a magmatic-like negative Eu anomaly, and Th/U ratios. These are interpreted as late-magmatic alteration, potentially close to the seafloor. Rim B1 are depleted in MREE, which shows the presence in the rock of a LREE-MREE-rich mineral such as lawsonite, titanite or apatite (lawsonite pseudomorphs and apatite are present in the rock); they yield a negative Eu anomaly indicating the persistence of plagioclase. These are interpreted as greenschist/lower blueschist facies metamorphic recrystallization, as no garnet-related HREE depletion can be seen. These zones yield a few dates around 90 Ma. A third mosaic zone composition (B2) is peculiar with MREE depletion, a slight enrichment in HREE, a negligible negative Eu anomaly, indicative of the absence of plagioclase, but also the incorporation of high amounts of Hf (up to 1.8 wt%). These are believed to be the result of recrystallization during garnet breakdown (garnet being the

source of the excess Hf and HREE), near eclogite facies conditions (where plagioclase is not stable).

These zones are intergrown at the  $\mu\text{m}$  scale, and inclusion-rich. Thus dating separate events was impossible, even by ion microprobe. The few youngest ages (90 to 87 Ma) are taken as the maximum age of the metamorphic recrystallization.

More readily reactive U-Th phases in the Halilbağı unit are allanite and florencite. Lawsonite sometimes contains significant Th (up to 200 ppm), but higher amounts of common Pb (up to 250 ppm). Titanite and rutile contain very little Th and U ( $<0.5$  ppm in measured grains). The dated florencite grains overgrown by allanite in sample SHS03 yield ages with low precision due to high amount of common Pb (98% common  $^{206}\text{Pb}$  in allanite, around 50% common  $^{208}\text{Pb}$  in florencite). The florencite cores yield  $98 \pm 10$  Ma and the allanite rims  $88 \pm 10$  Ma.

The three obtained ages (**Figure 3 - 29**) are in the same range as the most recent Lu-Hf data, but their precision is poor due to mosaic textures in zircon and the high amount of common Pb in U/Th-bearing accessory phases dated here.

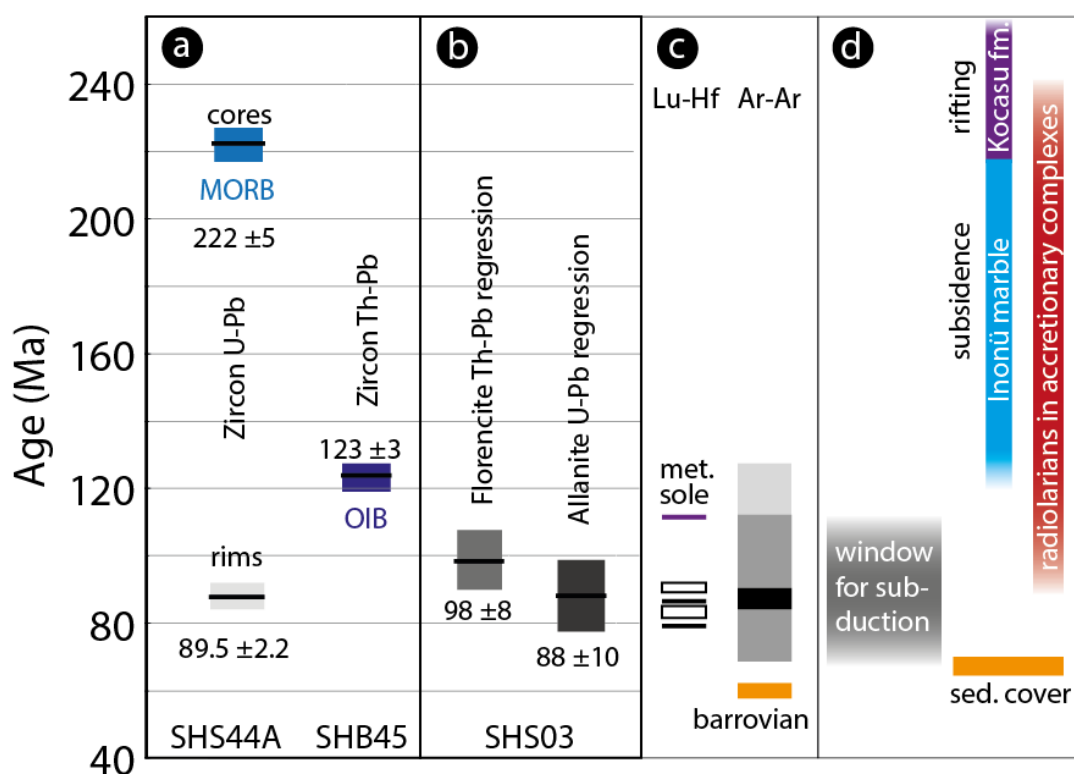


**Figure 3 - 29** Summary of ages compared with literature constraints. a. Average  $^{206}\text{Pb}$ - $^{238}\text{U}$  ages obtained on Halilbağı zircon. b. Florencite Th-Pb regression age and Allanite Th-Pb regression age of impure quartzite SHB03. c. Summary of Lu-Hf and Ar-Ar ages of Halilbağı lithologies (see Figure

3 – 4 for references). d. Geodynamic activity in the Tavşanlı zone (Kaya et al. 2001; Önen 2003; Göncüoğlu et al. 2006; Gökten and Floyd 2007; Pourteau et al. 2016).

## 6.5 Place of Halilbağı unit in subducting structure

Our geochemical data suggests that the Halilbağı unit is formed by different slices of seafloor, including metabasites of different ages and geochemical affinities, metasediments and serpentinites, similar to accretionary complexes of much lesser metamorphic grades (Plunder et al. 2015). It is however unclear if the assemblage of different slices within the Halilbağı unit happened at low-PT in an accretionary wedge or more at depth in the subduction channel. The latter possibility was explored by Davis and Whitney (2006, 2008), where they report three possible slices experiencing lawsonite and epidote stability at different stages, and thus coming from different depths/temperature regimes. They concluded that at least the exhumation story was common within the Halilbağı unit. Our ages can neither refute nor confirm this scenario by lack of precision, the older age of 98 Ma obtained in the florencite cores could hint to a protracted prograde history, such as Fornash et al. (2016) interpret from Ar-Ar ages. These could be recording low P-T metamorphism within the accretionary wedge prior to the entrainment into subduction.

This study showed that the Halilbağı unit can be considered as the eastern equivalent of the Devlez formation as an oceanic complex. There, Plunder et al. (2015) showed that the Devlez fm. had gone to lesser P-T than the coherent sequences underneath (such as the Kocasu fm.). Here in the Sivrihisar massif however, the Halilbağı unit records the highest P-T, similar to the Kocasu fm. in the West.

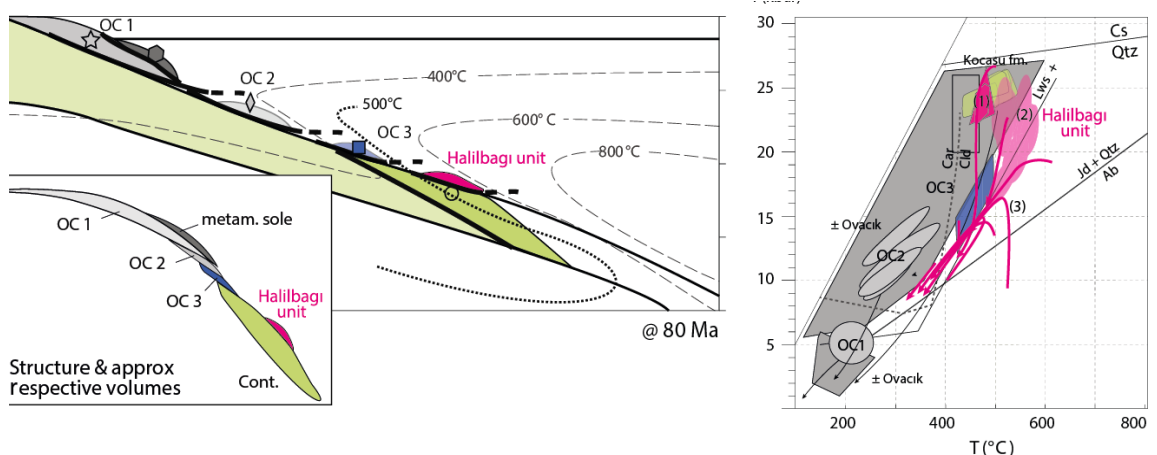


**Figure 3 - 30 Updated Halilbağı unit position on Plunder et al. (2015) figures 10 and 11. P-T estimates for the Halilbağı unit from (1) Çetinkaplan et al. (2008); (2) Davis & Whitney (2008); (3) Davis & Whitney (2006)**

This shows that the exhumation dynamics for both parts of the Tavşanlı zone are not identical, with the exhumation of deeper oceanic complex in the Sivrihisar unit. In both cases though, the oceanic complexes that have been subducted to depth represent a much smaller volume than the more continental carbonate platform (see Plunder et al. 2015). In the Tavşanlı zone, we thus see several oceanic complexes with similar petrologic and geochemical characteristics exhumed from a broad range of depth within the subduction zone (**Figure 3 - 30**), indicating a very dynamic environment of accretion-subduction of material from the top of the down-going plate.

## 7 Conclusions

- Mafic rocks in the Halilbağı unit mostly yield a sediment signature, with sills/flow basalts of OIB and MORB affinity, and lenses of oceanic serpentinites.
- Magmatic zircons in a MOR-type leucogabbro were dated at  $222 \pm 5$  Ma, and an OIB Fe-Ti gabbro at  $123 \pm 5$  Ma.
- Detrital zircons in a calcsilicate sediment yield a provenance from both the Gondwana margin (e.g. Arabian-Egyptian shield) and either the Sakarya zone Carboniferous arc or the easternmost Variscan detritus.
- The presence of OIB and MORB, serpentinite lenses, as well as Triassic and Jurassic magmatic ages are best explained by a composite origin of the Halilbağı unit. The ages correspond to both the base and the top of the coherent carbonate platform in the coherent Orhaneli units, within the range of radiolarites present in the accretionary complexes. We thus confirm previous studies making the Halilbağı unit the equivalent of the Ovacık complex in the western Tavşanlı zone: a composite unit sampling distal seafloor lithologies, similar to widespread cretaceous accretionary complexes in the Tavşanlı-Ankara region.
- SHRIMP metamorphic ages are obtained in the U-Th-Pb system in minerals allanite (retrograde), florencite (prograde) and zircon (multi-phased), which yield  $88 \pm 10$  Ma,  $98 \pm 8$  Ma and  $89.5 \pm 2.2$  Ma respectively. Florencite yields potential for dating the prograde stages of metamorphism in Ca-poor rocks but requires further standard development to investigate matrix bias with respect to monazite and allanite.

## **Chapter 4**

# **Fluid circulation in subducted crust investigated by in situ O isotopes and trace elements in zircon, garnet, apatite and lawsonite (HP-LT Halilbağ ı unit, Turkey).**

### **1 Introduction**

In understanding element cycling in the Earth's mantle, the processes happening in the subducting slab are key, as the slab is the main locus of element transfer from the crust to the mantle. From their oceanic floor protoliths, subducted lithologies undergo major transformations as they dehydrate and deform on their way to sub-arc depths. Metasomatism (e.g. Bebout and Barton 1989) and mechanical mixing (e.g. Penniston-Dorland et al. 2014) between rock types are two dominant processes in the subduction slab which may have long lasting consequences on element recycling. Fluids are the main agent for chemical transfers in the slab, as they catalyse reactions, enable deformation and seismicity, and transfer mass within the subducting slab, to the plate interface and eventually to the overlying mantle. The resulting major and trace-element chemistry of sub-arc lithologies will control what dehydration fluids and melts will permeate to the mantle wedge, and which elements will remain in the slab. This case study uses the Halilbağ ı unit in the Tavşanlı zone in Turkey as a natural laboratory for studying the interaction of different subducting plate lithologies through fluid exchanges during their history at the plate interface. It builds on and contributes to work in better understanding the subduction factory, from the sea floor to sub-arc depths.

Slab dehydration and fluid-rock interactions are complex, because of two main factors: first, fluid flow and deformation are tightly intertwined in subduction dynamics (subduction deformation regimes are presented in Figure 4 - 1). At shallow levels in the seismic zone, abundant fluids (e.g. Hacker 2008) are a major player in seismicity and deformation (e.g. Vrolijk 1987; Byrne and Fisher 1990; Breeding and Ague 2002; Bachmann et al. 2009). The modelling of subduction geotherms is complicated at depth by the upward migration of fluids creating heat advection, as well as the depth and extent of slab-mantle coupling below the seismic zone to the maximum decoupling depth MDD (Wada and Wang 2009; Penniston-Dorland and Kohn 2015). Slab-mantle decoupling is subordinate to the presence of hydrated deformable lithologies in the mantle wedge (e.g. Scambelluri and Tonarini 2012), and thus the depth of the MDD, usually around 80 km

(Figure 4 - 1), can change according to the specific subduction zone fluid regime, which in turns determines where the temperature for main dehydration reactions is obtained in the slab lithologies (Syracuse et al. 2010; Schmidt and Poli 2014). The field record of HP-LT rocks is valuable to study how fluid influxes correlate with temperature and deformation changes in different subduction zones.

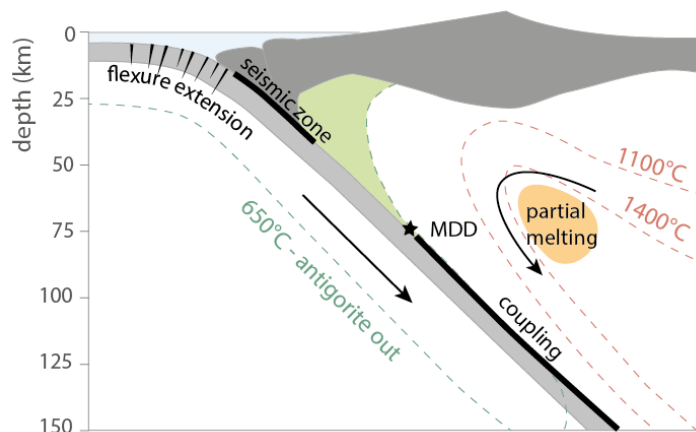


**Figure 4 - 1 Sketch of subduction tectonic environments in the subduction zone (modified from Hilaret and Reynard 2009)**

Second, the subducting slab, made of oceanic mantle, crust and sediments, is heterogeneous in composition and rheology. Although studies have shown that the slab component comprises elements of both metasediments and mafic and ultramafic oceanic crust (Kessel et al. 2005; Spandler and Pirard 2013), the modalities of mechanical and chemical interactions between these two reservoirs are critical to the understanding of sub-arc processes. Both oceanic crust alteration by interaction with seawater and sediments (Miller and Cartwright 2000; Spandler et al. 2004), and the evolution of mélanges at the slab interface - made of mechanical and chemical hybridization of slab lithologies (Marschall and Schumacher 2012) - are thought to play an important role in the geochemical evolution of the slab. The mineralogy and chemistry of these modified and hybridized lithologies are suspected to control the generation and chemical composition of the slab component through dehydration and melting in sub-arc regions. The interaction of sediment-derived fluids with mafic and ultramafic rocks can be traced by fluid-mobile, incompatible trace elements and Sr- and Pb-isotopic studies. However, it is much more difficult to trace the influx of trace element poor fluids from mafic or ultramafic rocks with sediments. This work aims at pinpointing the P-T conditions at which fluid-rock interaction and isotopic mixing occur between different rock types of the subducted slab, and untangling seafloor from subduction hybridization.

Oxygen isotopes are used as monitors for influences of fluids originated in sediments (heavy), or oceanic crust (light) fluids. Indeed, the signatures present in different reservoirs of the subducting slab are diverse. Sediments are rich in the heavy isotope of oxygen ( $\delta^{18}\text{O} = 15\text{-}25\text{ ‰}$ ), whereas the altered oceanic crust and yield intermediate signatures depending on different temperatures of interaction with seawater (12 ‰ –LT to 3 ‰ – HT). Previous studies have used whole-rock or mineral separate signatures to identify where sediment-dominated fluids (e.g. Bebout and Barton 1989; Miller et al. 2001), mafic-dominated fluids (e.g. Philippot et al. 2007), or no significant modification (Barnicoat and Cartwright 1995) are found in different subducted terranes. Here, as outlined in the thesis **Introduction**, the novelty of the method used is the in situ analysis of minerals. This study distinguishes mineral growth zones to establish how much and at which stages of the P-T evolution oxygen is exchanged between sedimentary lithologies and the mafic/ultramafic parts of the slab during subduction metamorphism.

In situ oxygen isotopes in garnet growth zones have been used by a few previous studies of subduction processes: in the Monviso eclogites (Rubatto and Angiboust 2015), in the Franciscan (Russell et al. 2013; Errico et al. 2013; Page et al. 2014), and in the high-pressure rocks of Corsica (Martin et al. 2014b). These studies allowed recognizing fluids of varying signatures during the subduction history of garnet-bearing rocks. Here, the aim is combining garnet data with those from other metamorphic minerals to get a record that is as complete as possible for the reconstruction of the fluid history during subduction, in a range of lithologies. A range of target minerals is used in this study. (i) Zircon is a robust mineral used for oxygen in magmatic and metamorphic settings (Peck et al. 2003; Valley 2003; Page et al. 2014). (ii) Apatite is a ubiquitous fluid-reactive mineral (Smith and Yardley 1999; Spear and Pyle 2002; Li and Hermann 2015) used routinely for in situ oxygen analysis in fossils (Rigo and Joachimski 2010; Trotter et al. 2015), and very recently investigated for geological processes (Sun et al. 2016). (iii) Lawsonite is a trace-element- and water- rich mineral thought to play a significant role in slab-mantle transfer processes (Spandler et al. 2003; Dragovic et al. 2012; Martin et al. 2014a; Vitale Brovarone and Beyssac 2014) and which has not yet been used for in situ oxygen; exploratory results in collaboration with Laure Martin are presented. In each mineral, trace element analysis will allow linking fluid circulations to P-T conditions (similar to work done in zircon and garnet: Rubatto 2002; Martin et al. 2011; Gauthiez-Putallaz et al. 2016; **Chapter 2**), but also identifying changes in fluid-mobile trace-elements along the P-T path (for instance Sr/Pb variations identified in lawsonite by Martin et al. 2014a). These mineral data are then compared to whole rock (WR) analyses to assess the influence of metasomatism on overall signatures.

The chosen field area – the Tavşanlı zone in Turkey – contains some of the best preserved lawsonite eclogites, an invaluable record of cold subduction processes. The main focus is the Halilbağı unit, in the Sivrihisar massif (see maps and context in **Chapter 3**). Previous studies have focused on the petrography and the low-T, high- P trajectory of the Halilbağı metabasites (Gautier 1984; Whitney and Davis, 2006; Davis and Whitney 2006; Çetinkaplan et al. 2008; Davis and Whitney 2008; Whitney et al., 2014). These studies estimated the maximum P-T conditions as 23-25 kbar, 550°C (see summary of P-T determinations in **Chapter 3**). Most unusual is the cold gradient of exhumation, as most Halilbağı rocks escape overprinting and retrogression and contain pristine lawsonite, a rare occurrence worldwide (Tsujimori et al. 2006; Whitney and Davis 2006). The paleogeography of the Halilbağı unit is less investigated, although insights are provided by Çetinkaplan et al. (2008), as well as broader scale studies (Okay and Whitney 2010; Plunder et al. 2013; Plunder et al. 2015; Pourteau et al. 2016). In **Chapter 3**, new geochronological and geochemical data are presented to provide a clearer geodynamic background to the Halilbağı unit. The main conclusions are that the Halilbağı unit is an oceanic complex similar to accretionary units in the western part of the Tavşanlı zone (e.g. Plunder et al. 2015) formed by a juxtaposition of contrasted distal (cherts, MORB and OIB basalts and gabbros, serpentinites) and continental margin lithologies (detrital and carbonate-rich sediments) that was subducted and exhumed along with other oceanic complexes, close to the plate boundary. This area thus provides the opportunity to study the interaction between different lithologies of the subducting slab, down to the maximum decoupling depth (around 80 km).

The timing of subduction is assumed to be Cretaceous, with most ages related to the peak of metamorphism around 90 Ma (e.g. Mulcahy et al. 2014; Fornash et al. 2016, this study, full summary of available data in **Chapter 3**). Retrograde blueschist assemblages are dated at ca 85 Ma, and a recent study of prograde assemblages concludes that samples have come from different P-T-t trajectories, with prograde ages around 93 Ma (Pourteau, pers. comm.). Such conclusions have also been drawn by Davis and Whitney (2008), on the base of P-T and deformation only. Ar-Ar studies hint to a more protracted history with earliest ages around 125 Ma (Fornash et al. 2016), similar ages in earlier studies were questioned on the basis of the possible presence of excess argon (Sherlock and Kelley 2002). Fornash et al. (2016) assign phengite recrystallization to phases of deformation and fluid flow in the Halilbağı unit. That work ties into deformation studies of the Sivrihisar massif (Gautier 1984; Teyssier et al. 2010; Whitney et al. 2014) that show an increase of deformation intensity towards the northern contact of the Halilbağı unit to the low-grade peridotitic unit, assigned to exhumation-related deformation (Whitney et al. 2014).



Geochemical studies of the Sivrihisar/ Halilbağı unit are scarce. Cr zoning in lawsonite has been related to fluid influxes (Sherlock 1999), and another study has reported halogen concentrations in amphibole, lawsonite, phengite and apatite and concluded that the rocks were depleted in Cl at shallow subduction levels but that F is retained (Pagé et al. 2016). A first part of the dataset on lawsonite trace-elements presented in this chapter was published in Martin et al. (2014a), paper provided in *Appendix A4*. In this thesis, **Chapter 3** provided additional data for impure quartzite SHB046, and petrography and trace-element data acquired on sample SV03-103 provided by D. Whitney (Davis and Whitney 2008). The preliminary work on sample SV03-103 highlighted the fractal heterogeneity of some metabasitic lithologies, thus impairing the ability for distinguishing small scale vs large scale equilibration processes. In this work, the focus is thus on typical examples of the lithologies (marble, impure quartzite, metachert, serpentinite, metabasites: lawsonite eclogite and lawsonite blueschist), on samples that are as homogenous as possible at the thin section to hand specimen scale.

The current study aims at shedding more light on fluid circulation between different rock types in the subducting slab, which are well preserved in the Tavşanlı zone, by combining in situ mineral  $\delta^{18}\text{O}$  analysis with in situ trace-element analysis, and integrating it with WR signatures.

## 2 Methods

Mineral mounting and imaging methods are presented in **Chapter 3**.

### 2.1 Mineral chemistry

Qualitative chemical analyses on spots were obtained with a solid state Energy Dispersive (EDS) detector on the Research School of Earth Sciences – RSES -- JEOL SEM instrument using an acceleration voltage of 15V and a current of 60-70 nA. Analyses were checked for stoichiometry and for garnet, UWG2 was measured as a secondary standard. The EDS measurements were within 5% of published values for this garnet (Valley et al. 1995). The SEM EDS was also used to produce chemical maps by scanning the beam across the field of view. For major elements (over 5 element wt%) the settings used were a short dwell time (0.5 ms) with 5 to 10 frame repetitions.

Garnet and clinopyroxene EMPA analyses were performed on a JEOL JXA-8900R at the Department of Earth Sciences, University of Minnesota. An acceleration of 15 keV, a beam current of 20 nA, and a beam diameter of 1 micron were used. Elements were acquired using diffraction crystals LiF for Cr ka, Ti ka, LiFH for Mn ka, Ni ka, Fe ka, LiF for Cr ka, Ti ka, LiFH for Mn ka, Ni ka, Fe ka, PETJ for Ca ka, K ka, and TAP for Si ka, Na ka, Mg ka, Al ka. The

standards were anorthite, feldspar, silicate for Ca, chromite, spinel, oxide for Cr, ilmenite, oxide for Ti, pyrope, garnet, silicate for Si, albite, plagioclase, feldspar, silicate for Na, almandine, garnet, silicate for Fe, microcline (asbestos), feldspar, silicate for K,  $\text{Mg}_2\text{SiO}_4$  (synth) for Mg,  $\text{Ni}_2\text{SiO}_4$  for Ni, and spessartine, garnet, silicate for Mn and Al. The peak and off-peak counting time was 20 seconds for all elements. Standard intensities were corrected for standard drift over time. A ZAF matrix correction was applied.

Trace elements were measured on an ArF excimer laser coupled to a quadrupole Inductively Coupled Plasma Mass Spectrometer (ICP-MS) Agilent 7700 at the RSES at ANU, using the setup described in Eggins et al. (1998). The laser was tuned to a frequency of 5 Hz and energy of 50 mJ (corresponding to a HV of around 26-27kV). Spot sizes of 22 and 28  $\mu\text{m}$  for zircon and of 62  $\mu\text{m}$  for garnet were used. Three international glass standards were measured in every run: NIST 610 and 612, as well as BCR-2G. The counts were standardised to NIST 610 (zircon) and NIST 612 (garnet) glasses and accuracy was monitored by analysing BCR-2G glass. Recent data for the NIST glasses (Jochum et al., 2011; Spandler et al., 2011) differ from previous estimations (Pearce et al., 1997) by as much as 5 to 10% for certain elements (Cl, Nb, P, Sc, Sn, Ta) in NIST 610 and NIST 612 (As, F, P, Ti). Values of Spandler et al. (2011) have been used for data reduction. Data were acquired over a 65 seconds analysis that included a 20 s background and the reference materials were measured after every eight unknowns. Stoichiometric Si was employed as internal standard for zircon ( $\text{SiO}_2$ : 31.6 wt%) and garnet ( $\text{SiO}_2$ : 42 wt%). Reproducibility and accuracy as assessed on the BCR-2G glass were within 10% or less across all analysed elements. The data was reduced with the freeware Iolite (Paton et al. 2011) and its data-reduction scheme for trace-elements (Woodhead et al. 2007).

Trace element slit-profiles were done on garnet. They are performed by scanning the surface of the mineral with a slit that is moved laterally at rates from of 3 to 5  $\mu\text{m}/\text{s}$ . The size of the slit is 5 by 50  $\mu\text{m}$ . Scans on the primary standard (NIST 610 glass) are performed for 2 minutes roughly every 3 measurement. No secondary standard is used. Most of the profile data are used in a qualitative manner. When possible, profiles were measured from the lowest concentration side to the higher concentration side to avoid “tail” effects in the signal.

## **2.2 Oxygen isotope analysis**

Oxygen and carbon isotopes in carbonates were measured with Joe Cali at RSES using a Thermo MAT 253 and Kiel IV microcarbonate preparation device. WR powders were weighed according to previously measured Leco C contents so that the carbonate weight was around 40  $\mu\text{g}$ , for a maximal sample weight of 200  $\mu\text{g}$ . The samples were weighed into glass thimbles. The samples

are then dissolved in 105%  $\text{H}_3\text{PO}_4$  at  $90^\circ\text{C}$  and analysed alongside standards NBS 18 and NBS 19 to calibrate the  $\delta^{18}\text{O}$  composition. The external precision for the measurements is  $\pm 0.04$  ‰ for  $\delta^{13}\text{C}$  and  $\pm 0.06$  ‰ for  $\delta^{18}\text{O}$ . All carbonates were treated as calcite for data reduction purposes (no additional fractionation coefficients were used).

Oxygen isotopes were measured in de-carbonated WR powders by the Institute of Geological and Nuclear Sciences (GNS; Lower Hutt, New Zealand) using laser fluorination (Reactant:  $\text{BrF}_5$ , following the method of Sharp 1990). For de-carbonation, 2.5 g aliquots were treated with 10%  $\text{HCl}$ , then rinsed to neutral pH. This was repeated twice. They were subsequently weighed to determine the carbonate content.

Lawsonite crystals were mounted both as grain separates and as composite mounts containing thin section cuts, or polished blocks of rock. Lawsonite crystals range from  $50\ \mu\text{m}$  to 2-3 mm in size. Lawsonite analyses were performed on a Cameca 1280 Ion Microprobe at the Centre for Mineral Characterisation and Analysis in University of Western Australia, Perth with Laure Martin. The primary beam used in a  $\text{Cs}^+$  source, with an intensity varying between 3.05 and 2.78 nA. Counts per second on the secondary peak were ca.  $2.4 \times 10^9$  on  $^{16}\text{O}$  and ca.  $4.8 \times 10^6$  on  $^{18}\text{O}$  the lawsonite standard CAL. Peak shape and stability on lawsonite were not as good as on the garnet standard UWG2, but stabilised during the first hour of the session. After set up, a few sets of standards were analysed. A steep downhole fractionation behaviour was observed, similar to what is seen in apatite (L. Martin pers. comm.) In order to mitigate that effect, a  $20 \times 20\ \mu\text{m}$  raster was used during analysis, resulting in a broader and flatter spot of ca.  $35\ \mu\text{m}$  diameter. This reduced the internal SE by a factor of 2 down from 0.015 to ca. 0.008 on ratios, and also increased the reproducibility down to ca. 0.3 ‰ ( $1\sigma$ ). The standard CAL is used ( $\text{LF } \delta^{18}\text{O}_{\text{VSMOW}} = 8.10\text{‰}$ , L. Martin, unpublished), embedded in the same mount, it is measured every 6 unknowns. Drift correction was applied when drift on standard values was over 0.5 ‰.

Antigorite  $\delta^{18}\text{O}$  analysis was performed by M-R. Schicchitano on SHRIMP 2 on polished rock cubes, following the method described in Rubatto and Angiboust (2015). The apatite  $\delta^{18}\text{O}$  analysis method is described in **Chapter 1**.

Zircon oxygen isotopes were analysed on the same mounts as U-Pb dating with the SHRIMP II instrument following the procedure described in Ickert et al. (2008). The standard Temora ( $\delta^{18}\text{O}_{\text{VSMOW}} = 8.2\text{‰}$ , Black et al. 2004) was used. Analyses consist of 5 scans of 20 s for a total counting time of 100 s. The reproducibility of TEM zircons was within 0.5‰ ( $2\sigma$ ) during each analytical session. Raw data were processed with the in-house software POXI.

Garnet oxygen isotopes are measured on SHRIMP II and SHRIMP SI following the method of Martin et al. (2014b). Analyses consist of 5 scans of 20 s for a total counting time of 100s and the standards are measured every 5 unknowns. The reproducibility of the standard UWG2 (Valley et al. 1995), is within 0.3‰ ( $2\sigma$ ) for the analytical sessions. A matrix correction for grossular content was made according to calibrations by Martin et al. (2014b) acquired in the same year as the unknown analyses, with similar running parameters. Garnet chemistry was acquired by EDS analysis, measured a posteriori next to each SHRIMP spot after a slight re-polish. Error propagation for oxygen isotope analyses follows Martin et al. (2014b).

### **3 Sample description and mineral composition**

The samples were chosen to represent the variability in lithologies and geochemical signatures that could document contrasts in  $\delta^{18}\text{O}$ . The samples were taken from homogenous parts of layered outcrops in order to focus on heterogeneities over 10 cm in scale, aside from the pod samples SV03-103, SHB53 and SHB42 that are layered at the thin section scale.

Three types of lithologies are identified using immobile geochemical indicators in **Chapter 3** (Table 4 - 1). A number of mafic pod and layers have magmatic protoliths, with MORB (group 2) or OIB (group 3) signatures. Other mafic layers show a sediment-like REE signature and deviations in major elements compared to their magmatic equivalents, and are interpreted as mixed lithologies (group 1). Finally, a variety of metasediments were sampled, varying from impure quartzite to impure marbles and calcsilicates.

**Table 4 - 1. Halilbağı sample description and summary of analyses performed in this study, see Chapter 3 for dating and WR geochemistry**

Sample	Locality	Rock type	Mineralogy	U-Pb or Th-Pb Dating	Trace-element Affinity	Oxygen isotope analysis					
						WR-c	WR-s	Ap	Lws	Grt	Zrn
SHB05	h	Eclogite pod	Omp, gln, grt, lws, amp, rt, tn, ap		MORB	x	x	x	x	x	
SHB08	h	Blueschist layer	Gln, lws, omp, WM		MORB	x	x	x			
SHB12	h	Eclogite pod	Omp, WM, grt, chl, ep, rt, tn, ap		MORB	x	x	x	x	x	
SHS26	h	Serpentine pod	Atg, opq, cal		MORB	x	x				
SHS44A	sh	Lws-phen-grt layer	Qz, grt, WM, ep, all, lws rel., ap, zrn	<b>222 ±5 Ma</b> 89.5 ±2 Ma	MORB		x	x		x	x
SHS44B	sh	Blueschist layer	Grt, gln, qz, ep, amp, WM, lws rel., omp rel., ap, rt, zrn		MORB		x	x		x	
SHB45	sh	Eclogite layer	Omp, Gln, grt, WM, lws rel., rt, tn	<b>123 ±3 Ma</b>	OIB		x	x		x	x
SV01-75	h	Blueschist	Gln, WM, lws, grt (...)		(Mafic)				x		x
SHB53	h	Eclogite pod	Omp, gln, WM, lws, grt, ep, rt, tn, aln		Mafic sed.		x	x			
SV12-13F	h	Eclogite pod	Omp, WM, lws, grt (...)		(Mafic sed.)				x		x
SHB02	h	Omph-lws layer	Lws, omp, qz, opq		Mafic sed.	x					
SHB42C	sh	Chl-lws-grt pod	Chl, grt, ep, lws rel., cal, WM, qz, opq		Mafic sed.	x					
SHB32A	i	Lws-chl pod	Lws, Chl, opq, tn, some ep		Mafic sed.		x	x		x	
SHB32B (ep)	i	Ep-chl-lws pod	Ep, chl, lws, opq, tn, qz		Mafic sed.		x				
SHB50B	i	Gln micaschist layer	Gln, lws, omp, grt, WM, qz, opq, rt, tn, ep-aln, chl, amp		Mafic sed.		x	x		x	x
SHS03	h	Impure quartzite layer	Qz, lws, WM, grt, ep, flo, aln, opq, tur	<b>98 ±8 Ma</b> <b>88 ±10 Ma</b>	Sed.		x	x		x	x
SHS46	h	Impure quartzite layer	Qz, lws, WM, ep, flo, all, opq, tur		Sed.		x				
SIS53	i	Impure quartzite layer	Qz, WM, lws, gln, opq		Sed.		x	x			
SIS52	i	Piemontite quartzite layer	Qz, opq, ep, cal, WM, tur		Sed.	x	x	x			
SHM23B	h	Calcsilicate layer	Qz, cal, WM, opq	<b>3.5 Ga –</b> <b>280 Ma</b>	Sed.	x	x	x			
SHS27	h	Calcsilicate layer	Cal, opq, chl, WM, ep, qz, lws		Sed.	x	x	x			
SGM21	g	Impure marble layer	Cal, qz, WM, ep, opq		Sed.	x	x	x			
SHM04	h	Marble layer	Cal, opq		Sed.	x					

Locality: h: Halilbağı; sh: South Halilbağı; i: İkipinar; g: Günyüzü

 Dating: zircon (straight font) or other accessories (*italic font*). Protolith ages are in **bold font**, metamorphic ages are in regular font.

Trace-element affinity in brackets ( ) is assumed and not measured. WR-c: Whole-rock carbonates; WR-s: Whole-rock silicates

### 3.1 Metabasites (groups 2 and 3) and serpentinite

SHB05 is a retrogressed lawsonite eclogite boulder found in the river bed of the Halilbağı creek. It contains abundant lawsonite, as well as clinopyroxene relicts in a corona of glaucophane (Figure 4 - 2). Some clinopyroxene relicts are peppered with rutile exsolutions, and could represent relict magmatic pyroxene; clinopyroxene is otherwise unzoned and contain an aegirine component (Figure 4 - 5,  $Ae_{19-29}$ ,  $Jd_{14-27}$ ,  $Q_{54-64}$ , *Appendix table A4 - 2*). 3 mm garnet crystals are unzoned with the exception of minor Mn depletion towards the rim (Figure 4 - 3, Figure 4 - 4, *Appendix table A4 - 3*,  $Gr_{S21-23}$ ,  $Prp_{3-7}$ ,  $Sps_{5-26}$ ,  $Alm_{50-66}$ ). Garnet contains inclusions of lawsonite, glaucophane and clinopyroxene. Rutile is overgrown by a corona of titanite. Lawsonite forms polycrystalline aggregates that have a square shape, potentially pseudomorphs after plagioclase or an earlier generation of lawsonite. The bigger lawsonite crystals have cores rich in inclusions of glaucophane needles. The pseudomorphic lawsonite aggregates, together with groups of glaucophane and omphacite might be a relic of fine-grained gabbroic texture. This sample contains pyrite, which is sometimes oxidised, in line with signs of weathering across the sample. A small vein is present in hand sample (2 cm long, 2 mm wide), filled predominantly by lawsonite. SHB05 garnets and clinopyroxene yield 450°C using the Ravna (2000) thermometer for a pressure of 20 kbar, with  $Fe^{3+}$  contents calculated by charge balance in clinopyroxene. The uncertainty on these temperatures is high because of minor compositional variations and the hypothesis made for pressure, and is around  $\pm 50^\circ C$ .

SHB08 is a lawsonite blueschist with minor calcite found within 50 m of the contact with the serpentinite-gabbro unit. It contains lawsonite patches and veins as large as 1 cm within a fine-grained glaucophane and chlorite matrix. The patches could be filled vacuoles, or the result of veining and boudinage.

SHB12 is a phengite-bearing lawsonite eclogite that outcrops as a boudin within metasedimentary schists. It contains a matrix of omphacite, phengite and chlorite, with 2-4 mm garnet crystals. Garnet crystals have a core-rim texture in BSE (Figure 4 - 4a) with rims enriched in Mn and Mg (core:  $Gr_{S22-25}$ ,  $Prp_{15-20}$ ,  $Sps_{5-11}$ ,  $Alm_{51-53}$ ; rim:  $Gr_{S20-27}$ ,  $Prp_{7-9}$ ,  $Sps_{10-19}$ ,  $Alm_{51-58}$ , Figure 4 - 3). Rims of this composition form along garnet fractures and edges, along irregular boundaries (Figure 4 - 4a). Garnets are sometimes chloritised. A lawsonite vein (3 mm wide) is found in sample SHB12B. Lawsonite is also found in garnet pressure shadows in a similar sample collected by K. Fornash. Large rutile grains (400  $\mu m$ ) and some titanite are present, mostly around rutile. This sample contains small allanite grains overgrown by epidote. Most minerals show zoning with BSE-lighter rims, generally enriched in Fe over Mg. Typically, clinopyroxene has  $Fe^{3+}$ -rich rims (core:  $Ae_{3-8}$ ,  $Jd_{40-43}$ ,  $Q_{52-55}$ ; rim:  $Ae_{9-24}$ ,  $Jd_{20-41}$ ,  $Q_{49-63}$ , Figure 4 - 5a) along grain boundaries and fractures,

forming similar textures as garnet (Figure 4 - 4e). Along chlorite halos around garnet, clinopyroxene has Fe-rich aegirine rims that are the brightest in BSE ( $Ae_{40-49}$ ,  $Jd_{31-39}$ ,  $Q_{12-29}$ ). Garnet-clinopyroxene temperatures for rim compositions in SHB12B are ca.  $535 \pm 50^\circ\text{C}$ .

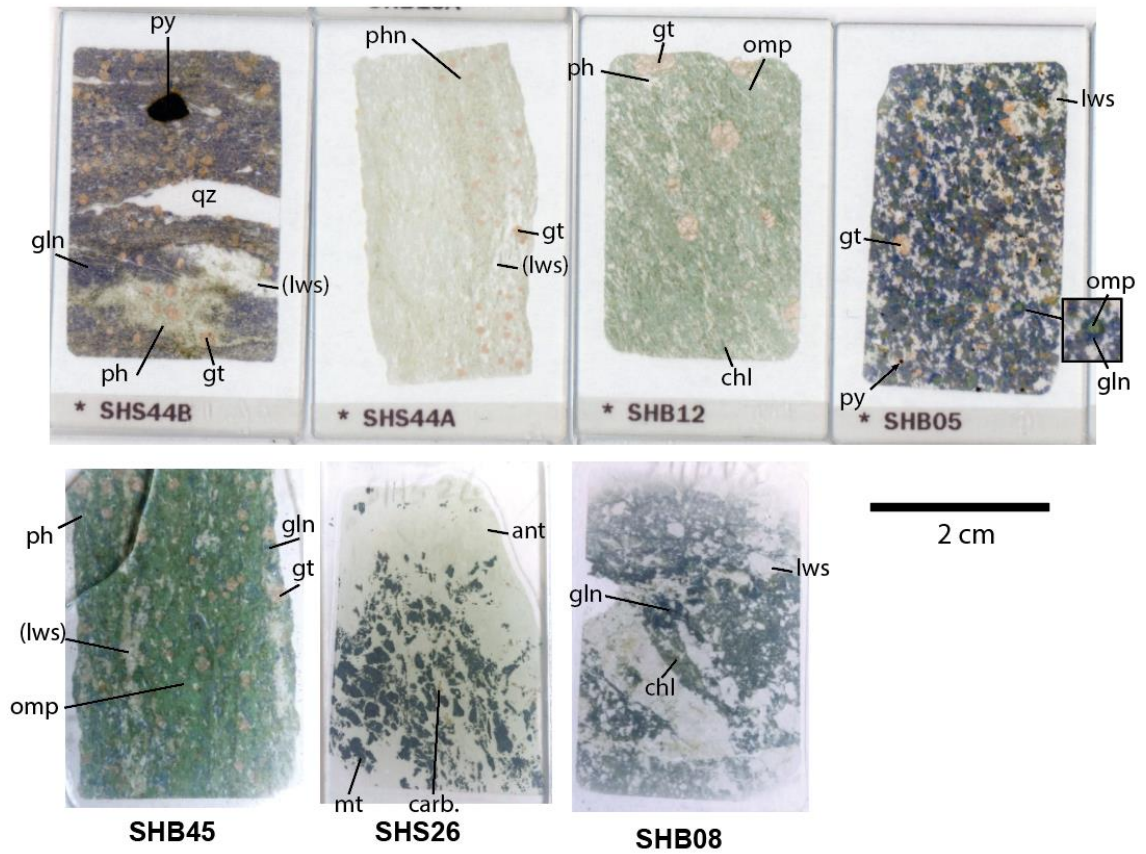


Figure 4 - 2. Thin section scans of Halilbaği metabasites and serpentinite (SHS26) with indication of main mineral phases. Mineral abbreviations are from (Whitney and Evans 2010).

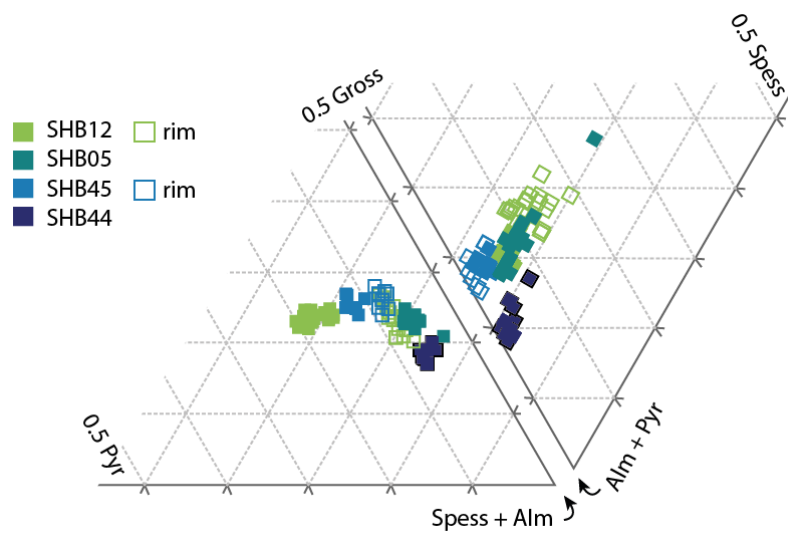


Figure 4 - 3. Garnet compositions of Halilbaği meta-igneous rocks, SEM data.

SHB44 is a blueschist (SHB44B), with a qtz-ph (lws)-grt layer (SHS44A). In this sample, all lawsonite is retrogressed in polymineralic pseudomorphs including epidote. In the mafic part, small relicts of omphacite are found, overgrown by glaucophane. Garnet grains are 2-4 mm in size and little zoning is seen apart from Mn depletion and Fe increase towards the rims (Grs<sub>17-20</sub>, Prp<sub>5-7</sub>, Sps<sub>1-8</sub>, Alm<sub>69-75</sub>, Figure 4 - 3, Figure 4 - 4d). Selvages of qtz-ap, qz-ap-omp and qz-ph-(lws)-gt-ap are found. Clinopyroxene have Fe-rich rims (bright in BSE, not analysed by EMPA). In the leucocratic layer, garnet grains are 2 mm in diameter; they contain inclusions of zircon and lawsonite relicts, and are of similar composition as in the mafic part of the sample (Grs<sub>17-19</sub>, Prp<sub>5-7</sub>, Sps<sub>1-4</sub>, Alm<sub>71-75</sub>). Some garnet grains are chloritized at the rim. Abundant zircon and apatite are present. Zircons show spongy and skeletal textures, possibly due to fluid-related dissolution-precipitation and metamictisation. Epidote and allanite are present in lawsonite pseudomorphs

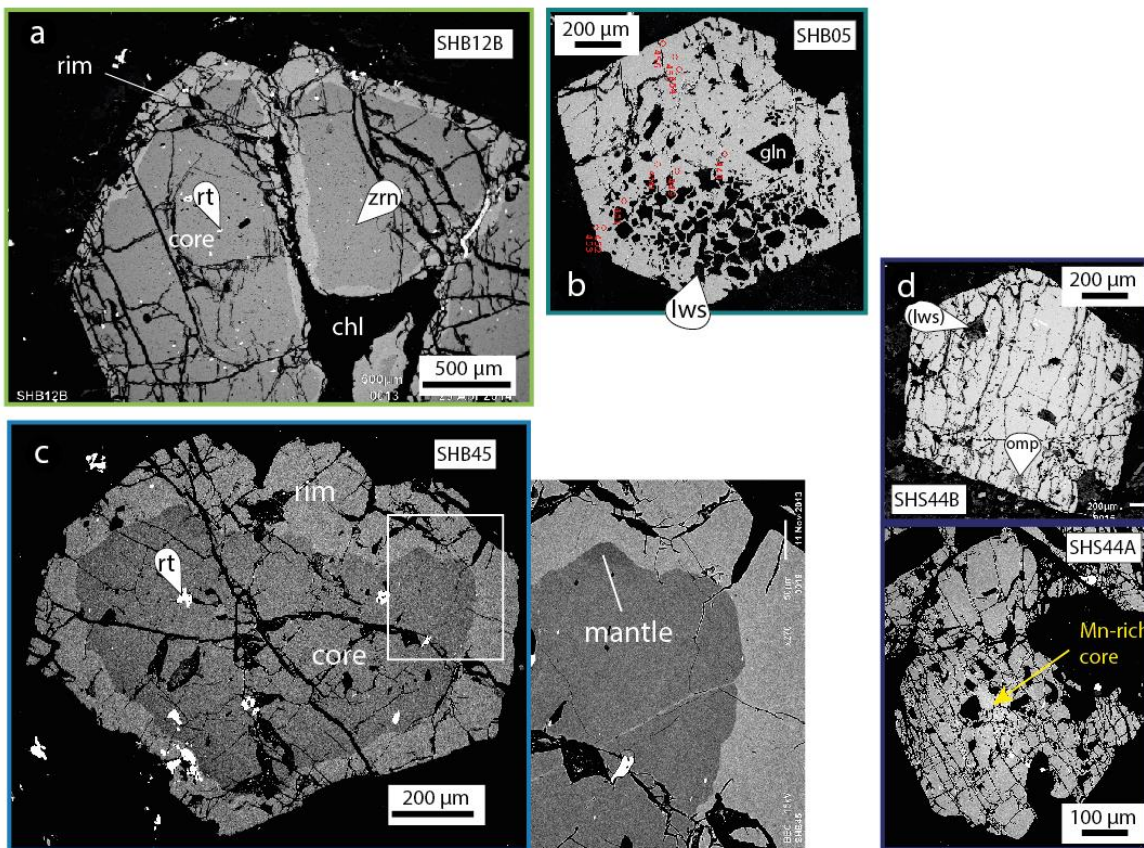


Figure 4 - 4. BSE images of Halilbağlı meta-magmatic rock garnets

SHB45 is a phengite-bearing lawsonite eclogite, where lawsonite is also retrogressed. Omphacite is dominant, forming elongated grains with inclusion-rich cores. Glaucophane and phengite form the groundmass. In some layers, lawsonite is dominant and is preserved as box-shaped pseudomorphs with epidote and white mica. Garnet grains are 4 mm in size and display core-rim zoning (Figure 4 - 4c). Cores are more HREE-rich and Fe-rich compared to the rims (core: Grs<sub>24-</sub>



27, Prp<sub>10-13</sub>, Sps<sub>3-5</sub>, Alm<sub>58-60</sub>; rim: Grs<sub>24-28</sub>, Prp<sub>7-9</sub>, Sps<sub>1-5</sub>, Alm<sub>60-65</sub>, Figure 4 - 3). Garnet cores contain inclusions of titanite and lawsonite, garnet rims contain rutile. SHB45 also contains zoned clinopyroxene (Figure 4 - 5), with omphacite cores (Ae<sub>8-12</sub>, Jd<sub>35-44</sub>, Q<sub>49-54</sub>) surrounded by more aegirine-rich rims (Ae<sub>16-22</sub>, Jd<sub>23-29</sub>, Q<sub>53-59</sub>). The rim compositions are seen along grain boundaries, but also along cracks. Similarly to garnet rims, clinopyroxene rims show irregular boundaries possibly indicating dissolution-reprecipitation. Grt-cpx temperature is ca. 475°C ±50°C for rim compositions in SHB45. Rutile is abundant throughout the rock, especially in lawsonite-rich layers. A few zircons were separated from the rock.

SHS26 is a serpentinite pod described in detail in **Chapter 3**, made of antigorite and magnetite. The serpentinite contains pods of orange carbonate, and veinlets of white calcite. It is surrounded by a rim of talc and carbonate (see details in **Chapter 3**), within mixed metasediments and mafic schists.

### 3.2 Mixed metabasites (group 1)

SHB02 is a lawsonite-omphacite layer, with small grain size (Figure 4 - 7). Lawsonite and omphacite form small prisms aligned with the foliation, with minor chlorite. Some lawsonite crystals are bigger and squared, and have inclusion-rich cores. Small quartz and calcite veins are present. The sample contains minor amounts of calcite and minor phengite in some layers. Some almond-shaped zones contain bigger lawsonite crystals surrounded by chlorite. Inclusion-rich apatite crystals are visible in thin section.

SHB42 is a metre-sized pod, with several mineralogical layers. The outside shell of the pod is mainly chlorite and, towards the inside, the fine-grained chlorite hosts 5 mm lawsonite pseudomorphs. The next layer is fine-grained, with small epidote-quartz veinlets, in a matrix of fine-grained epidote and chlorite, with large lawsonite pseudomorphs and small (<1mm) garnet crystals (SHB42C). Calcite and oxides are present. The core of the pod is made of a slightly coarser-grained rock with garnet and lawsonite blasts, now replaced by white mica and epidote.

SV01-75 is a blueschist sample provided by D. Whitney. The sample is dominated by glaucophane and contains large (5 mm) lawsonite crystals with sector zoning, and garnet that displays BSE-dark mantles and small BSE-light Mn-rich rims with irregular boundaries (Figure 4 - 8a,e, core: Grs<sub>25-29</sub>, Prp<sub>8-11</sub>, Sps<sub>2-11</sub>, Alm<sub>56-58</sub>; mantle: Grs<sub>31</sub>, Prp<sub>12</sub>, Sps<sub>1</sub>, Alm<sub>56</sub>; rim: Grs<sub>25-28</sub>, Prp<sub>6</sub>, Sps<sub>8-12</sub>, Alm<sub>57-58</sub>).

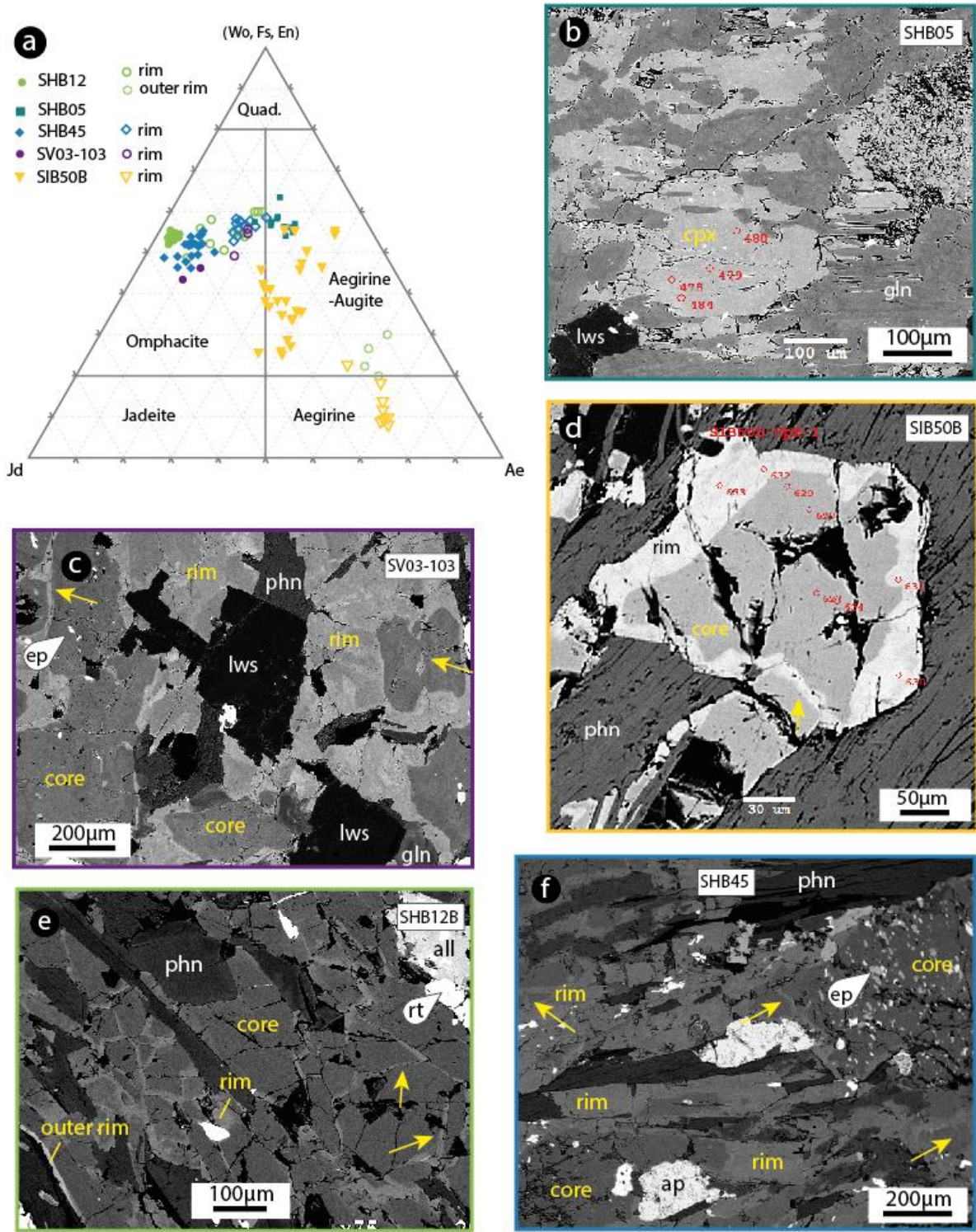
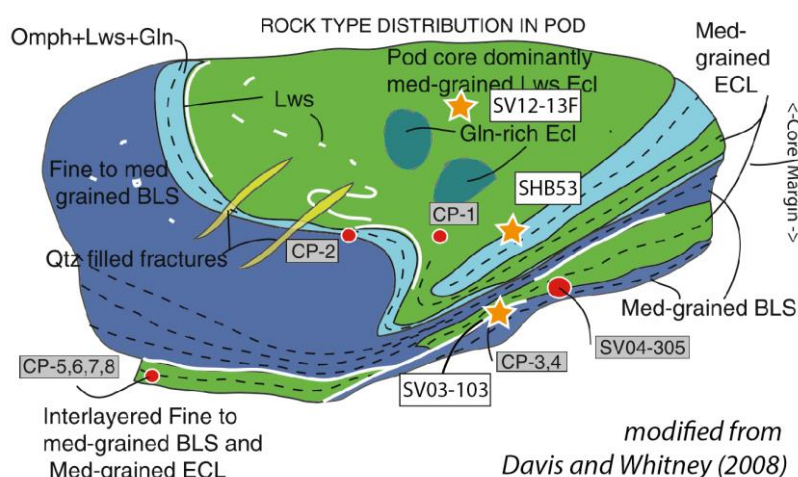


Figure 4 - 5. a. End-member composition of clinopyroxenes. EMPA data, normalisation is to 4 cations,  $Fe^{3+}$  calculated by charge balance. Arrow indicate  $Fe^{3+}$ -rich rims along fractures.

SHB53 and SV03-103 (provided by D. Whitney) are part of the rim of a mafic pod described in detail in Davis and Whitney (2006, 2008), Figure 4 - 6. SV12-13F is part of the core of the same pod (supplied by K. Fornash), and it is a lawsonite eclogite with a matrix of omphacite and phengite with large poikilitic grains of lawsonite and garnet.



**Figure 4 - 6. Sketch of composite mafic pod from Davis and Whitney (2008) with samples studied in this study for oxygen isotopes and trace elements.**

Garnet is zoned, with patchy core zones that contain BSE-darker mantle zones, both cut by BSE-light rims with sharp and irregular boundaries growing along fractures, inclusions and garnet edges that form expressed crystallographic faces. The core is low in Mg and Mn, the mantles see an increase in Mg, and the rims a decrease in Mg and increase in Mn (core: Grs<sub>30</sub>, Prp<sub>6</sub>, Sps<sub>5</sub>, Alm<sub>59</sub>; mantle: Grs<sub>29</sub>, Prp<sub>16</sub>, Sps<sub>7</sub>, Alm<sub>48</sub>; rim: Grs<sub>26</sub>, Prp<sub>8</sub>, Sps<sub>10</sub>, Alm<sub>56</sub>). Lawsonite and garnet have inclusions of quartz and epidote. Similar textures are observed in SV03-103 garnets, where the channels can be seen in BSE but also in Mg and Mn maps (Figure 4 - 9b). In the lawsonite-rich zone of SV03-103 (see Martin et al. 2014a), two large (4-5 mm) garnet crystals displays oscillatory-zoned cores (Figure 4 - 9a), the oscillations involve Ca, Mn to a lesser extent, as well as REE, Y and Cr. Lawsonite shows similar oscillatory zoning (see Martin et al. 2014a). The inner part of these cores contain quartz inclusions, the outer part of these garnet cores contain omphacite inclusions. Neither quartz nor omphacite is present in the lawsonite-rich zone matrix, with only phengite, lawsonite, garnet and minor allanite, zircon and rutile. In SV12-13F, outer garnet rims are quite thick and show nice euhedral faces, and are enriched in Mn. Garnet rims are sparser in SV03-103.

SHB53 is a lawsonite-phengite-omphacite-glaucophane-garnet rock, with a 2 mm wide omphacite-chlorite vein, with lawsonite selvages. It contains large rutile grains with titanite rims. Garnets are inclusion rich (mainly glaucophane) and epidote is a minor phase.

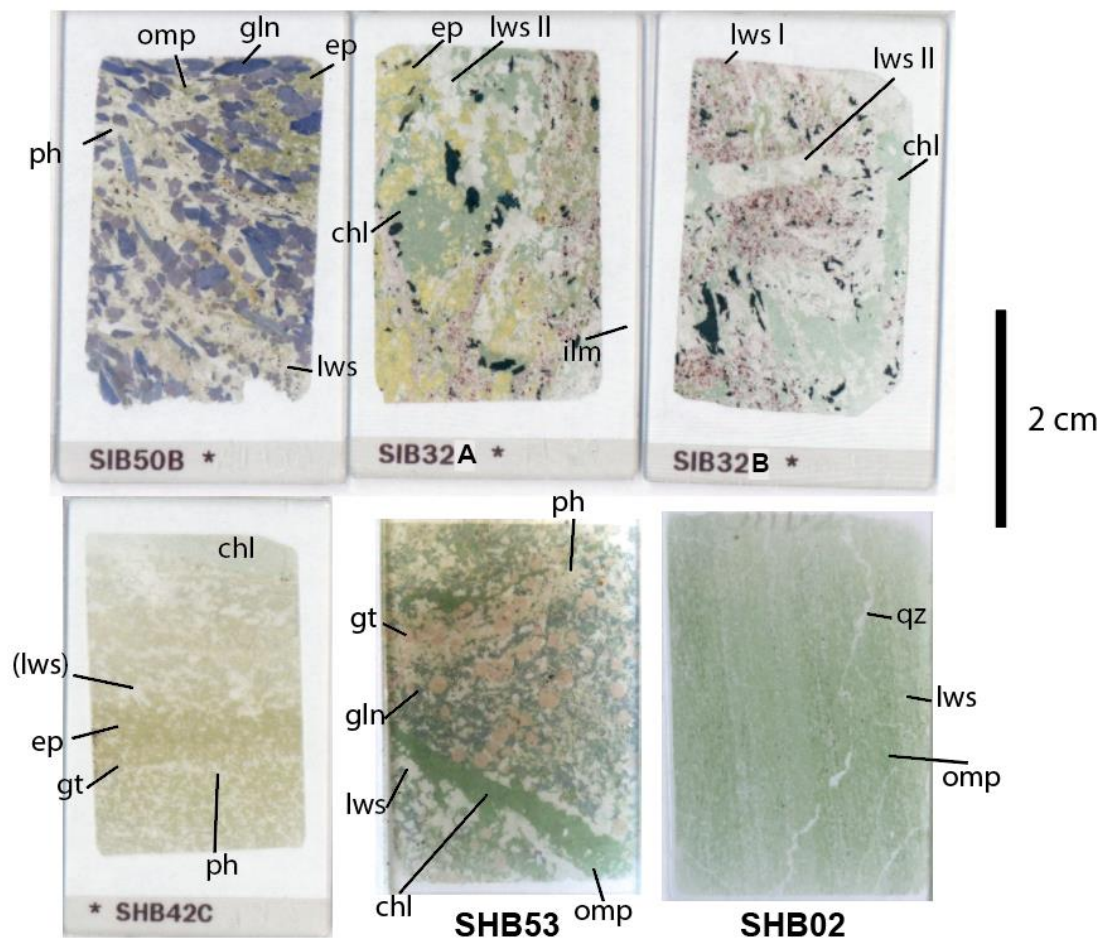


**Figure 4 - 7. Thin section scans of Halilbağı mixed metabasites with indication of main mineral phases**

SIB32 is a 1 m mafic pod found within metasediments (Figure 3 - 11 in **Chapter 3**). Its outer shell is made of chlorite with some lawsonite. The inner part of the pod is a lawsonite-chlorite-titanite-oxide rock, with some parts containing epidote together with lawsonite (SIB32B). Lawsonite forms rosettes of pink crystals that are full of oxide inclusions (SIB32A). These pink agglomerates are cut by lawsonite-chlorite-oxide veins where crystals grow epitaxially this second-generation lawsonite is clear of inclusions. Titanite crystals are big (500  $\mu\text{m}$ ) and also contain inclusion-rich cores. Pink lawsonite and epidote agglomerates are cut by veins of chlorite, oxide and clear lawsonite.

SIB50B is a phengite-glaucophane layer with large (up to 5 mm) euhedral glaucophane in a matrix of phengite. Lawsonite is present as smaller crystals, more common in some layers. Clinopyroxene and epidote are restricted to a portion of the thin section. Clinopyroxenes have BSE-dark cores ( $\text{Ae}_{26-41}$ ,  $\text{Jd}_{8-34}$ ,  $\text{Q}_{25-56}$ , Figure 4 - 5) and BSE-light rims in some areas, following grain boundaries that are aegirine-rich ( $\text{Ae}_{65-72}$ ,  $\text{Jd}_{17-22}$ ,  $\text{Q}_{8-18}$ ). Garnets are small and euhedral (<100  $\mu\text{m}$ ) and are present as inclusions in all phases Garnet is spessartine-rich ( $\text{Grs}_{15-20}$ ,  $\text{Prp}_{1-7}$ ,

Sps<sub>40-69</sub>, Alm<sub>14-34</sub>, Figure 4 - 8b) and contain rutile and zircon inclusions. In one-sub layer, lawsonite is more abundant and has inclusion-rich cores, giving it a pink colour. Glaucophane contains inclusions of allanitic epidote, as well as clear lawsonite inclusions.

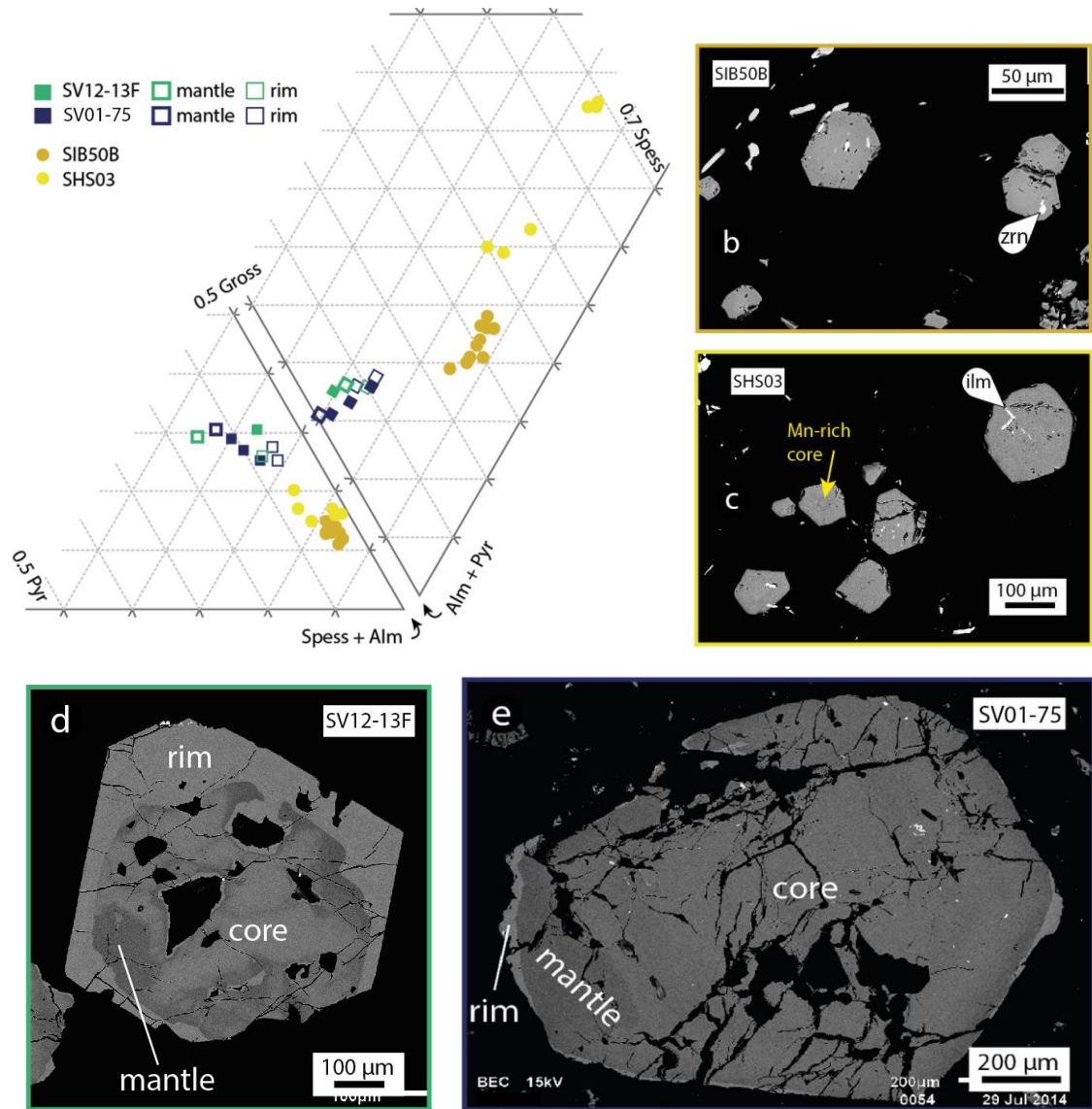


Figure 4 - 8. a. End-member composition of garnet in mixed metabasites and metasediments. b-c. BSE images of garnets from metasediments. d-e. BSE images of garnet in mixed metabasites.

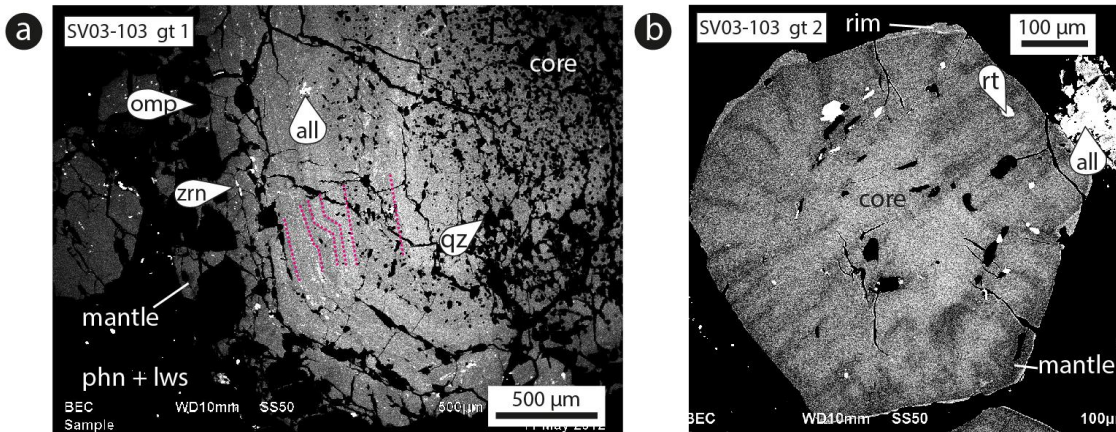


Figure 4 - 9. a. High-contrast BSE image of garnet showing oscillations in BSE brightness in the core (highlighted by pink dashed lines), correlating with Ca and trace-elements in SV03-103 lawsonite rich zone. b. High-contrast BSE image of garnet showing reequilibration channels in SV03-103 lawsonite-rich zone.

### 3.3 Metasediments

SHS03 and SHS46 are impure quartzite layers from the same outcrop. Their matrix is composed of ribbons of quartz with minor phengite (Figure 4 - 10). SHS03 is a garnet-bearing layer; the garnet crystals are 500  $\mu\text{m}$  to 1 mm in size, and are concentrated in a chlorite-rich zone. SHS03 garnets are euhedral and spessartine-rich ( $\text{Grs}_{13-14}$ ,  $\text{Prp}_{3-5}$ ,  $\text{Sp}_{27-34}$ ,  $\text{Alm}_{49-56}$ , Figure 4 - 8). Both samples contain lawsonite concentrated in layers, and which has cores rich in inclusions of a variety of minerals (see more details in Martin et al. 2014a). SHS03 also contains florencite crystals that are 500  $\mu\text{m}$  in size and are surrounded by an allanite corona (described in more detail in **Chapter 3**, Figure 3 -23). Small epidote prisms are also present. Glaucophane forms elongated prisms with dark blue pleochroic rims. SIS53 is a similar lithology coming from the nearby locality of Ikipinar. It contains lawsonite but not garnet, and has minor epidote in some layers.

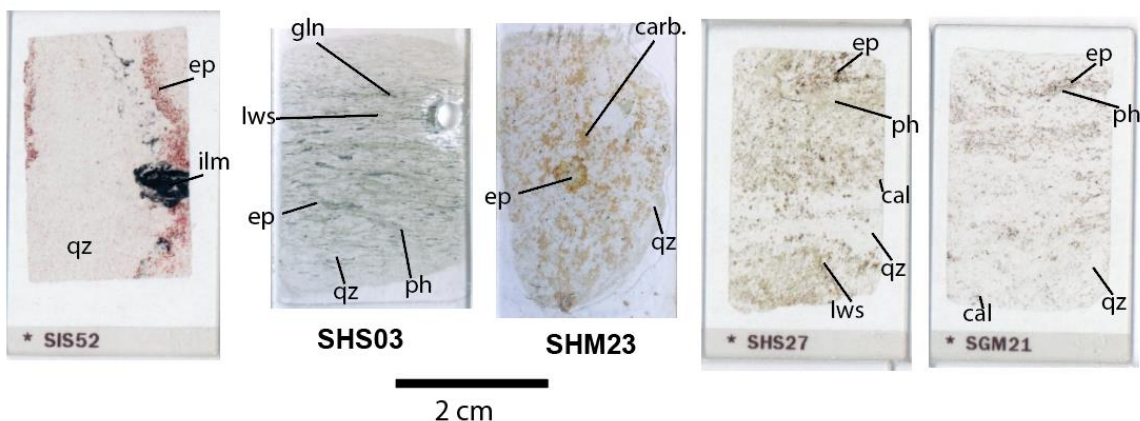


Figure 4 - 10. Thin section scans of Halilbağı metasediments with indication of major phases.

SIS52 is a Mn-rich quartzite dominated by quartz with layers of ilmenite and piemontite. Quartz crystals are rich in micro-inclusions. Automorphic and interstitial calcite is present, as well as phengite. Accessories are apatite and tourmaline; tourmaline has inclusion-rich cores.

SHS27 is a calc-silicate layer with quartz, phengite and abundant lawsonite, calcite and epidote. The lawsonite crystals show resorption features. Both lawsonite and epidote have inclusion-rich cores. Chlorite is a minor phase. The sample is highly heterogeneous with calcite zones, phengite selvages and lawsonite-rich layers.

SHM23B is a calc-silicate layer, made of quartz and white mica, with interstitial orange carbonate. It contains accessory oxides, apatite and detrital zircons. The carbonate is orange in colour and forms poikilitic patches around quartz, as well as small agglomerates. Quartz grains are dusty, phengite flakes are small and randomly oriented. Potential lawsonite pseudomorphs as epidote-quartz aggregates.

SHM04 is a pure marble with accessory apatite, phengite and oxides.

SGM21 is an impure marble, dominated by calcite with quartz, white mica, epidote and oxides. In the more impure layers, some calcite and oxide aggregates could represent lawsonite pseudomorphs. This sample is part of the Günyüzü area, and has seen a slight Barrovian overprint (chlorite zone at ca. 400°C, high-pressure zone of Seaton et al. 2009, 2014).

## 4 Oxygen isotopes

This study is based on a survey of oxygen isotopes, across 20 samples. The samples were measured as Whole-Rock (WR) powders for silicates and carbonates, and zircon, garnet, apatite and lawsonite were analysed in situ by SIMS. The WR results are presented first, following by a summary of in situ data. The in situ oxygen data are supported by trace element zoning in the minerals of interest. Fractionation models are used as a link between WR and mineral data.  $\delta^{18}\text{O}$  is expressed in ‰ calculated against the VSMOW standard.

**Table 4 - 2. Summary of WR  $\delta^{18}\text{O}$  and  $\delta^{13}\text{C}$  analyses. SE for silicates and carbonates is 0.1‰.**

Sample	Silicate $\delta^{18}\text{O}$	Carbonate $\delta^{18}\text{O}$	WR $\delta^{18}\text{O}$ (VSMOW)	$\delta^{13}\text{C}$ (VPDB)	% carb*
SHB05	15.4		<b>15.4</b>		0
SHB08	15.3	18.0	<b>15.4</b>	0.8	3
SHB02	<i>na</i>	17.1	<i>Na</i>	-1.2	6
SHB42CA	<i>na</i>	19.0	<i>Na</i>	0.5	2
SHB42CB	<i>na</i>	19.0	<i>Na</i>	0.7	2
SHB12B	11.0		<b>11.0</b>		0
SHB53	12.2		<b>12.2</b>		0
SIB32	12.2		<b>12.2</b>		0
SIB50B	13.7		<b>13.7</b>		0
SHS44A	16.9		<b>16.9</b>		0
SHS44B	17.0		<b>17.0</b>		0
SHB45A	15.6		<b>15.6</b>		0
SHS26	13.8		<b>13.8</b>		0
SHS46	18.5		<b>18.5</b>		0
SHS03	20.0		<b>20.0</b>		0
SIS52	22.5	22.9	<b>22.5</b>	3.2	1
SIS53	18.9		<b>18.9</b>		0
SGM21	26.8	25.4	<b>26.5</b>	2.1	26
SHM23B	19.5	21.4	<b>19.9</b>	-6.3	21
SHS27	20.5	19.1	<b>19.9</b>	1.4	40
SHM04		22.3	<b>22.3</b>	3.9	100
<i>SHS26 orange carbonates</i>		22.2		-6.8	
<i>SHS26 white carbonates</i>		22.0		-5.4	
<i>SIB32 alteration crust</i>		25.3		-1.2	

\* LECO LOI assuming all C is  $\text{CaCO}_3$ , calibrated with pure marble SHM04.



## 4.1 WR silicates and carbonates

All measured silicate WR samples yield  $\delta^{18}\text{O}$  heavy values, between 11.0 and 26.8 ‰ (Table 4 - 2). Meta-magmatic (Group 2 and 3 samples in **Chapter 3**) samples yield varied values, between 11.0 ‰ for SHB12B, ca 15 ‰ for SHB05, SHB08 and SHB45, and a higher ca. 17 ‰ for SHS44A and SHS44B. The serpentinite SHS26 also yields a high value at 13.8 ‰. Intermediate samples (Group 1 in **Chapter 3**) yield silicate  $\delta^{18}\text{O}$  in the lower range of magmatic samples with SHB53 and SIB32 at 12.2 ‰, and SIB50B at 13.7 ‰. Metasediments yield more uniform silicates values between 18.5 ‰ for SHS46 and 22.5 ‰ for SIS52.

The  $\delta^{18}\text{O}$  values for the carbonate fractions are similar to the silicate value for most analysed metasediments (within 1.4 ‰). In the metabasite SHB08 and calcsilicate SHM23B, carbonates yield a higher  $\delta^{18}\text{O}$  at +2.7 ‰ and +1.9 ‰ respectively compared to the silicate value. Two different generations of carbonates: orange globules along magnetite zones, and white seams in fractures in serpentinite SHS26 yield similar values at ca 22 ‰. The alteration crust measured around SIB32 yields a high value at 25.3 ‰.

$\delta^{13}\text{C}$  values were obtained together with the  $\delta^{18}\text{O}$  analysis of the carbonate fraction. These are variable between -6.8 to 3.9.

## 4.2 Mineral data

Hisograms for garnet, lawsonite and apatite analysis are presents in Figure 11 for selected samples. A summary of all oxygen data is presented in Figure 4 - 12. In the latter figure, individual in situ analyses are regrouped into probability density plots made with Isoplot (Ludwig 2012). Represented as probability density curves, in half of the samples the analyses define a single bell-curve, corresponding to a normally -distributed population with a homogenous  $\delta^{18}\text{O}$ . Zoning is seen in half of the analysed samples SHS27, SHS3, SHB53-SV12-13F, SHB45, SHB44A, SHB12B and SV01-75. In most cases, equilibrium fractionation order in mineral  $\delta^{18}\text{O}$  is preserved for metamorphic minerals (e.g. Zheng 1993a, b, 1996a), with garnet < lawsonite (zoizite) < apatite < carbonates. Apatite > carbonate in metasedimentary rocks SGM21 and SHS27, which indicates isotopic disequilibrium between these two phases. Zircon (SHB45, SHB44A) yields much lower values than garnet for a similar fractionation coefficient, which is also indicative of isotopic disequilibrium. These occurrences of isotopic disequilibrium are investigated by looking at mineral zoning in detail (see Figure 4 – 11 and following discussion).

Antigorite yields a homogenous composition in serpentinite SHS26, at  $13.4 \pm 0.3$  ‰ (1sd, n=28, Appendix table A4 – 4).

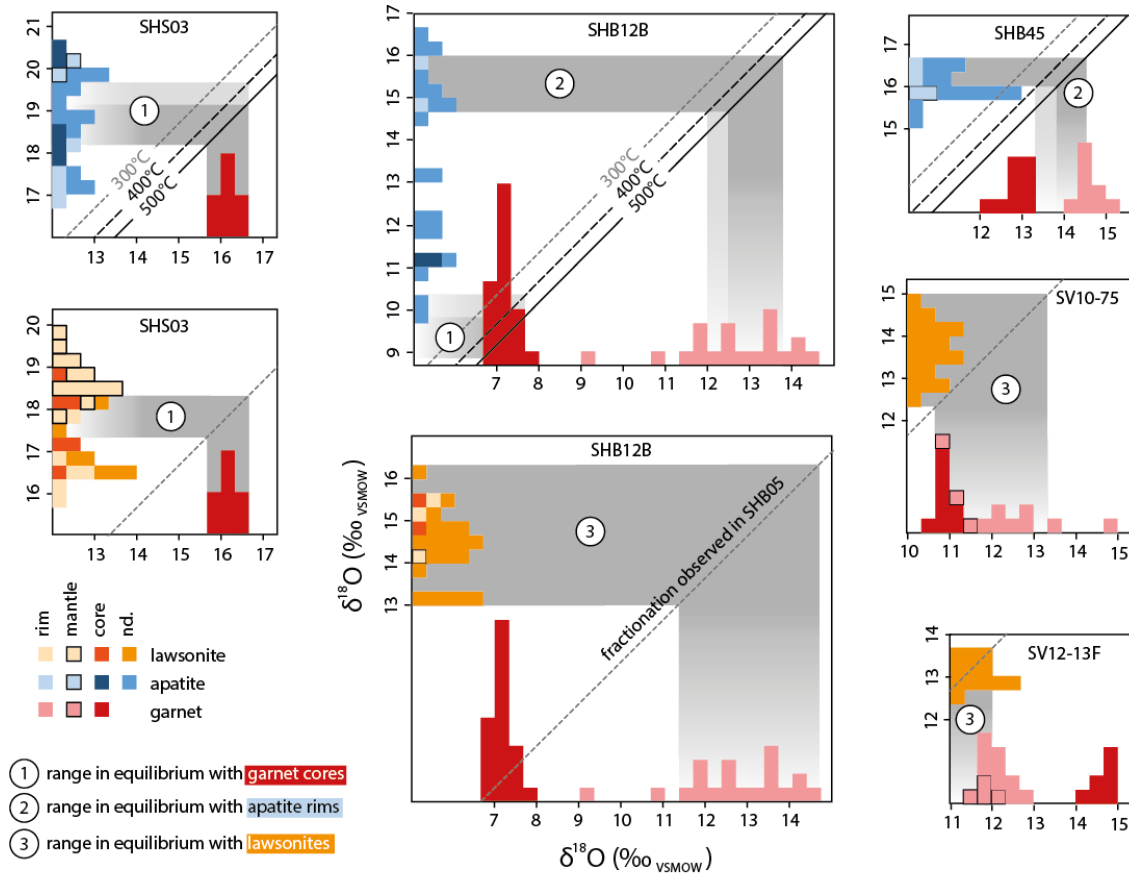


Figure 4 - 11.  $\delta$  -  $\delta$  histogram plots showing fractionation between minerals in heterogeneous samples. Each square element in histograms represents one analysis. The fractionation lines for garnet-apatite are drawn from Zheng (1996) and Zheng (1993a). For lawsonite-garnet, as no fractionation equation is known and the data is used in a relative manner, the fractionation of ca. +1.7 ‰ observed between these two minerals in the homogenous sample SHB05 is shown. Numbered grey areas are shown as a reading guide to indicate potential equilibrium between phases.

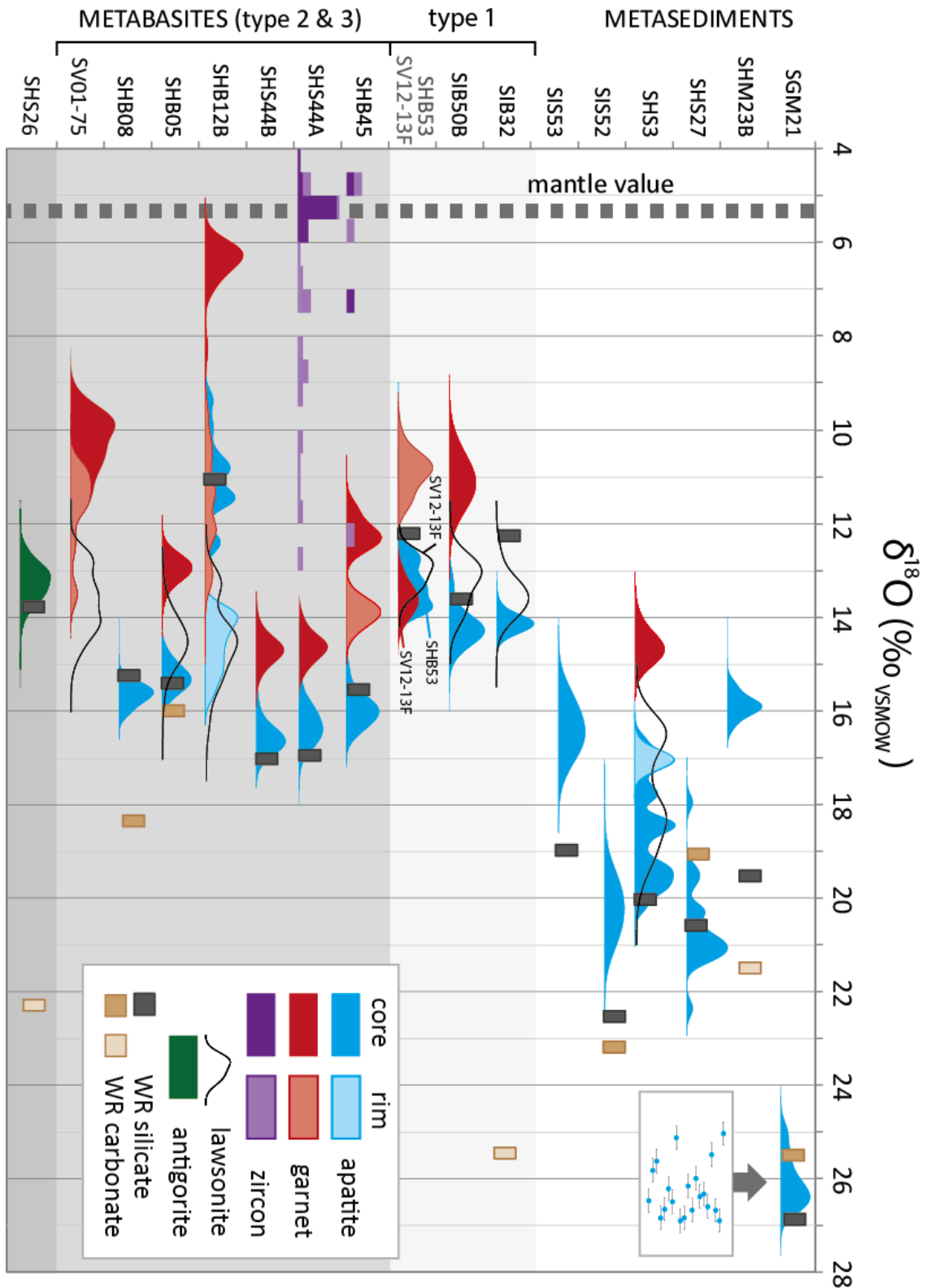
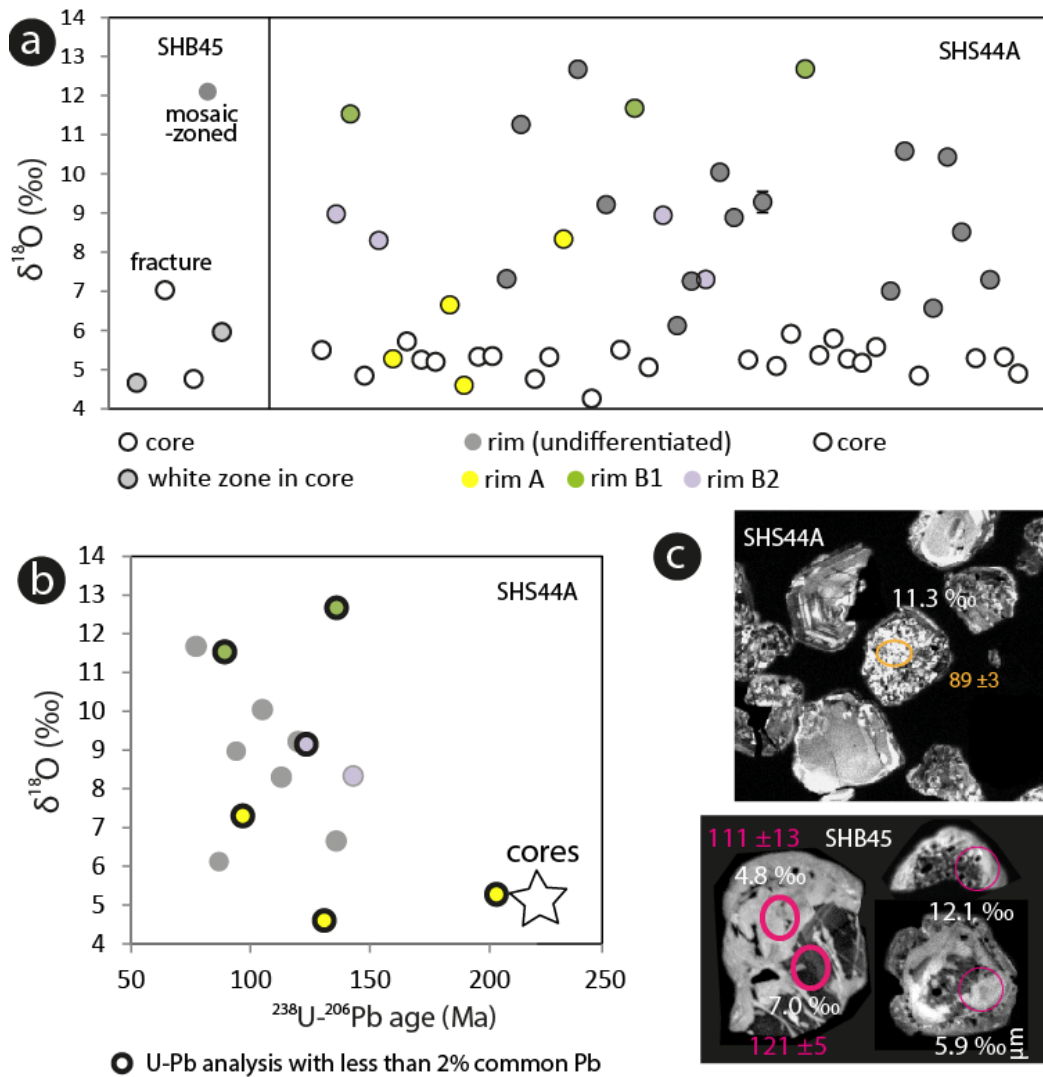


Figure 4 - 12. Summary of in situ  $\delta^{18}\text{O}$  analyses, represented as probability density plots. Each sample is on a line, each colour represents a different mineral. Mantle value is from *Eiler (2001)*. Probability density plots are made with Isoplot, using individual data with propagated standard repeatability.

As a general rule, apatite and lawsonite seem to be in equilibrium with garnet rim values at the temperatures garnet is stable (ca. 400-500°C, detailed for heterogeneous samples in Figure 4 – 11). This relation is less clear in SHS03, where core-rim relationships are documented in two apatite grains only, and a single generation of garnet is present. Figure 4 - 11 highlights that this work does not aim at deriving fractionation between minerals with a precision of the tenth of a permil, but rather to compare different populations of minerals that show heterogeneities up to 7 ‰, as in SHB12B, in order to trace disequilibrium processes. To deduce more about mineral equilibration and metasomatism, results are reviewed in detail for each mineral below, in light of major and trace element zoning.

#### **4.2.1 Zircon**

Zircon U-Pb ages, trace-element data and textures are described in **Chapter 3**. Here, the  $\delta^{18}\text{O}$  dataset is presented for magmatic samples SHS44A and SHB45. In both samples, magmatic oscillatory-zoned cores yield mantle-like values (Figure 4 - 13a, *Appendix table A4 – 5*). An average of  $5.2 \pm 0.4$  ‰,  $n=22$  can be calculated in SHS44A. More spread out values are measured in the handful of SHB45 zircons, between 4.5 and 7.0 ‰. The spread in SHB45 is likely due to fractures and inclusions that could not be avoided or to the small number of grains recovered.



**Figure 4 - 13. a.** Zircon  $\delta^{18}\text{O}$  analyses in sample sSHB45 and SHS44A, by order of time during the session. SE on single measurement is usually smaller than the symbol. **b.**  $\delta^{18}\text{O}$  vs  $^{207}\text{Pb}$ -corrected SHRIMP  $^{206}\text{Pb}$ - $^{238}\text{U}$  ages on same zones. In this sample, a large proportion of analyses were discarded due to inclusions introducing large common-Pb contents. Only bold symbols show data that has less than 2% common  $^{206}\text{Pb}$ . The colour scheme is the same as the same sample in a. **c.** CL images of SHS44A and SHB45 zircon grains showing age and  $\delta^{18}\text{O}$  data. Spot diameter is ca. 25  $\mu\text{m}$ .

In both samples, mosaic-zoned domains yield higher values (one measurement of 12 ‰ in SHB45, values varying from the magmatic value up to 13.0 ‰ in SHS44A). In SHS44A, rim A yields core-like or slightly higher values (up to 8.7 ‰), whereas rim B1 yields the highest values at ca. 12 ‰. Rim B2 yields intermediate values at 7-9 ‰. There is no obvious relationship between rim  $\delta^{18}\text{O}$  and age (Figure 4 - 13b), which indicates that the two systems might be de-coupled in the zircon recrystallization textures.

## 4.2.2 Garnet

In samples SHS44A ( $14.6 \pm 0.3\text{‰}$ , n=9), SHS44B ( $14.7 \pm 0.2\text{‰}$ , n=10), SIB50B ( $11.5 \pm 0.2\text{‰}$ , n=6), SHB05 ( $13.0 \pm 0.2\text{‰}$ , n=20), and SHS03 ( $14.6 \pm 0.3\text{‰}$ , n=12), garnets yield analyses that have a similar spread in  $\delta^{18}\text{O}$  as the standard UWG2 ( $0.28\text{‰}$  std dev.), and are thus considered homogenous for  $\delta^{18}\text{O}$ . In the samples that show light BSE rims, however,  $\delta^{18}\text{O}$  is zoned between core and rim (Figure 4 – 11, Figure 4 - 12, Figure 4 - 14, *Appendix table A4 – 6*).

The most complex sample is the lawsonite eclogite SV12-13F, in which garnets have cores with irregular dark zones toward the outside (mantle), surrounded by euhedral BSE-bright rims. The oxygen composition of the different domains is notable with cores at  $13.6 \pm 0.3\text{‰}$  (n=7), the mantle zones at  $10.6 \pm 0.3\text{‰}$  (n=4) and the rims at  $11.0 \pm 0.3\text{‰}$  (n=9), see Figure 4 - 14a. In this sample, the three zones have no major difference in trace-element contents (*Appendix table A4 – 7*), such as Sc (variations from 16 to 61ppm, not systematic between zones), or P (from 33 to 45 ppm across zones). The most notable changes are a lesser Cr content in mantles (47-71 ppm) and rims (68-101 ppm) compared to cores (104-181 ppm), as well as Ti: 822-1064 ppm in cores to 215-346 in mantles and 320-323 ppm in rims. Cores yield variably HREE-depleted patterns (Figure 4 - 15), showing Rayleigh fractionation towards the outer core. Mantles yield HREE enriched patterns similar to the most enriched cores. Rims have a markedly different composition with MREE and HREE enrichment compared to cores and mantles, up to similar or higher values for Lu.

In blueschist SV01-75 (Figure 4 - 14b) cores have a homogeneous oxygen isotope composition with a  $\delta^{18}\text{O}$  of  $9.8 \pm 0.3\text{‰}$  (n=9). In one crystal the BSE-darker mantle was also analysed, and yields  $\delta^{18}\text{O}$  values similar to the core ( $10.4 \pm 0.3\text{‰}$ , n=3). The rim however yields heavier values at  $11.1 \pm 0.3\text{‰}$  (n=8) in one grain and higher at 13.5 and 12.4 ‰ in the other analysed garnet crystals. In this sample, variable enrichments of HREE can be seen in garnet cores in the two grains analysed (Figure 4 - 15). In grain 2, the mantles are enriched in HMREE compared to the cores, in grain 1, the rims show depletion in LMREE compared to the cores.

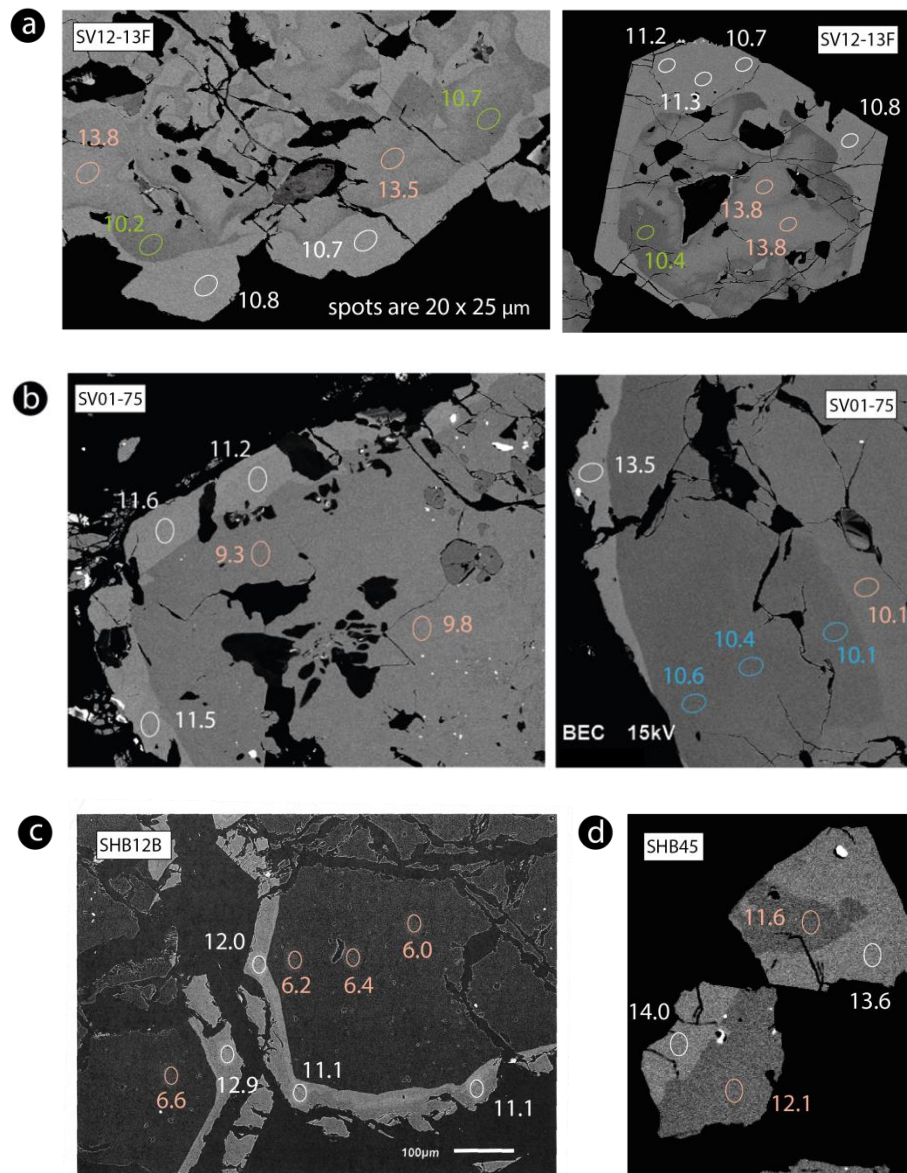


**Figure 4 - 14.** BSE images of Halilbağı  $\delta^{18}\text{O}$ -zoned garnets. Spots are ca. 20x 25  $\mu\text{m}$ .  $\delta^{18}\text{O}$  values are in ‰.

In eclogite SHB12B, garnet cores have a homogeneous  $\delta^{18}\text{O}$  value across and within grains of  $6.3 \pm 0.3\text{‰}$ ,  $n= 24$ , whereas rims yield much higher values from 8.2 to 13.3 ‰ (Figure 4 - 14c, an average would yield  $11.4 \pm 1.3\text{‰}$ ,  $n=20$ ). The rims however show some variation within a single rim and across grains, which mirrors variations in BSE brightness indicative of major and trace element zoning. This intra-rim zoning was investigated for trace-elements using a LA-ICP-MS slit profile (*Appendix figure A4 – 8*). In SHB12B garnets, profiles show a peak in garnet-compatible elements such as Mn, Y, Lu, Yb, Er and Tm at the interface between core and rim. Other elements such as Zr and Ni are to the contrary depleted at the interface. MREE show a gradual decrease in the rim, as seen in the spot analyses (Figure 4 - 15), whereas LREE are

depleted at the interface, their concentration trending towards larger values next to the crystal edge. Cr and Mg are depleted in the rim. A number of elements show no variation between core and rim: Fe, Ca, Zn, P, Rb and Sr show a very slight depletion in the rim.

Eclogite SHB45 yields higher absolute  $\delta^{18}\text{O}$  values: the cores are homogenous at  $12.1 \pm 0.3\%$ ,  $n=10$ , and the rims are at  $13.9 \pm 0.2\%$ ,  $n=9$  apart from one analysis at  $16.8\%$  that is likely the results of an inclusion. The core-rim interface was also investigated for trace elements by a slit profile (*Appendix figure A4–9*). In SHB45, the interface concentration peak in garnet-compatible elements is only seen in Mn. HREE show a rather flat profile with a slight depletion compared to the cores (Figure 4 - 15), as most minor elements (Cr, Zn, P, Ni, Sr, Rb) and Ca, Fe. MREE and LREE are depleted at the interface and their concentration increases towards the edge of the crystal, similarly to Zr. The main features shared by samples SHB12B and SHB45 are an increase of Mn at the interface, and a drop in Mg# and L-MREE in the rims.

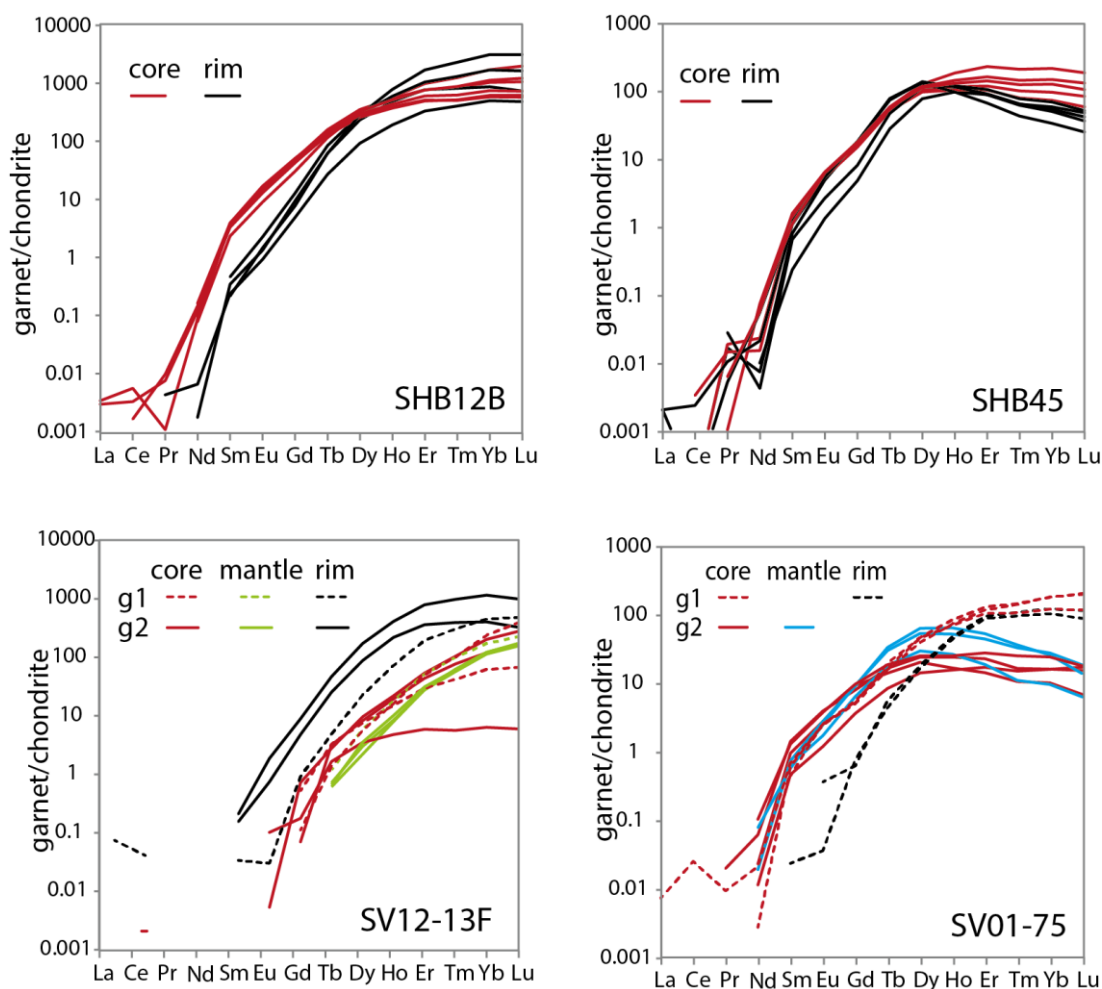
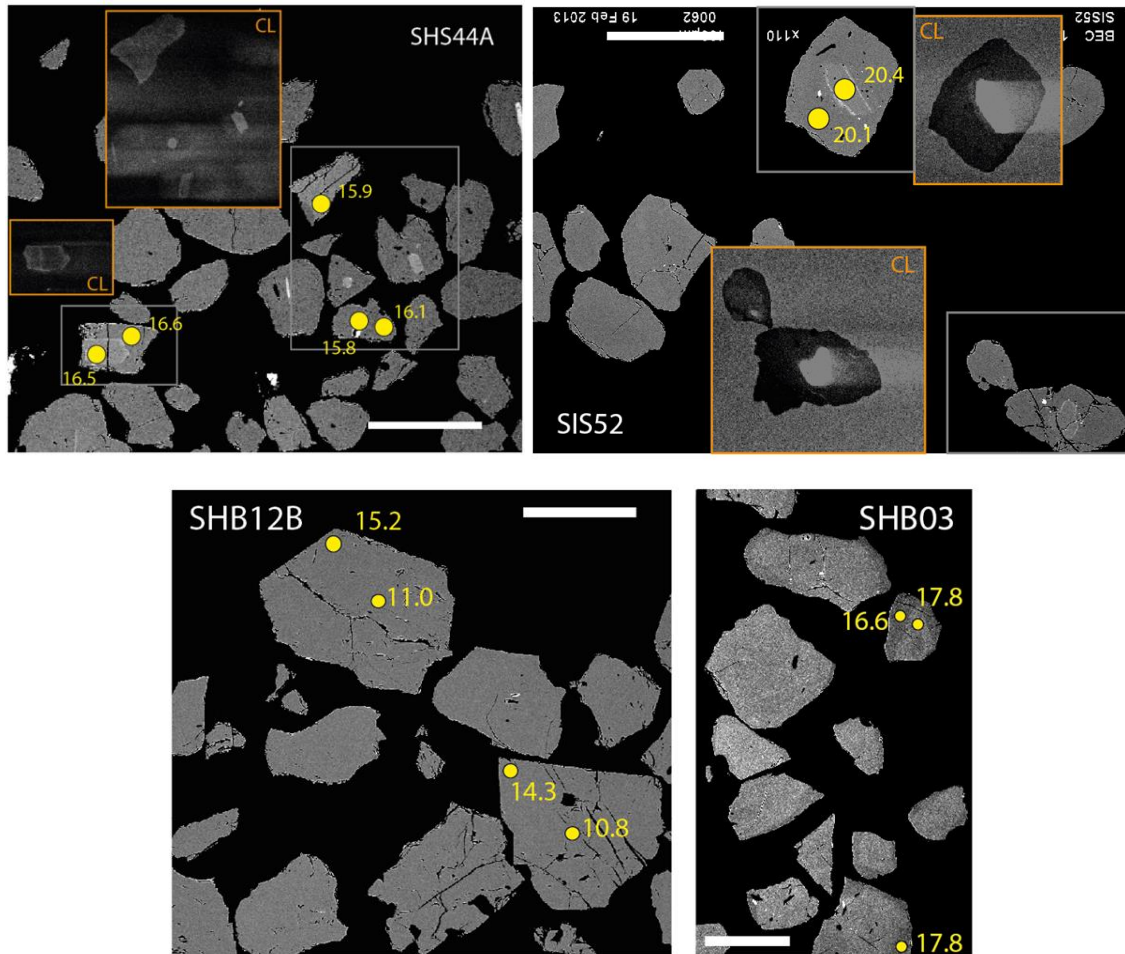


Figure 4 - 15. Chondrite-normalised REE concentrations in  $\delta^{18}\text{O}$  zoned garnets



### 4.2.3 Apatite

The oxygen isotope results for apatites are presented in detail in Chapter 1, and are plotted in Figure 4 - 12, the data table is provided in *Appendix table A1 – 1*. As most apatite samples are homogenous for  $\delta^{18}\text{O}$  but show BSE zoning (Figure 4 - 16), the  $\delta^{18}\text{O}$  data are described in light of chemical zoning in the apatites identified by BSE and LA-ICP-MS analysis. The complete apatite REE dataset is plotted in the *Appendix figure A4 – 10*.



**Figure 4 - 16. BSE images of Halilbağı apatites, with CL when available.  $\delta^{18}\text{O}$  in ‰ is presented with the analysis spots, around 25x25  $\mu\text{m}$  in size. Scale bar is 200 $\mu\text{m}$ .**

Two types of zoning can be seen in Halilbağı apatites. First, in some samples, both magmatic, mixed and sedimentary, REE-rich BSE- and CL-bright cores can be seen (Figure 4 - 16), usually rounded and outlined by small fluid and mineral inclusions. In metasediments SIB50B, SIS52 and SIS53, the cores are LREE-enriched (1000 chondrite) and are overgrown by LREE-poor rims (0.1-1 chondrite in SIS52, ca 10 chondrite in SIS53 and SIB50B, *Appendix table A4 – 1 and figure A4 - 10*), the latter show a pronounced positive anomaly in Ce in SIS52. Rim analyses are depleted in HREE compared to MREE in SIB50B and SIS53. Cores are also seen in samples of magmatic

origin, although they sometimes have less rounded shapes than in the previously described metasedimentary samples. Magmatic samples SHB44A, SHB44B and SHB05 contain BSE and CL-bright cores that are enriched in REE and yield a pronounced negative anomaly, even if none is present in the whole rock (Figure 4 - 17). They are surrounded by a mantle that is poorer in REE, and more specifically in LREE and HREE, with a Eu anomaly that is comparable to the WR.

Second, some apatites display less BSE contrast, but sometimes faint core and rim can be detected. In this case, the cores make up most of the apatite volume, and yield a much lesser amount of REE. This contrast can also be present in the mantles and rims of the previously described samples. The more faint core-rim contrast is best seen in quartzite SHS03, where rims are systematically depleted in most REE and spectacularly so in HREE compared to the cores (Figure 4 - 18). Eclogite SHB45 shows LREE and MREE depletion in the rims compared to the cores, in addition to a dip in HREE.

Core-rim REE relationships are less systematic in blueschist SHB08, eclogite SHB12B and SHB53, calcisilicate SHM23B and marble SGM21. In blueschist SHB08 and eclogites SHB12B and SHB53, apatites are variably depleted in LREE, down to 0.1 -1 chondrite (see SHB12B in Figure 4 - 18). In other samples such as calcisilicates SHS27, and SHM23B and marble SGM21, the BSE and REE zoning are restricted, but some grains analyses are enriched in MREE (up to 1000 chondrite in SHM23B) compared to other REE (ca 100 chondrite, slightly more in SHM23B). SGM21 and SHM23B display complex zoning in CL, which potentially correlates with MREE abundance.

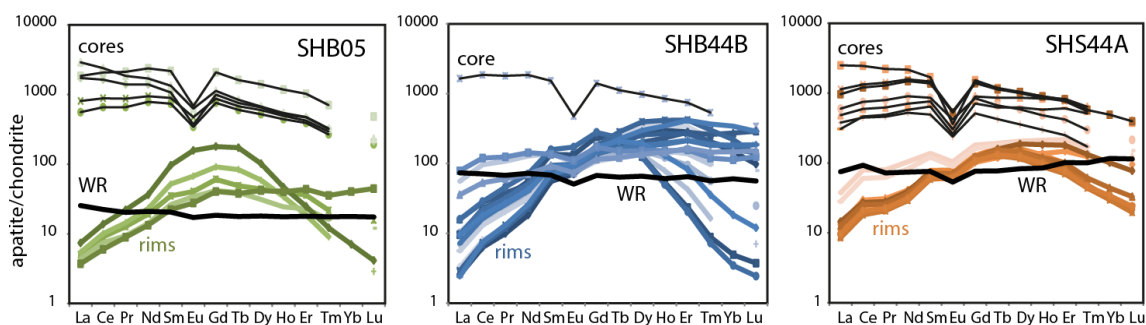


**Figure 4 - 17. Chondrite-normalised REE profiles for apatites with WR profile.**

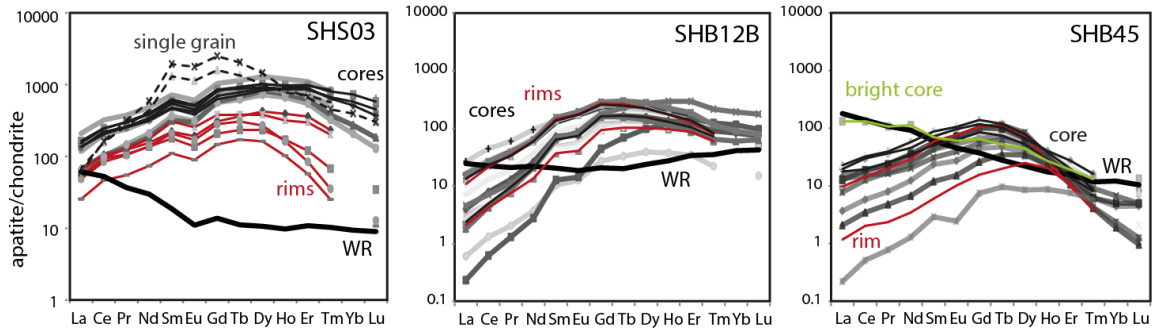


**Figure 4 - 18. Chondrite-normalised REE profiles for  $\delta^{18}\text{O}$ -zoned apatites samples, with WR profile in black. Thick lines in shades of grey are non-determined zones (e.g. no BSE contrast or fragmental grain).**

In contrast with this rich trace element zoning, most apatite samples and grains are homogenous for oxygen isotopes, as shown in **Chapter 1**. Particularly, the  $\delta^{18}\text{O}$  composition of small bright cores, in both metasedimentary and magmatic samples, is systematically identical to the mantles surrounding them (Figure 4 - 16, *Appendix table A1 - 1*). Some variation in  $\delta^{18}\text{O}$  is observed along the rims of apatite crystals in SHB03 and SHB12B. In SHB12B, in two grains, the cores yield lower  $\delta^{18}\text{O}$  of ca. 10 ‰ and the rims have a higher  $\delta^{18}\text{O}$  of ca. 15 ‰ (pictured in Figure 4 - 16). In SHB03, the variation is smaller and inverse, with cores at ca. 19.5 ‰ and rims at ca. 17 ‰. In SHB12B, LREE depletion does not correlate with  $\delta^{18}\text{O}$ , only in that the two most LREE-depleted profiles yield the two highest  $\delta^{18}\text{O}$ . Particularly, in the two grains that show 5 ‰ core-rim zoning in  $\delta^{18}\text{O}$ , core and rim REE composition are identical, but grain to grain variation is seen in REE. In SHS03, no good correlation is found between oxygen isotopes and REE with grain to grain variations occulting core-rim variations in  $\delta^{18}\text{O}$ . Nevertheless, the 3 most HREE depleted rim spectra are the lowest  $\delta^{18}\text{O}$ . In SHB45, despite large variations in LREE, no variations in  $\delta^{18}\text{O}$  are observed in the apatite rims. Some co-variation is observed between  $\delta^{18}\text{O}$  and Fe and is most spectacular in SHS03, where BSE-dark rims yield less Fe and a lower  $\delta^{18}\text{O}$  compared to BSE-bright cores (Figure 4 - 25c). Apatite  $\delta^{18}\text{O}$  changes show a weak co-variation with Sr/Pb, which is investigated in more detail (Figure 4 - 19c).

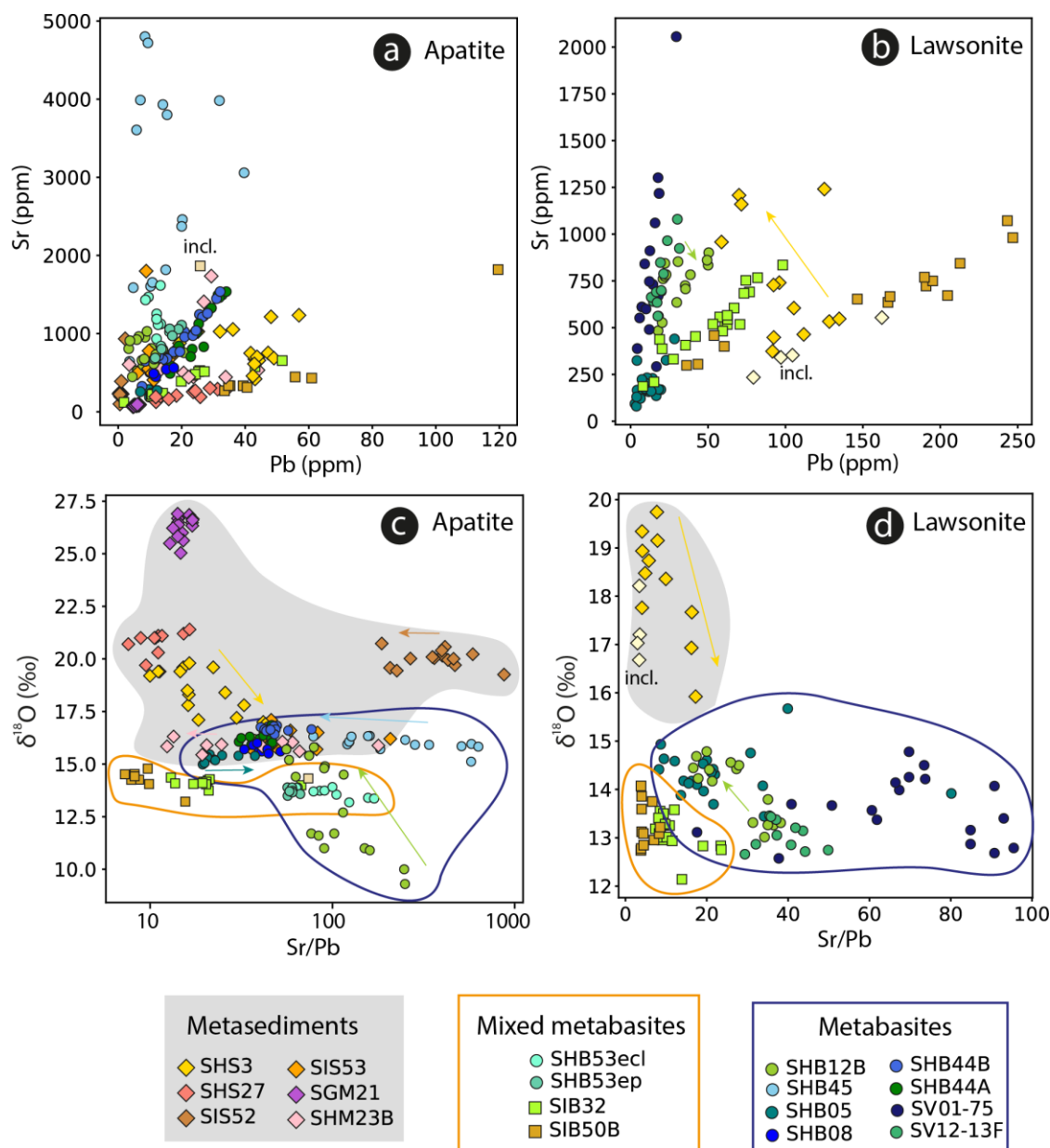


**Figure 4 - 19. Systematics of Sr and Pb concentration in apatite and lawsonite, and their correlation with  $\delta^{18}\text{O}$ . In c. and d., arrows point to core-rim evolution in single grains.**

The analysed apatite samples have significant variations in Sr-Pb systematics (Figure 4 - 19a). Apatite in metasedimentary samples yields low Sr contents (up to ca 1000 ppm). A few analyses above this concentration correspond to the LREE-rich cores, and might be affected by small inclusions. Pb contents are variable, from 0.1 ppm for SIS52 apatite to up to 60 ppm in metasediment SHS3. In the impure marble SGM21, contents in Sr and Pb are among the lowest and are constant across the analysed zones. Samples SIS52 and SHS27 produce Sr-Pb arrays that spread in Sr and Pb respectively, along an array of similar Sr/Pb. A similar behaviour is seen in apatite from intermediate samples SIB32 and SIB50B, which also has low Sr contents. Apatite in

Sample SHS03, SHM27 and SHM23B yields more scattered analyses. In metabasites, apatite is much richer in Sr compared to Pb (up to 5000 ppm Sr and 40 ppm Pb). Samples SHS44A and SHB44B form arrays of constant Sr/Pb, which is also observed in SHB53ep. A couple of apatite analyses in SHS44A deviate to higher Pb concentrations, a few analyses of SHB53ep deviate to higher Sr concentrations, with SHB53ecl at similar Pb but much higher Sr (up to 0.15 wt%). Some samples have homogenous Sr and Pb compositions such as SHB08 and SHB05. Apatite in two of the metabasites show significant scatter in Sr and Pb content: SHB45 yields high and variable Sr contents, with no particular systematics between analyses. SHB12B shows some small-scale variation for moderate amounts of both Sr and Pb. Sr/Pb and  $\delta^{18}\text{O}$  are compared in Figure 4 - 19c. In most samples, Sr/Pb varies without changes in  $\delta^{18}\text{O}$ . Typically, Sr/Pb decreases from core to rim, as is most seen in SHB45 with a change from 600 to 80. In SHB12B, higher  $\delta^{18}\text{O}$  rim values correspond to lower Sr/Pb ratios. A reverse trend is seen in SHS03 where the lowest  $\delta^{18}\text{O}$  rims yield higher Sr/Pb ratios.

#### 4.2.4 Lawsonite

Exploratory results are presented for lawsonite. They have been produced in collaboration with Laure Martin at the University of Western Australia, Perth. More emphasis is put into the interpretation of internal zoning in grains than on the absolute values measured because accuracy still bears uncertainties linked to method development. As the chemical variations between unknowns and the standard LWCAL are not larger than 1 wt% in the most abundant minor elements Fe and Ti (*Appendix table A4 – 11*), it is expected that matrix effects do not play a significant role.

In most samples analysed for oxygen isotopes (*Appendix table A4 – 12*), lawsonite samples measured in a single session show a similar repeatability as the standard with ca. 0.3 ‰ standard deviation (SHB05, SHB12B, SIB32, SV12-13F). In SHB05 and SIB50B, the spread is larger (0.45-0.48 ‰ 1 SD), but the difference between high and low values is still not significant (ca. 1 ‰). Samples SHB12B, SHS03 and SV01-75 have significant spread, over 2 to 3 ‰. In this case, no average is calculated as there is no singular statistical population.

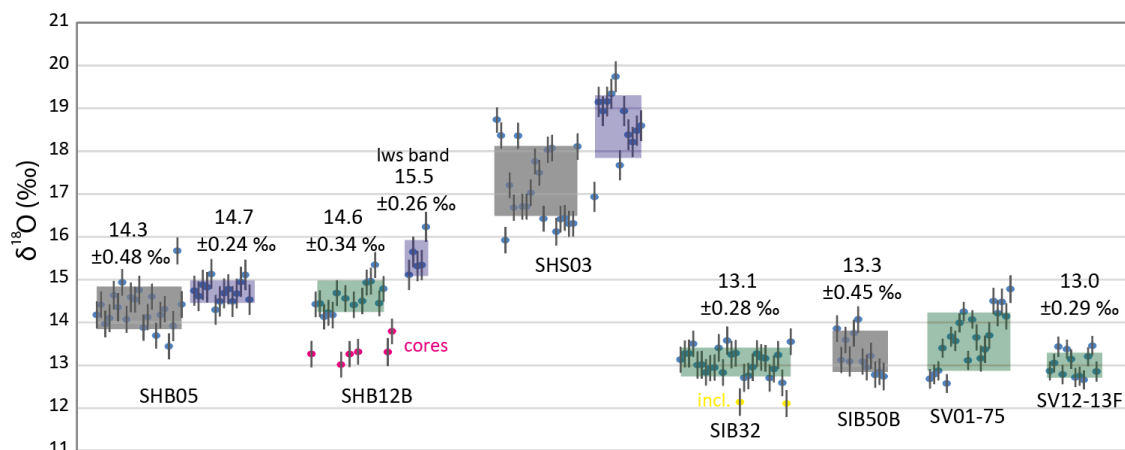


**Figure 4 - 20.  $\delta^{18}\text{O}$  analyses of lawsonite. Error bars are single measurement SE. Boxes represent 1 SD around the sample average. The box colour refers to the 3 sessions: black is for the grain mount, blue for the thin section mount and green for the rock chip mount. The analyses are standardised to LWCAL.**

In SHS03, lawsonite shows spectacular BSE zoning (Figure 4 - 21a). The crystals are made of BSE-bright and inclusion-rich cores that sometimes show some sector zoning. These cores are surrounded by BSE-intermediate mantles, BSE-brighter rims and by BSE-dark outer rims in some cases. These zones have varied REE concentrations: the cores are the richest in HREE (up to 1000 chondrite, Figure 4 - 21b, *Appendix table A4 - 11*); the mantle and rim are HREE-depleted and the BSE brightness corresponds to LREE abundance, where the outer rims have the lowest REE content (200 chondrite La, 10 chondrite Lu). In one grain in thin section,  $\delta^{18}\text{O}$  can be correlated to this zoning: core, mantle and inner rim yield similar high values between 18.9 and 19.7 ‰ (Figure 4 - 21a,c). The outer rim yields lower values of 17.7 and 16.9 ‰. Cores have high and variable Fe contents, potentially due to inclusions (1.4 to 2.3 wt%, Figure 4 - 25d), mantles are Fe-depleted (<1 wt%) and outer rims are mildly enriched in Fe (ca. 1-1.1 wt%).

In SHB12B, most lawsonite analyses were carried out in a grain mount, and grains are often fragmental and the textural relation between zones is hard to assess. Lawsonite zones with high  $\delta^{18}\text{O}$  have flat REE patterns with a slight HREE depletion (*Appendix figure A4 - 13*), with La/Sm around 0.5. Zones with a lower  $\delta^{18}\text{O}$  are more enriched in MREE and yield large depletion in LREE with La/Sm of ca 0.1. SHB12B lawsonite analyses that yield the heaviest  $\delta^{18}\text{O}$  are enriched in Fe from 0.8 to 1.4 wt% (see plot in next section, Figure 4 - 25d).

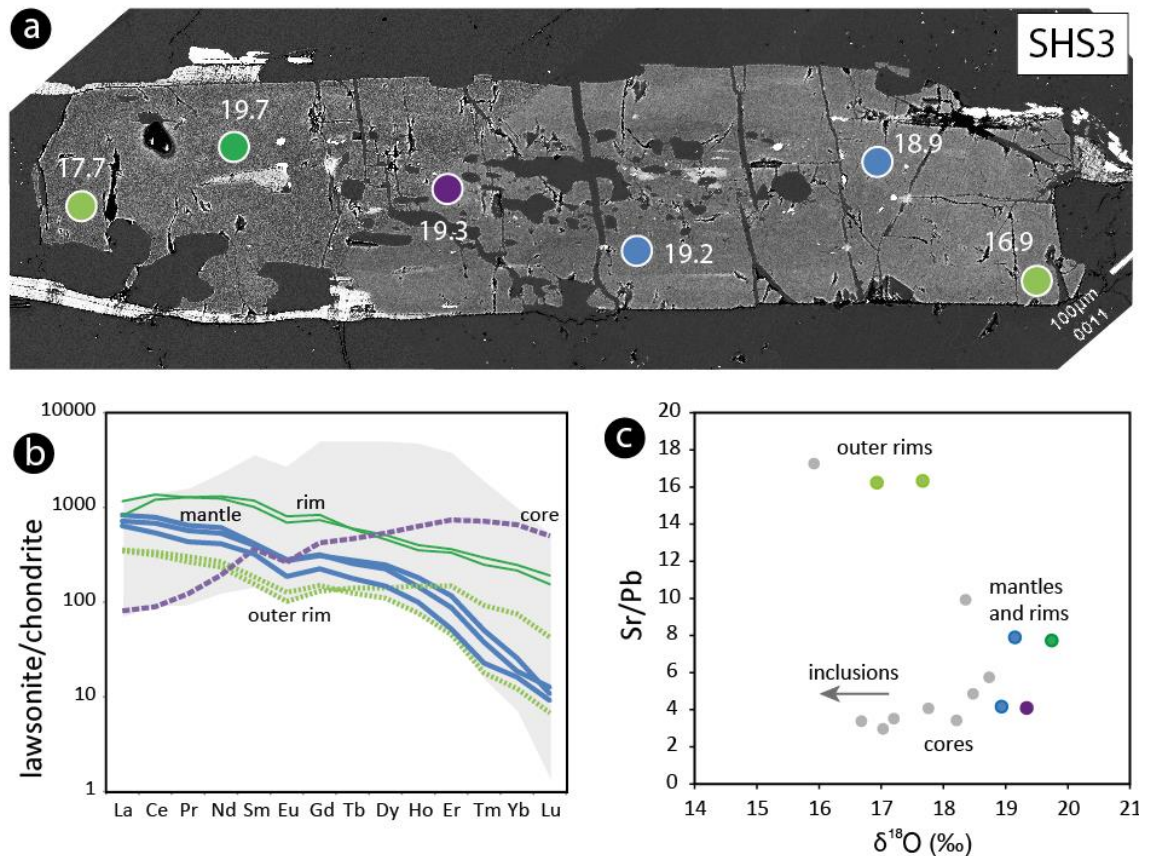


**Figure 4 - 21. a.** High-contrast BSE image of a zoned lawsonite crystal in SHS03, analysed in thin section. Circles represent the location of the SIMS  $\delta^{18}\text{O}$  analyses with value in ‰, the spot size is ca.  $25 \times 25 \mu\text{m}$ . **b.** Chondrite-normalised REE patterns for the crystal pictured in a. (zones are colour-coded, and for all analyses of SHS03 lawsonites in light grey. Some analyses are MREE-enriched, a composition that is not sampled in the pictured grain. **c.** Variation of Sr/Pb according to  $\delta^{18}\text{O}$  in lawsonite for sample SHS03 (light grey) and the pictured crystal (full symbols, colours track the picture). Similarly to REE, some inclusion-rich core compositions are not sampled in the pictured grain.

Similarly to apatite, some correlation can be seen between Sr/Pb and  $\delta^{18}\text{O}$  in lawsonite (Figure 4 - 19). In lawsonite, Sr/Pb is rather constant within sample (Figure 4 - 19a). Mafic samples SV01-75 and SV12-13F yield the highest Sr (up to 0.2 wt%) and the lowest Pb (ca 30 ppm). Intermediate rock SIS50B yields the highest Pb (up to 250 ppm) for  $250 < \text{Sr} < 1000 \text{ ppm}$ . SHB05 lawsonites are Sr and Pb-poor below 25 ppm Pb and 250 ppm Sr. SHS03 and SHB12B display more scatter. This can be tracked unto the Sr/Pb variation with  $\delta^{18}\text{O}$  (Figure 4 - 19d) where Sr/Pb is correlated with  $\delta^{18}\text{O}$  in SHB12B and SHS03. SHS03 zoning is seen in more detail in Figure 4 - 25, where a shift to lower  $\delta^{18}\text{O}$  and higher Sr/Pb is seen from mantle to rim in a single grain. Inversely to the behaviour seen in SHS03, in SHB12B, high- $\delta^{18}\text{O}$  rims yield lower Sr/Pb. The rims of both SHB12B and SHS03 converge to similar Sr/Pb around 20.

### 4.3 Fractionation modelling

In order to relate mineral  $\delta^{18}\text{O}$  composition to bulk-rock  $\delta^{18}\text{O}$ , and assess if some of the mineral variations are purely temperature-related fractionation along the T variation experienced by the rocks, simple models of  $\delta^{18}\text{O}$  fractionation within the rock assemblage are presented for the main rock types. These models aim at answering questions such as: is a measured mineral in equilibrium with the measured WR of the sample? Is the core-rim variation measured in a mineral attributable to temperature changes in a closed system? Or does it suggest an open system resulting in a change in WR  $\delta^{18}\text{O}$ ?

As no P-T pseudosections were produced during this work, the effect of phase changes is not taken into account here, to not add additional sources of uncertainty. These simple models mostly reflect the fractionation related to the overall rock content in  $\text{SiO}_2$ , and the variation in  $\text{SiO}_2$  content between coexisting phases, as  $\text{SiO}_2$  forms a strong bond that retains heavy oxygen preferentially. Effects linked to specific mineral structures (e.g. reaction with albite, see also effects of reactions modelled in Dora Maira Whiteschists, **Chapter 1**) are usually secondary in magnitude and are not examined here. Specifically at temperatures outside of the stability field of the assemblage preserved in the thin section, the preserved assemblage is used as a proxy for the “true” assemblage as its chemical composition is identical and thus the fractionation behaviour similar. Also, as is expanded in the discussion, each mineral is considered open for  $\delta^{18}\text{O}$  exchanges in the temperature range (400-600°C). This is likely not the case on the retrograde path as investigated by previous studies involving more sophisticated models involving diffusion (Eiler et al. 1992), but is probably a good assumption during prograde reactions when most of the assemblage recrystallizes. Moreover, diffusion might impact the signature recorded by the measured minerals. Garnet and zircon retain high-temperature signatures for oxygen (Watson and Cherniak 1997; Vielzeuf et al. 2005b), it thus gives a reliable record of the reactive bulk. Less is known about lawsonite and apatite.

These models are based on the modes of major minerals observed in thin section, and are constructed using the fractionation coefficients of Zheng (1993a, 1993b, 1996). As coefficients for lawsonite are not available, epidote is used as a proxy because of its similar composition (as done by Martin et al. 2014b. reproducing measured whole-rocks successfully). The inter-mineral fractionation is calculated, and then the relative values are adjusted either to a measured mineral composition or to the measured bulk-rock to obtain absolute values. More details about the modelling procedure can be found in Gauthiez-Putallaz et al. (2016) and in **Chapter 5**. The table of mineral modes used for the calculation is available in *Appendix table A4 – 14*.



First, constant WR models were constructed for three main rock types (calcsilicate metasediment, mafic and serpentinite, Figure 4 - 22) for a temperature range that overestimates the stability of minerals, allowing to estimate the maximum fractionation difference. In a mafic eclogite, the temperature-related fractionation is minimal as all minerals have similar SiO<sub>2</sub> contents; see also Russell et al. (2013). In this case, the strongest variation in  $\delta^{18}\text{O}$  over the T range can be expected from garnet and will be <0.5 ‰ during the temperatures where garnet is stable (between 450 and 600°C according to P-T estimates by Davis and Whitney, 2006 and Cetinkaplan et al., 2008). For apatite and epidote, the variation over the chosen temperature range is <0.5 ‰. In this rock, apatite and epidote marginally decrease in  $\delta^{18}\text{O}$  from 400 to 700°C, inversely to garnet. In the metasediment SHS27, due to the presence of 30% quartz and 30% calcite that concentrate heavy  $\delta^{18}\text{O}$ , the expected fractionation is much larger. Hypothetical garnet crystallising in this metasediment would see an increase in its  $\delta^{18}\text{O}$  value of 2 ‰ from 400 to 700°C. Similarly, increase in apatite and epidote  $\delta^{18}\text{O}$  of around 1 ‰ with increasing temperature can be expected in the calcite-bearing metasediment. The serpentinite model highlights that the silicate, oxide and carbonate fractions of the rock would yield radically different  $\delta^{18}\text{O}$  values at equilibrium (more than 10 ‰ spread at 400°C, 5 ‰ at 700°C), although the antigorite would only decrease ~1 ‰ in  $\delta^{18}\text{O}$  over the T range, as it represents the most abundant mineral. To sum up, in quartz-poor eclogites,  $\delta^{18}\text{O}$  changes related to temperature are expected to be minimal in garnet, apatite and lawsonite, which indicates that core-rim zoning present in metabasite garnets (SHB12B, SHB45, SV01-75 and SV12-13F) and SHB12B apatite cannot be attributed to temperature and are thus the sign of an open system. In quartz or calcite-rich metasediments, changes of up to 2 ‰ are expected in garnet, and up to 1 ‰ in apatite and lawsonite, zoning observed in SHS03 apatites is of ca. 2.5 ‰ and is thus also likely the sign of an open system. Only antigorite was measured in serpentinite, and no more than 1 ‰ variation in its mineral value is expected with temperature change.

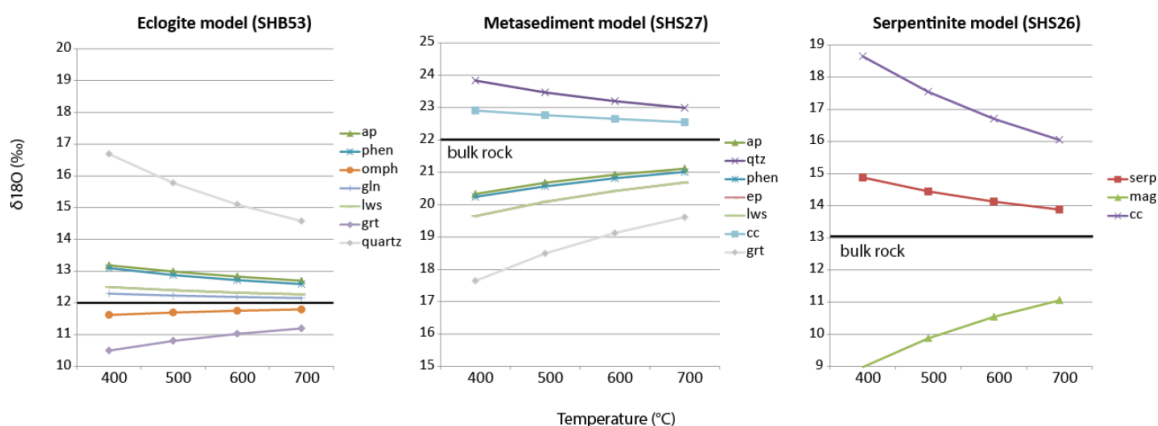


Figure 4 - 22. Modelling of equilibrium fractionation between metamorphic phases at constant WR, using assemblage and modes as observed in thin section. Fractionation coefficients used are from Zheng 1993a; Zheng 1993b; Zheng 1996. Phase stability is overstated in these diagrams, with the aim of providing maximal changes in  $\delta^{18}\text{O}$  according to temperature.

Table 4 - 3. Summary of WR recalculations based on equilibrium fractionation. Magmatic WR recalculated from zircon was produced using the relationship by Valley 2003.

Sample	zone	Measured values				Modelled WR		
		apatite	zircon	garnet	WR	zircon mag	apatite 400°C-500°C	garnet 400°C-550°C
SHB05		15.3		13	15.4		14.1 - 14.3	14.4 - 14.0
SHB08		15.7			15.4		14.8 - 15.0	
SHB12B	core rim	10.0* 15.0*		6.3 13.0*	11		<b>8.7 - 8.9</b> <b>13.7 - 13.9</b>	<b>7.7 - 7.3</b> <b>14.3 - 14.0</b>
SHB45	core rim	16	5*	12.2 13.9	15.6	<b>5.4</b>	14.5 - 14.8	<b>13.4 - 13.1</b> 15.1 - 14.8
SHS44A	core rim	16.2	5.3 12.0*	14.6	16.9	<b>6.1</b>	15.8 - 15.9	17.0 - 16.3
SHS44B		16.6		14.7	17		15.5 - 15.7	16.3 - 15.9
SHB53		12.7			12.2		11.5 - 11.7	
SIB32		14.1			12.2		13.3 - 13.4	
SIB50B		14.2		11.5	13.7		13.4 - 13.5	13.4 - 12.9
SGM21		26.1			26.5		28.1 - 27.7	
SHM23B		15.9			19.9		18.9 - 18.3	
SHS27		20.3			19.9		<b>22 - 21.7</b>	
SHS3	core rim	19.5* 17.0*		14.6	20		21.7 - 21.3 <b>18.2 - 17.8</b>	19.5 - 18.2
SIS52		20.2			22.5		22.9	
SIS53		16.3			18.9		18.3	

\* representative value for a chosen mineral zone (not an average of all analyses, non-normal distribution) Values deviating by more than 1.5 ‰ from the measured WR are indicated in bold.

Second, the hypothetical WR in equilibrium with measured mineral values are modelled and presented in Table 4 - 3. In this model, mineral modes are assumed to be as observed in the thin section for each sample, and temperature is set to values that are approximate brackets to the crystallisation interval for the given mineral. As the temperature profiles show, this procedure is

more reliable in metabasites where the uncertainty related to the assumption made for temperature is small. In metasediments, the uncertainty of a garnet-based calculation is larger, and the modelled value has to be taken as an indication only if the temperature of equilibration cannot be constrained.

The main results are that in most samples, the modelled WR from each measured mineral is similar to the measured WR within the estimated uncertainty of ca. 1 ‰. This indicates that in these samples, there is no indication for oxygen isotope disequilibrium. For a subset of samples that show mineral zoning (SHB12B, SHB45, SHS03, SHS44A), this modelling reinforces the hypothesis of an open-system: the largest contrasts are present in eclogite SHB12B, with a WR modelled of 7.3-7.7 ‰ and 14.0-14.3 ‰ from the measured garnet cores and the garnet rims respectively, that are both distinct of the measured WR value of 11.0 ‰. Hints for an open-system are also identified in SHS27, where the WR values modelled from apatite at 21.7-22.0 are higher than the measured WR value at 19.9 ‰, however this is subject to a larger uncertainty due to the magnitude of fractionation in quartz and calcite-rich rocks.

## 5 Discussion

The measurement of in situ oxygen in metamorphic minerals allows uncovering several steps of the fluid evolution of the Halilbağı rocks from their oceanic protoliths to peak P and T at about 23 kbar, 550°C, and the start of exhumation. The aim of this study is to combine the records present in zircon, garnet, apatite and lawsonite to track  $\delta^{18}\text{O}$  changes along the subduction and exhumation paths. The oxygen isotope or elemental zoning in metamorphic minerals is discussed below for P-T and fluid composition indications. Any relict of protolith signatures is discussed considering also to what extent these signatures are altered at low T before the growth of the main metamorphic assemblage. A fluid history is assembled with information gathered across minerals and rock types. This approach allows reconstructing which rock types in the Halilbağı unit were affected by HP fluid events, and gives indication of what the fluid source and composition might have been. Finally, the effect of fluid-rock interaction on WR composition is explored.

### 5.1 Evidence of fluid-rock interaction in zoned minerals

#### 5.1.1 Zircon zoning

Zircons in MORB leucogabbro SHS44A record magmatic growth at  $222 \pm 5$  Ma (see U-Pb and trace-element data and discussion in **Chapter 3**). These cores yield a mantle value of  $\delta^{18}\text{O}$  of  $5.2 \pm 0.4\text{‰}$ . The complex textures with porosity and mosaic-like zoning in rim A, rim B1 and rim B2 (defined on the basis of trace-element content in **Chapter 3**, Figure 3 - 18) resemble what

was previously described for zircon that underwent intense fluid alteration and recrystallization, and that can be found at varied P-T conditions ranging from seafloor (Schwartz et al. 2010; Grimes et al. 2013) to LT-HP conditions (Tomaschek et al. 2003; Rubatto et al. 2008). In some of these cases, a deviation in  $\delta^{18}\text{O}$  is observed: Grimes et al. (2013) investigated the the Oman and Trodos plagiogranites and reported lower  $\delta^{18}\text{O}$  signatures (1.5 to 4.7 ‰) in the mosaic zircon rims than in the magmatic cores. The zircon rims were interpreted as hydrothermal zones, potentially crystallised from a low  $\delta^{18}\text{O}$  fluid at high temperatures. In the case of the SHS44A zircons, a heavy-  $\delta^{18}\text{O}$  fluid shifted the zircon value from 5.3 ‰ in the cores to 12 ‰ in the rims (Figure 4 - 13), indicating either low-temperature interaction with seawater or the input of sedimentary signature at the metamorphic stage.  $\delta^{18}\text{O}$  and age do not correlate systematically in rims (Figure 4 - 13b): as seen in previous studies (see Rubatto, 2017; Grimes et al. 2013), alteration can induce partial resetting and increase the potential for a mixing at the microscale and de-coupling between signatures. Rim B1 is interpreted to represent the end-member of growth under HP conditions. Its main characteristics are (i) no pronounced Eu anomaly indicating the absence of plagioclase and (ii) depletion in MREE suggesting co-crystallisation with a MREE-rich phase such as lawsonite or titanite. This rim yields ages around 90 Ma, which can be tentatively interpreted as prograde to peak metamorphic crystallisation. These rims record the highest  $\delta^{18}\text{O}$  values of ca. 12 ‰, which represent a minimum estimate for the zircon domain crystallised at prograde to peak conditions. The different REE chemistry (see **Chapter 3**) and varying  $\delta^{18}\text{O}$  composition (Figure 4 - 13) of recrystallized zones A and B2 hint at more complexity in the fluid-zircon interaction history with potential sub-solidus and retrograde stages, that however cannot be fully resolved.

Five  $\delta^{18}\text{O}$  analyses on the rare zircons in SHB45 allow speculatively sketching a similar evolution for this OIB gabbro sample: low values around the mantle value for the magmatic cores, and a single high value at 12 ‰ for the spongy rim. More analyses are required to confirm this hypothesis.

### 5.1.2 Garnet zoning

In most mafic and metasedimentary samples, garnet is not zoned in  $\delta^{18}\text{O}$ . However, four mafic samples show  $\delta^{18}\text{O}$  zoning linked to the presence of Mg-rich rims. Garnets yield generally high  $\delta^{18}\text{O}$  values up to 14.7 ‰. The lowest value is found in eclogite SHB12B (6.2 ‰), other metabasites yield high values that converge toward the value measured in the quartzite SHS03 (14.6 ‰).

Mg-poor outer garnet rims are observed in 5 mafic samples (SHB12B, SHB45, SV01-75, SV12-13F and SV03-103, Figure 4 - 23). These rims grow from a dissolution surface that is irregular,

and follows cracks and inclusions into the garnet. In some samples, this rim is large (up to 300  $\mu\text{m}$  width in SHB45, replacing >50% of the garnet), but in others it is partial and small (20  $\mu\text{m}$ ) e.g. SV01-75. The size of the rims is different in different compositional sections in SV03-103: garnet in the omphacite-rich zones have 100  $\mu\text{m}$  rims whereas the Mg-poor garnet rim is almost absent in the lawsonite-rich section. In places, the rim growth is coupled to dissolution of the pre-existing garnet as is shown by Rayleigh-like depletion in Mn, Y and HREE at the core-rim interface (e.g. profile in the core crack of SHB12B garnet, *Appendix figure A4 – 8*) in the inner part of the rim. This re-incorporation of garnet-compatible elements is interpreted as a loss of garnet volume due to dissolution. In other grains and samples, it is not clear if the rim is new growth around dissolved garnet or is replacing garnet core, as the profiles are flat for garnet-compatible elements at the interface. The rim shows euhedral edges indicating growth, at least in samples where garnets is not affected by chloritization (e.g. SV12-13F), Most rims show an enrichment in MREE and sometimes HREE, which could either be brought by the fluid, or reflect the dissolution of REE-bearing phases such as garnet, allanite and lawsonite, equilibrated at the scale of the sample.

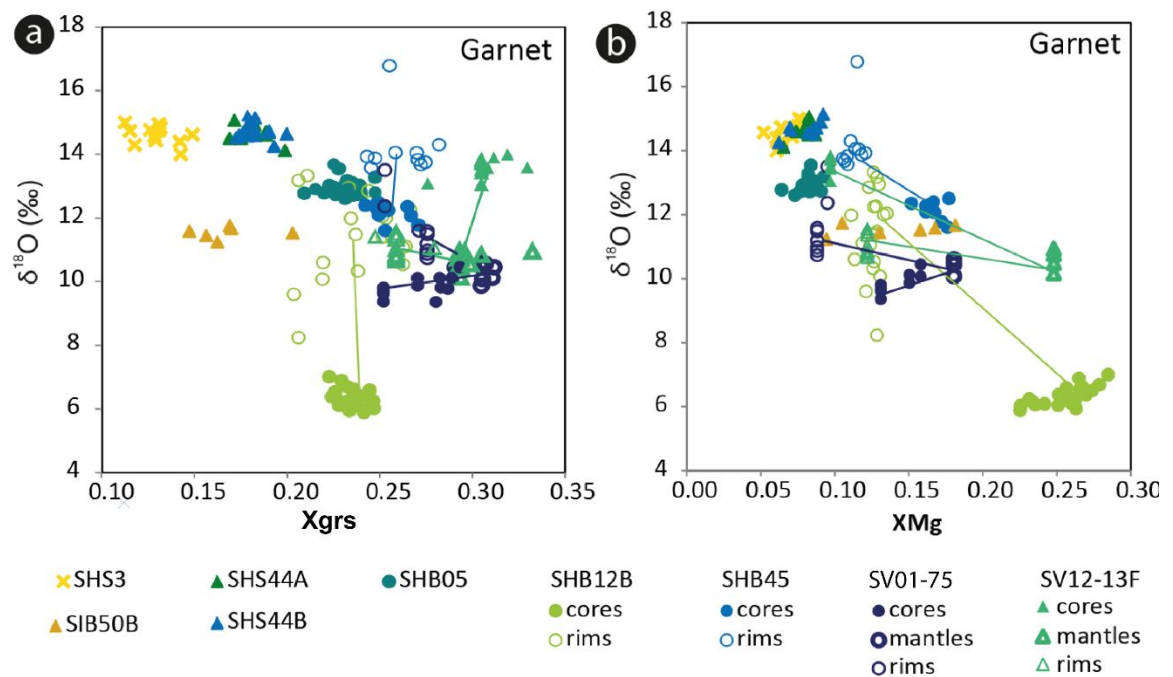


**Figure 4 - 23. Variation of  $\delta^{18}\text{O}$  according to garnet  $X_{\text{grs}}$  and  $X_{\text{Mg}}$ . Ties indicate zoning as observed in single grains.**

These garnet rims usually show a  $\delta^{18}\text{O}$  that is heavier than the garnet cores it surrounds, around 11-12 ‰ in samples SV12-13F, SHB12B and SV01-75 with the exception of outer rim in (up to 13 ‰) eclogite SHB12B, ca. 14 ‰ in sample SHB45 and up to 14 ‰ for the few small rims in SV01-75. The high  $\delta^{18}\text{O}$  garnet rim in all samples has a rather homogenous Mg# (10-15, Figure

4 - 23), in contrast to the cores which show more variability in composition across samples (8-25). If one takes Mg# as a relative indication for temperature, the homogeneous composition suggests that the rims crystallised at similar temperatures in all samples, with Mg# higher than core in SV01-75 and SV03-103, and lower than core in SHB12B and SHB45. The core-rim contrast seen in SHB12B at ca +6‰ is among the largest  $\delta^{18}\text{O}$  contrasts reported for garnet (Vielzeuf et al. 2005a; Page et al. 2014; Martin et al. 2014b). The texture of the rims is similar to the garnets in lawsonite schist 09028 of Martin et al. (2014b) and the garnets from a Franciscan amphibolite (Page et al. 2014b) but have a reverse  $\delta^{18}\text{O}$  behaviour, indicative of a different fluid source than in other studies, with a more prominent sedimentary influence (see below).

Additionally to the Mg-poor rims, garnet textures such as re-equilibration channels transitioning to Mg-rich rims are observed in samples SV03-103 and SV12-13F, as well as a Mg-rich mantle in SV01-75. They resemble what has been described in eclogite garnets of several localities as well as amphibolites (e.g. Whitney et al. 1996), sometimes linked to atoll textures (e.g. Cheng et al. 2007). In these instances, sub-grain boundaries or fluid channels allow partial replacement of the major elements in garnets typically with a change in Mg# (Konrad-Schmolke et al. 2007; Faryad et al. 2010). These textures are interpreted as a re-equilibration mechanism of the prograde cores when increasing temperature at thermal peak or the start of exhumation, with the catalysing presence of fluids. In SV12-13F, a  $\delta^{18}\text{O}$  contrast is present between the core that yields a high  $\delta^{18}\text{O}$  at ca. 14 ‰ and the cross cutting zones at ca. 11 ‰. In the preliminary data obtained for SV03-103, no such contrasts can be observed since the cores also yield 10 ‰ on average (*Appendix figure A4 – 15*). Both of these mantles thus seem to have equilibrated with a fluid of ca. 11-12 ‰, although the fluid can only be identified in SV12-13F, as the core of the garnet records a contrasted bulk composition.

In SV03-103, a lawsonite-rich layer interpreted as a vein by Davis and Whitney (2008) is present, in which garnet and lawsonite cores display oscillatory Ca, REE and Cr zoning, which have elsewhere been interpreted as the result of fluid-influx-related disequilibrium (Sherlock 1999). SV03-103 vein garnets also contains inclusions of rock-forming minerals that are not present in the matrix (quartz, followed by omphacite towards the rim). Such inclusions are likely to be the result of prograde growth and are not observed in other samples of this study. These oscillatory zones could thus be the result of prograde fluid circulations in this rock. These two samples are taken from the pod described in Davis and Whitney (2008): SV03-103 is sampled from the edge of the pod, and SV12-13F from the core. In SV03-103, garnets in the vein as well as the matrix yield a homogenous garnet  $\delta^{18}\text{O}$  of ca. 9-10 ‰, similar to the signature observed in the garnet recrystallized zones and rims of sample SV12-13F from the same mafic pod. If the zoning seen

in vein minerals is an indicator of protracted fluid influxes, it is possible that the SV03-103 area of the pod was equilibrated with lower  $\delta^{18}\text{O}$  fluids prior to the start of the garnet crystallisation, whereas the core of the pod retained high values until a more pervasive fluid event at peak conditions.

In summary, garnet in several mafic samples show the influx of high-  $\delta^{18}\text{O}$  fluids at two stages: during prograde-peak metamorphism (Mg-rich re-equilibration channels) and at the start of exhumation (dissolution of prograde garnet and growth of a Mg-poor rim). This change in  $\delta^{18}\text{O}$  is not followed by systematic changes in garnet-compatible trace-element concentrations, which are likely linked to local redistribution.

### 5.1.3 Apatite zoning

Apatite is present in all samples except for the pure marble SHM04. Apatite is variably F-rich, depending on lithology, with metasediments such as quartzite SIS52 and SIS53 having all A site occupied by F, compared to metabasites with only half the A site filled with F, the rest assumed to be  $\text{H}_2\text{O}$ . In all samples, apatite is low in Cl (below EMPA detection limit). The concentrations measured in this study are similar to what Pagé et al. (2016) found in western Tavşanlı zone apatites, where Cl content was measured by SIMS at the 100-250 ppm level. These low contents in Cl, at the low temperatures in the Halilbağı rocks, are an indication that the fluids were likely not Cl-rich (Kusebauch et al. 2015; Li and Hermann 2015). This has been interpreted by Pagé et al. (2016) as a sign that Cl escaped the system early in the subduction history, during early dehydration. No intra-sample zoning is seen in Cl, nor detected in F (uncertainty due to orientation effects is ca. 0.5 wt% F). This indicates that either the fluid content didn't vary in F and Cl, or that these elements were re-equilibrated. Indeed, Brenan (1993) proposed that diffusional equilibration of Cl in apatite is efficient at temperatures of 400°C, similar to oxygen (Farver and Giletti 1989).

Apatite contain REE-rich cores with a pronounced negative Eu anomaly in a few magmatic samples of MORB signature. Their composition is similar to magmatic apatites (e.g. Belousova et al. 2002; Morton and Yaxley 2007), and they are therefore interpreted as relicts of the protolith, similar to the few zircons cores in the same sample. In metasediments, trace-element rich cores are also present. However, they are much more enriched in LREE than the supposed magmatic apatite cores. In the metasediments the apatite cores could represent early growth when no other REE-bearing mineral is competing for LREE (pre-lawsonite and epidote), or detrital apatite from alkaline magmatic sources (Belousova et al. 2002).

As shown in **Chapter 1**, the temperature that the Halilbağı rocks experienced is higher than the closure temperature for oxygen in apatites of the size measured. This discussion takes care in distinguishing signatures that are primary to those who could have been disturbed by diffusion. However it is not to say that diffusion is envisaged as the primary process to induce heterogeneity in these apatites: recent works have shown that dissolution-reprecipitation is crucial in understanding trace element and isotopic changes in these minerals (Putnis and Putnis 2007; Niedermeyer et al. 2009; Jonas et al. 2014; Kusenbauch et al. 2015). Without more data on mineral structure (e.g. TEM analyses), textural information and the composition in REE that are very slow to diffuse in apatite (Figure 4 – 24) are used to distinguish, where possible, between these two processes.

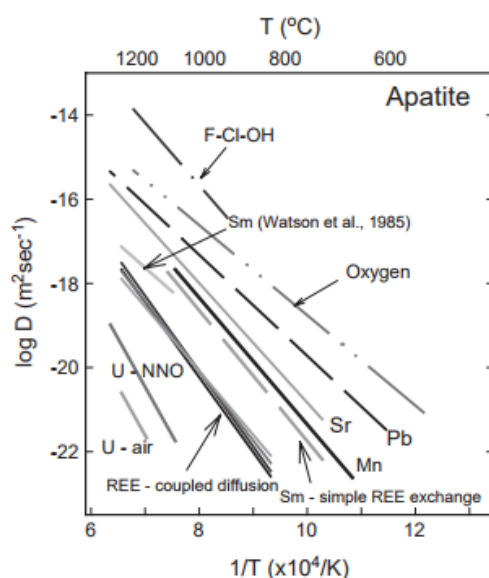


**Figure 4 - 24. Summary of diffusion data for cations and anions in apatite, from Cherniak (2005).**

In both metasediments and mafic rocks the apatite REE-rich cores yield the same  $\delta^{18}\text{O}$  composition as the rims. Particularly, in eclogite SHS44A, the REE-rich apatite cores yield a  $\delta^{18}\text{O}$  value that is much higher than what is recorded by magmatic zircon cores in the same rock. This is taken as an indication that the apatite cores are diffusionally re-equilibrated for  $\delta^{18}\text{O}$ . The preservation of distinctive REE signatures indicates that the cores were not recrystallized, but rather thermally re-equilibrated by diffusion. An overview of elemental diffusion in apatite is presented in Figure 4 - 24 from Cherniak (2005). The re-equilibration of  $\delta^{18}\text{O}$  signatures (and potentially F-Cl-OH) is consistent if the apatite cores resided for a few Ma above their closure temperature (estimated to ca. 350-400°C for 50  $\mu\text{m}$  grains in **Chapter 1** using data from Farver and Giletti 1989 and Hammerli et al. 2014 and pers. comm.). As a result, the  $\delta^{18}\text{O}$  signatures in the cores cannot be used to infer the  $\delta^{18}\text{O}$  information about the rock protolith or early prograde evolution.



$\delta^{18}\text{O}$  zoning is observed in the metamorphic apatite rims for samples SHB12B and SHS03. This zoning does not correlate with REE zoning: the apatite rims could have been altered by diffusion and not represent a primary signature. The possibility that they formed by dissolution-precipitation is at odds with the observation that they have similar REE composition as the inner region of the same crystals. In contrast,  $\delta^{18}\text{O}$  yields systematic changes linked to Sr/Pb. Pb and Sr are some of the fastest-diffusion cations in apatite (Cherniak and Ryerson 1993), so it is possible that they diffused into the crystal similarly to O. Additionally, as outlined by Farver and Giletti (1989) and Brenan (1993), diffusion of anions in apatite is highly anisotropic: they diffuse at much faster rates along the c-axis than along the a-axis, O diffusing slower than F, Cl and OH. The different diffusivities are likely the reason for apparent de-coupling between  $\delta^{18}\text{O}$  and REE concentrations (apatite is virtually closed to REE diffusion at the observed temperatures). Regardless of the recrystallization or diffusion process, the apatite rim composition indicates equilibration with a  $\delta^{18}\text{O}$ -enriched and low Sr/Pb fluid. Apatite rims also show a depletion in Fe in some cases.

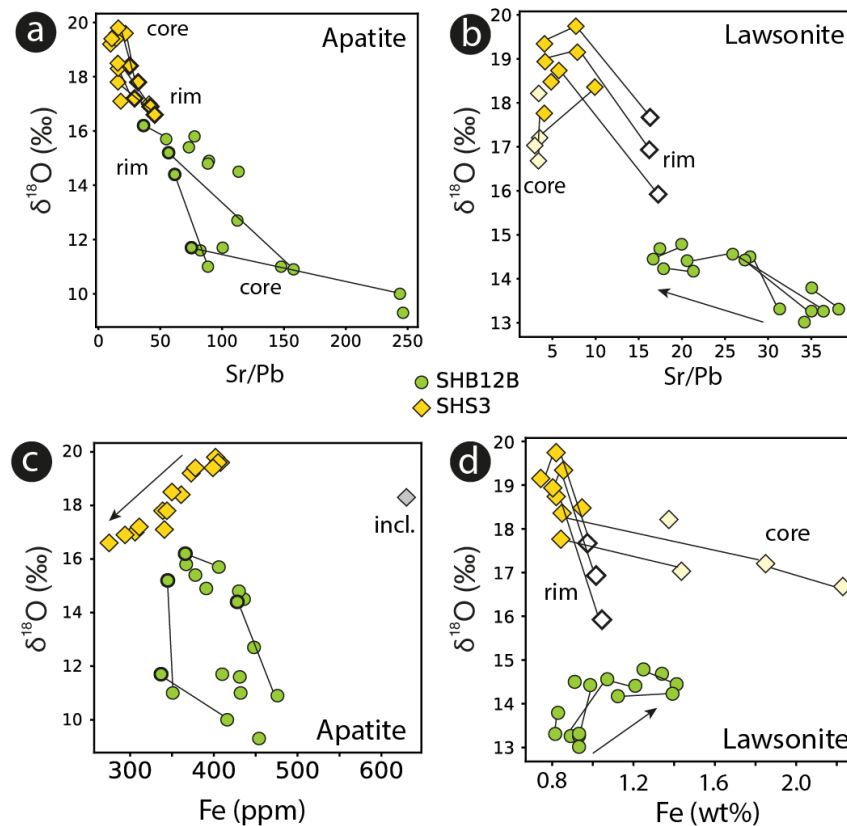


**Figure 4 - 25. Individual grain  $\delta^{18}\text{O}$  vs. Sr/Pb and Fe systematics in apatites and lawsonite. Ties indicate zoning in individual grains. Cores are indicated by a lighter shade of yellow, rims by a thicker symbol outline.**

In quartzite SHS03, in contrast, BSE shows core-rim zoning with bright cores and dark rims. This zoning correlates best with Fe contents (high in the cores and low in the rims) and is an indication of new growth or recrystallization of apatite. The SHS03 apatite rims yield higher Sr/Pb, lower  $\delta^{18}\text{O}$  and lower Fe concentrations than the corresponding cores. The lower Fe contents measured in SHS03 apatite rims (and to a smaller extent SHB12B) could be due to three factors (i) higher  $f\text{O}_2$ , as Fe is incorporated as  $\text{Fe}^{2+}$  in apatite; (ii) redistribution of Fe from apatite to another phase; (iii) lower temperature crystallization of the rims, as higher temperatures result in more Fe incorporation in apatite (Li and Hermann 2015).

The apatite rim compositions for SHB12B and SHS03 are similar at around 16 ‰  $\delta^{18}\text{O}$ , and Sr/Pb around 50 (Figure 4 - 25), suggesting that rims in the two samples equilibrated (likely by dissolution-reprecipitation) with a similar fluid. Such convergence is also seen in the full dataset, with the most values converging at these values (Figure 4 - 19c). Some metasedimentary samples yield homogenous Sr/Pb and do not follow this trend, such as SGM21, SIB50B and SHS27. SGM21 and SHS27 contain large modal amount of calcite, which might act as a buffer for Sr/Pb at low values (ca. 15). Another calcsilicate sample, SHM23B, displays core-rim zoning towards lower ratios, and might have equilibrated with carbonate material at a later stage.

In summary, apatite in most samples reflects the oxygen isotope composition of the bulk-rock according to equilibrium fractionation at temperatures of ca. 400°C. Any  $\delta^{18}\text{O}$  contrast correlated with REE-enriched magmatic/prograde apatite cores has been lost due to diffusion, if ever it was present. However, in two samples, outer rims record a  $\delta^{18}\text{O}$  change compared to the cores, and indicate a fluid influx also reflected in Sr/Pb. This fluid influx yields a higher  $\delta^{18}\text{O}$  and lower Sr/Pb in eclogite SHB12B and a lower  $\delta^{18}\text{O}$  and higher Sr/Pb in quartzite SHS03. It thus seems that both  $\delta^{18}\text{O}$  and Sr/Pb can be used to track metasomatism in apatites on the retrograde path from 450-500°C.

#### **5.1.4 Lawsonite zoning**

The  $\delta^{18}\text{O}$  data for lawsonite, although preliminary, show significant zoning in two samples: SHB12B and SHS03, the same that contain zoned apatite. These changes are attributed to growth zoning, in the absence of data on diffusion for these elements in lawsonite. In SHS03, lawsonite shows strong core-rim BSE zoning follow the crystallographic shape and, similar to apatite, this zoning is correlated with changes in Sr/Pb. In SHB12B, rims have a higher  $\delta^{18}\text{O}$  and a lower Sr/Pb, whereas in SHB03 the opposite is observed. These two samples converge toward similar Sr/Pb values of ca. 18, as also observed in apatite. Over the entire dataset, the convergence toward a

unique value is not as strong as seen in apatite, with most of sample SV01-75 retaining much higher values in Sr/Pb, up to 80.

Correlation between Sr and Pb in lawsonite has been observed in sample SV03-103, previously published in Martin et al. (2014a). In this work, it was identified that lawsonite in metasomatic sample COE5 from Corsica transitions from low Sr/Pb in the cores, similar to metasedimentary lawsonite, to high Sr/Pb in the rims and the vein, similar to mafic samples. This change was attributed to an influx of mafic-derived fluid into a rock of sedimentary origin; this could also be the case for Martin et al. (2014a) quartzite SHB046, a sample from the same outcrop as SHS03. In our dataset, the endmembers are represented by mafic sample SV01-75, in which lawsonite yields high Sr/Pb, and lawsonite in metasediments SHS03 (cores) and SIB50B, which yield low Sr/Pb. The correlation between  $\delta^{18}\text{O}$  and Sr/Pb in samples SHB03 and SHSB12B is a strong indication that changes in Sr/Pb in lawsonite can track metasomatic events, confirming conclusions by Martin et al. (2014a). In SHB12B and SHB03, the outer lawsonite rims are also enriched in Fe. This enrichment is interpreted as an indication of oxidising conditions since Fe is primarily included as  $\text{Fe}^{3+}$  in lawsonite (Martin et al. 2014a), similarly to what is seen in the aegirine-rich rims of clinopyroxene in SHB12B.

In summary,  $\delta^{18}\text{O}$  zoning is observed in two samples in lawsonite. Lawsonite zoning in  $\delta^{18}\text{O}$  correlates with Sr/Pb and Fe and all can be used for tracking metasomatism, similar to apatite. However, in the case of lawsonite, the diffusion rates of oxygen are unknown.

## 5.2 Protolith $\delta^{18}\text{O}$ and early metasomatism

The  $\delta^{18}\text{O}$  signatures observed at the mineral scale and in the bulk are the cumulative result of a sequence of processes, a general model presenting three stages of metasomatism is presented as shown first in Figure 26. The signatures present in the sedimentary and magmatic protoliths are first modified by the results of seafloor alteration (stage 0), mechanical or chemical mixing of sedimentary and magmatic signatures either by the deposition of volcano-sedimentary layers or by melange-formation processes in the accretionary prism (stage 1), and finally fluid-rock interaction during subduction (stages 2 and 3). These processes will be investigated by discussing first the pre-metamorphic processes (current section), and then the high-pressure fluid circulations (section 5.3).

The origin of protoliths in the Halilbağı unit was investigated in **Chapter 3**. Based on WR geochemistry and zircon U-Pb dating it was concluded that the Halilbağı unit is made of an assemblage of rock types of different affinity and ages, of oceanic and continental margin origin.

The Halilbağlı rocks are geochemically and geochronologically similar to the less-metamorphic oceanic complexes of the Tavşanlı area, which can be related to the Izmir-Ankara ophiolitic complexes. The only oxygen isotope data available for the Tavşanlı zone are not directly relevant for this study as they are on different rock types: magnesite veins in the serpentinite of the ophiolite unit (Kahya 2014), or on the post-continental magmatic rocks (Mutlu 2012). One previous study measured  $\delta^{18}\text{O}$  (VSMOW) of 12 to 17 ‰ for the OIB pillow lavas in the Kılıçlar locality of the ophiolitic melange of the Izmir-Ankara suture, interpreted as a fore-arc accretionary prism (Gökten and Floyd 2007). In this case, the pillow lavas in prehnite-pumpellyite facies retain a magmatic  $^{87}\text{Sr}/^{86}\text{Sr}$  ratio at ca. 0.704, which was interpreted as an indication that the pillow-lavas were not mechanically mixed with sediments, but rather hydrothermally altered. Such elevated  $\delta^{18}\text{O}$  values of 12 to 17 ‰ are at the upper range of what is expected for seafloor mafic lithologies altered at low temperatures in the upper part of the oceanic sequence (Gregory and Taylor 1981), and could be due to further fluid circulations in the accretionary prism.

SHS44A and SHB45 magmatic zircon cores provide direct constraints on the magmatic  $\delta^{18}\text{O}$  of this leucogabbro and alkali basalt: zircon  $\delta^{18}\text{O}$  is of  $5.2 \pm 0.4\text{‰}$  for SHS44A and 4.5-6 ‰ for SHB45 (stage 0 in Figure 4 - 27). These two zircon values correspond to a modelled WR of 5.7 at 6 ‰ respectively, using an empirical formula by Valley (2003). This indicates that at magmatic temperatures, the protolith of these two rocks had mantle-like oxygen composition. These magmatic values can be extrapolated to other rocks of similar magmatic MORB and OIB immobile trace-element signatures identified in **Chapter 3**: SHB05, SHB08, SHB12B and SHB44B.

In contrast to these mantle-like values, the modelled  $\delta^{18}\text{O}$  values for the metabasites based on the analysed garnet cores range from 8 to 16 ‰ (following Stage 1 in Figure 4 - 27). The highest modelled  $\delta^{18}\text{O}$  values are from the south of Halilbağlı (SHS44A and B, modelled WR 17.0 and 16.3 ‰), followed by rocks from central Halilbağlı at 14.4 ‰ (boulder SHB05) see map in Figure 3 - 5. Similarly, in eclogite SHB45 and blueschist SV01-75 garnet cores yield modelled WR at 13.3 ‰ and ca. 11.5 ‰ respectively. The garnet cores in eclogite SHB12B provide the lowest modelled WR value of ca. 8‰, which still is far from the mantle value of  $\sim 5.5\text{‰}$ . Garnet is not a magmatic mineral, but grows early in the metamorphic evolution and thus its core  $\delta^{18}\text{O}$  composition is likely to represent the WR value at the early stage of metamorphism. These 8‰ to 16 ‰ signatures are interpreted as reflecting variable early alteration of the metabasalts (see also Putlitz et al. 2000).

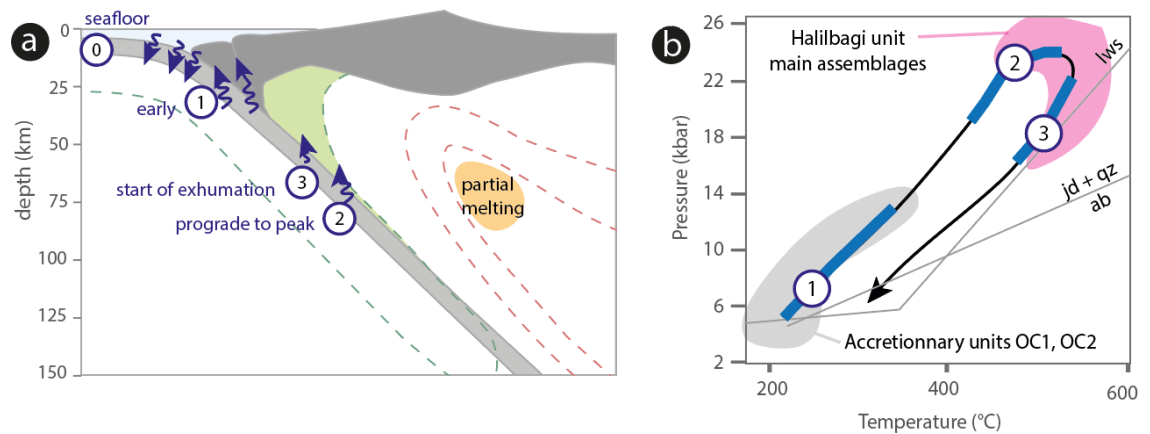


**Figure 4 - 26. a. Schematic representation of fluid pulses documented in the Halilbağı unit with regard to the subduction zone. b. P-T path with indications of fluid-rock interaction stages. The P-T field for the Accretionary units OC1 and OC2 and the main reactions are from Plunder et al. (2015), the P-T field for the Halilbağı unit main assemblages is a compilation of Çetinkaplan et al. (2008) and Davis and Whitney (2006,2008).**

In summary, relicts of magmatic oxygen isotope signatures in Halilbağı rocks only present in rare zircon cores in SHS44A and SHB45; mantle-like signatures that were likely original in all the MOR and OIB mafic rocks were obliterated before the crystallisation of the high-pressure (blueschist or eclogite) assemblage. The result is an elevated  $\delta^{18}\text{O}$  between 11 and 17 ‰ for all measured WR of mafic samples (Figure 4 - 27). The measured values correspond to the higher end of seafloor altered basalts, similar to the Gökten and Floyd (2007) Izmir-Ankara suture prehnite-pumpellyite pillow basalts. Ophiolites and oceanic drilling studies (Muehlenbachs and Clayton 1972; Gregory and Taylor 1981; Staudigel et al. 1995) show that heavy values  $\delta^{18}\text{O}$  in basalts can be attained by circulation of seawater at surficial levels where temperature is low and can reach even higher  $\delta^{18}\text{O}$  when sediments are present (e.g. Fouillac and Javoy 1988). Oceanic alteration, especially in the presence of sediments, is thus a likely process for the enrichment in  $^{18}\text{O}$  (stage 0 in Figure 4 - 26a). An alternate setting for the enrichment of  $^{18}\text{O}$  in Halilbağı metabasites is the accretionary prism and early (pre-garnet) subduction (stage 1 in Figure 4 - 26a, b). An enrichment trend has previously been observed by Bebout and Barton (1989) and Miller et al. (2001) in the WR of metabasites in sediment-rich subducted terranes of the Catalina Schist and Corsica, respectively. Miller et al. (2001) found a large span of  $\delta^{18}\text{O}$  values for metabasites and meta pillow-lavas, from 6 to 16 ‰, which they ascribe to hydrothermal alteration, with minor modification from subduction-related fluids, especially present at lithological interfaces (Martin et al. 2011; Vitale Brovarone et al. 2014). Bebout and Barton (1989) found various degrees of homogenisation for metasedimentary and metabasitic garnet-free 400°C blueschists, which  $\delta^{18}\text{O}$  was shifted towards equilibrium with water of ca. 13 ‰ along fluid conduits.

The serpentinite SHS26 also yields heavy  $\delta^{18}\text{O}$  with a measured WR of 13.8 ‰, which is consistent with its main mineral antigorite, measured at 13.4 ‰. These serpentinite pods have previously been interpreted as mantle wedge slices (Whitney et al. 2014), in which the high  $\delta^{18}\text{O}$  value would imply that mantle wedge was serpentinised by sedimentary fluids with high  $\delta^{18}\text{O}$ . A simpler explanation is that these lenses represent oceanic serpentinites such as present in lower grade oceanic complexes (Plunder et al. 2013) that equilibrated with seawater at low temperatures or sediments in the accretionary prism, similarly to the metabasites. The latter hypothesis is supported by the REE and trace element signature of this rock that resemble that of an olivine-rich cumulate, in line with an oceanic protolith (see **Chapter 3**) and not a mantle wedge peridotite protolith.

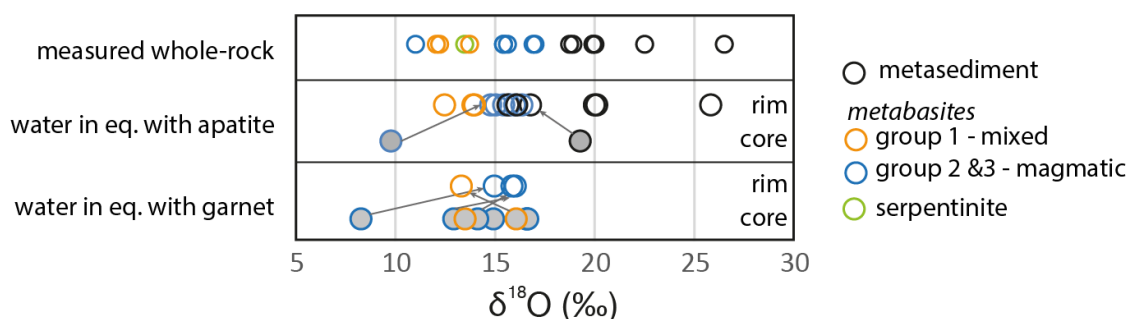


**Figure 4 - 27. Overview of measured WR  $\delta^{18}\text{O}$  and value for water equilibrated with mineral zones at 500°C, following fractionation coefficients by Zheng (1993a, 1996) at 500°C. Straight ties indicate core-rim relationship in a single sample.**

WR REE and trace-element patterns (see **Chapter 3**) indicate that intermediate lithologies SHB53, SIB50B, SIB32 are likely a mix between volcanic and sedimentary components (e.g. volcanoclastic). These samples yield a measured WR  $\delta^{18}\text{O}$  between 12.2-13.7 ‰, which is within the range of  $\delta^{18}\text{O}$  measured in rocks that yield magmatic-like REE patterns and magmatic relicts. Similar to purely magmatic metabasites, heavy signature can be traced back to at least early garnet growth in SIB50B and SV03-103, SV12-13F, where garnet cores yield modelled WR  $\delta^{18}\text{O}$  of ca 13 ‰, 11 ‰ and 15 ‰ respectively. The intermediate lithologies studied here are similar in  $\delta^{18}\text{O}$  to the pillow breccias of Miller et al. (2001), that yield a  $\delta^{18}\text{O}$  of 12-15 ‰, values that are higher than the pillow-lavas in the same sequence.

The metasediments co-deposited with these metabasites yield a range of elevated values, from 18.9 to 22.5 ‰ with the exception of the Günyüzü marble SGM21 which yields a higher value at 26.5 ‰. These values are similar to oceanic sediments analysed by Bebout (1991) in the Catalina schist, or the sediments in the Corsica HP ophiolite analysed by Miller et al. (2001). As sediment

$\delta^{18}\text{O}$  signatures can span a wide range in un-metamorphosed sequences, these rocks do not provide additional information on the pre- or early-subduction hydrothermal phase.

### 5.3 High-pressure fluid events

The first evidence for open system behaviour in the metamorphic assemblages is seen in the difference between garnet core and rim in eclogite SV12-13F (stage 2, Figure 4 - 28). The garnet core yields high  $\delta^{18}\text{O}$  values of 14 ‰, with a corresponding modelled bulk rock value of ca. 15 ‰, whereas the garnet rim yields a  $\delta^{18}\text{O}$  of 11 ‰, testifying to a high-pressure re-equilibration with a lower- $\delta^{18}\text{O}$  fluid of 12.7 ‰. The re-equilibration is speculated to occur before the end of the prograde path, toward the end of garnet growth (Figure 4 - 26b). Similar HP metasomatism has been observed in other eclogite terranes, leading to the dissolution of the cores and the formation of atoll garnets (e.g. Cheng et al. 2007, Martin et al. 2014b). Similar channel-like textures are present in metasomatic garnets from the Monviso (Angiboust et al. 2011; Rubatto and Angiboust 2015), and have been interpreted as healed fractures recrystallizing blueschist-facies garnet cores at peak conditions along major shear zones. The difference in temperature between the growth of garnet cores (estimated at 500°C by Davis and Whitney, 2008) and the rims (max T ca. 580°C, min T ca. 500°C) cannot be responsible for such a  $\delta^{18}\text{O}$  change, especially since a higher temperature would induce a marginally higher  $\delta^{18}\text{O}$  in garnet (Figure 4 - 22). This event is only recorded in one outcrop and thus little can be gathered of the composition of this fluid at a regional scale. As the re-equilibrated garnet zones are homogenous in  $\delta^{18}\text{O}$ , it is likely that the system was buffered by fluid composition. The re-equilibration mechanism marked by the replacement features in the garnet cores contrasts with the dissolution-reprecipitation recorded in the Mg-poor rims (see below). This might indicate a contrast in the fluid properties (potentially pH or  $f\text{O}_2$ ) that would explain a different reactivity with garnet.

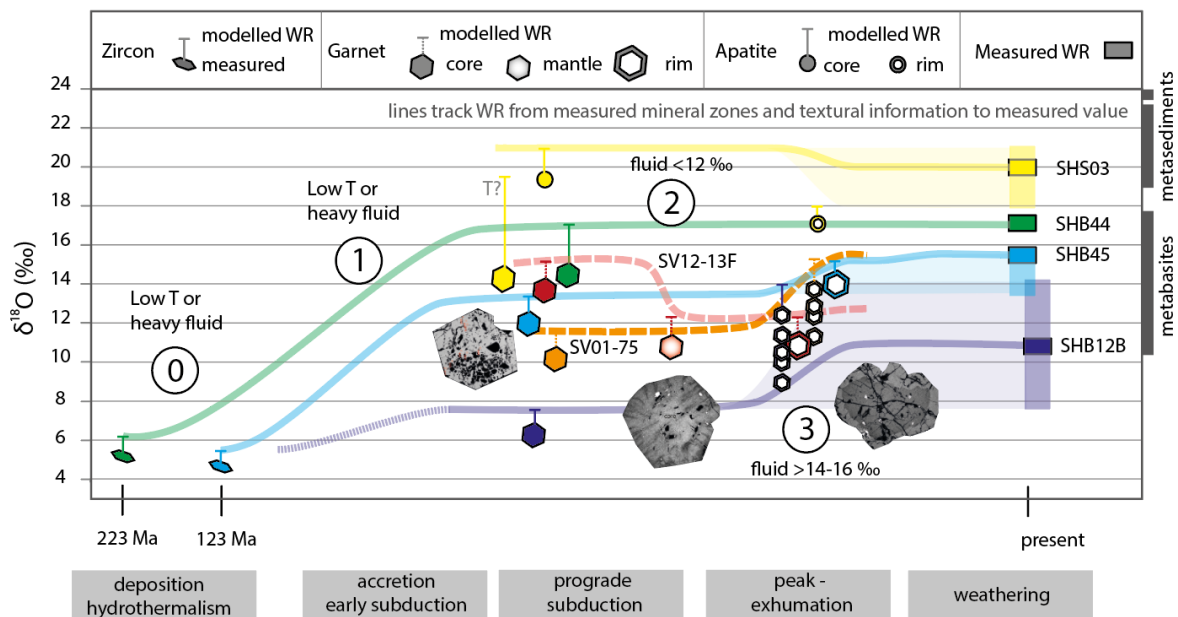


**Figure 4 - 28. WR  $\delta^{18}\text{O}$  vs time trajectories documented by in situ analysis and WR modelling in Halilbağlı lithologies. Measured values are indicated by mineral symbols, corresponding modelled WR value is indicated by the vertical bar on the left.**

Mg-poor and Fe-rich rims in garnet and clinopyroxene are interpreted as fluid-related recrystallisation in lawsonite eclogites SHB12B, SHB45, SV12-13F as well as in lawsonite blueschist SV01-75A. The garnet Mg-poor rim cross-cut stage 2 core re-equilibration in SV01-75A and thus occurred at a later phase: stage 3 in Figure 4 - 28. Here, a model is presented where the fluid circulation is presented as episodic. There is no evidence in the sample where both stage 2 and stage 3 are observed for continuity between these two phases characterised by contrasting  $\delta^{18}\text{O}$  signatures and garnet composition. However, the relative duration of these phases cannot be determined here. The garnet rims in SHB12B can be linked to the co-crystallisation of new lawsonite, thus a potential enrichment in Ca. This stage is characterised by strong  $\delta^{18}\text{O}$  change in garnet rim in the three samples, as well as apatite and lawsonite  $\delta^{18}\text{O}$  zoning in SHB12B (apatites were not investigated in SV12-13F and SV01-75A). The garnet rims yield higher  $\delta^{18}\text{O}$  than garnet cores in all but SV12-13F where the rims have a similar signature as the stage 2 re-equilibrated zones in the cores. The rim growth is coupled with some core dissolution, as shown by the replacement textures around cracks, but also by the concentration of garnet-compatible elements (e.g. Mn, Lu and Y) at the recrystallization front (SHB12B, SHB45). Some garnet rims are homogenous for oxygen, which is an indication of fluid-buffering. In these samples, the water in equilibrium with the rims at  $500^\circ\text{C}$  is 12.7 ‰ to 15.8 ‰. In other samples such as SHB12B, and to a lesser extent SV01-75, garnet rims show variable  $\delta^{18}\text{O}$  compositions. In SHB12B, the higher values are measured towards the outside of the rims, whereas in SV01-75, the difference is observed between large rims around garnet 1 with lower values, and much smaller rims around garnet 2 with higher values. These variations may indicate that the system was not fluid-buffered,



and only a minimum value for the fluid can be calculated from the highest  $\delta^{18}\text{O}$  measured in rims. For these two sample, the fluid  $\delta^{18}\text{O}$  would be  $>14.9$  and  $>15.4$  ‰. (Figure 4 - 27).

Similar fluid values are obtained from apatite in SHB12B: apatite rims in this sample yield  $\delta^{18}\text{O}$  values up to 15.3 ‰ that are in equilibrium with the values measured in garnet (Figure 4 - 27), and with a fluid value of ca. 14.8 ‰. Similar to apatite, lawsonite shows an increase in  $\delta^{18}\text{O}$  towards the rim, but as lawsonite fractionation with water is uncertain, no fluid value is calculated. In contrast with the metabasitic samples, metasedimentary sample SHS03 contains reversely zoned lawsonite and apatite: in this sample, cores have high values and rims lower values. The water in equilibrium with the lowest rim apatite values is maximum ca. 16.8 ‰. Garnet rim  $\delta^{18}\text{O}$ , together with apatite  $\delta^{18}\text{O}$  (on the hypothesis that other apatites have equilibrated with the latest fluid), converges toward a fluid value ca. 14-16 ‰ (Figure 4 - 27), which is the highest reported for subduction fluids, and shows the dominance of heavily altered oceanic crust and sediment signature.

Some indication about the fluid trace-element composition can be gathered from garnet, apatite and lawsonite. Cr is subtly enriched in SHB45 garnet rims, and depleted in SHB12B rims. No major zoning is seen in other garnet trace-elements such as Zn. Apatite in SHB12B yields interesting information about fluid-mobile elements: both core and rim yield undetectable Cl, an indication the fluid is low in Cl, as interpreted from apatites in the western part of the Tavşanlı zone by Pagé et al. (2016). Also, the apatite rims yield a lower Sr/Pb, which suggests that the fluid carried Sr and removed Pb from eclogite SHB12B. Apatite and lawsonite rims in quartzite SHS03 yield higher Sr/Pb, with a gain in Sr and a loss in Pb compared to the cores, thus showing a convergence towards the ratios observed in eclogite SHB12B apatite and lawsonite rims. The Sr/Pb to which rims converge is ca. 18 for lawsonite and 50 for apatite. It has been proposed that lawsonite records the reactive bulk-rock Sr/Pb (Martin et al. 2014a), in which case the intermediate values between mafic and sedimentary lithologies show a contribution of both sources into the fluid composition. It is striking that Sr/Pb and  $\delta^{18}\text{O}$  ratios converge to a well-defined value: Sr/Pb of ca. 18 in lawsonite which is a proxy for WR value (Figure 4 - 19), and equilibrated with a fluid of  $\delta^{18}\text{O}$  ca. 16 ‰ (Figure 4 - 19, Figure 4 - 27). This is likely representative of a fluid permeating the entire unit at high-pressure conditions.

There are several indications of an oxidising nature of this fluid. The associated Fe-rich rims on clinopyroxene, which also display fluid related textures with propagation along grain boundaries and cracks, are systematically enriched in  $\text{Fe}^{3+}$ , which is interpreted as the sign that the fluid is oxidising. In a parallel way, lawsonite rims are enriched in Fe (mostly incorporated as  $\text{Fe}^{3+}$ ), and

apatites depleted in Fe (mostly incorporated as  $\text{Fe}^{2+}$ ). Oxidising fluids could be generated by interaction with C-bearing metasediments, such as by dissolution of marbles or other carbonate-bearing lithologies. This oxidation is the reverse of that seen by Liu et al. (2016) and Angiboust et al. (2012) in slightly higher grade eclogites. In these studies, the oxidised Fe-Ti gabbro protolith is reduced during subduction. While Angiboust et al. (2012) report a late stage oxidising stage, the opposite situation is observed in the Tavşanlı samples, with reducing conditions prevailing in the prograde evolution, before retrogression in oxidising conditions. These differences could hint at highly variable oxidation histories in subducting slabs depending on carbonate-rich sediment availability. The  $\text{Fe}^{3+}$  increase in clinopyroxene and lawsonite rims could also be the result of retrogression: as shown by Groppo and Castelli (2010), more oxidised assemblages are stable at lower P-T (these authors studied assemblages at 21 kbar, from 460 to 500°C, conditions very similar to the Halilbağı unit, but the rims would here be retrograde).  $\text{Fe}^{3+}$  could be liberated in the reactive bulk by the destabilisation of epidote with decreasing temperature or increasing pressure, or by external fluids.

The P-T conditions of the second HP fluid event (stage 3, Figure 4 - 26) are in the stability field of garnet, omphacite and lawsonite (affected minerals) for mafic samples, and these minerals are stable at peak conditions. The presence of similar  $\delta^{18}\text{O}$  enriched garnet rims in blueschist SV01-75 suggests that this event occurred at P-T conditions where mafic rocks contain omphacite or glaucophane-dominated assemblages depending on their chemistry (SHB12B has no glaucophane, SV01-75 no omphacite, and SHB45 a similar amount of both). As an indication, grt-cpx temperatures calculated between garnet and omphacite rims for a pressure of 20 kbar is ca. 510°C for SHB12B and ca. 480°C for SHB45. Similar temperatures were obtained by K. Fornash using the same method (unpublished PhD thesis, 2016) on SV12-13F. Fornash also measured phengites in a twin sample for SHB12, which yields P-T conditions of 23 kbar, 530°C (K. Fornash unpublished PhD thesis). These P-T conditions coincide with the beginning of exhumation and a change in deformation patterns close to the maximum decoupling depth (MDD) as described in Whitney et al. (2014) at  $500 \pm 50$  °C (Figure 4 - 26, Figure 4 - 29). In Teyssier et al. (2010) and Whitney et al. (2014), the change of vorticity between eclogite facies rocks (high degree of simple shear, phase 2 in Figure 4 - 29) and retrograde blueschists (significant amount of pure shear, lower degree of simple shear, phase 3 in Figure 4 - 29), is interpreted as a thinning of the subduction channel close to the MDD, and the extrusion of the Halilbağı unit. This change in vorticity is associated to a change in deformation pattern: from the formation of isoclinal folds (F2, Gautier 1984; Seaton et al. 2009; Teyssier et al. 2010b; Davis 2011; Whitney et al. 2014) to an increase

in pure shear linked to the start of exhumation, leading to the development of the strongly deformed mylonitic zone close to the current contact with the peridotitic unit to the North.

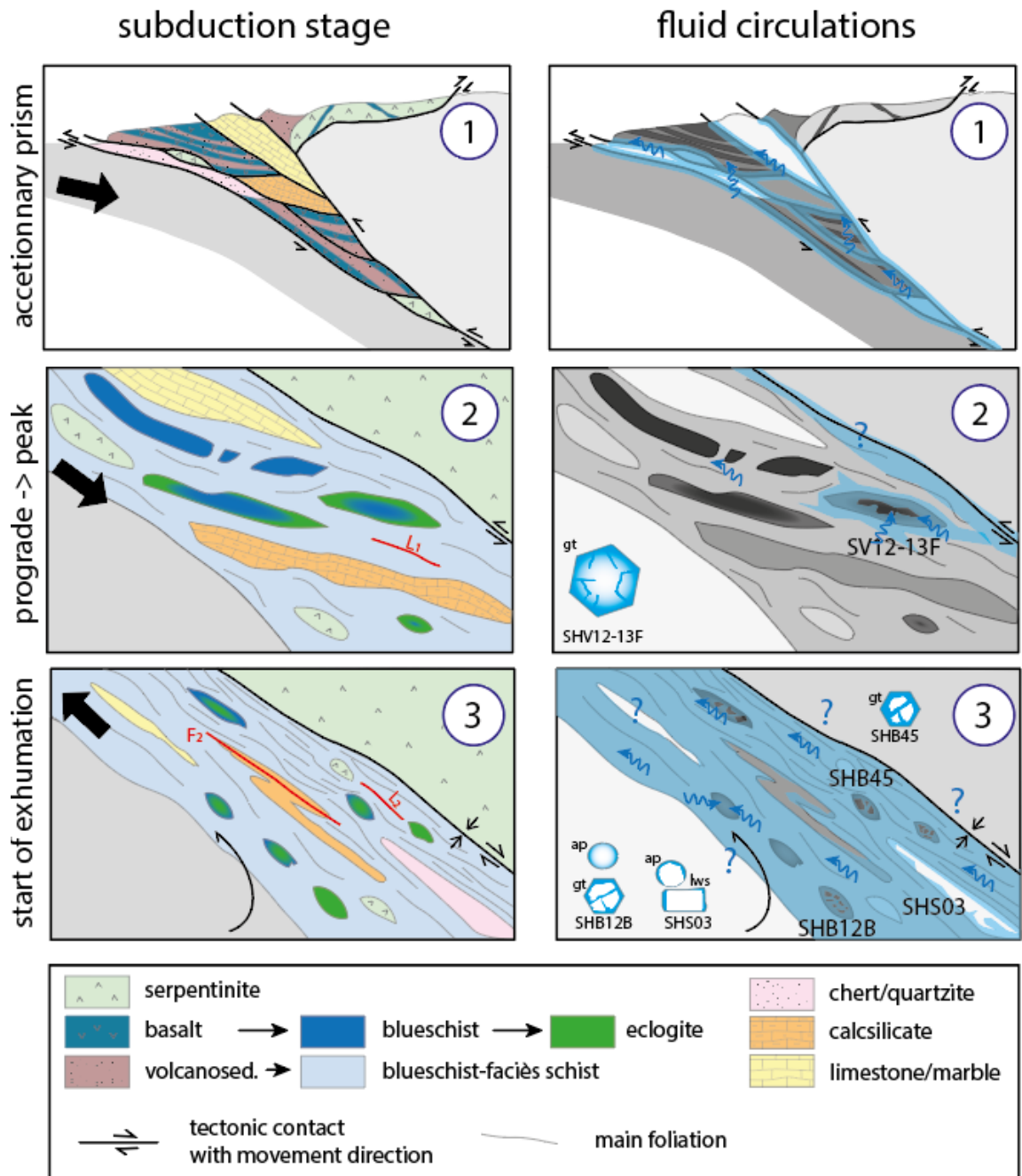


Figure 4 - 29. Schematic representation of the three phases of subduction-related fluid-rock interaction in the Halilbağı unit, with geological relationships in the left panel and corresponding fluid flow pattern in the right panel. (1) Accretionary prism phase, from representations in Pourteau et al. (2016) and Plunder et al. (2015), with fluid flow along shear zones and mechanical mixing (2) Prograde to peak fluid-induced recrystallization, observed in eclogite SV12-13F: Blueschist to eclogite prograde transition, simple shear phase in Davis and Whitney (2008) and Teyssier et al. (2010), (3) Pervasive fluid flow at the start of exhumation seen across the unit, phase of pure shear, drawn from cross section in Whitney et al. (2014).

The change in deformation regime could have created opportunities for fluid flow across the Halilbağı rocks and mafic boudins in particular (stage 3 in Figure 4 - 29), as this deformation has been linked to the hydration of clinopyroxene-dominated assemblages into glaucophane-dominated assemblages at the edges of the boudins (e.g. Davis and Whitney 2008). It is to note that 5 metabasites that show stage 3 fluid-rock interaction are situated throughout the Halilbağı unit, ranging from 500 m to 5 km away from the mylonitic shear zone forming the current contact with the peridotitic unit to the North. Fluid flow was thus not concentrated within the shear zone, but pervasive across the unit (Figure 4 - 29, stage 3). Moreover, mineral signatures in  $\delta^{18}\text{O}$  and Sr/Pb show a convergence to a common signature across the unit and across lithologies (Figure 4 - 19), which indicates that fluid exchanges happen at the unit scale, affecting mafic rocks as well as metasediments.

In the Halilbağı unit, high pressure fluids were dominated by a sedimentary component, which is different from fluids identified in other subducted oceanic sequence where there is a stronger ultramafic influence, such as in the Franciscan (Errico et al. 2013; Page et al. 2014), the early stages in the Monviso (Rubatto and Angiboust 2015), and some areas in Corsica (Martin et al. 2014b). The sediment-derived fluid circulation described here is closer to what documented in the Catalina schists (Bebout and Barton 1989), where at lower pressure, a large sedimentary influence is present. As in the Catalina schists, the Halilbağı unit contains relatively small mafic bodies compared to more coherent slices of oceanic crust (Monviso, Corsica), where sediments are a minor percentage of the outcrop, or melanges dominated by ultramafic matrix (Franciscan). The dynamic environment of successive accretion (accumulation of an accretionary prism) and underplating (entrainment of accretionary prism units in the subduction) documented in the Tavşanlı zone (Plunder et al. 2015, **Chapter 3**) could be responsible for the pervasive low temperature fluid circulation and the equilibration of  $\delta^{18}\text{O}$  and Pb in a sediment-rich environment, in the accretionary prism and early subduction stages giving rise to the large positive Pb anomalies and generally heavy pre-HP  $\delta^{18}\text{O}$  signatures recorded in Halilbağı metabasites. The cold conditions recorded during subduction and exhumation stages in the Tavşanlı zone in general and the Halilbağı unit in particular (Whitney and Davis 2006) might also preclude or delay large amounts of serpentinite dehydration which is the main provider for fluids from ultramafic rocks and would have diluted the sedimentary signature. Although the main HP fluid circulation event happened during the start of exhumation in the Halilbağı unit, the syn-subduction extrusion dynamics (Teyssier et al. 2010; Whitney et al. 2011; Whitney et al. 2014) allowing the exhumation of the Halilbağı unit make it potentially relevant to continuing subduction zones, reflecting deformation regime changes near the MDD, by opposition of collision-related exhumation and fluid events.

## 5.4 Chemical WR changes and hybridisation

Four fluid events (stages 0 to 3) are identified in Halilbağlı lithologies, including the seafloor or accretionary prism mixing and high-pressure fluid exchanges. These events produce rims in garnet, clinopyroxene, lawsonite and apatite. In this section, the effect of fluid metasomatism on whole-rock composition during subduction is investigated.

### 5.4.1 Mechanism for WR metasomatism

The modality of fluid circulation changes at the different stages of fluid-rock interaction. Low-temperature interactions at the seafloor or in the accretionary prism is the product of high water/rock ratio and creates clay and other low-temperature minerals. It is likely coupled and favoured by mechanical mixing such as sedimentation of volcanoclastic layers, re-sedimentation by gravity and seismic events (mass transport deposits, Strasser et al. 2012), brecciation along faults and deformation in the accretionary wedge (Barany and Karson 1989; Froitzheim and Manatschal 1996). The present litostratigraphic relationships in the Halilbağlı unit are attributed to these processes that created lenses of small bodies of mafic and even ultramafic rocks within a heterogeneous matrix of metasediments, with variable clastic and carbonatic component. In the Halilbağlı sequence, due to the paucity of magmatic, sedimentary or low grade mineral relicts, it is hard to establish whether the chemical exchanges occurred in the seafloor (stage 0) or in accretionary stage (stage 1). It can however be concluded that by the early stages of HP metamorphism (core of the garnet) mafic rocks were already heavily altered and their oxygen signature intensely modified and shifted to higher  $\delta^{18}\text{O}$ .

Once the metabasites achieved blueschist to eclogite facies conditions, two behaviours are observed: (a) mafic rocks that largely remained impermeable to fluids, where metamorphic minerals are in equilibrium with the measured WR and yield no zoning in  $\delta^{18}\text{O}$ , such as SHS44A, SHS44B and SHB05; and (b) rocks that show significant interaction with fluids at different stages to produce shift in  $\delta^{18}\text{O}$ , as in SV12-13F (stage 2 and 3 in Figure 4 - 28, Figure 4 - 29). Stage 2 fluid is evidenced by local re-equilibration or recrystallisation of garnet cores along subgrain boundaries. At stage 3, garnet rim growth was in equilibrium with an external fluid of heavier  $\delta^{18}\text{O}$  composition, and thus likely entering from the surrounding sediments. In garnet and clinopyroxene, stage 3 is expressed as dissolution-reprecipitation forming a reaction front along grain boundaries, fractures and inclusions, leading to the growth of rims of contrasted composition. This fluid exchange likely occurred at near-peak conditions or at the start of exhumation (Figure 4 - 26), where garnet growth is made possible by a change in the reactive bulk composition. At this stage input of external fluids in the mafic rocks is more pervasive, and is documented even in the most intact mafic pods (Figure 4 - 29).

For example, in SHB12B, the measured WR  $\delta^{18}\text{O}$  is 11.0 ‰. This can be related as half way between the WR  $\delta^{18}\text{O}$  extrapolated from garnet cores, indicative of the starting material: ca. 7.5 ‰, and the rim signatures, equilibrated with the fluid: a maximum of 14.3 ‰. This corresponds to a percentage of replacement of minimum 50% of the oxygen atoms in the sample, if the highest rim signature represents equilibrium with the fluid. This is reflected in the textures seen in the sample, where BSE-bright rims in garnet, omphacite and phengite represent half of the area (proxy for volume) in the thin section. In SHB45, the measured WR is 15.6 ‰, which is marginally higher than the modelled WR in equilibrium with the garnet rims (14.8 ‰), which shows that a later stage of interaction with  $\delta^{18}\text{O}$ -heavy water could have happened after the end of garnet growth. A similar exercise can be done with the WR modelled from apatite core-rim zoning in SHS03. The measured WR in quartzite SHS03 is 20.0 ‰, the WR reconstructed from the cores yields ca. 21.5 ‰, and from the rims ca. 18 ‰, which corresponds to a replacement percentage of ca. 40%. In terms of  $\delta^{18}\text{O}$ , the interaction with external fluids result in a homogenisation of metabasitic rocks towards a heavy value between 12 and 17 ‰ furthering a tendency achieved for most lithologies in the oceanic/accretionary stage, before garnet growth. These calculations show that the reactions forming garnet rims during stage 2 did not occur in a closed system, where ca. half of the oxygen atoms are from the fluid, but in a dynamic system involving a high fluid/rock ratio. Chemical changes in WR will depend on the capacity of the fluid to transport elements, and the compatibility of elements in the phases that crystallise. The mineral data show that Sr and Pb are mobile elements, as they vary together with  $\delta^{18}\text{O}$ . Fe and Mg concentration changes between garnet core and rims, but this could be due to repartition between different phases.

As expected, pervasive infiltration of aqueous fluids modifies the major element composition (replacement of ca. 50% of oxygen atoms, changes in  $\text{Fe}^{3+}$ , potential changes in Ca) of the reactive assemblage, by the process of dissolution-reprecipitation. Consequently, it is not correct to consider a closed system for rim-forming reactions in most mafic and some sedimentary Halilbağı samples. Especially, P-T path determinations based on isochemical pseudosections must be interpreted with care in samples where an open system is demonstrated, and  $\text{Fe}^{3+}$  should be considered as an important component in such rocks.

#### **5.4.2 Influence of metasomatism on WR trace-element signatures**

In the two metabasites that best preserve magmatic signatures up to stage 3, the main changes observed in trace element composition are in Pb, Sr, and Cs, Rb and Ba (Figure 4 - 30a). Compared to their magmatic supposed protolith composition (EMORB and OIB, respectively), SHB45 and SHB12 are enriched in Pb and depleted in Sr. Cs, Rb and Ba may have been buffered by a similar fluid as they show similar concentrations in both samples, with Cs notably enriched

compared to Rb and Ba. Additionally, SHB12 is enriched in HREE, but it cannot be excluded that this HREE enrichment is a sampling bias related to variable garnet (HREE rich phase) abundance in the two sub-layers. While oxygen signatures are efficiently homogenised at the WR scale, even if the mineral data show a convergence in Sr/Pb in different samples, the convergence in Sr/Pb is not observed in the WR (Figure 4 - 30b). This discrepancy could be explained by the unreactive behaviour during ca. 500°C fluid metasomatism of lawsonite and apatite cores which are major hosts for Sr and Pb. Mineral zoning is better at recording relative changes over time, whereas the bulk rock remains a mixture superposing stages. Mobile elements (Cs, Rb, Ba) are mostly hosted in phengite, which is very reactive during recrystallization, and to a lesser amount lawsonite and apatite. No changes can be observed in HFSE likely hosted in zircon and rutile that do not readily react. These results echo previous studies that showed limited trace-element redistribution between lithologies from lawsonite blueschist to eclogite facies (Spandler et al. 2003), and also show that HFSE and REE, fluid mobile elements and oxygen isotopes are strongly decoupled at the WR scale at these conditions.

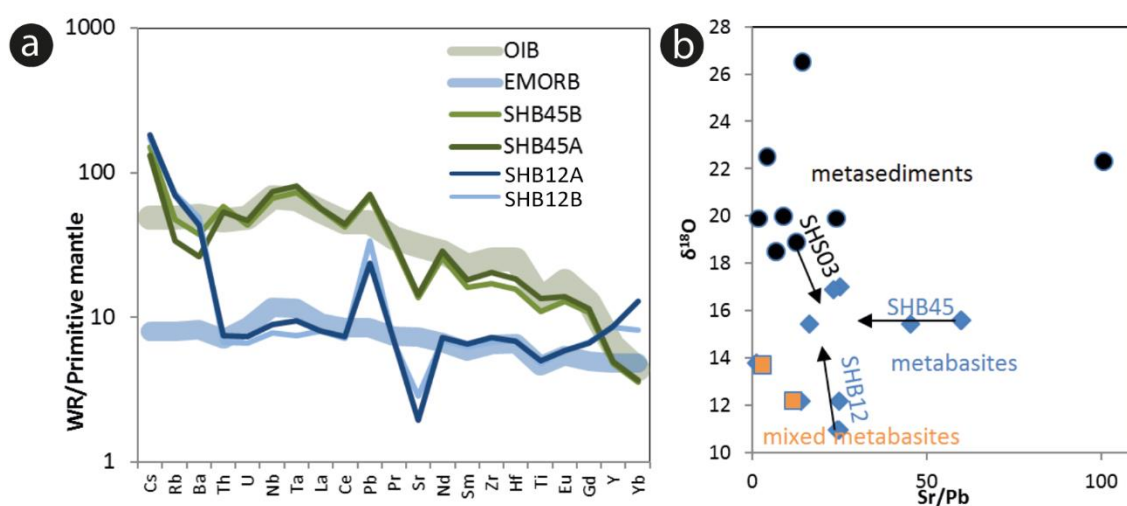


**Figure 4 - 30. a. Primitive mantle normalised trace element patterns for samples SHB45 and SHB12; b. variation of  $\delta^{18}\text{O}$  vs Sr/Pb in Halilbağı WR. Arrows show variation seen in lawsonite core-rim, as lawsonite records reactive bulk Sr/Pb.**

The whole dataset, representing the accumulation of oceanic crust alteration, early subduction mixing and HP fluid exchanges, shows more variation in trace elements (Figure 4 - 31). The main feature is a pronounced positive Pb anomaly in all samples regardless of rock type. Notably, the Pb anomaly is smallest in clastic metasediment SIS53 and is even present in the marble and the serpentinite. Most samples are enriched in Sr with respect to the primitive mantle, but most patterns have a negative Sr anomaly, except the serpentinite and the marble SHM04 that yield low concentrations overall but still 20 times the primitive mantle in Sr.

Apart from these pronounced features, the diversity in trace-element patterns is likely to reflect heterogeneity in the protoliths entering the subduction (cf. **Chapter 2**), especially among mafic rocks of magmatic origin, similarly to what is observed in other oceanic sequences such as in New Caledonia (Spandler et al. 2004). The variation in trace elements is smaller for the type 1 metabasites (mixed lithologies) with the exclusion of Cs, Rb and Ba, which have large variations. These rocks contain elevated amounts of trace elements with a large Pb anomaly, varying positive and negative anomalies in Sr. They yield a GLOSS-like REE pattern (cf **Chapter 3**), which is typical of sediments in this unit. The similarity in trace-element pattern is striking, and contrasts to the large variations seen in mineralogy and major element composition (cf **Chapter 3**). As REE variations are not observed in samples metasomatised at high pressure, the REE signature is likely due to mechanical mixing at the fine scale between mafic volcanic and sediments at depositional and oceanic/accretionary stage. The resulting trace-element signatures (Figure 4 - 31) are similar to the melange average of Marschall and Schumacher (2012, Figure 4 - 32) in their enrichment in incompatible elements, the positive anomaly in Pb, negative Eu anomaly, but differ in their low Ba contents and lack of a Nb and Ta anomaly. These rock types yield a rather homogenous  $\delta^{18}\text{O}$  of 12.2-13.7 ‰, that would agree with buffering in a fluid-rich low temperature system such as an accretionary prism (e.g. Bebout 1991).

In summary, some metabasitic lithologies are mixed with a sedimentary component before the crystallisation of their metamorphic assemblage, where others kept a pristine signature for all but fluid-mobile elements, and were later homogenised for  $\delta^{18}\text{O}$ . The mixed lithologies in the Halilbağı unit do not reflect the high level of high-pressure chemical hybridisation seen in some melange zones, where high-pressure accessory mineral control on trace-element composition is documented (Marschall and Schumacher 2012), but rather the result of mechanical mixing on the seafloor or accretionary prism, while some mafic lithologies preserve their magmatic signatures down to the maximum decoupling depth. This decoupling between fluid mobile elements such as Sr, Pb and to some extent oxygen isotopes, compared to REE such as Nd has been observed in settings of oceanic crust alteration (Staudigel et al. 1995), as well as low to mid temperatures in the Catalina schist (King et al. 2006; Sievers et al. 2016). The result of both mechanical mixing and fluid-rock interactions in the Halilbağı unit converge towards a signature where incompatible trace elements and oxygen isotopes are dominated by sedimentary signature (e.g. GLOSS-like pattern in mixed lithologies, Pb enrichment across the unit and during HP fluid circulations in mafic lithologies such as SHB12B), but Sr is influenced by mafic rock types (Sr is abundant in altered metabasites such as SHB45 and enriched in metasediment SHS03 during HP fluid circulation). If the Halilbağı unit was to be brought to sub-arc conditions and interacted with fluids



from serpentinite dehydration, it could at a small scale create the mixture of sedimentary and altered oceanic crust subduction components identified in arc magmas (e.g. Elliott et al. 1997).

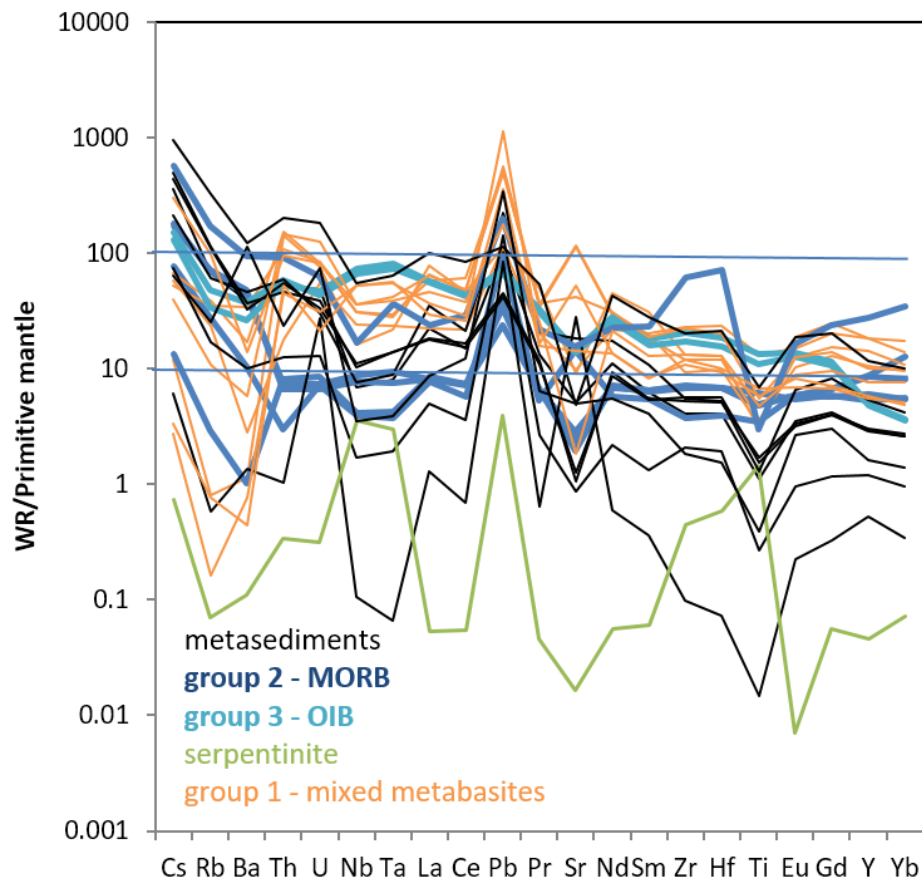


Figure 4 - 31. Primitive mantle normalised trace-element patterns for Halilbaşı WR samples

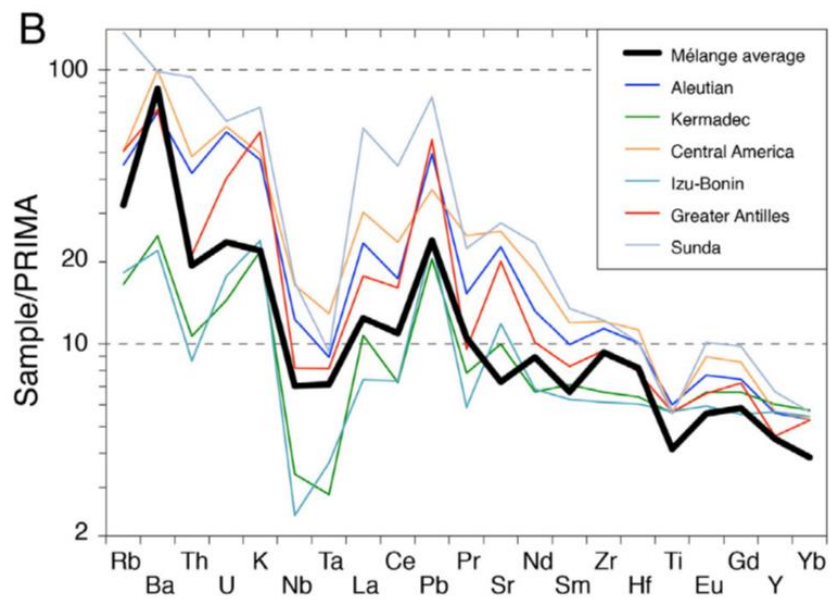


Figure 4 - 32. From *Marschall and Schumacher (2012)*, trace-element patterns for typical arc magmas compared to the average melange.

## 6 Conclusions

Core-rim  $\delta^{18}\text{O}$  zoning is observed in Halilbağı unit garnets, zircons, apatites and lawsonites, with variations up to 6‰. In six samples (four metabasites, one metasediment and one meta-leucogabbro) containing these zoned minerals, it is thus possible to pin-point fluid circulations to one of four possible stages: (0) of seafloor alteration, (1) accretionary prism alteration, before garnet growth, (2) prograde to peak fluid circulation, during peak garnet growth and (3) fluid circulation during the onset of exhumation and garnet dissolution-reprecipitation.

A thorough homogenisation of  $\delta^{18}\text{O}$  signatures is observed in the Halilbağı unit, reflecting low grade processes as well as high pressure fluid influxes. WR  $\delta^{18}\text{O}$  converge towards a range of values of 12-18 ‰ for metabasites and 18-22 ‰ for metasediments. In several metabasites across the investigated unit, some proportion of magmatic  $\delta^{18}\text{O}$  signature was preserved until nearing the maximum decoupling depth, where pervasive fluid influx is seen along grain boundaries and fractures. This HP fluid pulse identified by unit-wide garnet and clinopyroxene recrystallization, has an oxidising signature, and a  $\delta^{18}\text{O}$  of ca. 12-15 ‰, both compatible with equilibration with metasediments. This  $\delta^{18}\text{O}$  HP equilibration is accompanied by a variation of Sr and Pb seen in apatite and lawsonite. Sr, Pb, Cs, Rb and Ba are identified as the main mobile elements during this phase. Trace-elements are not homogenised as readily as  $\delta^{18}\text{O}$ : some mafic lithologies are the result of mechanical mixing at low grade with sediments and yield GLOSS-like signatures, but those who escaped these interactions preserve near-magmatic trace-element signatures, indicating that trace-elements are not liberated from these lithologies despite pervasive fluid flow at 500-550°C, 15-25 kbar.

Although several stages of fluid-rock interactions are detected, the main chemical vectors changing in the seafloor, accretionary prism, subduction and early exhumation stages are similar, leading to a homogenisation in  $f\text{O}_2$ ,  $\delta^{18}\text{O}$ , Sr/Pb and Cs, Rb and Ba across the unit, in a sediment-dominated environment. The homogenisation to a sedimentary signature is most efficiently seen at low P-T (seafloor or accretionary prism), where fluid-rock interaction is coupled to mechanical mixing, and to a lesser extent at the start of exhumation where deformation allows pervasive fluid influx in previously untouched boudins.

Finally, this study demonstrates the relevance of apatite and lawsonite as tracers of fluid events. The Sr – Pb ratio in both these phases allows identifying sedimentary or mafic influences in the fluid composition during prograde to retrograde evolution, as well as their  $\delta^{18}\text{O}$  signature, as far as they are not reset by diffusion. Indeed, the rate of diffusion of oxygen in apatite allows an

insight into late fluid events in these rocks, as they cooled quickly from 500-450°C. More work is needed in the refinement of  $\delta^{18}\text{O}$  analysis for lawsonite, and the study of its diffusion behaviour.



## Chapter 5

# Tracking heavy $\delta^{18}\text{O}$ signatures in the Archaean crust, a combined *in situ* and WR oxygen isotope study in Archaean metasedimentary rocks from the Itsaq complex, West Greenland.

## 1 Introduction

The emergence of continents and their interactions with the ocean and atmosphere in the early Earth is key to understanding early life and plate tectonics. Geochemical signatures offer precious clues about these early events. Among them, oxygen isotopes have been used as a tracer for surficial processes, as strongest oxygen isotope fractionation happens by fluid-rock interaction at low temperature (e.g. Lawrence and Taylor, 1971; Gregory and Taylor, 1981). Notably, analysis of heavy  $\delta^{18}\text{O}$  in Hadean zircons yielded the first evidence for early crust formation involving liquid water (e.g. Wilde et al. 2001; Trail et al. 2007; Kemp et al. 2010; Rizo et al. 2012). In this study, the formation and crustal evolution of the source of heavy  $\delta^{18}\text{O}$  signatures is investigated through the analysis of sedimentary rocks in their geological context, in Eo- and Mesoarchaeon supracrustal sequences.

The Isua supracrustal belt, in the Itsaq complex in Western Greenland, yields well-preserved complex 3.7 and 3.8 Ga crustal successions thought to be the remnants of two proto-arcs (Nutman et al., 2015c, Figure 5 - 1). Geochemical and isotopic investigations in Isua led to pioneering discoveries about Eoarchaeon crust differentiation (e.g. Harper and Jacobsen, 1992; Bennett et al., 1993), oceanic and atmospheric processes (e.g. Mojzsis et al., 2003; Bolhar et al., 2004) or the beginning of life (e.g. Schidlowski et al., 1979; Nutman et al., 2016). This thesis focuses on novel evidence for Eo- and Mesoarchaeon weathering processes, and their expression in the sedimentary record in paragneisses. This study of oxygen isotopes signatures, examines how they travel from sedimentary burial to metamorphism at mid crustal levels.

The method used is the *in situ* measurement of oxygen isotopes in zircon (magmatic and metamorphic) and garnet (metamorphic), combined with whole-rock  $\delta^{18}\text{O}$  to track  $\delta^{18}\text{O}$  signature changes. Two volcanoclastic metasedimentary sequences were chosen as the target of this study: one is a mid-crustal chlorite-garnet schist belonging to a 3.7 Ga unit in the Isua supracrustal belt,

the second is a lower crustal quartz-biotite-amphibolite belonging to the nearby Tikeraq complex at  $\geq 2.9$  Ga. First, the  $\delta^{18}\text{O}$  data are used to establish if any important fluid circulation or metasomatism affected these rocks during metamorphism. Second, protolith signatures are discussed and then compared to other regional values in order to investigate the degree of surface alteration and sedimentation processes in the early Archaean.

## 1.1 General context

The Isua supracrustal belt contains several tectonic packages of different ages, geochemical signatures and metamorphic histories (e.g. Nutman et al., 1997; Rollinson, 2002; Nutman and Friend, 2009). The two main terranes have ages of about 3700 Ma and 3800 Ma respectively (Nutman and Friend 2009) and are interpreted as the fragments of two proto-arcs (e.g. Nutman et al., 2015c). The 3700 Ma unit is made of several slivers of mafic volcanic rocks overlain by banded-iron formation (BIF) and more carbonate-rich sedimentary rocks. Additionally, some dunite lenses are intercalated in these units. The magmatic rocks show an evolution from boninite to more arc-like tholeiite, andesite and dacites signatures that would represent a transition from fluid-fluxing mantle melting to melting of a mafic protolith at garnet-present conditions (Nutman et al. 2014).

Within the 3700 Ma package, this study focuses on a sub-terrane made of schists (B2 unit in Nutman et al., 1984, Nutman and Bridgewater, 1986) that belongs to the *northwestern tectonic package* of Appel et al. (1998) (Figure 5 - 2). This sub-terrane is made of a pile of mafic (B2) to felsic (B1) composition, both with volcanoclastic protoliths. These rocks are chosen for this study because they represent the largest mass of detrital metasedimentary rocks of the Isua supracrustal belt, and one of the largest preserved from Earth's early history. They yield mafic to intermediate composition such as andesite or dacite (Rosing 1999; Bolhar et al. 2004; Bolhar et al. 2005). This sediment pile is interpreted by Nutman et al. (2015b) as an arc-related volcano-sedimentary package.

Nutman et al. (1997) and Kamber et al. (2005) separated a few zircon grains from felsic units and garnet micaschists. They obtained dates of  $3711 \pm 6$  Ma,  $3707 \pm 9$  Ma,  $3713 \pm 6$  Ma and an age of  $3704 \pm 13$  Ma. These ages are within error of dates obtained for the felsic B1 unit ( $3710 \pm 4$  Ma) and for banded iron formations ( $3707 \pm 6$  Ma), all from Nutman et al. (1997). These ages are interpreted as depositional ages, with zircons of volcanic origin (see petrological description in Nutman et al. 1997).

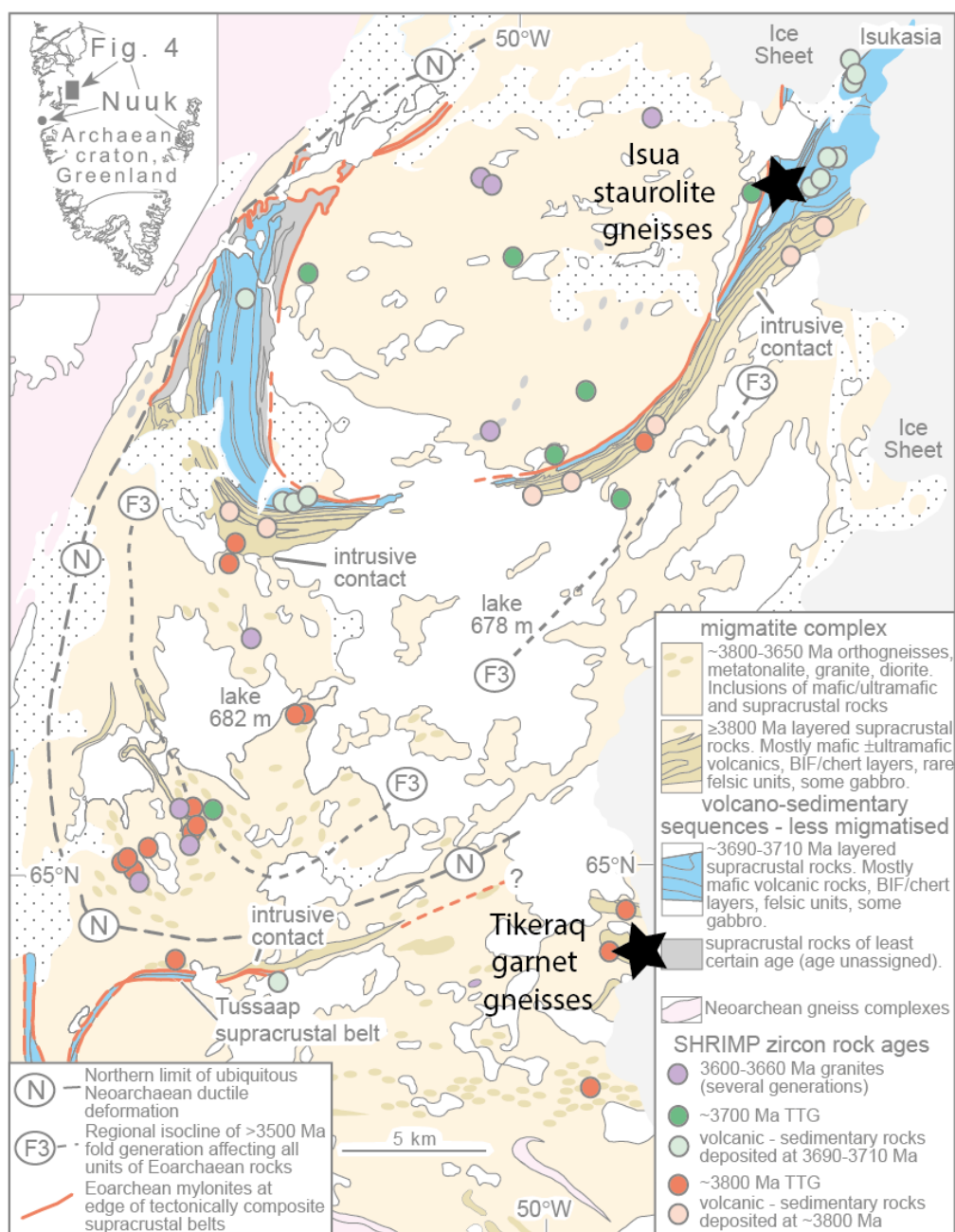


**Figure 5 - 1. Map of tectonic units and ages in the northern part of the Itsaq Gneiss Complex, from Nutman et al. (2013). Sampling localities are shown by stars.**

A second sampling site was chosen in an area 20 km south of the Isua supracrustal belt: Tikerqa (Figure 5 - 1). This area was revisited by V. Bennett, A. Nutman and C. Friend in 2010 prior the 2012 expedition. An exploratory isotopic study by V. Bennett revealed old components such as a Sm-Nd isochron age  $\geq 3.8$  Ga for layered gabbros. In contact with the layered gabbros is an extensive (a few hundreds of metres outcrop length) unit of garnet-schists that potentially represent an older equivalent of the B2 schists. There is no literature data available on these rocks that had not seen the visit of scientists since the mapping of Chadwick in the early 1950's.

Metamorphism is of higher grade in the Tikeraq area: the rocks show evidences of partial melting (see section 3.1.3).

## 1.2 Tectonics and metamorphic events

In the Isua supracrustal belt, based on field precise mapping and numerous U-Pb zircon ages, Nutman and Friend (2009) propose a tectonic model for the assembly of the Northern 3.7 Ga terrane and the Southern 3.8 Ga terrane. The schists that are the focus of this study are part of the the *northwestern tectonic package* in the 3700 Ma terrane, but yield a different metamorphic history than the coeval *central tectonic domain* of Appel et al. (1998) that outcrop to the SE. The northern tectonic domain preserves a consistent younging towards the SE (Nutman and Friend 2009) and thus no apparent folding, whereas the central domain contains numerous isoclinal folds. This difference is also marked in the garnet zoning that is different between the two domains (Rollinson 2002; Rollinson 2003). A chronology for events following the assembly of the *northwestern-* and *central tectonic domain* is proposed by Nutman and Friend (2009): the two main packages (3700 Ma and 3800 Ma) stacked on top of each other around 3.69 to 3.66 Ga following cessation of flat subduction. This event was followed by thermal relaxation and extension starting at circa 3.66 Ga, with the intrusion of the mafic Inaluk dikes of various chemistry. At 3.65 to 3.60 Ga, a period of shearing and intrusion of crustally-derived graites and pegmatites is recorded.

According to this interpretation, most of the metamorphism observed in the Isua supracrustal belt is 3.65-3.60 Ga, and reflects a high geotherm gradient during extensive to transtensive tectonics (e.g. Friend and Nutman, 2005). This is reflected in ages recorded by metamorphic minerals (Crowley 2003; Nutman et al. 2014). A S-N gradient is present in the Isua belt: most of the 3.8 Ga package is preserved in a greenschist/lower amphibolite facies parageneses whereas the tonalites in the northern part of the massif shows an upper amphibolite facies (Friend and Nutman 2005). This early metamorphism was overprinted by a later Neoproterozoic greenschist/lower amphibolite facies event that yields much higher temperatures in the Southern part of the Itsaq complex (.garnulite facies, e.g. Nutman et al., 2015b).



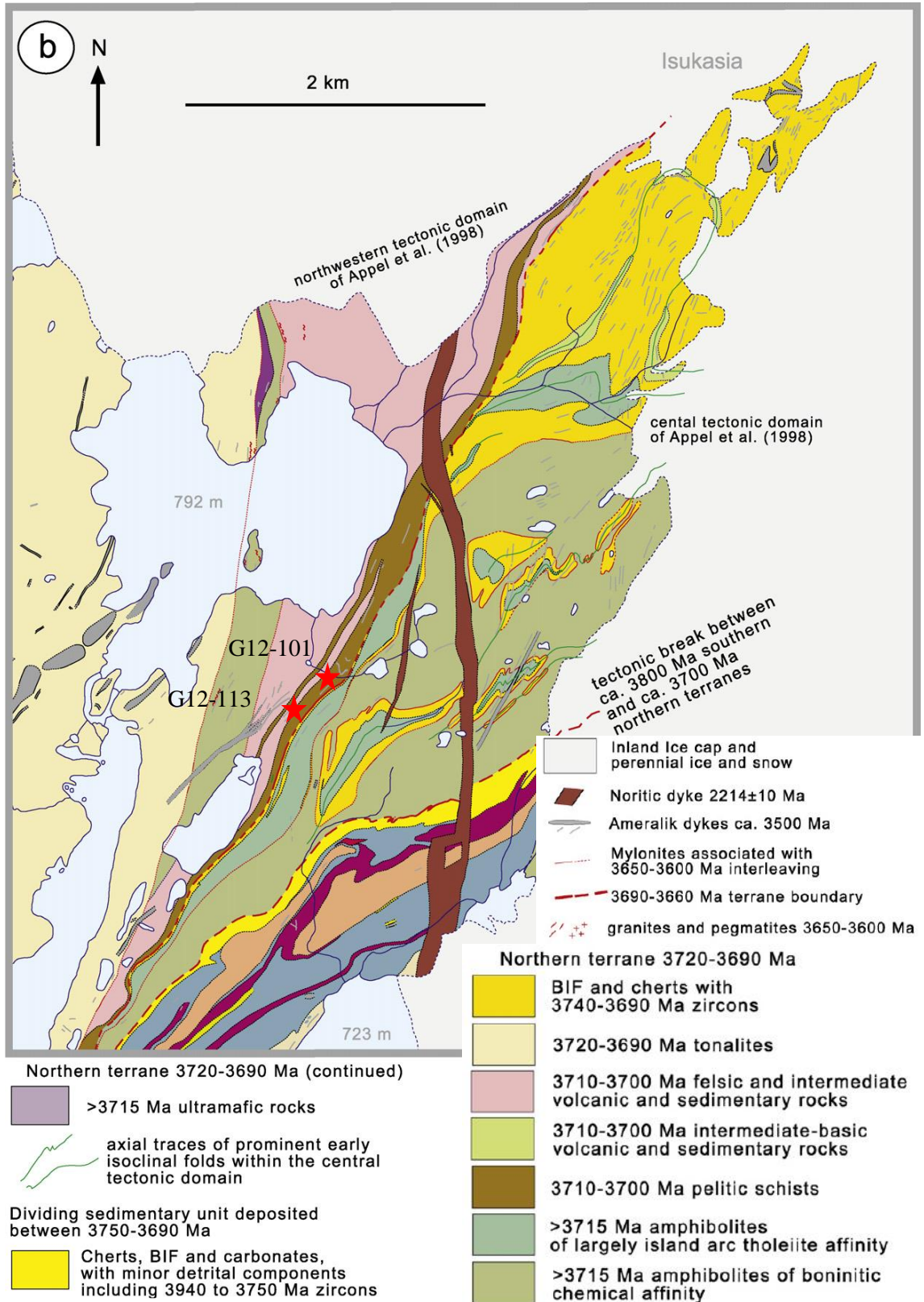


Figure 5 - 2. Interpretative map of the eastern end of the Isua supracrustal belt, from Nutman and Friend (2009). Sampling localities are indicated by red stars.

Another model based on the Eastern part of the Isua supracrustal belt (Komiya et al. 1999; Hayashi et al. 2000; Komiya et al. 2002; Arai et al. 2014) proposes a progressive North to South and West to East increase in maximum P-T experienced, which overprints tectonic boundaries such as defined by Nutman et al. (2009) or Rollinson (2003). The authors of this alternate model (e.g. Komiya et al. 2012) interpret the current P-T conditions recorded by plagioclase, amphibole, staurolite, biotite and garnet as the result of one main episode of metamorphism within a subduction-like accretionary complex. However, this interpretation contradicts abundant integrated field, petrographic and U-Pb mineral geochronology evidences for polymetamorphism in several distinct Archaean events.

The schist unit of the Isua supracrustal belt is staurolite and kyanite-bearing, and thereby contains barrovian assemblages typical of crustal thickening. The few studies done on the metamorphic assemblages in these rocks (Boak and Dymek 1982; Rollinson 2002; Rollinson 2003) report P-T conditions of about 600°C and 6 kbar (Boak and Dymek, 1982). Garnet zoning in these schists shows distinct growth and resorption stages documenting several metamorphic events (Blichert-Toft and Frei 2001; Rollinson 2003) as early as 3.7 Ga. The timing of this first metamorphic event can be tracked in higher temperature lithologies in the gneiss dome: high-pressure granulite enclaves have been found in pegmatite dikes in the central gneisses and could be linked to the same higher-pressure crustal thickening episode (Nutman et al. 2014; Nutman et al. 2015c). Zircon crystallisation in presence of garnet was dated in high-pressure granulites at around 3.66 Ga (Nutman et al. 2014). Also, a titanite age was obtained by Crowley (2003) around 3632-3620 Ma for amphibolite-faciès metamorphism.

In Tikeraq, no previous data is available about metamorphism. According to field observations, sedimentary rocks and 3.5 Ga mafic Ameralik dykes preserve upper amphibolite – granulite facies, which is postulated to be as the expression of the pan-Itsaq metamorphic event that reached high grade in the southern part of the Isukasia terrane (A. Nutman and C. Friend pers. comm.). This event reset most isotopic systems at around 2.8 – 2.9 Ga (e.g. Nutman et al., 2002; Nutman et al., 2015b). In a mafic layered sequence underlying the sedimentary schists that are the focus of this study, several levels contain garnet, clinopyroxene, quartz and feldspar. According to our field observations, this assemblage is identical to what is described by Nutman et al. (2014) in an Isua enclave, where it is interpreted as a relic of high pressure granulite facies, dated at 3.66 Ga. If this is confirmed, these rocks could record lower crustal conditions similarly to the Isua enclave described by Nutman et al. (2014), however much younger.

Extensive oxygen isotope investigations have been carried out in the Itsaq Gneiss Complex. Oxygen isotopes have been measured in many lithologies, apart from the B2 schists, either as whole rock (Baadsgaard et al. 1986; Cates and Mojzsis 2006; Furnes et al. 2007; Pope et al. 2012) or mineral separates (Cates and Mojzsis 2006; Pope et al. 2012) as well as in situ in zircon and olivine grains (Cates and Mojzsis 2006; Hiess et al. 2009; Hiess et al. 2011). The data obtained is mostly close to mantle value ( $\delta^{18}\text{O}_{\text{VSMOW}}$  ca. +5 ‰) and differentiated magmatic rocks (+6-8 ‰, e.g. Furnes et al., 2007), Some samples yield lower values (<+5‰) that are assigned to high-temperature alteration (Hiess et al. 2011; Pope et al. 2012). One study identified higher values (>15‰) that are interpreted as the result of low-temperature alteration (Nutman et al. 2015a). A summary is provided in the discussion, together with a compilation of available data for the Isua 3.7 Ga package.

There has been some debate about the preservation of isotopic signatures throughout metamorphism for such ancient rocks, and thus to the validity of interpreting whole-rock and mineral data in terms of protolith or other Early Archaean processes. Indeed several authors argue for pervasive isotopic resetting and/or a metasomatic origin of Isua lithologies (Gruau et al. 1996; Rose et al. 1996). On the basis of oxygen isotopes, it has been shown by Baadsgaard et al. (1986) and Hiess et al. (2009) that the 3.6 Ga granites that intrude the central gneiss interacted with low  $\delta^{18}\text{O}$  fluids. Baadsgaard et al. (1986) present evidence for circulation of meteoric fluids along fault systems.

The current study aims at identifying heavy  $\delta^{18}\text{O}$  lithologies in the 3.7 Ga package of the Isua supracrustal belt, and assessing how these signatures evolve during burial at mid-crustal level and subsequent metamorphic evolution, up to the bulk rock value measured at present.

## 2 Methods

### 2.1 WR geochemistry

Major elements were measured on fused discs at Geoscience Australia (GA) with Liz Webber and Bill Pappas. Fused discs were produced using an Initiative Scientific Products Fusilux 4X4 Fusion Machine using a proportion of 6.000 g of flux for 1.000 g of sample, fusing at 1100°C for 10 min (13 min for carbonates) in platinum crucibles. Some iodine vapor was used to get the fused tabs to separate better from the platinum crucibles. Two fluxes were used: X-ray flux 12:22 (35.3%  $\text{Li}_2\text{B}_4\text{O}_7$  - tetraborate, 64.7%  $\text{LiBO}_2$  – metaborate) for silicates and X-ray flux 57:43 (57% tetraborate, 43% metaborate) for samples that contained more than 30%  $\text{CaCO}_3$ . The fluxes are certified for containing 0-1ppm of Pb, Ni, Mn, Cd, Zn, Co, Ag; 1-5 ppm K, Cu, Se, As, Al, Sn,

Na, Fe; 2-10 ppm Si, S, Ca and Mg. Powder aliquots were measured on a C/H/moisture analyser Leco RC-612 at GA.

Fused discs were recovered from XRF analysis and mounted in epoxy. The discs were cut in their centre and polished using 3 and 1 µm diamond paste. WR trace elements were measured the RSES ArF excimer laser coupled to a quadrupole Inductively Coupled Plasma Mass Spectrometer (ICP-MS) Agilent 7700 using the setup described in Eggins et al. (1998). The laser was tuned to a frequency of 5 Hz and energy of 50 mJ (corresponding to a HV of around 26-27kV). The spot size was set to 103 µm. 20 s were measured on the background before analysis and 45 s for the signal. The reported value is the average of 3 spots in the same tab. NIST 610 and 612 were used for high (>100 ppm) and low-concentration elements respectively and the BCR rhyolite was used as a secondary standard. Reproducibility and accuracy as assessed on the BCR-2G glass were within 10% or less across all analysed elements. The data was reduced with the freeware Iolite (Paton et al. 2011) and its data-reduction scheme for trace-elements (Woodhead et al. 2007).

## 2.2 Mineral chemistry

Qualitative chemical analyses on spots were obtained with a solid state Energy Dispersive (EDS) detector on the RSES JEOL SEM instrument using an acceleration voltage of 15V and a current of 60-70 nA. Analyses were checked for stoichiometry and for garnet, UWG2 was measured as a secondary standard. The EDS measurements were within 5% of published values for this garnet (Valley et al. 1995). The SEM EDS was also used to produce chemical maps by scanning the beam across the field of view. For major elements (over 5 element wt%) the settings used were a short dwell time (0.5 ms) with 5 to 10 frame repetitions.

Trace elements were measured on an ArF excimer laser coupled to a quadrupole Inductively Coupled Plasma Mass Spectrometer (ICP-MS) Agilent 7700 at the Research School of Earth Sciences – RSES – at ANU), using the setup described in Eggins et al. (1998). The laser was tuned to a frequency of 5 Hz and energy of 50 mJ (corresponding to a HV of around 26-27kV). Spot sizes of 22 and 28 µm for zircon and of 62 µm for garnet were used. Three international standards were measured in every run: NIST 610 and 612 glasses, as well as the rhyolite BCR. The counts were standardised to NIST 610 (zircon) and NIST 612 (garnet) glasses and accuracy was monitored by analysing BCR-2G glass. BCR is a natural material that was used as a secondary standard to check for accuracy in the results. Recent data for the NIST glasses (Jochum et al., 2011; Spandler et al., 2011) differ from previous estimations (Pearce et al., 1997) by as much as 5 to 10% for certain elements (Cl, Nb, P, Sc, Sn, Ta) in NIST 610 and NIST 612 (As, F, P, Ti). Values of Spandler et al. (2011) have been used for data reduction. Data were acquired

over a 65 seconds analysis that included a 20 s background and the reference materials were measured after every eight unknowns. Stoichiometric Si was employed as internal standard for zircon ( $\text{SiO}_2$ : 31.6 wt%) and garnet ( $\text{SiO}_2$ : 42 wt%). Reproducibility and accuracy as assessed on the BCR-2G glass were within 10% or less across all analysed elements. The data was reduced with the freeware Iolite (Paton et al. 2011) and its data-reduction scheme for trace-elements (Woodhead et al. 2007).

### 2.3 SHRIMP oxygen isotopes

Zircon oxygen isotopes were analysed on the same mounts as U-Pb dating with the SHRIMP II instrument following the procedure described in Ickert et al. (2008). The standard Temora ( $\delta^{18}\text{O}_{\text{VSMOW}}=8.2\text{‰}$ , Black et al. 2004) was used. Analyses consist of 5 scans of 20 s for a total counting time of 100 s. In the first session (sample G04-46), blocs of four standards are measured every 10 unknowns. In the second session (samples G03-100 and G12-165), the same parameters are used but one standard is measured every 3 unknowns. The reproducibility of TEM zircons was within 0.5‰ ( $2\sigma$ ) during each analytical session. Raw data were processed with the in-house software POXI.

Garnet oxygen isotopes are measured on SHRIMP II and SHRIMP SI following the method of Martin et al. (2014b). The standard used for Isua garnets is UWG2 (Valley et al. 1995). Analyses consist of 5 scans of 20s for a total counting time of 100 s and the standards are measured every 5 unknowns. The reproducibility of UWG2 is within 0.3‰ ( $2\sigma$ ) for the analytical sessions. A matrix correction for grossular content was made according to calibrations by Martin et al. (2014b) acquired in the same year as the unknown analyses, with similar running parameters. Garnet chemistry was acquired by EDS analysis, measured a posteriori next to each SHRIMP spot after a slight re-polish. Error propagation for oxygen isotope analyses follows Martin et al. (2014b).

### 2.4 SHRIMP U-Pb dating

Zircon U-Pb dating was performed on the SHRIMP II at RSES, according to the method described in Williams (1998). Standards and unknown were analysed with a spot size of around  $20 \times 25 \mu\text{m}$ . Temora zircon (U-Pb age of 417 Ma, Black et al. 2003) was used as standard for internal mass fractionation and U concentration (160 ppm). The calibration error during the analytical sessions was 1.5% and this uncertainty was propagated to individual analyses. Ratios were corrected for common Pb according to the measured  $^{204}\text{Pb}/^{206}\text{Pb}$  ( $^{4/6}\text{R}_m$ ) and the non-radiogenic  $^{204}\text{Pb}/^{206}\text{Pb}$  ( $^{4/6}\text{R}_c$ ) following the method described in Williams (1998), i.e  $f_{206} = ^{4/6}\text{R}_m / ^{4/6}\text{R}_c$ . The  $^{4/6}\text{R}_c$  composition was assumed to be that predicted by Stacey and Kramers (1975) model. Most analyses yield less

than 2% common  $^{206}\text{Pb}$ , so the choice of the common Pb model has no significant incidence on ages, Data reduction was performed using MS Excel extensions SQUID 2.5 (Ludwig 2009) and Isoplot 4 (Ludwig 2012).

### 3 Results

#### 3.1 Sample petrology and garnet zoning

Three samples were studied in detail for garnet zoning (G12-101, G12-113 and G12-165), two of them, (G12-101 and G12-113) for thin section petrology also (see sample location on Figure 5 - 2). Another two samples were provided by V.Bennett and A. Nutman for zircon analysis (chips of G04-46 and zircon separates of G03-100).

**Table 5 - 1. Sample characteristics. Mineral abbreviations are from Whitney and Evans (2010).**

Sample #	Rocktype	Area	Latitude	Longitude	Assemblage	Met.faciès
G12-101	chlorite-garnet schist	Isua	65°10'26.5"	49°49'40.2"	Chl – Grt - Qz – Ms - Pl -Tur - Ilm - Cal	Amphibolite
G12-113	garnet-chlorite fels	Isua	65°10'18.6"	49°49'58.6"	Chl – Grt – Qz - Ms - St -Cld – Tur - Ilm	Amphibolite
G04-46	plagioclase-amphibole gneiss	Isua	...	...	Qtz – Pl - Bt – Chl – Grt - Ilm - Zrn	Amphibolite
G12-165	garnet-amphibole gneiss	Tikeraq	64°58'40.8"	49°56'54.5"	Grt – Qz - Pl – Bt - Amp - Ep	Granulite
G03-100	...	Tikeraq	...	...	... - Zrn	Granulite

##### 3.1.1 Mafic schists G12-101 and G12-113

The B2 unit, Nutman et al. (1986, 1997), is made of layered biotite-chlorite-garnet schists where staurolite and kyanite have been identified (Boak and Dymek, 1982). In the field it is present as an

extensive sequence of layered mafic schists. Most layers are coarse-grained with cm-sized garnets embedded in a matrix of chlorite with quartz layers (Figure 5 - 3), and quartz and calcite veinlets. Many layers contain pale-blue pseudomorphs (Figure 5 - 3d, e) suggestive of kyanite, but thin section inspection shows that they are made of finely grained white mica interspersed with staurolite relicts and chloritoid. In some instances (e.g. sample G12-113, Figure 5 – 5a), staurolite relicts are large enough to suggest the pale-blue pseudomorphs mentioned above were prior staurolite.

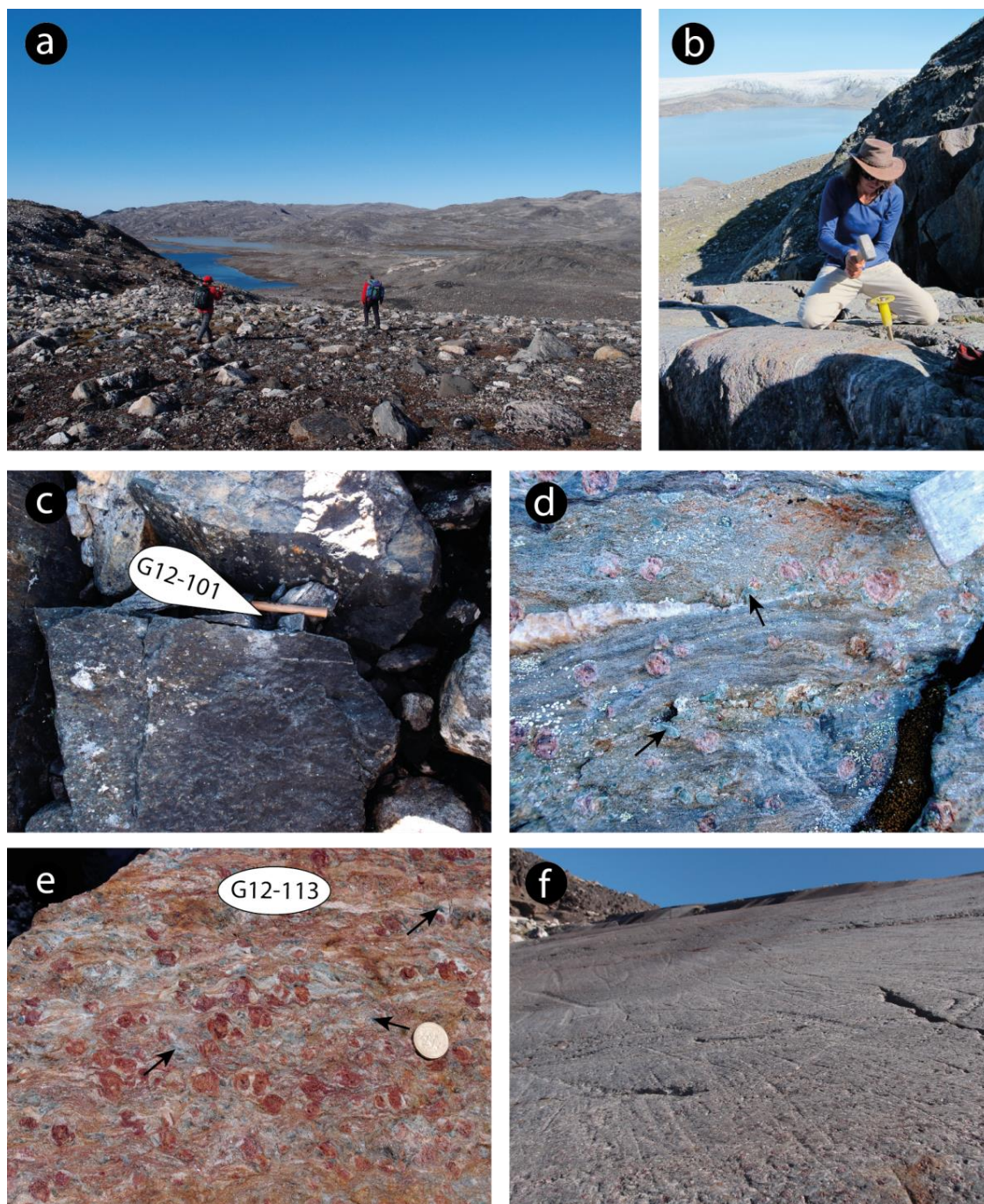


**Figure 5 - 3. a.** A. Nutman and C. Friend heading down the escarpment formed by the mafic schists, walking on moraine cover. **b.** L. Gauthiez Putallaz sampling mafic schists from a glacially polished surface showing compositional layering. **c.** Sample G12-101 was taken from a chlorite-rich layer. **d.** Centimetre-sized garnets (4cm hammer wedge for scale) and staurolite pseudomorphs (indicated by black arrows) in a layer below G12-101. Sample G12-113 was taken from a detached bloc showing rotational texture in cm-sized garnets (Danish kroner coin for scale), together with staurolite pseudomorphs (indicated by black arrows). **f.** Cliff formed by layered mafic schists, showing glacial polish and scour marks.

On the basis of garnet textures and preserved mineralogy, two samples were chosen for a more detailed study. G12-101 is a fine-layered plagioclase-chlorite-garnet-quartz-tourmaline schist

with 5-10 mm garnets (Figure 5 - 4), whereas G12-113 is a more quartz-rich garnet-chlorite-quartz fels with tourmaline and numerous staurolite pseudomorphs containing relict staurolite (Figure 5 - 4, Figure 5 - 5a). Some of these staurolite pseudomorphs contain chloritoid needles that grow over staurolite relicts, statically over the main foliation. (Figure 5 - 5c). In both samples, garnets show rotational features compared to the foliation.

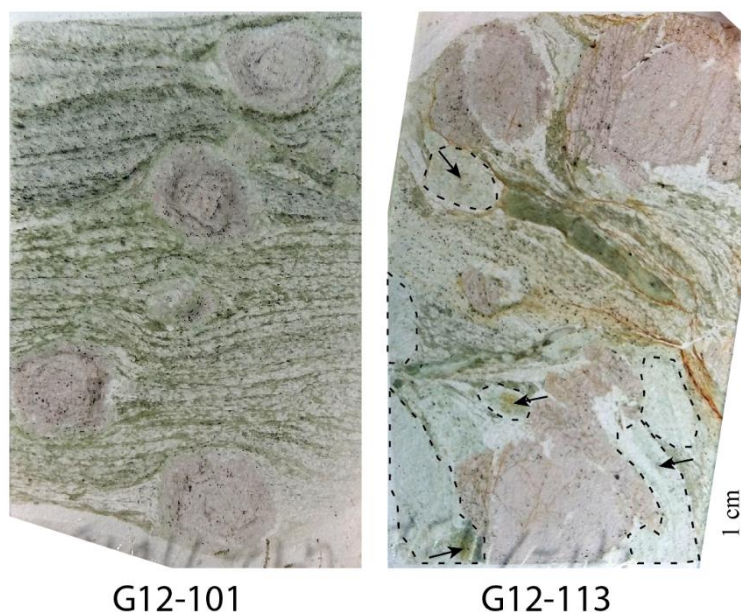


**Figure 5 - 4. Thin-section scans of samples G12-101 and G12-113. In G12-113, dotted lines outline staurolite pseudomorphs, arrows indicate staurolite relicts.**

A garnet that showed the most complete textural record was chosen in each of the two samples. The studied garnet is 8 mm across in G12-101 and 15 mm across in G12-113. The investigated garnets (sample G12-101 and G12-113) show a similar zoning pattern consisting of 4 domains identified in texture and major elements (Figure 5 - 6a,b,c). Zone I, at the core, is Mn-rich and Ca-poor (G12-101-I: Prp<sub>4-5</sub>, Grs<sub>8-9</sub>, Sps<sub>13-19</sub>, Alm<sub>68-73</sub>; G12-113-I: Prp<sub>4-5</sub>, Grs<sub>5-7</sub>, Sps<sub>9-18</sub>, Alm<sub>72-81</sub>) showing a bell-shaped manganese profile, this zone yields numerous quartz inclusions in G12-113, the inclusions define an internal foliation (Figure 5 - 7b). Zone II is a first rim richer in Ca, containing decreasing amounts of Mn (G12-101-II: Prp<sub>4-5</sub>, Grs<sub>15-21</sub>, Sps<sub>8-14</sub>, Alm<sub>64-72</sub>; G12-113-II: Prp<sub>4-5</sub>, Grs<sub>8-11</sub>, Sps<sub>6-8</sub>, Alm<sub>79-81</sub>) this zone yields rotated inclusion trails, branching off the core foliation. Zone III is a second rim that is Ca-rich but Mn-poor (G12-101-III: Prp<sub>4-6</sub>, Grs<sub>19-21</sub>, Sps<sub>1-5</sub>, Alm<sub>71-73</sub>; G12-113-III: Prp<sub>4-6</sub>, Grs<sub>7-16</sub>, Sps<sub>1-5</sub>, Alm<sub>77-85</sub>), it yields more rotated inclusion trails. Lastly, Zone IV is an outer rim that is Ca-poor and more Mg-rich (G12-101-IV: Prp<sub>6-9</sub>, Grs<sub>5-12</sub>, Sps<sub>0-4</sub>, Alm<sub>79-85</sub>; G12-113-IV: Prp<sub>6-10</sub>, Grs<sub>3-8</sub>, Sps<sub>0-1</sub>, Alm<sub>85-88</sub>), inclusion poor. Very sharp transitions are observed between core and first rim as well as first and second rim in G12-101 (Figure 5 - 5d, Figure 5 - 6a). They are underlined by the presence of small mineral and fluid inclusions.



In G12-113, ilmenite, rutile, plagioclase, quartz, tourmaline and chlorite can be observed as inclusions in zone I. In zone II, rutile, ilmenite, tourmaline and quartz can be found. A complex inclusion contains rutile, ilmenite calcite and tourmaline. Zone III yields tourmaline and ilmenite, while rutile can be observed in cracks. Zone IV is generally inclusion-poor, but in one instance, it contains composite inclusions of staurolite and chloritoid (Figure 5 - 5a), similarly to pseudomorphs seen in the matrix.

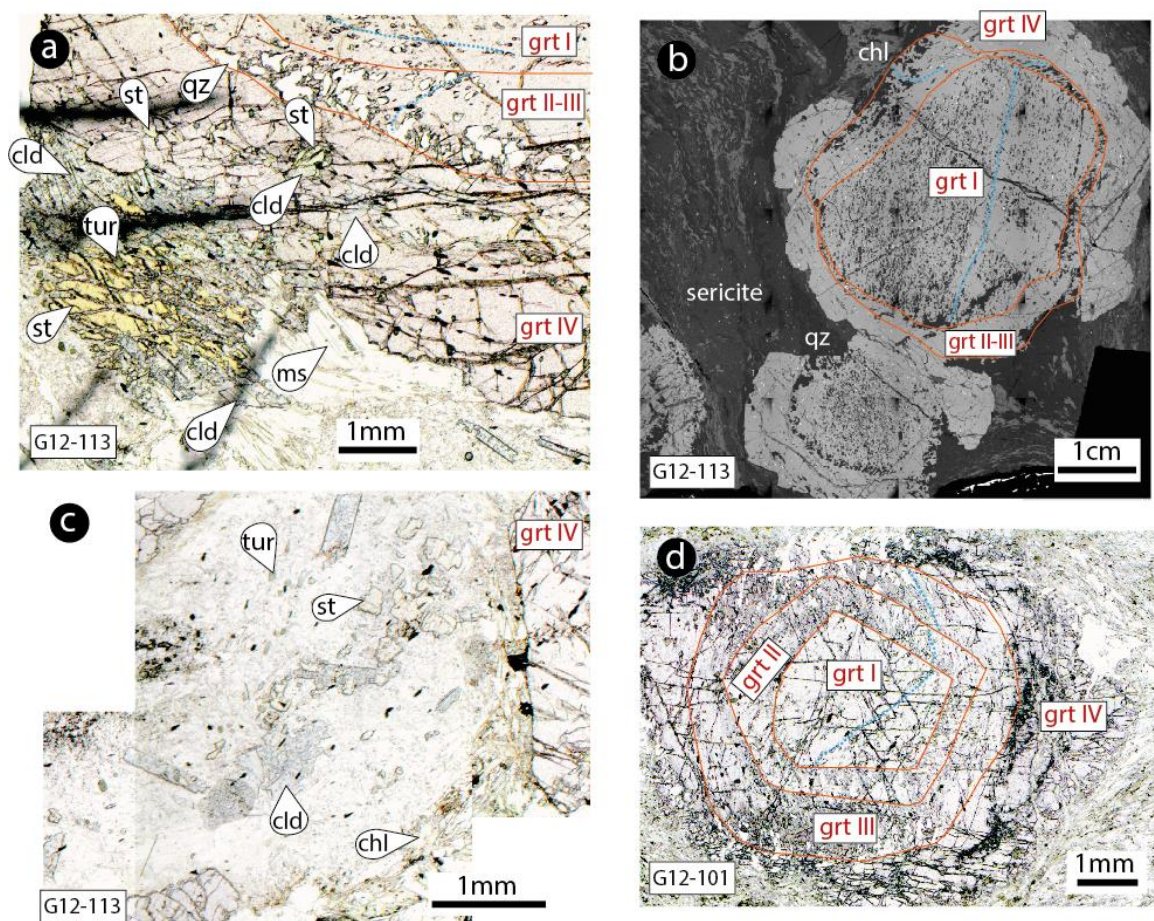


**Figure 5 - 5. a. G12-113 transmitted light mosaic of matrix and garnet inclusion mineralogy: Grt-IV contains inclusion of relict staurolite and of chloritoid. Grt-I to IV correspond to chemical zones described below. b. G12-113 BSE mosaic of two garnets showing the rotation of inclusion trails (blue dotted lines) and the textural changes between zones (red lines). c. G12-113 transmitted light image showing chloritoid growing on relict staurolite in a staurolite pseudomorph. d. G12-101 transmitted light image showing rotating inclusion trails (blue dotted lines) and different growth zones (red lines).**

The core, zone I, is the most enriched in HREE in both samples (Figure 5 - 6d, *Appendix table A5 - 1*), with a gradual depletion towards the outer core similar to what is observed for Mn, a marker of Rayleigh fractionation during garnet growth. This is marked with a change in HREE concentrations of two orders of magnitude in sample G12-113 that contains large garnets. Zone I yields a marked Eu anomaly in both samples, which is significant of the presence of plagioclase in the co-existing assemblage. Zone II and zone III yield no Eu anomaly in both samples, which

suggests that plagioclase reacted out or significantly decreased in abundance during this stage. The HREE content of these garnet zones is generally lower than zone I, indicating that most HREE were fractionated and stored in the garnet cores. However, HREE content of zone II and III is variable, which shows that HREE-bearing phases were reacting at the time of garnet crystallization. Zone IV yields different REE signatures in the two samples. In sample G12-113, zone IV yields a small to non-existent negative Eu anomaly indicating little plagioclase present. It has extreme depletion in HREE which is interpreted as an effect of the fractionation of HREE in the large garnet cores and previous rims. In G12-101, a marked negative Eu anomaly is present, indicating the presence of plagioclase in the co-existing assemblage.

The HREE and MREE contents are slightly higher than zone III which indicates that these elements were redistributed by either garnet dissolution or the participation of another matrix phase. The presence of a negative Eu anomaly in G12-101 is correlated to the presence of plagioclase in the matrix (mode about 40%), which contrasts with the absence of significant negative Eu anomaly in G12-113, where only small amounts of plagioclase can be found, in parts of the matrix that preserve small-scale layering (mode about 0.5-1%). It is reasonable to make the assumption that matrix minerals equilibrated in the same conditions in the two samples; as a consequence, the presence or absence of significant plagioclase in the matrix and consequently Eu anomaly in garnet correlates in matrix and zone IV with differences in reactive bulk chemistry rather than metamorphic conditions.

### **3.1.2 Sample G04-46**

G04-46 is a layered felsic gneiss in which amphibole and chlorite-rich layers contain more garnet than quartz-rich layers. In quartz-rich layers, garnet grows in a skeletal texture which impedes the interpretation of outwards growth zoning. Garnets in the amphibole-rich layers yield concentric zoning that is similar to what is observed in the biotite schists G12-113 and G12-101. Oxygen analysis could not be performed in these garnets.

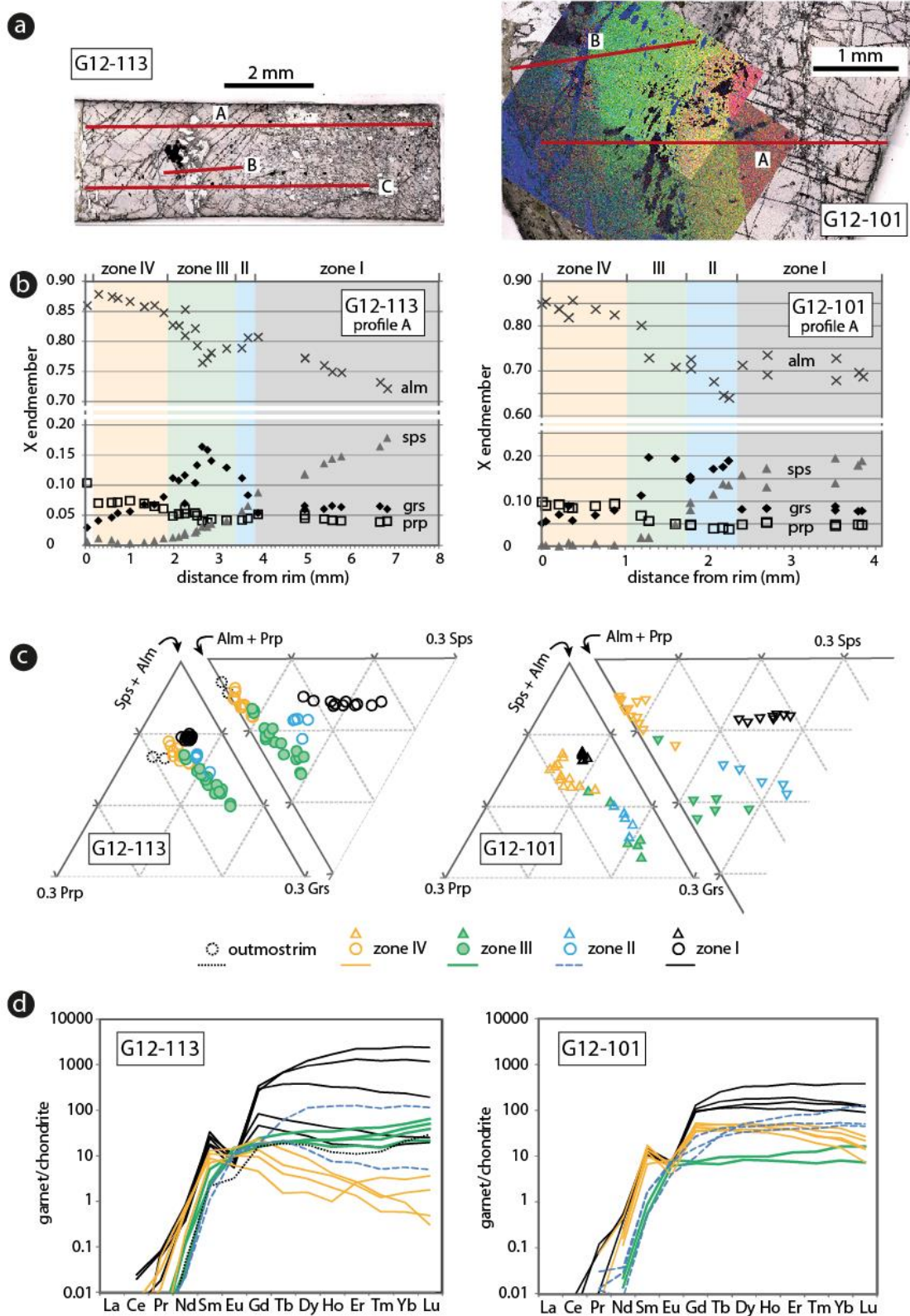


**Figure 5 - 6. Chemical characteristics of B2 schists garnets. a.** Transmitted light mosaic of analysed garnets in the epoxy mount with profile lines. For sample G12-101, EDS composite maps of Mn (red), Ca (green) and Mg (blue) are superimposed. **b** EDS endmember composition profiles according to distance to rim (analysis position projected on profile line, zones are distinguished on textural and chemical information). **c.** Endmember compositions in two triangular diagrams created with the program Triplot. **d.** LA-ICPMS REE composition of different zones normalised to CI chondrites of *Sun & McDonough (1989)*.

### 3.1.3 Tikeraq

The Tikeraq garnet-gneiss unit, with fist-sized garnets, has a thickness of up to a few hundred meters and layering can be followed on the outcrop scale (Figure 5 - 7). It is composed of layers containing various amounts of quartz, clinopyroxene, plagioclase and garnets that vary in size from 5 cm to 10 cm. The garnets sometimes show rotational features. In some layers, they are surrounded by quartz and plagioclase segregations that are akin to leucosomes, thus suggesting partial melting (Figure 5 - 7b). In a few instances, garnet has an annulus of quartzo-feldspathic material in between the core and the rim (Figure 5 - 7b, see garnet vertically below G12-165). Several samples were taken in a N-S cross-section to form a composite sample for zircon separation. A euhedral garnet of 5cm across was sampled as G12-165.

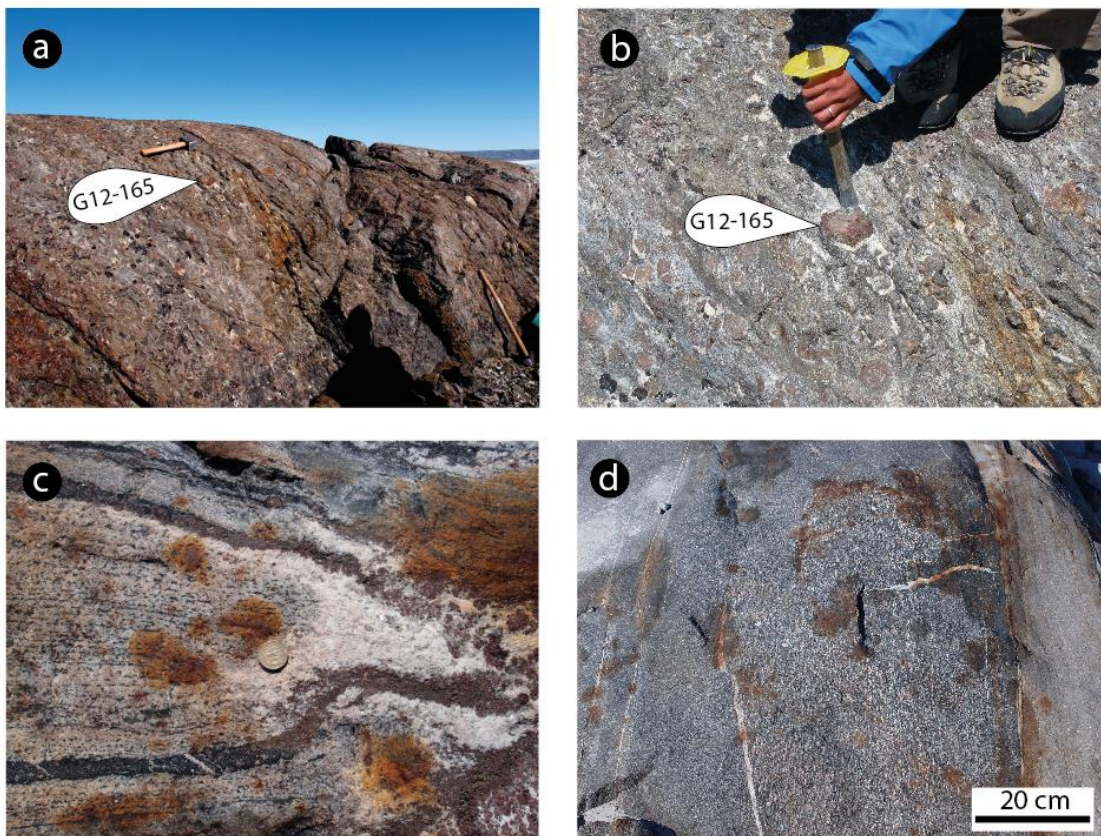


**Figure 5 - 7. a. Sampling site of garnet G12-165 showing compositional layering. b. Extraction of garnet G12-165, note the quartzo-feldspathic thin layers around garnet.. c. Evidence of partial melting in another Tikeraq lithology: Quartzo-feldspathic selvage and garnet restite at the right of the coin. d. Ameralik dyke with well-developed amphibolite-facies paragenesis (amphibole, plagioclase and garnet).**

G12-165 core contains numerous inclusions of epidote, plagioclase, quartz and ilmenite, with assemblages of chlorite, pyrite and Fe-oxides in cracks (Figure 5 - 8b). The garnet core yields quartz and ilmenite inclusions aligned on an undeformed foliation (core: Prp<sub>7</sub>, Grs<sub>19</sub>, Sps<sub>11</sub>, Alm<sub>63</sub>, Figure 5 - 8b,c). Towards the rim, the foliation is rotated and no epidote inclusions are seen (rim

1: Prp<sub>18</sub>, Grs<sub>10</sub>, Sps<sub>3</sub>, Alm<sub>69</sub>). This zone is rich in plagioclase inclusions and appears as a white middle rim in hand specimen. The outer rim (rim 2a: Prp<sub>19</sub>, Grs<sub>13</sub>, Sps<sub>1</sub>, Alm<sub>67</sub>; rim 2b: Prp<sub>25</sub>, Grs<sub>8</sub>, Sps<sub>2</sub>, Alm<sub>65</sub>) contains small inclusions of quartz (quartz inclusion becomes smaller towards rim 3) while the ilmenite inclusions are large and oriented along the inner rim foliation direction. Finally, the very edge of the garnet is partly retrogressed giving rise to chlorite. Plagioclase patches are present in the matrix, in contact with the rim.

Tikeraq schist garnet G12-165 was excessively large for sample preparation and complete major and trace element profiles could not be obtained. Instead, a core-rim section of garnet was prepared in 3 1 inch mounts that were individually polished and imaged (blocs A, B and C in Figure 5 - 8a). The garnet shows a smooth core to rim zoning in major elements (Figure 5 - 8c). No sharp chemical transitions could be observed in BSE (Figure 5 - 8b). Late resorption is present and is visible as thin BSE-light rims at the contact of garnet and chlorite. Spessartine content decreases from core to rim with corresponding increasing almandine and pyrope, with the exception of rim 2b showing a small increase in Mn (Figure 5 - 8c,d). It is however possible that the section analysed does not sample the very core of the garnet given a rather flat profile in Mn in the outer core area. Grossular contents are higher in the core and in rim 2a, and lower in rim 1 and rim 2b (Figure 5 - 8d). The presence of such variations, as well as changes in Fe, Mn and Mg contents is an indication that diffusion did not reset the garnet composition in this sample.

The REE content of the core zone (measured in the outer core) is surprisingly the most depleted in MREE and HREE (Figure 5 - 8e, *Appendix table A5 - 1*). It yields a small negative Eu anomaly. Rim 1 is more enriched in MREE and HREE, which indicates that garnet resorption and/or a MREE-rich phase reacted to make these elements available to garnet. Rim 1 yields a very pronounced negative Eu anomaly indicating the presence of plagioclase (which is coherent with the inclusion suite described). Rim 2a shows a small Eu anomaly and an enrichment in MREE indicating the contribution of a reacting phase such as apatite, titanite or epidote/allanite, and a decrease in HREE comparable to rim 1 composition. Rim 2b is strikingly similar to rim 1 with a strong Eu anomaly and a similar enrichment in HREE.

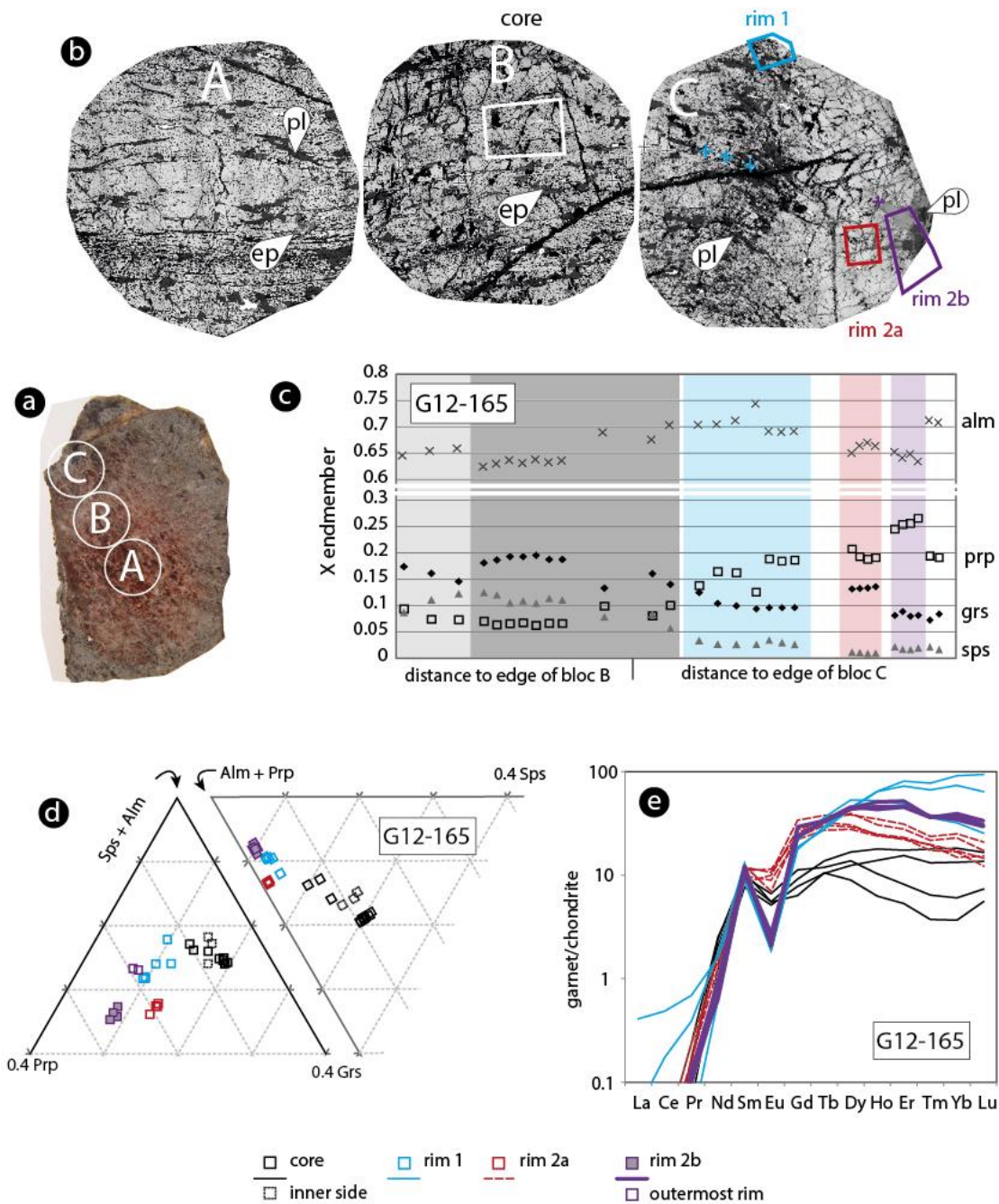


Figure 5 - 8. a. Photograph of a cut slice through garnet G12-165. White circles indicate polished 2,5 cm blocs. b. BSE mosaics of polished blocks (diameter: 2,5 cm) showing curving inclusion trails. Solid lines outline cut outs that were included in the SHRIMP epoxy mount for oxygen isotope analysis. Crosses indicate the position of EDS analyses outside of the cutouts. c. EDS endmember profile through bloc B and C. d. Chemical variation from core to rim. e. REE composition of the different garnet zones normalised to CI chondrites from Sun and McDonough (1989).

### 3.2 WR Geochemistry

Whole-rock major and trace elements were measured in G04-46, G12-101 and G12-113 (Table 5 - 2).

G12-101 and G12-113 have parallel patterns and are enriched in incompatible elements compared to the primitive mantle, and yield a marked negative Nb-Ta anomaly (Figure 5 – 9, right panel). G12-101 yields a positive anomaly in Rb and Ba. Generally, these two samples are comparable to the more mafic rocks in Nutman et al. (2013) although G12-101 the more depleted type and G12-113 the more enriched type. G12-101 is rich in Cr (1033 ppm) and Ni (434 ppm) which are other indicators that its protolith might be richer in mafic minerals such as olivine, cpx and spinel compared to G12-113 (Cr: 31 ppm, Ni: 17 ppm). G12-101 yields a pattern that is similar to positive Eu anomaly samples of Bolhar et al. (2005).

G04-46 is enriched in incompatible elements, similar to a diorite from Nutman et al. (2013), Figure 5 - 9, left panel. G04-46 yields a negative anomaly in Nb-Ta, but also in Sr, Eu and Ti, showing the fractionation of plagioclase and a Ti phase, which are also typical of other Isua rocks (e.g. Nutman et al., 2013 tonalite), even though the Ti negative anomaly is more pronounced in this sample. G04-46 also yields a negative anomaly in Ba. G04-46 yields a pattern that is similar to felsic volcanogenic samples of Bolhar et al. (2005).

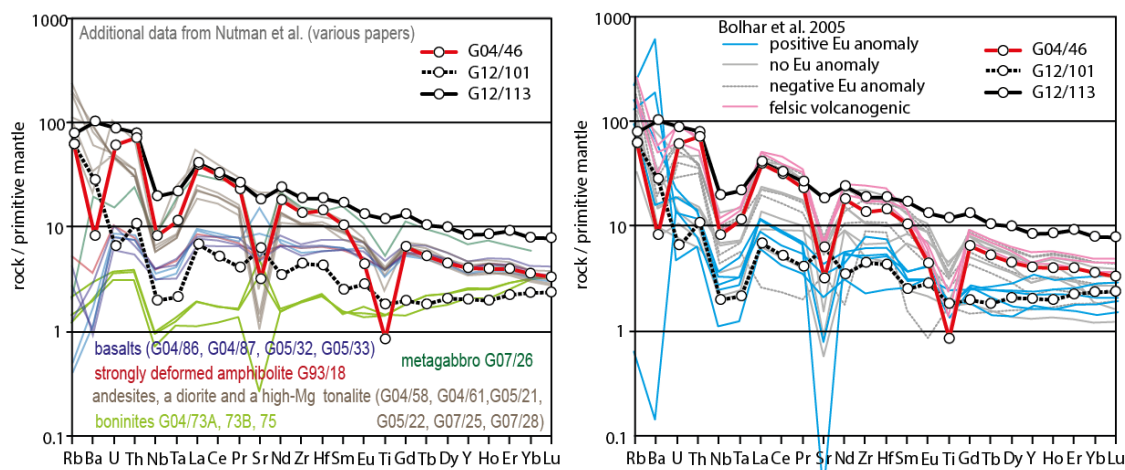


**Figure 5 - 9. Trace-element patterns normalised to primitive mantle from Sun and McDonough (1989) with literature values for a. 3.7 Ga magmatic lithologies from Nutman et al. (2013, 2015) b. Sedimentary lithologies in Isua (Bolhar et al. 2005).**

Table 5 - 2. XRF Major and LA-ICP-MS trace element composition of Isua samples.

	<b>G04-46</b>	<b>G12-101</b>	<b>G12-113</b>
<b>XRF (wt%)</b>		<b>chl-grt-qz-pl-tur</b>	<b>chl-grt-qz-st</b>
SiO <sub>2</sub>	75.6	51.7	60.9
Al <sub>2</sub> O <sub>3</sub>	10.1	20.5	16.0
Fe <sub>2</sub> O <sub>3</sub>	6.9	13.0	13.4
MnO	0.1	0.2	0.7
MgO	2.6	4.1	2.2
CaO	1.5	2.4	1.1
Na <sub>2</sub> O	1.3	3.2	1.7
K <sub>2</sub> O	0.7	1.3	1.2
P <sub>2</sub> O <sub>5</sub>	bdl	bdl	bdl
TiO <sub>2</sub>	0.2	0.4	0.4
<b>XRF Sum</b>	<b>98.9</b>	<b>96.7</b>	<b>97.6</b>
H <sub>2</sub> O (LECO wt%)	2.0	3.7	2.1
CO <sub>2</sub> (LECO wt%)	0.2	0.7	0.1
<b>Total Sum</b>	<b>101.3</b>	<b>101.3</b>	<b>100.0</b>
<b>LA-ICP-MS (ppm)</b>			
Sc	12.3	45.4	42.7
Ti	1083	2341	15554
V	29.0	204	469
Cr	76.1	1033	30.8
Mn	500	1369	1602
Co	14.5	60.0	39.6
Ni	47.3	434	17.6
Cu	3.5	5.5	18.4
Zn	38.0	96.5	135
Ga	14.8	23.4	51.6
Ge	11.0	7.6	6.2
Rb	39.6	39.7	50.6
Sr	66.5	132	389
Y	18.3	9.1	38.3
Zr	152	49.9	212
Nb	5.9	1.4	14.1
Cs	0.9	0.4	1.3
Ba	57.6	198	723
La	27.2	4.7	28.5
Ce	56.0	9.2	59.0
Pr	6.4	1.1	7.4
Nd	24.6	4.7	32.7
Sm	4.6	1.1	7.6
Eu	0.7	0.5	2.2
Gd	3.8	1.2	8.0
Tb	0.6	0.2	1.1
Dy	3.3	1.5	7.3
Ho	0.6	0.3	1.4
Er	1.9	1.1	4.4
Tm	0.3	0.2	0.6
Yb	1.8	1.1	3.9
Lu	0.2	0.2	0.6
Hf	4.5	1.3	5.8
Ta	0.5	0.1	0.9
W	0.5	1.3	0.9
Pb	7.3	14.5	10.9
Th	6.2	0.9	6.8
U	1.0	0.1	1.8



### 3.3 U-Pb dating

Sparse small prismatic zircons were recovered from gneiss G04-46. They are mostly oscillatory zoned (Figure 5 - 10a), which is a common feature of magmatic zircons (Hoskin and Schaltegger 2003). The zircons present embayments and very small (<10 microns) and CL-bright overgrowths, that could not be analysed because of their size. It is speculated that the overgrowths are significant of a metamorphic-fluid related dissolution-reprecipitation event, potentially during metamorphism.

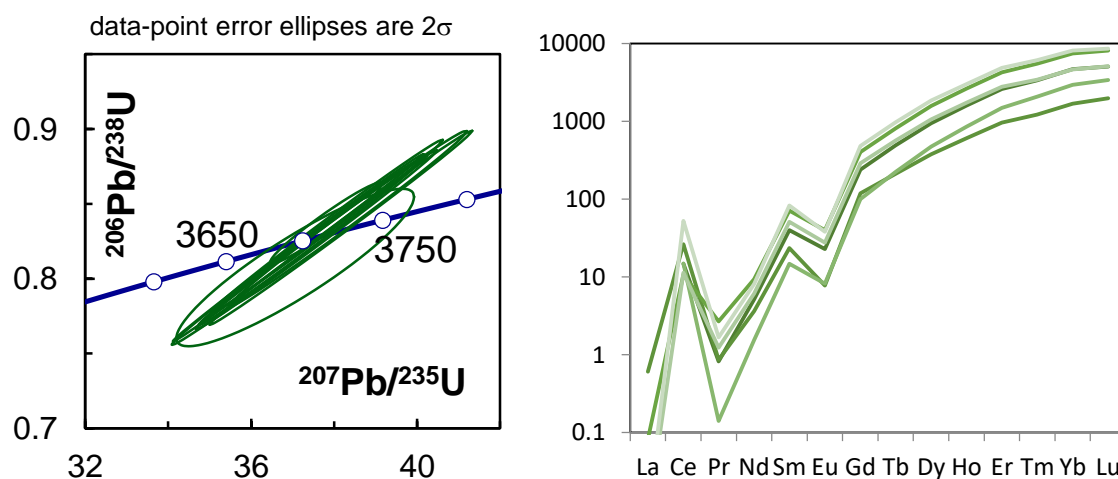
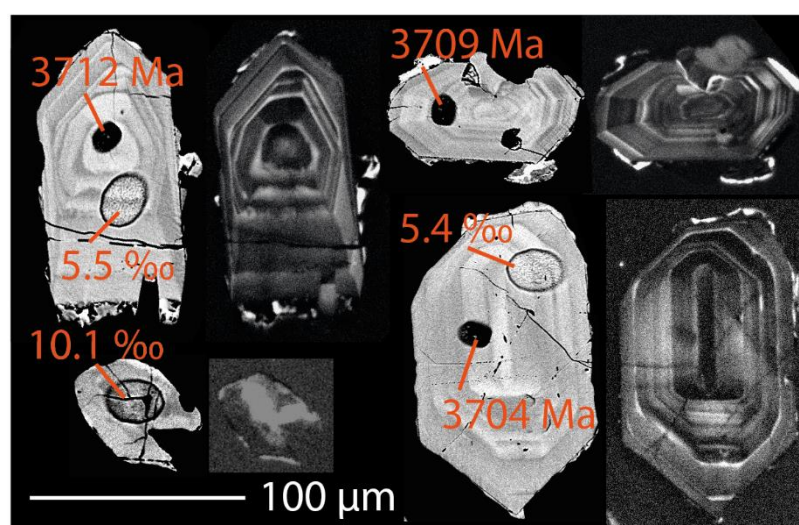


Figure 5 - 10. a. High-contrast BSE (left) and CL images (right) of selected zircon grains from felsic gneiss G04-46. U-Pb dating SHRIMP pits with 204-corrected  $^{206}\text{Pb}$ - $^{207}\text{Pb}$  age, oxygen isotope SHRIMP pits with measured value in ‰. b. Weatherill Concordia plot of 204-corrected data. c. LA-ICP-MS REE composition normalised to CI chondrites of Sun and McDonough (1989).

Clean oscillatory zones in G04-46 zircons yield an average  $^{206}\text{Pb}$ - $^{207}\text{Pb}$  age of  $3709 \pm 4$  Ma MSWD 1.2 (weighted by data-point errors only, 1 of 11 rejected) and a Concordia age of  $3709 \pm 6$  Ma

(95% confidence, probability of concordance 0.895) (Figure 5 - 10a,b; *Appendix table A5 – 2*). They yield Th/U between 0.6 and 1.1. Their common Pb content is below 1% in all cases.

The oscillatory zones yield a negative Eu anomaly and a positive Ce anomaly, together with a HREE enrichment. The profiles are similar to what is seen for Phanerozoic magmatic zircons (Figure 5 - 10c, *Appendix table A5 – 3*).

### 3.4 Oxygen isotopes

#### 3.4.1 Whole-rock

Whole-rock oxygen isotope were measured for samples G12-113, G12-101 and G04-46 by A. Chivas in the University of Wollongong using the conventional fluorination technique (see method in Nutman et al., 2015a). They yield  $\delta^{18}\text{O}_{\text{VSMOW}}$  values between +11.8 and +13.0 ‰. G12-101 and G04-46 duplicates yielding only 0.0 and 0.1 ‰ difference, within the analytical uncertainty given for single analyses (Table 5 - 3). The results for G12-113 diverge slightly with 1.1 ‰ between the two duplicates. This can be attributed to the higher alteration of this sample (traces of oxidation in fractures) and thus the heterogenous distribution and reaction of altered minerals in the two fractions used for oxygen analysis.

**Table 5 - 3. Fluorination WR oxygen data.**

Sample	First analysis		Duplicate, further hand-crushed	
	$\delta^{18}\text{O}_{\text{VSMOW}}$ (‰)	1 $\sigma$ error	$\delta^{18}\text{O}_{\text{VSMOW}}$ (‰)	1 $\sigma$ error
G12-101	+11.8	0.1	+11.6	0.1
G12-113	+12.6	0.1	+11.5	0.1
G04-46	+13.0	0.1	+13.0	0.1

#### 3.4.2 Garnet ion microprobe measurements

In a cross section strip of G12-113 garnet, 2 rim to core profiles were measured for oxygen isotopes using the ion microprobe. Ca-rich zones II and III are thin on this garnet, a third and more detailed profile of that area was measured separately (Figure 5 - 11, *Appendix table A5 – 4*). In G12-113, zone I yields an average corrected  $\delta^{18}\text{O}$  of  $+9.2 \pm 0.1$  ‰ (1sd, n=11), Zone II  $+9.7 \pm 0.3$  ‰ (1sd, n=5), zone III  $+9.4 \pm 0.2$  ‰ (1sd, n=19) and zone IV  $8.7 \pm 0.3$  ‰ (1sd, n=15). Averages are reported with the standard deviation of the population (1 $\sigma$  level). External uncertainty for these populations calculated following formula in Martin et al. (2014b) is on the

range of 0.5-0.6 ‰ ( $2\sigma$ ), dominated by the grossular and spessartine matrix calibration error. For consistency, both grossular and spessartine corrections were applied in all measurements, even though the correction for spessartine is negligible for zone III and IV compositions. In profile A, the rim value seems to be lower at the interface between zone II and IV, correlating negatively with grossular content.

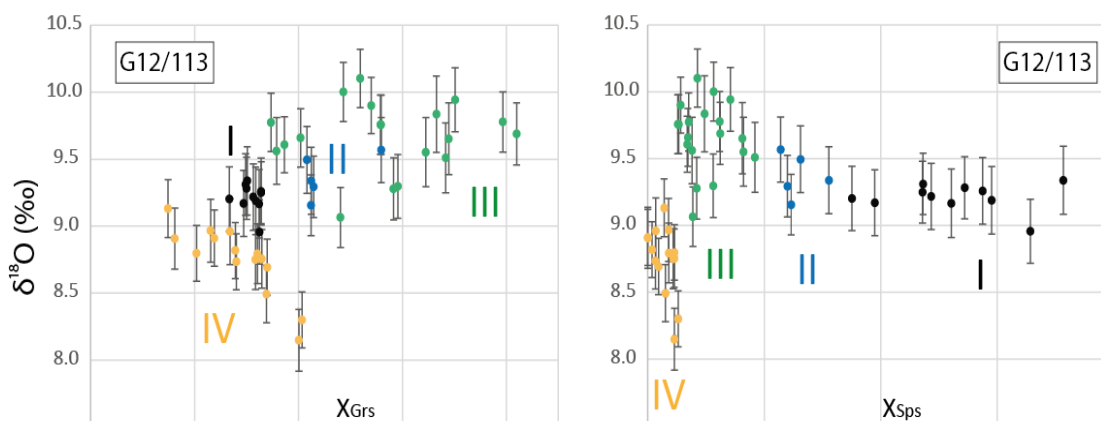


**Figure 5 - 11. SHRIMP oxygen isotope analyses from profiles in G12/113 and G12/101 garnets, displayed according to their EDS grossular and spessartine endmember content. Picture of mounted pieces and profile positions are indicated on Figure 5 - 6. Figure 5 - 6a.  $\delta^{18}\text{O}_{\text{VSMOW}}$  values are plotted with  $1\sigma$  error bars. Colour coding in the symbol represents the garnet zone as identified by texture and major elements in Figure 5 - 6.**

Two profiles were measured in sample G12-101 garnet (rim to core: 4 mm). In this smaller garnet, less variation is observed from core to rim, from a  $\delta^{18}\text{O}_{\text{VSMOW}}$  of  $+9.4 \pm 0.2$  (1sd,  $n=8$ ) in the core (zone I), Zone II  $+9.4 \pm 0.2$  ‰ (1sd,  $n=6$ ), zone III  $+9.7 \pm 0.1$  ‰ (1sd,  $n=4$ ), to a value of  $+9.3 \pm 0.2$  (1sd,  $n=13$ ) in the external rim (IV).

4 pieces of G12-165 garnet were analysed as the garnet was too big to do a continuous core rim profile. Rim 1 piece was cut in the curved-inclusion trail rim; Rim 2a and Rim 2b were cut in the outer uniform rim (Figure 5 - 8a). After matrix correction, the 4 pieces yield a homogeneous  $\delta^{18}\text{O}_{\text{VSMOW}}$  of ca.  $+9$  ‰ (Figure 5 - 12). Zone averages are: core  $+8.5 \pm 0.2$  ‰ (1sd,  $n=7$ ), rim 1  $+8.8 \pm 0.1$  ‰ (1sd,  $n=4$ ), rim 2a  $+9.3 \pm 0.1$  ‰ (1sd,  $n=4$ ), rim 2b  $+9.0 \pm 0.1$  ‰ (1sd,  $n=4$ ). The Mg-poorer outmost rim yields  $8.4 \pm 0.2$ ‰.

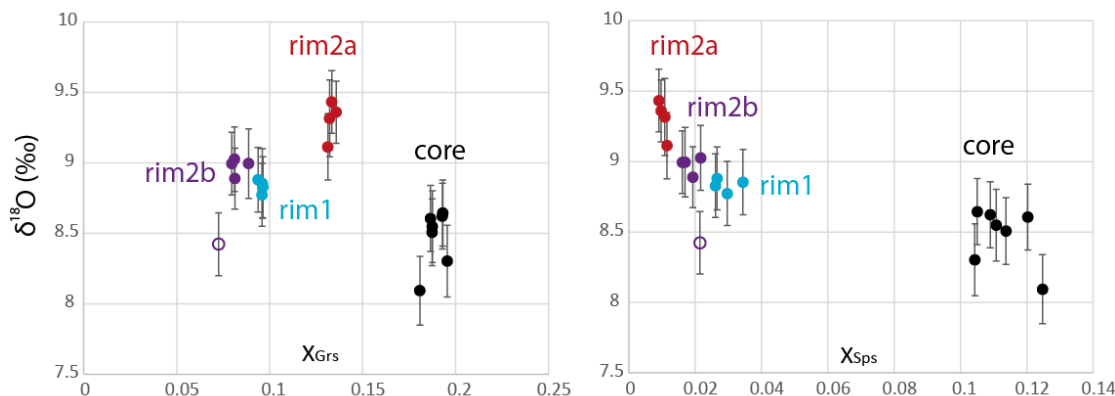


**Figure 5 - 12. SHRIMP oxygen isotope composition of G12-165 garnet fragments displayed according to the EDS proportions of grossular and spessartine endmembers. Fragment positions are indicated on Figure 5 - 8b.  $\delta^{18}\text{O}_{\text{VSMOW}}$  values are plotted with  $1\sigma$  error bars. Colour coding in the symbol represents the garnet zone as identified by texture and major elements in Figure 5 - 8b,c .**

### 3.4.3 Zircon ion microprobe measurements

Oxygen isotopes were measured in oscillatory- zoned zircons as well as the few CL lighter rims in sample G04-46 (Figure 5 - 13, *Appendix table A5 – 5*). The zircons present very small and CL-bright overgrowths but could not be analysed for oxygen isotopes because of their size and proximity to epoxy. The results return a homogenous population of typical mantle  $\delta^{18}\text{O}_{\text{VSMOW}}$  value at  $+5.4 \pm 0.4\text{‰}$  ( $1\sigma$ ,  $n=20$ ). One light zone measured in a heavily fractured grain yields a value of  $+10.1 \pm 0.4\text{‰}$  ( $1\sigma$ ). This could be a hint of the composition of the metamorphic overgrowths, but without more information, it is not used for the interpretation. because it could be a result of the contamination in the fracture. One zircon was analysed as an inclusion in garnet and also yields a mantle-like value of  $+6.0\text{‰}$  (Figure 5 – 13a); at this occasion, two spots in the surrounding garnet were analysed against the zircon standard, and corrected for typical zircon-garnet IMF; they are presented as indicative in Figure 5 – 13. Even with the large uncertainty associated with the lack of proper standardisation, they show a disequilibrium with the zircon included in the garnet at ca.  $+9,5 \text{‰}$ .

G12-165 zircons were dated by A. Nutman and V. Bennett, they yield one population of 2.95-3.00 Ga metamorphic ages. G12-165 zircons yield  $\delta^{18}\text{O}_{\text{VSMOW}}$  from  $+8.5$  to  $+10.5 \text{‰}$ . The distribution peaks at  $10.5 \text{‰}$ , with a smaller amount of lower values (Figure 5 - 14d); the average for all analyses is  $9.9 \pm 0.6\text{‰}$  ( $1\sigma$ ,  $n=20$ ). This spread is double of what is measured in the standard Temora II during the same session ( $1\sigma$  0.26). As no systematic core-rim variation was observed, it is likely that this spread in values reflects inter-layer assemblage variability in this composite sample. CL zoning explains some of the  $\delta^{18}\text{O}$  variation: light cores yield a  $\delta^{18}\text{O}_{\text{VSMOW}}$  value of  $+10.6 \pm 0.1\text{‰}$  ( $1\sigma$ ,  $n=4$ ) and unzoned grains yield a lower  $\delta^{18}\text{O}_{\text{VSMOW}}$  value of  $+9.4 \pm 0.5\text{‰}$  ( $1\sigma$ ,  $n=8$ ).

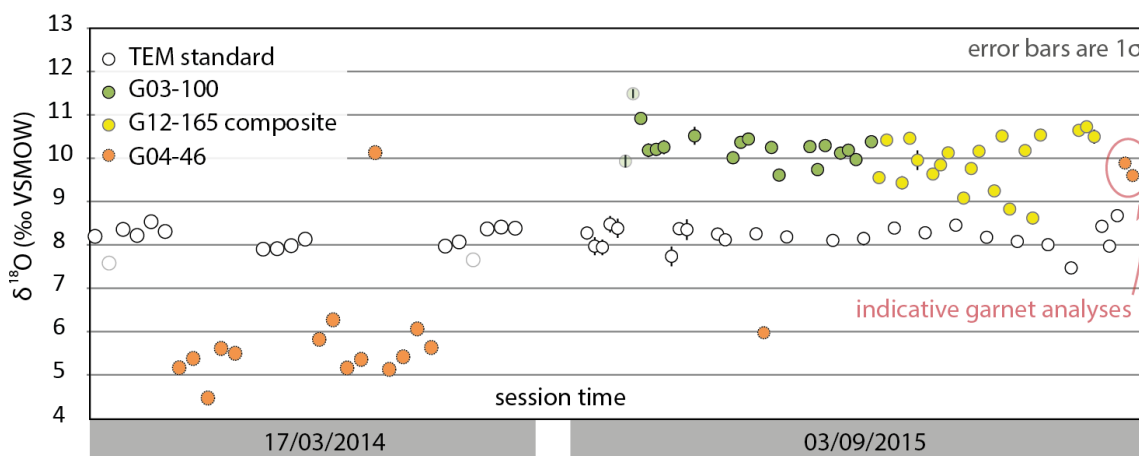


Figure 5 - 13. SHRIMP oxygen isotope analyses of Isua and Tikeraq zircons plotted along session time (arbitrary scale).  $1\sigma$  error bars are usually smaller than the symbols, they represent the measurement errors. Shaded symbols are data points that were rejected on the basis of instrument parameters.

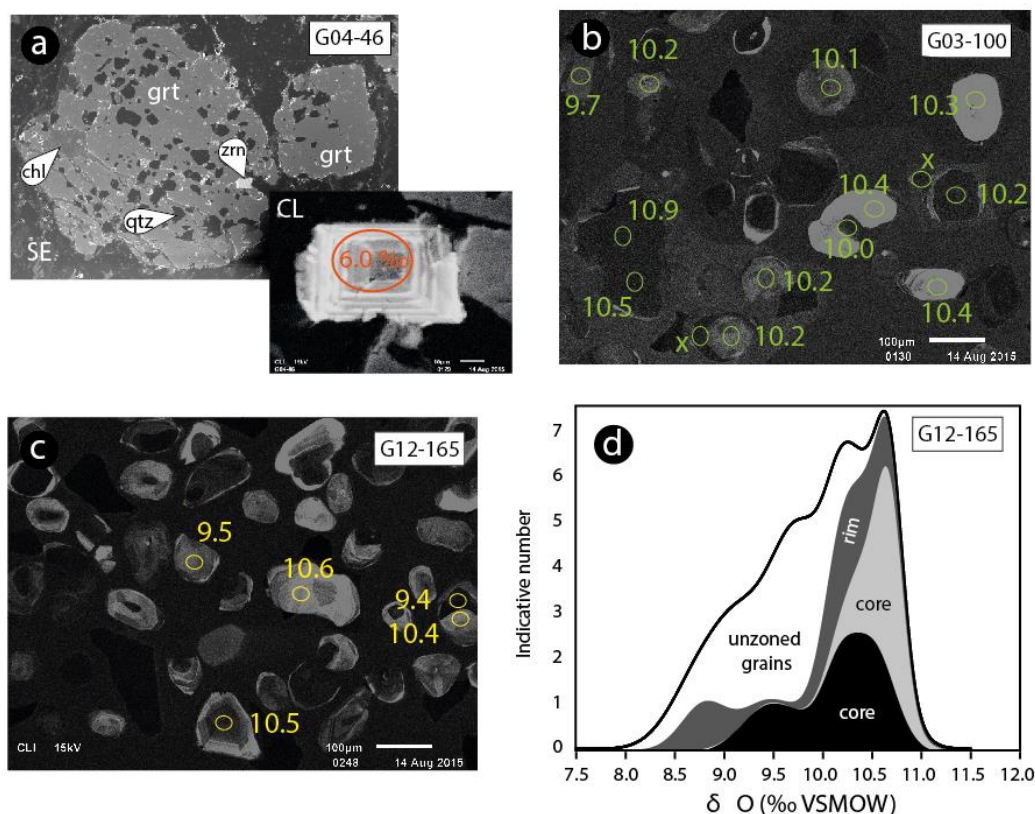
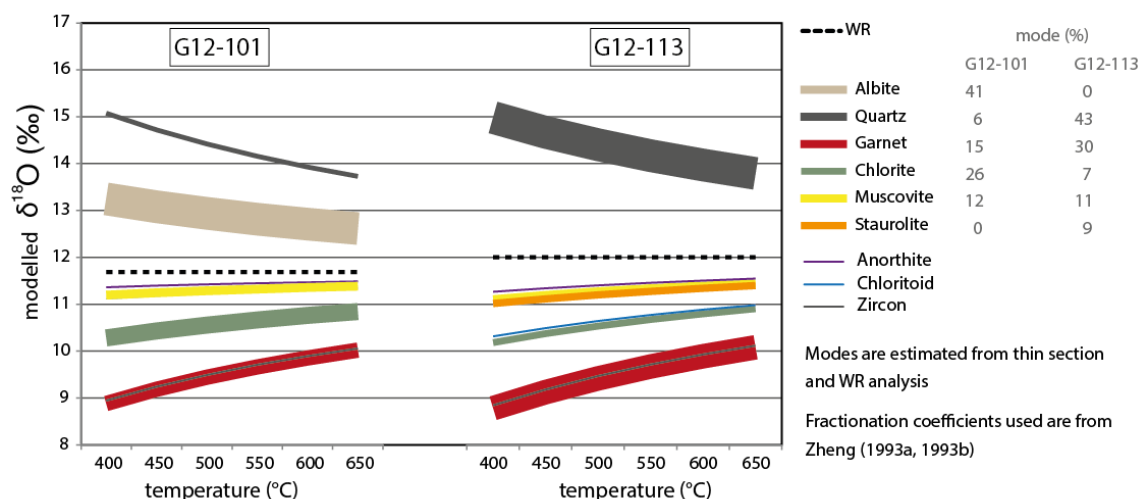


Figure 5 - 14. Probability density plot of in situ  $\delta^{18}\text{O}$  analyses of G12-165 zircons according to their CL-texture.

G03-100 zircons yield a homogenous value of  $+10.2 \pm 0.3\text{‰}$  (1sd,  $n=17$ ), with a standard deviation that is comparable to what is observed in the primary standard (1sd 0.26). Several core-rim pairs were analysed with no variation.

### 3.4.4 Fractionation modelling

In order to be able to draw a link between mineral  $\delta^{18}\text{O}$  and WR  $\delta^{18}\text{O}$ , a simple model of equilibrium fractionation of oxygen isotopes in a closed system is proposed. This exercise is intended to monitor the influence that mineral modes have on the repartition of  $^{18}\text{O}$  following the laws of equilibrium fractionation in a closed system. For instance (model is not shown here), in a hypothetical rock that would be made of 99% quartz and 1% garnet, quartz would yield the WR value, and virtually all  $\delta^{18}\text{O}$  change due to temperature fractionation would be accommodated by garnet (ca. 3‰ between 450°C and 600°C Valley et al., 1995). In the opposite case of a rock with 99% garnet and 1% quartz, the garnet value (close to the WR value) would barely change, but quartz would change by 3‰. As a result, two rocks that have the same WR  $\delta^{18}\text{O}$  and the same thermal history can yield garnet with significantly different absolute  $\delta^{18}\text{O}$  and  $\delta^{18}\text{O}$  zoning if they yield different mineralogy or mineral modes.



**Figure 5 - 15. Results of constant WR  $\delta^{18}\text{O}$  and constant assemblage fractionation modelling in G12-101 and G12-113. Fractionation between minerals are calculated using the Zheng (1993a; 1993b) fractionation coefficients at a set temperature. The whole-rock value is calculated from the combination of mineral modes and mineral values, then all values are shifted (using the MS excel goal seek function) so that the WR value equates the measured fluorination value. Line colour indicates the mineral, line weight is scaled to modal amount in sample. Anorthite, chloritoid and zircon are shown as spectator minerals with a mode of 0.**

In the present model (Figure 5 - 15), mineral modes and WR  $\delta^{18}\text{O}$  are kept constant to measured WR values, while the effect of temperature is the output. This is obviously a simplification as parageneses are likely to change over the investigated interval (as demonstrated by staurolite reacting out to chloritoid in G12-113, see also Ferry et al., 2014). However this approach is sufficiently robust, because  $\delta^{18}\text{O}$  fractionation, sensitive to the strength of chemical bonding, varies on a first order according to  $\text{SiO}_2$  content in silicate minerals and only as a secondary level to mineral structure (e.g. Zheng 1993a). This approach, using the observed mineral modal

amounts, avoids uncertainties linked to the estimation of parageneses and phase equilibria during an evolving P-T. It is much more rudimentary than the thermodynamic phase model by Kohn, (1993) but can still predict how much  $\delta^{18}\text{O}$  zoning in garnet expected along a T change according to quartz/albite modal content. Effects of garnet fractionation of  $\delta^{18}\text{O}$  (by storage of lighter than WR  $\delta^{18}\text{O}$  in the core) are not taken into account here, then have been shown to be mostly negligible (Kohn 1993).

Mineral modes are estimated using thin section observations, and adjusted using WR XRF data such as  $\text{K}_2\text{O}$ ,  $\text{NaO}$  and  $\text{CaO}$  to constrain modes of white mica and plagioclase. This produces a chemically viable model (critical to  $\delta^{18}\text{O}$  fractionation is  $\text{SiO}_2$  content, as outlined above). Modes used are listed in Figure 5 - 15 and results for samples G12-113 and G12-101 are presented in Figure 5 - 15. The model predicts the value of garnet at  $450^\circ\text{C}$  to be around one permil lower than at  $600^\circ\text{C}$  (in a closed system where WR  $\delta^{18}\text{O}$  is kept constant). This is in line with similar models presented in Gauthiez-Putallaz et al. (2016) and Martin et al. (2014b) for quartz- or albite- bearing rocktypes, and with more sophisticated models such as (Kohn et al. 1993) predicting ca. 1‰ per  $100^\circ\text{C}$ .

## 4 Discussion

### 4.1 WR $\delta^{18}\text{O}$ records 3.7 Ga signatures in the B2 schists

This study combines WR  $\delta^{18}\text{O}$  with contextualised SHRIMP mineral data (zircon and garnet) to present a detailed account of  $\delta^{18}\text{O}$  evolution in the B2 schists. This is based on geochemical analysis of mineral zones to be able to link them to geological events. In the discussion, I consider the available information on the timing of garnet growth in the B2 schists, to then be able to use in situ  $\delta^{18}\text{O}$  in garnet to track potential WR changes during its growth. The values recorded by garnet are then compared to zircon (representative of magmatic source-material) and present WR to provide a complete picture of fluid-rock interactions and  $\delta^{18}\text{O}$  signature preservation in the B2 schists.

#### 4.1.1 Garnet growth in Isua B2 schists

Zoned garnets have the potential for recording multiple tectonic events, and thus variable  $\delta^{18}\text{O}$  signatures. A first step is identifying growth zones and their relationship to metamorphic stages in the Isua supracrustal belt. In B2 samples G12-113 and G12-101, garnets are chemically zoned, as observed by previous authors in other samples from the same unit (Rollinson, 2002; Rollinson, 2003, and to a lesser extent Boak & Dymek, 1982). These garnet zones have sharp boundaries and are thought related to several stages of growth, and potentially several metamorphic events

(Rollinson 2002). Here, a summary of new and literature data on B2 garnets is presented, and put into context of broader studies on Isua geodynamics.

The core of the garnet (zone I, corresponding to Grt 1 in Rollinson 2002), in samples G12-101 and G12-113, yields bell-shaped patterns in both Mn and HREE such as Y, which is interpreted as Rayleigh fractionation. Rollinson (2003) reported flat patterns in the cores, and suggested they have been re-equilibrated by subsequent metamorphic events. It is possible that Rollinson (2003) did not use equatorial cuts in the garnets. In G12-113 core, the HREE depletion toward the edges yield to extreme 'volcano-type' patterns with a peak at MREE such as observed in similarly large garnets in ultra-high pressure schists in Gauthiez-Putallaz et al. (2016), **Chapter 2**. This is postulated to be imposed by the modal abundance of garnet in these samples. The garnet cores yield a negative Eu anomaly that is much more pronounced than in the whole rock. This indicates that garnet cores crystallised in the presence of plagioclase. Boak & Dymek (1982) calculated garnet-biotite temperatures of  $583 \pm 30$  and  $542 \pm 19^\circ\text{C}$  for garnet cores from two samples. The core inclusions show a straight layering or foliation, which suggests no rotational deformation during its growth. The Boak & Dymek (1982) core temperatures ca.  $570^\circ\text{C}$  and the presence of plagioclase (detected as Eu negative anomaly) would indicate amphibolite facies.

Two Ca-rich rims (zone II and III) are overgrowing the core. These are described in several samples by Rollinson (2003) as oscillatory zoned, Garnet 2. These rims have a sharp contact with the core. In G12-101, the Ca-rich rims are depleted outwards in HREE and Mn. In G12-113, the HREE become depleted and then enriched, in an oscillation pattern that resembles what is seen in Ca, and could be indicative of the influence of a fluid. These Ca-rich rims yield no Eu anomaly in both samples which indicates that plagioclase was likely not present in the rock (or present only in minor amounts, or with an albitic composition that does not incorporate significant  $\text{Eu}^{2+}$ ; J. Hermann, pers. comm.). Rollinson (2002) calculated a temperature of  $650^\circ\text{C}$  (574-654) for the early Garnet 2. These rims show rotational inclusion trails that branch on the zone I straight trails, and quartz is often present in the garnet pressure shadows which indicates deformation and rotation of the garnet during growth. The increased Ca in garnet is commonly interpreted as the sign of increased pressure (Rollinson 2002; Rollinson 2003). This record of increased pressure is in agreement with the presence of kyanite in some samples (Boak and Dymek 1982) of the same unit, where they estimate the minimal peak pressure at 6 kbar. In G12-113 and other staurolite-bearing layers, the Ca-rich garnet rims seem texturally contemporaneous to staurolite porphyroblasts (now partially replaced by pseudomorphs) that deflect the main foliation. A higher-pressure environment is confirmed by the absence of plagioclase, as plagioclase can react to form epidote-group minerals and amphibole at higher P conditions. Increased oxygen fugacity,



with the influx of a fluid, could also be responsible for the formation of epidote at the expense of plagioclase, but could not as readily explain the increased Ca in garnet. The Ca-rim, at 650°C (Rollinson, 2002) with presence of staurolite and absence of plagioclase, with no indication of partial melting, is assumed to have grown in medium/high-P amphibolite conditions typical of Barrovian-type metamorphism.

The outer Mg-rich and Ca-poor zone IV that overgrows zone III corresponds to Garnet 3 in Rollinson (2003). This zone has a higher Mg# that corresponds to lower garnet-biotite temperatures as calculated by Rollinson (2002): 530°C (490-534) and Boak and Dymek (1982):  $450 \pm 12$  °C and  $439 \pm 27$  °C. The discrepancy between the two estimations might be due to the different calibrations used (Perchuk and Lavrent'eva, 1983 and Ferry and Spear, 1978 respectively). In sample G12-101, garnet zone IV yields a negative Eu anomaly, significant of the presence of calcium-bearing plagioclase, whereas it does not in G12-113. This reflects the matrix mineralogy: G12-101 yields 40 mode % of plagioclase, whereas only small areas yield minor plagioclase in G12-113. This difference in plagioclase content is attributed to differences in reactive bulk between these two rocks. Sample G12-113 is poorer in Ca and Na and it contains more garnet, Ca is likely to be stored in the garnet cores and Ca-rich rims and thus not available to form new plagioclase. This potential for removal of components from the reactive bulk due to the abundance of garnet is shown by HREE and Mn concentration in the cores in the same sample. Garnet zone IV appears to grow statically on previous foliation, and it is not present where quartz-filled pressure shadows are located. It grows over staurolite pseudomorphs in G12-113 and occasionally yields inclusion of chloritoid that grows at the expense of staurolite relicts, as seen in the matrix. Zone IV formed at lower temperatures (450-530°C, Rollinson 2002; Boak and Dymek, 1982), in the presence of the matrix assemblage minerals plagioclase and chloritoid, which are indicative of upper greenschist – amphibolite facies. This is a lower temperature than recorded by the inner zones of the garnet (garnet-biotite temperature of 650°C, Rollinson 2002, and presence of staurolite). Formation of garnet on the retrograde path is not common in Barrovian evolution of metapelites. It is thus possible that this zone formed during a separate tectonic event whose peak temperature was lower, and is thus the result of a prograde reaction and not a retrograde reaction. This is supported by the textural evidence (static growth over foliated rock, growth over staurolite pseudomorphs after staurolite retrogression).

The succession of these three growth zones can be correlated to Archaean tectonic events proposed in the literature. First, the Ca-rich rims (zone II and III), equilibrated to higher amphibolite facies, record higher temperatures than in Ameralik metamorphosed dykes cross-cutting the Isua supracrustal belt (intruded at 3.50 Ga, maximal temperature of metamorphic

equilibration of around 550°C). This demonstrates that garnet zones I to III grew during Early Archaean, before the intrusion of the Ameralik dykes. A distinctive signature is the higher pressure recorded by zone II-III. This mid-high P signature can be correlated to a crust-stacking event during the 3.69-3.66 Ga assembly of the 3.70 and the 3.80 Ga packages, the Itsaqlia orogeny described by Nutman et al. (2015b). Crust-stacking was followed by extensional high-heat flow pan-Itsaq Gneiss Complex metamorphism to ca. 3.60 Ga (Nutman et al. 2014; Nutman et al. 2015c). The chronology of the crust-stacking and extensional events was established on the basis of cross-cutting relationships (see summary in Nutman and Friend, 2009) as well as a rare relict high-pressure granulite with an age of 3.66 Ga in the central gneisses (Nutman et al. 2014; Nutman et al. 2015c) together with titanite and zircon ages of 3632-3620 Ma for amphibolite-faciès metamorphism (Crowley and Myers 2002; Crowley 2003).

Growth zone I in the garnet cores is specific to the tectonic slice containing the B2 unit, and is not recorded in garnet anywhere else in the Isua supracrustal belt (Rollinson 2002). The growth of the cores could either be related to prograde 3.69-3.60 Ga metamorphism before assembly of the 3.7 Ga package subdomains, or could be the result of high heat-flow metamorphism during the arc crust buildup, shortly after deposition of the B2 mafic schists in the environment described by (Nutman et al. 2015b).

In the rock matrix, the retrogression of staurolite into chloritoid, corresponding to the growth of zone IV garnet rim could correspond to the late Archaean metamorphic event in the upper greenschist facies to lower amphibolite facies that is also observed in Ameralik dykes in the Isua Supracrustal Belt. This post Ameralik dyke metamorphism probably involved two events, one at ca. 2.95 Ga and the other at ca. 2.7 Ga (e.g. Nutman et al. 2015b and references therein). In the Eastern ISB, N-S dykes dated at 2.8 Ga have the same metamorphic assemblages and fabric as 3.5 Ga Ameralik dykes (A. Nutman, pers. comm.), which suggests that the ca. 2.7 Ga event yields the Neoproterozoic thermal peak and is likely responsible for the chloritoid and zone IV garnet growth in the B2 schists.

This study shows that interpreting metamorphism in these rocks as a single event (e.g. Komiya et al., 2002) is untenable. The garnet zoning and the presence and absence of plagioclase is the indication of different metamorphic stages at possibly low and high-P geotherms that are difficult to reconcile with prograde to retrograde evolution along a single P-T path.

#### **4.1.2 Tracking WR $\delta^{18}\text{O}$ through geologic time**

The whole-rock oxygen isotope composition of the Isua 3.70 Ga metasedimentary rocks is heavy (ca. +12 ‰), in both mafic layers (G12-101, G12-113) and felsic volcanogenic layers (G04-

46). This signature can be tracked back through time by measuring minerals that preserve early stages of metamorphism (garnet)  $\delta^{18}\text{O}$ , and can be correlated to geologic events.

In felsic layer G04-46: zircon grains which yield a magmatic age of 3710 Ma, and mantle-like  $\delta^{18}\text{O}$  (+5.4 ‰ on average) are interpreted as volcanic relicts. These zircons indicate that magmatic source-material of the B2 schists was mantle-derived and not altered when it crystallised. The zircon value can be extrapolated to the WR  $\delta^{18}\text{O}$  of the evolved magma it crystallises in (e.g. Valley et al., 2003). If a fractionation factor of ca. -2 ‰ is used, one obtains a value of 7-8 ‰ for the magma that formed G04-46 (this can vary with  $\text{SiO}_2$  in the melt). Zircons were not separated in the more mafic samples G12-101 and G12-113, so no direct evidence for its magmatic precursor source-material  $\delta^{18}\text{O}$  can be obtained, although magmatic rocks inferred on trace-element basis to be the source for the mafic G12-101 and G12-113 also yield low  $\delta^{18}\text{O}$  of 6-8 ‰ (see discussion in next section). The offset between the magmatic value (7-8 ‰ derived from zircon) and the WR sedimentary value (11-12 ‰) is attributed to surficial weathering (see discussion in next section).

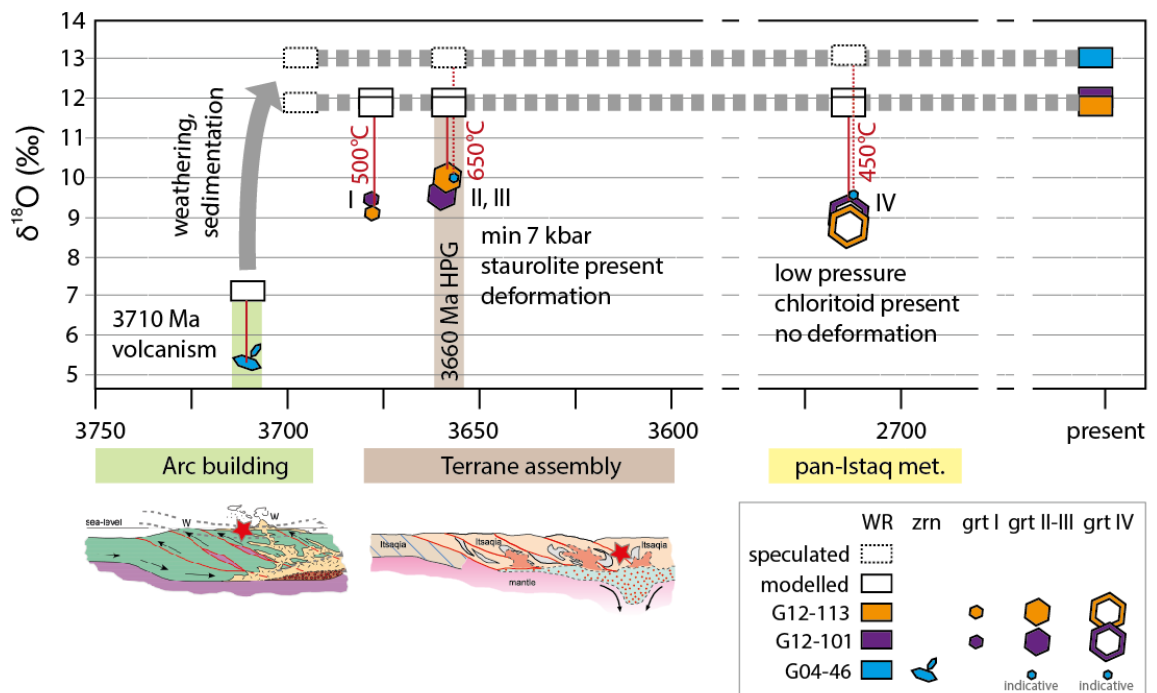


Figure 5 - 16. Summary of  $\delta^{18}\text{O}$  data for B2 schists on the timeline of tectonic events in the Isua Supracrustal Belt. Measured values are shown in filled symbols. Red tied show equilibrium relationships, approximate temperatures of  $\delta^{18}\text{O}$  equilibration are shown in red. Sketch for arc building is taken from Nutman et al. (2014), and for terrane assembly from (2015c). Red stars indicate the position of B2 schists at the different stages. G04-46 garnet data are standardized to zircon and not matrix-corrected according to previous analysis sessions where both garnet and zircon were analysed, the true value would be about 2 ‰ different. They are taken as an indication that the garnets yield heavy values in opposition to mantle values.

Throughout metamorphism, WR  $\delta^{18}\text{O}$  can be tracked by measuring garnet  $\delta^{18}\text{O}$  (Figure 5 - 16). G12-101 and G12-113 record garnet values of +8.7 to +9.7 ‰ that are much higher than the  $\delta^{18}\text{O}$  values of inherited magmatic zircon. These garnet values record the WR value throughout metamorphism, throughout the residence of these metasedimentary rocks in Archaean crust. All garnet zones, in both mafic samples (and the few indicative analyses in G04-46) yield similar heavy values ( $+9.5 \pm 1$  ‰). This implies that the metasedimentary rocks had acquired their heavy  $\delta^{18}\text{O}$  on the surface, and introduced heavy  $\delta^{18}\text{O}$  in the Archean crust before 3.69 Ga (age attributed to the garnet cores), and certainly before 3.5 Ga (age of lower grade cross-cutting dykes). Using the fractionation model, the garnet value in both samples is accurately predicted between 8.8 and 10.1 ‰ using the WR value for a temperature of 400-650°C. This indicates that the value measured in WR today reflects the WR  $\delta^{18}\text{O}$  during garnet growth within a permil.

Lower magnitude (ca. 1‰) core-rim variations in the garnets are detectable using SHRIMP. By modelling equilibrium fractionation in the co-equilibrating assemblage, it is shown that this  $\delta^{18}\text{O}$  zoning can be expected from temperature variations alone, and do not require the input of external fluids. For instance, in G12-113, modelling the temperature of equilibration at a constant WR of +12.0‰ (measured WR) yields 418°C for garnet core (I) and rim (IV) (9‰), and 618°C for garnet zone II-III (10‰). These temperatures are close to what has been estimated on the base of garnet-biotite thermometry by previous authors. Modelling predicts a slightly lesser  $\delta^{18}\text{O}$  variation over that range of temperature in G12-101 assemblage (ca. 0.8 ‰), however, the variation measured between zone III and zone IV (rim) is 0.4‰ which is barely resolvable with SHRIMP. This discrepancy could be due to assemblage variations such as the disappearance of albite (mode 40%) during growth of zone II and III that are not taken into account in the model. In both cases, the variation between garnet zones is small and can be attributed to temperature variations during garnet growth. As such, from  $\delta^{18}\text{O}$  measurements in garnet, G12-101 and G12-113 underwent no significant metasomatism since the growth of the first garnet (zone I).

In summary, the B2 sediments contain a volcanic component with mantle-derived  $\delta^{18}\text{O}$  signature and acquired a heavier  $\delta^{18}\text{O}$  signature after crystallisation of their magmatic source-rock and before the first metamorphic event in the stability field of garnet. They then were present as a high- $\delta^{18}\text{O}$  body at mid-crustal levels in both an early and a late Archaean metamorphic events.

## 4.2 Isua B2 schists are the results of weathering on the Eoarchaeon surface.

### 4.2.1 Magmatic source-material of the B2 schists

This work provides new geochronological and trace-element data that add to previous studies (Dymek et al. 1983; Jacobsen and Dymek 1988; Nutman et al. 1997; Bolhar et al. 2005; Kamber et al. 2005; Grew et al. 2015) that looked into the origin of the detrital material found in the B2 schists.

From major and trace-element data, it has been inferred that the B2 schists are of predominant mafic source (Dymek et al. 1983; Bolhar et al. 2005). Garnet-chlorite schists G12-101, together with *positive Eu anomaly samples* of Bolhar et al. (2005) and garnet micaschists of Dymek et al. (1983) yield depleted incompatible trace-element patterns that show the contribution of depleted mafic sources such as the boninites (Polat et al. 2002; Nutman et al. 2015b) that are a good match for low REE abundances in these samples (Figure 5 - 9). This is correlated with higher contents in Cr and Ni indicating mafic to ultramafic sources. G12-113 yields a parallel trace-element pattern, but much more enriched. Notably, this more enriched rock does not show negative anomalies in Ti and Sr, as seen in andesites, that would be an indication of a more fractionated source. In this sample, overall trace-element enrichment could be the result of the sedimentary sorting of trace-element bearing minerals to the expense of trace-element poor minerals during the sedimentation process. Given the size of garnets in G12-113 (up to 2 cm), it is also possible that garnets were oversampled during the sample preparation which would give an artificially enriched pattern. Previous studies have shown that these rocks yield near-chondritic initial  $\epsilon_{\text{Hf}}$  values (-0.6, +1.11; Hoffmann et al. 2010), which indicates that they are the product of juvenile sources, and not of older crust. These values also exclude the contribution of large amounts of fresh boninites as the latter yield much higher initial  $\epsilon_{\text{Hf}}$  values (+3.5 to +12.9; Hoffmann et al. 2010). Altered boninites, on the contrary, drift towards lower values (+0.9 to +6.3) and could be a potential source.

A more fractionated source is also present as shown by the incompatible-element enriched trace-element pattern of G04-46 (Figure 5 - 9), identical to volcanogenic samples in Bolhar et al. (2005) and fresh andesites (Nutman et al. 2013). These samples yield negative anomalies in Ti, Sr and Eu that are characteristic of fractional crystallisation of Ti oxydes and plagioclase. As such, G04-46 potentially represents a volcanic layer representing the more evolved source. This more fractionated magmatic component is a good candidate for the source of the volcanic zircons also found in mafic layers of the B2 schists (Nutman et al. 1997; Kamber et al. 2005). In a 1 kg of sample G04-46 (142 ppm WR Zr), about 50 zircons were separated, which is more than previous

authors found in other more typically mafic B2 layers. The zircons yield magmatic CL zoning and REE profiles, as well as mantle-like  $\delta^{18}\text{O}$  (ca. 5.3 ‰). They yield a concordia age of  $3709 \pm 6$  Ma which is identical to previous ages of 3700-3710 Ma previously identified in the B2 unit. This age is interpreted as the eruption/deposition age for this layer, and as the crystallization/eruption age of the fractionated magmatic source contributing to the B2 metasedimentary rocks.

Overall, these results confirm that the B2 schists are the product of erosion of mafic crust, during a period of active andesitic volcanism at 3700-3710 Ma, as has been proposed previously (Nutman et al. 1984; Nutman et al. 1997; Kamber et al. 2005). This age of deposition is within the same range as the ages found by Nutman et al. (1997) in the felsic B1 unit outcropping at a lower level in the *northwestern tectonic domain*, as well as chemical sediments in the *central tectonic domain*. The following discussion will focus on the alteration of this primary material before deposition to present, following the angle of oxygen isotopes.

#### **4.2.2 Mechanism of weathering /diagenesis**

In this study, we document the heaviest WR  $\delta^{18}\text{O}$  rock types in the Isua supracrustal belt 3700 Ma package. These rocks mirror findings by Nutman et al. (2015) from the 3800 Ma package, where they describe volcanic rocks weathered at low temperature in-situ, with WR  $\delta^{18}\text{O}_{\text{VSMOW}}$  as high as +16‰. There are two main lines of evidence for low temperature weathering in the B2 schists: major elements and oxygen isotopes.

First, as shown in Figure 5 - 17 and by previous authors, the major element composition of the mafic schists in the B2 unit form a trend from the andesite field down to the weathered corner of the diagram, corresponding to soils composition (similar to plots by Bolhar et al. 2005). This trend represents leaching of low-temperature fluid-soluble elements, namely by replacement of plagioclases by kaolinite (or similar reactions forming clay minerals, see Ohata and Arai, 2007 for more details). B1 felsic schists show less of the weathering signature, yet still diverge from the magmatic fields represented by coeval magmatic rocktypes inferred to be the source for these sediments.

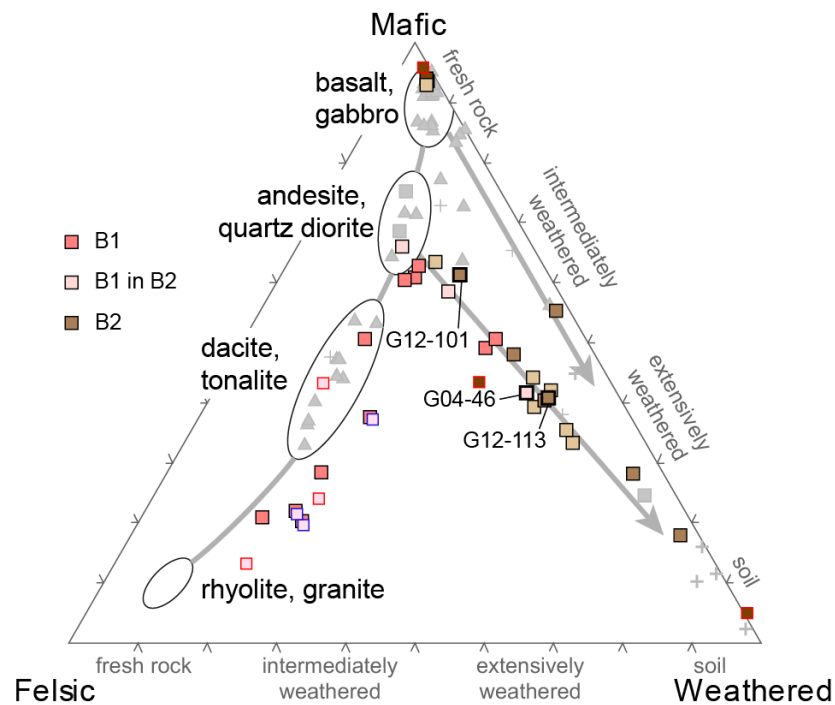


**Figure 5 - 17. Weathering diagram of Ohata & Arai (2007) representing multi-oxide indicators of weathering in the WR of G12-101, G12-113 and G04-46 together with B1 felsic schists and B2 mafic schists (pink and brown squares), with representative 3.7Ga package lithologies (gray symbols, Nutman et al. 2015). B1 and B2 literature data is from Nutman et al. (2013) – black outlines, Bolhar et al. (2005) - blue outlines.**

In this study, heavy  $\delta^{18}\text{O}$  signatures measured in metasedimentary rocks yield further support low-temperature alteration, independently from potentially different Archaean sedimentation dynamics. Most literature oxygen isotope data for the Isua 3.7 Ga rocks (Figure 5 - 18) are comparable to equivalent Phanerozoic magmatic processes: mantle-like  $\delta^{18}\text{O}$  for mafic plutonic lithologies, slightly higher as would be predicted by magmatic fractionation for tonalities and more felsic magmatic lithologies. The BIF and other chemical metasedimentary rocks record signatures from +12 to +20 ‰ (Perry et al. 1978; Pope et al. 2012). The values measured in pillow-lavas (Furnes et al. 2007) and serpentinites (Pope et al. 2012), thought to be the result of high-temperature interaction with seawater, have been used to derive information about the Archaean oceans. In a few localities of the Itsaq Gneiss Complex, much heavier values are present, which are thought to reflect the presence of surficial weathering, in low temperature conditions. Such samples are from an extensive felsic schist unit in the 3.8 Ga package (Nutman et al. 2015, Pope et al. 2012 supplementary data but not interpreted), biotite-quartz-garnet rocks in the Akilia region (Cates & Mojzsis, 2006), as well as a few felsic schists and others in the 3.7 Ga Isua package (Pope et al. 2012, supplementary data but not interpreted).

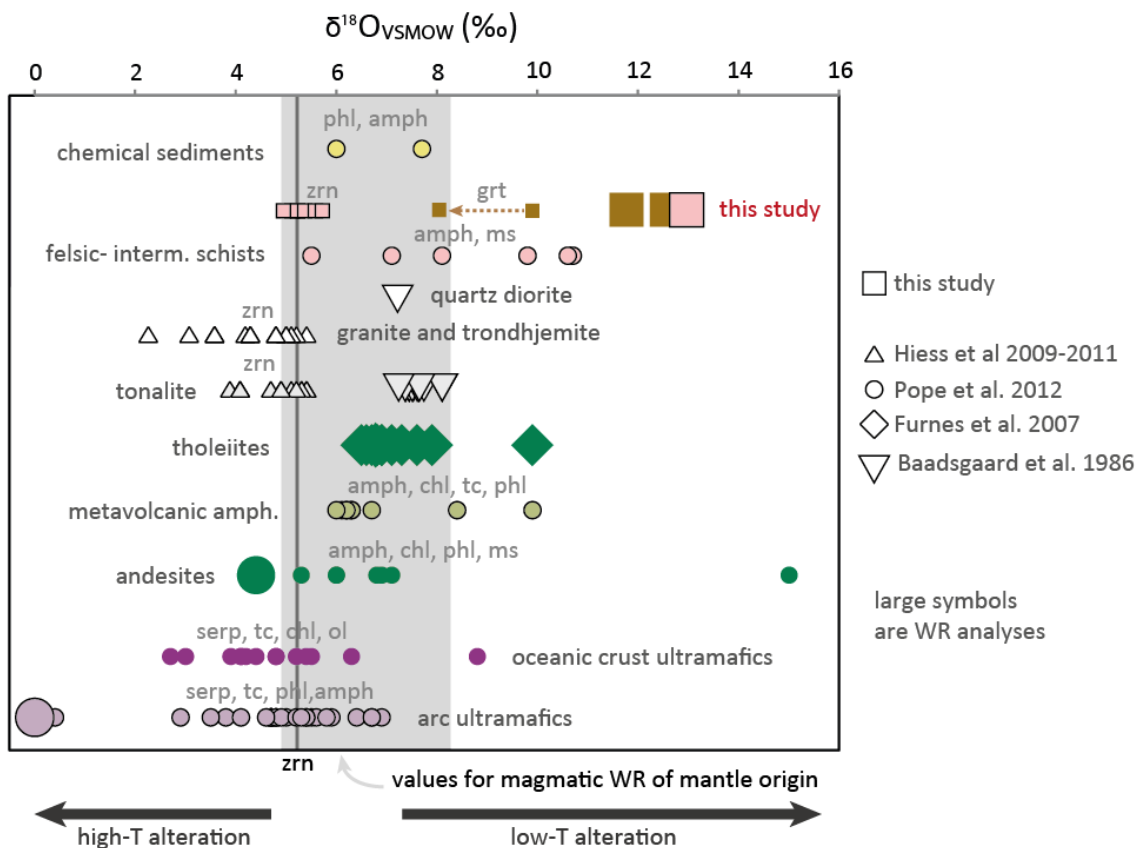


**Figure 5 - 18. Summary of oxygen isotope data for rocks of the 3700 Ma package of the Isua supracrustal belt, extracted from *Hiess et al. (2009)*; *Hiess et al. (2011)*; *Pope et al. (2012)*; *Furnes et al. (2007)*; *Baadsgaard et al. (1986)* according to the geochronology and mapping of *Nutman & Friend (2009)*. Mantle zircon value is taken from (Valley et al. 1998).**

Magmatic lithologies inferred to be the source for the B2 sedimentary rocks (boninites, island-arc-tholeiites and andesites, Figure 5 - 18) which outcrop in the Isua supracrustal belt yield mantle-like or just slightly more evolved  $\delta^{18}\text{O}$  signatures in whole-rock. This is also recorded by magmatic zircons in G04-46 that yield mantle-like values (+4.5 to +6 ‰). The  $\delta^{18}\text{O}$  recorded in G12-101, G12-113 and G04-46 are the highest reported for Isua 3.7 Ga rocks and thus cannot be directly inherited from their magmatic source-rocks. Low-temperature alteration is needed to bring the whole-rock  $\delta^{18}\text{O}_{\text{VSMOW}}$  value to +12 ‰ as recorded by the three samples studied here. Temperatures required to enrich the  $\delta^{18}\text{O}$  of silicates to this degree are below 200°C (e.g. Sheppard and Gilg, 1996 and references therein). The foremost mechanism by which this is achieved today is the formation of kaolinite, smectite and other clay minerals in weathering of magmatic/volcanic rocks exposed to the surface (e.g. Savin and Epstein, 1970). During this process, the  $\delta^{18}\text{O}$  of the material increases with the proportion of clay formed. From a starting point of 8 ‰, it would take the formation of about 20% kaolinite or other clay minerals in the rock to alter the composition to 12 ‰, 40% to get to 16 ‰ (Lawrence & Taylor 1976). A weathered andesite horizon at a ~3700 Ma unconformity has been identified in the *eastern*



*tectonic domain* (A. Nutman and A. Chivas, pers. comm.) and yield heavy values around +16 ‰. This locality could be the example of the source-material for the B2 schists, in place.

Increase in  $\delta^{18}\text{O}$  can also be caused by transport and diagenesis. Further along the sedimentation process, the  $\delta^{18}\text{O}$  can be further increased by the sorting of heavy  $\delta^{18}\text{O}$  minerals such as magmatic quartz if present but mostly weathering minerals such as clays. Bolhar et al. (2005) exclude significant weathering during transport on the basis of the absence of strong correlation between weathering indexes and  $\text{SiO}_2$  content. According to Bolhar et al. (2005),  $\text{SiO}_2$  variations, that cannot be attributed to the source material since they do not correlate with incompatible trace elements, are another indication of short transport distances and poor sedimentary mixing. Last, the formation of authigenic clay minerals during diagenesis can also be a mechanism for  $\delta^{18}\text{O}$  increase if the temperature remains low, this however is not one of the primary mechanisms today (Savin and Epstein, 1970). There are indications for low-temperature interaction with sea water in the B2 schists. Bolhar et al. (2005) use the presence of mild positive Eu anomalies as a signature of interaction with seawater, this would indicate that some diagenetic reactions have taken place and have potentially further enriched the sediments in  $^{18}\text{O}$ . The presence of tourmaline in the garnet schists has been reported by previous authors (Appel 1984; Chaussidon et al. 1997) and more recently, they have been analysed for in situ boron isotopes (Grew et al. 2015). In the latter study, light B signatures were found, in agreement with previous estimates of what interaction with sea-water would produce. The proposed source for the B incorporated in B2 schists is marine clays, the B being then re-hosted in tourmaline during diagenesis and metamorphism. The presence of tourmaline in the garnet cores observed here confirms that the B incorporation occurred before the first stage of metamorphism where garnet was stable, most likely by adsorption on clay minerals during diagenesis.

### 4.3 Tikeraq

Tikeraq garnet G12-165 records four growth zones. The core grows statically over a foliation marked by straight quartz inclusion trails. It yields epidote inclusions, a weak negative Eu anomaly (indicative of not much plagioclase in the paragenesis) and a high grossular content that are an indication for a mid-high pressure (e.g. epidote-amphibolite metamorphism). The first rim shows rotation in the quartz inclusion trails, it yields a marked negative Eu anomaly that indicates the presence of plagioclase in the co-crystallising assemblage (plagioclase is also present as inclusions), lower Ca and Mn content. This rim is more typical of amphibolite-faciès. Rim 1 is overall more enriched in HREE and MREE than the outer core, which shows the remobilisation of REE from garnet and MREE-bearing phases. This might be an indication for partial melting. A second rim grows statically over the foliation, where quartz inclusion trails disappear. This rim

repeats the same pattern as core and rim 1, with rim 2a having weak Eu anomaly and more Ca (no plagioclase, higher pressure), and rim 2b a strong Eu anomaly and less Ca, in equilibrium with matrix plagioclase. This overall double pattern mirrors what is seen in the field as ‘double garnets’ and suggest two cycles of decreasing pressure and increasing temperature, potentially both including partial melting in their HT phase.

Zircons in G03-100 and G12-165 are of soccerball shape, have complicated CL textures with light or dark cores overgrown by light rims. Some light cores yield embayments filled by darker mantles. Embayments are the sign of zircon destabilisation, which could be the sign of fluid or melt-related dissolution (e.g. Taylor et al., 2014). All of these zones are sector-zoned, with some oscillatory-zoning in lighter zones, which is a common feature for zircons crystallising in a melt (Hoskin and Schaltegger, 2003). They yield homogenous heavy  $\delta^{18}\text{O}$  around 9 ‰ which is in equilibrium with garnet values around 9 ‰. Thus these zircons grew in the same WR  $\delta^{18}\text{O}$  as the garnet and are likely metamorphic and not relict magmatic crystals which would most likely yield juvenile and mantle-like  $\delta^{18}\text{O}$ . Since partial melting evidence is ubiquitous in the field, the zircons are interpreted to be the result of different stages of HT metamorphism and partial melting.

Age constraints for the Tikeraq garnet gneisses from unpublished work by V. Bennett and A. Nutman are a both a Hf model age of ca. 2980 Ma and a zircon U-Pb age of ca. 2980 Ma (no differences between CL zones were detected). The Hf model age is interpreted as the age for the source material of these gneisses, which would be juvenile Mesoarchaeon mafic magmatism. The U-Pb age, on the contrary, is interpreted as the age of HT metamorphism (because of zircon homogenous age, soccerball shape and heavy  $\delta^{18}\text{O}$ ). The different CL zones would reflect punctuated growth in a short time-frame. This interpretation implies a quick (within age resolution) recycling of sediments into the lower crust, as observed in the much older Isua B2 schists, but at a later stage. The U-Pb ages and Hf model age measured in the Tikeraq garnet schists are much younger than the Eorchaean Hf model age obtained for the layered gabbros that lie directly under them (V. Bennett, pers. comm.), which would imply the presence of a large tectonic unconformity between these two units, at the base of the garnet-bearing schists.

The main information obtained from  $\delta^{18}\text{O}$  measurements in garnet and zircon is that the system is internally buffered: no external fluid or melt influxes are identified. The isotopically heavy signature measured in the Tikeraq garnets and zircon also suggests that they are made of low-temperature altered material, in a similar scenario to the much older Isua schists. In this case, as we have not found relict detrital minerals in these schists, the latter interpretation is more

speculative as the source material could (potentially but not probable) have been isotopically heavy to start with.

G12-165 garnet records homogenous  $\delta^{18}\text{O}$  from core to rim. Vielzeuf et al. (2005b) suggest that oxygen diffuses as quickly as Ca in garnet, and slower than Mn, Fe and Mg. In G12-165, Mn, Mg and Ca zoning is preserved so the zoning in  $\delta^{18}\text{O}$  is interpreted as a primary feature, not the result of diffusion, despite the likely high (650-700°C) temperatures required for the apparition of partial melting. G03-100 zircons yield a homogenous population around +10 ‰, across CL zoning. This indicates that  $\delta^{18}\text{O}$  was internally buffered during and in-between the episodes of growth recorded by the zircons (HT metamorphism and partial melting). Similarly, composite sample G12-165 yield one population of unzoned grains with  $\delta^{18}\text{O}$  around +9,5 ‰ (in equilibrium with the G12-165 garnet sample), and one population of zoned grains that yields  $\delta^{18}\text{O}$  around +10,5 ‰, with no systematic variation between CL zones (similar to G03-100). The slight variation between these two populations is attributed to compositional variations due to layering, which is an indication of local equilibration and melt production.

If at least some zircons grew during anatexis (e.g the light CL zones showing oscillatory zoning), the melt  $\delta^{18}\text{O}$  would be around +11 to +12.5 ‰ (minimum), using a fractionation of -2.2 ‰ for zircon – granitic melt (Valley et al. 2003).

#### 4.4 Heavy $\delta^{18}\text{O}$ mid-crustal lithologies in the Archaean

Isua B2 and Tikeraq schists are two examples of sedimentary-derived lithologies that brought heavy  $\delta^{18}\text{O}$  into the crust in the Archaean. The B2 schists have metamorphic conditions corresponding to mid-crustal levels (see Nutman et al. 2015b). In the same metamorphic event, the corresponding lower-crustal level could be represented by 3.66 Ga high-pressure granulite enclaves in >3.6 Ga tectonites (Nutman et al. 2014). In Tikeraq, a lower crustal level is sampled with metamorphic zircons that likely formed during anatexis of metasediments record high  $\delta^{18}\text{O}$  at 2.98 Ga.

In both cases, burial immediately followed sedimentation (within 10 to 50 My maximum, Figure 5 - 16), which demonstrates the possibility for early and fast recycling of surficial  $\delta^{18}\text{O}$  in the early Archaean crust, as also shown for Archaean high-grade metasediments in the Pilbara, Australia (François et al. 2014). In opposition to refractory BIFs and dolomites or low-volume altered horizons (3.8 Ga Isua package weathered volcanics, Nutman et al. 2015a) and sedimentary layers (e.g. Akilia island metasedimentary rocks, Cates and Mojzsis, 2006), these rocks provide a volumetrically important fertile source for heavy  $\delta^{18}\text{O}$  crustal magmas (undiluted +12 ‰) that

can explain heavy  $\delta^{18}\text{O}$  zircons as the result of S-type granite formation early in Earth's history (Mojzsis et al. 2001; Peck et al. 2001; Trail et al. 2007).

Sagduction processes such as suggested in the Pilbara (e.g. Thébauda and Rey, 2013) could account for similar recycling of heavy  $\delta^{18}\text{O}$  signatures, but are not favoured in the Isua area. Crustal tectonic models proposed so far for the Isua area on the basis of structural and petrographic studies are akin to modern subduction (Komiya et al. 1999; Hayashi et al. 2000; Arai et al. 2014) or flat subduction (Friend and Nutman 2005; Nutman et al. 2014; Nutman et al. 2015c; Kaczmarek et al. 2016) followed by orogeny. Sediment burial to mid- to lower-crustal depth would be possible in the orogeny stage where slivers of arc crust are juxtaposed and stacked.

## 5 Conclusion

Garnets from the the Isua 3.7 Ga metasedimentary rocks are zoned in major, trace elements and mineral inclusions. They record three metamorphic events starting in the Eoarchaeon: a proposed first high-heat flow event during arc formation, followed by the stacking of the 3.7 and 3.8 Ga terranes at 3.69 to 3.60 Ga. Lastly, the rock matrix records a greenschist/lower amphibolite facies overprint that could be linked to a Neoarchaeon event. The  $\delta^{18}\text{O}$  composition measured in B2 schists (WR, garnet) is heavy (ca. +10 ‰) for all but volcanic zircons (ca. +5.3 ‰). The relatively constant  $\delta^{18}\text{O}$  across garnet domains indicate that the present whole-rock value likely reflects the rock's sedimentary protolith, and did not evolve significantly during metamorphism when the rocks were buried ad mid-crustal depths.

These schists are thought to be the product of erosion of a 3700-3710 Ma proto arc involving both mafic and felsic components, such as the felsic and mafic rocks outcropping to the east and the west of the sampling area.  $\delta^{18}\text{O}$  offset between magmatic relicts (zircons) in these sediments and the rest of the material forming the rock is the result of low-temperature alteration, such as weathering on the surface of this proto-arc around 3700 Ma. This confirms findings by Nutman et al (2015) in the 3800 Ma package

Heavy  $\delta^{18}\text{O}$  signatures are also measured in garnet and metamorphic zircons from micaschists of the Tikeraq locality (ca. 10 ‰). Anatectic melts in equilibrium with the zircons and garnets yield a modelled value of around 12 ‰. Together with the Isua B2 schists, these sedimentary lithologies are the remnants of high  $\delta^{18}\text{O}$  components in mid to lower levels of the Archaean crust, at 3.7 and 2.9 Ga.

## Conclusion

This study explored using in situ  $\delta^{18}\text{O}$  analysis to document fluid-rock exchanges in subduction and mid-crustal rocks. Using trace elements and petrography to link mineral signatures to the rock evolution, a complex history of metamorphic fluid circulations were reconstructed in three settings: in the UHP whiteschists of the Dora Maira continental unit, in the lawsonite eclogites and blueschists from the Tavşanlı zone, and in the Early-Archaean metasediments from the Isua supracrustal belt.

This study contributed to expanding SHRIMP  $\delta^{18}\text{O}$  analysis and textural analysis to metamorphic minerals beyond garnet and zircon, to obtain a more complete picture of fluid circulations and cover a wider range of metamorphic conditions. This method is particularly suited to accessory phases (monazite, apatite, rutile) that have limited compositional variation, provide otherwise useful geochemical information, and may be difficult to analyse in bulk due to their low modal abundance and/or internal zoning. This investigation addressed some of the main challenges in ion microprobe oxygen analyses: repeatability of standard analysis, matrix effects related to compositional variations and orientation effects. SHRIMP analysis of previously characterised standard materials achieved a repeatability of 0.2 to 0.4 ‰ ( $1\sigma$ ) for apatite and monazite. Beyond the analytical measurement, this work highlights that corrections of measured oxygen isotope analyses are needed for compositional variations in monazite and orientation effects in rutile. A matrix-correction scheme was successfully established for monazite which brings the external error to about 0.4 ‰. A correction scheme could not be determined for SHRIMP  $^{18}\text{O}/^{16}\text{O}$  measurement for rutile where intra sample variations can reach 5 ‰. In apatite oxygen isotope measurements do not show any compositional matrix effect within the achieved precision of 0.2 ‰. However, modelling of oxygen isotope diffusion in apatite showed that for samples that have resided above 400-450°C diffusional re-equilibration has to be considered when interpreting the data.

Zircon, garnet, apatite and monazite in situ  $\delta^{18}\text{O}$  analysis was applied to geological samples. In the Dora Maira Whiteschists (Western Alps), the convergence of multiple lines of evidence stemming from thermodynamic modelling and in situ methods allowed establishing a complete P-T-t-fluid path for the subduction and exhumation of the UHP whiteschists. Zircon and monazite show multiple growth zones during metamorphism that are distinct in chemistry. Thermodynamic modelling in the relatively simple KFMASH chemistry of the whiteschists coupled with inclusion relationships and trace element chemistry allowed attributing zircon and monazite formation at 35-34 Ma to the prograde path. The reactivity of zircon (and monazite) is attributed to break down of hydrous minerals chlorite and talc by prograde reactions, liberating fluid pulses that lead to the

partial dissolution of magmatic zircons and the crystallisation of metamorphic rims. These fluids were internal derived and thus were not responsible for the metasomatism of the whiteschists, which must have occurred earlier in their evolution. This study shows that the prograde metamorphic minerals already recorded a low  $\delta^{18}\text{O}$  and high Mg at low temperature conditions, before antigorite dehydration, which is a major source of fluids in the subducting slab. The conclusion drawn, is that, similarly to lower-grade whiteschists across the Alpine orogeny, the low  $\delta^{18}\text{O}$  - high-Mg signature of the Dora Maira UHP whiteschists originated from a granite that was likely metasomatised on the seafloor during Permian rifting. In summary, this study thus allowed to (i) derive a prograde P-T-t-fluid path and investigate prograde recrystallization processes for zircon, and (ii) shed more light on the origin of metasomatism in the Dora Maira whiteschists.

The Tavşanlı high pressure zone of central Turkey is characterised by a large variety of lithologies. This study aimed to identify the amount of interlayering and hybridisation related to pre-subduction history and to subduction processes. The geodynamic study based on trace elements and geochronology showed that the Halilbağı unit is a composite assemblage of distal and proximal seafloor slivers with varying geochemical signature and ages, much like accretionary units recognised to the west. Thus, part of the chemical heterogeneity is due to pre- or early-subduction processes, and significant changes in  $\delta^{18}\text{O}$  in its lithologies are due to alteration and metasomatism before deep subduction.

Rare relicts of zircons and garnet cores preserve the mantle-like magmatic  $\delta^{18}\text{O}$  signature, but the whole rock and metamorphic minerals in all samples yield sediment-like  $\delta^{18}\text{O}$  values of 12-25 ‰. This shows that most lithologies either mechanically mixed with sediments (resulting in mixed REE signatures) or equilibrated through metasomatism (magmatic REE signatures, with mobility of Pb, Sr, Cs, Rb, Ba). Fluid circulation at high pressure is observed in 5 samples, where garnet, apatite and/or lawsonite show  $\delta^{18}\text{O}$  zoning. They involve a fluid with a  $\delta^{18}\text{O}$  of ca. 15 ‰ and that carries an intermediate Sr/Pb signature. This fluid circulation is likely enabled by the change in rheology previously described in this unit at the start of exhumation, close to 80 km depth.

The Early Archaean Isua metasediments and Late Archaean Tikeraq metasediments are derived by weathering of mafic magmatic material. For the Isua samples, the source material can be identified by comparing trace-element patterns and correspond to weathered olivine-bearing boninites and more evolved andesites. Detrital zircons in the Isua metasediment preserve mantle like  $\delta^{18}\text{O}$  values and yield a U-Pb age of 3705 Ma, The Isua metasediments record some of the highest bulk rock  $\delta^{18}\text{O}$  values in the supracrustal belt at 11-12 ‰, and Tikeraq sediments a value

---

of ca. 10 ‰. This concurs with major element indicators to indicate a surficial weathering processes. In both cases, the sediments were metamorphosed shortly (10-50 Ma) after deposition, as recorded by the presence of HP garnets related to a higher pressure event dated by others at ca. 3660-3690 Ma event in Isua, and a metamorphic U-Pb age of 2980 Ma in Tikeraq zircons. This shows that quick recycling of surficial signatures to mid-crustal (Isua) or lower-crustal (Tikeraq) levels is possible in the Archaean. The migmatites and associated zircons present in the Tikeraq metasediments show how this can result in the production of high  $\delta^{18}\text{O}$  magmas and zircons in the Early Earth.

All three studies show that surface or seafloor alteration were main processes that imprinted the  $\delta^{18}\text{O}$  signature recorded in metamorphic rocks. During metamorphism, measurable changes in oxygen isotope composition are recorded in specific rocktypes in the Halilbađı unit. This shows that metamorphic fluid-liberation processes (hydrous mineral breakdown and/or crustal dehydration melting) are secondary to the primary alteration that formed hydrated lithologies. Therefore, analysis of in situ minerals is often the only way to distinguish between these different phases and identifying metamorphic fluid circulations. In all three studies, relicts of zircon preserve the original protolith magmatic or detrital signature, and robust metamorphic minerals (e.g. garnet, monazite, zircon, apatite, lawsonite) can track alteration and metasomatism during metamorphism.





## References

- Aleinikoff JN, Schenck WS, Plank MO, et al (2006) Deciphering igneous and metamorphic events in high-grade rocks of the Wilmington Complex, Delaware: Morphology, cathodoluminescence and backscattered electron zoning, and SHRIMP U-Pb geochronology of zircon and monazite. *Geol Soc Am Bull* 118:39–64. doi: 10.1130/B25659.1
- Amato JM, Johnson CM, Baumgartner LP, Beard BL (1999) Rapid exhumation of the Zermatt-Saas ophiolite deduced from high-precision SmNd and RbSr geochronology *Earth and Planetary Science Letters* 171:425–438
- Andrews MG, Baxter EF, Pollington AD, et al (2010) Oxygen and strontium isotope zonation in shear zone garnet: Evidence for open system exchange. *Geochim Cosmochim Acta* 74:A23–A23.
- Angiboust S, Agard P, Raimbourg H, et al (2011) Subduction interface processes recorded by eclogite-facies shear zones (Monviso, W. Alps). *Lithos* 127:222–238. doi: 10.1016/j.lithos.2011.09.004
- Angiboust S, Langdon R, Agard P, et al (2012) Eclogitization of the Monviso ophiolite (W. Alps) and implications on subduction dynamics. *J Metamorph Geol* 30:37–61. doi: 10.1111/j.1525-1314.2011.00951.x
- Appel PWU (1984) Tourmaline in the Early Archean Isua Supracrustal Belt, West Greenland. *J Geol* 92:599–605.
- Appel PWU, Fedo CM, Moorbath S, Myers J (1998) Recognizable primary volcanic and sedimentary features in a low-strain domain of the highly deformed, oldest known (~ 3.7–3.8 Gyr) Greenstone Belt, Isua, West Greenland. *Terra Nov* 10:57–62. doi: 10.1046/j.1365-3121.1998.00162.x
- Arai T, Omori S, Komiya T, Maruyama S (2014) Intermediate P/T-type regional metamorphism of the Isua Supracrustal Belt, southern west Greenland: The oldest Pacific-type orogenic belt? *Tectonophysics* 662:22–39. doi: 10.1016/j.tecto.2015.05.020
- Ayers JC, Loflin M, Miller CF, et al (2006) In situ oxygen isotope analysis of monazite as a monitor of fluid infiltration during contact metamorphism: Birch Creek Pluton aureole, White Mountains, eastern California. *Geology* 34:653–656.
- Baadsgaard H, Nutman AP, Rosing MT, et al (1986) Alteration and metamorphism of Amitsoq gneisses from the Isukasia area, West Greenland: Recommendations for isotope studies of the early crust. *Geochim Cosmochim Acta* 50:2165–2172. doi: [http://dx.doi.org/10.1016/0016-7037\(86\)90071-2](http://dx.doi.org/10.1016/0016-7037(86)90071-2)
- Bachmann R, Glodny J, Oncken O (2009) Abandonment of the South Penninic–Austroalpine palaeosubduction zone, Central Alps, and shift from subduction erosion to accretion: constraints from Rb/Sr.
- Barany I, Karson JA (1989) Basaltic breccias of the Clipperton fracture zone (east Pacific): sedimentation and tectonics in a fast-slipping oceanic transform. *Geol Soc Am Bull* 101:204–220. doi: 10.1130/0016-7606(1989)101<0204:BBOTCF>2.3.CO;2
- Barbarand J, Pagel M (2001) Cathodoluminescence study of apatite crystals. *Am Mineral* 86:473–484.

## References

---

- Barnicoat AC, Cartwright I (1995) Focused fluid flow during subduction: Oxygen isotope data from high-pressure ophiolites of the western Alps. *Earth Planet Sci Lett* 132:53–61. doi: 10.1016/0012-821X(95)00040-J
- Bebout GE (1991) Geometry and mechanisms of fluid flow at 15 to 45 kilometer depths in an Early Cretaceous Accretionary Complex. *Geophys Res Lett* 18:923–926. doi: 10.1029/91GL00949
- Bebout GE, Barton MD (1989) Fluid flow and metasomatism in a subduction zone hydrothermal system: Catalina Schist terrane, California. *Geology* 17:976–980.
- Belousova E, Griffin WL, O'Reilly S (2002) Apatite as an indicator mineral for mineral exploration: trace-element compositions and their relationship to host rock type.
- Beltrando M, Rubatto D, Manatschal G (2010) From passive margins to orogens: The link between ocean-continent transition zones and (ultra) high-pressure metamorphism *Geology* 38:559-562
- Bennett VC, Nutman AP, McCulloch MT (1993) Nd isotopic evidence for transient, highly depleted mantle reservoirs in the early history of the Earth. *Earth Planet Sci Lett* 119:299–317. doi: 10.1016/0012-821X(93)90140-5
- Black LP, Kamo SL, Allen CM, et al (2003) TEMORA 1: a new zircon standard for Phanerozoic U–Pb geochronology. *Chem Geol* 200:155–170. doi: [http://dx.doi.org/10.1016/S0009-2541\(03\)00165-7](http://dx.doi.org/10.1016/S0009-2541(03)00165-7)
- Black LP et al. (2004) Improved  $^{206}\text{Pb}/^{238}\text{U}$  microprobe geochronology by the monitoring of a trace element-related matrix effect; SHRIMP, ID–TIMS, ELA–ICP–MS and oxygen isotope documentation for a series of zircon standards *Chem Geol* 205:115-140
- Blichert-Toft J, Frei R (2001) Complex Sm–Nd and Lu–Hf isotope systematics in metamorphic garnets from the Isua supracrustal belt, West Greenland. *Geochim Cosmochim Acta* 65:3177–3189. doi: [http://dx.doi.org/10.1016/S0016-7037\(01\)00680-9](http://dx.doi.org/10.1016/S0016-7037(01)00680-9)
- Boak J, Dymek RF (1982) Metamorphism of the ca. 3800 Ma supracrustal rocks at Isua, West Greenland: implications for early Archaean crustal evolution. *Earth Planet Sci Lett* 59:155–176. doi: [http://dx.doi.org/10.1016/0012-821X\(82\)90123-6](http://dx.doi.org/10.1016/0012-821X(82)90123-6)
- Bolhar R, Kamber BS, Moorbath S, et al (2004) Characterisation of early Archaean chemical sediments by trace element signatures. *Earth Planet Sci Lett* 222:43–60. doi: 10.1016/j.epsl.2004.02.016
- Bolhar R, Kamber BS, Moorbath S, et al (2005) Chemical characterization of earth's most ancient clastic metasediments from the Isua Greenstone Belt, southern West Greenland. *Cosmochim Acta* 69:1555–1573.
- Breecker DO, Sharp ZD (2007) A monazite oxygen isotope thermometer. *Am Mineral* 92:1561–1572. doi: 10.2138/am.2007.2367
- Breeding C, Ague JJ (2002) Slab-derived fluids and quartz-vein formation in an accretionary prism, Otago Schist, New Zealand.
- Brenan J (1993) Kinetics of fluorine, chlorine and hydroxyl exchange in fluorapatite. *Chem Geol* 110:195–210. doi: 10.1016/0009-2541(93)90254-G
- Breton N Le, Thompson AB (1988) Fluid-absent (dehydration) melting of biotite in metapelites in the early stages of crustal anatexis. *Contrib to Mineral Petrol* 99:226–237. doi: 10.1007/BF00371463
- Byrne T, Fisher D (1990) Evidence for a Weak and Overpressured Decollement Beneath Sediment-Dominated Accretionary Prisms. *J Geophys Res* 95:9081–9097. doi: 10.1029/JB095iB06p09081

- 
- Carr PA, Norman MD, Bennett VC (2017) Assessment of crystallographic orientation effects on secondary ion mass spectrometry (SIMS) analysis of cassiterite. *Chem Geol* 467:122–133. doi: 10.1016/j.chemgeo.2017.08.003
- Carrigan CW, Mukasa SB, Haydoutov I, Kolcheva K (2005) Age of Variscan magmatism from the Balkan sector of the orogen, central Bulgaria. *Lithos* 82:125–147. doi: 10.1016/j.lithos.2004.12.010
- Carry N, Gueydan F, Marquer D, Brun JP (2011) HP–UHP metamorphism as an indicator of slab dip variations in the Alpine arc *Int J Earth Sci* 100:1087–1094
- Cates NL, Mojzsis SJ (2006) Chemical and isotopic evidence for widespread Eoarchean metasedimentary enclaves in southern West Greenland. *Geochim Cosmochim Acta* 70:4229–4257. doi: 10.1016/j.gca.2006.05.014
- Çetinkaplan M, Candan O, Oberhänsli R, Bousquet R (2008) Pressure-temperature evolution of lawsonite eclogite in Sivrihisar; Tavşanlı Zone-Turkey. *Lithos* 104:12–32. doi: 10.1016/j.lithos.2007.11.007
- Chacko T, Cole DR, Horita J (2000) Chapter 7 - Natural abundance of the stable isotopes of C, O and H. *Stable Isot Hydrog Carbon Oxyg* 89–124. doi: 10.2307/1296391
- Chaussidon M, Uitterdijk Appel PW, Appel PWU (1997) Boron isotopic composition of tourmalines from the 3.8-Ga-old Isua supracrustals, West Greenland: implications on the  $\delta^{11}\text{B}$  value of early Archean seawater. *Chem Geol* 136:171–180. doi: 10.1016/S0009-2541(96)00140-4
- Cheng H, Nakamura E, Kobayashi K, Zhou Z (2007) Origin of atoll garnets in eclogites and implications for the redistribution of trace elements during slab exhumation in a continental subduction zone. *Am Mineral* 92:1119–1129. doi: 10.2138/am.2007.2343
- Cherniak D (2005) Uranium and manganese diffusion in apatite. *Chem Geol* 219:297–308. doi: 10.1016/j.chemgeo.2005.02.014
- Cherniak DJ, Zhang XY, Nakamura M, Watson EB (2004) Oxygen diffusion in monazite. *Earth Planet Sci Lett* 226:161–174. doi: 10.1016/j.epsl.2004.07.027
- Chopin C (1984) Coesite and Pure Pyrope in High-Grade Blueschists of the Western Alps - a 1st Record and Some Consequences *Contrib Mineral Petrol* 86:107–118 doi:Doi 10.1007/Bf00381838
- Chopin C, Monie P (1984) A Unique Magnesiochloritoid-Bearing, High-Pressure Assemblage from the Monte-Rosa, Western Alps - Petrologic and Ar-40-Ar-39 Radiometric Study *Contrib Mineral Petrol* 87:388–398 doi:Doi 10.1007/Bf00381295
- Chopin C, Schertl HP (1999) The UHP unit in the Dora-Maira massif, Western Alps *Int Geol Rev* 41:765–780
- Clarke GL, Powell R, Fitzherbert JA (2006) The lawsonite paradox: A comparison of field evidence and mineral equilibria modelling. *J Metamorph Geol* 24:715–725. doi: 10.1111/j.1525-1314.2006.00664.x
- Coggon R, Holland T (2002) Mixing properties of phengitic micas and revised garnet-phengite thermobarometers *J Metamorph Geol* 20:683–696
- Cogolu E, Krummenacher D (1967) Problemes geochronometriques dans la partie NW de l'Anatolie Centrale (Turquie). *Schweiz Miner Petrol Mitt* 47:825–833.
- Compagnoni R, Hirajima T (2001) Superzoned garnets in the coesite-bearing Brossasco-Isasca Unit, Dora-Maira massif, Western Alps, and the origin of the whiteschists *Lithos* 57:219–236 doi:Doi 10.1016/S0024-4937(01)00041-X

- Compagnoni R, Rolfo F, Groppo C, Hirajima T, Turello R (2012) Geological map of the ultra-high pressure Brossasco-Isasca unit (Western Alps, Italy) *Journal of Maps* 8:465-472
- Condie KC, Belousova E, Griffin WL, Sircombe KN (2009) Granitoid events in space and time: Constraints from igneous and detrital zircon age spectra. *Gondwana Res* 15:228–242. doi: 10.1016/j.gr.2008.06.001
- Costa F, Dohmen R, Chakraborty S (2008) time Scales of Magmatic Processes from Modeling the Zoning Patterns of Crystals. *Rev Mineral Geochemistry* 69:545–594. doi: 10.2138/rmg.2008.69.14
- Crank J (1975) Methods of Solution when the Diffusion Coefficient is Constant. In: *The mathematics of diffusion*. p 414
- Crowley JL (2003) U-Pb geochronology of 3810–3630 Ma granitoid rocks south of the Isua greenstone belt, southern West Greenland. *Precambrian Res* 126:235–257. doi: 10.1016/s0301-9268(03)00097-4
- Crowley JL, Myers J (2002) Timing and nature of multiple 3700–3600 Ma tectonic events in intrusive rocks north of the Isua greenstone belt, southern West Greenland.
- de Capitani C, Petrakakis K (2010) The computation of equilibrium assemblage diagrams with Theriak/Domino software *Am Mineral* 95:1006-1016
- Davis PB (2011) Petrotectonics of lawsonite eclogite exhumation: Insights from the Sivrihisar massif, Turkey. *Tectonics* 30:1–17. doi: 10.1029/2010TC002713
- Davis PB, Whitney DL (2006) Petrogenesis of lawsonite and epidote eclogite and blueschist, Sivrihisar Massif, Turkey. *J Metamorph Geol* 24:823–849. doi: DOI 10.1111/j.1525-1314.2006.00671.x
- Davis PB, Whitney DL (2008) Petrogenesis and structural petrology of high-pressure metabasalt pods, Sivrihisar, Turkey. *Contrib to Mineral Petrol* 156:217–241. doi: DOI 10.1007/s00410-008-0282-4
- Delaloye M, Bingol E (2000) Granitoids from Western and Northwestern Anatolia: Geochemistry and Modeling of Geodynamic Evolution. *Int Geol Rev* 42:241–268. doi: 10.1080/00206810009465081
- Didier A, Putlitz B, Baumgartner LP, et al (2017) Evaluation of potential monazite reference materials for oxygen isotope analyses by SIMS and laser assisted fluorination. *Chem Geol* 450:199–209. doi: 10.1016/j.chemgeo.2016.12.031
- Dilek Y, Thy P (2006) Age and petrogenesis of plagiogranite intrusions in the Ankara mélangé, central Turkey. *Isl Arc* 15:44–57. doi: 10.1111/j.1440-1738.2006.00522.x
- Dragovic B, Samanta LM, Baxter EF, Selverstone J (2012) Using garnet to constrain the duration and rate of water-releasing metamorphic reactions during subduction: An example from Sifnos, Greece. *Chem Geol* 314:9–22. doi: DOI 10.1016/j.chemgeo.2012.04.016
- Dymek RF, Boak J, Gromet L (1983) Average sedimentary rock rare Earth element patterns and crustal evolution: Some observations and implications from the 3800 Ma ISUA supracrustal belt, West Greenland.
- Eggins S, Kinsley PJ, Shelley MG (1998) Deposition and element fractionation processes during atmospheric pressure laser sampling for analysis by ICP-MS. *Appl Surf Sci* 127:278–286. doi: 10.1016/S0169-4332(97)00643-0
- Eiler J (2001) Oxygen isotope variations of basaltic lavas and upper mantle rocks.

- 
- Eiler JM, Baumgartner LP, Valley JW (1992) Intercrystalline stable isotope diffusion: a fast grain boundary model. *Contrib Miner Pet* 12:543–557.
- Elderfield H, Schultz a. (1996) Mid-Ocean Ridge Hydrothermal Fluxes and the Chemical Composition of the Ocean. *Annu Rev Earth Planet Sci* 24:191–224. doi: 10.1146/annurev.earth.24.1.191
- Errico JC, Barnes JD, Strickland A, Valley JW (2013) Oxygen isotope zoning in garnets from Franciscan eclogite blocks: Evidence for rock-buffered fluid interaction in the mantle wedge. *Contrib to Mineral Petrol* 166:1161–1176. doi: 10.1007/s00410-013-0915-0
- Etheridge MA, Wall VJ, Cox SF, Vernon RH (1984) High fluid pressures during regional metamorphism and deformation: Implications for mass transport and deformation mechanisms. *J Geophys Res* 89:4344–4358. doi: 10.1029/JB089iB06p04344
- Ewing TA, Rubatto D, Beltrando M, Hermann J (2015) Constraints on the thermal evolution of the Adriatic margin during Jurassic continental break-up: U-Pb dating of rutile from the Ivrea-Verbano Zone, Italy. *Contrib to Mineral Petrol*. doi: 10.1007/s00410-015-1135-6
- Ewing TA, Rubatto D, Eggins S (2009) In situ measurement of Hf isotopes in rutile by LA-MC-ICPMS. *Geochim Cosmochim Acta* 73:A347–A347.
- Ewing TA, Rubatto D, Eggins SM, Hermann J (2011) In situ measurement of hafnium isotopes in rutile by LA-MC-ICPMS: Protocol and applications. *Chem Geol* 281:72–82. doi: 10.1016/j.chemgeo.2010.11.029
- Farver JR, Giletti BJ (1989) Oxygen and strontium diffusion kinetics in apatite and potential applications to thermal history determinations. *Geochim Cosmochim Acta* 53:1621–1631. doi: [http://dx.doi.org/10.1016/0016-7037\(89\)90243-3](http://dx.doi.org/10.1016/0016-7037(89)90243-3)
- Faryad SW, Kláková H, Nosál L (2010) Mechanism of formation of atoll garnet during high-pressure metamorphism. *Mineral Mag* 74:111–126. doi: 10.1180/minmag.2010.074.1.111
- Ferrando S (2012) Mg-metasomatism of metagranitoids from the Alps: genesis and possible tectonic scenarios *Terra Nova* 24:423–436
- Ferrando S, Frezzotti ML, Petrelli M, Compagnoni R (2009) Metasomatism of continental crust during subduction: the UHP whiteschists from the Southern Dora-Maira Massif (Italian Western Alps) *J Metamorph Geol* 27:739–756 doi:DOI 10.1111/j.1525-1314.2009.00837.x
- Ferry JM, Ushikubo T, Kita NT, Valley JW (2010) Assessment of grain-scale homogeneity and equilibration of carbon and oxygen isotope compositions of minerals in carbonate-bearing metamorphic rocks by ion microprobe. *Geochim Cosmochim Acta* 74:6517–6540. doi: 10.1016/j.gca.2010.08.039
- Ferry JM, Kitajima K, Strickland A, Valley JW (2014) Ion microprobe survey of the grain-scale oxygen isotope geochemistry of minerals in metamorphic rocks. *Geochim Cosmochim Acta* 144:403–433. doi: 10.1016/j.gca.2014.08.021
- Ferry JM, Spear FS (1978) Experimental calibration of the partitioning of Fe and Mg between biotite and garnet. *Contrib to Mineral Petrol* 66:113–117. doi: 10.1007/BF00372150
- Ford M, Duchêne S, Gasquet D, Vanderhaeghe O (2006) Two-phase orogenic convergence in the external and internal SW Alps *J Geol Soc London* 163:815–826
- Fornash KF, Cosca MA, Whitney DL (2016) Tracking the timing of subduction and exhumation using  $^{40}\text{Ar}/^{39}\text{Ar}$  phengite ages in blueschist- and eclogite-facies rocks (Sivrihisar, Turkey). *Contrib to Mineral Petrol*. doi: 10.1007/s00410-016-1268-2

- Fortier SM, Lüttge A (1995) An experimental calibration of the temperature dependence of oxygen isotope fractionation between apatite and calcite at high temperatures (350–800°C). *Chem Geol* 125:281–290. doi: 10.1016/0009-2541(95)00084-Y
- Fouillac AM, Javoy M (1988) Oxygen and hydrogen isotopes in the volcano-sedimentary complex of Huelva (Iberian Pyrite Belt): example of water circulation through a volcano-sedimentary sequence. *Earth Planet Sci Lett* 87:473–484. doi: 10.1016/0012-821X(88)90010-6
- François C, Philippot P, Rey PF, Rubatto D (2014) Burial and exhumation during Archean sagduction in the East Pilbara Granite-Greenstone Terrane. *Earth Planet Sci Lett* 396:235–251. doi: 10.1016/j.epsl.2014.04.025
- Franz L, Romer RL, de Capitani C (2013) Protoliths and phase petrology of whiteschists *Contrib Mineral Petrol* 166:255-274
- Frezzotti M, Selverstone J, Sharp Z, Compagnoni R (2011) Carbonate dissolution during subduction revealed by diamond-bearing rocks from the Alps *Nat Geosci* 4:703-706
- Friend CRL, Nutman AP (2005) Complex 3670–3500 Ma orogenic episodes superimposed on juvenile crust accreted between 3850 and 3690 Ma, Itsaq Gneiss Complex, southern West Greenland.
- Froitzheim N, Manatschal G (1996) Kinematics of Jurassic rifting, mantle exhumation, and passive-margin formation in the Austroalpine and Penninic nappes (eastern Switzerland). *Geol Soc Am Bull* 108:1120–1133. doi: 10.1130/0016-7606(1996)108<1120:KOJRME>2.3.CO;2
- Furnes H, de Wit M, Staudigel H, et al (2007) A vestige of Earth's oldest ophiolite. *Science* (80- ) 315:1704–1707. doi: 10.1126/science.1139170
- Ganguly J, Tirone M (1999) Diffusion closure temperature and age of a mineral with arbitrary extent of diffusion: Theoretical formulation and applications. *Earth Planet Sci Lett* 170:131–140. doi: 10.1016/S0012-821X(99)00089-8
- Ganguly J, Tirone M (2001) Relationship between cooling rate and cooling age of a mineral: Theory and applications to meteorites. *Meteorit Planet Sci* 36:167–1. doi: 10.1111/j.1945-5100.2001.tb01817.x
- Gauthiez-Putallaz L, Rubatto D, Hermann J (2016) Dating prograde fluid pulses during subduction by in situ U-Pb and oxygen isotope analysis. *Contrib to Mineral Petrol* 171:1–20. doi: 10.1007/s00410-015-1226-4
- Gautier Y (1984) Deformation et métamorphismes associés à la suture Thethysienne en Anatolie centrale (Région de Sivrihisar, Turquie). Université d'Orsay, Paris
- Gebauer D, Schertl HP, Brix M, Schreyer W (1997) 35 Ma old ultrahigh-pressure metamorphism and evidence for very rapid exhumation in the Dora Maira Massif, Western Alps *Lithos* 41:5-24 doi:Doi 10.1016/S0024-4937(97)82002-6
- Geisler T, Schaltegger U, Tomaschek F (2007) Re-equilibration of zircon in aqueous fluids and melts *Elements* 3:43-50
- Gökten E, Floyd PA (2007) Stratigraphy and geochemistry of pillow basalts within the ophiolitic mélange of the Izmir-Ankara-Erzincan suture zone: Implications for the geotectonic character of the northern branch of Neotethys. *Int J Earth Sci* 96:725–741. doi: 10.1007/s00531-006-0132-4
- Göncüoğlu MC, Yaliniz MK, Tekin UK (2006) Geochemistry, tectono-magmatic discrimination and radiolarian ages of basic extrusives within the Izmir-Ankara Suture Belt (NW Turkey): Time constraints for the neotethyan evolution. *Ofioliti* 31:25–38.

- 
- Gregory CJ, Rubatto D, Allen CM, et al (2007) Allanite micro-geochronology: A LA-ICP-MS and SHRIMP U-Th-Pb study. *Chem Geol* 245:162–182. doi: 10.1016/j.chemgeo.2007.07.029
- Gregory RT, Taylor HP (1981) An oxygen isotope profile in a section of Cretaceous oceanic crust, Samail Ophiolite, Oman: Evidence for  $\delta^{18}\text{O}$  buffering of the oceans by deep (>5 km) seawater-hydrothermal circulation at mid-ocean ridges. *J Geophys Res Solid Earth* 86:2737–2755. doi: 10.1029/JB086iB04p02737
- Grevel C, Schreyer W, Grevel KD, Schertl HP, Willner AP (2009) REE distribution, mobilization and fractionation in the coesite-bearing 'pyrope quartzite' and related rocks of the Dora-Maira Massif, Western Alps *Eur J Mineral* 21:1213-1224 doi:Doi 10.1127/0935-1221/2009/0021-1967
- Grew E, Dymek RF, De Hoog JCM, et al (2015) Boron isotopes in tourmaline from the ca. 3.7-3.8Ga Isua supracrustal belt, Greenland: Sources for boron in Eoarchean continental crust and seawater. *Geochim Cosmochim Acta* 163:156–177. doi: 10.1016/j.gca.2015.04.045
- Grimes CB, Ushikubo T, Kozdon R, Valley JW (2013) Perspectives on the origin of plagiogranite in ophiolites from oxygen isotopes in zircon. *Lithos* 179:48–66. doi: 10.1016/j.lithos.2013.07.026
- Groppo C, Castelli D (2010) Prograde P-T evolution of a lawsonite eclogite from the Monviso meta-ophiolite (Western Alps): Dehydration and redox reactions during subduction of oceanic FeTi-oxide gabbro. *J Petrol* 51:2489–2514. doi: 10.1093/petrology/egq065
- Gruau G, Rosing MT, Bridgwater D, Gill R (1996) Resetting of Sm -- Nd systematics during metamorphism of > 3.7-Ga rocks: implications for isotopic models of early Earth differentiation. *Chem Geol* 133:225–240. doi: 10.1016/S0009-2541(96)00092-7
- Hacker BR (2008) H<sub>2</sub>O subduction beyond arcs. *Geochemistry, Geophys Geosystems*. doi: 10.1029/2007GC001707
- Hacker BR, Peacock SM, Abers GA, Holloway SD (2003) Subduction factory 2. Are intermediate-depth earthquakes in subducting slabs linked to metamorphic dehydration reactions? *J Geophys Res Solid Earth*. doi: 10.1029/2001JB001129
- Hammerli J, Kemp AIS, Spandler CJ (2014) Neodymium isotope equilibration during crustal metamorphism revealed by in situ microanalysis of REE-rich accessory minerals. *Earth Planet Sci Lett* 392:133–142. doi: 10.1016/j.epsl.2014.02.018
- Harper C, Jacobsen S (1992) Evidence from coupled <sup>147</sup>Sm–<sup>143</sup>Nd and <sup>146</sup>Sm–<sup>142</sup>Nd systematics for very early (4.5-Gyr) differentiation of the Earth's mantle. *Lett to Nat* 360:728–732. doi: 10.1038/360728a0
- Harrison TM, Wielicki MM (2016) From the Hadean to the Himalaya: 4.4 Ga of felsic terrestrial magmatism. *Am Mineral* 101:1348–1359. doi: 10.2138/am-2016-5516
- Hattori KH, Guillot S (2007) Geochemical character of serpentinites associated with high- to ultrahigh-pressure metamorphic rocks in the Alps, Cuba, and the Himalayas: Recycling of elements in subduction zones. *Geochemistry, Geophys Geosystems* 8:n/a-n/a. doi: 10.1029/2007GC001594
- Hayashi M, Komiya T, Nakamura Y, Maruyama S (2000) Archean Regional Metamorphism of the Isua Supracrustal Belt, Southern West Greenland: Implications for a Driving Force for Archean Plate Tectonics. *Int Geol Rev* 42:1055–1115. doi: 10.1080/00206810009465128

- Hermann J, Rubatto D (2003) Relating zircon and monazite domains to garnet growth zones: age and duration of granulite facies metamorphism in the Val Malenco lower crust. *J Metamorph Geol* 21:833–852.
- Hermann J, Rubatto D (2009) Accessory phase control on the trace element signature of sediment melts in subduction zones. *Chem Geol* 265:512–526. doi: 10.1016/j.chemgeo.2009.05.018
- Hermann J, Rubatto D, Korsakov A, Shatsky VS (2001) Multiple zircon growth during fast exhumation of diamondiferous, deeply subducted continental crust (Kokchetav Massif, Kazakhstan) *Contrib Mineral Petrol* 141:66–82
- Hermann J, Rubatto D (2014) 4.9—subduction of continental crust to mantle depth: geochemistry of ultrahigh-pressure rocks *Treatise on geochemistry*, 2nd edn Elsevier, Oxford:309–340
- Hiess J, Bennett VC, Nutman AP, Williams IS (2009) In situ U–Pb, O and Hf isotopic compositions of zircon and olivine from Eoarchaeon rocks, West Greenland: New insights to making old crust. *Geochim Cosmochim Acta* 73:4489–4516.
- Hiess J, Bennett VC, Nutman AP, Williams IS (2011) Archaean fluid-assisted crustal cannibalism recorded by low  $\delta^{18}\text{O}$  and negative  $\epsilon\text{Hf}(T)$  isotopic signatures of West Greenland granite zircon. *Contrib to Mineral Petrol* 161:1027–1050. doi: 10.1007/s00410-010-0578-z
- Hilaret N, Reynard B (2009) Stability and dynamics of serpentinite layer in subduction zone. *Tectonophysics* 465:24–29. doi: 10.1016/j.tecto.2008.10.005
- Hoffmann J, Münker C, Polat A, et al (2010) Highly depleted Hadean mantle reservoirs in the sources of early Archean arc-like rocks, Isua supracrustal belt, southern West Greenland. *Cosmochim Acta* 74:7236–7260. doi: 10.1016/j.gca.2010.09.027
- Holland T, Powell R (1998) An internally consistent thermodynamic data set for phases of petrological interest *J Metamorph Geol* 16:309–343
- Hoskin PWO, Schaltegger U (2003) The composition of zircon and igneous and metamorphic petrogenesis. *Rev Mineral geochemistry* 53:27–62.
- Huberty JM, Kita NT, Kozdon R, et al (2010) Crystal orientation effects in  $\delta^{18}\text{O}$  for magnetite and hematite by SIMS. *Chem Geol* 276:269–283. doi: 10.1016/j.chemgeo.2010.06.012
- Hu G, Clayton RN (2003) Oxygen isotope salt effects at high pressure and high temperature and the calibration of oxygen isotope geothermometers *Geochimica et Cosmochimica Acta* 67:3227–3246
- Ickert RB et al (2008) Determining high precision, in situ, oxygen isotope ratios with a SHRIMP II: analyses of MPI-DING silicate-glass reference materials and zircon from contrasting granites. *Chem Geol* 257:114–128. doi: 10.1016/j.chemgeo.2008.08.024
- Ito M, Ganguly J (2006) Diffusion kinetics of Cr in olivine and  $^{53}\text{Mn}$ – $^{53}\text{Cr}$  thermochronology of early solar system objects.
- Jacobsen S, Dymek RF (1988) Nd and Sr isotope systematics of clastic metasediments from Isua, West Greenland: Identification of pre-3.8 Ga Differentiated Crustal Components. *J Geophys Res* 93:338.
- Janots E, Negro F, Brunet F, et al (2006) Evolution of the REE mineralogy in HP-LT metapelites of the Sebide complex, Rif, Morocco: Monazite stability and geochronology. *Lithos* 87:214–234. doi: 10.1016/j.lithos.2005.06.008
- Janots E, Engi M, Berger A, et al (2008) Prograde metamorphic sequence of REE minerals in pelitic rocks of the Central Alps: Implications for allanite-monazite-xenotime phase



- 
- relations from 250 to 610°C. *J Metamorph Geol* 26:509–526. doi: 10.1111/j.1525-1314.2008.00774.x
- Jeon H, Williams IS, Chappell BW (2012) Magma to mud to magma: Rapid crustal recycling by Permian granite magmatism near the eastern Gondwana margin *Earth and Planetary Science Letters* 319–320:104–117 doi:<http://dx.doi.org/10.1016/j.epsl.2011.12.010>
- Jochum KP, Weis U, Stoll B, et al (2011) Determination of reference values for NIST SRM 610–617 glasses following ISO guidelines. *Geostand Geoanalytical Res* 35:397–429.
- John T, Scherer EE, Haase K, Schenk V (2004) Trace element fractionation during fluid-induced eclogitization in a subducting slab: Trace element and Lu-Hf-Sm-Nd isotope systematics. *Earth Planet Sci Lett* 227:441–456. doi: 10.1016/j.epsl.2004.09.009
- John T, Scherer EE, Schenk V, et al (2010) Subducted seamounts in an eclogite-facies ophiolite sequence: The Andean Raspas Complex, SW Ecuador. *Contrib to Mineral Petrol* 159:265–284. doi: 10.1007/s00410-009-0427-0
- John T et al. (2012) Volcanic arcs fed by rapid pulsed fluid flow through subducting slabs *Nat Geosci* 5:489–492
- Jonas L, John T, King HE, et al (2014) The role of grain boundaries and transient porosity in rocks as fluid pathways for reaction front propagation. *Earth Planet Sci Lett* 386:64–74. doi: 10.1016/j.epsl.2013.10.050
- Kaczmarek M-A, Müntener O, Rubatto D (2008) Trace element chemistry and U–Pb dating of zircons from oceanic gabbros and their relationship with whole rock composition (Lanzo, Italian Alps). *Contrib to Mineral Petrol* 155:295–312. doi: 10.1007/s00410-007-0243-3
- Kaczmarek M-A, Reddy SM, Nutman AP, et al (2016) Earth’s oldest mantle fabrics indicate Eoarchean subduction. *Nat Commun* 7:10665. doi: 10.1038/ncomms10665
- Kamber BS, Whitehouse MJ, Bolhar R (2005) Volcanic resurfacing and the early terrestrial crust: zircon U–Pb and REE constraints from the Isua Greenstone Belt, southern West Greenland. *Earth Planet* 240:276–290.
- Kaya O, Helvacı H, Kozur H, Sadeddin W (2001) Late Norian conodont age for a metacarbonate unit in NW Anatolia, Turkey. *Geobios* 34:527–532.
- Kemp AIS, Wilde SA, Hawkesworth C, et al (2010) Hadean crustal evolution revisited: New constraints from Pb-Hf isotope systematics of the Jack Hills zircons. *Earth Planet Sci Lett* 296:45–56. doi: 10.1016/j.epsl.2010.04.043
- Kessel R, Schmidt MW, Ulmer P, Pettke T (2005) Trace element signature of subduction-zone fluids, melts and supercritical liquids at 120–180 km depth. *Nature* 437:724–727. doi: 10.1038/nature03971
- King RL, Bebout GE, Moriguti T, Nakamura E (2006) Elemental mixing systematics and Sr-Nd isotope geochemistry of mélange formation: Obstacles to identification of fluid sources to arc volcanics. *Earth Planet Sci Lett* 246:288–304. doi: 10.1016/j.epsl.2006.03.053
- Kita NT, Huberty JM, Kozdon R, et al (2011) High-precision SIMS oxygen, sulfur and iron stable isotope analyses of geological materials: Accuracy, surface topography and crystal orientation. In: *Surface and Interface Analysis*. pp 427–431
- Kohn MJ (1993) Modeling of prograde mineral  $\delta^{18}\text{O}$  changes in metamorphic systems. *Contrib to Mineral Petrol* 113:249–261.
- Kohn MJ, Valley JW, Elsenheimer D, Spicuzza MJ (1993) O isotope zoning in garnet and staurolite: evidence for closed- system mineral growth during regional metamorphism. *Am. Mineral.* 78:988–1001.

- Kohn MJ, Corrie SL, Markley C (2015) The fall and rise of metamorphic zircon *Am Mineral* 100:897-908
- Kolodner K, Avigad D, McWILLIAMS M, et al (2006) Provenance of north Gondwana Cambrian–Ordovician sandstone: U–Pb SHRIMP dating of detrital zircons from Israel and Jordan. *Geol Mag* 143:367. doi: 10.1017/S0016756805001640
- Komiya T, Maruyama S, Masuda T, et al (1999) Plate tectonics at 3.8–3.7 Ga: field evidence from the Isua accretionary complex, southern West Greenland. *J* 107:515–554. doi: 10.1086/314371
- Komiya T, Hayashi M, Maruyama S, Yurimoto H (2002) Intermediate-P/T type Archean metamorphism of the Isua supracrustal belt: Implications for secular change of geothermal gradients at subduction zones and for Archean plate tectonics. *Am J Sci* 302:806–826. doi: 10.2475/ajs.302.9.806
- Konrad-Schmolke M, O’Brien PJ, Heidelbach F (2007) Compositional re-equilibration of garnet: the importance of sub-grain boundaries. *Eur J Mineral* 19:431–438. doi: 10.1127/0935-1221/2007/0019-1749
- Kusebauch C, John T, Whitehouse MJ, et al (2015) Distribution of halogens between fluid and apatite during fluid-mediated replacement processes. *Geochim Cosmochim Acta* 170:225–246. doi: 10.1016/j.gca.2015.08.023
- Kylander-Clark AR, Hacker BR, Mattinson CG (2012) Size and exhumation rate of ultrahigh-pressure terranes linked to orogenic stage Earth and Planetary Science Letters 321:115–120
- Lackey JS, Valley JW, Chen JH, Stockli DF (2008) Dynamic magma systems, crustal recycling, and alteration in the central Sierra Nevada batholith: the oxygen isotope record *J Petrol* 49:1397-1426
- Lackey JS, Valley JW, Hinke HJ (2006) Deciphering the source and contamination history of peraluminous magmas using  $\delta^{18}\text{O}$  of accessory minerals: examples from garnet-bearing plutons of the Sierra Nevada batholith *Contrib Mineral Petrol* 151:20-44
- Lapen TJ, Johnson CM, Baumgartner LP, Mahlen NJ, Beard BL, Amato JM (2003) Burial rates during prograde metamorphism of an ultra-high-pressure terrane: an example from Lago di Cignana, western Alps, Italy *Earth and Planetary Science Letters* 215:57-72
- Lawrence J, Taylor HP (1971) Deuterium and oxygen-18 correlation: Clay minerals and hydroxides in Quaternary soils compared to meteoric waters.
- Le Bas MJ, Le Maitre RW, Streckeisen A, Zanettin B (1986) A chemical classification of volcanic rocks based on the total alkali silica diagram. *J Petrol* 27:745–750. doi: 10.1093/petrology/27.3.745
- Li H, Hermann J (2015) Apatite as an indicator of fluid salinity: An experimental study of chlorine and fluorine partitioning in subducted sediments. *Geochim Cosmochim Acta* 166:267–297. doi: 10.1016/j.gca.2015.06.029
- Li X, Rusk B, Wang R, et al (2011) Rutile inclusions in quartz crystals record decreasing temperature and pressure during the exhumation of the Su-Lu UHP metamorphic belt in Donghai, East China. *Am Mineral* 96:964–973. doi: 10.2138/am.2011.3574
- Liu F, Liou J (2011) Zircon as the best mineral for P–T–time history of UHP metamorphism: A review on mineral inclusions and U–Pb SHRIMP ages of zircons from the Dabie–Sulu UHP rocks *J Asian Earth Sci* 40:1-39
- Liu Y, Santosh M, Yuan T, et al (2016) Reduction of buried oxidized oceanic crust during subduction. *Gondwana Res* 32:11–23. doi: 10.1016/j.gr.2015.02.014

- 
- Ludwig K (2009) SQUID 2 (rev. 2.50): A User's Manual Berkeley Geochronology Center Spec Pub 5:104p
- Ludwig KR (2012) User's Manual for Isoplot 3.75. A Geochronological Toolkit for Microsoft Excel. Berkeley Geochronol Center Spec Pub 5:75p.
- Lyon IC, Saxton JM, Turner GF, Hinton RW (1994) Isotopic fractionation in secondary ionization mass spectrometry. *Rapid Commun Mass Spectrom* 8:837–843. doi: 10.1016/S0168-1176(97)00143-2
- Manning CE (2004) The chemistry of subduction-zone fluids *Earth and Planetary Science Letters* 223:1-16
- Marschall HR, Schumacher JC (2012) Arc magmas sourced from mélange diapirs in subduction zones. *Nat Geosci* 5:862–867. doi: 10.1038/ngeo1634
- Martin LAJ, Balleve M, Boulvais P, et al (2011a) Garnet re-equilibration by coupled dissolution–reprecipitation: evidence from textural, major element and oxygen isotope zoning of “cloudy” garnet. *J Metamorph Geol* 29:213–231.
- Martin LAJ, Duchêne S, Deloule É, Vanderhaeghe O (2008) Mobility of trace elements and oxygen in zircon during metamorphism: Consequences for geochemical tracing. *Earth Planet Sci Lett* 267:161–174. doi: 10.1016/j.epsl.2007.11.029
- Martin LAJ, Hermann J, Gauthiez-Putallaz L, et al (2014a) Lawsonite geochemistry and stability - implication for trace element and water cycles in subduction zones. *J Metamorph Geol* 32:455–478. doi: 10.1111/jmg.12093
- Martin LAJ, Rubatto D, Crépisson C, et al (2014b) Garnet oxygen analysis by SHRIMP-SI: matrix corrections and application to high pressure metasomatic rocks from Alpine Corsica. *Chem Geol* 374:25–36.
- Martin LAJ, Rubatto D, Vitale Brovarone A, Hermann J (2011) Late Eocene lawsonite-eclogite facies metasomatism of a granulite sliver associated to ophiolites in Alpine Corsica. *Lithos* 125:620–640.
- Massonne H-J, Kennedy a., Nasdala L, Theye T (2007) Dating of zircon and monazite from diamondiferous quartzofeldspathic rocks of the Saxonian Erzgebirge – hints at burial and exhumation velocities. *Mineral Mag* 71:407–425. doi: 10.1180/minmag.2007.071.4.407
- Mattey D, Jackson DH, Harris NBW, Kelley S (1994) Isotopic constraints on fluid infiltration from an eclogite facies shear zone, Holsenøy, Norway. *J Metamorph Geol* 12:311–325. doi: 10.1111/j.1525-1314.1994.tb00025.x
- McCaig AM, Cliff RA, Escartin J, Fallick AE, MacLeod CJ (2007) Oceanic detachment faults focus very large volumes of black smoker fluids *Geology* 35:935-938
- Meschede M (1986) A method of discriminating between different types of mid-ocean ridge basalts and continental tholeiites with the Nb-Zr-Y diagram. *Chem Geol* 56:207–218. doi: 10.1016/0009-2541(86)90004-5
- Miller JA, Cartwright I (2000) Distinguishing between seafloor alteration and fluid flow during subduction using stable isotope geochemistry: Examples from Tethyan ophiolites in the Western Alps. *J Metamorph Geol* 18:467–482. doi: 10.1046/j.1525-1314.2000.00274.x
- Miller JA, Cartwright I, Buick IS, Barnicoat AC (2001) An O-isotope profile through the HP–LT Corsican ophiolite, France and its implications for fluid flow during subduction. *Chem Geol* 178:43–69. doi: 10.1016/S0009-2541(00)00428-9

- Mojzsis SJ, Harrison TM, Pidgeon RT (2001) Oxygen-isotope evidence from ancient zircons for liquid water at the Earth's surface 4,300 Myr ago. *Nature* 409:178–181. doi: 10.1038/35051557
- Mojzsis SJ, Coath C, Greenwood J, et al (2003) Mass-independent isotope effects in Archean (2.5 to 3.8 Ga) sedimentary sulfides determined by ion microprobe analysis. *Geochim Cosmochim Acta* 67:1635–1658. doi: 10.1016/S0016-7037(00)00059-0
- Morton A, Yaxley G (2007) Detrital apatite geochemistry and its application in provenance studies. *Geol Soc Am Spec Pap* 420 420:319–344. doi: 10.1130/2006.2420(19).
- Muehlenbachs K, Clayton RN (1972) Oxygen isotope geochemistry of submarine greenstones. *Canadian Journal of Earth Sciences* 9:471–478
- Mulcahy SR, Vervoort JD, Renne PR (2014) Dating subduction-zone metamorphism with combined garnet and lawsonite Lu-Hf geochronology. *J Metamorph Geol* 32:515–533. doi: 10.1111/jmg.12092
- Nutman AP, Allaart JH, Bridgwater D, et al (1984) Stratigraphic and geochemical evidence for the depositional environment of the early archaean isua supracrustal belt, southern west greenland. *Precambrian Res* 25:365–396. doi: 10.1016/0301-9268(84)90010-X
- Nutman AP, Bridgwater D (1986) Early Archaean Amitsoq tonalites and granites of the Isukasia area, southern West Greenland: development of the oldest-known sial. *Contrib to Mineral Petrol* 94:137–148
- Nutman AP, Bennett VC, Friend CRL, Rosing MT (1997) ~ 3710 and ≳ 3790 Ma volcanic sequences in the Isua (Greenland) supracrustal belt; structural and Nd isotope implications. *Chem Geol* 141:271–287. doi: [http://dx.doi.org/10.1016/S0009-2541\(97\)00084-3](http://dx.doi.org/10.1016/S0009-2541(97)00084-3)
- Nutman AP, Friend CRL, Bennett VC (2002) Evidence for 3650–3600 Ma assembly of the northern end of the Itsaq Gneiss Complex, Greenland: Implication for early Archaean tectonics. *Tectonics* 21:1005. doi: 10.1029/2000tc001203
- Nutman AP, Friend CRL (2009) New 1:20,000 scale geological maps, synthesis and history of investigation of the Isua supracrustal belt and adjacent orthogneisses, southern West Greenland: A glimpse of Eoarchaean crust formation and orogeny. *Precambrian Res* 172:189–211. doi: <http://dx.doi.org/10.1016/j.precamres.2009.03.017>
- Nutman AP, Bennett VC, Friend CRL, et al (2014) The Itsaq gneiss complex of Greenland: Episodic 3900 to 3660 Ma juvenile crust formation and recycling in the 3660 to 3600 Ma Isukasian orogeny. *Am J Sci*. doi: 10.2475/09.2013.03
- Nutman AP, Bennett VC, Chivas AR, et al (2015a) 3806Ma Isua rhyolites and dacites affected by low temperature Eoarchaean surficial alteration: Earth's earliest weathering. *Precambrian Res* 268:323–338. doi: 10.1016/j.precamres.2015.07.014
- Nutman AP, Bennett VC, Friend CRL (2015b) The emergence of the Eoarchaean proto-arc: Evolution of a c. 3700 Ma convergent plate boundary at Isua, southern West Greenland. *J Geol Soc London* 389:113–133
- Nutman AP, Bennett VC, Friend CRL (2015c) Proposal for a continent “Itsaqia” amalgamated at 3.66 Ga and rifted apart from 3.53 Ga: Initiation of a Wilson cycle near the start of the rock record. *Am J Sci* 315:509–536. doi: 10.2475/06.2015.01
- Nutman AP, Bennett VC, Friend CRL, et al (2016) Rapid emergence of life shown by discovery of 3,700-million-year-old microbial structures. *Nature* 1–12. doi: 10.1038/nature19355

- 
- Okay AI (1980) Mineralogy, Petrology, and Phase-Relations of Glaucophane-Lawsonite Zone Blue Schists from the Tavsanli Region, Northwest Turkey. *Contrib to Mineral Petrol* 72:243–255. doi: [Doi 10.1007/Bf00376143](https://doi.org/10.1007/Bf00376143)
- Okay AI (1984) Distribution and characteristics of the north-west Turkish blueschists. *Geol. Soc. Spec. Publ.* 17:455–466.
- Okay AI (1986) High-pressure/low-temperature metamorphic rocks of Turkey. In: *Geological Society of America Memoirs*. Geological Society of America, pp 333–347
- Okay AI (2002) Jadeite-chloritoid-glaucophane-lawsonite blueschists in northwest Turkey: Unusually high P/T ratios in continental crust. *J Metamorph Geol* 20:757–768. doi: [10.1046/j.1525-1314.2002.00402.x](https://doi.org/10.1046/j.1525-1314.2002.00402.x)
- Okay AI, Kelley S (1994) Tectonic setting, petrology and geochronology of jadeite+ glaucophane and chloritoid+ glaucophane schists from north-west Turkey. *J Metamorph Geol* 12:455–466.
- Okay AI, Satir M, Shang CK (2008) Ordovician metagranitoid from the Anatolide-Tauride Block, northwest Turkey: Geodynamic implications. *Terra Nov* 20:280–288. doi: [10.1111/j.1365-3121.2008.00818.x](https://doi.org/10.1111/j.1365-3121.2008.00818.x)
- Okay AI, Whitney DL (2010) Blueschists, eclogites, ophiolites and suture zones in northwest turkey: A review and a field excursion guide. *Ofioliti* 35:131–172.
- Oliver NHS, Bons PD (2001) Mechanisms of fluid flow and fluid-rock interaction in fossil metamorphic hydrothermal systems inferred from vein-wallrock patterns, geometry and microstructure. *Geofluids* 1:137–162. doi: [10.1046/j.1468-8123.2001.00013.x](https://doi.org/10.1046/j.1468-8123.2001.00013.x)
- Önen A (2003) Neotethyan ophiolitic rocks of the Anatolides of NW Turkey and comparison with Tauride ophiolites. *J Geol Soc London* 160:947–962
- Otamendi JE, Jesús D, Douce AEP, Castro A (2002) Rayleigh fractionation of heavy rare earths and yttrium during metamorphic garnet growth. *Geology* 30:159–162.
- Özbey Z, Ustaömer T, Robertson AHF, Ozbey Z (2013) Mesozoic magmatic and sedimentary development of the Tavşanlı Zone (NW Turkey): implications for rifting, passive margin development and ocean crust emplacement. *Geol Soc London, Spec Publ* 372:141–165. doi: [10.1144/SP372.17](https://doi.org/10.1144/SP372.17)
- Page FZ, Ushikubo T, Kita NT, et al (2007) High-precision oxygen isotope analysis of picogram samples reveals 2 um gradients and slow diffusion in zircon. *Am Mineral* 92:1772–1775. doi: [10.2138/am.2007.2697](https://doi.org/10.2138/am.2007.2697)
- Page FZ, Kita NT, Valley JW (2010) Ion microprobe analysis of oxygen isotopes in garnets of complex chemistry. *Chem Geol* 270:9–19. doi: <http://dx.doi.org/10.1016/j.chemgeo.2009.11.001>
- Page FZ, Essene EJ, Mukasa SB, Valley JW (2014) A garnet-zircon oxygen isotope record of subduction and exhumation fluids from the Franciscan complex, California. *J Petrol* 55:103–131. doi: [10.1093/petrology/egt062](https://doi.org/10.1093/petrology/egt062)
- Pagé L, Hattori KH, de Hoog JCM, Okay AI (2016) Halogen (F, Cl, Br, I) behaviour in subducting slabs: A study of lawsonite blueschists in western Turkey. *Earth Planet Sci Lett* 442:133–142. doi: [10.1016/j.epsl.2016.02.054](https://doi.org/10.1016/j.epsl.2016.02.054)
- Paquette JL, Montel JM, Chopin C (1999) U-Th-Pb dating of the Brossasco ultrahigh-pressure metagranite, Dora-Maira massif, western Alps. *Eur J Mineral* 11:69–77
- Paton C, Hellstrom J, Paul B, et al (2011) Iolite: Freeware for the visualisation and processing of mass spectrometric data. *J Anal At Spectrom* 26:2508–2518. doi: [10.1039/c1ja10172b](https://doi.org/10.1039/c1ja10172b)

- Peacock SA (1990) Fluid Processes in Subduction Zones. *Science* (80- ) 248:329–337. doi: 10.1126/science.248.4953.329
- Pearce JA (1996) A user's guide to basalt discrimination diagrams. In: Wyman, D.A., Ed., *Trace Element Geochemistry of Volcanic Rocks: Applications for Massive Sulphide Exploration*, Geological Association of Canada, Short Course Notes, Vol. 12, 79-113.
- Pearce JA, Cann JR (1973) Tectonic setting of basic volcanic rocks determined using trace element analyses. *Earth Planet Sci Lett* 19:290–300. doi: 10.1016/0012-821X(73)90129-5
- Pearce JA, Peate DW (1995) Tectonic Implications of the Composition of Volcanic ARC Magmas. *Annu Rev Earth Planet Sci* 23:251–285. doi: 10.1146/annurev.ea.23.050195.001343
- Pearce NJG, Perkins WT, Westgate JA, et al (1997) A compilation of new and published major and trace element data for NIST SRM 610 and NIST SRM 612 glass reference materials. *Geostand Newsl* 21:115–144.
- Peck WH, Valley JW, Wilde SA, Graham CM (2001) Oxygen isotope ratios and rare earth elements in 3.3 to 4.4 Ga zircons: Ion microprobe evidence for high  $\delta^{18}\text{O}$  continental crust and oceans in the early Archean. *Geochim Cosmochim Acta* 65:4215–4229. doi: 10.1016/S0016-7037(01)00711-6
- Peck WH, Valley JW, Graham CM (2003) Slow oxygen diffusion rates in igneous zircons from metamorphic rocks. *Am Mineral* 88:1003–1014.
- Penniston-Dorland SC, Gorman JK, Bebout GE, et al (2014) Reaction rind formation in the Catalina Schist: Deciphering a history of mechanical mixing and metasomatic alteration. *Chem Geol* 384:47–61. doi: 10.1016/j.chemgeo.2014.06.024
- Penniston-Dorland SC, Kohn MJ (2015) The global range of subduction zone thermal structures from exhumed blueschists and eclogites: Rocks are hotter than models. *EPSL* 428:243-254
- Perchuk LL, Lavrent'eva I V. (1983) *Experimental Investigation of Exchange Equilibria in the System Cordierite-Garnet-Biotite*. Springer New York, pp 199–239
- Perry E, Ahmad S, Swulius T (1978) The oxygen isotope composition of 3,800 my old metamorphosed chert and iron formation from Isukasia, West Greenland. *J Geol* 86:223-239
- Philippot P, Blichert-Toft J, Perchuk A, Costa S, Gerasimov V (2001) Lu–Hf and Ar–Ar chronometry supports extreme rate of subduction zone metamorphism deduced from geospeedometry *Tectonophysics* 342:23-38
- Philippot P, Busigny V, Scambelluri M, Cartigny P (2007) Oxygen and nitrogen isotopes as tracers of fluid activities in serpentinites and metasediments during subduction. *Mineral Petrol* 91:11–24. doi: 10.1007/s00710-007-0183-7
- Plank T, Langmuir C (1998) The chemical composition of subducting sediment and its consequences for the crust and mantle. *Chem Geol* 145:325-394
- Plunder A, Agard P, Chopin C, Okay AI (2013) Geodynamics of the Tavsanlı zone, western Turkey: Insights into subduction/obduction processes. *Tectonophysics* 608:884–903. doi: 10.1016/j.tecto.2013.07.028
- Plunder A, Agard P, Chopin C, et al (2015) Accretion, underplating and exhumation along a subduction interface: From subduction initiation to continental subduction (Tavsanlı zone, W. Turkey). *Lithos* 226:233–254. doi: 10.1016/j.lithos.2015.01.007

- 
- Polat A, Hofmann A, Rosing MT (2002) Boninite-like volcanic rocks in the 3.7–3.8 Ga Isua greenstone belt, West Greenland: geochemical evidence for intra-oceanic subduction zone processes in the early. *Chem Geol* 184:231–254. doi: 10.1016/S0009-2541(01)00363-1
- Pollington AD, Baxter EF (2010) High resolution Sm-Nd garnet geochronology reveals the uneven pace of tectonometamorphic processes Earth and Planetary Science Letters 293:63-71 doi:DOI 10.1016/j.epsl.2010.02.019
- Pope ECE, Bird DK, Rosing MT (2012) Isotope composition and volume of Earth's early oceans. *Proc Natl Acad Sci U S A* 109:4371–4376. doi: 10.1073/pnas.1115705109
- Pourteau A, Scherer EE, Schmidt A, Bast R (2014) Internal P-T-t Structure of Subduction Complexes — Insights from Lu-Hf Geochronology on Garnet and Lawsonite (Halilbağ, Central Anatolia). Abstract AGU Fall Meeting V24C-02
- Pourteau A, Oberhänsli R, Candan O, et al (2016) Neotethyan closure history of western Anatolia: a geodynamic discussion. *Int J Earth Sci* 105:203–224. doi: 10.1007/s00531-015-1226-7
- Putlitz B, Matthews A, Valley JW (2000) Oxygen and hydrogen isotope study of high-pressure metagabbros and metabasalts (Cyclades, Greece): Implications for the subduction of oceanic crust. *Contrib to Mineral Petrol* 138:114–126. doi: 10.1007/s004100050012
- Putnis A, Putnis C V. (2007) The mechanism of reequilibration of solids in the presence of a fluid phase. *J Solid State Chem* 180:1783–1786. doi: 10.1016/j.jssc.2007.03.023
- Putnis A, John T (2010) Replacement processes in the Earth's crust. *Elements* 6:159–164.
- Pyle JM, Spear FS, Rudnick RL, McDonough WF (2001) Monazite–xenotime–garnet equilibrium in metapelites and a new monazite–garnet thermometer. *J Petrol* 42:2083–2107.
- Ravna K (2000) The garnet–clinopyroxene Fe<sup>2+</sup>–Mg geothermometer: an updated calibration. *J Met Geol* 18(2) doi: 10.1046/j.1525-1314.2000.00247.x
- Rigo M, Joachimski MM (2010) Palaeoecology of Late Triassic Conodonts: Constraints from Oxygen Isotopes in Biogenic Apatite. *Acta Palaeontol Pol* 55:471–478. doi: 10.4202/app.2009.0100
- Rizo H, Boyet M, Blichert-toft J, et al (2012) The elusive Hadean enriched reservoir revealed by <sup>142</sup>Nd deficits in Isua Archaean rocks. *Nature* 490:96–100. doi: 10.1038/nature11565
- Rizvanova N et al. (2000) Zircon reaction and stability of the U-Pb isotope system during interaction with carbonate fluid: experimental hydrothermal study *Contrib Mineral Petrol* 139:101-114
- Rojay B, Altner D, Altner SÖ, et al (2004) Geodynamic significance of the Cretaceous pillow basalts from North Anatolian Ophiolitic Mélange Belt (Central Anatolia, Turkey): geochemical and paleontological constraints. *Geodin Acta* 175:349–361.
- Rollinson H (2002) The metamorphic history of the Isua Greenstone Belt, West Greenland. *Geol Soc London, Spec Publ* 199:329–350. doi: 10.1144/GSL.SP.2002.199.01.16
- Rollinson H (2003) Metamorphic history suggested by garnet-growth chronologies in the Isua Greenstone Belt, West Greenland. In: *Precambrian Research*. pp 181–196
- Rose N, Rosing MT, Bridgwater D (1996) The origin of metacarbonate rocks in the Archaean Isua supracrustal belt, West Greenland. *Am J Sci* 296:1004–1044. doi: 10.2475/ajs.296.9.1004

- Rosing MT (1999)  $^{13}\text{C}$ -Depleted Carbon Microparticles in >3700-Ma Sea-Floor Sedimentary Rocks from West Greenland. *Science* (80- ) 283:674–676. doi: 10.1126/science.283.5402.674
- Rubatto D (2002) Zircon trace element geochemistry: partitioning with garnet and the link between U-Pb ages and metamorphism *Chem Geol* 184:123-138 doi:Pii S0009-2541(01)00355-2
- Rubatto D, Hermann J (2001) Exhumation as fast as subduction? *Geology* 29:3-6 doi: 10.1130/0091-7613(2001)029<0003:Eafas>2.0.Co;2
- Rubatto D, Hermann J (2003) Zircon formation during fluid circulation in eclogites (Monviso, Western Alps): Implications for Zr and Hf budget in subduction zones *Geochimica et Cosmochimica Acta* 67:2173-2187 doi:Doi 10.1016/S0016-7037(02)01321-2
- Rubatto D, Müntener O, Barnhoorn A, Gregory CJ (2008) Dissolution-reprecipitation of zircon at low-temperature, high-pressure conditions (Lanzo Massif, Italy). *Am Mineral* 93:1519–1529. doi: Doi 10.2138/Am.2008.2874
- Rubatto D, Putlitz B, Gauthiez-Putallaz L, et al (2014) Measurement of in-situ oxygen isotope ratios in monazite by SHRIMP ion microprobe: Standards, protocols and implications. *Chem Geol* 380:84–96.
- Rubatto D, Angiboust S (2015) Oxygen isotope record of oceanic and high-pressure metasomatism: a P–T–time–fluid path for the Monviso eclogites (Italy). *Contrib to Mineral Petrol* 170:44. doi: 10.1007/s00410-015-1198-4
- Russell AK, Kitajima K, Strickland A, et al (2013) Eclogite-facies fluid infiltration: Constraints from  $\delta^{18}\text{O}$  zoning in garnet. *Contrib to Mineral Petrol* 165:103–116. doi: 10.1007/s00410-012-0794-9
- Savin SM, Epstein S (1970) The oxygen and hydrogen isotope geochemistry of ocean sediments and shales. *Geochim Cosmochim Acta* 34:43–63. doi: 10.1016/0016-7037(70)90150-X
- Scambelluri M, Tonarini S (2012) Boron isotope evidence for shallow fluid transfer across subduction zones by serpentinitized mantle. *Geology* 40:907–910. doi: 10.1130/G33233.1
- Schärer U (1984) The effect of initial  $^{230}\text{Th}$  disequilibrium on young U-Pb ages: the Makalu case, Himalaya *Earth and Planetary Science Letters* 67:191-204
- Scherrer N, Gnos E, Chopin C (2001) A retrograde monazite-forming reaction in bearthite-bearing high-pressure rocks.
- Schidlowski M, Appel PWU, Eichmann R, Junge CE (1979) Carbon isotope geochemistry of the 3.7 Ga-yr-old Isua sediments, West Greenland: implications for the Archaean carbon and oxygen cycles. *Geochim Cosmochim Acta* 43:189–199. doi: 10.1016/0016-7037(79)90238-2
- Schmidt MW, Poli S (2014) 4.19. Devolatilization during subduction. *Crust, Treatise Geochemistry* (eds HD Holl KK Turekian, Second Ed Elsevier-Pergamon, Oxford 669–701.
- Schwartz JJ, John BE, Cheadle MJ, et al (2010) Dissolution-reprecipitation of igneous zircon in mid-ocean ridge gabbro, Atlantis Bank, Southwest Indian Ridge. *Chem Geol* 274:68–81. doi: 10.1016/j.chemgeo.2010.03.017
- Schwartz S, Guillot S, Reynard B, et al (2013) Pressure–temperature estimates of the lizardite/antigorite transition in high pressure serpentinites. *Lithos* 178:197–210. doi: 10.1016/j.lithos.2012.11.023



- 
- Schertl HP, Schreyer W (1996) Mineral Inclusions in Heavy Minerals of the Ultrahigh-Pressure Metamorphic Rocks of the Dora-Maira Massif and Their Bearing on the Relative Timing of the Petrological Events *Earth Processes: Reading the Isotopic Code*:331-342
- Schertl HP, Schreyer W, Chopin C (1991) The Pyrope-Coesite Rocks and Their Country Rocks at Parigi, Dora Maira Massif, Western Alps - Detailed Petrography, Mineral Chemistry and Pt-Path *Contrib Mineral Petrol* 108:1-21 doi:Doi 10.1007/Bf00307322
- Schertl HP, Schreyer W (2008) Geochemistry of coesite-bearing "pyrope quartzite" and related rocks from the Dora-Maira Massif, Western Alps *Eur J Mineral* 20:791-809 doi:Doi 10.1127/0935-1221/2008/0020-1862
- Schmidt A, Mezger K, O'Brien PJ (2011) The time of eclogite formation in the ultrahigh pressure rocks of the Sulu terrane: constraints from Lu–Hf garnet geochronology *Lithos* 125:743-756
- Schreyer W (1973) Whiteschist: a high-pressure rock and its geologic significance *The Journal of Geology*:735-739
- Seaton NCA, Whitney DL, Teyssier C, et al (2009) Recrystallization of high-pressure marble (Sivrihisar, Turkey). *Tectonophysics* 479:241–253. doi: DOI 10.1016/j.tecto.2009.08.015
- Seaton NCA, Teyssier C, Whitney DL, Heizler MT (2014) Quartz and calcite microfabric transitions in a pressure and temperature gradient, Sivrihisar, Turkey. *Geodin Acta* 26:191–206. doi: 10.1080/09853111.2013.858952
- Sharp ZD (1990) A laser-based microanalytical method for the in situ determination of oxygen isotope ratios of silicates and oxides. *Geochim Cosmochim Acta* 54:1353–1357. doi: 10.1016/0016-7037(90)90160-M
- Sharp ZD, Essene EJ, Hunziker JC (1993) Stable Isotope Geochemistry and Phase-Equilibria of Coesite-Bearing Whiteschists, Dora-Maira Massif, Western Alps. *Contrib to Mineral Petrol* 114:1–12. doi: Doi 10.1007/Bf00307861
- Sharp Z, Barnes J (2004) Water-soluble chlorides in massive seafloor serpentinites: a source of chloride in subduction zones *Earth and Planetary Science Letters* 226:243-254
- Sheppard S, Gilg H, Sheppard, S. M. F., Gilg H a. (1996) Stable isotope geochemistry of clay minerals. *Clay Miner* 31:1–24.
- Sherlock SC (1999) Oscillatory Zoned Chrome Lawsonite in the Tavşanlı Zone, Northwest Turkey. *Mineral Mag* 63:687–692. doi: 10.1180/minmag.1999.063.5.06
- Sherlock SC, Arnaud NO (1999) Flat plateau and impossible isochrons: Apparent  $^{40}\text{Ar}$ - $^{39}\text{Ar}$  geochronology in a high-pressure terrain. *Geochim Cosmochim Acta* 63:2835–2838. doi: 10.1016/S0016-7037(99)00116-7
- Sherlock SC, Kelley S, Inger S, et al (1999)  $^{40}\text{Ar}$ -  $^{39}\text{Ar}$  and Rb-Sr geochronology of high-pressure metamorphism and exhumation history of the Tavsanli Zone, NW Turkey. *Contrib Miner Pet* 137:46–58. doi: doi:10.1007/PL00013777
- Sherlock SC, Kelley S (2002) Excess argon evolution in HP-LT rocks: a UVLAMP study of phengite and K-free minerals, NW Turkey. *Chem Geol* 182:619–636. doi: Pii S0009-2541(01)00345-XDoi 10.1016/S0009-2541(01)00345-X
- Sievers NE, Tenore J, Penniston-Dorland SC, Bebout GE (2016) Fingerprints of forearc element mobility in blueschist-facies metaconglomerates, Catalina Schist, California. *Int Geol Rev* 0:1–12. doi: 10.1080/00206814.2016.1253038

## References

---

- Simon G, Chopin C, Schenk V (1997) Near-end-member magnesiochloritoid in prograde-zoned pyrope, Dora-Maira massif, western Alps *Lithos* 41:37-57 doi:Doi 10.1016/S0024-4937(97)82004-X
- Skora S, Baumgartner LP, Mahlen NJ, et al (2006) Diffusion-limited REE uptake by eclogite garnets and its consequences for Lu–Hf and Sm–Nd geochronology. *Contrib to Mineral Petrol* 152:703–720.
- Smith M, Yardley BWD (1999) Fluid evolution during metamorphism of the Otago Schist, New Zealand:(II) influence of detrital apatite on fluid salinity. *J Met Geol* 17(2) doi: 10.1046/j.1525-1314.1999.00190.x
- Spandler CJ, Hermann J, Arculus RJ, Mavrogenes JA (2003) Redistribution of trace elements during prograde metamorphism from lawsonite blueschist to eclogite facies; implications for deep subduction-zone processes. *Contrib to Mineral Petrol* 146:205–222. doi: 10.1007/s00410-003-0495-5
- Spandler CJ, Hermann J, Arculus RJ, Mavrogenes JA (2004) Geochemical heterogeneity and element mobility in deeply subducted oceanic crust; insights from high-pressure mafic rocks from New Caledonia. *Chem Geol* 206:21–42. doi: 10.1016/j.chemgeo.2004.01.006
- Spandler CJ, Pettke T, Rubatto D (2011) Internal and external fluid sources for eclogite-facies veins in the Monviso Meta-ophiolite, Western Alps: Implications for fluid flow in subduction zones. *J Petrol* 52:1207–1236. doi: 10.1093/petrology/egr025
- Spandler CJ, Pirard C (2013) Element recycling from subducting slabs to arc crust: A review. *Lithos* 170–171:208–223.
- Spear FS, Pyle JM (2002) Apatite, Monazite, and Xenotime in Metamorphic Rocks. *Rev Mineral Geochemistry* 48:293–335. doi: 10.2138/rmg.2002.48.7
- Stacey JS t, Kramers J (1975) Approximation of terrestrial lead isotope evolution by a two-stage model. *Earth Planet Sci Lett* 26:207–221.
- Staudigel H, Davies GR, Hart SR, et al (1995) Large scale isotopic Sr, Nd and O isotopic anatomy of altered oceanic crust: DSDP/ODP sites 417/418. *Earth Planet Sci Lett* 130:169–185. doi: 10.1016/0012-821X(94)00263-X
- Strasser M, Henry P, Kanamatsu T, et al (2012) Scientific Drilling of Mass-Transport Deposits in the Nankai Accretionary Wedge: First Results from IODP Expedition 333. In: *Submarine Mass Movements and Their Consequences*. Springer Netherlands, Dordrecht, pp 671–681
- Sun S-S, McDonough WF (1989) Chemical and isotopic systematics of oceanic basalts: implications for mantle composition and processes. *Geol Soc London, Spec Publ* 42:313–345.
- Sun Y, Wiedenbeck M, Joachimski MM, et al (2016) Chemical and oxygen isotope composition of gem-quality apatites: Implications for oxygen isotope reference materials for secondary ion mass spectrometry (SIMS). *Chem Geol* 440:164–178. doi: 10.1016/j.chemgeo.2016.07.013
- Syracuse EM, van Keken PE, Abers GA, et al (2010) The global range of subduction zone thermal models. *Phys Earth Planet Inter* 183:73–90. doi: 10.1016/j.pepi.2010.02.004
- Tatsumi Y, Eggins S (1995) *Subduction zone magmatism*. Blackwell Science Cambridge 211p
- Taylor R, Clark C, Reddy SM (2012) The effect of grain orientation on secondary ion mass spectrometry (SIMS) analysis of rutile. *Chem Geol* 300:81–87. doi: 10.1016/j.chemgeo.2012.01.013

- 
- Taylor RJM, Clark C, Fitzsimons ICW, et al (2014) Post-peak, fluid-mediated modification of granulite facies zircon and monazite in the Trivandrum Block, southern India. *Contrib Miner Pet.* doi: 10.1007/s00410-014-1044-0
- Teyssier C, Whitney DL, Toraman E, Seaton NCA (2010) Lawsonite vorticity and subduction kinematics. *Geology* 38:1123–1126. doi: 10.1130/G31409.1
- Thébauda N, Rey PF (2013) Archean gravity-driven tectonics on hot and flooded continents: Controls on long-lived mineralised hydrothermal systems away from continental margins. *Precambrian Res* 229:93–104. doi: 10.1016/j.precamres.2012.03.001
- Tilton GR, Schreyer W, Schertl HP (1991) Pb-Sr-Nd Isotopic Behavior of Deeply Subducted Crustal Rocks from the Dora Maira Massif, Western Alps, Italy-Ii - What Is the Age of the Ultrahigh-Pressure Metamorphism *Contrib Mineral Petrol* 108:22-33 doi:Doi 10.1007/Bf00307323
- Tomaschek F, Kennedy AK, Villa IM, et al (2003) Zircons from Syros, Cyclades, Greece—recrystallization and mobilization of zircon during high-pressure metamorphism. *J Petrol* 44:1977–2002.
- Tomkins HS, Powell R, Ellis D (2007) The pressure dependence of the zirconium-in-rutile thermometer. *J Metamorph Geol* 25:703–713. doi: 10.1111/j.1525-1314.2007.00724.x
- Touret JLR (2001) Fluids in metamorphic rocks. *Lithos* 55:1–25. doi: 10.1016/S0024-4937(00)00036-0
- Trail D, Mojzsis SJ, Harrison TM, et al (2007) Constraints on Hadean zircon protoliths from oxygen isotopes, Ti-thermometry, and rare earth elements. *Geochemistry, Geophys Geosystems*. doi: 10.1029/2006GC001449
- Trail D, Bindeman IN, Watson EB, Schmitt AK (2009) Experimental calibration of oxygen isotope fractionation between quartz and zircon *Geochimica et Cosmochimica Acta* 73:7110-7126
- Tropper P, Manning CE (2008) The current status of titanite-rutile thermobarometry in ultrahigh-pressure metamorphic rocks: The influence of titanite activity models on phase equilibrium calculations. *Chem Geol* 254:123–132. doi: 10.1016/j.chemgeo.2008.03.010
- Trotter JA, Williams IS, Barnes CR, et al (2008) Did Cooling Oceans Trigger Ordovician Biodiversification? Evidence from Conodont Thermometry. *Science* (80- ) 321:550–554. doi: 10.1126/science.1155814
- Trotter JA, Williams IS, Nicora A, et al (2015) Long-term cycles of Triassic climate change: A new  $\delta^{18}\text{O}$  record from conodont apatite. *Earth Planet Sci Lett* 415:165–174. doi: 10.1016/j.epsl.2015.01.038
- Tsujimori T, Sisson VB, Liou JG, et al (2006) Very-low-temperature record of the subduction process: A review of worldwide lawsonite eclogites. *Lithos* 92:609–624. doi: 10.1016/j.lithos.2006.03.054
- Ustaömer PA, Ustaömer T, Robertson AHF (2012) Ion probe U–Pb dating of the central Sakarya basement: a peri-Gondwana terrane intruded by Late Lower Carboniferous subduction/collision-related granitic rocks. *Turkish J Earth Sci* 21:905–932. doi: 10.3906/yer-1103-1
- Valley JW (2003) Oxygen isotopes in zircon. *Rev Mineral geochemistry* 53:343–385. doi: 10.2113/0530343

## References

---

- Valley JW, Bindeman IN, Peck WH (2003) Empirical calibration of oxygen isotope fractionation in zircon. *Geochim Cosmochim Acta* 67:3257–3266. doi: 10.1016/S0016-7037(00)00090-5
- Valley JW, Kinny PD, Schulze DJ, Spicuzza MJ (1998) Zircon megacrysts from kimberlite: oxygen isotope variability among mantle melts. *Contrib to Mineral Petrol* 133:1–11. doi: 10.1007/s004100050432
- Valley JW, Kitchen N, Kohn MJ, et al (1995) UWG-2, a garnet standard for oxygen isotope ratios: Strategies for high precision and accuracy with laser heating. *Geochim Cosmochim Acta* 59:5223–5231. doi: [http://dx.doi.org/10.1016/0016-7037\(95\)00386-X](http://dx.doi.org/10.1016/0016-7037(95)00386-X)
- Vielzeuf D, Champenois M, Valley JW, et al (2005a) SIMS analyses of oxygen isotopes: matrix effects in Fe–Mg–Ca garnets. *Chem Geol* 223:208–226.
- Vielzeuf D, Veschambre M, Brunet F (2005b) Oxygen isotope heterogeneities and diffusion profile in composite metamorphic-magmatic. *Am Mineral* 90:463–472. doi: 10.2138/am.2005.1576
- Vitale Brovarone A, Alard O, Beyssac O, et al (2014) Lawsonite metasomatism and trace element recycling in subduction zones. *J Metamorph Geol* 32:489–514. doi: 10.1111/jmg.12074
- Vitale Brovarone A, Beyssac O (2014) Lawsonite metasomatism: A new route for water to the deep Earth. *Earth Planet Sci Lett* 393:275–284. doi: 10.1016/j.epsl.2014.03.001
- von Blackenburg F (1992) Combined high-precision chronometry and geochemical tracing using accessory minerals: applied to the Central-Alpine Bergell intrusion (central Europe). *Chem Geol* 100:19–40. doi: 10.1016/0009-2541(92)90100-J
- Vrolijk P (1987) Tectonically driven fluid flow in the Kodiak accretionary complex, Alaska. *Geology* 15:466–469. doi: 10.1130/0091-7613(1987)15<466:TDFFIT>2.0.CO;2
- Wada I, Wang K (2009) Common depth of slab-mantle decoupling: Reconciling diversity and uniformity of subduction zones. *Geochemistry, Geophys Geosystems* 10:n/a-n/a. doi: 10.1029/2009GC002570
- Watson EB, Cherniak D (1997) Oxygen diffusion in zircon. *Earth Planet Sci Lett* 148:527–544. doi: 10.1016/S0012-821X(97)00057-5
- White R, Powell R, Clarke G (2002) The interpretation of reaction textures in Fe-rich metapelitic granulites of the Musgrave Block, central Australia: constraints from mineral equilibria calculations in the system  $K_2O$ – $FeO$ – $MgO$ – $Al_2O_3$ – $SiO_2$ – $H_2O$ – $TiO_2$ – $Fe_2O_3$ . *J Metamorph Geol* 20:41–55
- White R, Powell R, Holland T (2007) Progress relating to calculation of partial melting equilibria for metapelites. *J Metamorph Geol* 25:511–527
- Whitney DL, Mechum TA, Dilek Y, Kuehner SM (1996) Modification of garnet by fluid infiltration during regional metamorphism in garnet through sillimanite-zone rocks, Dutchess County, New York. *Am Mineral* 81:696–705. doi: 10.2138/am-1996-5-617
- Whitney DL (2002) Coexisting andalusite, kyanite, and sillimanite: Sequential formation of three  $Al_2SiO_5$  polymorphs during progressive metamorphism near the triple point, Sivrihisar, Turkey. *Am Mineral* 87:405–416.
- Whitney DL, Davis PB (2006) Why is lawsonite eclogite so rare? Metamorphism and preservation of lawsonite eclogite, Sivrihisar, Turkey. *Geology* 34:473–476. doi: 10.1130/G22259.1
- Whitney DL, Evans BW (2010) Abbreviations for names of rock-forming minerals. *Am Mineral* 95:185–187. doi: 10.2138/am.2010.3371

- 
- Whitney DL, Teyssier C, Toraman E, et al (2011) Metamorphic and tectonic evolution of a structurally continuous blueschist-to-Barrovian terrane, Sivrihisar Massif, Turkey. *J Metamorph Geol* 29:193–212. doi: 10.1111/j.1525-1314.2010.00915.x
- Whitney DL, Teyssier C, Seaton NCA, Fornash KF (2014) Petrofabrics of high-pressure rocks exhumed at the slab-mantle interface from the “point of no return” in a subduction zone (Sivrihisar, Turkey). *Tectonics* 33:2315–2341. doi: 10.1002/2014TC003677
- Wilde SA, Valley JW, Peck WH, Graham CM (2001) Evidence from detrital zircons for the existence of continental crust and oceans on the Earth 4.4 Gyr ago. *Nature* 409:175–178. doi: 10.1038/35051550
- Williams IS (1998) U–Th–Pb geochronology by ion microprobe. *Rev Econ Geol* 7:1–35.
- Williams IS, Compston W, Chappell BW (1983) Zircon and monazite U–Pb systems and the histories of I-type magmas, Berridale Batholith, Australia. *J Petrol* 24:76–97. doi: 10.1093/petrology/24.1.76
- Winchester JA, Floyd PA (1977) Geochemical discrimination of different magma series and their differentiation products using immobile elements. *Chem Geol* 20:325–343. doi: 10.1016/0009-2541(77)90057-2
- Wingate MTD, Compston W (2000) Crystal orientation effects during ion microprobe U–Pb analysis of baddeleyite. *Chem Geol* 168:75–97. doi: 10.1016/S0009-2541(00)00184-4
- Woodhead JD, Hellstrom J, Hergt JM, et al (2007) Isotopic and elemental imaging of geological materials by laser ablation inductively coupled plasma-mass spectrometry. *Geostand Geoanalytical Res* 31:331–343.
- Zack T (2013) A cold slab-mantle interface: Constraints from exceptionally well preserved lawsonite eclogites. *Mineral Mag* 77:2574.
- Zack T, Moraes R, Kronz A (2004) Temperature dependence of Zr in rutile: empirical calibration of a rutile thermometer. *Contrib to Mineral Petrol* 148:471–488.
- Zanchi A, Garzanti E, Larghi C, et al (2003) The Variscan orogeny in Chios (Greece): Carboniferous accretion along a Palaeotethyan active margin. *Terra Nov* 15:213–223. doi: 10.1046/j.1365-3121.2003.00483.x
- Zhang Z-M, Shen K, Sun W-D, Liu Y-S, Liou J, Shi C, Wang J-L (2008) Fluids in deeply subducted continental crust: petrology, mineral chemistry and fluid inclusion of UHP metamorphic veins from the Sulu orogen, eastern China *Geochimica et Cosmochimica Acta* 72:3200-3228
- Zhang Z, SCHERTL HP, Wang J, Shen K, Liou J (2009) Source of coesite inclusions within inherited magmatic zircon from Sulu UHP rocks, eastern China, and their bearing for fluid–rock interaction and SHRIMP dating *J Metamorph Geol* 27:317-333
- Zheng Y (1991) Calculation of oxygen isotope fractionation in metal oxides. *Geochim Cosmochim Acta* 55:2299–2307.
- Zheng Y-F (1993a) Calculation of oxygen isotope fractionation in anhydrous silicate minerals. *Geochim Cosmochim Acta* 57:1079–1091.
- Zheng Y-F (1993b) Calculation of oxygen isotope fractionation in hydroxyl-bearing silicates. *Earth Planet Sci Lett* 120:247–263.
- Zheng YF (1996) Oxygen isotope fractionations involving apatites: Application to paleotemperature determination. *Chem Geol* 127:177–187. doi: 10.1016/0009-2541(95)00088-7

## References

---

Zheng Y-F (2009) Fluid regime in continental subduction zones: petrological insights from ultrahigh-pressure metamorphic rocks *J Geol Soc London* 166:763-782

## **Electronic appendix contents**

### **A1 – Appendix to chapter 1**

**Publication PDF:** Rubatto D, Putlitz B, **Gauthiez-Putallaz L**, et al (2014) Measurement of in-situ oxygen isotope ratios in monazite by SHRIMP ion microprobe: Standards, protocols and implications. *Chem Geol* 380:84–96.

**Table A1 – 1:** EMPA apatite data

**Table A1 – 2:** Apatite oxygen isotope composition determined by SHRIMP

**Table A1 – 3:** LA-ICP-MS data for DM1C rutiles

**Table A1 – 4:** LA-ICP-MS data for SHB12B, SHB45 and WOD rutiles

**Table A1 - 5:** Rutile oxygen isotope composition determined by SHRIMP

**Table A1 - 6:** EBSD orientation data for rutile

### **A2 – Appendix to chapter 2**

**Publication PDF:** **Gauthiez-Putallaz L**, Rubatto D, Hermann J (2016) Dating prograde fluid pulses during subduction by in situ U-Pb and oxygen isotope analysis. *Contrib to Mineral Petrol* 171:1–20.

**Table A2 – ESM1:** Garnet trace-element composition determined by LA-ICP-MS

**Table A2 – ESM2:** Zircon trace-element composition determined by LA-ICP-MS

**Table A2 – ESM3:** Monazite trace-element composition determined by LA-ICP-MS

**Figure A2 – ESM4:** Pseudosection for sample DM51 calculated using Theriak-Domino and the Holland and Powell database

**Table A2 - ESM5:** SHRIMP U-Pb analyses of zircon

**Table A2 - ESM6:** SHRIMP U-Pb analyses of monazite

**Table A2 – ESM7:** Zircon oxygen isotope composition determined by SHRIMP

**Table A2 – ESM8:** Garnet oxygen isotope composition determined by SHRIMP

**Table A2 – ESM9:** Monazite oxygen isotope composition determined by SHRIMP

### **A3 – Appendix to chapter 3**

**Table A3 – 1:** LA-ICP-MS Whole-rock trace element analyses

**Table A3 – 2:** SHRIMP U-Pb analyses of zircon

**Table A3 – 3:** Zircon trace-element composition determined by LA-ICP-MS

**Table A3– 4:** SHRIMP Th-Pb analyses for SHB45 zircons

**Table A3 - 5:** SHRIMP U-Pb analyses of allanite

**Table A3 - 6:** SHRIMP Th-Pb analyses of florencite

#### **A4 – Appendix to chapter 4**

**Publication PDF:** Martin LAJ, Hermann J, **Gauthiez-Putallaz L**, et al (2014a)  
Lawsonite geochemistry and stability - implication for trace element and water cycles in subduction zones. *J Metamorph Geol* 32:455–478.

**Table A4 – 1:** Apatite trace-element composition determined by LA-ICP-MS

**Table A4 – 2:** EMPA data for clinopyroxene

**Table A4 – 3:** EMPA data for garnet

**Table A4 – 4:** Antigorite oxygen isotope composition determined by SHRIMP

**Table A4 - 5:** Zircon oxygen isotope composition determined by SHRIMP

**Table A4 - 6:** Garnet oxygen isotope composition determined by SHRIMP

**Table A4 - 7:** Garnet trace-element composition determined by LA-ICP-MS

**Figure A4 - 8:** Garnet trace-element LA-ICP-MS slit profile for sample SHB12B

**Figure A4 - 9:** Garnet trace-element LA-ICP-MS slit profile for sample SHB45

**Figure A4 - 10:** Apatite rare-earth element concentrations normalised to chondrite

**Table A4 - 11:** Lawsonite trace-element composition determined by LA-ICP-MS

**Table A4 - 12:** Lawsonite oxygen isotope composition determined by SIMS

**Figure A4 - 13:** Lawsonite rare-earth element concentrations normalised to chondrite

**Table A4 - 14:** Mineral modes observed in thin section

**Figure A4 - 15:** Preliminary SHRIMP oxygen isotope data for sample SV03-103

#### **A5 – Appendix to chapter 5**

**Table A5 – 1:** Garnet trace-element composition determined by LA-ICP-MS

**Table A5 – 2:** SHRIMP U-Pb analyses of zircon for sample G04-46

**Table A5 – 3:** Zircon trace-element composition determined by LA-ICP-MS for G04-46

**Table A5– 4:** Garnet oxygen isotope composition determined by SHRIMP

**Table A5 - 5:** Zircon oxygen isotope composition determined by SHRIMP



# **A1 – Appendix to Chapter 1**

A1 - **Publication PDF:** Rubatto D, Putlitz B, **Gauthiez-Putallaz L**, et al (2014) Measurement of in-situ oxygen isotope ratios in monazite by SHRIMP ion microprobe: Standards, protocols and implications. Chem Geol 380:84-96.

This publication has been removed due to copyright restrictions.

It can be accessed online at:

<https://www.sciencedirect.com/science/article/abs/pii/S0009254114002289>

Table A1-1: EMPA apatite data

Sample EMPA #	DUR C 1 / 1 .	DUR C 2 / 1 .	DUR C 24 / 1 .	DUR C 25 / 1 .	DUR C 49 / 1 .	DUR C 50 / 1 .	DUR C 77 / 1 .	DUR C 78 / 1 .	DUR C 109 / 1 .	DUR C 110 / 1 .	DUR C 133 / 1 .
spot size	20	20	20	20	20	20	20	20	20	20	20
F	3.6	3.4	3.5	3.5	3.5	3.5	3.5	3.4	3.6	3.5	3.5
F stdev	0.4	0.4	0.4	0.4	0.4	0.4	0.4	0.4	0.4	0.4	0.4
<i>F corr*</i>											
Cl	0.41	0.31	0.39	0.34	0.37	0.39	0.40	0.40	0.38	0.36	0.37
CaO	53.8	52.7	52.3	52.6	52.9	52.3	52.4	53.1	53.3	53.3	53.2
P <sup>2</sup> O <sup>5</sup>	40.6	40.3	39.4	39.9	39.6	39.4	40.1	39.9	40.2	40.7	41.2
FeO	<0.09	<0.09	<0.09	<0.09	<0.09	<0.09	<0.09	<0.09	<0.09	<0.09	<0.09
SrO	<0.10	<0.10	<0.10	<0.10	<0.10	<0.10	<0.10	<0.10	<0.10	<0.10	<0.10
MnO	<0.07	<0.07	<0.07	<0.07	<0.07	<0.07	<0.07	<0.07	<0.07	<0.07	<0.07
Ce <sup>2</sup> O <sup>3</sup>	0.49	0.46	0.56	0.50	0.51	0.53	0.58	0.49	0.57	0.53	0.59
Total	99.0	97.3	96.2	96.9	97.0	96.1	97.1	97.3	98.0	98.6	99.0
<i>Corr. Total*</i>											
Sample EMPA #	DUR C 164 / 1 .	DUR C 26 / 1 .	DUR C 27 / 1 .	DUR C 47 / 1 .	DUR C 48 / 1 .	DUR r 59 / 1 .	DUR r 60 / 1 .	DUR r 51 / 1 .	DUR r 52 / 1 .	DUR r 53 / 1 .	DUR r 54 / 1 .
spot size	20	10	10	10	10	20	20	20	20	20	20
F	3.5	3.5	3.5	3.5	3.5	3.6	3.9	3.8	3.6	3.8	3.9
F stdev	0.4	0.4	0.4	0.4	0.4	0.4	0.4	0.4	0.4	0.4	0.4
<i>F corr*</i>						3.3	3.5	3.5	3.3	3.4	3.5
Cl	0.36	0.37	0.35	0.36	0.37	0.41	0.38	0.38	0.37	0.36	0.38
CaO	53.8	52.4	53.6	53.0	53.2	50.6	51.3	51.9	51.9	51.5	51.0
P <sup>2</sup> O <sup>5</sup>	42.7	40.7	40.9	38.7	39.5	38.1	39.5	38.3	39.1	38.8	38.6
FeO	<0.09	<0.09	<0.09	<0.09	<0.09	<0.09	<0.09	<0.09	<0.09	<0.09	<0.09
SrO	0.12	<0.10	<0.10	<0.10	<0.10	<0.10	<0.10	<0.10	<0.10	<0.10	<0.10
MnO	<0.07	<0.06	<0.06	<0.06	<0.06	<0.07	<0.07	<0.07	<0.07	<0.07	<0.07
Ce <sup>2</sup> O <sup>3</sup>	0.56	0.48	0.58	0.46	0.47	0.64	0.58	0.48	0.63	0.54	0.62
Total	101.1	97.5	98.9	96.1	97.2	93.4	95.7	94.9	95.7	95.0	94.6
<i>Corr. Total*</i>						93.0	95.2	94.4	95.3	94.6	94.1

\* F values adjusted down 10% as per Li and Hermann (2015) for randomly oriented samples

Table A1-1: EMPA apatite data

Sample	DUR C	DUR C	DUR r	DUR r	SGM21	SGM21	SGM21	SGM21	SGM21	SGM21	SGM21
EMPA #	134 / 1 .	163 / 1 .	57 / 1 .	58 / 1 .	135 / 1 .	136 / 1 .	137 / 1 .	138 / 1 .	139 / 1 .	140 / 1 .	141 / 1 .
spot size	20	20	20	20	20	20	20	20	20	20	20
F	3.6	3.6	3.8	3.9	4.3	4.2	4.1	4.1	4.4	4.2	4.3
F stdev	0.4	0.4	0.4	0.4	0.5	0.5	0.5	0.5	0.5	0.5	0.5
<i>F corr*</i>			3.4	3.5	3.9	3.8	3.7	3.7	4.0	3.8	3.9
Cl	0.39	0.39	0.38	0.38	<0.03	<0.03	<0.03	<0.03	<0.03	<0.03	<0.03
CaO	53.6	54.3	51.8	51.5	53.8	53.4	55.0	53.8	53.6	54.2	54.0
P <sup>2</sup> O <sup>5</sup>	40.9	43.0	38.7	39.2	41.3	41.6	41.5	42.5	42.0	41.9	41.9
FeO	<0.09	<0.09	<0.09	<0.09	<0.09	<0.09	<0.09	<0.09	<0.09	<0.09	<0.09
SrO	<0.10	<0.10	<0.10	<0.10	<0.10	<0.10	<0.10	<0.10	<0.10	<0.10	<0.10
MnO	<0.07	<0.07	<0.07	<0.07	<0.07	<0.07	<0.07	<0.07	<0.07	<0.07	<0.07
Ce <sup>2</sup> O <sup>3</sup>	0.54	0.63	0.61	0.51	<0.08	<0.08	<0.08	<0.08	<0.08	<0.08	<0.08
Total	99.0	102.0	95.3	95.7	99.5	99.3	100.6	100.5	100.0	100.4	100.3
<i>Corr. Total*</i>			94.8	95.1	99.0	98.8	100.2	100.0	99.5	99.9	99.8

Sample	DUR r	DUR r	SHB05	SHB05	SHB05	SHB05	SHB05	SHB05	SHB08	SHB08	SHB08
EMPA #	55 / 1 .	56 / 1 .	128 / 1 .	129 / 1 .	130 / 1 .	29 / 1 .	30 / 1 .	31 / 1 .	89 / 1 .	90 / 1 .	91 / 1 .
spot size	20	20	20	20	20	10	10	10	20	20	20
F	3.5	3.5	2.6	2.7	2.7	2.5	2.9	2.6	2.8	2.4	3.0
F stdev	0.4	0.4	0.3	0.3	0.3	0.3	0.3	0.3	0.3	0.3	0.4
<i>F corr*</i>	3.2	3.1	2.3	2.5	2.4	2.2	2.6	2.3	2.5	2.2	2.7
Cl	0.39	0.34	<0.03	<0.03	<0.03	<0.03	<0.03	<0.03	<0.03	<0.03	<0.03
CaO	52.0	51.5	53.5	54.0	53.7	53.0	53.4	52.8	53.3	53.7	53.1
P <sup>2</sup> O <sup>5</sup>	39.6	38.7	42.7	41.0	41.6	40.4	40.8	40.2	41.3	40.7	41.9
FeO	<0.09	<0.09	<0.09	<0.09	<0.09	0.26	<0.09	<0.09	<0.09	<0.09	<0.09
SrO	<0.10	<0.10	<0.10	<0.10	<0.10	<0.10	<0.10	<0.10	<0.10	<0.10	<0.10
MnO	<0.07	<0.07	0.07	<0.07	<0.07	0.10	<0.06	0.09	0.14	0.11	0.09
Ce <sup>2</sup> O <sup>3</sup>	0.55	0.54	<0.08	<0.08	<0.08	<0.08	<0.08	<0.08	<0.08	<0.08	<0.08
Total	96.2	94.6	98.9	97.8	98.1	96.3	97.3	95.8	97.7	97.1	98.1
<i>Corr. Total*</i>	95.7	94.2	98.6	97.4	97.7	95.9	96.9	95.4	97.3	96.8	97.8

\* F values adjusted

Table A1-1: EMPA apatite data

Sample EMPA #	SHB05 28 / 1 .	SHB05 131 / 1 .	SHB05 132 / 1 .	SHB05 127 / 1 .	SHB12B 14 / 1 .	SHB12B 15 / 1 .	SHB12B 16 / 1 .	SHB12B 17 / 1 .	SHB12B 18 / 1 .	SHB12B 19 / 1 .	SHB12B 20 / 1 .
spot size	20	20	20	20	20	20	20	20	20	20	20
F	2.6	2.4	2.8	2.8	2.3	2.2	2.2	2.2	2.2	2.3	2.5
F stdev	0.3	0.3	0.3	0.3	0.3	0.3	0.3	0.3	0.3	0.3	0.3
<i>F corr*</i>	2.3	2.2	2.5	2.5	2.1	2.0	2.0	2.0	2.0	2.0	2.2
Cl	<0.03	<0.03	<0.03	<0.03	<0.03	0.04	<0.03	<0.03	<0.03	<0.03	<0.03
CaO	51.7	53.3	54.0	53.0	52.5	53.1	53.2	52.7	52.5	52.3	52.3
P <sup>2</sup> O <sup>5</sup>	40.2	41.4	42.0	41.6	41.1	40.5	40.1	39.8	40.2	40.0	41.0
FeO	<0.09	<0.09	<0.09	<0.09	<0.09	<0.09	<0.09	<0.09	<0.09	<0.09	<0.09
SrO	<0.10	<0.10	<0.10	<0.10	<0.10	<0.10	<0.10	0.10	<0.10	<0.10	0.12
MnO	<0.07	<0.07	<0.07	<0.07	<0.07	<0.07	<0.07	<0.07	<0.07	<0.07	<0.07
Ce <sup>2</sup> O <sup>3</sup>	0.17	<0.08	<0.08	<0.08	<0.08	<0.08	<0.08	<0.08	<0.08	<0.08	<0.08
Total	94.7	97.3	98.8	97.6	96.1	95.9	95.6	94.8	95.0	94.7	96.0
<i>Corr. Total*</i>	94.4	96.9	98.5	97.1	95.7	95.6	95.2	94.5	94.7	94.3	95.6

Sample EMPA #	SHB08 92 / 1 .	SHB08 93 / 1 .	SHB12B 4 / 1 .	SHB12B 13 / 1 .	SHB12B 8 / 1 .	SHB12B 9 / 1 .	SHB12B 10 / 1 .	SHB12B 11 / 1 .	SHB12B 12 / 1 .	SHB44A 117 / 1 .	SHB44A 118 / 1 .
spot size	20	20	20	20	20	20	20	20	20	20	20
F	2.6	2.5	2.2	2.2	2.4	2.3	2.4	2.2	2.1	3.1	3.0
F stdev	0.3	0.3	0.3	0.3	0.3	0.3	0.3	0.3	0.3	0.4	0.4
<i>F corr*</i>	2.4	2.3	2.0	2.0	2.1	2.1	2.1	2.0	1.9	2.8	2.7
Cl	<0.03	<0.03	<0.03	0.04	<0.03	<0.03	0.05	<0.03	<0.03	<0.03	<0.03
CaO	53.8	54.0	52.9	53.0	53.0	53.4	52.7	52.9	52.6	53.0	53.8
P <sup>2</sup> O <sup>5</sup>	40.9	41.6	41.3	40.0	41.3	41.0	41.2	40.2	41.1	41.0	41.3
FeO	<0.09	<0.09	<0.09	<0.09	<0.09	<0.09	<0.09	<0.09	<0.09	0.09	<0.09
SrO	<0.10	<0.10	<0.10	<0.10	<0.10	<0.10	<0.10	0.14	0.14	<0.10	0.18
MnO	0.13	0.09	<0.07	<0.07	<0.07	0.07	0.08	<0.07	<0.07	0.07	<0.07
Ce <sup>2</sup> O <sup>3</sup>	<0.08	<0.08	<0.08	<0.08	<0.08	<0.08	<0.08	<0.08	<0.08	<0.08	<0.08
Total	97.6	98.3	96.6	95.5	96.8	97.0	96.6	95.4	96.1	97.4	98.3
<i>Corr. Total*</i>	97.2	98.0	96.3	95.1	96.4	96.6	96.2	95.1	95.8	96.9	97.9

\* F values adjusted

Table A1-1: EMPA apatite data

Sample EMPA #	SHB12B 21 / 1 .	SHB12B 22 / 1 .	SHB12B 5 / 1 .	SHB12B 23 / 1 .	SHB12B 6 / 1 .	SHB12B 7 / 1 .	SHB44B 114 / 1 .	SHB44B 115 / 1 .	SHB44B 116 / 1 .	SHB45 122 / 1 .	SHB45 123 / 1 .
spot size	20	20	20	20	20	20	20	20	20	20	20
F	2.3	2.7	2.4	2.0	2.4	2.2	3.2	3.2	3.2	3.6	3.5
F stdev	0.3	0.3	0.3	0.2	0.3	0.3	0.4	0.4	0.4	0.4	0.4
<i>F corr*</i>	2.0	2.5	2.1	1.8	2.2	2.0	2.9	2.9	2.8	3.2	3.2
Cl	<0.03	<0.03	0.04	0.05	<0.03	<0.03	<0.03	<0.03	<0.03	<0.03	<0.03
CaO	52.8	52.4	52.9	52.5	52.8	53.6	53.5	54.1	52.9	54.1	53.7
P <sup>2</sup> O <sup>5</sup>	39.7	40.3	41.3	40.5	40.8	41.1	41.6	41.3	41.7	41.9	42.4
FeO	<0.09	<0.09	<0.09	<0.09	<0.09	<0.09	<0.09	<0.09	<0.09	<0.09	<0.09
SrO	<0.10	<0.10	<0.10	0.14	0.15	<0.10	0.11	0.14	0.18	0.63	0.17
MnO	<0.07	<0.07	<0.07	<0.07	<0.07	0.08	<0.07	<0.07	<0.07	<0.07	<0.07
Ce <sup>2</sup> O <sup>3</sup>	<0.08	<0.08	<0.08	<0.08	<0.08	<0.08	<0.08	<0.08	<0.08	<0.08	<0.08
Total	94.9	95.6	96.7	95.4	96.2	97.0	98.5	98.9	97.9	100.2	99.9
<i>Corr. Total*</i>	94.5	95.2	96.4	95.1	95.9	96.7	98.1	98.5	97.6	99.8	99.5

Sample EMPA #	SHB44A 119 / 1 .	SHB44A 120 / 1 .	SHB44A 121 / 1 .	SHS44A 33 / 1 .	SHS44A 34 / 1 .	SHB44B 111 / 1 .	SHB53 ecl 97 / 1 .	SHB53 ecl 98 / 1 .	SHB53 ep 103 / 1 .	SHB53 ep 104 / 1 .	SHB53 ep 105 / 1 .
spot size	20	20	20	10	10	20	20	20	20	20	20
F	3.3	3.3	3.4	3.4	3.1	3.2	2.4	2.5	2.4	2.3	2.3
F stdev	0.4	0.4	0.4	0.4	0.4	0.4	0.3	0.3	0.3	0.3	0.3
<i>F corr*</i>	3.0	3.0	3.0	3.0	2.8	2.9	2.2	2.2	2.1	2.1	2.1
Cl	<0.03	<0.03	<0.03	<0.03	<0.03	<0.03	<0.03	<0.03	<0.03	<0.03	<0.03
CaO	53.4	53.6	53.0	53.2	51.5	53.9	53.5	53.4	53.3	53.0	53.1
P <sup>2</sup> O <sup>5</sup>	41.9	40.9	41.7	40.5	39.4	41.6	40.4	41.3	40.6	40.5	41.3
FeO	<0.09	<0.09	<0.09	<0.09	<0.09	<0.09	<0.09	<0.09	<0.09	<0.09	<0.09
SrO	0.11	0.10	0.20	<0.10	<0.10	0.15	<0.10	<0.10	<0.10	0.21	0.24
MnO	0.11	0.08	<0.07	<0.06	<0.06	<0.07	<0.07	<0.07	<0.07	<0.07	<0.07
Ce <sup>2</sup> O <sup>3</sup>	<0.08	<0.08	<0.08	<0.08	<0.08	<0.08	<0.08	<0.08	<0.08	<0.08	<0.08
Total	98.8	98.0	98.3	97.3	94.1	98.9	96.6	97.4	96.4	96.2	97.0
<i>Corr. Total*</i>	98.4	97.6	97.9	96.8	93.6	98.6	96.1	97.0	96.0	95.8	96.7

\* F values adjusted

Table A1-1: EMPA apatite data

Sample	SHB45	SHB45	SHB45	SHB45	SHB45	SHB45	SHB53 ecl	SHB53 ecl	SHM23	SHM23	SHM23
EMPA #	124 / 1 .	125 / 1 .	126 / 1 .	35 / 1 .	36 / 1 .	37 / 1 .	95 / 1 .	96 / 1 .	74 / 1 .	75 / 1 .	76 / 1 .
spot size	20	20	20	10	10	10	20	20	20	20	20
F	3.4	3.2	3.3	3.1	3.2	3.3	2.4	2.4	3.5	3.5	3.9
F stdev	0.4	0.4	0.4	0.4	0.4	0.4	0.3	0.3	0.4	0.4	0.4
<i>F corr*</i>	3.1	2.9	2.9	2.8	2.9	2.9	2.2	2.2	3.2	3.1	3.5
Cl	<0.03	<0.03	<0.03	<0.03	<0.03	<0.03	<0.03	<0.03	<0.03	<0.03	<0.03
CaO	54.0	53.6	53.7	53.1	52.4	52.6	52.7	53.4	52.9	53.5	53.5
P <sup>2</sup> O <sup>5</sup>	41.8	41.9	40.9	40.0	40.3	40.0	40.3	41.2	41.1	40.4	40.6
FeO	<0.09	<0.09	<0.09	<0.09	<0.09	<0.09	<0.09	<0.09	<0.09	<0.09	<0.09
SrO	0.38	0.38	0.37	<0.10	0.2015	0.2725	0.14	<0.10	<0.10	0.16	<0.10
MnO	<0.07	<0.07	<0.07	<0.06	<0.06	<0.06	<0.07	<0.07	<0.07	<0.07	<0.07
Ce <sup>2</sup> O <sup>3</sup>	<0.08	<0.08	<0.08	0.13	<0.08	<0.08	<0.08	<0.08	<0.08	<0.08	<0.08
Total	99.6	99.1	98.3	96.5	96.1	96.2	95.7	97.2	97.6	97.6	98.2
<i>Corr. Total*</i>	99.3	98.8	97.9	96.0	95.7	95.8	95.3	96.8	97.2	97.2	97.6

Sample	SHB53 ep	SHB53 ep	SHB53 ep	SHM23	SHM23	SHM23	SHM23	SHM23	SHS3	SHS3	SHS3
EMPA #	106 / 1 .	107 / 1 .	108 / 1 .	69 / 1 .	70 / 1 .	71 / 1 .	72 / 1 .	73 / 1 .	79 / 1 .	88 / 1 .	80 / 1 .
spot size	20	20	20	20	20	20	20	20	20	20	20
F	2.5	2.6	2.8	3.6	3.5	3.7	3.7	3.9	3.4	3.3	3.2
F stdev	0.3	0.3	0.3	0.4	0.4	0.4	0.4	0.4	0.4	0.4	0.4
<i>F corr*</i>	2.2	2.3	2.5	3.2	3.2	3.3	3.3	3.5	3.0	3.0	2.8
Cl	<0.03	<0.03	<0.03	<0.03	<0.03	<0.03	<0.03	<0.03	<0.03	<0.03	<0.03
CaO	54.3	53.3	53.4	53.5	53.3	52.8	53.6	52.6	53.1	52.9	52.4
P <sup>2</sup> O <sup>5</sup>	41.0	42.1	41.5	40.4	40.2	40.6	40.9	40.1	40.0	41.0	40.4
FeO	<0.09	<0.09	<0.09	<0.09	<0.09	<0.09	<0.09	<0.09	<0.09	<0.09	<0.09
SrO	0.14	<0.10	0.15	<0.10	<0.10	<0.10	<0.10	<0.10	<0.10	0.11	<0.10
MnO	<0.07	<0.07	<0.07	<0.07	<0.07	<0.07	<0.07	<0.07	0.08	0.18	0.16
Ce <sup>2</sup> O <sup>3</sup>	<0.08	<0.08	<0.08	<0.08	<0.08	<0.08	<0.08	<0.08	<0.08	<0.08	<0.08
Total	97.9	98.0	97.9	97.6	97.0	97.2	98.3	96.6	96.6	97.6	96.3
<i>Corr. Total*</i>	97.6	97.7	97.6	97.1	96.6	96.7	97.8	96.2	96.2	97.2	95.8

\* F values adjuste

Table A1-1: EMPA apatite data

Sample EMPA #	SHS27 68 / 1 .	SHS27 61 / 1 .	SHS27 62 / 1 .	SHS27 63 / 1 .	SHS27 64 / 1 .	SHS27 65 / 1 .	SHS27 66 / 1 .	SHS27 67 / 1 .	SHS27 45 / 1 .	SHS27 46 / 1 .	SIB32 153 / 1 .
spot size	20	20	20	20	20	20	20	20	10	10	20
F	3.3	3.7	3.6	3.4	3.4	3.4	3.9	3.7	3.4	3.8	2.3
F stdev	0.4	0.4	0.4	0.4	0.4	0.4	0.4	0.4	0.4	0.4	0.3
<i>F corr*</i>	3.0	3.3	3.2	3.0	3.1	3.1	3.5	3.4	3.0	3.4	2.1
Cl	<0.03	<0.03	<0.03	<0.03	<0.03	<0.03	<0.03	<0.03	<0.03	<0.03	<0.03
CaO	53.1	52.8	52.7	52.4	52.3	52.6	53.1	53.1	52.7	52.0	54.1
P <sup>2</sup> O <sup>5</sup>	40.4	40.5	39.9	39.9	40.0	39.7	41.0	40.2	39.2	38.7	42.2
FeO	<0.09	<0.09	<0.09	<0.09	<0.09	<0.09	<0.09	<0.09	<0.09	<0.09	<0.09
SrO	<0.10	<0.10	<0.10	<0.10	<0.10	<0.10	<0.10	<0.10	<0.10	<0.10	<0.10
MnO	0.07	0.07	0.10	<0.07	<0.07	<0.07	0.08	0.09	<0.06	0.06	<0.07
Ce <sup>2</sup> O <sup>3</sup>	<0.08	<0.08	<0.08	<0.08	<0.08	<0.08	<0.08	<0.08	<0.08	<0.08	<0.08
Total	97.0	97.1	96.3	95.8	95.8	95.7	98.1	97.2	95.4	94.7	98.7
<i>Corr. Total*</i>	96.6	96.7	95.9	95.4	95.3	95.3	97.7	96.7	95.0	94.3	98.3

Sample EMPA #	SHS3 81 / 1 .	SHS3 82 / 1 .	SHS3 83 / 1 .	SHS3 84 / 1 .	SHS3 85 / 1 .	SHS3 86 / 1 .	SHS3 87 / 1 .	SIB32 150 / 1 .	SIB32 151 / 1 .	SIB32 152 / 1 .	SIS52 158 / 1 .
spot size	20	20	20	20	20	20	20	20	20	20	20
F	3.3	3.2	3.2	3.3	3.3	3.3	3.5	2.8	2.5	2.4	4.0
F stdev	0.4	0.4	0.4	0.4	0.4	0.4	0.4	0.3	0.3	0.3	0.5
<i>F corr*</i>	3.0	2.9	2.9	2.9	3.0	3.0	3.1	2.6	2.2	2.2	3.6
Cl	<0.03	<0.03	<0.03	<0.03	<0.03	<0.03	<0.03	<0.03	<0.03	<0.03	<0.03
CaO	52.8	52.5	52.5	52.5	53.1	52.2	52.8	53.2	54.1	54.0	54.1
P <sup>2</sup> O <sup>5</sup>	40.2	41.0	40.1	40.2	40.5	40.5	40.4	42.1	41.8	42.1	42.6
FeO	<0.09	<0.09	<0.09	<0.09	<0.09	<0.09	<0.09	<0.09	<0.09	<0.09	0.25
SrO	<0.10	<0.10	<0.10	0.14	0.16	<0.10	<0.10	<0.10	<0.10	<0.10	0.13
MnO	0.19	0.14	0.21	0.13	0.11	0.18	0.20	0.08	<0.07	<0.07	0.07
Ce <sup>2</sup> O <sup>3</sup>	<0.08	<0.08	<0.08	<0.08	<0.08	<0.08	<0.08	<0.08	<0.08	<0.08	<0.08
Total	96.7	96.9	96.2	96.3	97.2	96.2	96.9	98.2	98.5	98.6	101.3
<i>Corr. Total*</i>	96.2	96.5	95.7	95.9	96.8	95.8	96.5	97.9	98.1	98.2	100.8

\* F values adjusted



Table A1-1: EMPA apatite data

Sample	SIB32	SIB50B	SIB50B	SIB50B	SIB50B	SIB50B	SIB50B	SIB50B	SIB50B	SIS52	SIS52	SIS52	SIS52
EMPA #	154 / 1 .	142 / 1 .	143 / 1 .	144 / 1 .	145 / 1 .	38 / 1 .	39 / 1 .	40 / 1 .	162 / 1 .	155 / 1 .	156 / 1 .	157 / 1 .	
spot size	20	20	20	20	20	10	10	10	20	20	20	20	
F	2.5	2.8	3.1	2.7	3.1	3.1	2.7	2.7	4.5	4.4	3.6	3.8	
F stdev	0.3	0.3	0.4	0.3	0.4	0.4	0.3	0.3	0.5	0.5	0.4	0.4	
F corr*	2.3	2.5	2.8	2.4	2.8	2.8	2.4	2.4	4.1	4.0	3.2	3.4	
Cl	<0.03	<0.03	<0.03	<0.03	<0.03	<0.03	<0.03	<0.03	<0.03	<0.03	<0.03	<0.03	
CaO	54.0	53.3	53.1	53.6	53.7	52.7	52.1	51.7	54.9	54.2	53.9	54.6	
P <sup>2</sup> O <sup>5</sup>	42.3	41.3	41.3	41.2	41.6	40.2	39.4	39.6	43.2	43.7	42.7	43.5	
FeO	<0.09	<0.09	<0.09	<0.09	<0.09	0.11	0.27	0.10	<0.09	<0.09	0.36	<0.09	
SrO	<0.10	<0.10	<0.10	<0.10	<0.10	0.2007	<0.10	<0.10	<0.10	<0.10	<0.10	<0.10	
MnO	<0.07	0.18	0.15	0.19	0.13	0.10	0.18	0.16	<0.07	<0.07	0.07	<0.07	
Ce <sup>2</sup> O <sup>3</sup>	<0.08	<0.08	<0.08	<0.08	<0.08	0.16	<0.08	<0.08	<0.08	<0.08	<0.08	<0.08	
Total	98.9	97.7	97.8	97.9	98.6	96.6	94.7	94.3	102.7	102.4	100.6	102.0	
Corr. Total*	98.5	97.3	97.4	97.5	98.2	96.3	94.3	93.9	102.2	101.9	100.2	101.5	

Sample	SIS52	SIS52	SIS52	SIS52	SIS52	SIS53	SIS53	SIS53	SIS53	SIS53	SIS53
EMPA #	159 / 1 .	160 / 1 .	161 / 1 .	41 / 1 .	42 / 1 .	146 / 1 .	147 / 1 .	148 / 1 .	149 / 1 .	43 / 1 .	44 / 1 .
spot size	20	20	20	10	10	20	20	20	20	10	10
F	4.5	4.5	4.6	4.3	4.2	3.3	3.2	3.1	3.1	3.4	3.2
F stdev	0.5	0.5	0.5	0.5	0.5	0.4	0.4	0.4	0.4	0.4	0.4
F corr*	4.1	4.0	4.1	3.8	3.8	3.0	2.9	2.8	2.8	3.1	2.9
Cl	<0.03	<0.03	<0.03	0.04	<0.03	<0.03	<0.03	<0.03	<0.03	<0.03	<0.03
CaO	54.6	54.3	54.5	51.6	51.2	53.7	54.4	53.8	53.7	52.1	52.3
P <sup>2</sup> O <sup>5</sup>	43.5	44.3	43.0	39.1	37.4	41.9	41.8	41.7	42.3	38.3	40.7
FeO	<0.09	<0.09	<0.09	0.28	0.20	<0.09	<0.09	<0.09	<0.09	<0.09	0.15
SrO	<0.10	<0.10	<0.10	<0.10	0.1558	<0.10	<0.10	0.12	<0.10	0.1078	0.1659
MnO	<0.07	0.01	<0.07	0.09	<0.06	0.08	0.15	0.10	<0.07	0.12	<0.06
Ce <sup>2</sup> O <sup>3</sup>	<0.08	<0.08	<0.08	0.40	0.50	<0.08	<0.08	<0.08	<0.08	<0.08	0.14
Total	102.7	103.1	102.1	95.9	93.7	99.1	99.7	98.8	99.2	94.2	96.7
Corr. Total*	102.2	102.6	101.6	95.4	93.3	98.7	99.3	98.5	98.8	93.7	96.3

\* F values adjusted

**Table A1- 2: Apatite oxygen isotope composition determined by SHRIMP. C: core, M: mantle, R: rim**

Spot	$^{18}\text{O}/^{16}\text{O}$	$\pm 95\% \text{ cl}$	$\delta^{18}\text{O} (\text{‰})$	$\pm \text{SE}$
SGM21-01C	0.00208499	1.85E-07	25.04	0.09
SGM21-2	0.00208882	2.28E-07	26.91	0.11
SGM21-3R	0.00208798	1.21E-07	26.50	0.06
SGM21-4	0.00208741	1.72E-07	26.22	0.08
SGM21-5C	0.00208832	1.89E-07	26.66	0.09
SGM21-6R	0.00208870	1.39E-07	26.84	0.07
SGM21-7R	0.00208621	2.59E-07	25.63	0.12
SGM21-8	0.00208662	2.29E-07	25.83	0.11
SGM21-9C	0.00208794	2.28E-07	26.48	0.11
SGM21-10	0.00208881	1.70E-07	26.90	0.08
SGM21-11C	0.00208836	2.47E-07	26.68	0.12
SGM21-12R	0.00208592	1.71E-07	25.49	0.08
SGM21-13C	0.00208821	1.63E-07	26.60	0.08
SGM21-14C	0.00208765	1.58E-07	26.33	0.08
SGM21-15	0.00208776	1.33E-07	26.39	0.06
SGM21-16	0.00208697	2.57E-07	26.00	0.12
SGM21-17R	0.00208836	1.79E-07	26.68	0.09
SGM21-18	0.00208730	9.90E-08	26.16	0.05
SGM21-19	0.00208870	2.02E-07	26.84	0.10
SGM21-20	0.00208518	1.73E-07	25.13	0.08
		<b>average</b>	26.3	
		<b>std. dev.</b>	0.57	

Spot	$^{18}\text{O}/^{16}\text{O}$	$\pm 95\% \text{ cl}$	$\delta^{18}\text{O} (\text{‰})$	$\pm \text{SE}$
SHB05-1	0.00206482	1.75E-07	15.39	0.08
SHB05-2	0.00206352	1.61E-07	14.76	0.08
SHB05-3C	0.00206481	8.70E-08	15.39	0.04
SHB05-4C	0.00206475	7.80E-08	15.36	0.04
SHB05-5C	0.00206467	1.72E-07	15.32	0.08
SHB05-6R	0.00206451	1.42E-07	15.24	0.07
SHB05-7	0.00206412	1.71E-07	15.05	0.08
SHB05-8	0.00206439	1.38E-07	15.18	0.07
SHB05-9	0.00206474	1.74E-07	15.35	0.08
SHB05-10C	0.00206398	8.50E-08	14.98	0.04
SHB05-11	0.00206424	1.28E-07	15.11	0.06
SHB05-12R	0.00206446	1.49E-07	15.22	0.07
SHB05-13	0.00206489	2.70E-07	15.43	0.13
SHB05-14	0.00206352	2.31E-07	14.76	0.11
SHB05-15	0.00206450	1.49E-07	15.24	0.07
SHB05-16	0.00206404	1.29E-07	15.01	0.06
SHB05-17	0.00206525	1.58E-07	15.60	0.08
SHB05-18	0.00206488	1.37E-07	15.42	0.07
SHB05-19	0.00206564	1.37E-07	15.79	0.07
SHB05-20C	0.00206486	1.34E-07	15.41	0.06
SHB05-21	0.00206496	1.22E-07	15.46	0.06
SHB05-22R	0.00206483	1.82E-07	15.40	0.09
		<b>average</b>	15.3	
		<b>std. dev.</b>	0.25	

<b>Instrument:</b>	SHRIMP II
<b>Session:</b>	13.03.2013
<b>DUR repeatability:</b>	0.23 ‰ (1 $\sigma$ )

Table A1- 2: Apatite oxygen isotope composition determined by SHRIMP. C: core, M: mantle, R: rim

Spot	$^{18}\text{O}/^{16}\text{O}$	$\pm 95\%$ cl	$\delta^{18}\text{O}$ (‰)	$\pm\text{SE}$
SHB45-1M	0.00206576	1.57E-07	15.85	0.08
SHB45-2R	0.00206677	2.20E-07	16.34	0.11
SHB45-3	0.00206638	1.28E-07	16.15	0.06
SHB45-4R	0.00206618	3.16E-07	16.05	0.15
SHB45-5	0.00206590	9.50E-08	15.92	0.05
SHB45-6M	0.00206572	1.58E-07	15.83	0.08
SHB45-7	0.00206595	1.24E-07	15.94	0.06
SHB45-8	0.00206592	1.04E-07	15.93	0.05
SHB45-9	0.00206671	1.50E-07	16.31	0.07
SHB45-10	0.00206519	2.04E-07	15.57	0.10
SHB45-11	0.00206621	1.11E-07	16.07	0.05
SHB45-12	0.00206547	2.18E-07	15.71	0.11
SHB45-13	0.00206670	1.73E-07	16.31	0.08
SHB45-14	0.00206425	2.61E-07	15.12	0.13
SHB45-15	0.00206675	1.96E-07	16.33	0.09
SHB45-16	0.00206598	2.48E-07	15.96	0.12
SHB45-17	0.00206590	1.57E-07	15.92	0.08
		<b>average</b>	16.0	
		<b>std. dev.</b>	0.31	

<b>Instrument:</b>	SHRIMP II
<b>Session:</b>	13.03.2013
<b>DUR repeatability:</b>	0.23 ‰ (1 $\sigma$ )

Spot	$^{18}\text{O}/^{16}\text{O}$	$\pm 95\%$ cl	$\delta^{18}\text{O}$ (‰)	$\pm\text{SE}$
SHB12B-1	0.00205928	2.69E-07	12.69	0.13
SHB12B-2	0.00206280	9.60E-08	14.41	0.05
SHB12B-3	0.00205925	1.29E-07	12.68	0.06
SHB12B-4	0.00206258	1.65E-07	14.30	0.08
SHB12B-5	0.00206376	1.05E-07	14.88	0.05
SHB12B-6C	0.00205574	1.25E-07	10.97	0.06
SHB12B-7R	0.00206298	1.78E-07	14.49	0.09
SHB12B-8	0.00206437	2.00E-07	15.17	0.10
SHB12B-9R	0.00206479	2.07E-07	15.38	0.10
SHB12B-10	0.00205573	1.22E-07	10.96	0.06
SHB12B-11C	0.00205566	1.45E-07	10.93	0.07
SHB12B-12	0.00205698	1.22E-07	11.58	0.06
SHB12B-13	0.00206276	1.22E-07	14.39	0.06
SHB12B-14	0.00206539	8.20E-08	15.67	0.04
SHB12B-15	0.00206655	1.09E-07	16.24	0.05
SHB12B-16	0.00205721	1.47E-07	11.69	0.07
SHB12B-17	0.00205367	1.59E-07	9.96	0.08
SHB12B-18	0.00205717	2.02E-07	11.67	0.10
SHB12B-19	0.00206571	2.28E-07	15.83	0.11
SHB12B-20	0.00205488	1.52E-07	10.55	0.07
SHB12B-21	0.00205711	1.31E-07	11.64	0.06
SHB12B-22	0.00206359	1.34E-07	14.79	0.06
SHB12B-23	0.00205238	1.78E-07	9.33	0.09
		<b>average</b>	13.1	
		<b>std. dev.</b>	2.12	

Table A1- 2: Apatite oxygen isotope composition determined by SHRIMP. C: core, M: mantle, R: rim

Spot	$^{18}\text{O}/^{16}\text{O}$	$\pm 95\% \text{ cl}$	$\delta^{18}\text{O} (\text{‰})$	$\pm \text{SE}$
SHS44A-1	0.00206783	1.78E-07	16.86	0.09
SHS44A-2	0.00206670	2.62E-07	16.31	0.13
SHS44A-3R	0.00206730	1.82E-07	16.60	0.09
SHS44A-4	0.00206680	1.55E-07	16.36	0.07
SHS44A-5	0.00206582	1.06E-07	15.88	0.05
SHS44A-6C	0.00206703	1.28E-07	16.47	0.06
SHS44A-7C	0.00206568	2.18E-07	15.81	0.11
SHS44A-8	0.00206590	2.18E-07	15.92	0.11
SHS44A-9R	0.00206637	6.70E-08	16.15	0.03
SHS44A-10R	0.00206721	2.01E-07	16.56	0.10
SHS44A-11	0.00206457	4.45E-07	15.27	0.22
SHS44A-12R	0.00206620	2.38E-07	16.06	0.12
SHS44A-13	0.00206656	1.86E-07	16.24	0.09
SHS44A-14C	0.00206564	1.46E-07	15.79	0.07
SHS44A-16	0.00206651	2.79E-07	16.21	0.14
SHS44A-17C	0.00206692	1.25E-07	16.42	0.06
SHS44A-18	0.00206375	1.93E-07	14.87	0.09
SHS44A-19R	0.00206717	1.45E-07	16.54	0.07
SHS44A-20	0.00206707	3.64E-07	16.49	0.18
SHS44A-21	0.00206745	1.26E-07	16.67	0.06
SHS44A-22	0.00206654	2.04E-07	16.23	0.10
SHS44A-23	0.00206613	1.26E-07	16.03	0.06
SHS44A-24	0.00206732	1.07E-07	16.61	0.05
SHS44A-25	0.00206764	6.45E-07	16.76	0.31
		<b>average</b>	16.2	
		<b>std. dev.</b>	0.46	

Spot	$^{18}\text{O}/^{16}\text{O}$	$\pm 95\% \text{ cl}$	$\delta^{18}\text{O} (\text{‰})$	$\pm \text{SE}$
SHS44B-1C	0.00206769	2.38E-07	16.79	0.11
SHS44B-2	0.00206771	1.47E-07	16.80	0.07
SHS44B-3R	0.00206692	2.72E-07	16.42	0.13
SHS44B-4	0.00206738	1.25E-07	16.64	0.06
SHS44B-5	0.00206763	1.90E-07	16.76	0.09
SHS44B-6	0.00206726	2.04E-07	16.58	0.10
SHS44B-7	0.00206741	1.82E-07	16.65	0.09
SHS44B-8	0.00206738	1.82E-07	16.64	0.09
SHS44B-9	0.00206740	1.94E-07	16.65	0.09
SHS44B-10	0.00206729	2.71E-07	16.59	0.13
SHS44B-11	0.00206723	1.58E-07	16.57	0.08
SHS44B-12	0.00206670	2.39E-07	16.31	0.12
SHS44B-13	0.00206639	1.13E-07	16.16	0.05
SHS44B-14	0.00206557	1.61E-07	15.76	0.08
SHS44B-15	0.00206724	1.59E-07	16.57	0.08
SHS44B-16	0.00206675	1.68E-07	16.33	0.08
SHS44B-17	0.00206733	2.38E-07	16.62	0.12
SHS44B-18	0.00206727	1.88E-07	16.59	0.09
SHS44B-19	0.00206777	1.84E-07	16.83	0.09
SHS44B-20	0.00206745	2.14E-07	16.67	0.10
SHS44B-21	0.00206741	2.23E-07	16.65	0.11
SHS44B-22	0.00206729	2.46E-07	16.60	0.12
SHS44B-23	0.00206781	1.88E-07	16.85	0.09
		<b>average</b>	16.6	
		<b>std. dev.</b>	0.24	

<b>Instrument:</b>	SHRIMP II
<b>Session:</b>	13.03.2013
<b>DUR repeatability:</b>	0.23 ‰ (1 $\sigma$ )

**Table A1- 2: Apatite oxygen isotope composition determined by SHRIMP. C: core, M: mantle, R: rim**

Spot	$^{18}\text{O}/^{16}\text{O}$	$\pm 95\%$ cl	$\delta^{18}\text{O}$ (‰)	$\pm\text{SE}$
SIB50B-1C	0.00206285	1.94E-07	14.26	0.09
SIB50B-2C	0.00206298	1.24E-07	14.32	0.06
SIB50B-3R	0.00206318	2.74E-07	14.42	0.13
SIB50B-4R	0.00206340	3.09E-07	14.53	0.15
SIB50B-5R	0.00206338	1.52E-07	14.51	0.07
SIB50B-6C	0.00206277	1.19E-07	14.22	0.06
SIB50B-7C	0.00206282	1.33E-07	14.25	0.06
SIB50B-8	0.00206071	1.40E-07	13.22	0.07
SIB50B-9	0.00206393	1.53E-07	14.78	0.07
SIB50B-10	0.00206259	2.17E-07	14.13	0.11
SIB50B-11	0.00206308	1.46E-07	14.37	0.07
SIB50B-12	0.00206242	1.74E-07	14.05	0.08
SIB50B-13	0.00206234	2.14E-07	14.01	0.10
SIB50B-14	0.00206286	1.26E-07	14.26	0.06
SIB50B-15	0.00206167	1.84E-07	13.69	0.09
		<b>average</b>	14.2	
		<b>std. dev.</b>	0.37	

Spot	$^{18}\text{O}/^{16}\text{O}$	$\pm 95\%$ cl	$\delta^{18}\text{O}$ (‰)	$\pm\text{SE}$
------	-------------------------------	---------------	---------------------------	----------------

<b>Instrument:</b>	SHRIMP II
<b>Session:</b>	13.03.2013
<b>DUR repeatability:</b>	0.23 ‰ (1 $\sigma$ )

Table A1- 2: Apatite oxygen isotope composition determined by SHRIMP. C: core, M: mantle, R: rim

Spot	$^{18}\text{O}/^{16}\text{O}$	$\pm 95\%$ cl	$\delta^{18}\text{O}$ (‰)	$\pm\text{SE}$
SIS52-1C	0.00207659	1.54E-07	20.40	0.07
SIS52-2R	0.00207596	1.93E-07	20.09	0.09
SIS52-3R	0.00207578	1.10E-07	20.01	0.05
SIS52-4C	0.00207568	2.16E-07	19.96	0.10
SIS52-5R	0.00207669	2.49E-07	20.45	0.12
SIS52-6M	0.00207682	2.85E-07	20.51	0.14
SIS52-7M	0.00207791	2.33E-07	21.04	0.11
SIS52-8R	0.00207763	1.97E-07	20.91	0.09
SIS52-10	0.00207727	2.66E-07	20.73	0.13
SIS52-11	0.00207797	1.68E-07	21.07	0.08
SIS52-12C	0.00207747	2.10E-07	20.83	0.10
SIS52-13R	0.00207516	1.53E-07	19.71	0.07
SIS52-14M	0.00207608	1.43E-07	20.15	0.07
SIS52-15M	0.00207584	2.12E-07	20.04	0.10
SIS52-16R	0.00207493	2.20E-07	19.59	0.11
SIS52-17R	0.00207462	1.33E-07	19.44	0.06
SIS52-18	0.00207580	2.24E-07	20.02	0.11
SIS52-19	0.00207489	8.60E-08	19.58	0.04
SIS52-20C	0.00207424	2.55E-07	19.26	0.12
SIS52-21	0.00207622	1.79E-07	20.22	0.09
SIS52-22	0.00207507	2.44E-07	19.66	0.12
SIS52-23	0.00207695	2.33E-07	20.58	0.11
SIS52-24	0.00207691	1.97E-07	20.56	0.09
		<b>average</b>	20.2	
		<b>std. dev.</b>	0.52	

Spot	$^{18}\text{O}/^{16}\text{O}$	$\pm 95\%$ cl	$\delta^{18}\text{O}$ (‰)	$\pm\text{SE}$
SIS53-1R	0.00206797	2.38E-07	16.20	0.12
SIS53-2	0.00206702	2.51E-07	15.74	0.12
SIS53-3C	0.00206690	2.04E-07	15.69	0.10
SIS53-4C	0.00206860	1.79E-07	16.51	0.09
SIS53-5	0.00206745	1.06E-07	15.95	0.05
SIS53-6	0.00206713	8.80E-08	15.80	0.04
SIS53-7	0.00206676	4.89E-07	15.61	0.24
SIS53-8	0.00206713	1.62E-07	15.80	0.08
SIS53-9	0.00206881	2.46E-07	16.61	0.12
SIS53-10	0.00206841	2.28E-07	16.42	0.11
SIS53-11	0.00206795	1.90E-07	16.20	0.09
SIS53-12	0.00206850	1.31E-07	16.46	0.06
SIS53-13	0.00206862	1.35E-07	16.52	0.07
SIS53-14	0.00206976	1.40E-07	17.08	0.07
SIS53-15	0.00206935	1.23E-07	16.88	0.06
SIS53-16C	0.00206883	1.20E-07	16.63	0.06
SIS53-17R	0.00206847	1.33E-07	16.45	0.06
SIS53-18	0.00206853	1.95E-07	16.48	0.09
SIS53-19	0.00206919	1.14E-07	16.80	0.06
		<b>average</b>	16.3	
		<b>std. dev.</b>	0.43	

<b>Instrument:</b>	SHRIMP II
<b>Session:</b>	17.03.2013
<b>DUR repeatability:</b>	0.44 ‰ (1 $\sigma$ )

Table A1- 2: Apatite oxygen isotope composition determined by SHRIMP. C: core, M: mantle, R: rim

Spot	$^{18}\text{O}/^{16}\text{O}$	$\pm 95\%$ cl	$\delta^{18}\text{O}$ (‰)	$\pm\text{SE}$
SHB53ep-1	0.00207426	2.29E-07	13.73	0.11
SHB53ep-2	0.00207452	1.13E-07	13.86	0.05
SHB53ep-3	0.00207422	1.92E-07	13.71	0.09
SHB53ep-4	0.00207305	1.10E-07	13.14	0.05
SHB53ep-5	0.00207440	9.20E-08	13.80	0.04
SHB53ep-6	0.00207411	1.97E-07	13.66	0.10
SHB53ep-7	0.00207395	7.00E-08	13.58	0.03
SHB53ep-8	0.00207451	1.86E-07	13.85	0.09
SHB53ep-9	0.00207376	8.60E-08	13.49	0.04
SHB53ep-10	0.00207339	1.18E-07	13.30	0.06
SHB53ep-11	0.00207426	1.57E-07	13.73	0.08
SHB53ep-12	0.00207378	3.60E-08	13.49	0.02
SHB53ep-13	0.00207460	1.87E-07	13.89	0.09
SHB53ep-14	0.00207405	9.70E-08	13.63	0.05
SHB53ep-15	0.00207460	2.04E-07	13.89	0.10
SHB53ep-16	0.00207229	2.63E-07	12.77	0.13
SHB53ep-17	0.00207432	2.87E-07	13.76	0.14
SHB53ep-18	0.00207238	1.85E-07	12.82	0.09
		<b>average</b>	13.6	
		<b>std. dev.</b>	0.34	

Spot	$^{18}\text{O}/^{16}\text{O}$	$\pm 95\%$ cl	$\delta^{18}\text{O}$ (‰)	$\pm\text{SE}$
SHB53ec-1	0.00207350	3.20E-08	13.36	0.02
SHB53ec-2	0.00207464	1.72E-07	13.91	0.08
SHB53ec-3	0.00207457	2.75E-07	13.88	0.13
SHB53ec-4	0.00207420	8.20E-08	13.70	0.04
SHB53ec-5	0.00207429	1.10E-07	13.74	0.05
SHB53ec-6	0.00207307	2.03E-07	13.15	0.10
SHB53ec-7	0.00207460	2.69E-07	13.89	0.13
SHB53ec-8	0.00207313	2.86E-07	13.18	0.14
SHB53ec-9	0.00207208	1.61E-07	12.67	0.08
SHB53ec-10	0.00207171	1.72E-07	12.49	0.08
SHB53ec-11	0.00207427	2.48E-07	13.73	0.12
SHB53ec-12	0.00207390	3.63E-07	13.55	0.17
SHB53ec-13	0.00207237	1.74E-07	12.81	0.08
SHB53ec-14	0.00207357	1.76E-07	13.40	0.08
SHB53ec-15	0.00207263	2.29E-07	12.94	0.11
SHB53ec-16	0.00207351	2.03E-07	13.37	0.10
SHB53ec-17	0.00207013	2.09E-07	11.73	0.10
SHB53ec-18	0.00207217	2.40E-07	12.72	0.12
		<b>average</b>	13.2	
		<b>std. dev.</b>	0.59	

Instrument:	SHRIMP SI
Session:	04.04.2013
DUR repeatability:	0.14 ‰ (1 $\sigma$ )

Table A1- 2: Apatite oxygen isotope composition determined by SHRIMP. C: core, M: mantle, R: rim

Spot	$^{18}\text{O}/^{16}\text{O}$	$\pm 95\% \text{ cl}$	$\delta^{18}\text{O} (\text{‰})$	$\pm \text{SE}$
SHS3-1C	0.00208295	1.96E-07	17.83	0.09
SHS3-2	0.00208660	9.80E-08	19.59	0.05
SHS3-3R	0.00208041	8.60E-08	16.59	0.04
SHS3-4R	0.00208160	6.40E-08	17.17	0.03
SHS3-5	0.00208505	2.01E-07	18.84	0.10
SHS3-6C	0.00208395	9.90E-08	18.31	0.05
SHS3-7R	0.00208280	2.74E-07	17.75	0.13
SHS3-8C	0.00208712	1.70E-07	19.84	0.08
SHS3-9M	0.00208702	1.07E-07	19.79	0.05
SHS3-10R	0.00208121	8.00E-08	16.98	0.04
SHS3-11C	0.00208775	9.90E-08	20.15	0.05
SHS3-12	0.00208669	2.73E-07	19.64	0.13
SHS3-13	0.00208413	1.87E-07	18.39	0.09
SHS3-14C	0.00208239	3.59E-07	17.55	0.17
SHS3-15M	0.00208628	1.30E-07	19.43	0.06
SHS3-16	0.00208619	1.69E-07	19.39	0.08
SHS3-17	0.00208149	2.11E-07	17.12	0.10
SHS3-18	0.00208118	1.94E-07	16.97	0.09
SHS3-19	0.00208437	2.54E-07	18.51	0.12
SHS3-20	0.00208395	1.09E-07	18.31	0.05
SHS3-21	0.00208081	1.65E-07	16.90	0.08
SHS3-22	0.00208417	2.14E-07	18.52	0.10
SHS3-23	0.00208554	7.70E-08	19.19	0.04
SHS3-24	0.00208571	2.17E-07	19.27	0.10
		<b>average</b>	18.4	
		<b>std. dev.</b>	1.10	

Spot	$^{18}\text{O}/^{16}\text{O}$	$\pm 95\% \text{ cl}$	$\delta^{18}\text{O} (\text{‰})$	$\pm \text{SE}$
SIB32-1	0.00206418	2.63E-07	14.36	0.13
SIB32-1b	0.00207589	1.56E-07	14.17	0.08
SIB32-2	0.00207572	5.10E-08	14.08	0.02
SIB32-3	0.00207501	6.30E-08	13.74	0.03
SIB32-4	0.00207589	2.64E-07	14.17	0.13
SIB32-5	0.00207563	1.56E-07	14.04	0.08
SIB32-6	0.00207561	1.94E-07	14.03	0.09
SIB32-7	0.00207613	2.29E-07	14.28	0.11
SIB32-8	0.00207613	1.61E-07	14.28	0.08
SIB32-9	0.00207575	1.06E-07	14.10	0.05
SIB32-10	0.00207567	1.34E-07	14.06	0.06
SIB32-11	0.00207603	2.00E-07	14.24	0.10
SIB32-12	0.00207589	1.15E-07	14.17	0.06
SIB32-13	0.00207560	1.84E-07	14.03	0.09
SIB32-14	0.00207588	1.75E-07	14.16	0.08
SIB32-15	0.00207554	1.74E-07	14.00	0.08
SIB32-16	0.00207562	1.01E-07	14.04	0.05
		<b>average</b>	14.1	
		<b>std. dev.</b>	0.14	

<b>Instrument:</b>	SHRIMP SI
<b>Session:</b>	04.04.2013
<b>DUR repeatability:</b>	0.14 ‰ (1 $\sigma$ )



Table A1- 2: Apatite oxygen isotope composition determined by SHRIMP. C: core, M: mantle, R: rim

Spot	$^{18}\text{O}/^{16}\text{O}$	$\pm 95\%$ cl	$\delta^{18}\text{O}$ (‰)	$\pm \text{SE}$
SHB08-1	0.00207906	5.90E-08	15.94	0.03
SHB08-2	0.00207842	3.08E-07	15.63	0.15
SHB08-3	0.00207830	2.05E-07	15.58	0.10
SHB08-4	0.00207916	1.52E-07	15.99	0.07
SHB08-5	0.00207824	1.57E-07	15.54	0.08
SHB08-6	0.00207857	2.09E-07	15.71	0.10
SHB08-7	0.00207831	3.43E-07	15.58	0.17
SHB08-8	0.00207859	5.90E-08	15.71	0.03
SHB08-9	0.00207790	2.56E-07	15.38	0.12
SHB08-10	0.00207797	9.90E-08	15.42	0.05
		average	15.6	
		std. dev.	0.20	

Spot	$^{18}\text{O}/^{16}\text{O}$	$\pm 95\%$ cl	$\delta^{18}\text{O}$ (‰)	$\pm \text{SE}$
SHM23B-1C	0.00207926	2.59E-07	16.04	0.12
SHM23B-2C	0.00207883	1.79E-07	15.83	0.09
SHM23B-3R	0.00207982	1.10E-07	16.31	0.05
SHM23B-4R	0.00207885	1.82E-07	15.84	0.09
SHM23B-5	0.00207837	1.94E-07	15.61	0.09
SHM23B-6	0.00207893	1.67E-07	15.88	0.08
SHM23B-7R	0.00207803	2.01E-07	15.44	0.10
SHM23B-8C	0.00207897	5.80E-08	15.90	0.03
SHM23B-9	0.00207904	1.95E-07	15.93	0.09
SHM23B-10	0.00207931	6.10E-08	16.06	0.03
		average	15.9	
		std. dev.	0.24	

Spot	$^{18}\text{O}/^{16}\text{O}$	$\pm 95\%$ cl	$\delta^{18}\text{O}$ (‰)	$\pm \text{SE}$
SHS27-1C	0.00208783	3.04E-07	20.30	0.15
SHS27-2	0.00208779	1.77E-07	20.27	0.08
SHS27-3R	0.00209216	2.83E-07	22.39	0.14
SHS27-4C	0.00208627	2.30E-07	19.54	0.11
SHS27-5	0.00208859	1.68E-07	20.66	0.08
SHS27-6R	0.00208958	1.00E-07	21.14	0.05
SHS27-7	0.00209009	1.35E-07	21.39	0.06
SHS27-8	0.00208971	2.15E-07	21.20	0.10
SHS27-9R	0.00208953	2.72E-07	21.12	0.13
SHS27-10C	0.00208302	2.12E-07	17.97	0.10
SHS27-11	0.00208921	1.59E-07	20.96	0.08
SHS27-12	0.00208991	1.96E-07	21.30	0.09
SHS27-13	0.00208873	1.14E-07	20.73	0.05
SHS27-14	0.00208927	8.70E-08	20.99	0.04
SHS27-15	0.00208664	2.41E-07	19.72	0.12
SHS27-16	0.00208909	1.79E-07	20.91	0.09
SHS27-17	0.00208793	1.18E-07	20.34	0.06
SHS27-18	0.00208989	1.58E-07	21.29	0.08
SHS27-19	0.00208595	1.48E-07	19.38	0.07
SHS27-20	0.00208924	2.81E-07	20.98	0.13
		average	20.6	
		std. dev.	0.94	

Instrument:	SHRIMP SI
Session:	04.04.2013
DUR repeatability:	0.14 ‰ (1 $\sigma$ )

**Table A 1 - 3: LA-ICP-MA data for DM1C rutiles.** Temperature in °C calculated following Tomkins et al. (2007).

	DM1C Rutile_1	DM1C Rutile_2	DM1C Rutile_3	DM1C Rutile_4	DM1C Rutile_5	DM1C Rutile_6	DM1C Rutile_7	DM1C Rutile_8	DM1C Rutile_9	DM1C Rutile_10	DM1C Rutile_11	DM1C Rutile_12
<b>Al (ppm)</b>	1973	1779	2103	1976	1552	1452	1423	1597	2102	1732	1677	1594
<b>Si (ppm)</b>	1184	1170	1196	1102	1129	1217	1188	1135	1152	1153	1145	1150
<b>Sc (ppm)</b>	8.4	10.0	2.3	5.1	3.6	2.0	3.4	2.8	2.1	2.9	3.1	2.9
<b>V (ppm)</b>	565	640	675	595	648	822	852	794	655	711	724	726
<b>Cr (ppm)</b>	118	110	96	108	128	117	135	109	107	138	148	153
<b>Mn (ppm)</b>	bdl	bdl	bdl	bdl	bdl	bdl	bdl	bdl	bdl	bdl	bdl	bdl
<b>Fe (ppm)</b>	152	255	105	181	597	307	343	493	345	567	549	357
<b>Y (ppm)</b>	0.61	0.06	0.04	0.07	0.97	0.36	0.11	0.23	0.19	0.17	0.25	0.13
<b>Zr (ppm)</b>	146	143	146	142	139	139	143	136	154	143	140	152
<b>Nb (ppm)</b>	5187	5040	5026	4901	5021	5229	5159	5071	5221	5050	5159	5022
<b>Mo (ppm)</b>	0.96	3.33	6.72	5.02	1.22	1.89	1.18	1.35	1.59	3.28	1.76	1.07
<b>Ba (ppm)</b>	bdl	bdl	bdl	bdl	bdl	bdl	bdl	bdl	bdl	bdl	bdl	bdl
<b>Dy (ppm)</b>	0.242	bdl	bdl	0.016	0.226	0.080	0.022	0.046	0.017	0.029	0.037	0.018
<b>Er (ppm)</b>	0.045	0.001	bdl	0.003	0.113	0.026	0.009	0.027	0.016	0.017	0.024	0.004
<b>Yb (ppm)</b>	0.029	0.007	bdl	bdl	0.198	0.026	0.006	0.021	0.022	0.017	0.033	0.017
<b>Hf (ppm)</b>	7.10	6.25	5.74	5.00	6.76	6.81	6.67	6.50	7.47	6.80	6.73	6.02
<b>Ta (ppm)</b>	487	461	459	418	428	528	473	494	522	529	501	464
<b>W (ppm)</b>	304	508	488	567	217	175	241	245	263	278	221	364
<b>Pb (ppm)</b>	2.59	0.05	bdl	0.11	0.28	0.50	0.13	1.26	bdl	0.11	0.11	0.16
<b>Th (ppm)</b>	10.30	0.17	bdl	0.28	0.47	0.31	0.03	0.35	0.02	0.02	0.03	0.03
<b>U (ppm)</b>	3.52	2.28	5.17	2.46	3.27	3.09	0.55	0.63	0.89	0.75	1.02	1.18
<b>T 20 kbar</b>	636	634	636	634	632	632	634	630	639	634	632	638
<b>T 30 kbar</b>	676	675	676	674	672	672	674	671	680	674	673	679
<b>Nb/Ta</b>	10.7	10.9	11.0	11.7	11.7	9.9	10.9	10.3	10.0	9.5	10.3	10.8

**Table A 1 - 3: LA-ICP-MA data for DM1C rutiles.** Temperature in °C calculated following Tomkins et al. (2007).

	DM1C Rutile_13	DM1C Rutile_14	DM1C Rutile_15	DM1C Rutile_16	DM1C Rutile_17	DM1C Rutile_19	DM1C Rutile_20	DM1C Rutile_21	DM1C Rutile_22	DM1C Rutile_23	DM1C Rutile_24	LOD
<b>Al (ppm)</b>	2098	1551	1704	1460	1443	2190	1450	1452	1533	1628	1518	<b>129</b>
<b>Si (ppm)</b>	1653	1256	1174	1110	1158	2240	1066	1152	1208	1537	1134	<b>103</b>
<b>Sc (ppm)</b>	11.6	20.3	3.0	2.8	1.5	2.3	2.2	1.7	1.9	2.5	1.8	<b>0.5</b>
<b>V (ppm)</b>	765	797	724	779	710	755	754	787	653	716	758	<b>59</b>
<b>Cr (ppm)</b>	136	149	136	117	117	103	104	134	121	136	100	<b>11</b>
<b>Mn (ppm)</b>	0.24	bdl	bdl	0.24	bdl	bdl	bdl	bdl	bdl	bdl	bdl	<b>0.12</b>
<b>Fe (ppm)</b>	467	377	418	361	349	334	311	272	404	458	374	<b>29</b>
<b>Y (ppm)</b>	0.34	0.08	0.29	0.29	0.09	0.17	0.08	0.06	0.10	0.05	0.06	<b>0.01</b>
<b>Zr (ppm)</b>	148	153	147	138	146	133	134	144	142	143	139	<b>12</b>
<b>Nb (ppm)</b>	5000	4925	5208	5067	5134	4986	4980	5111	4983	5081	5040	<b>414</b>
<b>Mo (ppm)</b>	7.45	11.48	0.68	1.04	0.73	1.15	1.25	0.97	3.87	1.40	0.95	<b>0.26</b>
<b>Ba (ppm)</b>	bdl	bdl	bdl	bdl	bdl	0.530	bdl	bdl	bdl	0.246	bdl	<b>0.017</b>
<b>Dy (ppm)</b>	0.042	bdl	0.059	0.060	0.010	0.029	bdl	bdl	0.017	bdl	0.007	<b>0.005</b>
<b>Er (ppm)</b>	0.034	0.003	0.029	0.032	0.002	0.009	0.001	bdl	0.003	bdl	bdl	<b>0.001</b>
<b>Yb (ppm)</b>	0.034	bdl	0.038	0.032	bdl	0.012	bdl	bdl	bdl	bdl	bdl	<b>0.003</b>
<b>Hf (ppm)</b>	5.58	5.55	7.31	6.80	7.61	6.45	6.41	6.86	5.70	6.07	6.87	<b>0.52</b>
<b>Ta (ppm)</b>	464	457	515	513	511	477	512	477	457	485	386	<b>39</b>
<b>W (ppm)</b>	558	575	213	188	217	233	227	232	450	352	187	<b>27</b>
<b>Pb (ppm)</b>	0.94	bdl	0.39	0.31	0.34	0.30	0.05	0.16	0.23	1.69	0.12	<b>0.04</b>
<b>Th (ppm)</b>	bdl	bdl	0.08	0.13	0.19	0.16	0.02	0.07	0.05	0.01	0.16	<b>0.01</b>
<b>U (ppm)</b>	1.57	1.68	1.02	1.78	1.88	2.52	1.45	1.30	1.09	0.98	1.79	<b>0.14</b>
<b>T 20 kbar</b>	636	639	636	631	636	629	629	635	633	634	632	
<b>T 30 kbar</b>	677	679	677	672	676	669	669	675	674	674	672	
<b>Nb/Ta</b>	10.8	10.8	10.1	9.9	10.1	10.4	9.7	10.7	10.9	10.5	13.1	

**Table A1- 4: LA-ICP-MS data for SHB12B, SHB45 and WOD rutiles.** Temperature in °C calculated following Tomkins et al. (2007).

	Rutile_2	Rutile_8	Rutile_5	Rutile_3	Rutile_6	Rutile_4	Rutile_10	Rutile_11	Rutile_1	Rutile_9	Rutile_7	Rutile_12
	SHB12B	SHB12B	SHB12B	SHB12B	SHB12B	SHB12B	SHB12B	SHB12B	SHB12B	SHB12B	SHB12B	SHB12B
<b>Al (ppm)</b>	154.2	137.2	132.1	136.4	162	130.7	103.9	90.9	161.7	147	145	103
<b>Si (ppm)</b>	2858	3133	2883	3040	2821	2975	2944	2764	2821	3099	2971	2974
<b>P (ppm)</b>	18.8	23.5	13.9	20.5	21.6	22.9	27.4	23.8	25.1	25.8	28.9	27
<b>Sc (ppm)</b>	2.21	2.11	2.63	2.27	2.44	2.33	0.85	1.87	2.89	2.83	0.94	1.91
<b>V (ppm)</b>	765.6	810.2	805.9	791.8	812.2	801.1	732.6	815.4	821.8	850.1	811.3	700.5
<b>Cr (ppm)</b>	951	762	711	710	727	732.1	954	888	942	820	687	826
<b>Mn (ppm)</b>	bdl	0.76	1.63	bdl	0.71	bdl	3.53	3.26	bdl	0.83	10.81	2.87
<b>Fe (ppm)</b>	9474	10053	10013	9388	9560	9118	9850	11900	9055	9901	11340	10910
<b>Co (ppm)</b>	0.151	0.11	0.219	0.158	0.199	0.099	0.06	0.173	0.104	0.117	0.505	0.2
<b>Ni (ppm)</b>	0.32	0.9	0.34	0.71	0.21	1.06	0.77	0.86	0.12	1.09	0.49	0.24
<b>Cu (ppm)</b>	22.53	20.04	22.2	22.36	23.1	21.6	20.9	20.4	22.1	22.1	19.8	20.9
<b>Zn (ppm)</b>	8.36	7.86	9.13	8.63	8.76	8.53	8	7.66	10.2	8.5	8.12	9.8
<b>Y (ppm)</b>	bdl	bdl	bdl	bdl	bdl	bdl	bdl	bdl	bdl	bdl	bdl	bdl
<b>Zr 90 (ppm)</b>	66.08	68.84	68.9	69.26	69.66	70.13	75.12	75.8	78.78	80.8	96.5	114.9
<b>Zr 91(ppm)</b>	64.6	69.2	68.2	70	69.3	68.8	75.1	77.1	77.6	81.4	94.4	114.4
<b>Nb (ppm)</b>	3675	3688	3414	3485	3396	3473	3789	4022	5288	5068	1630	567.7
<b>Mo (ppm)</b>	1.24	1.3	1.3	1.37	1.23	1.17	2.49	1.26	1.63	1.47	2.72	3.04
<b>Sn (ppm)</b>	17.17	19	17.6	17.9	18.5	18.4	20	22.1	22.2	23	21.5	16.7
<b>Sb (ppm)</b>	2.04	2.2	2.32	2.11	1.89	2.22	2.33	1.99	2.54	2.89	1.56	2.26
<b>Hf (ppm)</b>	3.12	3.4	3.41	3.37	3.43	3.46	3.67	3.43	4.01	4.37	4.43	5.04
<b>Ta (ppm)</b>	98.23	125.96	111.08	112.49	108.27	111.1	114.11	128.3	197.7	196.1	108.11	28.59
<b>W (ppm)</b>	47.25	63.7	57.19	60.59	57.34	60.2	67.2	102.1	308.6	360.5	4.92	22.74
<b>Pb (ppm)</b>	0.019	0.013	0.0074	bdl	bdl	0.025	0.095	0.08	0.021	0.028	0.061	0.152
<b>U (ppm)</b>	0.084	0.051	0.079	0.0478	0.075	0.06	0.282	0.329	0.0765	0.097	0.17	0.055
<b>T 20 kbar</b>	580	583	583	583	584	584	589	589	592	594	606	618
<b>T 10 kbar</b>	542	545	545	545	545	546	550	551	553	555	567	578
<b>Nb/Ta</b>	37.4	29.3	30.7	31.0	31.4	31.3	33.2	31.3	26.7	25.8	15.1	19.9

**Table A1- 4: LA-ICP-MS data for SHB12B, SHB45 and WOD rutiles.** Temperature in °C calculated following Tomkins et al. (2007).

	Rutile_13	Rutile_17	Rutile_16	Rutile_14	Rutile_21	Rutile_20	Rutile_19	Rutile_18	Rutile_15	Rutile_22	WOD_1	WOD_2
	SHB12B	SHB45	SHB45	SHB45	SHB45	SHB45	SHB45	SHB45	SHB45	SHB45	WOD	WOD
<b>Al (ppm)</b>	77.7	134.9	81.1	95.9	94.2	88	92.4	75.2	101.3	79	8.19	15.9
<b>Si (ppm)</b>	3019	2780	2739	2843	2638	2614	2561	2754	2840	2780	3107	2935
<b>P (ppm)</b>	22.7	21.1	21.7	20.7	24.5	30.2	21.7	24.1	24.6	25.8	22.9	23.4
<b>Sc (ppm)</b>	2.39	2.81	2.29	2.44	1.93	1.52	2.14	2.24	2.42	2.01	19.8	19.73
<b>V (ppm)</b>	709.5	781.1	628.2	686.8	685.4	620.7	662.6	597.9	705.7	684.3	2354	2352
<b>Cr (ppm)</b>	903	1139	729	799	871	794	674	763	562.9	697	11630	11451
<b>Mn (ppm)</b>	3	0.91	1.65	1.69	2.03	2.18	1.15	0.64	2.02	1.98	bdl	1.23
<b>Fe (ppm)</b>	9030	11598	9738	10730	10330	9850	9970	9328	10520	10040	2152	1914
<b>Co (ppm)</b>	0.135	0.191	0.124	0.163	0.165	0.132	0.143	0.128	0.108	0.166	0.007	0.057
<b>Ni (ppm)</b>	0.63	1.07	0.77	1.7	0.55	2.7	0.76	0.71	2.03	1.34	1.45	0.18
<b>Cu (ppm)</b>	21.5	19.4	19.5	20.9	20	20.3	20	20.9	19.6	18.71	21.98	22.15
<b>Zn (ppm)</b>	8.65	7.24	8	8.1	7.54	6.47	7.39	8.07	7.09	7.71	8.74	9.6
<b>Y (ppm)</b>	2.55	bdl	bdl	bdl	bdl	bdl	bdl	bdl	bdl	bdl	bdl	bdl
<b>Zr 90 (ppm)</b>	116.7	90.5	93.7	95.2	103	111.4	117.9	118.6	120.3	129.1	602.8	674.4
<b>Zr 91(ppm)</b>	117.4	87.5	95.2	95.3	103.3	110.9	115.4	117.9	120.6	128.1	602.1	669.7
<b>Nb (ppm)</b>	627.4	421.9	483.1	413.9	439.5	742.4	448.9	722.7	575.2	1109.8	1903	1825
<b>Mo (ppm)</b>	4.49	2.71	4.84	3.27	3.3	3.63	3.77	4.44	3.37	5.23	47.9	56.3
<b>Sn (ppm)</b>	25.2	17.5	19.5	15	17.1	14.8	15	12.7	14.3	23.6	576	365.2
<b>Sb (ppm)</b>	2.05	1.22	1.94	1.84	1.74	1.54	2.06	2.19	2.4	2.86	5.6	6.1
<b>Hf (ppm)</b>	6.88	5.1	5.24	4.78	4.65	4.6	4.99	4.92	5.34	7.1	32.6	32.37
<b>Ta (ppm)</b>	36.7	24.86	20.79	23	22.99	19.23	23.07	26.85	31.59	81.34	204.6	221
<b>W (ppm)</b>	33.6	6.9	6.8	4.33	3.42	5.94	5.3	6.7	16.62	260.8	13936	13600
<b>Pb (ppm)</b>	9.26	0.078	0.062	0.051	0.49	0.141	0.099	0.92	0.087	0.049	342	346.4
<b>U (ppm)</b>	0.128	0.324	0.232	0.238	0.128	0.102	0.137	0.177	0.073	0.089	164.3	155.1
<b>T 20 kbar</b>	619	601	604	605	610	616	620	620	621	627	709	720
<b>T 10 kbar</b>	579	562	565	566	571	576	580	581	582	586	709	720
<b>Nb/Ta</b>	17.1	17.0	23.2	18.0	19.1	38.6	19.5	26.9	18.2	13.6	9.3	8.3

**Table A1- 4: LA-ICP-MS data for SHB12B, SHB45 and WOD rutiles.** Temperature in °C calculated following Tomkins et al. (2007).

	WOD_3	WOD_4	WOD_5	
	WOD	WOD	WOD	LOD
<b>Al (ppm)</b>	10.29	6.92	4.11	<b>0.5</b>
<b>Si (ppm)</b>	2940	2919	2827	<b>98</b>
<b>P (ppm)</b>	24	29.7	18.5	<b>8.6</b>
<b>Sc (ppm)</b>	19.02	21.93	19.01	<b>0.14</b>
<b>V (ppm)</b>	2360	2517	2419	<b>0.05</b>
<b>Cr (ppm)</b>	11548	11800	11570	<b>1.0</b>
<b>Mn (ppm)</b>	bdl	bdl	0.21	<b>0.5</b>
<b>Fe (ppm)</b>	2329	2487	2070	<b>13</b>
<b>Co (ppm)</b>	-0.0006	0.004	0.0054	<b>0.02</b>
<b>Ni (ppm)</b>	0.2	1.08	0.94	<b>1.41</b>
<b>Cu (ppm)</b>	20.8	19.6	19.3	<b>0.34</b>
<b>Zn (ppm)</b>	8.03	8.18	7.85	<b>0.21</b>
<b>Y (ppm)</b>	bdl	bdl	bdl	<b>0.46</b>
<b>Zr 90 (ppm)</b>	600.6	634.7	663.7	<b>0.004</b>
<b>Zr 91(ppm)</b>	599.9	636.7	663.3	<b>0.007</b>
<b>Nb (ppm)</b>	1888	2255	1817	<b>0.04</b>
<b>Mo (ppm)</b>	50.5	41.7	59.6	<b>0.010</b>
<b>Sn (ppm)</b>	564	743	343.5	<b>0.03</b>
<b>Sb (ppm)</b>	6.55	6.91	6.32	<b>1.21</b>
<b>Hf (ppm)</b>	32.55	33.38	31.89	<b>0.18</b>
<b>Ta (ppm)</b>	199.7	285.2	220.6	<b>0.01</b>
<b>W (ppm)</b>	13770	15470	13430	<b>0.001</b>
<b>Pb (ppm)</b>	367.5	338.4	346.9	<b>0.01</b>
<b>U (ppm)</b>	163.6	150.4	153.1	<b>0.02</b>
<b>T 20 kbar</b>	709	714	718	
<b>T 10 kbar</b>	709	714	718	
<b>Nb/Ta</b>	9.5	7.9	8.2	

Table A1 - 5: Rutile oxygen isotope composition determined by SHRIMP

Spot	$^{18}\text{O}/^{16}\text{O}$	$\pm 95\% \text{ cl}$	$\delta^{18}\text{O} (\text{‰})$	$\pm \text{SE}$
WOD-1	0.00200402	9.00E-08	-0.25	0.04
WOD-2	0.00200736	1.35E-07	1.42	0.07
WOD-3	0.00200191	1.39E-07	-1.31	0.07
WOD-4	0.00200125	6.10E-08	-1.63	0.03
WOD-5	0.00200294	2.50E-07	-0.79	0.12
WOD-6	0.00200469	1.29E-07	0.08	0.06
WOD-7	0.00200099	1.01E-07	-1.76	0.05
WOD-8	0.00200253	8.50E-08	-1.00	0.04
WOD-9	0.00200647	8.40E-08	0.97	0.04
WOD-10	0.00200403	1.68E-07	-0.25	0.08
WOD-11	0.00200474	2.60E-07	0.11	0.13
WOD-12	0.00200293	5.20E-08	-0.80	0.03
WOD-13	0.00200574	1.64E-07	0.61	0.08
WOD-14	0.00200257	2.43E-07	-0.97	0.12
WOD-15	0.00200233	2.80E-07	-1.09	0.14
WOD-16	0.00200585	2.00E-07	0.66	0.10
WOD-17	0.00200412	1.62E-07	-0.20	0.08
WOD-18	0.00199926	2.12E-07	-2.63	0.11
WOD-19	0.00200425	1.51E-07	-0.14	0.08
WOD-20	0.00200432	1.96E-07	-0.10	0.10
WOD-21	0.00200467	1.94E-07	0.07	0.10
WOD-22	0.00200161	1.99E-07	-1.46	0.10
WOD-23	0.00200251	1.32E-07	-1.01	0.07
WOD-24	0.00200616	2.79E-07	0.82	0.14
WOD-25	0.00200284	1.10E-07	-0.84	0.06
WOD-26	0.00200403	1.06E-07	-0.25	0.05
		<b>average</b>	-0.5	
		<b>std. dev.</b>	0.94	

Spot	$^{18}\text{O}/^{16}\text{O}$	$\pm 95\% \text{ cl}$	$\delta^{18}\text{O} (\text{‰})$	$\pm \text{SE}$
DM1C-1	0.00200967	1.62E-07	2.57	0.08
DM1C-2	0.00200790	2.55E-07	1.68	0.13
DM1C-3	0.00200897	1.64E-07	2.22	0.08
DM1C-4	0.00200949	1.35E-07	2.48	0.07
DM1C-5	0.00200588	8.10E-08	0.68	0.04
DM1C-6	0.00200573	1.81E-07	0.60	0.09
DM1C-7	0.00200466	1.18E-07	0.07	0.06
DM1C-8	0.00200553	9.00E-08	0.50	0.04
DM1C-9	0.00200479	2.45E-07	0.13	0.12
DM1C-10	0.00200414	1.78E-07	-0.19	0.09
DM1C-11	0.00200893	1.58E-07	2.20	0.08
DM1C-12	0.00200578	1.77E-07	0.63	0.09
DM1C-13	0.00200912	1.99E-07	2.30	0.10
DM1C-14	0.00200984	2.11E-07	2.65	0.10
DM1C-15	0.00200644	1.24E-07	0.96	0.06
DM1C-16	0.00200505	7.00E-08	0.26	0.03
		<b>average</b>	1.2	
		<b>std. dev.</b>	1.03	

<b>Instrument:</b>	SHRIMP SI
<b>Session:</b>	12.07.2013
<b>WOD repeatability:</b>	0.93 ‰ (1 $\sigma$ )

Table A1 - 5: Rutile oxygen isotope composition determined by SHRIMP

Spot	$^{18}\text{O}/^{16}\text{O}$	$\pm 95\%$ cl	$\delta^{18}\text{O}$ (‰)	$\pm \text{SE}$
DM52-1	0.00200859	1.90E-07	2.03	0.09
DM52-2	0.00201047	1.42E-07	2.97	0.07
DM52-3	0.00200800	7.40E-08	1.73	0.04
DM52-4	0.00200971	2.50E-07	2.59	0.12
DM52-5	0.00200471	6.60E-08	0.09	0.03
DM52-6	0.00201074	1.31E-07	3.10	0.07
DM52-7	0.00200837	7.30E-08	1.92	0.04
DM52-8	0.00201085	6.10E-08	3.16	0.03
DM52-9	0.00201008	1.23E-07	2.77	0.06
DM52-10	0.00200451	1.49E-07	-0.01	0.07
DM52-11	0.00201067	2.03E-07	3.07	0.10
DM52-12	0.00200904	1.13E-07	2.25	0.06
DM52-13	0.00200631	2.73E-07	0.89	0.14
DM52-14	0.00200727	1.50E-07	1.37	0.07
DM52-15	0.00200860	1.18E-07	2.03	0.06
		<b>average</b>	2.0	
		<b>std. dev.</b>	1.03	

Spot	$^{18}\text{O}/^{16}\text{O}$	$\pm 95\%$ cl	$\delta^{18}\text{O}$ (‰)	$\pm \text{SE}$
RSHB12B-1	0.00200977	1.59E-07	2.62	0.08
RSHB12B-2	0.00200791	1.60E-07	1.69	0.08
RSHB12B-3	0.00200882	1.78E-07	2.14	0.09
RSHB12B-4	0.00201145	2.50E-07	3.46	0.12
RSHB12B-5	0.00200578	2.79E-07	0.63	0.14
RSHB12B-6	0.00201253	9.10E-08	4.00	0.05
RSHB12B-7	0.00200764	1.76E-07	1.55	0.09
RSHB12B-8	0.00200731	2.53E-07	1.39	0.13
RSHB12B-9	0.00200927	1.56E-07	2.37	0.08
RSHB12B-10	0.00201201	2.07E-07	3.73	0.10
RSHB12B-11	0.00200830	1.29E-07	1.88	0.06
RSHB12B-12	0.00200455	1.23E-07	0.01	0.06
RSHB12B-13	0.00200824	2.22E-07	1.85	0.11
RSHB12B-14	0.00200609	1.64E-07	0.78	0.08
		<b>average</b>	2.0	
		<b>std. dev.</b>	1.17	

<b>Instrument:</b>	SHRIMP SI
<b>Session:</b>	12.07.2013
<b>WOD repeatability:</b>	0.93 ‰ (1 $\sigma$ )



Table A1 - 5: Rutile oxygen isotope composition determined by SHRIMP

Spot	$^{18}\text{O}/^{16}\text{O}$	$\pm 95\%$ cl	$\delta^{18}\text{O}$ (‰)	$\pm \text{SE}$
RSHB45-1	0.00201848	1.23E-07	6.97	0.06
RSHB45-2	0.00201808	1.13E-07	6.76	0.06
RSHB45-3	0.00202131	2.17E-07	8.38	0.11
RSHB45-4	0.00201556	9.50E-08	5.51	0.05
RSHB45-5	0.00201966	2.69E-07	7.55	0.13
RSHB45-6	0.00201955	1.88E-07	7.50	0.09
RSHB45-7	0.00202092	1.24E-07	8.19	0.06
RSHB45-8	0.00201972	7.60E-08	7.58	0.04
RSHB45-9	0.00202179	1.91E-07	8.62	0.09
RSHB45-10	0.00202042	1.43E-07	7.93	0.07
RSHB45-11	0.00201826	1.92E-07	6.85	0.10
RSHB45-12	0.00202091	2.65E-07	8.18	0.13
RSHB45-13	0.00202050	2.44E-07	7.97	0.12
RSHB45-14	0.00201819	8.40E-08	6.82	0.04
RSHB45-15	0.00201913	1.58E-07	7.29	0.08
		<b>average</b>	7.5	
		<b>std. dev.</b>	0.81	

Spot	$^{18}\text{O}/^{16}\text{O}$	$\pm 95\%$ cl	$\delta^{18}\text{O}$ (‰)	$\pm \text{SE}$
------	-------------------------------	---------------	---------------------------	-----------------

<b>Instrument:</b>	SHRIMP SI
<b>Session:</b>	12.07.2013
<b>WOD repeatability:</b>	0.93 ‰ (1 $\sigma$ )

Table A1 - 6: EBSD orientation data for rutile

Index	Xpos	Ypos	Euler1(°)	Euler2(°)	Euler3(°)	MAD(°)	AFI	BC	BS
WOD1	10.968	-113.5	105.8083	89.61653	48.72533	0.37	115	79	6
WOD1A	101.93	-134.1	154.5346	128.7292	89.22884	0.53	117	79	6
WOD2	-1.29	89.681	179.147	102.9769	85.38513	0.4	105	95	6
WOD3	114.19	-110.9	80.58455	114.1156	48.59218	0.44	102	63	6
WOD4	29.678	-112.2	80.41234	106.9608	30.86388	0.54	101	67	0
WOD5	-5.806	97.423	80.07635	107.1992	30.3427	0.37	110	73	6
WOD6	32.681	27.381	109.2513	76.63912	28.97638	0.55	119	64	6
WOD7	-120	7.7422	80.45907	114.1651	49.0008	0.41	117	69	6
WOD8	-20.64	-117.4	67.83733	119.8989	27.21637	0.42	106	77	6
WOD9	98.068	-100	178.6678	103.6186	85.17265	0.51	103	55	6
WOD10	12.258	56.776	155.3381	129.2582	0.005495	0.35	100	66	6
WOD11	10.323	88.39	105.7578	89.8465	49.24606	0.43	117	74	6
WOD12	3.2259	13.548	89.05999	105.5467	48.14161	0.41	110	69	6
WOD13	-7.742	29.678	132.8185	90.45959	11.76007	0.49	107	63	6
WOD14	103.87	39.356	1.205608	98.29018	39.19124	0.61	97	67	6
WOD15	-66.45	-48.38	32.97004	144.7585	46.18458	0.66	107	58	6
WOD16	41.292	-63.22	23.15855	117.7314	80.43438	0.53	113	72	6
WOD17	-166.4	-20.64	42.16356	37.84679	3.207433	0.37	104	74	6
WOD18	-11.61	-134.8	46.29895	120.6931	39.0837	0.62	105	68	6
WOD19	-62.58	-80	98.88804	94.0824	58.34079	0.29	103	67	6
WOD20	-18.06	36.13	137.7675	54.69249	44.76706	0.47	118	64	6
SHB12-1	36.775	96.132	10.67823	111.6373	54.96539	0.55	115	65	6
SHB12-2	-5.806	88.39	158.2516	66.92821	54.75109	0.42	122	73	6
SHB12-3	-118.7	120	22.64333	138.6133	70.25522	0.39	98	53	6
SHB12-4	160	-23.87	108.1358	98.64495	83.00006	0.57	94	62	6
SHB12-5	85.809	29.678	178.7106	107.5062	41.426	0.42	111	67	6
SHB12-6	-42.58	-27.74	142.3431	94.77699	76.75352	0.42	108	69	6
SHB12-7	-23.22	-73.55	90.76779	93.41248	41.88414	0.34	108	73	6
SHB12-8	0.6451	47.098	98.53456	94.55331	40.22252	0.61	117	71	6
SHB12-9	-61.93	-23.87	45.1173	49.29768	57.66355	0.32	95	56	6
SHB12-10	-65.16	-86.45	148.8132	85.1801	80.50087	0.56	118	68	6
SHB45-1	-99.35	-11.61	125.013	95.46036	33.38751	0.47	104	77	6
SHB45-2	116.13	7.7422	110.9914	88.885	38.64002	0.64	97	64	6
SHB45-3	-13.54	29.033	153.6258	82.1783	26.44941	0.55	113	68	6
SHB45-4	70.97	131.61	4.043903	94.56102	33.46521	0.65	102	70	6
SHB45-5	-121.2	81.293	99.72154	14.69773	63.92895	0.7	88	73	6
SHB45-6	-36.77	-55.48	165.7349	47.16143	77.5932	0.37	111	67	6
SHB45-7	107.1	53.55	177.2302	34.64821	17.65144	0.33	89	55	4
SHB45-8	-23.87	-165.8	171.5288	73.10251	65.98783	0.46	111	75	6
SHB45-9	79.358	-129	63.20818	134.6045	83.01835	0.4	86	62	6
SHB45-10	-80	-10.32	81.88138	62.69186	54.69755	0.42	99	58	6
SHB45-11	42.582	-70.97	123.0254	156.1189	15.24313	0.44	94	58	6
SHB45-12	45.163	1.9355	177.4471	73.91949	26.28527	0.58	101	64	6
SHB45-13	3.8711	91.616	28.97612	110.7568	56.53217	0.46	104	65	6
SHB45-14	-46.45	-25.8	38.73469	11.90951	6.859113	0.27	91	46	4
SHB45-15	-100	32.259	170.7484	72.98676	66.40583	0.46	92	60	5

**Table A1 - 6: EBSD orientation data for rutile**

<b>Index</b>	<b>Xpos</b>	<b>Ypos</b>	<b>Euler1(°)</b>	<b>Euler2(°)</b>	<b>Euler3(°)</b>	<b>MAD(°)</b>	<b>AFI</b>	<b>BC</b>	<b>BS</b>
DM1C-1	-74.84	7.097	1.663733	65.24103	0.609278	0.63	107	71	6
DM1C-2	58.066	56.131	141.9619	72.98611	70.11866	0.41	106	70	6
DM1C-3	34.84	-64.51	63.31118	91.65391	76.18944	0.45	103	62	6
DM1C-4	44.517	92.261	50.8832	94.9462	17.81355	0.33	116	63	6
DM1C-5	7.7422	-123.8	123.3222	85.37761	49.9004	0.4	111	69	6
DM1C-6	-72.26	-6.451	49.64607	113.8833	60.15071	0.29	100	65	6
DM1C-7	-41.93	-110.9	116.67	57.19402	61.48095	0.27	103	68	6
DM1C-8	-45.16	80.003	170.9156	98.55453	65.97195	0.45	100	59	6
DM1C-9	57.421	-32.9	160.8993	130.2657	72.10203	0.28	120	68	6
DM1C-10	-26.45	50.969	50.56946	24.14871	51.76156	0.42	109	61	6
DM1C-12	114.84	98.713	95.10492	95.52505	59.57379	0.44	102	62	6
DM1C-13	-95.48	74.841	15.10687	94.70253	11.44061	0.4	122	83	6
DM1C-15	170.97	-10.32	70.17439	79.19953	29.62185	0.56	101	66	6
DM1C-16	5.8066	45.163	5.883895	91.4837	79.27881	0.49	100	73	6
DM52-1	-2.58	-3.871	119.0723	86.47896	21.74559	0.36	102	75	6
DM52-2	168.39	9.0326	3.891518	72.92622	13.16438	0.54	94	62	6
DM52-3	-65.8	78.067	136.7946	89.90492	21.10413	0.45	99	76	6
DM52-4	171.61	71.615	84.99051	79.71198	16.55671	0.61	100	65	6
DM52-5	-67.74	50.969	141.3833	111.3936	41.08619	0.33	110	83	6
DM52-6	-27.09	-32.9	24.76114	93.77282	15.6415	0.36	104	67	6
DM52-7	54.195	76.777	61.16831	70.27061	45.53254	0.64	105	65	6
DM52-8	-36.13	7.7422	104.8708	87.64407	4.896894	0.5	109	70	6
DM52-9	99.358	-38.71	60.86583	71.41564	7.11997	0.43	94	61	6
DM52-10	-123.2	-66.45	175.37	79.31032	50.11879	0.7	92	76	6
DM52-11	39.356	-20	42.76253	83.33564	11.62921	0.58	109	66	6
DM52-12	-20.64	70.97	85.58278	79.44115	16.18761	0.36	107	71	6
DM52-13	-180	-16.77	134.2348	93.34064	28.64554	0.4	104	69	6
DM52-14	-96.13	-115.4	118.7368	86.51245	22.18628	0.36	98	71	6
DM52-15	167.74	112.26	0.984824	72.95379	15.75359	0.35	109	63	6

## **A2 – Appendix to Chapter 2**

**A2 - Publication PDF: Gauthiez-Putallaz L, Rubatto D, Hermann J (2016) Dating prograde fluid pulses during subduction by in situ U-Pb and oxygen isotope analysis. Contrib to Mineral Petrol 171:1-20.**

This publication has been removed due to copyright restrictions.

It can be accessed online at:

<https://link.springer.com/article/10.1007/s00410-015-1226-4>

**A2 - Electronic Supplementary Material 1:** Garnet trace-element composition determined by laser ablation ICP-MS

Elemental analyses are in ppm.

	DM1C-1	DM1C-2	DM1C-3	DM1C-4	DM1C-5	DM51-6	DM51-5	DM51-4	DM51-3	DM51-2	DM51-1			
profiles	Core					Rim					Core		Rim	
P	271.3	386.7	373.6	614.1	435.4	59.0	62.5	182.4	423.9	496.9	496.4			
Ca	9680.0	9270.0	8040.0	6390.0	5450.0	404.9	480.8	548.8	636.3	826.2	734.3			
Sc	283.0	162.1	101.1	25.96	9.85	2.35	2.80	6.67	13.74	32.38	29.43			
Ti	71.7	60.2	105.5	89.0	51.1	92.9	135.9	129.6	115.4	135.4	137.8			
Cr	3.77	4.32	13.30	9.00	7.60	10.06	14.31	16.48	15.74	8.27	5.76			
Mn	987.7	584.4	269.2	70.3	38.1	2.08	1.79	3.57	7.24	9.40	11.52			
Fe	55190	49760	34250	16440	13390	2784	6414	12752	18299	22629	24659			
Rb	0.129	0.089	0.062	0.026	0.023	4.85	0.15	0.09	0.12	0.08	0.12			
Sr	0.050	0.032	0.028	<0.009	<0.009	0.83	0.03	0.04	0.04	0.05	0.04			
Y	350.3	313.5	292.7	134.2	61.6	1.74	3.04	8.89	10.48	18.06	18.52			
Zr	1.59	2.92	2.00	3.66	0.82	3.09	6.77	5.56	4.25	5.44	5.71			
La	<0.002	<0.002	<0.002	<0.002	<0.002	0.025	0.010	0.007	0.007	0.010	<0.004			
Ce	<0.003	<0.003	<0.003	<0.003	<0.003	0.101	0.030	0.012	0.007	0.013	0.015			
Pr	<0.005	<0.005	<0.005	<0.005	<0.005	0.033	0.014	0.006	<0.003	0.004	0.005			
Nd	<0.014	<0.014	0.027	<0.014	<0.014	0.351	0.523	0.125	0.035	0.097	0.113			
Sm	0.27	0.23	0.23	0.08	0.03	2.46	2.43	0.75	0.27	0.29	0.36			
Eu	0.10	0.15	0.08	0.03	0.04	0.34	0.53	0.20	0.06	0.08	0.07			
Gd	2.53	2.55	2.08	1.40	0.85	2.75	6.14	2.58	0.98	1.21	1.46			
Tb	1.51	1.74	1.48	0.90	0.62	0.15	0.49	0.55	0.24	0.29	0.30			
Dy	29.03	27.72	26.41	15.58	8.57	0.48	1.01	2.67	1.82	2.35	2.74			
Ho	11.27	10.26	10.08	4.85	2.21	0.05	0.12	0.31	0.44	0.61	0.71			
Er	57.30	44.80	43.00	15.11	5.31	0.19	0.20	0.67	1.06	2.20	2.33			
Tm	12.50	8.46	7.78	1.90	0.51	0.02	0.02	0.06	0.11	0.32	0.32			
Yb	108.70	65.10	54.20	9.94	2.32	0.27	0.20	0.37	0.56	1.82	2.09			
Lu	17.13	8.96	6.91	1.11	0.27	0.03	0.05	0.05	0.09	0.23	0.35			
Hf	0.00	0.04	0.01	0.04	0.01	0.08	0.12	0.12	0.10	0.04	0.04			
Pb	<0.003	<0.003	<0.003	<0.003	<0.003	0.75	0.23	0.27	0.26	0.37	0.53			
Th	<0.005	<0.005	<0.005	<0.005	<0.005	0.11	0.008	<0.005	<0.005	<0.005	0.009			
U	<0.008	<0.008	<0.008	<0.008	<0.008	0.02	0.011	<0.008	<0.008	<0.008	<0.008			

**A2 - Electronic Supplementary Material 2:** Zircon trace-element composition determined by laser ablation ICP-MS  
Elemental analyses are in ppm unless indicated otherwise.

Analysis	DM1c-04	DM1c-09	DM1c-15	DM1c-07	DM1c-17	DM1c-11	DM1c-08	DM1c-14	DM1c-03	DM1c-16	DM1c-10	DM51-02	DM51-04
zone	core	core	core	rim	rim	rim	rim	rim	rim	rim	rim	outer rim	outer rim
Ti	2.84	0.96	3.90	5.08	4.40	6.60	4.90	3.90	4.16	9.60	6.00	4.86	4.84
Y	994.0	978.0	1499.0	280.0	320.2	440.0	450.0	436.9	409.2	682.0	572.6	106.0	79.0
Zr Wt%	45.1	46.9	43.9	44.4	44.5	43.5	46.7	46.2	44.1	45.7	44.5	45.2	45.2
Hf wt%	1.10	1.15	1.24	1.27	1.30	1.29	1.32	1.33	1.29	1.34	1.26	1.31	1.35
U	295.9	429.0	1059.0	100.4	59.1	56.9	125.0	337.0	260.5	379.2	279.9	207.3	210.8
Th	103.10	138.80	250.00	2.70	2.09	4.61	1.98	10.70	2.92	9.05	24.80	17.75	26.55
Pb	2.47	3.34	6.17	<0.11	<0.11	<0.11	<0.11	0.25	<0.11	<0.11	0.47	<0.11	<0.11
Nb	3.63	3.82	5.43	1.25	0.95	1.37	1.35	1.09	1.47	2.65	2.00	1.92	2.16
Ta	1.73	1.42	3.30	0.84	0.52	0.82	0.84	0.69	0.93	1.50	1.31	0.98	1.07
La	<0.01	<0.01	<0.01	0.01	0.01	<0.01	<0.01	<0.01	<0.01	0.12	0.01	<0.01	<0.01
Ce	3.37	3.97	4.54	4.23	1.78	1.58	2.00	0.67	1.07	1.32	1.24	30.40	30.60
Pr	0.03	0.05	0.04	0.01	<0.01	<0.01	<0.01	0.01	<0.01	0.13	0.03	0.01	0.02
Nd	0.96	1.21	0.87	0.15	<0.05	<0.05	<0.05	0.12	<0.05	1.08	0.60	0.32	0.35
Sm	2.74	2.95	3.18	0.71	0.36	0.52	0.57	0.47	0.32	1.21	1.15	1.58	1.59
Eu	0.10	0.07	0.08	0.29	0.23	0.25	0.25	0.15	0.14	0.29	0.22	0.31	0.33
Gd	20.94	20.80	25.99	9.32	7.08	9.26	7.42	5.46	4.79	9.38	9.62	3.77	4.15
Tb	7.50	7.27	9.79	5.26	4.38	6.35	4.80	3.12	3.20	4.90	4.57	0.57	0.59
Dy	93.50	93.00	133.30	57.90	55.40	78.70	68.10	44.90	46.35	67.20	59.50	5.81	5.27
Ho	34.04	35.20	49.90	9.23	10.70	14.30	15.14	13.88	12.63	20.47	17.96	2.74	2.33
Er	165.60	167.80	253.20	15.36	20.91	26.92	40.40	46.60	43.20	81.50	74.80	21.40	17.10
Tm	33.40	33.80	52.60	1.32	1.77	2.41	5.14	6.32	6.94	15.20	14.20	7.40	5.56
Yb	311.80	317.00	499.00	6.58	8.87	11.22	34.30	44.10	55.90	131.50	128.40	94.00	79.00
Lu	57.31	57.10	92.70	0.84	1.09	1.27	4.70	6.90	8.84	22.01	22.30	21.70	18.50
Th/U	0.35	0.32	0.24	0.03	0.04	0.08	0.02	0.03	0.01	0.02	0.09	0.09	0.13
Eu/Eu*	0.0	0.0	0.0	0.2	0.2	0.2	0.2	0.2	0.2	0.2	0.1	0.4	0.4
LuN/HoN	3.7	3.6	4.1	0.2	0.2	0.2	0.7	1.1	1.6	2.4	2.8	17.6	17.6

Analysis	DM51-06	DM51-07	DM51-10	DM51-12	DM51-14	DM51-16	DM52-23	DM52-10	DM52-24	DM52-04	DM52-06	DM52-15	DM52-17
zone	outer rim	inner rim	inner rim	outer rim	inner rim	inner rim	core	core	core	outer rim	outer rim	outer rim	outer rim
Ti	5.50	3.73	3.70	3.40	12.30	4.60	3.40	5.52	7.90	6.40	4.12	4.60	5.00
Y	53.2	249.0	174.8	52.0	926.0	174.2	2067.0	2644.0	5200.0	98.8	189.7	521.0	25.6
Zr Wt%	45.5	45.3	46.0	45.5	47.6	44.5	45.2	45.1	45.7	46.0	45.6	44.5	43.7
Hf wt%	1.34	1.37	1.36	1.34	1.38	1.31	1.58	1.20	1.25	1.39	1.36	1.39	1.36
U	228.9	309.0	148.9	338.0	933.0	159.6	1672.0	1147.0	1911.0	724.0	500.1	269.0	458.0
Th	18.73	18.20	5.87	16.21	126.90	11.56	50.20	93.70	717.00	19.40	7.04	2.20	16.29
Pb	<0.11	0.36	<0.11	0.22	0.46	<0.11	1.53	4.35	15.02	<0.11	<0.11	<0.11	<0.11
Nb	1.87	5.05	4.60	1.77	8.34	4.88	3.40	3.11	35.90	1.49	1.09	2.09	1.68
Ta	1.15	3.40	2.92	1.10	4.50	2.89	4.44	2.67	17.69	0.82	0.61	1.71	1.17
La	<0.01	0.01	<0.01	0.02	<0.01	<0.01	<0.01	0.19	0.09	0.02	<0.01	<0.01	0.02
Ce	19.20	1.38	0.43	40.67	16.59	1.27	0.87	2.15	29.61	4.72	0.66	0.79	45.20
Pr	0.01	0.01	<0.01	0.03	0.02	<0.01	<0.01	0.12	0.27	0.04	<0.01	<0.01	0.03
Nd	0.27	0.12	<0.05	0.50	0.38	0.10	0.19	1.35	5.81	0.57	0.11	<0.05	0.55
Sm	1.00	0.30	0.20	2.04	2.24	0.35	1.53	3.80	15.19	1.70	0.82	0.37	3.30
Eu	0.18	0.08	0.06	0.46	0.48	0.06	0.05	0.18	0.32	0.34	0.24	0.16	0.77
Gd	2.42	2.04	1.14	6.25	12.56	1.60	15.97	30.00	106.30	6.16	6.46	4.63	11.44
Tb	0.41	0.85	0.40	0.76	3.72	0.41	8.92	14.22	40.00	1.59	2.51	2.92	1.53
Dy	3.49	13.30	6.67	5.83	52.00	7.04	146.10	211.00	511.00	14.10	26.04	49.20	6.10
Ho	1.51	6.88	4.46	1.60	27.70	4.37	65.50	85.70	183.60	3.03	5.69	15.29	0.73
Er	10.00	56.00	45.10	7.60	213.90	45.68	383.20	459.70	872.00	9.90	15.51	55.20	2.14
Tm	2.96	20.64	19.44	1.44	72.10	19.37	93.00	101.40	163.40	1.54	2.20	8.26	0.32
Yb	38.80	288.90	290.00	13.50	942.00	309.70	987.00	1000.00	1417.00	12.00	15.32	61.40	2.20
Lu	9.10	67.10	72.70	2.21	227.30	77.90	190.70	179.40	241.80	2.06	2.47	9.50	0.40
Th/U	0.08	0.06	0.04	0.05	0.14	0.07	0.03	0.08	0.38	0.03	0.01	0.01	0.04
Eu/Eu*	0.3	0.2	0.3	0.4	0.2	0.2	0.02	0.04	0.02	0.29	0.22	0.2	0.3
LuN/HoN	13.4	21.6	36.2	3.1	18.2	39.6	6.5	4.6	2.9	1.5	1.0	1.4	1.2



Analysis	DM52-21	DM52-26	DM52-27	DM52-13	DM52-25	DM52-11	DM52-05	DM52-07	DM52-08	DM52-14	DM52-09	DM52-28	DM52-03	DM52-20
zone	outer rim	outer rim	outer rim	outer rim	outer rim	outer rim	outer rim	outer rim	outer rim	outer rim	outer rim	outer rim	outer rim	inner rim
Ti	7.50	3.10	6.70	8.55	12.00	10.50	7.23	4.37	6.40	6.75	7.20	7.20	7.50	4.60
Y	486.0	73.5	79.6	435.3	348.0	798.0	319.1	129.0	201.0	288.5	17.4	246.2	775.0	993.0
Zr Wt%	46.8	43.8	46.0	45.8	43.6	46.6	45.2	45.2	44.8	45.6	46.4	44.2	46.3	43.4
Hf wt%	1.51	1.36	1.42	1.37	1.34	1.34	1.38	1.35	1.31	1.36	1.41	1.34	1.40	1.39
U	408.0	704.0	955.0	587.0	455.0	707.0	375.0	103.1	153.3	403.1	780.0	173.6	637.5	164.6
Th	14.68	11.48	16.58	12.29	14.36	29.40	15.77	8.39	15.94	8.73	17.86	14.57	7.93	1.42
Pb	<0.11	<0.11	0.17	<0.11	0.23	0.43	<0.11	<0.11	<0.11	<0.11	0.14	<0.11	<0.11	<0.11
Nb	2.73	1.59	1.83	2.43	2.12	3.85	2.56	0.90	1.57	2.10	1.60	1.70	3.50	4.48
Ta	2.47	1.04	1.15	1.32	1.00	2.06	1.40	0.60	0.92	1.26	1.13	1.01	2.15	3.63
La	<0.01	<0.01	0.08	<0.01	0.04	<0.01	<0.01	<0.01	<0.01	<0.01	<0.01	<0.01	<0.01	<0.01
Ce		1.60	1.84	1.25	5.23	1.26	1.01	0.52	0.94	0.79	12.70	0.64	1.20	0.51
Pr	0.02	<0.01	0.08	<0.01	0.11	0.01	0.02	<0.01	0.01	0.01	0.04	<0.01	<0.01	<0.01
Nd	0.23	0.14	0.55	0.23	1.04	0.30	0.43	0.06	0.23	0.18	0.56	0.14	0.15	<0.05
Sm	0.86	0.99	2.24	1.99	2.39	2.39	2.46	1.17	2.09	1.49	2.36	2.04	1.12	0.17
Eu	0.32	0.24	0.62	0.61	0.57	0.59	0.70	0.33	0.60	0.48	0.39	0.65	0.34	0.08
Gd	7.54	5.06	11.41	16.69	14.46	19.41	18.22	8.71	14.50	12.13	7.15	16.41	0.34	3.31
Tb	3.11	1.32	2.40	5.88	4.90	7.12	5.20	2.22	3.60	4.14	0.91	4.30	0.34	2.41
Dy	39.40	10.47	13.40	54.65	44.70	83.70	42.30	16.72	26.50	36.22	3.80	32.90	0.34	53.60
Ho	13.90	2.14	2.19	12.35	9.97	25.60	9.28	3.67	5.68	8.04	0.45	7.11	0.34	27.57
Er	67.80	6.37	6.97	40.22	32.20	119.90	29.65	12.21	18.54	27.06	1.12	23.43	0.34	180.50
Tm	13.81	1.06	1.21	6.50	4.90	25.10	4.76	1.80	2.84	4.26	0.18	3.68	0.34	47.26
Yb	136.40	8.46	10.61	51.30	37.00	254.00	35.80	13.64	21.90	30.36	1.68	26.46	0.34	513.00
Lu	24.90	1.45	1.82	8.20	6.08	44.20	5.49	1.99	3.20	4.82	0.25	4.23	0.34	105.90
Th/U	0.04	0.02	0.02	0.02	0.03	0.04	0.04	0.08	0.10	0.02	0.02	0.08	0.01	0.01
Eu/Eu*	0.3	0.3	0.3	0.2	0.2	0.2	0.2	0.2	0.2	0.2	0.3	0.2	0.2	0.2
LuN/HoN	4.0	1.5	1.8	1.5	1.4	3.8	1.3	1.2	1.3	1.3	1.2	1.3	1.5	8.5

Analysis	DM52-16	DM53-04	DM53-05	DM53-06	DM53-07	DM53-09	DM53-10	DM53-11	DM53-12	DM53-14	DM53-15	DM53-16	
zone	inner rim	outer rim	outer rim	outer rim	inner rim	inner rim	outer rim	inner rim	core	core	inner rim	inner rim	
Ti	4.60	5.70	6.80	5.20	4.40	9.40	6.00	3.20	4.40	2.66	7.30	9.10	
Y	1115.0	58.7	24.2	7.2	119.3	1089.0	162.0	139.6	1915.0	1361.0	468.9	646.0	
Zr Wt%	44.6		45.6	45.4	45.9	45.6	44.4	46.9	46.5	46.2	44.7	44.8	44.9
Hf wt%	1.35		1.36	1.35	1.36	1.45	0.81	1.35	1.41	1.19	1.15	1.35	1.3
U	359.0	297.30	443.00	51.20	235.50	80.20	333.70	158.00	573.00	593.00	1328.00	816.00	
Th	1.72	14.68	35.20	25.16	4.97	44.27	19.60	9.27	91.50	147.50	33.00	23.04	
Pb	<0.11	<0.11	0.30	<0.11	<0.11	0.16	0.19	<0.11	2.33	3.51	0.15	0.18	
Nb	5.80	0.85	1.54	0.95	3.77	7.20	2.08	4.60	2.01	2.76	17.32	6.57	
Ta	3.46	0.6	0.9	0.7	3.0	0.8	1.1	3.2	1.3	1.5	9.3	4.3	
La	<0.01	<0.01	0.02	<0.01	<0.01	<0.01	0.01	<0.01	<0.01	<0.01	<0.01	<0.01	
Ce	0.40	1.82	16.05	97.20	0.29	3.20	4.94	0.56	1.31	2.81	1.72	1.97	
Pr	<0.01	<0.01	0.02	0.06	<0.01	<0.01	0.03	<0.01	0.04	0.05	<0.01	<0.01	
Nd	<0.05	0.17	0.72	1.35	<0.05	0.26	0.33	<0.05	0.85	1.08	0.16	0.18	
Sm	0.24	0.94	2.85	5.71	0.19	2.21	1.35	0.25	3.31	4.20	0.98	1.32	
Eu	0.12	0.22	0.63	1.08	0.08	0.65	0.30	0.05	0.08	0.14	0.25	0.39	
Gd	3.77	3.65	10.05	11.11	1.83	17.73	6.03	1.39	29.10	29.90	6.33	8.73	
Tb	3.08	0.97	1.24	0.71	0.52	5.69	1.35	0.40	11.99	10.48	1.98	2.37	
Dy	66.60	8.52	5.11	2.15	6.81	77.50	15.90	6.19	164.60	133.70	27.48	35.21	
Ho	31.70	1.78	0.83	0.21	3.42	29.37	5.01	3.56	63.90	45.00	12.44	17.05	
Er	194.70	4.96	3.75	0.52	25.75	153.70	26.00	33.80	327.10	199.50	79.20	114.60	
Tm	50.40	0.66	0.83	0.10	7.98	33.02	6.30	14.55	69.00	37.80	20.41	31.33	
Yb	549.00	4.01	9.20	1.18	107.60	292.40	68.00	233.00	639.00	326.00	213.30	336.50	
Lu	111.90	0.64	1.75	0.27	25.30	47.75	13.60	59.70	117.70	57.60	39.05	65.00	
Th/U	0.00	0.05	0.08	0.49	0.02	0.55	0.06	0.06	0.16	0.25	0.02	0.03	
Eu/Eu*	0.2	0.3	0.3	0.4	0.3	0.2	0.3	0.2	0.0	0.0	0.2	0.3	
LuN/HoN	7.8	0.8	4.7	2.8	16.4	3.6	6.0	37.2	4.1	2.8	7.0	8.5	

**A2 - Electronic Supplementary Material 3: Monazite trace-element composition determined by laser ablation ICP-MS**

Elemental analyses are in ppm unless indicated otherwise.

Spot name	DM1C-1	DM1C-2	DM1C-3	DM1C-4	DM1C-5	DM1C-6	DM1C-7	DM1C-8	DM1C-9	DM1C-10	DM1C-11
Zone	outer zone	inner zone	outer zone	outer zone	outer zone	outer zone	inner zone	outer zone	outer zone	outer zone	outer zone
Si	1750	2317	2092	2130	1678	1714	2140	1750	1480	1670	1966
Ca	28000	27820	38350	48800	30900	31460	28940	31200	28200	29900	37060
Y	13990	36300	19530	14040	18740	21110	30320	11520	14750	23600	20480
La	62900	37150	55600	45900	71300	50670	41620	60800	73100	53500	52460
Ce	177300	133400	130400	113200	160600	144200	139900	149700	168100	162100	123000
Pr	24170	22650	17460	15960	20400	22010	22890	20100	22170	24540	16850
Nd	113500	114500	79500	74200	86700	105500	112700	94100	96400	114000	77800
Sm	30390	31040	21520	21870	20950	28310	30190	24960	24170	33400	21740
Eu	2890	2781	2268	2323	2175	2763	2743	2517	2427	3100	2396
Gd	27700	23770	22900	23930	21560	26060	23330	24420	22930	28060	23400
Tb	3470	2775	3011	3121	2821	3231	2665	3072	2845	3430	3089
Dy	11120	11840	10930	10530	10300	11900	10920	9750	9560	12590	11420
Ho	663.0	1408.0	806.0	638.0	767.2	954.0	1219.0	534.4	622.0	1065.0	861.0
Er	450.0	2320.0	774.4	418.0	744.3	1009.0	1859.0	323.8	540.0	1244.0	831.0
Tm	13.87	165.40	39.23	13.90	36.93	49.10	117.50	9.40	23.60	66.80	39.68
Yb	32.60	600.00	125.50	30.80	111.80	136.40	382.30	21.71	66.20	200.00	117.40
Lu	2.51	47.40	9.42	2.40	8.22	9.55	28.60	1.85	4.80	14.43	8.33
Pb	430.00	402.70	482.20	736.00	378.00	469.70	391.50	513.10	392.00	419.00	524.70
Th wt%	16.47	14.01	16.49	27.30	12.96	16.76	14.42	17.73	13.64	15.49	18.21
U	4890	24830	53910	8400	47520	15860	26230	2794	32200	20600	39770
Th/U	33.7	5.6	3.1	32.5	2.7	10.6	5.5	63.5	4.2	7.5	4.6

Spot name	DM1C-17	DM1C-18	DM1C-19	DM1C-20	DM1C-21	DM1C-22	DM1C-23	DM1C-24	DM1C-25	DM1C-26	DM1C-27	DM1C-28
Zone	outer zone	outer zone	outer zone	outer zone	inner zone	inner zone	outer zone	outer zone	outer zone	inner zone	outer zone	outer zone
Si	2107	1750	2770	1558	1843	1625	1965	2190	2315	2262	2070	2160
Ca	35980	21400	51300	26210	24420	29460	33710	44100	44800	26530	40100	41400
Y	18940	11120	21000	14550	32540	25230	16960	20010	18480	31970	19740	20030
La	48500	75200	31860	69010	34120	38170	51100	43200	42780	36610	48200	39800
Ce	120200	179000	84100	160600	129500	120500	125500	112900	101300	126600	116300	106200
Pr	16550	22610	12430	20760	21920	19050	17450	16400	13940	20900	16090	15410
Nd	75350	101500	62400	90500	109800	94100	81400	78900	65080	103800	76100	74800
Sm	18660	24600	18280	21420	28990	24930	21710	20370	16230	27500	21120	22180
Eu	2076	2376	2135	2157	2552	2391	2288	2243	1725	2540	2251	2405
Gd	19940	23000	22570	20100	22270	20850	22480	23100	17160	22130	22740	23620
Tb	2572	2690	3029	2487	2554	2405	2869	2995	2238	2573	2995	3136
Dy	9870	8890	11060	8610	10750	9850	10070	10720	8990	10890	10860	10880
Ho	811.0	523.0	854.0	595.7	1250.0	1041.0	734.2	807.0	805.2	1248.0	829.0	846.0
Er	837.0	353.0	856.0	527.6	1957.0	1435.0	667.0	808.0	800.0	2028.0	769.0	999.0
Tm	42.30	13.60	45.46	24.40	134.80	84.00	31.40	45.61	34.20	148.00	37.90	65.20
Yb	124.00	38.10	131.10	69.20	468.00	258.00	90.70	142.40	84.20	550.00	111.00	236.00
Lu	9.30	3.06	8.69	4.94	37.20	19.50	6.71	9.60	5.81	46.20	8.10	19.90
Pb	519.10	335.00	745.00	320.90	346.70	432.50	515.20	619.00	666.10	383.20	569.00	631.00
Th wt%	18.70	12.42	25.45	10.80	12.10	15.18	18.02	20.07	24.26	13.08	20.24	23.37
U	24440	10100	41460	44860	22020	27010	21570	46900	24400	23670	38100	11060
Th/U	7.7	12.3	6.1	2.4	5.5	5.6	8.4	4.3	9.9	5.5	5.3	21.1

Spot name	DM1C-29	DM1C-30	DM1C-31	DM1C-32	DM51-1	DM51-2	DM51-3	DM51-4	DM51-5	DM51-6	DM51-7	DM51-8
Zone	outer zone	inner zone	outer zone	inner zone								
Si	2300	1990	2410	2090	14360	3604	2170	7110	10660	15500	4000	10830
Ca	49100	28500	49000	30800	299	9980	17700	9370	11580	13980	12530	491
Y	19950	41100	21620	32800	12.07	807	1930	474	1036	416.9	1308	54.1
La	39200	35840	36750	38840	144500	143300	126800	132400	127900	109600	123800	153500
Ce	98800	125900	95400	128800	286200	266100	253000	262600	261100	244200	256800	290000
Pr	13890	20490	13310	21360	31760	27770	27000	29250	30380	30580	29160	34100
Nd	66500	101100	65400	104600	119500	98800	103200	110000	118900	126700	108600	123800
Sm	18440	28930	18880	29210	17340	13350	15600	17300	19050	25710	15660	18260
Eu	2075	2808	2185	2758	702	671.3	755	828	949	1379	808	854
Gd	21760	24680	22290	24280	2495	3568	3950	4006	4720	7050	4315	3847
Tb	2839	3016	3036	2890	34.43	151.6	213.7	129.1	176.4	208.7	183.9	79.8
Dy	10450	13080	11260	11940	20.57	359.3	615	245	412.4	303.4	461.2	71.7
Ho	843.0	1605.0	885.0	1339.0	1.22	35.39	63.60	20.99	43.70	18.64	54.80	3.80
Er	863.0	2960.0	893.0	2200.0	bdl	56.20	103.00	33.40	74.50	27.76	113.90	bdl
Tm	49.50	241.00	46.44	166.00	0.26	3.05	5.93	1.69	4.48	1.53	8.81	0.29
Yb	158.00	981.00	136.30	632.00	0.74	10.20	18.40	5.23	13.49	5.41	34.90	1.02
Lu	11.90	86.60	9.37	54.50	0.09	1.00	1.35	0.46	1.02	0.53	3.35	0.10
Pb	709.00	408.00	725.00	442.00	298.90	534.60	336.00	627.00	599.00	936.00	581.00	222.20
Th wt%	24.57	14.83	24.29	16.63	10.54	6.09	8.79	8.42	12.23	17.69	7.88	7.91
U	34570	23690	29220	19150	1966	1241	3570	1377	2075	4150	1180	1787
Th/U	7.1	6.3	8.3	8.7	53.6	49.1	24.6	61.1	58.9	42.6	66.8	44.3

Spot name	DM51-10	DM51-11	DM51-12	DM51-13	DM51-14	DM51-15	DM51-16	DM51-17	DM51-18	DM51-19	DM51-20	DM51-21	DM51-22
Zone													
Si	3690	15490	9060	5511	15750	4510	12960	3910	1920	6200	5610	12240	7020
Ca	8580	4760	13180	13060	460	12920	1770	13220	14870	7820	11000	2840	15100
Y	922	525	664.9	1071	87	1134	151	1893	837	465	2950	40.96	2437
La	159900	143400	142600	127100	157100	138000	152500	114500	107900	130200	121100	124300	103300
Ce	279400	297600	261800	258100	307500	263700	297300	235200	217300	255800	239300	252200	224000
Pr	28370	33000	26860	28750	34500	27890	32500	26890	24230	28480	26820	28510	25560
Nd	100700	130700	95800	106700	129600	101400	123100	103900	89500	104200	100400	109000	100700
Sm	13440	21450	14320	16490	17870	14560	18470	14950	12660	14010	13980	17140	17480
Eu	725	1099	761	861.8	604	763	934	736	633.1	631	715	853	1059
Gd	3899	5250	4139	4696	2055	4142	4630	3850	2984	2811	3740	3772	6102
Tb	190	164.2	164	207.4	36.6	172.7	133.4	182.1	135.1	87.4	220.5	70.2	303.5
Dy	476.7	257	345.8	500	44	423.3	156.3	533	339.5	175.3	753	50.1	902
Ho	41.83	22.90	30.13	44.96	4.10	48.77	8.67	66.10	28.44	17.25	99.00	2.16	104.80
Er	59.60	42.60	43.69	66.50	bdl	93.00	bdl	132.90	37.12	32.50	227.00	bdl	178.30
Tm	3.10	2.40	2.26	3.56	0.71	6.80	0.53	11.16	1.77	1.92	21.50	0.42	11.41
Yb	10.03	8.44	7.12	11.08	3.40	24.97	1.56	40.90	4.74	6.53	95.40	2.23	39.09
Lu	0.93	0.74	0.67	0.91	0.37	2.26	0.16	3.45	0.34	0.57	8.76	0.27	3.46
Pb	401.80	504.00	676.80	587.10	340.00	674.80	349.30	358.70	288.30	355.90	275.90	397.70	910.00
Th wt%	5.86	14.54	8.27	9.24	12.27	8.12	10.60	9.00	7.62	8.01	9.11	10.15	11.62
U	1842	3254	1862	1966	1132	1266	2407	1335	2756	1274	2217	2586	2464
Th/U	31.8	44.7	44.4	47.0	108.4	64.1	44.0	67.4	27.6	62.9	41.1	39.2	47.2

Spot name	DM51-23	DM51-24	DM51-25	DM51-26	DM51-27	DM51-28	DM51-29	DM51-31	DM51-32	DM52-02b	DM52-3	DM52-4	DM52-5
Zone													
Si	8980	12000	10690	10960	11230	11500	3223	13620	12310	2150	11310	3670	9580
Ca	4170	4430	3420	202	493	1290	7680	421	660	8590	1416	13530	3860
Y	32.1	237	192.1	7.62	24.1	21.6	447.8	18.5	42.9	10384	233.1	6610	821
La	123400	132100	134400	138900	133700	131800	145000	132600	137900	142500	133100	118100	133300
Ce	249600	268200	263100	275300	265000	259000	249900	263100	270000	254300	268100	248900	275200
Pr	28180	29280	29600	30570	28880	28920	24830	29400	30580	25360	31050	28160	31480
Nd	105100	109900	111400	116700	108500	108900	84100	111100	116100	90800	121300	109800	124200
Sm	14110	15890	15990	15300	14680	14760	10060	15610	15880	15660	24680	18520	26540
Eu	646	758	810	604.6	624.1	602	503.7	693	711	1236	1697	1161	2077
Gd	2336	3210	4008	1873	2058	1977	2730	2660	2970	9611	11880	9130	16210
Tb	48.2	81.7	118.1	24.38	29.68	31	106.2	37.2	61.8	1122.6	530.7	906	993
Dy	40.6	132	156.2	15.22	25.37	26.1	227.9	23.3	55.3	4778	493	3326	1296
Ho	1.64	11.20	8.77	0.93	1.59	1.42	18.76	1.23	2.57	428.10	11.90	297.20	39.23
Er	bdl	21.60	bdl	bdl	bdl	bdl	25.10	bdl	bdl	415.70	bdl	319.90	29.47
Tm	0.18	1.12	0.57	0.14	0.20	0.17	1.05	0.28	0.20	16.83	0.56	14.37	1.14
Yb	0.40	3.34	1.80	0.25	0.47	0.32	2.95	1.18	0.72	42.16	2.88	37.93	5.07
Lu	0.04	0.37	0.18	0.03	0.05	0.03	0.24	0.16	0.07	3.32	0.38	3.18	0.60
Pb	296.10	449.00	391.00	227.30	259.10	277.90	501.80	297.90	283.20	188.10	232.90	344.50	248.80
Th wt%	8.48	11.15	9.36	8.43	8.52	9.22	5.22	10.37	9.79	3.55	8.00	7.08	7.56
U	975	2231	1765	1184	1367	1568	1178	1996	1557	9150	4114	4880	6410
Th/U	87.0	50.0	53.0	71.2	62.3	58.8	44.3	52.0	62.9	3.9	19.4	14.5	11.8

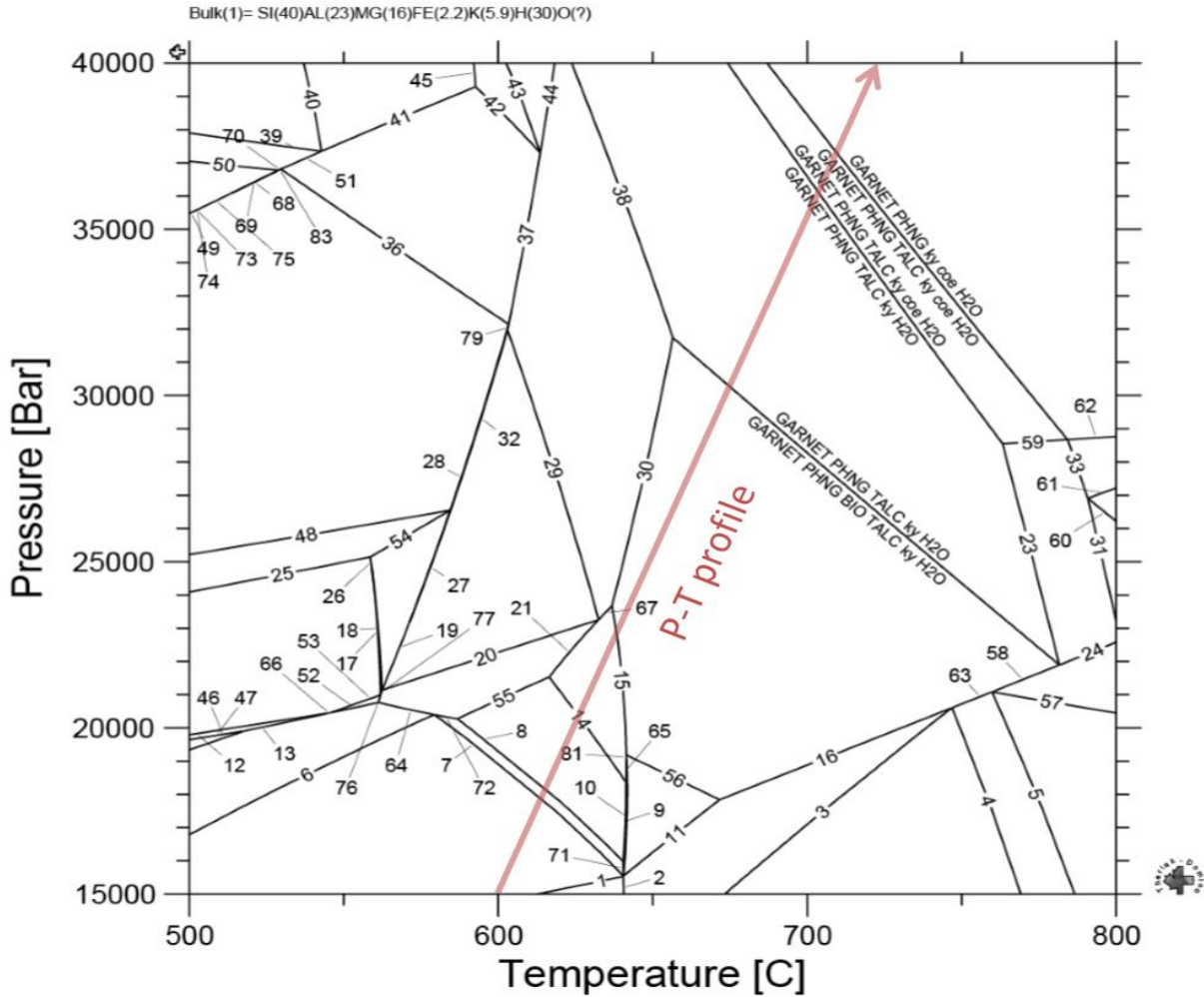
Spot name	DM52-6	DM52-7	DM52-9	DM52-10	DM52-11	DM52-12	DM52-13	DM52-14	DM52-15	DM52-16	DM52-17	DM52-18	DM52-19	DM52-20
Zone														
Si	7130	5150	5090	9270	11510	1670	11860	2453	4500	4490	12070	5720	4670	5200
Ca	9320	11200	11900	4640	4090	15880	7400	13020	13360	12670	4050	5630	10600	8810
Y	1354	2169	2223	4060	676	9790	3270	3014	2335	8500	123.7	5800	2340	3870
La	124000	124200	119000	126600	144200	112900	123900	115300	122800	120600	139500	142300	125700	134300
Ce	251100	251600	247500	266100	284400	226100	257400	234700	253000	242600	286000	267300	258800	264200
Pr	28420	28450	28310	30760	31790	25510	30500	26910	28230	27430	32800	28930	30070	29580
Nd	110000	110800	114400	123100	123700	99770	123100	103600	112500	107600	129700	107700	119800	112000
Sm	21900	21100	19630	27090	22260	18520	26800	19160	21230	19430	21120	18250	20860	18080
Eu	1652	1338	1106	2154	1284	1255	1865	1187	1359	1230	1037	1231	1328	1215
Gd	13560	9650	8430	19080	7930	9440	16820	7237	9640	8650	5027	8940	9940	9270
Tb	1060	594	671	1683	349.1	827	1406	361.7	610	671	136.5	815	766	812
Dy	1934	1220	1839	4070	529	2905	3130	912	1284	2300	139.4	2890	1911	2496
Ho	65.01	85.40	108.00	214.00	27.40	337.00	161.00	95.20	90.90	288.00	6.43	245.00	116.80	186.60
Er	35.47	104.10	74.80	144.40	32.91	630.00	105.60	163.40	111.80	640.00	bdl	233.00	94.50	168.60
Tm	1.10	5.12	2.19	4.51	1.30	49.13	3.15	10.30	5.67	60.20	0.48	9.00	3.31	6.66
Yb	4.37	14.62	5.72	13.10	3.89	171.60	8.78	29.90	15.73	232.30	1.52	23.40	9.38	18.82
Lu	0.62	1.03	0.55	1.35	0.34	12.96	0.98	1.93	1.08	18.55	0.16	1.83	0.81	1.61
Pb	374.60	262.50	386.50	246.50	281.10	242.30	414.00	215.60	285.70	257.40	295.70	267.80	397.80	355.70
Th wt%	7.75	6.89	7.35	7.30	8.53	7.02	11.21	6.18	7.24	7.60	9.91	5.64	7.67	6.68
U	5191	7060	3910	4790	7610	6212	5270	4477	7210	6420	8270	9100	5020	4398
Th/U	14.9	9.8	18.8	15.2	11.2	11.3	21.3	13.8	10.0	11.8	12.0	6.2	15.3	15.2



Spot name	DM52-21	DM52-22	DM52-23	DM52-24	DM52-25	DM53-1	DM53-2	DM53-3	DM53-4	DM53-5	DM53-6	DM53-7	DM53-8	DM53-9
Zone														
Si	2050	8860	14590	9100	2980	13890	4918	14460	4570	12210	4950	18080	3593	13040
Ca	7660	4090	4500	6440	11260	679	12000	1310	13430	3930	13680	590	9450	2120
Y	457	5360	2340	650	2295	34.3	852	73.9	1652	550	1161	53.0	1091	183
La	149500	124900	119300	136200	124600	140100	144700	141900	122100	141700	124800	147000	154500	148100
Ce	275700	258700	257700	267400	249100	278700	256900	285000	252700	286800	258300	292300	265800	287800
Pr	28460	30310	30930	31130	28330	30590	25650	31150	28450	32670	29350	32560	25970	31570
Nd	99550	119700	127300	120900	108600	115400	91700	117200	108800	122300	110500	124600	87400	118400
Sm	14110	24130	25270	20930	18740	17500	12350	18090	16890	17740	16670	19450	10850	17160
Eu	832	2028	1845	1231	1252	793	649	939	863	785	861	864	607.4	935
Gd	4900	16270	13710	7340	9570	3326	3525	4665	4726	3480	4820	3910	3198	4605
Tb	244.5	1482	980	350.9	773	71.7	149.2	130.4	216.9	125.7	224.4	86	154.7	139.7
Dy	400.3	4250	2190	554.1	1924	57.4	350.5	111.7	585.0	262.0	577.0	74.0	438.8	166.8
Ho	20.62	276.00	123.00	26.68	110.50	2.46	36.70	4.15	65.90	25.90	48.20	3.91	44.78	8.73
Er	bdl	209.10	89.70	29.00	84.20	bdl	64.8	bdl	123.7	45.5	64.6	bdl	69.1	bdl
Tm	0.74	7.39	2.83	1.27	2.89	0.30	4.06	0.35	8.32	2.37	3.11	0.38	3.83	0.69
Yb	2.07	21.80	7.50	3.86	7.99	0.78	14.45	1.29	30.10	7.98	8.88	1.04	11.14	2.68
Lu	0.19	1.87	0.68	0.29	0.75	0.08	1.29	0.14	2.44	0.75	0.67	0.12	0.90	0.25
Pb	190.90	285.30	434.00	306.00	371.70	312.40	693.80	368.70	670.00	463.00	689.00	396.60	515.00	376.00
Th wt%	3.19	7.56	11.74	8.88	6.53	10.16	7.40	11.59	8.73	10.09	8.70	14.14	5.43	11.07
U	3870	5995	6160	6400	4161	2101	1477	2591	1779	1729	1990	2417	1552	2523
Th/U	8.2	12.6	19.1	13.9	15.7	48.4	50.1	44.7	49.1	58.4	43.7	58.5	35.0	43.9

Spot name	DM53-10	DM53-11	DM53-12	DM53-13	DM53-14	DM53-15	DM53-16
Zone							
Si	3520	12050	12460	3370	10770	3187	4190
Ca	10160	1550	1410	14150	140	11160	8940
Y	1396	107.9	108	444.4	7.02	1363	1211
La	147200	152600	156900	119300	148500	127700	143300
Ce	256900	296600	291900	239400	297700	247000	265600
Pr	26010	31780	33000	27620	32920	25750	27830
Nd	93300	122000	121100	102800	124300	93300	98200
Sm	12010	17770	17600	14460	15200	12700	12840
Eu	650.5	936	955	725.8	513	711	668
Gd	3488	4670	4850	3521	1539	3867	3605
Tb	177.6	147.1	159	154.1	24.68	188.8	175.1
Dy	535.5	167.7	181.0	307.8	16.0	547.8	490.0
Ho	55.92	5.71	6.01	19.12	0.81	56.87	50.10
Er	89.8	bdl	bdl	21.6	bdl	89.0	80.3
Tm	5.39	0.25	0.27	0.82	0.15	5.25	4.93
Yb	16.97	0.85	1.08	2.30	0.24	15.52	15.60
Lu	1.32	0.10	0.10	0.18	0.03	1.23	1.20
Pb	587.90	305.90	316.00	338.10	220.30	522.00	516.40
Th wt%	6.22	9.46	9.86	7.89	8.16	6.74	6.33
U	1697	1963	2065	3519	785	1708	1389
Th/U	36.7	48.2	47.7	22.4	103.9	39.5	45.6

**A2 - Electronic Supplementary Material 4: Pseudosection for sample DM51 calculated using Theriak-Domino and the Holland and Powell database (see text for details)**



Numbered reactions:

- 1): CHLR PHNG TALC ky q = CHLR PHNG BIO TALC ky q
- 2): CHLR PHNG BIO TALC ky q = PHNG BIO TALC ky q H2O
- 3): PHNG BIO TALC ky q H2O = BIO TALC ky q H2O
- 4): BIO TALC ky q H2O = GARNET BIO TALC ky q H2O
- 5): GARNET BIO TALC ky q H2O = GARNET BIO ky q H2O
- 6): CHTD CHLR PHNG TALC ky q = CHLR PHNG TALC ky q
- 7): CHLR PHNG TALC ky q = CHLR PHNG TALC ky q H2O
- 8): CHLR PHNG TALC ky H2O = CHLR PHNG TALC ky q H2O
- 9): CHLR PHNG TALC ky H2O = CHLR PHNG BIO TALC ky H2O
- 10): CHLR PHNG BIO TALC ky H2O = PHNG BIO TALC ky H2O
- 11): PHNG BIO TALC ky H2O = PHNG BIO TALC ky q H2O
- 12): CHTD CRPH CHLR PHNG TALC = CHTD CRPH CHLR PHNG TALC q
- 13): CHTD CRPH CHLR PHNG TALC q = CHTD CHLR PHNG TALC ky q
- 14): GARNET CHLR PHNG TALC ky H2O = CHLR PHNG TALC ky H2O

- 15): GARNET CHLR PHNG TALC ky H2O = GARNET PHNG BIO TALC ky H2O
- 16): GARNET PHNG BIO TALC ky H2O = PHNG BIO TALC ky q H2O
- 17): CHTD CRPH CHLR PHNG TALC = CHTD CRPH CHLR PHNG TALC H2O
- 18): CHTD CRPH CHLR PHNG TALC H2O = CHTD CRPH PHNG TALC H2O
- 19): CHTD CRPH PHNG TALC H2O = CHTD PHNG TALC ky H2O
- 20): CHTD PHNG TALC ky H2O = CHTD CHLR PHNG TALC ky H2O
- 21): CHTD CHLR PHNG TALC ky H2O = GARNET CHLR PHNG TALC ky H2O
- 22): GARNET PHNG BIO TALC ky H2O = GARNET PHNG TALC ky H2O
- 23): GARNET PHNG TALC ky H2O = GARNET PHNG TALC ky q H2O
- 24): GARNET PHNG TALC ky q H2O = GARNET PHNG BIO ky q H2O
- 25): CHTD CRPH PHNG TALC = CHTD CRPH CHLR PHNG TALC
- 26): CHTD CRPH CHLR PHNG TALC = CHTD CRPH PHNG TALC H2O
- 27): CHTD CRPH PHNG TALC H2O = CHTD CRPH PHNG TALC ky H2O
- 28): CHTD CRPH PHNG TALC ky H2O = CHTD PHNG TALC ky H2O
- 29): CHTD PHNG TALC ky H2O = GARNET CHTD PHNG TALC ky H2O
- 30): GARNET CHTD PHNG TALC ky H2O = GARNET PHNG BIO TALC ky H2O
- 31): GARNET PHNG TALC q H2O = GARNET PHNG TALC ky q H2O
- 32): CHTD CRPH PHNG TALC ky = CHTD CRPH PHNG TALC ky H2O
- 33): GARNET PHNG TALC ky q H2O = GARNET PHNG ky q H2O
- 34): GARNET PHNG TALC ky H2O = GARNET PHNG TALC ky coe H2O
- 35): GARNET PHNG ky coe H2O = GARNET PHNG TALC ky coe H2O
- 36): CHTD CRPH PHNG TALC ky = GARNET CHTD CRPH PHNG TALC ky
- 37): GARNET CHTD CRPH PHNG TALC ky = GARNET CHTD PHNG TALC ky H2O
- 38): GARNET CHTD PHNG TALC ky H2O = GARNET PHNG TALC ky H2O
- 39): GARNET CHTD PHNG TALC tpz = GARNET CHTD PHNG TALC ky tpz
- 40): GARNET CHTD PHNG TALC tpz = GARNET CHTD CRPH PHNG TALC tpz
- 41): GARNET CHTD CRPH PHNG TALC tpz = GARNET CHTD CRPH PHNG TALC ky
- 42): GARNET CHTD CRPH PHNG TALC = GARNET CHTD CRPH PHNG TALC ky
- 43): GARNET CHTD CRPH PHNG TALC = GARNET CHTD CRPH PHNG TALC H2O
- 44): GARNET CHTD CRPH PHNG TALC H2O = GARNET CHTD PHNG TALC ky H2O
- 45): GARNET CHTD CRPH PHNG TALC tpz = GARNET CHTD CRPH PHNG TALC
- 46): CHTD CHLR PHNG TALC q = CHTD CHLR PHNG TALC ky q
- 47): CHTD CRPH CHLR PHNG TALC q = CHTD CHLR PHNG TALC q
- 48): CHTD CRPH PHNG TALC ky = CHTD CRPH PHNG TALC
- 49): CHTD PHNG TALC ky tpz = CHTD CRPH PHNG TALC ky
- 50): GARNET CHTD PHNG TALC ky tpz = CHTD PHNG TALC ky tpz
- 51): GARNET CHTD PHNG TALC ky tpz = GARNET CHTD CRPH PHNG TALC ky
- 52): CHTD CRPH CHLR PHNG TALC ky = CHTD CHLR PHNG TALC ky q
- 53): CHTD CRPH CHLR PHNG TALC = CHTD CRPH CHLR PHNG TALC ky
- 54): CHTD CRPH PHNG TALC H2O = CHTD CRPH PHNG TALC
- 55): CHLR PHNG TALC ky H2O = CHTD CHLR PHNG TALC ky H2O
- 56): GARNET PHNG BIO TALC ky H2O = PHNG BIO TALC ky H2O
- 57): GARNET PHNG BIO ky q H2O = GARNET BIO ky q H2O
- 58): GARNET PHNG BIO ky q H2O = GARNET PHNG BIO TALC ky H2O
- 59): GARNET PHNG TALC ky coe H2O = GARNET PHNG TALC ky q H2O
- 60): GARNET PHNG q H2O = GARNET PHNG TALC q H2O
- 61): GARNET PHNG q H2O = GARNET PHNG ky q H2O
- 62): GARNET PHNG ky coe H2O = GARNET PHNG ky q H2O
- 63): GARNET PHNG BIO TALC ky H2O = GARNET BIO TALC ky q H2O
- 64): CHTD CHLR PHNG TALC ky H2O = CHTD CHLR PHNG TALC ky q
- 65): GARNET CHLR PHNG TALC ky H2O = CHLR PHNG BIO TALC ky H2O
- 66): CHTD CRPH CHLR PHNG TALC = CHTD CHLR PHNG TALC ky q
- 67): GARNET CHTD PHNG TALC ky H2O = GARNET CHLR PHNG TALC ky H2O
- 68): CHTD PHNG TALC ky tpz = CHTD CRPH PHNG TALC ky tpz

- 69): CHTD CRPH PHNG TALC ky tpz = CHTD CRPH PHNG TALC ky
- 70): CHTD CRPH PHNG TALC ky tpz = CHTD CRPH PHNG TALC ky
- 71): CHLR PHNG TALC ky q H2O = CHLR PHNG BIO TALC ky H2O
- 72): CHTD CHLR PHNG TALC ky H2O = CHLR PHNG TALC ky q H2O
- 73): CHTD PHNG TALC ky tpz = CHTD CRPH PHNG TALC ky tpz
- 74): CHTD CRPH PHNG TALC ky tpz = CHTD CRPH PHNG TALC ky
- 75): CHTD PHNG TALC ky tpz = CHTD CRPH PHNG TALC ky
- 76): CHTD CRPH CHLR PHNG TALC ky = CHTD CHLR PHNG TALC ky H2O
- 77): CHTD CRPH CHLR PHNG TALC H2O = CHTD CHLR PHNG TALC ky H2O
- 78): CHTD CRPH PHNG TALC ky = CHTD CRPH PHNG TALC H2O
- 79): CHTD CRPH PHNG TALC ky H2O = GARNET CHTD PHNG TALC ky H2O
- 80): CHLR PHNG TALC ky q H2O = PHNG BIO TALC ky q H2O
- 81): GARNET CHLR PHNG TALC ky H2O = PHNG BIO TALC ky H2O
- 82): GARNET PHNG TALC ky coe H2O = GARNET PHNG ky q H2O
- 83): GARNET CHTD PHNG TALC ky tpz = CHTD CRPH PHNG TALC ky tpz
- 84): CHTD CHLR PHNG TALC ky H2O = CHLR PHNG TALC ky q
- 85): CHTD PHNG TALC ky tpz = CHTD CRPH PHNG TALC ky

**A2 - Electronic Supplementary Material 5: SHRIMP U-Pb analyses of zircon (all uncertainties are at 1 sigma level)**

Spot Name	zone	comm.		Th (ppm)	Th/U	Corr <sup>206</sup> Pb/ <sup>238</sup> U	% err	<sup>207</sup> Pb corr. <sup>206</sup> Pb/ <sup>238</sup> U Age (Ma)	1s err	Total		Total	
		<sup>206</sup> Pb (%)	U (ppm)							<sup>206</sup> Pb/ <sup>238</sup> U	% err	<sup>207</sup> Pb/ <sup>206</sup> Pb	% err
DM1C-1	rim	2.25	89	8	0.10	.006	2.1	34.6	0.8	181.71	2.1	.0645	8.2
DM1C-3	rim	4.39	56	3	0.05	.006	2.6	35.0	1.0	175.78	2.6	.0815	10.0
DM1C-5	rim	0.96	166	1	0.01	.005	1.7	34.6	0.6	184.16	1.7	.0543	7.1
DM1C-6	rim	0.33	409	3	0.01	.006	1.2	36.0	0.4	177.85	1.2	.0493	4.4
DM1C-7	rim	0.49	580	4	0.01	.005	1.1	34.8	0.4	183.89	1.1	.0506	3.8
DM1C-2*	rim	0.67	274	4	0.02	.005	1.4	32.6	0.5	195.90	1.4	.0520	5.5
DM1C-4*	rim	0.63	1006	24	0.02	.010	0.9	63.6	0.6	100.19	0.9	.0523	1.9
DM1C-8*	rim	0.32	329	45	0.14	.027	3.2	172.0	5.4	36.85	3.2	.0521	2.1
DM1C-9*	rim	1.20	120	11	0.10	.005	2.1	30.9	0.7	205.61	2.1	.0562	9.3
DM51-1	outer rim	0.00	817	29	0.03	.005	1.0	33.9	0.3	190.15	1.0	.0456	3.3
DM51-5	outer rim	0.47	582	31	0.05	.005	1.1	33.1	0.4	193.56	1.1	.0504	5.1
DM51-6	outer rim	0.00	915	26	0.03	.005	1.0	35.3	0.3	182.26	1.0	.0453	3.1
DM51-7	outer rim	0.78	165	30	0.18	.005	1.7	32.4	0.6	196.97	1.7	.0529	7.2
DM51-13	outer rim	0.78	382	19	0.05	.005	1.3	34.7	0.4	183.75	1.3	.0529	4.7
DM51-15	outer rim	1.64	312	36	0.11	.005	1.3	34.2	0.5	185.10	1.3	.0597	4.9
DM51-12*	outer rim	0.17	800	24	0.03	.008	1.0	48.4	0.5	132.45	1.0	.0483	3.0
DM51-2	inner rim	0.55	225	11	0.05	.005	1.4	34.5	0.5	185.36	1.4	.0511	5.9
DM51-3	inner rim	0.89	243	19	0.08	.005	1.4	33.9	0.5	187.78	1.4	.0537	5.5
DM51-8	inner rim	0.10	248	16	0.06	.005	1.4	35.0	0.5	183.70	1.4	.0475	5.8
DM51-9	inner rim	3.23	293	15	0.05	.006	1.3	34.3	0.5	181.30	1.3	.0723	4.2
DM51-10	inner rim	0.23	204	7	0.04	.006	1.5	35.4	0.6	181.32	1.5	.0485	7.0
DM51-14	inner rim	1.17	133	18	0.13	.005	1.9	33.4	0.7	190.25	1.9	.0559	8.7
DM51-4*	inner rim	0.57	633	47	0.07	.009	1.0	60.2	0.6	106.03	1.0	.0518	2.9
DM51-11*	inner rim	0.85	191	23	0.12	.019	1.1	118.6	1.3	53.40	1.1	.0552	3.3
DM52-1.1	core	0.02	1181	1212	1.03	.040	0.8	250.3	2.0	25.25	0.8	.0513	0.9
DM52A-18	core	1.67	2061	151	0.07	.039	0.9	240.4	2.4	25.87	0.9	.0644	4.2
DM52A-21	core	0.95	1184	303	0.26	.041	0.9	253.6	2.3	24.68	0.9	.0589	1.6
DM52A-28	core	0.06	1321	520	0.39	.042	0.8	268.0	2.1	23.54	0.8	.0521	1.4
DM52A-29	core	0.14	931	343	0.37	.042	0.8	266.8	2.1	23.64	0.8	.0527	1.1
DM52B-14	core	0.02	2762	79	0.03	.042	0.8	263.0	2.0	24.01	0.8	.0517	0.6

Spot Name	zone	comm. <sup>206</sup> Pb (%)	U (ppm)	Th (ppm)	Th/U	Corr <sup>206</sup> Pb/ <sup>238</sup> U	% err	<sup>207</sup> Pb corr.	1s err	Total	% err	Total	% err
								<sup>206</sup> Pb/ <sup>238</sup> U		<sup>206</sup> Pb/ <sup>238</sup> U		<sup>207</sup> Pb/ <sup>206</sup> Pb	
DM52A-30*	core	1.72	418	226	0.54	.026	1.0	163.9	2.0	38.17	1.0	.0630	7.9
DM52-2	outer rim	0.30	1161	35	0.03	.005	0.9	34.7	0.3	184.52	0.9	.0491	2.6
DM52B-4	outer rim	0.00	641	9	0.01	.005	1.0	35.0	0.4	183.97	1.0	.0458	3.7
DM52A-17	outer rim	0.21	681	10	0.01	.005	1.0	34.9	0.4	183.80	1.0	.0484	3.5
DM52A-20	outer rim	0.24	782	38	0.05	.005	1.0	35.1	0.4	182.74	1.0	.0487	5.0
DM52A-22	outer rim	0.47	886	9	0.01	.006	1.0	35.4	0.3	180.67	1.0	.0505	3.0
DM52A-23	outer rim	0.20	1768	29	0.02	.005	0.9	35.2	0.3	182.12	0.9	.0483	2.2
DM52A-24	outer rim	0.08	774	10	0.01	.005	1.0	35.2	0.4	182.55	1.0	.0473	3.4
DM52A-26	outer rim	0.21	1043	16	0.02	.005	0.9	35.2	0.3	182.39	0.9	.0484	2.9
DM52A-27	outer rim	0.41	585	18	0.03	.005	1.2	34.3	0.4	186.77	1.2	.0499	3.9
DM52B-10	outer rim	0.00	814	26	0.03	.005	1.0	35.1	0.3	183.84	1.0	.0446	3.2
DM52B-12	outer rim	0.00	925	19	0.02	.005	1.0	34.7	0.3	185.68	1.0	.0453	3.0
DM52B-13	outer rim	0.79	311	27	0.09	.005	1.3	34.0	0.4	187.63	1.3	.0529	4.8
DM52B-15	outer rim	0.31	674	9	0.01	.005	1.0	35.0	0.4	183.37	1.0	.0492	3.4
DM52A-19*	outer rim	0.18	1531	67	0.04	.006	0.9	36.1	0.3	177.56	0.9	.0482	2.3
DM52B-11	inner rim	0.35	311	4	0.01	.005	1.5	34.4	0.5	186.10	1.5	.0495	8.2
DM52B-16	inner rim	0.14	722	11	0.02	.005	1.0	35.3	0.4	182.09	1.0	.0479	3.2
DM52A-25	inner rim	1.05	308	3	0.01	.006	1.3	35.2	0.5	180.83	1.3	.0550	5.0
DM52B-3*	inner rim	0.29	663	14	0.02	.015	0.9	96.5	0.9	66.11	0.9	.0503	2.0

\* analysis excluded from average calculation.

**A2 - Electronic Supplementary Material 6: SHRIMP U-Pb analyses of monazite (all uncertainties are at 1 sigma level)**

Spot Name	Zone	% initial <sup>206</sup> Pb	common** <sup>207</sup> Pb/ <sup>206</sup> Pb	Total <sup>206</sup> Pb/ <sup>238</sup> U	% error	Total <sup>207</sup> Pb/ <sup>206</sup> Pb	% error	<sup>206</sup> Pb/ <sup>238</sup> U	±1 sigma %	<sup>206</sup> Pb/ <sup>238</sup> U Age (Ma)	±1 sigma
DM1C-2*	inner zone	33.30	0.838	0.0091	1.3	0.31	1.4	0.00608	0.49	39.1	0.6
DM1C-5*	inner zone	24.87	0.838	0.0076	1.7	0.24	1.5	0.00571	0.58	36.7	0.7
DM1C-9*	inner zone	7.13	0.838	0.0061	1.6	0.10	2.2	0.00567	0.53	36.4	0.6
DM1C-10*	inner zone	10.84	0.838	0.0059	1.0	0.13	4.4	0.00527	0.41	33.9	0.4
DM1C-19*	inner zone	25.95	0.838	0.0093	1.8	0.25	13.3	0.00688	1.93	44.2	3
DM1C-23*	inner zone	32.44	0.838	0.0085	5.6	0.30	1.6	0.00575	1.80	36.9	2
DM1C-1	outer zone	5.74	0.838	0.0056	1.5	0.09	1.5	0.00529	0.49	34.0	0.5
DM1C-4	outer zone	6.73	0.838	0.0058	2.0	0.10	4.1	0.00541	0.67	34.7	0.7
DM1C-6	outer zone	4.69	0.838	0.0056	1.7	0.08	1.5	0.00537	0.55	34.5	0.6
DM1C-7	outer zone	3.61	0.838	0.0057	1.4	0.08	2.4	0.00546	0.45	35.1	0.5
DM1C-8	outer zone	5.42	0.838	0.0058	1.2	0.09	4.3	0.00551	0.42	35.4	0.5
DM1C-11	outer zone	9.27	0.838	0.0059	2.3	0.12	5.2	0.00535	0.78	34.4	0.8
DM1C-13	outer zone	4.94	0.838	0.0057	1.3	0.09	1.4	0.00539	0.43	34.6	0.5
DM1C-14	outer zone	3.96	0.838	0.0056	1.9	0.08	1.2	0.00542	0.60	34.8	0.7
DM1C-15	outer zone	3.82	0.838	0.0055	1.5	0.08	1.2	0.00531	0.47	34.1	0.5
DM1C-16	outer zone	5.03	0.838	0.0057	1.2	0.09	1.2	0.00538	0.39	34.6	0.4
DM1C-17	outer zone	3.11	0.838	0.0055	2.0	0.07	2.5	0.00532	0.65	34.2	0.7
DM1C-18	outer zone	3.93	0.838	0.0055	2.1	0.08	1.2	0.00533	0.66	34.3	0.7
DM1C-20	outer zone	8.45	0.838	0.0059	1.5	0.11	2.8	0.00538	0.49	34.6	0.5
DM1C-21	outer zone	5.75	0.838	0.0057	1.0	0.09	1.9	0.00534	0.32	34.4	0.3
DM1C-22	outer zone	9.76	0.838	0.0059	1.4	0.12	3.4	0.00536	0.48	34.5	0.5
DM1C-24	outer zone	5.49	0.838	0.0058	1.6	0.09	1.4	0.00548	0.51	35.3	0.6
DM1C-12*	outer zone	12.05	0.838	0.0061	1.8	0.14	2.2	0.00538	0.60	34.6	0.7
DM1C-3*	outermost zone	13.52	0.838	0.0058	1.4	0.15	1.0	0.00505	0.45	32.5	0.5
DM51-1		45.99	0.750	0.0118	1.2	0.41	3.9	0.00567	1.52	36.5	2
DM51-2		26.11	0.750	0.0076	3.0	0.25	3.5	0.00537	1.07	34.5	1
DM51-3		85.46	0.750	0.0716	3.1	0.73	0.5	0.00250	4.75	16.1	2
DM51-4		24.20	0.750	0.0083	4.3	0.24	5.5	0.00607	1.57	39.0	2
DM51-5		63.60	0.750	0.0177	2.6	0.55	1.0	0.00502	1.21	32.3	1
DM51-6		72.00	0.750	0.0391	4.7	0.62	4.5	0.00732	6.86	47.0	10
DM51-7		72.50	0.750	0.0393	3.2	0.62	2.1	0.00713	3.43	45.8	5
DM51-8		85.17	0.750	0.1106	3.0	0.73	0.9	0.00384	8.23	24.7	6
DM51-9		60.13	0.750	0.0200	2.3	0.52	5.9	0.00646	4.39	41.5	6
DM52-1		33.03	0.716	0.0074	2.5	0.27	2.3	0.00494	0.91	31.8	0.9
DM52-2		51.63	0.716	0.0113	2.4	0.39	5.4	0.00547	2.23	35.1	2.5



Spot Name	Zone	% initial <sup>206</sup> Pb	common** <sup>207</sup> Pb/ <sup>206</sup> Pb	Total <sup>206</sup> Pb/ <sup>238</sup> U	% error	Total <sup>207</sup> Pb/ <sup>206</sup> Pb	% error	<sup>206</sup> Pb/ <sup>238</sup> U	±1 sigma %	<sup>206</sup> Pb/ <sup>238</sup> U Age (Ma)	±1 sigma
DM52-3		36.42	0.716	0.0078	2.4	0.29	1.1	0.00495	0.81	31.8	0.8
DM52-4		64.16	0.716	0.0141	2.2	0.48	1.9	0.00504	1.41	32.4	1.4
DM52-6		72.87	0.716	0.0193	2.8	0.53	0.7	0.00523	1.08	33.6	1.1
DM52-9		63.15	0.716	0.0143	3.8	0.47	1.2	0.00528	1.41	34.0	1.5
DM52-10		37.54	0.716	0.0087	2.8	0.30	1.4	0.00542	0.94	34.8	1.0
DM52-11		23.40	0.716	0.0069	1.7	0.20	6.1	0.00532	0.95	34.2	1.0
DM52-12		36.16	0.716	0.0084	1.8	0.29	1.3	0.00538	0.63	34.6	0.7
DM52-13		33.25	0.716	0.0077	2.8	0.27	1.7	0.00512	0.95	32.9	1.0
DM52-14		45.72	0.716	0.0098	2.3	0.35	2.0	0.00534	0.96	34.3	1.0
DM52-15		35.03	0.716	0.0084	4.7	0.28	5.1	0.00546	1.83	35.1	2.0
DM52-16		34.54	0.716	0.0080	2.2	0.28	2.1	0.00525	0.82	33.8	0.9
DM52-17		41.52	0.716	0.0091	2.1	0.32	2.6	0.00531	0.96	34.1	1.0
DM52-18		36.96	0.716	0.0082	2.0	0.29	1.2	0.00516	0.69	33.1	0.7
DM52-5*		47.52	0.716	0.0091	1.6	0.36	1.8	0.00477	0.77	30.7	0.7
DM52-7*		13.23	0.716	0.0064	2.1	0.14	8.4	0.00553	0.91	35.5	1.0
DM52-8*		60.46	0.716	0.0144	2.8	0.45	2.0	0.00570	1.40	36.7	1.6

\* analysis excluded from average calculation.

\*\*common Pb composition used for <sup>207</sup>Pb-based correction

**A2 - Electronic Supplementary Material 7: Zircon oxygen isotope composition determined by SHRIMP (all uncertainties are at 2 sigma level)**

Title	domain	$^{18}\text{O}/^{16}\text{O}$	$\pm 95\% \text{ cl}$	$\delta^{18}\text{O}\text{‰}$	$\pm 2\text{SE}$
DM1C1-1R	rim	0.002043379	1.72E-07	6.39	0.17
DM1C-2.1	rim	0.002044136	1.79E-07	6.76	0.18
DM1C-3.1	core	0.002051031	9.80E-08	10.13	0.10
DM1C-4.1	core	0.002050003	2.51E-07	9.63	0.24
DM1C-5.1	rim	0.002045041	1.48E-07	7.21	0.14
DM1C-6.1	rim	0.002043520	2.41E-07	6.46	0.24
DM1C-7.1	rim	0.002043226	1.84E-07	6.32	0.18
DM1C-8.1	core	0.002051428	1.20E-07	10.33	0.12
DM1C-9.1	rim	0.002043776	1.65E-07	6.59	0.16
DM1C-10.1	core	0.002051454	2.23E-07	10.34	0.22
DM1C-11.1	rim	0.002041617	1.43E-07	5.53	0.14
DM1C-12.1	rim	0.002042968	1.02E-07	6.19	0.10
DM1C-13.1	rim	0.002043301	1.75E-07	6.36	0.17
DM1C-14.1	rim	0.002042982	9.30E-08	6.20	0.09
DM1C-15.1	core	0.002050189	1.39E-07	9.72	0.14
DM1C-16.1	core	0.002050992	1.80E-07	10.11	0.18
DM1C-17.1	core	0.002049813	1.36E-07	9.54	0.13
DM1C-18.1	rim	0.002042699	1.74E-07	6.06	0.17
DM1C-19.1	core	0.002050129	1.65E-07	9.69	0.16
DM1C-20.1	rim	0.002044328	1.22E-07	6.86	0.12
DM51-1.1	outer rim	0.002043043	2.19E-07	6.23	0.21
DM51-3.1	outer rim	0.002043755	1.09E-07	6.58	0.11
DM51-5.1	inner rim	0.002042690	1.05E-07	6.06	0.10
DM51-6.1	outer rim	0.002042330	1.81E-07	5.88	0.18
DM51-7.1	outer rim	0.002044220	1.16E-07	6.80	0.11
DM51-8.1	core	0.002050812	1.58E-07	10.02	0.15
DM51-9.1	core	0.002050371	1.86E-07	9.81	0.18
DM51-10.1	core	0.002051601	1.77E-07	10.41	0.17
DM51-11.1	outer rim	0.002043580	1.73E-07	6.49	0.17
DM51-12.1	outer rim	0.002043389	2.35E-07	6.40	0.23
DM51-13.1	core	0.002051994	1.71E-07	10.60	0.17
DM51-14.1	outer rim	0.002042574	2.40E-07	6.00	0.23
DM51-15.1	outer rim	0.002043519	1.20E-07	6.46	0.12
DM51-16.1	outer rim	0.002041336	1.83E-07	5.40	0.18
DM51-17.1	core	0.002051404	1.69E-07	10.31	0.17
DM51-18.1	outer rim	0.002043802	1.80E-07	6.60	0.18
DM51-20.1	inner rim	0.002043135	1.24E-07	6.27	0.12
DM51-19.1*	core	0.002047171	1.89E-07	8.25	0.18
DM51-2.1*	outer rim	0.002045300	1.20E-07	7.33	0.12
DM51-4.1*	core	0.002047510	1.03E-07	8.41	0.10
DM52-1.1	core	0.002051572	2.28E-07	10.40	0.22
DM52-2.1	inner rim	0.002044378	2.12E-07	6.88	0.21
DM52-3.1	outer rim	0.002044116	2.03E-07	6.75	0.20
DM52-4.1	core	0.002049976	1.32E-07	9.62	0.13
DM52-5.1	outer rim	0.002043889	1.71E-07	6.64	0.17
DM52-6.1	inner rim	0.002043404	2.38E-07	6.41	0.23
DM52-6.2	outer rim	0.002043546	1.44E-07	6.48	0.14
DM52-7.1	core	0.002051286	2.21E-07	10.26	0.22
DM52-8.1	outer rim	0.002044202	1.32E-07	6.80	0.13

Title	domain	$^{18}\text{O}/^{16}\text{O}$	$\pm 95\% \text{ cl}$	$\delta^{18}\text{O}\text{‰}$	$\pm 2\text{SE}$
DM52-9.1	core	0.002049998	1.38E-07	9.63	0.13
DM52-10.1	core	0.002050091	1.86E-07	9.67	0.18
DM52-11.1	outer rim	0.002044070	1.24E-07	6.73	0.12
DM52-12.1	outer rim	0.002044730	1.36E-07	7.05	0.13
DM52-13.1	core	0.002051943	2.28E-07	10.58	0.22
DM52-14.1	outer rim	0.002044429	2.01E-07	6.91	0.20
DM52-14.2	outer rim	0.002044163	1.94E-07	6.78	0.19
DM52-15.1	outer rim	0.002044598	2.38E-07	6.99	0.23
DM52-16.1	core	0.002053102	2.18E-07	11.14	0.21
DM52-17.1	core	0.002052599	1.73E-07	10.90	0.17
DM52-18.1	core	0.002050174	1.72E-07	9.71	0.17
DM53-1.1	core	0.002047727	1.62E-07	8.52	0.16
DM53-2.1	outer rim	0.002043771	1.00E-07	6.58	0.10
DM53-3.1	outer rim	0.002042493	2.33E-07	5.96	0.23
DM53-4.1	outer rim	0.002043092	1.52E-07	6.25	0.15
DM53-5.1	outer rim	0.002042719	2.56E-07	6.07	0.25
DM53-6.1	core	0.002050051	2.30E-07	9.65	0.22
DM53-7.1	outer rim	0.002043073	1.60E-07	6.24	0.16
DM53-8.1	core	0.002052008	1.49E-07	10.61	0.15
DM53-9.1	outer rim	0.002043824	1.86E-07	6.61	0.18
DM53-10.1	core	0.002050085	2.25E-07	9.67	0.22
DM53-11.1	outer rim	0.002043393	1.62E-07	6.40	0.16
DM53-12.1	core	0.002050005	1.48E-07	9.63	0.14
DM53-13.1	core	0.002050064	1.75E-07	9.66	0.17
DM53-14.1	outer rim	0.002042978	1.39E-07	6.20	0.14
DM53-15.1	outer rim	0.002043634	1.98E-07	6.52	0.19
DM53-16.1	core	0.002050883	1.26E-07	10.06	0.12
DM53-17.1	outer rim	0.002043367	1.73E-07	6.39	0.17
DM53-18.1	outer rim	0.002042956	2.08E-07	6.19	0.20
DM53-19.1	outer rim	0.002042651	2.76E-07	6.04	0.27
DM53-20.1	outer rim	0.002042462	1.61E-07	5.95	0.16

\* mixed analysis excluded from average calculation.

**A2 - Electronic Supplementary Material 8: Garnet oxygen isotope composition determined by SHRIMP (all uncertainties are at 2 sigma level)**

Title	domain	PrPDM as primary standard				Xgross	Xprp	Xalm	UWG2 as primary standard				matrix corrected		
		$^{18}\text{O}/^{16}\text{O}$	$\pm 95\% \text{ cl}$	$\delta^{18}\text{O}\text{‰}$	$\pm 2\text{SE}$				$^{18}\text{O}/^{16}\text{O}$	$\pm 95\% \text{ cl}$	$\delta^{18}\text{O}\text{‰}$	$\pm 2\text{SE}$	$\delta^{18}\text{O}\text{‰}$	$\pm 2\text{SE}$	
DM1C-19	core	0.002039133	4.24E-07	6.92	0.21	0.03	0.87	0.09	0.002039155	3.77E-07	4.22	0.19	4.22	0.55	
DM1C-20	core	0.002039997	6.27E-07	7.35	0.31	0.04	0.86	0.10	0.002040031	2.45E-07	4.65	0.12	4.65	0.47	
DM1C-6	core	0.002039954	3.47E-07	7.33	0.17	0.04	0.85	0.11	0.002040026	1.41E-07	4.65	0.07	4.65	0.42	
<i>profile</i>															
DM1C-5	core	0.002039708	4.19E-07	7.21	0.21	0.03	0.87	0.10	0.002039916	1.6E-07	4.59	0.08	4.59	0.43	
DM1C-10		0.002039962	4.03E-07	7.33	0.20	0.04	0.86	0.09	0.002039754	1.81E-07	4.51	0.09	4.51	0.44	
DM1C-1		0.002039433	7.05E-07	7.07	0.35	0.03	0.88	0.09	0.002039379	2.6E-07	4.33	0.13	4.33	0.47	
DM1C-15		0.002039386	4.73E-07	7.05	0.23	0.03	0.90	0.07	0.002039358	1.83E-07	4.32	0.09	4.32	0.44	
DM1C-9		0.002039862	4.06E-07	7.28	0.20	0.03	0.90	0.06	0.002039670	1.72E-07	4.47	0.08	4.47	0.43	
DM1C-16		0.002038830	3.86E-07	6.77	0.19	0.02	0.91	0.06	0.002038788	1.73E-07	4.04	0.08	4.04	0.43	
DM1C-8		0.002038451	4.1E-07	6.59	0.20	0.03	0.93	0.04	0.002038355	2.82E-07	3.83	0.14	3.83	0.49	
DM1C-2		0.002038724	7.41E-07	6.72	0.36	0.03	0.93	0.04	0.002038543	2.71E-07	3.92	0.13	3.92	0.48	
DM1C-17		0.002038664	1.36E-07	6.69	0.07	0.02	0.94	0.04	0.002038733	2.32E-07	4.01	0.11	4.01	0.46	
DM1C-7		0.002038326	2.13E-07	6.53	0.10	0.02	0.95	0.03	0.002038431	2.82E-07	3.86	0.14	3.86	0.49	
DM1C-18		0.002037622	6.47E-07	6.18	0.32	0.03	0.95	0.03	0.002037612	2.11E-07	3.46	0.10	3.46	0.45	
DM1C-3		0.002037912	5.2E-07	6.32	0.25	0.02	0.96	0.02	0.002038100	1.58E-07	3.70	0.08	3.70	0.43	
DM1C-11		0.002038047	4.29E-07	6.39	0.21	0.02	0.96	0.02	0.002038018	1.84E-07	3.66	0.09	3.66	0.44	
DM1C-12		0.002037758	2.86E-07	6.25	0.14	0.02	0.96	0.02	0.002037699	1.74E-07	3.51	0.09	3.51	0.43	
DM1C-13		0.002037933	7.65E-07	6.33	0.38	0.02	0.96	0.02	0.002037805	2.84E-07	3.56	0.14	3.56	0.49	
DM1C-14		0.002038501	6.22E-07	6.61	0.31	0.02	0.95	0.02	0.002038442	2.03E-07	3.87	0.10	3.87	0.45	
DM1C-4	rim	0.002037223	6.29E-07	5.99	0.31	0.02	0.96	0.02	0.002036970	2.59E-07	3.15	0.13	3.15	0.47	
<i>profile</i>															
DM51-1	core	0.002036896	2.79E-07	5.83	0.14	0.00	0.96	0.03	0.002036890	1.86E-07	3.11	0.09	3.11	0.44	
DM51-2		0.002038274	6.24E-07	6.50	0.31	0.00	0.97	0.03	0.002038311	3.61E-07	3.81	0.18	3.81	0.53	
DM51-23		0.002038917	5.37E-07	6.82	0.26	0.00	0.97	0.03	0.002038769	2.71E-07	4.03	0.13	4.03	0.48	
DM51-3		0.002036955	2.46E-07	5.85	0.12	0.00	0.96	0.03	0.002036892	2.21E-07	3.11	0.11	3.11	0.46	
DM51-25		0.002037842	3.07E-07	6.29	0.15	0.00	0.97	0.03	0.002037863	3.22E-07	3.59	0.16	3.59	0.51	
DM51-4		0.002037882	2.24E-07	6.31	0.11	0.00	0.97	0.03	0.002037730	2.24E-07	3.52	0.11	3.52	0.46	
DM51-5		0.002036716	2.75E-07	5.74	0.13	0.00	0.97	0.03	0.002036737	2.35E-07	3.04	0.12	3.04	0.46	
DM51-24		0.002038668	3.26E-07	6.70	0.16	0.00	0.97	0.03	0.002038795	2.08E-07	4.04	0.10	4.04	0.45	
DM51-6		0.002036179	7.47E-07	5.47	0.37	0.00	0.97	0.03	0.002036336	2.58E-07	2.84	0.13	2.84	0.47	
DM51-7		0.002036997	4.65E-07	5.88	0.23	0.00	0.97	0.03	0.002036929	2.63E-07	3.13	0.13	3.13	0.48	
DM51-8		0.002036610	6.13E-07	5.68	0.30	0.00	0.98	0.02	0.002036584	2.3E-07	2.96	0.11	2.96	0.46	
DM51-9		0.002037179	3.52E-07	5.96	0.17	0.00	0.98	0.02	0.002037015	2.04E-07	3.17	0.10	3.17	0.45	
DM51-10		0.002037601	4.18E-07	6.17	0.21	0.00	0.98	0.02	0.002037562	1.84E-07	3.44	0.09	3.44	0.44	
DM51-11		0.002036748	7.6E-07	5.75	0.37	0.00	0.98	0.02	0.002036621	2.83E-07	2.98	0.14	2.98	0.49	

Title	domain	PrPDM as primary standard				Xgross	Xprp	Xalm	UWG2 as primary standard				matrix corrected			
		$^{18}\text{O}/^{16}\text{O}$	$\pm 95\% \text{ cl}$	$\delta^{18}\text{O}\text{‰}$	$\pm 2\text{SE}$				$^{18}\text{O}/^{16}\text{O}$	$\pm 95\% \text{ cl}$	$\delta^{18}\text{O}\text{‰}$	$\pm 2\text{SE}$	$\delta^{18}\text{O}\text{‰}$	$\pm 2\text{SE}$		
DM51-12		0.002037792	4.15E-07	6.27	0.20	0.00	0.98	0.02	0.002037585	3.17E-07	3.45	0.16	3.45	0.51		
DM51-13		0.002037216	3.41E-07	5.98	0.17	0.00	0.98	0.01	0.002037347	5.2E-07	3.33	0.26	3.33	0.65		
DM51-14		0.002036265	5.48E-07	5.52	0.27	0.00	0.99	0.01	0.002036308	1.88E-07	2.82	0.09	2.82	0.44		
DM51-15		0.002037311	6.41E-07	6.03	0.31	0.00	0.99	0.01	0.002037146	2.73E-07	3.24	0.13	3.24	0.48		
DM51-16		0.002038482	6.45E-07	6.60	0.32	0.00	0.99	0.01	0.002038402	3.02E-07	3.85	0.15	3.85	0.50		
DM51-18		0.002037080	6.68E-07	5.92	0.33	0.00	0.99	0.00	0.002037185	2.48E-07	3.25	0.12	3.25	0.47		
DM51-17		0.002037273	2.59E-07	6.01	0.13	0.00	1.00	0.00	0.002037164	2.42E-07	3.24	0.12	3.24	0.47		
DM51-19		0.002037658	1.48E-07	6.20	0.07	0.00	1.00	0.00	0.002037693	2.29E-07	3.50	0.11	3.50	0.46		
DM51-20		0.002038292	5.37E-07	6.51	0.26	0.00	1.00	0.00	0.002038254	2.27E-07	3.78	0.11	3.78	0.46		
DM51-22	rim	0.002037394	9.54E-07	6.07	0.47	0.00	0.99	0.01	0.002037361	4.08E-07	3.34	0.20	3.34	0.57		
				6.09	0.36											
DM52-1		0.002040536	3.87E-07	7.61	0.19	0.02	0.92	0.06	0.002040455	3.95E-07	4.86	0.19	4.86	0.56		
DM52-2		0.002038182	6.24E-07	6.46	0.31	0.00	0.99	0.01	0.002038322	2.89E-07	3.81	0.14	3.81	0.49		
DM52-3		0.002038635	3.62E-07	6.68	0.18	0.00	0.98	0.02	0.002038719	1.67E-07	4.01	0.08	4.01	0.43		
DM52-4		0.002038908	5.85E-07	6.81	0.29	0.00	0.98	0.02	0.002039149	2.07E-07	4.22	0.10	4.22	0.45		
DM52-5		0.002039621	1.79E-07	7.16	0.09	0.03	0.89	0.09	0.002039570	1.49E-07	4.42	0.07	4.42	0.43		
DM52-6		0.002038110	4.71E-07	6.42	0.23	0.00	0.99	0.01	0.002038277	2.24E-07	3.79	0.11	3.79	0.46		
DM52-7		0.002039263	2.14E-07	6.99	0.11	0.00	0.98	0.01	0.002039262	2.04E-07	4.27	0.10	4.27	0.45		
DM52-8		0.002039017	5.31E-07	6.87	0.26	0.00	0.96	0.04	0.002039163	3.67E-07	4.22	0.18	4.22	0.54		
DM52-9		0.002039320	4.79E-07	7.02	0.24	0.00	0.98	0.02	0.002039527	2.05E-07	4.40	0.10	4.40	0.45		
DM52-10		0.002038619	6.5E-07	6.67	0.32	0.00	0.98	0.02	0.002038517	2.31E-07	3.91	0.11	3.91	0.46		
PrPDM-1						0.01	0.95	0.04	0.002036124	1.5E-07	2.73	0.07	2.73	0.43		
PrPDM-2						0.01	0.95	0.04	0.002036546	1.9E-07	2.94	0.09	2.94	0.44		
PrPDM-3						0.01	0.96	0.04	0.002035844	1.62E-07	2.60	0.08	2.60	0.43		
PrPDM-4						0.01	0.96	0.04	0.002035829	3.06E-07	2.59	0.15	2.59	0.50		
PrPDM-5						0.00	0.97	0.02	0.002036592	1.41E-07	2.96	0.07	2.96	0.42		
PrPDM-6						0.00	0.98	0.02	0.002036980	3.26E-07	3.15	0.16	3.15	0.51		
PrPDM-7						0.00	0.97	0.02	0.002036642	3.42E-07	2.99	0.17	2.99	0.52		
PrPDM-8						0.00	0.97	0.02	0.002036556	1.98E-07	2.95	0.10	2.95	0.44		
PrPDM-10						0.00	0.97	0.02	0.002036772	1.75E-07	3.05	0.09	3.05	0.44		
PrPDM-11						0.01	0.95	0.04	0.002036559	2.5E-07	2.95	0.12	2.95	0.47		
PrPDM-12						0.01	0.95	0.04	0.002036507	1.87E-07	2.92	0.09	2.92	0.44		
PrPDM-13						0.01	0.95	0.04	0.002036905	1.98E-07	3.12	0.10	3.12	0.44		
PrPDM-14						0.01	0.95	0.04	0.002036686	1.9E-07	3.01	0.09	3.01	0.44		
PrPDM-15						0.00	0.98	0.02	0.002036564	2.2E-07	2.95	0.11	2.95	0.45		

**A2 - Electronic Supplementary Material 9: Monazite oxygen isotope composition determined by SHRIMP (all uncertainties are at 2 sigma level)**

Title	zone	$^{18}\text{O}/^{16}\text{O}$	$\pm 95\% \text{ cl}$	$\delta^{18}\text{O}\text{‰}$	$\pm 2\text{SE}$	Si wt%	Ca wt%	corrected $\delta^{18}\text{O}\text{‰}$	$\pm 2\text{SE}$
DM1C-1	outer zone	0.002037203	1.88E-07	3.80	0.18	0.15	2.69	6.16	0.18
DM1C-2	inner zone	0.002036498	1.06E-07	3.46	0.10	0.14	3.20	6.37	0.10
DM1C-3	outer zone	0.002035963	1.08E-07	3.20	0.11	0.14	3.36	6.28	0.11
DM1C-4	outer zone	0.002036478	1.88E-07	3.45	0.18	0.12	2.89	6.02	0.18
DM1C-5	outer zone	0.002037201	1.48E-07	3.80	0.15	0.09	2.39	5.82	0.15
DM1C-6	outer zone	0.002036060	1.34E-07	3.24	0.13	0.19	3.70	6.70	0.13
DM1C-7	outer zone	0.002036517	1.48E-07	3.47	0.15	0.15	3.53	6.74	0.15
DM1C-8	outer zone	0.002038171	1.14E-07	4.28	0.11	0.11	2.46	6.37	0.11
DM1C-9	outer zone	0.002034957	1.10E-07	2.70	0.11	0.15	3.87	6.36	0.11
DM1C-10	outer zone	0.002035180	9.90E-08	2.81	0.10	0.15	3.38	5.93	0.10
DM1C-12	outer zone	0.002038101	1.81E-07	4.24	0.18	0.09	2.13	5.97	0.18
DM1C-13	inner zone	0.002040112	2.04E-07	5.22	0.20	0.09	1.81	6.61	0.20
DM1C-14	outer zone	0.002037136	9.70E-08	3.77	0.10	0.14	3.58	7.10	0.10
DM1C-15	outer zone	0.002037593	1.52E-07	3.99	0.15	0.10	2.26	5.88	0.15
DM1C-19	outer zone	0.002034496	1.36E-07	2.48	0.13	0.18	4.42	6.73	0.13
DM51-1		0.002040418	1.51E-07	5.37	0.15	1.61	0.05	6.10	0.15
DM51-2		0.002041180	1.62E-07	5.75	0.16	0.46	0.65	6.13	0.16
DM51-3		0.002041645	1.16E-07	5.97	0.11	1.18	0.05	6.33	0.11
DM51-4		0.002043062	1.86E-07	6.67	0.18	0.21	0.36	6.51	0.18
DM51-5		0.002041023	1.33E-07	5.67	0.13	0.20	1.13	6.34	0.13
DM51-6		0.002040466	1.29E-07	5.40	0.13	1.78	0.01	6.24	0.13
DM51-7		0.002041022	1.31E-07	5.67	0.13	0.36	0.67	5.98	0.13
DM51-8		0.002040115	2.12E-07	5.23	0.21	0.64	1.11	6.27	0.21
DM51-9		0.002039069	2.13E-07	4.71	0.21	1.92	0.05	5.71	0.21
DM51-10		0.002041145	8.20E-08	5.73	0.08	0.61	1.23	6.88	0.08
DM51-11		0.002041490	1.28E-07	5.90	0.12	0.86	0.04	5.96	0.12
DM51-12		0.002041070	1.03E-07	5.69	0.10	0.40	0.43	5.78	0.10
DM51-13		0.002040917	1.36E-07	5.62	0.13	1.47	0.20	6.40	0.13
DM51-14		0.002041602	1.50E-07	5.95	0.15	1.24	0.01	6.32	0.15
DM51-16		0.002041023	1.86E-07	5.67	0.18	0.21	1.04	6.26	0.18
DM51-17		0.002041084	1.17E-07	5.70	0.11	0.08	1.16	6.31	0.11

Title	zone	$^{18}\text{O}/^{16}\text{O}$	$\pm 95\% \text{ cl}$	$\delta^{18}\text{O}\text{‰}$	$\pm 2\text{SE}$	Si wt%	Ca wt%	corrected $\delta^{18}\text{O}\text{‰}$	$\pm 2\text{SE}$
DM52-1		0.002042355	1.52E-07	6.32	0.15	0.65	0.38	6.58	0.15
DM52-2		0.002042860	1.89E-07	6.57	0.19	1.07	0.02	6.79	0.19
DM52-3		0.002041785	6.90E-08	6.04	0.07	0.21	0.86	6.44	0.07
DM52-4		0.002042239	1.59E-07	6.26	0.16	0.38	0.73	6.66	0.16
DM52-5		0.002042694	1.08E-07	6.49	0.11	0.22	0.76	6.78	0.11
DM52-8		0.002042982	1.50E-07	6.63	0.15	1.06	0.04	6.86	0.15
DM52-9		0.002041707	1.95E-07	6.00	0.19	0.28	0.79	6.38	0.19
DM52-10		0.002043207	1.01E-07	6.74	0.10	0.13	0.56	6.73	0.10
DM52-11		0.002041993	1.54E-07	6.14	0.15	0.08	1.11	6.70	0.15
DM52-12		0.002044106	1.82E-07	7.18	0.18	0.07	0.27	6.80	0.18
DM52-13		0.002041333	1.30E-07	5.82	0.13	0.99	0.13	6.10	0.13
DM52-15		0.002042543	1.29E-07	6.41	0.13	1.08	0.20	6.84	0.13
DM53-1		0.002042054	1.10E-07	6.173682	0.11	1.11	0.03	6.45	0.11
DM53-2		0.002042998	1.34E-07	6.635327	0.13	0.35	0.55	6.81	0.13
DM53-3		0.002041067	1.49E-07	5.691135	0.15	1.37	0.02	6.18	0.15
DM53-4		0.002041975	1.00E-07	6.135069	0.10	0.45	0.29	6.11	0.10
DM53-5		0.002041288	1.23E-07	5.799177	0.12	1.64	0.01	6.52	0.12
DM53-6		0.002040289	1.18E-07	5.311004	0.12	0.41	0.75	5.76	0.12
DM53-7		0.002041447	7.70E-08	5.877025	0.07	1.10	0.03	6.14	0.07
DM53-8		0.002041327	9.70E-08	5.818455	0.09	0.47	0.56	6.11	0.09
DM53-9		0.002041848	1.06E-07	6.07331	0.10	0.97	0.27	6.48	0.10

## **A3 – Appendix to Chapter 3**



**Table A3 - 1 : LA-ICP-MS Whole-rock trace element analyses**

Standard deviation on three replicates of laser ablation on the same melted tab.

	SGM21		SHB02		SHB05		SHB08	
	ppm	std. dev.	ppm	std. dev.	ppm	std. dev.	ppm	std. dev.
Si	<b>310063</b>	3952	<b>216292</b>	4149	<b>224066</b>	1986	<b>205584</b>	5269
Sc	<b>9.6</b>	0.2	<b>25.2</b>	0.9	<b>42.9</b>	1.5	<b>32.3</b>	0.5
Ti	<b>1433</b>	28	<b>3841</b>	65	<b>8109</b>	146	<b>4477</b>	122
V	<b>58.2</b>	0.7	<b>157.8</b>	2.5	<b>292.0</b>	5.5	<b>260.4</b>	2.1
Cr	<b>36.0</b>	2.2	<b>119.2</b>	4.0	<b>73.5</b>	4.6	<b>236.8</b>	6.2
Mn	<b>466</b>	11	<b>1829</b>	22	<b>1186</b>	7	<b>993</b>	15
Co	<b>4.1</b>	0.1	<b>26.9</b>	0.9	<b>31.3</b>	0.8	<b>31.5</b>	0.3
Ni	<b>28.0</b>	1.9	<b>134.0</b>	4.2	<b>42.0</b>	1.7	<b>86.3</b>	1.1
Cu	<b>4.1</b>	0.2	<b>48.8</b>	1.0	<b>26.4</b>	1.2	<b>46.2</b>	1.6
Zn	<b>24.6</b>	1.9	<b>55.0</b>	2.7	<b>85.9</b>	3.2	<b>64.1</b>	0.9
Ga	<b>15.49</b>	0.83	<b>11.69</b>	0.27	<b>14.14</b>	0.04	<b>18.82</b>	0.65
Ge	<b>1.1</b>	0.9	<b>4.2</b>	0.9	<b>3.1</b>	0.8	<b>3.4</b>	0.4
Rb	<b>43.08</b>	0.56	<b>0.51</b>	0.03	<b>1.88</b>	0.06	<b>17.78</b>	0.18
Sr	<b>108.4</b>	1.8	<b>194.2</b>	5.0	<b>51.0</b>	0.5	<b>307.1</b>	5.8
Y	<b>13.6</b>	0.2	<b>83.6</b>	2.0	<b>24.3</b>	1.0	<b>27.5</b>	0.6
Zr	<b>46.3</b>	0.7	<b>148.0</b>	3.1	<b>78.5</b>	5.1	<b>42.1</b>	1.1
Nb	<b>4.90</b>	0.28	<b>11.55</b>	0.19	<b>2.99</b>	0.04	<b>2.81</b>	0.20
Cs	<b>2.85</b>	0.11	<b>0.10</b>	0.02	<b>0.11</b>	0.01	<b>0.60</b>	0.03
Ba	<b>273.3</b>	6.0	<b>8.0</b>	0.5	<b>7.1</b>	0.2	<b>73.6</b>	1.4
La	<b>15.27</b>	0.46	<b>53.68</b>	1.02	<b>5.81</b>	0.27	<b>5.28</b>	0.26
Ce	<b>26.67</b>	0.78	<b>81.22</b>	1.49	<b>13.20</b>	0.20	<b>10.30</b>	0.06
Pr	<b>3.65</b>	0.06	<b>13.72</b>	0.24	<b>1.81</b>	0.02	<b>1.45</b>	0.02
Nd	<b>14.91</b>	0.16	<b>60.49</b>	2.27	<b>9.16</b>	0.56	<b>7.71</b>	0.17
Sm	<b>2.79</b>	0.08	<b>13.78</b>	0.42	<b>2.88</b>	0.02	<b>2.42</b>	0.08
Eu	<b>0.60</b>	0.05	<b>3.18</b>	0.07	<b>0.92</b>	0.03	<b>0.98</b>	0.02
Gd	<b>2.49</b>	0.05	<b>14.88</b>	0.14	<b>3.52</b>	0.12	<b>3.45</b>	0.07
Tb	<b>0.37</b>	0.03	<b>2.11</b>	0.07	<b>0.62</b>	0.02	<b>0.62</b>	0.01
Dy	<b>2.30</b>	0.08	<b>13.67</b>	0.35	<b>4.24</b>	0.08	<b>4.44</b>	0.04
Ho	<b>0.47</b>	0.01	<b>2.69</b>	0.12	<b>0.92</b>	0.03	<b>0.96</b>	0.03
Er	<b>1.38</b>	0.07	<b>7.99</b>	0.39	<b>2.72</b>	0.16	<b>2.91</b>	0.18
Tm	<b>0.20</b>	0.02	<b>1.03</b>	0.01	<b>0.42</b>	0.02	<b>0.42</b>	0.02
Yb	<b>1.30</b>	0.08	<b>6.87</b>	0.22	<b>2.76</b>	0.09	<b>2.66</b>	0.15
Lu	<b>0.19</b>	0.01	<b>0.97</b>	0.01	<b>0.41</b>	0.04	<b>0.37</b>	0.01
Hf	<b>1.26</b>	0.03	<b>4.01</b>	0.28	<b>2.09</b>	0.16	<b>1.21</b>	0.07
Ta	<b>0.33</b>	0.03	<b>0.90</b>	0.01	<b>0.17</b>	0.02	<b>0.15</b>	0.02
W	<b>3.83</b>	0.29	<b>0.74</b>	0.15	<b>0.45</b>	0.04	<b>0.55</b>	0.04
Pb	<b>7.51</b>	0.13	<b>8.07</b>	0.22	<b>3.05</b>	0.02	<b>6.77</b>	0.07
Th	<b>4.49</b>	0.10	<b>12.24</b>	0.39	<b>0.70</b>	0.04	<b>0.26</b>	0.01
U	<b>1.01</b>	0.07	<b>1.59</b>	0.04	<b>0.18</b>	0.01	<b>0.15</b>	0.01

Table A3 - 1 : LA-ICP-MS Whole-rock trace element analyses

	SHB12A		SHB12B		SHB42CA		SHB42CB	
	ppm	std. dev.	ppm	std. dev.	ppm	std. dev.	ppm	std. dev.
Si	<b>217812</b>	2339	<b>224311</b>	2167	<b>194672</b>	1257	<b>179681</b>	866
Sc	<b>37.2</b>	1.0	<b>42.7</b>	1.1	<b>22.2</b>	0.2	<b>18.8</b>	0.6
Ti	<b>6193</b>	53	<b>6463</b>	19	<b>4683</b>	33	<b>4293</b>	34
V	<b>206.1</b>	1.4	<b>218.8</b>	1.4	<b>132.6</b>	1.4	<b>137.2</b>	0.5
Cr	<b>374.2</b>	8.9	<b>391.6</b>	5.8	<b>79.1</b>	1.8	<b>52.9</b>	2.3
Mn	<b>1785</b>	13	<b>1441</b>	18	<b>4979</b>	67	<b>6298</b>	85
Co	<b>34.1</b>	0.1	<b>24.8</b>	0.6	<b>46.4</b>	1.4	<b>51.9</b>	0.1
Ni	<b>179.5</b>	7.3	<b>146.6</b>	1.6	<b>147.3</b>	1.8	<b>107.8</b>	2.7
Cu	<b>18.9</b>	0.7	<b>16.8</b>	0.9	<b>97.4</b>	0.6	<b>79.3</b>	0.9
Zn	<b>42.4</b>	0.7	<b>39.4</b>	1.0	<b>52.0</b>	0.3	<b>62.0</b>	1.1
Ga	<b>25.86</b>	0.89	<b>24.68</b>	1.40	<b>18.91</b>	0.60	<b>24.01</b>	0.51
Ge	<b>2.7</b>	0.4	<b>2.8</b>	0.6	<b>2.8</b>	0.2	<b>3.1</b>	0.3
Rb	<b>45.72</b>	1.01	<b>44.17</b>	0.66	<b>24.77</b>	0.52	<b>22.14</b>	0.36
Sr	<b>59.9</b>	0.4	<b>41.2</b>	0.5	<b>2407.4</b>	12.8	<b>2469.4</b>	9.2
Y	<b>38.9</b>	0.7	<b>39.6</b>	0.9	<b>47.8</b>	0.7	<b>64.3</b>	0.3
Zr	<b>75.7</b>	2.1	<b>81.3</b>	1.9	<b>133.3</b>	3.3	<b>105.9</b>	3.2
Nb	<b>5.53</b>	0.08	<b>6.31</b>	0.11	<b>22.26</b>	0.16	<b>22.29</b>	0.12
Cs	<b>1.36</b>	0.05	<b>1.44</b>	0.02	<b>0.53</b>	0.01	<b>0.41</b>	0.02
Ba	<b>339.5</b>	1.4	<b>303.6</b>	0.6	<b>117.8</b>	1.2	<b>237.9</b>	2.2
La	<b>5.53</b>	0.20	<b>5.55</b>	0.13	<b>39.87</b>	0.09	<b>45.10</b>	0.26
Ce	<b>12.73</b>	0.13	<b>13.05</b>	0.32	<b>108.28</b>	0.80	<b>81.63</b>	0.39
Pr	<b>1.82</b>	0.02	<b>1.87</b>	0.09	<b>9.57</b>	0.12	<b>9.94</b>	0.04
Nd	<b>9.40</b>	0.10	<b>9.78</b>	0.34	<b>39.63</b>	0.19	<b>41.36</b>	0.10
Sm	<b>2.78</b>	0.17	<b>2.90</b>	0.14	<b>8.23</b>	0.26	<b>8.86</b>	0.27
Eu	<b>0.99</b>	0.09	<b>0.98</b>	0.06	<b>1.74</b>	0.04	<b>2.12</b>	0.02
Gd	<b>4.00</b>	0.29	<b>3.94</b>	0.20	<b>7.66</b>	0.16	<b>9.26</b>	0.22
Tb	<b>0.74</b>	0.02	<b>0.69</b>	0.05	<b>1.17</b>	0.02	<b>1.42</b>	0.03
Dy	<b>6.01</b>	0.24	<b>5.49</b>	0.29	<b>7.54</b>	0.08	<b>9.37</b>	0.19
Ho	<b>1.38</b>	0.05	<b>1.44</b>	0.06	<b>1.52</b>	0.03	<b>1.93</b>	0.03
Er	<b>4.26</b>	0.19	<b>5.12</b>	0.16	<b>4.66</b>	0.11	<b>5.99</b>	0.08
Tm	<b>0.60</b>	0.01	<b>0.82</b>	0.04	<b>0.67</b>	0.00	<b>0.80</b>	0.02
Yb	<b>4.02</b>	0.04	<b>6.32</b>	0.28	<b>4.76</b>	0.13	<b>5.37</b>	0.06
Lu	<b>0.59</b>	0.02	<b>1.01</b>	0.05	<b>0.67</b>	0.02	<b>0.75</b>	0.01
Hf	<b>2.13</b>	0.10	<b>2.11</b>	0.05	<b>3.67</b>	0.21	<b>3.03</b>	0.02
Ta	<b>0.31</b>	0.04	<b>0.39</b>	0.01	<b>1.20</b>	0.02	<b>1.16</b>	0.03
W	<b>0.59</b>	0.02	<b>0.59</b>	0.04	<b>0.31</b>	0.07	<b>0.31</b>	0.04
Pb	<b>2.40</b>	0.16	<b>1.69</b>	0.07	<b>35.97</b>	0.63	<b>40.26</b>	0.56
Th	<b>0.57</b>	0.02	<b>0.64</b>	0.04	<b>13.20</b>	0.17	<b>9.32</b>	0.07
U	<b>0.14</b>	0.01	<b>0.15</b>	0.02	<b>1.74</b>	0.01	<b>1.77</b>	0.04

Table A3 - 1 : LA-ICP-MS Whole-rock trace element analyses

	SHB44B		SHB45A		SHB45B		SHB53	
	ppm	std. dev.	ppm	std. dev.	ppm	std. dev.	ppm	std. dev.
Si	<b>213607</b>	2591	<b>199532</b>	1238	<b>203530</b>	1806	<b>196900</b>	3185
Sc	<b>34.9</b>	0.5	<b>29.2</b>	0.5	<b>30.1</b>	0.2	<b>33.6</b>	0.3
Ti	<b>17368</b>	31	<b>17548</b>	130	<b>14322</b>	40	<b>7195</b>	103
V	<b>286.8</b>	1.9	<b>254.1</b>	1.7	<b>238.9</b>	4.7	<b>198.1</b>	2.2
Cr	<b>23.6</b>	1.2	<b>455.8</b>	2.6	<b>362.4</b>	5.0	<b>250.5</b>	4.2
Mn	<b>1351</b>	19	<b>1135</b>	8	<b>1179</b>	25	<b>2658</b>	30
Co	<b>38.0</b>	0.3	<b>44.3</b>	0.7	<b>41.5</b>	0.6	<b>27.0</b>	0.7
Ni	<b>96.5</b>	4.2	<b>185.1</b>	2.6	<b>135.5</b>	4.3	<b>129.4</b>	1.8
Cu	<b>23.8</b>	0.9	<b>70.0</b>	0.7	<b>81.1</b>	1.8	<b>17.1</b>	0.3
Zn	<b>100.6</b>	0.7	<b>87.7</b>	2.8	<b>84.0</b>	2.1	<b>76.9</b>	1.2
Ga	<b>20.92</b>	0.18	<b>21.59</b>	0.25	<b>25.30</b>	0.55	<b>24.31</b>	0.24
Ge	<b>4.1</b>	0.4	<b>3.9</b>	0.1	<b>4.0</b>	0.5	<b>4.2</b>	0.9
Rb	<b>14.81</b>	0.16	<b>21.51</b>	0.11	<b>30.29</b>	0.75	<b>6.92</b>	0.19
Sr	<b>208.4</b>	1.4	<b>301.8</b>	3.3	<b>287.5</b>	1.3	<b>885.1</b>	12.7
Y	<b>83.6</b>	0.4	<b>22.4</b>	0.2	<b>21.8</b>	0.2	<b>45.3</b>	0.2
Zr	<b>259.9</b>	0.7	<b>229.2</b>	2.5	<b>191.6</b>	3.5	<b>251.3</b>	4.2
Nb	<b>17.32</b>	0.17	<b>52.94</b>	0.66	<b>47.70</b>	0.62	<b>25.48</b>	0.39
Cs	<b>0.46</b>	0.03	<b>1.04</b>	0.06	<b>1.20</b>	0.07	<b>0.32</b>	0.01
Ba	<b>19.8</b>	0.6	<b>183.2</b>	1.4	<b>262.5</b>	3.1	<b>40.9</b>	1.1
La	<b>15.59</b>	0.05	<b>39.00</b>	0.16	<b>38.64</b>	0.20	<b>44.16</b>	0.73
Ce	<b>39.08</b>	0.32	<b>77.71</b>	0.81	<b>75.10</b>	0.63	<b>85.44</b>	1.25
Pr	<b>5.63</b>	0.04	<b>9.15</b>	0.03	<b>8.62</b>	0.08	<b>10.21</b>	0.37
Nd	<b>29.65</b>	0.04	<b>38.60</b>	0.22	<b>35.12</b>	0.25	<b>41.63</b>	0.95
Sm	<b>9.01</b>	0.06	<b>8.02</b>	0.27	<b>7.10</b>	0.06	<b>8.40</b>	0.36
Eu	<b>2.55</b>	0.07	<b>2.34</b>	0.03	<b>2.15</b>	0.03	<b>2.14</b>	0.07
Gd	<b>12.04</b>	0.19	<b>6.81</b>	0.07	<b>6.45</b>	0.27	<b>8.27</b>	0.34
Tb	<b>2.07</b>	0.01	<b>0.92</b>	0.06	<b>0.88</b>	0.03	<b>1.21</b>	0.02
Dy	<b>14.58</b>	0.25	<b>5.03</b>	0.22	<b>4.91</b>	0.12	<b>7.94</b>	0.16
Ho	<b>2.99</b>	0.01	<b>0.87</b>	0.01	<b>0.84</b>	0.02	<b>1.56</b>	0.07
Er	<b>9.40</b>	0.06	<b>2.28</b>	0.11	<b>2.24</b>	0.05	<b>4.73</b>	0.19
Tm	<b>1.24</b>	0.03	<b>0.26</b>	0.01	<b>0.28</b>	0.01	<b>0.67</b>	0.01
Yb	<b>8.66</b>	0.16	<b>1.81</b>	0.13	<b>1.76</b>	0.08	<b>4.85</b>	0.23
Lu	<b>1.25</b>	0.02	<b>0.23</b>	0.01	<b>0.24</b>	0.01	<b>0.72</b>	0.01
Hf	<b>7.23</b>	0.18	<b>5.71</b>	0.04	<b>4.81</b>	0.16	<b>6.27</b>	0.17
Ta	<b>0.98</b>	0.02	<b>3.31</b>	0.09	<b>3.01</b>	0.07	<b>1.70</b>	0.06
W	<b>6.51</b>	0.29	<b>0.55</b>	0.06	<b>0.57</b>	0.01	<b>0.44</b>	0.06
Pb	<b>8.18</b>	0.30	<b>5.05</b>	0.06	<b>4.78</b>	0.03	<b>35.19</b>	0.35
Th	<b>1.54</b>	0.02	<b>4.56</b>	0.13	<b>4.98</b>	0.02	<b>12.58</b>	0.31
U	<b>1.17</b>	0.05	<b>0.98</b>	0.01	<b>0.91</b>	0.06	<b>2.61</b>	0.06

Table A3 - 1 : LA-ICP-MS Whole-rock trace element analyses

	SHM04		SHM23B		SHS3		SHS26	
	ppm	std. dev.	ppm	std. dev.	ppm	std. dev.	ppm	std. dev.
Si	<b>4466</b>	225	<b>404077</b>	3028	<b>333634</b>	34304	<b>57976</b>	3561
Sc	<b>0.5</b>	0.03	<b>6.1</b>	0.2	<b>12.6</b>	2.3	<b>3.8</b>	0.3
Ti	<b>19</b>	1	<b>348</b>	13	<b>2019</b>	227	<b>1887</b>	110
V	<b>9.1</b>	0.3	<b>29.0</b>	0.2	<b>63.8</b>	6.2	<b>18.3</b>	1.0
Cr	<b>11.6</b>	0.7	<b>20.2</b>	1.1	<b>46.0</b>	8.2	<b>134.0</b>	5.4
Mn	<b>57</b>	1	<b>368</b>	12	<b>324</b>	35	<b>117</b>	7
Co	<b>0.9</b>	0.1	<b>1.7</b>	0.0	<b>8.4</b>	0.6	<b>28.4</b>	1.4
Ni	<b>8.0</b>	0.6	<b>19.3</b>	0.7	<b>32.0</b>	3.9	<b>570.5</b>	25.9
Cu	<b>7.7</b>	3.2	<b>12.0</b>	5.8	<b>9.3</b>	2.1	<b>24.0</b>	3.0
Zn	<b>8.2</b>	0.3	<b>17.7</b>	0.8	<b>42.9</b>	3.8	<b>10.3</b>	0.5
Ga	<b>0.37</b>	0.02	<b>4.08</b>	0.16	<b>19.69</b>	3.61	<b>0.41</b>	0.04
Ge	<b>bdl</b>		<b>0.8</b>	1.2	<b>1.0</b>	0.3	<b>1.0</b>	0.1
Rb	<b>0.37</b>	0.04	<b>10.79</b>	0.15	<b>72.17</b>	7.94	<b>0.04</b>	0.02
Sr	<b>598.1</b>	9.7	<b>18.1</b>	0.5	<b>26.6</b>	3.0	<b>0.35</b>	0.03
Y	<b>2.4</b>	0.02	<b>5.5</b>	0.1	<b>13.8</b>	1.3	<b>0.21</b>	0.01
Zr	<b>1.1</b>	0.2	<b>23.5</b>	1.8	<b>63.8</b>	8.6	<b>5.0</b>	0.2
Nb	<b>0.08</b>	0.02	<b>1.23</b>	0.03	<b>7.36</b>	1.26	<b>2.56</b>	0.22
Cs	<b>0.05</b>	0.01	<b>0.58</b>	0.04	<b>3.94</b>	0.33	<b>bdl</b>	
Ba	<b>9.4</b>	0.1	<b>71.1</b>	2.5	<b>259.8</b>	28.2	<b>0.8</b>	0.017
La	<b>0.88</b>	0.03	<b>3.46</b>	0.06	<b>12.21</b>	1.51	<b>0.04</b>	0.004
Ce	<b>1.22</b>	0.03	<b>6.34</b>	0.21	<b>27.43</b>	3.03	<b>0.10</b>	0.002
Pr	<b>0.18</b>	0.02	<b>0.74</b>	0.02	<b>3.00</b>	0.34	<b>0.01</b>	0.01
Nd	<b>0.80</b>	0.11	<b>2.97</b>	0.13	<b>11.82</b>	1.42	<b>0.08</b>	0.005
Sm	<b>0.16</b>	0.06	<b>0.59</b>	0.03	<b>2.39</b>	0.20	<b>0.03</b>	0.01
Eu	<b>0.04</b>	0.004	<b>0.16</b>	0.01	<b>0.53</b>	0.10	<b>bdl</b>	
Gd	<b>0.20</b>	0.03	<b>0.70</b>	0.03	<b>2.39</b>	0.29	<b>0.03</b>	0.01
Tb	<b>0.03</b>	0.005	<b>0.11</b>	0.00	<b>0.34</b>	0.01	<b>0.01</b>	0.001
Dy	<b>0.24</b>	0.03	<b>0.78</b>	0.05	<b>2.34</b>	0.23	<b>0.05</b>	0.01
Ho	<b>0.06</b>	0.001	<b>0.15</b>	0.01	<b>0.47</b>	0.05	<b>0.01</b>	0.001
Er	<b>0.20</b>	0.03	<b>0.52</b>	0.03	<b>1.44</b>	0.15	<b>0.04</b>	0.01
Tm	<b>0.04</b>	0.003	<b>0.09</b>	0.01	<b>0.22</b>	0.03	<b>0.01</b>	0.0004
Yb	<b>0.17</b>	0.01	<b>0.47</b>	0.05	<b>1.36</b>	0.18	<b>0.04</b>	0.01
Lu	<b>0.03</b>	0.005	<b>0.08</b>	0.01	<b>0.20</b>	0.03	<b>0.01</b>	0.002
Hf	<b>0.02</b>	0.01	<b>0.59</b>	0.06	<b>1.73</b>	0.14	<b>0.18</b>	0.02
Ta	<b>bdl</b>		<b>0.08</b>	0.01	<b>0.57</b>	0.07	<b>0.12</b>	0.01
W	<b>1.89</b>	0.10	<b>2.67</b>	0.29	<b>1.58</b>	0.20	<b>0.56</b>	0.02
Pb	<b>5.94</b>	0.20	<b>10.07</b>	0.03	<b>2.94</b>	0.23	<b>0.28</b>	0.02
Th	<b>0.09</b>	0.02	<b>1.08</b>	0.05	<b>3.90</b>	0.44	<b>0.03</b>	0.002
U	<b>0.57</b>	0.04	<b>0.27</b>	0.01	<b>0.81</b>	0.10	<b>0.01</b>	0.001

Table A3 - 1 : LA-ICP-MS Whole-rock trace element analyses

	SHS27		SHS44A		SHS46		SIB32	
	ppm	std. dev.	ppm	std. dev.	ppm	std. dev.	ppm	std. dev.
Si	<b>200468</b>	3070	<b>232460</b>	2728	<b>316358</b>	14376	<b>157194</b>	2504
Sc	<b>9.6</b>	0.2	<b>18.0</b>	0.5	<b>12.9</b>	1.1	<b>23.8</b>	0.4
Ti	<b>1692</b>	36	<b>3848</b>	48	<b>2214</b>	127	<b>8667</b>	143
V	<b>56.4</b>	0.8	<b>204.9</b>	3.8	<b>61.4</b>	2.8	<b>138.9</b>	3.6
Cr	<b>39.6</b>	1.1	<b>18.1</b>	0.9	<b>43.1</b>	3.0	<b>158.5</b>	2.8
Mn	<b>2249</b>	44	<b>1879</b>	37	<b>156</b>	5	<b>1153</b>	30
Co	<b>14.1</b>	0.5	<b>10.1</b>	0.2	<b>7.5</b>	0.4	<b>46.0</b>	1.4
Ni	<b>46.9</b>	0.5	<b>68.0</b>	0.7	<b>35.0</b>	2.2	<b>261.2</b>	4.1
Cu	<b>45.5</b>	0.5	<b>11.9</b>	0.6	<b>5.6</b>	0.2	<b>12.2</b>	0.4
Zn	<b>44.5</b>	1.5	<b>22.5</b>	0.9	<b>36.2</b>	2.4	<b>82.6</b>	3.9
Ga	<b>18.16</b>	0.78	<b>52.81</b>	1.11	<b>18.02</b>	1.18	<b>16.35</b>	0.46
Ge	<b>1.4</b>	0.8	<b>2.9</b>	0.6	<b>1.0</b>	0.2	<b>3.5</b>	0.6
Rb	<b>38.90</b>	1.39	<b>108.27</b>	1.96	<b>70.17</b>	3.41	<b>0.49</b>	0.07
Sr	<b>387.0</b>	6.4	<b>332.0</b>	2.1	<b>22.2</b>	1.3	<b>302.0</b>	2.3
Y	<b>24.7</b>	0.5	<b>126.3</b>	1.9	<b>13.1</b>	0.9	<b>25.3</b>	0.5
Zr	<b>61.1</b>	0.3	<b>694.7</b>	4.3	<b>58.8</b>	4.1	<b>133.2</b>	1.6
Nb	<b>5.50</b>	0.07	<b>11.88</b>	0.09	<b>7.89</b>	0.49	<b>37.26</b>	0.62
Cs	<b>1.69</b>	0.04	<b>4.54</b>	0.15	<b>3.47</b>	0.20	<b>0.03</b>	0.01
Ba	<b>321.7</b>	3.5	<b>660.5</b>	6.1	<b>229.5</b>	14.4	<b>3.1</b>	0.1
La	<b>24.12</b>	0.51	<b>16.38</b>	0.14	<b>12.75</b>	0.68	<b>20.50</b>	0.30
Ce	<b>37.57</b>	0.90	<b>52.07</b>	0.84	<b>29.29</b>	1.14	<b>46.09</b>	0.44
Pr	<b>5.72</b>	0.08	<b>6.12</b>	0.05	<b>3.19</b>	0.17	<b>4.39</b>	0.14
Nd	<b>23.91</b>	0.73	<b>30.79</b>	0.49	<b>12.79</b>	1.00	<b>18.61</b>	0.40
Sm	<b>4.87</b>	0.05	<b>10.23</b>	0.41	<b>2.44</b>	0.23	<b>3.63</b>	0.10
Eu	<b>1.11</b>	0.04	<b>2.75</b>	0.08	<b>0.57</b>	0.04	<b>1.17</b>	0.02
Gd	<b>4.89</b>	0.09	<b>14.06</b>	0.25	<b>2.37</b>	0.19	<b>4.03</b>	0.07
Tb	<b>0.67</b>	0.03	<b>2.54</b>	0.04	<b>0.35</b>	0.04	<b>0.60</b>	0.02
Dy	<b>4.09</b>	0.10	<b>18.63</b>	0.16	<b>2.27</b>	0.06	<b>4.06</b>	0.08
Ho	<b>0.79</b>	0.02	<b>4.24</b>	0.09	<b>0.48</b>	0.01	<b>0.88</b>	0.01
Er	<b>2.33</b>	0.12	<b>14.80</b>	0.13	<b>1.38</b>	0.09	<b>2.70</b>	0.04
Tm	<b>0.32</b>	0.01	<b>2.28</b>	0.01	<b>0.20</b>	0.02	<b>0.38</b>	0.004
Yb	<b>2.07</b>	0.18	<b>17.26</b>	0.04	<b>1.29</b>	0.06	<b>2.56</b>	0.004
Lu	<b>0.31</b>	0.02	<b>2.57</b>	0.01	<b>0.19</b>	0.01	<b>0.39</b>	0.02
Hf	<b>1.64</b>	0.14	<b>21.99</b>	0.23	<b>1.59</b>	0.13	<b>3.11</b>	0.14
Ta	<b>0.36</b>	0.01	<b>1.48</b>	0.06	<b>0.58</b>	0.03	<b>2.30</b>	0.12
W	<b>3.85</b>	0.25	<b>2.10</b>	0.16	<b>1.03</b>	0.11	<b>0.58</b>	0.11
Pb	<b>16.04</b>	0.08	<b>14.15</b>	0.47	<b>3.22</b>	0.13	<b>25.55</b>	0.96
Th	<b>5.08</b>	0.23	<b>7.89</b>	0.06	<b>4.64</b>	0.18	<b>4.42</b>	0.05
U	<b>0.64</b>	0.01	<b>1.31</b>	0.03	<b>0.71</b>	0.05	<b>0.44</b>	0.04

Table A3 - 1 : LA-ICP-MS Whole-rock trace element analyses

	SIB32ep		SIB50B		SIS52		SIS53	
	ppm	std. dev.	ppm	std. dev.	ppm	std. dev.	ppm	std. dev.
Si	<b>156853</b>	1399	<b>245658</b>	5140	<b>355643</b>	63207	<b>2347676</b>	435367
Sc	<b>40.7</b>	0.6	<b>26.2</b>	0.6	<b>9.2</b>	0.5	<b>55.1</b>	10.3
Ti	<b>7636</b>	23	<b>6183</b>	133	<b>513</b>	111	<b>9105</b>	1610
V	<b>149.4</b>	2.7	<b>138.8</b>	1.7	<b>9.3</b>	0.8	<b>179.2</b>	24.6
Cr	<b>116.3</b>	2.6	<b>208.1</b>	8.0	<b>17.5</b>	2.7	<b>140.4</b>	22.8
Mn	<b>1983</b>	16	<b>5365</b>	120	<b>4140</b>	796	<b>3917</b>	737
Co	<b>39.4</b>	0.3	<b>28.3</b>	0.7	<b>13.0</b>	2.8	<b>41.7</b>	7.4
Ni	<b>118.5</b>	0.6	<b>106.5</b>	2.2	<b>16.8</b>	3.6	<b>132.6</b>	19.5
Cu	<b>6.0</b>	0.3	<b>16.1</b>	0.8	<b>32.8</b>	6.4	<b>74.2</b>	12.1
Zn	<b>86.9</b>	1.1	<b>44.0</b>	1.2	<b>15.4</b>	3.1	<b>158.5</b>	41.4
Ga	<b>17.71</b>	0.13	<b>15.97</b>	0.45	<b>38.53</b>	1.78	<b>55.77</b>	8.66
Ge	<b>4.7</b>	0.3	<b>3.4</b>	0.1	<b>1.1</b>	1.6	<b>6.1</b>	4.5
Rb	<b>0.10</b>	0.01	<b>62.72</b>	1.42	<b>15.97</b>	3.14	<b>206.79</b>	40.57
Sr	<b>1113.9</b>	1.8	<b>38.6</b>	0.4	<b>106.3</b>	19.7	<b>103.6</b>	21.0
Y	<b>26.6</b>	0.3	<b>34.9</b>	1.1	<b>7.4</b>	1.2	<b>52.6</b>	11.2
Zr	<b>122.2</b>	2.0	<b>150.0</b>	2.8	<b>20.7</b>	4.5	<b>226.9</b>	58.4
Nb	<b>37.03</b>	0.43	<b>25.69</b>	0.75	<b>2.51</b>	0.38	<b>39.11</b>	6.43
Cs	<b>0.02</b>	0.01	<b>2.39</b>	0.06	<b>0.51</b>	0.15	<b>7.62</b>	1.96
Ba	<b>5.3</b>	0.6	<b>97.7</b>	3.7	<b>794.8</b>	146.3	<b>855.7</b>	159.8
La	<b>25.68</b>	0.32	<b>32.01</b>	0.41	<b>5.91</b>	1.07	<b>68.91</b>	11.51
Ce	<b>51.41</b>	0.12	<b>67.80</b>	0.99	<b>21.94</b>	3.87	<b>149.50</b>	27.13
Pr	<b>4.58</b>	0.07	<b>7.09</b>	0.11	<b>1.76</b>	0.28	<b>14.88</b>	2.92
Nd	<b>18.43</b>	0.14	<b>28.96</b>	0.27	<b>7.40</b>	1.33	<b>58.87</b>	12.27
Sm	<b>3.78</b>	0.14	<b>5.77</b>	0.24	<b>1.83</b>	0.27	<b>12.41</b>	2.29
Eu	<b>1.38</b>	0.04	<b>1.48</b>	0.11	<b>0.45</b>	0.09	<b>3.13</b>	0.78
Gd	<b>4.19</b>	0.08	<b>5.72</b>	0.06	<b>1.82</b>	0.53	<b>12.06</b>	3.02
Tb	<b>0.62</b>	0.02	<b>0.83</b>	0.06	<b>0.23</b>	0.04	<b>1.50</b>	0.39
Dy	<b>4.15</b>	0.12	<b>5.48</b>	0.14	<b>1.55</b>	0.25	<b>9.40</b>	1.83
Ho	<b>0.85</b>	0.01	<b>1.21</b>	0.03	<b>0.27</b>	0.02	<b>1.86</b>	0.36
Er	<b>2.66</b>	0.08	<b>3.83</b>	0.06	<b>0.78</b>	0.13	<b>5.53</b>	0.58
Tm	<b>0.38</b>	0.02	<b>0.55</b>	0.01	<b>0.11</b>	0.02	<b>0.75</b>	0.16
Yb	<b>2.43</b>	0.05	<b>3.77</b>	0.04	<b>0.68</b>	0.16	<b>4.97</b>	0.37
Lu	<b>0.39</b>	0.01	<b>0.52</b>	0.02	<b>0.09</b>	0.03	<b>0.65</b>	0.04
Hf	<b>2.92</b>	0.11	<b>4.01</b>	0.15	<b>0.48</b>	0.12	<b>6.51</b>	1.79
Ta	<b>2.24</b>	0.02	<b>1.59</b>	0.05	<b>0.16</b>	0.05	<b>2.62</b>	0.42
W	<b>0.42</b>	0.02	<b>2.26</b>	0.10	<b>1.13</b>	0.06	<b>13.57</b>	2.19
Pb	<b>80.11</b>	1.03	<b>12.64</b>	0.25	<b>24.55</b>	4.71	<b>8.13</b>	1.03
Th	<b>3.87</b>	0.08	<b>8.07</b>	0.09	<b>2.00</b>	0.43	<b>17.14</b>	4.28
U	<b>0.65</b>	0.03	<b>1.75</b>	0.05	<b>1.58</b>	0.27	<b>3.85</b>	0.29

Table A3 - 2: SHRIMP U-Pb analyses of zircon. Errors are 1 sigma.

Spot Name	%com 206	ppm U	ppm Th	<sup>232</sup> Th/ <sup>238</sup> U	207corr <sup>206</sup> Pb/ <sup>238</sup> U Date	1σ err	7corr <sup>206</sup> Pb* / <sup>238</sup> U	% err	Total <sup>238</sup> U/ <sup>206</sup> Pb	% err	Total <sup>207</sup> Pb / <sup>206</sup> Pb	%err	4corr <sup>207</sup> Pb* / <sup>235</sup> U	% err	4corr <sup>206</sup> Pb* / <sup>238</sup> U	% err	err corr
<i>Session 3 SHRIMP II</i>																	
<b>SHS44A</b>																	
SHS44A-1.1	1.0	366	189	0.53	123	3	0.0192	0.9	52	2.7	0.0565	1.1	0.131	4.0	0.0192	2.7	0.7
SHS44A-2.1	0.7	40	14	0.38	203	5	0.0320	0.8	31	2.6	0.0554	2.6	0.232	5.5	0.0320	2.6	0.5
SHS44A-3.1 R	1.4	206	81	0.41	89.2	3	0.0139	1.1	71	3.4	0.0592	1.7	0.091	6.6	0.0139	3.5	0.5
SHS44A-5.1b	1.0	225	44	0.20	131	1	0.0206	0.4	48	1.1	0.0567	1.1	0.128	5.0	0.0205	1.1	0.2
SHS44A-8.1	0.6	127	106	0.87	136	3	0.0213	0.7	47	2.2	0.0533	1.7	0.138	4.9	0.0213	2.2	0.5
SHS44A-10.1 R	0.7	267	63	0.24	88.1	3	0.0138	1.3	72	4.0	0.0530	2.3	0.090	5.6	0.0138	4.0	0.7
SHS44A-12.1 R	0.6	193	42	0.23	91.2	3	0.0142	1.1	70	3.6	0.0526	1.7	0.082	6.9	0.0141	3.6	0.5
SHS44A-17.1 R	0.7	150	60	0.41	89.5	1	0.0140	0.5	71	1.6	0.0533	3.3	0.087	6.6	0.0139	1.6	0.2
SHS44A-19.1	1.5	214	59	0.29	96.8	1	0.0151	0.5	65	1.4	0.0598	5.4	0.089	10.7	0.0150	1.4	0.1
excluded for commom 206Pb over 2%:																	
SHS44A-4.1	5.6	98	78	0.82	208	3	0.0329	0.5	29	1.1	0.0950	8.0	0.263	23.9	0.0332	1.8	0.1
SHS44A-5.1	3.1	469	232	0.51	136	8	0.0214	1.8	45	5.0	0.0731	29.5	0.185	36.8	0.0217	5.0	0.1
SHS44A-9.1	26.3	383	153	0.41	143	11	0.0224	2.6	33	4.6	0.2582	14.8	0.197	110.2	0.0228	7.5	0.1
SHS44A-14.1	2.2	141	72	0.53	120	3	0.0188	0.7	52	2.1	0.0656	10.1	0.128	20.5	0.0188	2.3	0.1
SHS44A-15.1	10.7	187	40	0.22	77.2	1	0.0120	0.5	74	1.1	0.1325	7.0	0.076	29.7	0.0120	1.6	0.1
SHS44A-16.1	5.3	156	43	0.28	95.4	3	0.0149	1.0	64	2.0	0.0899	19.1	0.116	36.9	0.0151	2.4	0.1
SHS44A-18.1	15.1	216	123	0.59	105	4	0.0164	1.1	52	3.0	0.1681	7.1	0.131	35.2	0.0166	3.6	0.1
SHS44A-21.1	8.4	187	104	0.58	113	5	0.0177	1.3	52	2.5	0.1149	21.2	0.156	42.7	0.0181	2.6	0.1
<b>SHB45</b>																	
SHB45-1.2 C	18.0	14	607	44.81	108	5	0.0169	1.5	49	3.4	0.1912	11.2	0.068	163.5	0.0165	6.1	0.0
SHB45-2.1 C	0.1	107	122	1.18	123	3	0.0193	0.7	52	2.3	0.0493	1.9	0.124	4.3	0.0193	2.3	0.5
SHB45-1.1 R	5.1	5	42	8.35	129	14	0.0201	3.5	47	10.9	0.0892	7.7	0.057	126.3	0.0185	12.1	0.1
SHB45-2.2 R	0.0	700	1282	1.89	130	2	0.0204	0.5	49	1.6	0.0486	0.8	0.136	1.8	0.0204	1.6	0.9
excluded on basis of REE, contamination																	
SHB45-3.1	0.9	662	330	0.51	133	3	0.0208	0.7	48	2.3	0.0561	0.7	0.145	2.9	0.0208	2.3	0.8
SHB45-4.1	0.5	363	196	0.56	241	13	0.0380	1.7	26	5.4	0.0549	0.7	0.282	5.5	0.0382	5.4	1.0

Table A3 - 2: SHRIMP U-Pb analyses of zircon. Errors are 1 sigma.

Spot Name	%com 206	ppm U	ppm Th	<sup>232</sup> Th/ <sup>238</sup> U	207corr <sup>206</sup> Pb/ <sup>238</sup> U Date	1σ err	7corr <sup>206</sup> Pb* / <sup>238</sup> U	% err	Total <sup>238</sup> U/ <sup>206</sup> Pb	% err	Total <sup>207</sup> Pb / <sup>206</sup> Pb	%err	4corr <sup>207</sup> Pb* / <sup>235</sup> U	% err	4corr <sup>206</sup> Pb* / <sup>238</sup> U	% err	err corr
Session 1 SHRIMP II																	
<b>SHS44A</b>																	
SHS44A-4 C	0.8	167	181	1.12	225	3	0.0355	0.4	28	1.2	0.0505	2.1	0.213	5.3	0.0352	1.2	0.2
SHS44A-5	1.4	443	189	0.44	108	3	0.0169	0.8	58	2.6	0.0571	4.8	0.108	7.9	0.0169	2.6	0.3
SHS44A-6 C	1.5	244	439	1.85	226	3	0.0357	0.4	28	1.2	0.0587	1.6	0.227	6.2	0.0355	1.2	0.2
SHS44A-7 C	0.3	336	151	0.46	219	2	0.0345	0.4	29	1.1	0.0506	1.4	0.226	2.6	0.0344	1.1	0.4
SHS44A-9	1.0	120	35	0.30	187	2	0.0295	0.4	34	1.2	0.0546	2.7	0.187	7.3	0.0294	1.3	0.2
SHS44A-10 C	0.5	64	60	0.97	226	4	0.0357	0.6	28	1.8	0.0486	3.7	0.219	7.3	0.0354	1.8	0.3
SHS44A-11 C	1.4	132	97	0.76	218	3	0.0345	0.4	29	1.2	0.0581	2.4	0.220	7.4	0.0343	1.3	0.2
excluded for commom 206Pb over 2%																	
SHS44A-1	28.7	683	344	0.52	173	4	0.0272	0.7	27	1.8	0.2722	2.8	0.150	32.8	0.0269	2.0	0.1
SHS44A-2	5.5	33	25	0.77	227	3	0.0359	0.5	28	1.5	0.0577	4.2	0.057	102.5	0.0342	2.1	0.0
SHS44A-3	3.3	66	56	0.87	214	5	0.0338	0.7	30	2.2	0.0510	3.4	0.107	29.7	0.0327	2.3	0.1
SHS44A-8	2.1	328	111	0.35	104	4	0.0163	1.1	60	3.4	0.0590	3.0	0.094	9.4	0.0162	3.5	0.4
SHS44A-12	9.4	507	316	0.64	133	2	0.0209	0.6	43	1.4	0.1303	6.5	0.163	27.3	0.0211	2.1	0.1
SHS44A-13	16.7	438	238	0.56	182	13	0.0287	2.4	29	6.1	0.1796	16.0	0.180	115.3	0.0285	7.9	0.1
SHS44A-14	7.0	412	206	0.52	162	4	0.0255	0.7	37	1.7	0.0977	11.1	0.143	44.3	0.0252	2.4	0.1
SHS44A-15	2.3	56	44	0.82	227	3	0.0358	0.4	28	1.4	0.0510	3.7	0.155	20.2	0.0350	1.6	0.1
<b>SHM23B</b>																	
SHM23B-13	0.0	935	302	0.33	328	4	0.052	0.42	19.2	1.3	0.0526	0.8	0.38	1.6	0.0522	1.3	0.8
SHM23B-6	2.3	802	214	0.28	405	13	0.065	1.09	15.0	3.4	0.0787	3.6	0.54	7.0	0.0653	3.4	0.5
SHM23B-15	0.2	1150	460	0.41	503	16	0.081	1.06	12.1	3.3	0.0700	0.5	0.77	3.3	0.0822	3.3	1.0
SHM23B-12	0.1	196	279	1.47	571	7	0.093	0.39	10.8	1.2	0.0601	1.2	0.76	1.8	0.0927	1.2	0.7
SHM23B-3	0.3	107	117	1.13	612	7	0.100	0.41	10.0	1.2	0.0625	1.5	0.83	2.5	0.0996	1.3	0.5
SHM23B-1	0.0	405	62	0.16	626	7	0.102	0.37	9.8	1.1	0.0600	0.7	0.84	1.3	0.1018	1.1	0.8
SHM23B-2	0.1	202	348	1.78	639	7	0.104	0.38	9.6	1.2	0.0615	1.0	0.88	1.6	0.1042	1.2	0.7
SHM23B-10	0.1	586	27	0.05	642	10	0.105	0.50	9.5	1.5	0.0617	0.7	0.88	1.7	0.1047	1.5	0.9
SHM23B-4	0.2	319	78	0.25	644	10	0.105	0.52	9.5	1.6	0.0614	0.8	0.87	1.9	0.1050	1.6	0.8
SHM23B-9	0.1	161	37	0.24	661	8	0.108	0.39	9.3	1.2	0.0626	1.1	0.91	1.9	0.1079	1.2	0.6



Table A3 - 2: SHRIMP U-Pb analyses of zircon. Errors are 1 sigma.

Spot Name	%com 206	ppm U	ppm Th	<sup>232</sup> Th/ <sup>238</sup> U	207corr <sup>206</sup> Pb/ <sup>238</sup> U Date	1σ err	7corr <sup>206</sup> Pb* / <sup>238</sup> U	% err	Total <sup>238</sup> U/ <sup>206</sup> Pb	% err	Total <sup>207</sup> Pb / <sup>206</sup> Pb	%err	4corr <sup>207</sup> Pb* / <sup>235</sup> U	% err	4corr <sup>206</sup> Pb* / <sup>238</sup> U	% err	err corr
Session 1 SHRIMP II - continued																	
SHM23B-11	1.6	504	216	0.44	642	23	0.105	1.21	8.9	3.7	0.1146	4.0	1.56	6.7	0.1103	3.7	0.6
SHM23B-7	0.0	241	25	0.11	743	11	0.122	0.51	8.2	1.6	0.0641	0.9	1.08	1.8	0.1222	1.6	0.9
SHM23B-8	0.0	1050	660	0.65	742	8	0.122	0.37	8.2	1.1	0.0665	0.4	1.12	1.2	0.1222	1.1	0.9
SHM23B-5	0.2	92	26	0.29	751	9	0.124	0.42	8.1	1.3	0.0628	1.4	1.04	2.2	0.1231	1.3	0.6
SHM23B-14	0.8	29	13	0.48	875	14	0.145	0.55	6.8	1.7	0.0724	2.2	1.31	4.9	0.1449	1.7	0.3
SHM23B-16	0.0	220	65	0.30	1988	31	0.361	0.58	2.6	1.6	0.1779	0.6	9.43	1.7	0.3852	1.6	0.9
Session 2 SHRIMP RG																	
<b>SHM23B</b>																	
SHM23B-35	0.1	733	172	0.24	282	5	0.045	0.60	22.3	1.9	0.0529	0.8	0.32	2.2	0.0448	1.9	0.87
SHM23B-95	0.0	597	264	0.46	284	7	0.045	0.77	22.2	2.4	0.0534	1.2	0.33	2.7	0.0451	2.4	0.89
SHM23B-83	0.0	524	294	0.58	297	9	0.047	0.95	21.2	2.9	0.0534	1.2	0.35	3.2	0.0472	2.9	0.93
SHM23B-86	0.2	508	289	0.59	297	9	0.047	0.97	21.2	3.0	0.0536	1.4	0.34	3.6	0.0472	3.0	0.85
SHM23B-59	0.1	653	166	0.26	311	4	0.049	0.42	20.3	1.3	0.0520	1.0	0.35	1.8	0.0493	1.3	0.74
SHM23B-39	0.1	260	107	0.42	311	4	0.049	0.45	20.2	1.4	0.0529	1.6	0.35	2.5	0.0494	1.4	0.56
SHM23B-99	0.8	656	311	0.49	311	5	0.050	0.51	20.1	1.6	0.0573	1.1	0.34	3.3	0.0494	1.6	0.49
SHM23B-27	0.1	324	94	0.30	312	5	0.050	0.51	20.2	1.6	0.0527	1.3	0.35	2.3	0.0495	1.6	0.68
SHM23B-73	0.1	1863	94	0.05	311	5	0.050	0.55	20.2	1.7	0.0529	0.6	0.36	1.8	0.0495	1.7	0.93
SHM23B-75	0.0	1065	207	0.20	314	4	0.050	0.41	20.1	1.3	0.0525	0.8	0.36	1.5	0.0499	1.3	0.85
SHM23B-43	0.2	1362	400	0.30	314	4	0.050	0.46	20.0	1.4	0.0548	0.7	0.37	1.7	0.0499	1.4	0.82
SHM23B-23	0.1	1156	383	0.34	314	6	0.050	0.59	20.0	1.8	0.0538	0.7	0.37	2.0	0.0500	1.8	0.91
SHM23B-60	0.2	505	315	0.65	317	4	0.050	0.43	19.9	1.3	0.0527	1.1	0.36	2.1	0.0503	1.3	0.64
SHM23B-79	0.0	171	70	0.42	318	5	0.051	0.48	19.8	1.5	0.0510	2.0	0.35	2.5	0.0505	1.5	0.59
SHM23B-94	0.1	338	139	0.42	318	4	0.051	0.46	19.7	1.4	0.0547	1.4	0.38	2.1	0.0506	1.4	0.67
SHM23B-31	0.1	174	83	0.49	322	6	0.051	0.62	19.5	1.9	0.0546	1.7	0.38	3.0	0.0513	1.9	0.65
SHM23B-72	0.0	751	319	0.44	322	4	0.051	0.42	19.5	1.3	0.0541	0.9	0.38	1.6	0.0513	1.3	0.79
SHM23B-28	0.0	543	119	0.23	328	5	0.052	0.47	19.2	1.5	0.0532	1.0	0.38	1.8	0.0522	1.5	0.80

Table A3 - 2: SHRIMP U-Pb analyses of zircon. Errors are 1 sigma.

Spot Name	%com 206	ppm U	ppm Th	<sup>232</sup> Th/ <sup>238</sup> U	207corr <sup>206</sup> Pb/ <sup>238</sup> U Date	1σ err	7corr <sup>206</sup> Pb* / <sup>238</sup> U	% err	Total <sup>238</sup> U/ <sup>206</sup> Pb	% err	Total <sup>207</sup> Pb / <sup>206</sup> Pb	%err	4corr <sup>207</sup> Pb* / <sup>235</sup> U	% err	4corr <sup>206</sup> Pb* / <sup>238</sup> U	% err	err corr
Session 2 SHRIMP RG - continued																	
SHM23B-47	0.1	382	163	0.44	328	4	0.052	0.44	19.1	1.3	0.0533	2.4	0.38	2.9	0.0522	1.4	0.46
SHM23B-45	-0.1	145	67	0.47	330	5	0.053	0.49	19.0	1.5	0.0554	2.0	0.41	3.0	0.0527	1.5	0.51
SHM23B-25	0.4	157	54	0.36	343	5	0.055	0.47	18.3	1.4	0.0538	1.8	0.38	3.9	0.0545	1.5	0.38
SHM23B-89	0.0	409	182	0.46	421	8	0.067	0.64	14.8	2.0	0.0562	1.1	0.52	2.3	0.0675	2.0	0.88
SHM23B-18	0.1	289	74	0.26	452	9	0.073	0.64	13.8	2.0	0.0555	1.1	0.55	2.4	0.0726	2.0	0.82
SHM23B-30	0.1	96	29	0.31	455	7	0.073	0.50	13.7	1.5	0.0553	1.9	0.55	2.8	0.0730	1.5	0.56
SHM23B-66	-0.1	283	541	1.98	524	7	0.085	0.46	11.8	1.4	0.0569	1.2	0.67	2.0	0.0847	1.4	0.70
SHM23B-90	0.2	250	176	0.73	544	13	0.088	0.77	11.3	2.4	0.0594	1.2	0.71	2.9	0.0880	2.4	0.83
SHM23B-85	-0.1	85	165	2.00	557	14	0.090	0.86	11.1	2.6	0.0601	2.0	0.76	3.6	0.0904	2.6	0.74
SHM23B-67	0.2	274	115	0.43	561	8	0.091	0.45	11.0	1.4	0.0587	1.1	0.71	2.1	0.0906	1.4	0.65
SHM23B-49	0.0	389	187	0.50	577	11	0.094	0.64	10.7	2.0	0.0609	0.9	0.79	2.2	0.0939	2.0	0.91
SHM23B-82	0.1	290	250	0.89	589	8	0.096	0.45	10.5	1.4	0.0598	1.0	0.78	1.8	0.0955	1.4	0.76
SHM23B-81	0.0	602	682	1.17	589	8	0.096	0.43	10.4	1.3	0.0599	0.7	0.79	1.5	0.0958	1.3	0.87
SHM23B-40	0.0	422	141	0.35	595	8	0.097	0.44	10.3	1.3	0.0602	0.8	0.80	1.6	0.0968	1.3	0.83
SHM23B-50	0.0	934	79	0.09	613	9	0.100	0.49	10.0	1.5	0.0604	0.6	0.83	1.6	0.0997	1.5	0.92
SHM23B-64	0.3	87	68	0.80	617	10	0.100	0.54	9.9	1.7	0.0617	1.8	0.81	3.5	0.1003	1.7	0.48
SHM23B-70	-0.1	264	41	0.16	617	8	0.100	0.45	10.0	1.4	0.0613	1.0	0.86	1.8	0.1006	1.4	0.77
SHM23B-41	0.0	244	49	0.21	622	13	0.101	0.72	9.9	2.2	0.0620	1.0	0.87	2.5	0.1015	2.2	0.89
SHM23B-48	0.0	541	541	1.03	628	8	0.102	0.43	9.8	1.3	0.0608	0.7	0.85	1.5	0.1023	1.3	0.86
SHM23B-68	0.0	286	104	0.38	634	8	0.103	0.45	9.7	1.4	0.0614	1.0	0.87	1.7	0.1033	1.4	0.80
SHM23B-55	0.0	238	42	0.18	636	9	0.104	0.47	9.7	1.4	0.0600	1.1	0.85	1.9	0.1035	1.4	0.76
SHM23B-38	0.0	186	174	0.96	641	9	0.104	0.47	9.6	1.5	0.0604	1.2	0.87	1.9	0.1044	1.5	0.77
SHM23B-74	0.0	354	232	0.68	643	9	0.105	0.44	9.5	1.4	0.0618	0.9	0.89	1.6	0.1050	1.4	0.83
SHM23B-58	0.0	200	152	0.79	645	9	0.105	0.48	9.5	1.5	0.0613	1.2	0.89	1.9	0.1053	1.5	0.77
SHM23B-63	0.2	154	125	0.84	650	9	0.106	0.49	9.4	1.5	0.0607	1.3	0.87	2.4	0.1058	1.5	0.64
SHM23B-32	0.5	25	15	0.64	664	15	0.109	0.74	9.2	2.3	0.0599	3.1	0.83	6.9	0.1077	2.3	0.33
SHM23B-62	0.1	271	143	0.54	661	9	0.108	0.48	9.3	1.5	0.0623	1.0	0.92	1.9	0.1080	1.5	0.77
SHM23B-80	0.7	37	15	0.42	668	14	0.109	0.69	9.1	2.1	0.0632	2.5	0.86	6.4	0.1086	2.1	0.33
SHM23B-98	0.1	97	40	0.43	663	11	0.108	0.55	9.2	1.7	0.0649	1.7	0.96	2.7	0.1087	1.7	0.63

Table A3 - 2: SHRIMP U-Pb analyses of zircon. Errors are 1 sigma.

Spot Name	%com 206	ppm U	ppm Th	<sup>232</sup> Th/ <sup>238</sup> U	207corr <sup>206</sup> Pb/ <sup>238</sup> U Date	1σ err	7corr <sup>206</sup> Pb* / <sup>238</sup> U	% err	Total <sup>238</sup> U/ <sup>206</sup> Pb	% err	Total <sup>207</sup> Pb / <sup>206</sup> Pb	%err	4corr <sup>207</sup> Pb* / <sup>235</sup> U	% err	4corr <sup>206</sup> Pb* / <sup>238</sup> U	% err	err corr
Session 2 SHRIMP RG - continued																	
SHM23B-33	0.0	132	18	0.14	668	12	0.109	0.63	9.2	1.9	0.0608	1.3	0.91	2.4	0.1089	1.9	0.80
SHM23B-101	0.1	234	36	0.16	677	9	0.111	0.46	9.1	1.4	0.0605	1.1	0.91	2.0	0.1104	1.4	0.72
SHM23B-20	0.0	757	110	0.15	701	11	0.115	0.53	8.7	1.6	0.0631	0.5	1.00	1.7	0.1149	1.6	0.95
SHM23B-69	0.0	261	198	0.79	720	10	0.118	0.46	8.5	1.4	0.0626	0.9	1.03	1.7	0.1181	1.4	0.80
SHM23B-26	0.0	757	475	0.65	729	9	0.120	0.42	8.3	1.3	0.0642	0.5	1.06	1.4	0.1198	1.3	0.92
SHM23B-84	0.2	146	92	0.65	757	11	0.125	0.51	8.0	1.5	0.0656	1.4	1.10	2.5	0.1246	1.6	0.62
SHM23B-97	0.0	424	264	0.64	757	10	0.125	0.44	8.0	1.3	0.0649	0.7	1.11	1.6	0.1246	1.3	0.86
SHM23B-88	0.6	70	56	0.83	781	15	0.129	0.65	7.7	2.0	0.0685	1.8	1.13	4.1	0.1286	2.0	0.48
SHM23B-92	0.0	163	170	1.07	868	12	0.144	0.49	6.9	1.5	0.0743	1.2	1.48	1.9	0.1451	1.5	0.77
SHM23B-53	0.1	204	102	0.52	899	13	0.150	0.51	6.7	1.5	0.0691	1.0	1.40	1.9	0.1494	1.5	0.79
SHM23B-51	0.1	275	82	0.31	933	20	0.156	0.72	6.4	2.2	0.0713	0.8	1.52	2.3	0.1559	2.2	0.93
SHM23B-93	0.0	100	64	0.66	958	15	0.160	0.54	6.2	1.6	0.0718	1.2	1.58	2.1	0.1603	1.6	0.77
SHM23B-57	0.0	378	341	0.93	961	13	0.161	0.45	6.2	1.4	0.0728	0.7	1.61	1.5	0.1611	1.4	0.90
SHM23B-91	0.1	213	79	0.38	966	13	0.162	0.48	6.2	1.4	0.0725	0.9	1.60	1.8	0.1617	1.4	0.80
SHM23B-61	0.1	131	128	1.01	1008	15	0.169	0.52	5.9	1.6	0.0734	1.1	1.69	2.0	0.1693	1.6	0.77
SHM23B-65	0.0	434	115	0.27	1011	13	0.170	0.44	5.9	1.3	0.0732	0.6	1.71	1.4	0.1698	1.3	0.92
SHM23B-71	0.1	125	56	0.46	1041	15	0.175	0.51	5.7	1.5	0.0738	1.0	1.76	2.0	0.1751	1.5	0.78
SHM23B-24	0.1	272	138	0.52	1046	14	0.176	0.45	5.7	1.3	0.0746	0.6	1.80	1.5	0.1761	1.3	0.89
SHM23B-56	0.2	52	7	0.15	1070	20	0.181	0.66	5.5	2.0	0.0748	1.6	1.81	3.0	0.1800	2.0	0.66
SHM23B-19	0.0	249	96	0.40	1138	15	0.193	0.47	5.2	1.4	0.0771	0.6	2.04	1.6	0.1930	1.4	0.90
SHM23B-42	0.0	148	112	0.78	1417	21	0.246	0.52	4.1	1.5	0.0913	0.7	3.09	1.7	0.2463	1.5	0.89
SHM23B-17	0.0	231	136	0.61	1800	24	0.322	0.49	3.1	1.4	0.1164	0.4	5.21	1.4	0.3245	1.4	0.96
SHM23B-34	0.0	636	111	0.18	1908	26	0.344	0.51	2.9	1.4	0.1202	0.2	5.72	1.4	0.3456	1.4	0.98
SHM23B-22	0.0	308	201	0.67	1952	26	0.354	0.49	2.8	1.3	0.1203	0.4	5.86	1.4	0.3539	1.3	0.96
SHM23B-96	0.0	575	573	1.03	2044	42	0.373	0.77	2.7	2.1	0.1272	0.3	6.54	2.1	0.3735	2.1	0.99
SHM23B-52	0.0	398	177	0.46	2130	29	0.391	0.51	2.5	1.3	0.1349	0.6	7.30	1.5	0.3926	1.3	0.90
SHM23B-100	0.0	169	90	0.55	2369	37	0.444	0.59	2.2	1.5	0.1800	0.4	11.36	1.5	0.4583	1.5	0.96
SHM23B-87	0.0	203	30	0.15	2405	61	0.452	0.97	2.2	2.4	0.1732	0.4	10.99	2.5	0.4612	2.4	0.99
SHM23B-46	0.0	106	100	0.97	2603	46	0.498	0.69	2.0	1.6	0.1770	0.5	12.16	1.7	0.4987	1.6	0.96

Table A3 - 2: SHRIMP U-Pb analyses of zircon. Errors are 1 sigma.

Spot Name	%com 206	ppm U	ppm Th	<sup>232</sup> Th/ <sup>238</sup> U	<sup>207</sup> corr <sup>206</sup> Pb/ <sup>238</sup> U Date	1σ err	<sup>7</sup> corr <sup>206</sup> Pb* / <sup>238</sup> U	% err	Total <sup>238</sup> U/ <sup>206</sup> Pb	% err	Total <sup>207</sup> Pb / <sup>206</sup> Pb	%err	<sup>4</sup> corr <sup>207</sup> Pb* / <sup>235</sup> U	% err	<sup>4</sup> corr <sup>206</sup> Pb* / <sup>238</sup> U	% err	err corr
Session 2 SHRIMP RG - continued																	
SHM23B-21	0.0	428	99	0.24	2725	41	0.526	0.59	1.9	1.3	0.1975	0.4	14.47	1.4	0.5317	1.3	0.95
SHM23B-77	0.0	97	39	0.42	3337	105	0.678	1.28	1.5	1.8	0.2736	1.6	25.51	2.4	0.6765	1.8	0.75
Rejected for detrital analyses:																	
SHM23B-76	1.0	1710	598	0.36	186	2	0.029	0.41	33.8	1.3	0.0595	0.7	0.21	4.8	0.0293	1.3	0.27
<i>high U - lost Pb</i>																	
SHM23B-44	0.4	836	788	0.97	971	114	0.163	4.04	6.1	12.2	0.0744	0.4	1.59	12.6	0.1625	12.2	0.97
<i>bad analysis</i>																	

**Table A3 - 3: Zircon trace-element composition determined by LA-ICP-MS. C: core, R A: rim A, R B1: rim B1, R B2: rim B2**

Analysis # zone	SHS44A	SHS44A	SHS44A	SHS44A	SHS44A	SHS44A	SHS44A	SHS44A	SHS44A	SHS44A	SHS44A	SHS44A
	zirc28-11 C	zirc28-12 C	zirc28-13 C	zirc28-14 C	zirc28-15 C	zirc28-16 C	zirc28-17 C	zirc28-18 C	zirc28-20 C	SHS44A-2 C	SHS44A-3 C	SHS44A-4 C
P	511	383	582	418.9	516	708	781	329	556			
Ca	45	25	101	56	107	119	bdl	100	97			
Sc	435.5	403.1	429.7	397.2	415.4	404.7	425.7	419.3	453.3			
Ti	10.88	3.13	12.65	7.09	10.75	5.1	8.62	6.2	13.6			
Fe	bdl	14.4	5.8	bdl	740	165	27.4	13.7	37			
Y	4131	1375	3630	2699	1929	3890	4718	1559	2556	2366	2570	3490
Zr (wt%)	45.1	43.7	43.4	42.8	42.2	43.2	43.0	45.0	46.8	44.3	43.1	46.0
Nb	2.07	4.94	5.3	2.5	2.08	25.4	13.88	4.77	3.67	4.34	1.98	3.91
La	0.0194	bdl	0.024	0.002	bdl	0.063	0.0022	0.011	bdl	0.0072	0.063	0.0015
Ce	6.59	9.14	11.45	6.92	5.82	24	32.12	6.95	9.03	8.67	5.2	12.64
Pr	0.249	0.0131	0.168	0.114	0.052	0.106	0.155	0.036	0.076	0.088	0.163	0.168
Nd	4.27	0.71	3.22	2.8	1.51	1.5	3.72	0.88	2.36	1.91	3.2	3.57
Sm	10.53	2.19	8.68	7.54	3.98	4.47	12.3	2.93	5.94	5.75	8.47	9.62
Eu	2.24	0.464	1.86	1.559	0.904	0.81	2.14	0.489	1.29	1.2	1.75	1.84
Gd	80.4	19.9	71.9	57.7	31.4	41.1	95.7	23.4	47.7	43.8	57	71.9
Tb	29.27	8.12	26.4	20.4	11.87	17.29	35.29	9.34	17.83	15.61	18.8	25.6
Dy	389	116.5	338	260.2	163.8	265.2	457.4	132.8	233.3	224.1	250	339
Ho	144	46.4	125.6	94.6	63.3	116.3	164.9	53.2	87.3	81.3	88.1	120.8
Er	683	238.7	601	444.4	313	644	780	266	416	388.1	408	555
Tm	136.7	51.56	116.2	84.5	65.5	138.3	150.9	54.1	83.3	77.2	79.7	110.4
Yb	1208	476	1026	747	589	1205	1305	516	754	707	728	994
Lu	199.3	83.9	174	126.3	104.1	168.2	212.6	88.3	124.9	116	121.7	162.3
Hf (wt%)	0.86	0.91	0.83	0.89	0.81	1.60	0.82	0.93	0.87	0.76	0.83	0.87
Ta	0.822	3.62	1.86	0.935	0.821	20	4.21	2.27	1.3	1.72	0.79	1.65
Pb	1.45	0.9	1.43	0.679	1.96	4.77	4.81	0.7	1.46	1.51	0.68	1.05
Th	72.9	44.16	71.3	31.93	81.9	223.8	222.3	26.4	76.7			
U	79.4	87.3	76.4	40.45	77	764	168.1	49.8	70.7			

**Table A3 - 3: Zircon trace-element composition determined by LA-ICP-MS. C: core, R A: rim A, R B1: rim B1, R B2: rim B2**

Analysis # zone	SHS44A SHS44A-5 C	SHS44A SHS44A-6 C	SHS44A SHS44A-7 C	SHS44A SHS44A-8 C	SHS44A SHS44A-9 C	SHS44A SHS44A-10 C	SHS44A SHB44A-30 C	SHS44A SHB44A-22 C	SHS44A SHB44A-26 C	SHS44A SHB44A-23 C	SHS44A SHB44A-19 C	SHS44A SHB44A-24 C
P												
Ca												
Sc												
Ti												
Fe												
Y	3210	3790	3703	2145	2401	1481	2560	6930	6660	5090	4900	5710
Zr (wt%)	46.1	42.6	41.8	42.6	46.9	42.4	40.3	39.3	46.0	45.7	41.3	44.3
Nb	2.74	6.89	6.96	3.13	2.28	2.45	5.8	36	51.3	40	24.17	50.8
La	0.0043	0.0049	0.0026	bdl	0.092	0.0157	0.299	0.96	0.129	0.158	0.289	0.72
Ce	9.7	17.75	22.76	6.83	6.01	5.58	12.49	53.2	74.2	40.5	39.4	79
Pr	0.185	0.17	0.156	0.093	0.136	0.056	0.31	0.8	0.366	0.383	0.299	0.71
Nd	3.81	3	2.9	1.95	2.84	1.09	3.84	10	6.23	6.6	6.03	8
Sm	9.6	9.69	8.5	5.12	7.81	3.43	7.21	20.6	18.3	16.5	13.1	15.5
Eu	1.93	1.89	1.923	1.301	1.44	0.713	0.83	2.38	1.87	1.81	1.56	2.24
Gd	69.1	75	69.7	40.97	50.5	24.6	49.1	137.3	126.6	103	92.1	94
Tb	23.6	26.9	25.7	15.29	17.7	9.76	18	48.2	47.7	35.8	35.4	34.9
Dy	310	362	344.4	197.3	231.4	131.3	230	637	610	477	473	499
Ho	113	128.7	125.4	72.2	81.6	49.6	88.2	235.8	227.1	174	181.8	194
Er	533	606	603	350.1	396	245.6	411	1153	1110	851	857	992
Tm	103.2	117.9	117.3	67.8	78.4	49.8	82.4	226.1	224.4	179.7	179.6	212.7
Yb	925	1042	1031	602	702	435	731	2083	2012	1753	1648	2033
Lu	149	174.6	174.3	104.8	121.9	78.4	128.9	356.2	341	320.2	284.5	367
Hf (wt%)	0.82	0.83	0.82	0.75	0.84	0.86	0.89	0.71	0.92	0.86	0.78	0.95
Ta	1.18	2.49	2.52	1.075	0.89	0.912	2.2	19.68	10.54	7.54	6.74	27.6
Pb	0.82	3.09	6.51	1.16	0.83	0.742	1.03	6.79	6.33	4.06	3.74	8
Th												
U												

**Table A3 - 3: Zircon trace-element composition determined by LA-ICP-MS. C: core, R A: rim A, R B1: rim B1, R B2: rim B2**

Analysis # zone	SHS44A	SHS44A	SHS44A	SHS44A	SHS44A	SHS44A	SHS44A	SHS44A	SHS44A	SHS44A	SHS44A
	SHB44A-18 C	SHB44A-20 C	zirc22-39 R A	zirc22-40 R A	zirc22-43 R A	zirc22-44 R A	zirc22-49 R A	zirc22-50 R A	SHB44A-29 R A	SHB44A-27 R A	SHB44A-17 R A
P			458	397	837	528	560	716			
Ca			420	170	230	190	850	70			
Sc			363	389	348.4	356.5	357.9	343.3			
Ti			5.5	8.83	3.67	6.57	13.8	3.03			
Fe			876	1060	1460	580	502	337			
Y	4910	5050	2555	2023	3510	3330	3500	3790	3640	3038	2570
Zr (wt%)	40.0	45.8	40.5	42.4	39.8	40.9	39.9	39.0	39.6	44.3	47.6
Nb	33.4	58.4	49.1	23.1	84.3	65.3	48.3	25.6	38.2	56.1	26.1
La	0.26	0.14	0.13	0.68	0.147	0.29	0.249	0.68	1.09	2.08	1.7
Ce	72.2	32.3	25.1	41	28	36.5	41.8	47.7	27.5	32.5	28
Pr	0.317	0.37	0.156	0.48	0.23	0.318	0.223	0.52	0.69	0.67	0.8
Nd	6.01	4.8	2.57	6	2.84	3.75	2.17	4.2	5.6	5.1	4
Sm	11.5	12.3	4.2	6.6	4.8	6.3	4.86	7.8	8.2	8.7	6
Eu	1.22	1.3	0.55	0.78	1.05	1.47	0.666	0.65	1.23	1.31	0.53
Gd	86.7	79.2	32.8	32.6	38.3	50.6	37.3	61.3	53.8	48.7	41.5
Tb	31.9	27.8	12.5	11.1	15.4	17.7	16.32	23.9	19.1	16.97	15.5
Dy	406	416	187	159	241	240	252.4	330	273	243	211
Ho	159.6	172	77.3	67.5	107.1	98.8	110.4	127	115	102.4	88.5
Er	804	927	468	378	642	550	631	613	633	595	487.7
Tm	168	210.6	122.7	100.5	149.8	133.3	146.7	122.5	150	142.1	135.3
Yb	1545	2180	1457	1147	1538	1452	1452	1082	1489	1580	1560
Lu	283	369	276.5	209.7	305	295	275.2	183.9	301	306	335
Hf (wt%)	0.89	0.83	1.00	0.85	0.82	1.57	0.85	1.01	0.73	0.79	1.19
Ta	7.72	13.8	55.6	5.61	44.1	63.7	16.85	12.3	14.8	17.82	8.4
Pb	3.44	7.04	6.1	3.76	10.8	9.44	6.97	3.97	9.3	5.96	3.34
Th			330	140	467	447	306.5	145.6			
U			588	328	770	737	492	179.2			

**Table A3 - 3: Zircon trace-element composition determined by LA-ICP-MS. C: core, R A: rim A, R B1: rim B1, R B2: rim B2**

Analysis #	SHS44A SHB44A-25	SHS44A SHB44A-16	SHS44A zirc22-42	SHS44A zirc22-46	SHS44A zirc22-41	SHS44A 41 bis	SHS44A SHB44A-15	SHS44A SHB44A-28	SHS44A SHB44A-13	SHS44A zirc22-45
zone	R A	R A	R B1	R B1	R B1	R B1	R B1	R B1	R B1	R B2
P			437	387	427	399				409
Ca			500	450	bdl	bdl				174
Sc			414.1	365.5	389	412.5				353.4
Ti			6.93	4.51	1.61	1.57				8.68
Fe			170	1200	24	30				2800
Y	2980	2620	2386	2023	1510	1361	2020	2061	1079	1938
Zr (wt%)	47.1	42.2	46.0	39.6	45.6	47.6	45.5	45.1	36.0	39.0
Nb	42.6	13	41.6	13.9	14.97	13.47	23.3	17.68	10.86	58.6
La	0.049	0.016	0.097	0.054	0.006	0.006	0.6	0.057	0	0.631
Ce	40	24.1	19.1	16.8	10.28	9.29	18.9	4.86	6.55	32.29
Pr	0.096	0.141	0.201	0.073	0.015	0.009	0.3	0.068	0.012	1.071
Nd	1.46	2.2	1.32	0.36	0.33	0.19	1.73	0.44	0.7	6.97
Sm	3.89	6.75	2.42	1.05	0.91	0.62	3	0.63	1.71	3.45
Eu	0.52	0.75	0.368	0.126	0.17	0.113	0.43	0.147	0.266	1.42
Gd	32.2	46.7	16.4	11.6	10.1	8.1	18	5.74	13.3	10.12
Tb	14.7	15.8	7.91	6.04	5.13	4.2	7.81	4.17	5.2	4.85
Dy	216	228	147.2	114.7	89.9	76.3	130.8	92.1	74.6	98.2
Ho	92.4	87.6	76.3	59.6	46.5	41.4	62.1	60.9	33.6	56.9
Er	521	478	513	432	301	276	432	537	219	477.7
Tm	124.5	113.6	147	116.9	79.6	75.7	142.4	186.8	62.9	159
Yb	1295	1217	1838	1420	838	798	2000	2810	798	2153
Lu	246.9	249.7	383	314	156.4	147.1	446	680	191.7	491.5
Hf (wt%)	0.98	0.96	0.98	0.94	0.88	0.91	1.03	1.01	0.81	1.83
Ta	14.6	3.89	9.88	2.52	11.72	11.38	5.98	4.11	3.54	100.5
Pb	4.38	3.34	7.22	5.52	4.22	3.64	3.9	3.75	1.41	9.63
Th			317.6	245	193.5	171.9				587
U			641	341.2	355.4	353				1122



**Table A3 - 3: Zircon trace-element composition determined by LA-ICP-MS. C: core, R A: rim A, R B1: rim B1, R B2: rim B2**

Analysis # zone	SHS44A	SHS44A	SHS44A	SHS44A	SHB45	SHB45	SHB45	SHB45	SHB45	SHB45	SHB45
	SHB44A-12 R B2	SHB44A-14 R B2	SHB44A-21 R B2	SHB44A-11 R B2	zirc22-36	SHB45-6	zirc22-33	zirc22-34	zirc22-32	SHB45-4	zirc22-31
P					57.4		45	32	23		34.4
Ca					86		55	180	bdl		122
Sc					370.7		425	371.9	391		362.2
Ti					2.8		10.12	3.52	7.21		2.97
Fe					710		650	97	229		137
Y	1912	1244	2222	1590	3090	2540	1078	739	560	508	371
Zr (wt%)	37.3	37.0	45.7	37.4	42.4	45.0	44.8	42.9	46.5	45.2	40.8
Nb	85.1	38.4	75.6	41.9	49.8	52.2	11.8	9.27	18.9	8.79	6.74
La	1.24	0.223	1.11	0.455	0.022	0.51	0.11	0.136	0.57	0.082	0.027
Ce	19	8.93	20.4	18.27	29.35	39.3	12.6	5.58	9.4	9.35	2.15
Pr	0.61	0.207	0.52	0.69	0.755	1.7	0.37	0.211	1	0.228	0.026
Nd	3.72	1.46	3.23	4.16	14.41	24.3	7	2.98	10.24	2.89	0.38
Sm	3.06	1.16	2.32	2.32	27.1	33.2	6.2	3.39	6.6	3.7	0.52
Eu	0.592	0.333	0.65	0.94	19.47	21.4	5.4	2.36	3.6	2.38	0.45
Gd	12.8	4.76	10.8	8.41	131	127	29.7	17.3	18.6	17	4.16
Tb	6.13	2.43	5.16	3.7	40.3	35.6	9.6	6.49	5.71	4.94	1.9
Dy	104.8	55.5	100.2	74.5	424	359	106	81.5	61.2	53.7	28.4
Ho	53.3	32.7	55.8	43.9	123.2	98	37.5	28.6	19.81	17.5	12.5
Er	384	274	431	373.4	482	370	180	126.1	87.2	79.6	64
Tm	114.2	90	143.3	125.8	82.8	62.4	35.7	25.2	17	15.7	12.9
Yb	1474	1250	1941	1723	606	469	337	208.3	134.6	138.9	118
Lu	319	289	431	412.1	84	65.5	52.2	33	20.7	23.8	19.6
Hf (wt%)	1.83	1.65	2.19	1.55	0.35	0.36	0.83	0.41	0.58	0.50	0.68
Ta	281	114.2	223.9	56.6	3.29	5.3	1.16	1.27	3	1.01	2.05
Pb	11	5.52	10.6	9.37	16.33	15.8	5.7	8.7	5.2	5.8	2.35
Th					1407	607	418	722	348	107	114
U					28.7	14	454	402	127.9	122	96

**Table A3 - 3: Zircon trace-element composition determined by LA-ICP-MS. C: core, R A: rim A, R B1: rim B1, R B2: rim B2**

Analysis # zone	SHB45 SHB45-5	SHB45 zirc22-35	SHB45 zirc22-38	SHB45 SHB45-3	SHB45 SHB45-8
P		45	34		
Ca		160	590		
Sc		361.8	433.5		
Ti		9.1	14.8		
Fe		1243	800		
Y	314	303	141	1950	496
Zr (wt%)	45.9	40.2	45.2	44.8	48.1
Nb	4.19	7.84	1	21.4	24.5
La	0.163	0.101	0.005	0.304	0.451
Ce	4.49	4.27	0.206	43.5	14
Pr	0.259	0.091	bdl	1.46	1.33
Nd	2.45	1.08	bdl	18.7	13
Sm	1.98	1.54	bdl	24.7	11.6
Eu	1.41	0.99	bdl	15	6.3
Gd	7.8	6.42	0.68	94	31.7
Tb	2.27	2.42	0.45	23.9	7.6
Dy	29.5	30.8	7.6	248	69.9
Ho	10.1	10.5	3.83	70.5	18.1
Er	52	49.4	20.7	282	69.8
Tm	10.28	9.2	4.7	48.6	12.1
Yb	97.6	86.3	54	387	98.9
Lu	18.7	14.5	12.4	58.4	14.9
Hf (wt%)	0.61	0.39	1.10	0.51	0.44
Ta	0.28	0.454	0.112	1.9	5.58
Pb	1.64	3.92	bdl	24	5.29
Th		241	2.88	1282	5
U		154	20.3	700	42

**Table A 3 - 4 : SHRIMP Th-Pb analyses for SHB45 zircons.** The U-Pb systametics of the same analyses are presented in Table A3 - 2.

Errors are 1 sigma.

	<b>%com208</b>	<b>U (ppm)</b>	<b>Th (ppm)</b>	$^{232}\text{Th}/^{238}\text{U}$	<b>Total</b> $^{208}\text{Pb}/^{232}\text{Th}$	<b>% err</b>	<b>207corr</b> $^{208}\text{Pb}/^{232}\text{Th}$ date	<b>1<math>\sigma</math> err</b>	<b>7corr</b> $^{208}\text{Pb}^*/^{232}\text{Th}$	<b>% err</b>
<b>SHB45</b>										
SHB45-1.2 C	<b>2.8</b>	14	607	44.81	0.00616	3.9	<b>121</b>	<b>5</b>	0.00599	3.9
SHB45-2.1 C	<b>0.0</b>	107	122	1.18	0.00617	1.7	<b>124</b>	<b>2</b>	0.00618	1.7
SHB45-1.1 R	<b>0.6</b>	5	42	8.35	0.00611	2.8	<b>122</b>	<b>3</b>	0.00608	2.8
SHB45-2.2 R	<b>4.7</b>	700	1282	1.89	0.00575	11.5	<b>111</b>	<b>13</b>	0.00548	11.6
excluded on basis of REE, contamination										
SHB45-3.1	<b>12.0</b>	662	330	0.51	0.00654	3.1	<b>116</b>	<b>4</b>	0.00575	3.2
<i>SHB45-4.1</i>	<b>5.0</b>	363	196	<i>0.56</i>	<i>0.01364</i>	<i>8.2</i>	<b>260</b>	<b>21</b>	<i>0.01295</i>	<i>8.2</i>

Table A3 - 5: SHRIMP U-Pb analyses of allanite and florencite.

Errors are 1 $\sigma$  unless otherwise specified

from TW

Spot	7-corr	7-corr	7-corr	% 232Th err /238U	% 206Pb err /238U	Total		207corr		C-Pb % 207 err /206	206Pb /238U Age	1 $\sigma$ err	7corr	Total % 238 err /206	Total % 207 err /206	% err			
	%com 206	%com 208	208Pb* /206Pb*			% 206Pb err /238U	% /232T h	206Pb /238U Age	206*				% 207 err /206						
<b>Allanite</b>																			
SHS3-1.1	<b>99.29</b>	<b>100.03</b>	-	-	7.7	2.8	1.95	1.7	0.530	2.2	0.841	<b>89.1</b>	<b>22</b>	0.0139	8.1	0.5	1.7	0.835	0.17
SHS3-2.1	<b>96.41</b>	<b>98.12</b>	1.07	7.0	2.0	3.9	0.38	2.8	0.386	2.8	0.841	<b>88.1</b>	<b>3</b>	0.0138	1.2	2.6	2.8	0.813	0.09
SHS3-3.1	<b>99.16</b>	<b>98.41</b>	3.98	13.0	10.2	5.7	1.52	5.1	0.313	2.5	0.841	<b>81.6</b>	<b>18</b>	0.0127	7.1	0.7	5.1	0.834	0.17
SHS3-4.1	<b>98.68</b>	<b>98.56</b>	2.26	8.3	4.9	5.8	1.02	5.2	0.434	2.6	0.841	<b>86.4</b>	<b>8</b>	0.0135	2.8	1.0	5.2	0.831	0.09
SHS3-4.2	<b>98.88</b>	<b>96.43</b>	6.79	10.8	17.3	4.6	1.14	4.0	0.140	2.2	0.841	<b>81.7</b>	<b>11</b>	0.0128	4.2	0.9	4.0	0.832	0.13
SHS3-5.2	<b>98.59</b>	<b>98.84</b>	1.71	9.9	4.4	4.3	1.12	3.7	0.522	2.2	0.841	<b>101</b>	<b>7</b>	0.0158	2.3	0.9	3.7	0.830	0.08
<b>Florencite</b>																			
SHS3F-2	<b>100.18</b>	<b>51.03</b>	-	-	203.2	6.0	0.46	5.6	0.010	2.0	0.822	-	-	-	-	2.2	5.6	0.823	0.73
SHS3F-3	<b>97.94</b>	<b>44.68</b>	128.27	45.6	273.9	9.3	0.54	5.6	0.009	7.2	0.822	-	-	-	-	1.8	5.6	0.806	0.92
SHS3F-4	<b>97.98</b>	<b>23.39</b>	346.15	37.3	335.0	4.5	0.23	4.0	0.006	2.0	0.822	-	-	-	-	4.4	4.0	0.806	0.73
SHS3F-5	<b>98.61</b>	<b>27.96</b>	399.89	123.4	191.5	5.0	0.18	3.9	0.007	3.0	0.822	-	-	-	-	5.6	3.9	0.811	1.64
SHS3F-6	<b>99.73</b>	<b>48.61</b>	835.91	392.7	132.1	7.8	0.29	6.3	0.010	4.6	0.822	-	-	-	-	3.4	6.3	0.820	1.02

**Table A3 - 6: SHRIMP Th-Pb analyses of florencite.** The U-Pb systematics of the same analyses are presented in Table A3 - 5.

	Total			Total			Comm			$^{232}\text{Th}/^{206}\text{Pb}_c$			$^{208}\text{Pb}/^{206}\text{Pb}_c$	
	$^{207}\text{Pb}/^{206}\text{Pb}$	% err	$^{208}\text{Pb}/^{206}\text{Pb}$	% err	$^{208}\text{Pb}/^{232}\text{Th}$	% err	$^{207}\text{Pb}/^{206}\text{Pb}$	f206	% err	% err	% err	% err	% err	
<b>SHS3F-2</b>	0.823	0.73	4.279	0.60	0.010	2.0	0.822	1.002	1.3	445.222	2.5	4.2718	1.4	
<b>SHS3F-3</b>	0.806	0.92	4.779	2.02	0.009	7.2	0.822	0.979	1.6	514.847	7.7	4.8794	2.6	
<b>SHS3F-4</b>	0.806	0.73	9.131	0.55	0.006	2.0	0.822	0.980	1.3	1503.400	2.4	9.3198	1.4	
<b>SHS3F-5</b>	0.811	1.64	7.689	1.16	0.007	3.0	0.822	0.986	2.9	1077.910	4.3	7.7971	3.1	
<b>SHS3F-6</b>	0.820	1.02	4.472	0.84	0.010	4.6	0.822	0.997	1.8	456.830	5.0	4.4845	2.0	

## **A4 – Appendix to Chapter 4**

A4 - **Publication PDF:** Martin LAJ, Hermann J, **Gauthiez-Putallaz L**, et al (2014a)  
Lawsonite geochemistry and stability - implication for trace element and water cycles in  
subduction zones. *J Metamorph Geol* 32:455-478.

This publication has been removed due to copyright restrictions.

It can be accessed online at:

<https://onlinelibrary.wiley.com/doi/full/10.1111/jmg.12093>

**Table A4-1. Apatite trace-element composition determined by La-ICP-MS. c: core, m: mantle, r:rim**

sample	SGM21	SGM21	SGM21	SGM21	SGM21	SGM21	SGM21	SGM21	SGM21	SGM21	SGM21	SGM21	SGM21	SGM21	SGM21
Analysis#	149	145	71	137	143	136	139	138	72	75	147	141	74	142	144
SHRIMP	SGM21-1	SGM21-10	SGM21-11	SGM21-12	SGM21-13	SGM21-14	SGM21-15	SGM21-16	SGM21-17	SGM21-3	SGM21-4	SGM21-5	SGM21-6	SGM21-7	SGM21-8
zone	c		c	r	c	c	r		r		r			r	c
EMPA	1									2	3	6	7		
Element (ppm)															
Li	1.2	0.4	0.18	0.8	0.44	bdl	3.2	0.5	0.66	1.27	bdl	0.2	1.12	0.2	3.7
Mg	453.4	438.9	332.5	452	441	444.6	449	472	328	325.8	430	432	323.1	453.9	376
Al	10.5	29	bdl	0.8	0.05	0.59	12.1	bdl	bdl	3.1	0.26	1.1	-0.26	0.12	2.9
Si	1461	1310	1433	1237	1541	1170	1580	1278	1430	1162	1240	1350	1149	1410	1480
Sc	0.179	0.169	0.154	0.139	0.064	0.14	0.073	0.094	0.112	0.15	0.111	0.061	0.103	0.074	-0.05
Ti	0.82	43	0.26	0.29	0.1	0.09	0.33	0.38	0.22	bdl	bdl	0	0.3	0.09	13.1
V	0.87	12.2	0.697	0.186	0.763	0.65	0.76	0.64	0.373	0.35	0.414	0.79	0.79	0.609	2.2
Cr	0.3	0.86	0.97	0.94	0.46	0.33	1.98	0.36	1.25	0.89	0.51	0.41	0.67	1.04	3.3
Mn	171.5	159	185.8	145.8	192.8	164	202	210.5	164.1	191.2	190	199	181.8	201.3	204
Fe	257	487	308.6	225	227	237	268	251	282.1	281	235	232	282.5	247	1160
Rb	0.084	0.133	-0.02	0.024	0.022	0.048	0.097	0.05	0.025	0.014	0.084	0.113	0.036	0.014	bdl
Sr	88.9	69.1	91	81.4	86.5	78.8	90.5	95.4	81.78	84.2	87.1	87.6	84.2	94.8	64.4
Y	191.6	265.9	160.5	300.1	187	115.5	261.4	243.1	247.8	299	317	273	206.3	220.9	590
Zr	24	0.49	bdl	0.006	bdl	bdl	0.006	bdl	bdl	0.0007	bdl	0.012	0.0055	0.0024	bdl
Cs	0.025	0.014	0.0025	0.008	0.002	bdl	0.031	0.004	0.0102	0.0113	bdl	0.008	0.0145	bdl	bdl
Ba	0.029	0.34	0.11	0.117	0.061	0.004	0.31	0.25	0.076	0.074	0	0.07	0.091	0.091	-0.0149
La	20.18	24.14	19.13	16.29	18.69	7.97	27	22.35	15.31	17.5	31.3	40.4	28.6	25.45	24.8
Ce	58.9	84.7	51.88	43.7	57.8	20.56	61.6	51.3	36.53	41.52	76.4	117.1	72.5	63.9	108
Pr	13.07	20.22	10.07	8.57	13.15	4.37	11.26	10.12	7.26	8.11	13.64	26	17.4	12.19	25.9
Nd	68.5	112.7	53.2	46.3	69.2	25.1	55.5	50.5	38.06	43.52	67.2	122	91.2	59.1	151
Sm	21.1	36.7	16.34	15.8	21.6	7.56	18.1	16.23	12.89	15.05	20.9	34.9	26.17	16.75	63
Eu	6.19	8.78	4.59	4.53	5.98	2.9	4.52	4.47	3.78	4.36	5.49	9.83	6.95	4.37	14.4
Gd	27.6	48.4	21	25.1	29.5	12.6	25	23.52	19.94	23.13	29.1	45	32.81	22.68	84
Tb	4.43	6.89	3.601	4.81	4.86	2.08	4.6	4.27	3.96	4.65	5.43	6.69	5.179	4.09	15
Dy	30.2	44.1	25.06	38.06	31.2	15.8	33.5	32.9	31.07	37.71	41.5	45.4	35.07	30.09	85.4
Ho	6.58	8.79	5.97	9.46	6.76	3.71	7.99	7.76	7.92	9.38	9.9	9.79	7.43	6.86	17.5
Er	23.18	25.61	20.66	34.12	21.94	12.84	29.41	26.78	29.32	34.42	37.2	29.4	23.05	24.62	42.1
Tm	3.47	3.34	3.379	5.58	3.04	2.2	4.63	4.01	4.818	5.67	5.6	4.34	3.465	3.82	4.03
Yb	24.94	21.36	24.55	39.5	22.49	15.94	33.3	29.59	36.39	42.37	44.1	30.8	23.91	28.79	21.1
Lu	3.3	2.6	3.54	5.18	3.02	1.97	4.8	4.31	5.1	6.13	5.79	3.79	3.197	3.85	2.29
Pb	6.19	5	6.52	6.5	5.19	4.74	6.5	6.52	5.9	6.06	6.69	5.24	5.26	6.39	4.65
Th	0.62	3.52	0.885	0.329	0.368	0.155	3.67	0.757	0.494	0.45	4.92	1.06	1.171	0.599	1
U	0.85	0.061	0.229	0.052	0.196	0.092	0.421	0.266	0.212	0.227	0.29	0.179	0.132	0.272	0.039



**Table A4-1. Apatite trace-element composition determined by La-ICP-MS. c: core, m: mantle, r:rim**

sample	SGM21	SGM21	SGM21	SGM21	SGM21	SHB05	SHB05	SHB05	SHB05	SHB05	SHB05	SHB05	SHB05	SHB05	SHB05
Analysis#	73	140	146	148	150	2	200	199	194	196	195	202	203	1	201
SHRIMP	SGM21-9					SHB05-1	SHB05-10	SHB05-12	SHB05-20	SHB05-21	SHB05-22	SHB05-5	SHB05-7	SHB05-8	SHB05-9
zone		c	c		r	r	c	r	c	c	r	c	c	r	r
EMPA			5	4			8	9		3		1	4	10	
Element ( $\mu\text{g}$ )															
Li	1.8	2.1	2.7	bdl	1	1.5	bdl	0.8	bdl	bdl	0.2	0	1.9	1.25	1.5
Mg	308.3	461	438	459	459		318	350.5	355.3	331.5	356.8	364.8	315		322.7
Al	42.1	0.02	330	0.21	0	0.22	1040	0.05	58	318	5.7	590	2320	0.16	510
Si	1378	1331	2040	1355	1343	1260	2120	1125	1920	2030	1520	2970	5060	1313	2450
Sc	0.139	0.075	0.1	0.124	0.136	0.099	0.25	0.071	0.86	0.54	0.103	0.9	1.95	0.147	0.75
Ti	0.94	0.36	290	bdl	0.11	0.33	6.6	0.41	1.6	3.1	174	2.74	7.9	0.28	1.2
V	0.89	0.73	48.1	0.683	0.632	0.02	4.3	0.059	1.58	1.92	0.3	2.35	14.15	0.042	3.49
Cr	0.84	0.81	1.06	0.83	0.17	0.24	1.5	0.49	0.94	0.92	0.98	1.04	1.96	-0.01	0.37
Mn	162.6	212.5	130	177.2	180.5	528	273	286.4	312.4	227	416.7	338.8	457	134.9	282
Fe	374	232	580	234	246	380	345	341	680	437	363	1132	2580	473	910
Rb	0.007	0.048	0.71	0.007	0.059	0.005	0.058	0.004	0.191	0.153	0.01	0.224	0.101	-0.016	0.087
Sr	84.6	95.8	74.9	84.6	92.5	256	186	262.6	259.2	208.5	286.1	220	252	272.9	247.4
Y	265.9	260.9	274	141.1	180.8	65.1	139	36.85	682	603	59.5	1553	773	61.7	777
Zr	3.9	0.0029	23	0.109	bdl	0.006	0.24	bdl	2.49	1.73	0.051	3.23	3.86	0.0061	2.67
Cs	0.0096	bdl	0.054	bdl	0.005	0.002	0.048	bdl	0.02	bdl	bdl	0	0.028	0.0008	bdl
Ba	0.033	0.103	2.2	0.006	0.101	bdl	0.19	0.166	0.65	0.21	0.042	0.78	0.38	0.07	0.67
La	25.67	22.15	32	14.48	12.53	0.88	65.4	1.032	191.5	132.3	1.194	439	688	1.751	410
Ce	77.3	51.3	119	44.2	31.32	3.67	131	4.58	542	404	5.54	1272	1470	8.44	1004
Pr	18.84	10.24	22.6	8.94	6.19	0.83	15.9	0.871	81.1	61.2	1.182	196.7	172	2.046	129.9
Nd	100.8	52	123.3	48.5	31.7	6.09	81	6.46	432.5	359	8.8	1087	779	16.64	638
Sm	33.27	16.55	41.1	14.89	10.91	3.3	23.2	3.9	132.3	109.4	5.2	321.9	198	14.29	158.8
Eu	8.98	4.7	8.88	4.41	3	1.56	4.76	1.92	26.58	19.36	2.28	38.5	35.4	8.88	20.76
Gd	44.4	24.25	55.3	18.9	14.91	8.08	30.5	8.3	173.5	151.8	12.05	415.7	225	35.71	198.3
Tb	7.26	4.77	8.66	3.23	3	1.374	4.75	1.422	24.52	21.77	1.77	58.4	30.4	6.23	27.4
Dy	48	34.4	52	21.93	22.56	10.29	26.6	7.65	147	128.6	10.84	345.6	165.7	25.06	160.5
Ho	10.17	8.07	9.28	4.92	5.39	2.2	5.47	1.33	26.91	24.2	2.21	64.4	29.7	2.548	28.2
Er	30.36	28.47	21.6	17.43	20.15	7	13.97	3.65	67.4	62.4	5.77	164.4	76.1	3.97	75.1
Tm	4.24	4.32	2.56	2.78	3.16	0.88	1.72	0.398	7.27	6.62	0.537	17.4	8.04	0.302	7.94
Yb	27.64	31.8	12	19.61	23.9	6.5	10.1	2.23	40.3	36.1	2.95	95.7	46.9	1.14	44.3
Lu	3.44	4.32	1.36	2.565	3.41	1.1	1.3	0.296	5.07	4.74	0.388	11.89	5.7	0.102	5.29
Pb	5.11	6.68	5.8	5.45	6.06	6.96	9.8	11.96	10.68	10.05	9.58	10.96	12.98	12.27	12.35
Th	0.251	0.773	8.1	0.243	0.603	0.0018	2.26	0.0047	4.67	2.76	bdl	10.74	31.3	0.011	15.7
U	0.111	0.295	0.34	0.146	0.264	0.0105	0.4	0.0147	1.136	0.819	0.028	2.19	5.1	0.058	1.48

**Table A4-1. Apatite trace-element composition determined by La-ICP-MS. c: core, m: mantle, r:rim**

sample	SHB05	SHB08	SHB08	SHB08	SHB08	SHB08	SHB08	SHB08	SHB08	SHB08	SHB12B	SHB12B	SHB12B	SHB12B	SHB12B	SHB12B
Analysis#	197	47	230	229	49	50	48	228	51	183	186	4	189	5	190	
SHRIMP		SHB08-1	SHB08-2	SHB08-3	SHB08-4	SHB08-5	SHB08-6	SHB08-7	SHB08-8	SHB12B-10	SHB12B-11	SHB12B-14	SHB12B-15	SHB12B-16	SHB12B-17	
zone																
EMPA	6		1			5	2	4			9	2	13	12	14	16
Element (ppm)																
Li	1.3	0.06	0.1	0	bdl	0.79	0.84	0.5	2.4	bdl	0.1	1.17	bdl	0.66	bdl	
Mg	341.6		343.3	349.7				351.2		358.4	364.8		360.4		363	
Al	0.21	0.17	2.5	25.5	0.34	0.03	0.14	0.56	1077	0.36	0.19	0.08	0.29	bdl	2.29	
Si	1058	1050	896	1031	941	958	1116	926	2940	1224	1216	1425	1152	1458	1255	
Sc	0.112	0.103	0.094	0.192	0.075	0.126	0.09	0.079	0.38	0.12	0.14	0.117	0.139	0.151	0.05	
Ti	0.21	0.23	0.73	0.35	0.16	0.09	-0.02	0.07	1.11	0.59	0.62	0.32	bdl	0.48	0.16	
V	0.016	0.018	0.034	0.256	0.009	0.012	0.0014	0.011	0.79	0.058	0.097	0.026	0.046	0.074	0.098	
Cr	0.9	0.39	0.87	1.07	0.53	0.57	0.51	1.15	0.7	0.68	0.47	0.52	0.59	0.82	0.81	
Mn	259	825	732	765	706	780	707	825	951	327.7	334.8	362	307.4	312.5	309.3	
Fe	368	288.8	227	301	277	283	286	196	2900	432	476	406	366	410.1	416	
Rb	0.037	0.002	0.053	0.06	0	bdl	bdl	0.045	0.134	0.029	0.035	0.001	0.041	0.029	0.011	
Sr	238.9	542	558	462.7	448.1	488.2	488	503	562	963	923	613	755	448	807	
Y	43.3	46.1	137.8	27.26	35.03	19.05	35.09	17.6	21.5	291.9	244.6	181	49.8	152.5	240.2	
Zr	bdl	bdl	bdl	0.003	0.0057	0.0026	0.0017	bdl	bdl	0.067	0.101	0.0044	bdl	0.042	0.067	
Cs	0.015	bdl	bdl	3.87	0.0078	bdl	0.001	bdl	9.47	0.005	bdl	bdl	0.001	0.0005	bdl	
Ba	0.003	0.56	0.14	2.02	0.094	0.062	0.05	0.245	1.43	0.066	0.055	0.048	0.014	0.028	0.009	
La	1.282	0.483	5.15	0.502	0.2	0.111	0.202	0.096	1.23	3.74	3.15	0.055	0.143	0.432	2.56	
Ce	6.18	2.323	17.27	1.57	1.134	0.494	1.326	0.517	1.05	16.12	14.14	0.38	0.801	2.649	13.13	
Pr	1.337	0.514	2.8	0.353	0.255	0.129	0.315	0.107	0.278	3.66	3.08	0.121	0.189	0.815	3.22	
Nd	10.57	3.5	15.96	2.1	1.96	0.8	2.42	0.74	1.65	26.73	27.2	1.26	1.69	9.7	27.4	
Sm	7.68	2.05	6.83	1.18	1.26	0.47	1.46	0.44	0.82	18.85	20.17	1.88	1.52	10.14	21.43	
Eu	3.79	1.014	3.32	0.648	0.705	0.305	0.719	0.296	0.396	9.54	9.68	0.802	0.709	4.49	9.93	
Gd	18.2	3.83	12.56	2.49	2.56	1.31	3	0.94	1.44	46.7	50.9	8.77	5.36	31.7	53.8	
Tb	3.02	0.882	2.52	0.536	0.667	0.293	0.659	0.285	0.378	8.89	8.89	2.49	1.187	5.67	9.53	
Dy	14.52	6.99	18.57	4.6	5.53	2.77	5.51	2.56	3.24	57.8	54.7	24.1	9.56	34.44	53.8	
Ho	1.862	1.756	4.47	0.999	1.281	0.7	1.256	0.664	0.87	10.77	9.54	6.48	2.048	6.17	9.47	
Er	2.98	5.72	15.11	3.56	4.7	2.4	4.43	2.51	2.76	27.18	21.95	23.4	5.51	14.44	20.26	
Tm	0.224	0.86	2.04	0.529	0.635	0.38	0.622	0.421	0.556	2.67	2.038	3.07	0.545	1.597	1.959	
Yb	0.75	5.56	13	3.92	4.35	2.72	4.06	3.14	3.7	14.49	10.06	18.47	3.15	9.65	10.11	
Lu	0.071	0.598	1.911	0.391	0.483	0.312	0.47	0.373	0.424	1.92	1.258	2.37	0.37	1.554	1.239	
Pb	10.33	15.1	13.9	11.97	11.84	11.16	11.34	9.9	17.5	6.52	5.85	11.19	20.72	4.46	3.31	
Th	0.0097	0.0058	0.0002	0.0172	bdl	bdl	bdl	0.0003	0.0002	0.0004	bdl	bdl	bdl	0.0132	0.022	
U	0.052	0.0102	0.033	bdl	bdl	bdl	bdl	0.0092	0.008	0.137	0.361	0.0022	0.0105	0.511	0.632	

**Table A4-1. Apatite trace-element composition determined by La-ICP-MS. c: core, m: mantle, r:rim**

sample	SHB12B	SHB12B	SHB12B	SHB12B	SHB12B	SHB12B	SHB12B	SHB12B	SHB12B	SHB12B	SHB12B	SHB12B	SHB12B	SHB44A	SHS44A	SHB44A
Analysis#	191	192	3	6	193	7	180	181	184	187	188	185	13	160		
SHRIMP	SHB12B-18	SHB12B-19	SHB12B-2	SHB12B-21	SHB12B-22	SHB12B-23	SHB12B-3	SHB12B-5	SHB12B-6	SHB12B-7	SHB12B-8	SHB12B-9	SHB44A-1	SHB44A-12	SHB44A-13	
zone									c	r		r	r		c	c
EMPA	15	17	6		19	20		7	4	3		5				
Element (ppm)																
Li	0.6	bdl	1.36	1.27	0	1.89	bdl	bdl	0.8	0.7	bdl	bdl	0.04	0.2	0.16	
Mg	394	360.7			370		308.4	368.9	370.1	335.3	362	414.3		445		
Al	11.1	0.29	12.1	bdl	57	bdl	6.8	0.02	2.66	1.3	0.47	23	0.05	0.24	0.07	
Si	1283	1162	1363	1411	1390	1252	1048	1173	1289	1070	1158	1457	1231	1923	1803	
Sc	0.1	0.062	0.197	0.128	0.125	0.199	0.108	0.108	0.106	0.185	0.129	0.075	0.16	0.169	0.232	
Ti	0.16	0.14	0.16	0.58	0.09	0.39	0.6	bdl	0.18	0.12	0.03	0.08	0.34	0.4	0.46	
V	0.071	0.067	0.176	0.075	0.229	0.061	0.115	0.069	0.149	0.146	0.1	0.085	0.023	0.228	0.472	
Cr	0.73	0.56	0.65	0.84	2.36	0.95	0.67	0.65	0.56	0.25	0.7	0.84	0.63	0.69	0.63	
Mn	313	358.6	358	351.2	326	316.8	358.4	339.4	307.2	326	348.1	327.7	64	221.2	123.8	
Fe	337	367	428	431	430	454	448	391	351	436	345	378	511	439	480	
Rb	0.082	0.043	0.015	0.049	0.046	0.048	0.07	0.039	0.052	0.073	0.037	0.051	0.088	0.197	0.172	
Sr	590	811	730.8	675.5	659	909	954	1136	525.8	1029	798	789	1494	490	705	
Y	145.2	214.8	200.5	430.7	147.5	333.8	275.8	289.8	178.7	253.3	175.9	139.3	264.9	1358	1265	
Zr	0.067	0.048	0.036	0.03	0.038	0.069	0.052	0.048	0.096	0.091	0.012	bdl	bdl	1.55	2.88	
Cs	0.004	bdl	0.0032	0.043	6.13	0.004	0.122	bdl	0.004	0.021	0.004	0.44	-0.0026	0.004	0.0063	
Ba	0.32	0.23	0.235	0.189	0.062	0.031	0.122	0.056	0.101	0.101	0.154	0.018	0.231	0.55	0.51	
La	0.621	1.694	0.939	1.074	1.017	3.56	6.31	3.98	0.563	3.61	0.744	0.499	3.42	591	228.1	
Ce	3.1	8.02	4.82	4.35	3.61	15.98	27.13	17.2	3.05	16.22	3.01	2.59	16.71	1502	737.8	
Pr	0.735	1.765	1.206	1.033	0.78	3.583	5.56	3.81	0.896	3.42	0.775	0.699	2.596	205.7	119.4	
Nd	7.1	16.62	11.92	9.32	7.24	28.75	43.5	30.62	9.33	27.4	7.3	6.18	17.88	988	678.5	
Sm	6.72	12.81	10.65	9.44	6.15	22.76	20.51	21.84	9.45	20.5	7.08	5.47	10.85	249.4	203.5	
Eu	3.02	6.02	4.54	4.95	2.61	10.94	9.49	10.91	4.16	9.97	3.14	2.3	3.54	20.23	29.7	
Gd	21.6	37.1	31.64	35.25	18	56.9	43.8	56.6	32.2	50.5	24	18.54	24.02	302.8	275.5	
Tb	4.04	6.57	5.97	8.26	3.87	10.84	7.09	10.08	5.98	9.05	4.5	3.71	5.71	42.66	40.81	
Dy	26.7	42.7	38.67	66.5	26.2	68.8	45.9	60.4	38	54	31.7	25.16	46.02	255.3	253.3	
Ho	5.48	8.08	7.4	15.99	5.62	12.25	9.27	10.6	7.04	9.22	6.52	5.26	9.96	49.2	48.77	
Er	15.81	21.67	19.74	46.76	15.11	29.9	24.74	26.34	16.69	21.94	17.61	13.89	28.65	128.3	130.3	
Tm	1.867	2.337	2.218	5.31	1.78	2.823	2.86	2.518	1.789	2.18	2.069	1.468	3.26	14.38	14.15	
Yb	12.41	13.76	13.32	30.91	10.51	14.54	17.3	13.62	9.17	10.89	12.56	8.52	16.23	78	78.9	
Lu	2.034	1.748	1.824	4.347	1.58	1.919	2.287	1.673	1.264	1.459	1.836	1.213	1.9	9.29	9.71	
Pb	7.85	10.44	11.85	8.19	7.45	3.69	8.49	12.72	5.94	9.08	14.07	10.79	32.76	16.34	22.82	
Th	0.027	0.0159	0.0022	0.0048	0.017	0.0006	0.0032	0.018	0.0106	0.034	0.0011	0.0019	0.0147	2.85	2.48	
U	0.37	0.202	0.257	0.212	0.321	0.275	0.058	0.61	0.467	0.471	0.254	0.185	0.177	0.716	0.722	

**Table A4-1. Apatite trace-element composition determined by La-ICP-MS. c: core, m: mantle, r:rim**

sample	SHS44A	SHS44A	SHS44A	SHB44A	SHB44A	SHB44A	SHB44A	SHS44A	SHS44A	SHS44A	SHS44A	SHS44A	SHS44A	SHS44B	SHB44B
Analysis#	158	159	164	15	17	16	18	157	166	165	167	162	161	151	22
SHRIMP	SHB44A-16	SHB44A-18	SHB44A-2	SHB44A-20	SHB44A-21	SHB44A-22	SHB44A-23	SHB44A-25	SHB44A-3	SHB44A-4	SHB44A-5	SHB44A-8		SHB44B-1	SHB44B-15
zone	c	r	c	r	r	r	r	r	r	c	r	c	c	c	
EMPA	2	7													1
<i>Element (ppm)</i>															
Li	1.3	0.34	bdl	0.09	0.04	0.59	0.27	0.7	bdl	bdl	bdl	0.3	bdl	bdl	0.45
Mg	401	434	347.8					459	329.7	323.8	357.5	344.5	349.5	439	
Al	0.63	7.1	0.23	0.09	0.15	0.04	0.14	0.38	0.7	0.01	0.24	34.8	0.47	0.26	0.23
Si	1300	1200	1110	1354	1220	1386	1205	1240	913	830	1039	1732	1575	1940	1285
Sc	0.131	0.12	0.324	0.125	0.115	0.117	0.184	0.064	0.049	0.29	0.137	0.395	0.221	0.174	0.171
Ti	0.26	3930	0.03	0.16	0.09	0.55	0.31	0.05	0.01	bdl	0.26	0.47	-0.1315	0.98	0.53
V	0.17	1.71	2.34	0.049	0.022	0.034	0.029	0.005	0.026	1.09	0.034	1.16	0.264	0.94	0.035
Cr	0	0.78	0.46	0.6	0.64	0.72	0.55	0.6	0.22	1.12	0.02	1.49	1.02	0.84	0.81
Mn	180	363	247.1	53	42.73	71.7	57.8	93.3	222	222.9	143.1	315	129	257	600
Fe	418	410	530	518	495	459	484	397	398	514	431	584	401	498	405
Rb	0.183	0.058	0.119	0.032	0.028	0.013	bdl	0.074	0.008	0.074	0.053	0.159	0.169	0.156	0.052
Sr	598	1011	802	1537	1495	1328	1461	1290	842	1016	1126	585	831	326	680
Y	947	216.4	730	167.6	127.4	163	142.1	189.7	299	455	270.9	1252	1287	1290	412
Zr	2.11	0.05	5.31	0.0013	bdl	bdl	0.002	bdl	0.0011	1.61	bdl	3.29	0.66	5.52	bdl
Cs	0	0.007	bdl	bdl	0.0097	0.0041	0.024	0.152	0.027	0.012	0.002	0.135	bdl	0.244	0.016
Ba	0.18	0.089	1.17	0.088	0.087	0.113	0.119	0.116	0.21	1.44	0.68	1.95	0.36	1.99	0.019
La	72.7	3.15	141.7	2.97	2.02	2.121	2.271	2.6	8.89	89.5	6.64	268.6	114.3	390	0.689
Ce	283	18	458.4	15.54	11.09	12.26	12.55	14.86	48.5	273	36.81	813	364	1140	4.51
Pr	45.3	2.87	73.8	2.39	1.917	2.113	2.074	2.44	7.39	42.6	5.76	130.9	57.6	167	1.21
Nd	264	18.66	411.6	16.61	13.28	14.74	14.05	16.97	47.4	239	37.4	718	322	847	10.37
Sm	95	9.82	126.5	10.56	8.67	10.01	9.1	11.59	20.3	72.8	17.95	216.4	112.4	226	9.46
Eu	14.6	3.13	23.6	3.96	3.43	3.81	3.44	4.46	5.83	13.38	5.05	30.87	17.03	26.8	4.21
Gd	141	20.28	167.8	24.23	21.35	24.08	21.41	25.4	35.9	101.8	31.9	282.2	178	279	28.6
Tb	22.5	4.29	24	5.44	4.55	5.45	4.72	5.9	6.9	15.29	6.56	40.85	30.85	40.4	7.1
Dy	153	34.59	144.4	35.7	28.56	36.21	30.5	39.3	50.5	87.8	47.2	245.8	211.8	241	63.1
Ho	31.6	7.42	26.29	6.52	4.85	5.94	5.36	7.1	11.55	16.26	10.37	46.63	45.5	46.3	14.7
Er	96.8	23.57	67.1	16.01	11.21	13.28	12.36	15.89	34.5	40	30.17	122.8	132	119	42.8
Tm	12.6	3.05	7.31	1.503	1.082	1.191	1.134	1.325	4.22	4.22	3.55	13.48	15.72	13.2	5.02
Yb	72	18.44	39.15	7.07	4.78	5.09	5.48	5.85	24.7	24.8	20.75	75.9	85.7	70	26.35
Lu	9.1	2.34	5.26	0.811	0.482	0.574	0.588	0.609	3.69	3.08	2.72	9.44	9.94	8.37	3.46
Pb	15.3	24.45	23.27	34.04	31.4	29.38	31.84	28.4	19.09	24.8	25.35	16.67	26.92	7.5	15.38
Th	13.8	0.025	1.329	0.058	0.0116	0.0131	0.0302	0.035	0.122	1.18	0.025	2.86	4.27	14.6	0.0016
U	2.44	0.089	0.492	0.239	0.199	0.122	0.172	0.112	0.044	0.345	0.043	0.71	1.21	0.471	0.038

**Table A4-1. Apatite trace-element composition determined by La-ICP-MS. c: core, m: mantle, r:rim**

sample	SHB44B	SHB44B	SHS44B	SHB44B	SHS44B	SHB44B	SHB44B	SHS44B	SHB44B	SHB44B	SHB44B	SHB44B	SHB44B	SHS44B	SHB44B
Analysis#	21	19	153	20	156	30	29	152	27	28	23	26	24	154	25
SHRIMP	SHB44B-18	SHB44B-19	SHB44B-2	SHB44B-20	SHB44B-21	SHB44B-22	SHB44B-23	SHB44B-3	SHB44B-4	SHB44B-5	SHB44B-6	SHB44B-6	SHB44B-7	SHB44B-8	SHB44B-9
zone															
EMPA			7					2							
Element (ppm)															
Li	bdl	bdl	0.4	bdl	bdl	0.09	0.71	2.2	0.82	0.17	bdl	0.08	0.44	2.4	0.33
Mg			463		439			457						459	
Al	0.14	0.03	0.95	0.02	0.01	0.03	117	bdl	0.06	0.11	0.11	0.21	0.21	0.49	0.29
Si	1259	1353	1273	1361	1343	1114	1333	1348	1172	1154	1284	1221	1200	1212	1116
Sc	0.138	0.125	0.11	0.169	0.133	0.156	0.153	0.118	0.1	0.136	0.099	0.126	0.117	0.047	0.102
Ti	0.36	0.41	0.09	0.07	0.24	0.25	1.13	0.39	0.26	0.41	0.59	0.28	0.25	0.34	0.18
V	0.037	0.034	0.034	0.025	0.042	0.018	0.28	0.034	0.016	0.057	0.032	0.05	0.039	0.072	0.025
Cr	0.82	0.85	0.41	0.9	0.06	1.05	0.92	0.68	0.67	0.65	0.78	0.63	0.73	0.5	0.44
Mn	889	605.2	91.5	60.2	399	473.2	665.3	93.8	832	120	333	662	67.5	280	800
Fe	340	402	394	488	418	300	365	382	374	422	457	384	511	398	357
Rb	0.096	0.026	0.034	-0.002	0.095	0.041	0.145	0.005	0.079	0.015	0.116	0.05	0.01	0.052	0.059
Sr	957	765.7	1245	1447	828	646	714.8	1223	668	1259	769	1039	1537	1211	974
Y	366.3	441.1	118	69.7	511	233	243.8	185.6	549.5	195.2	588.7	307.3	69.3	232.3	303.5
Zr	bdl	bdl	bdl	bdl	bdl	bdl	bdl	bdl	bdl	bdl	bdl	bdl	bdl	0.009	0.003
Cs	0.0033	0.0006	0.015	0.0019	0.016	bdl	0.0049	bdl	0.011	bdl	0.0017	0.006	bdl	0.012	0.005
Ba	0.048	0.14	0.145	0.128	0.122	0.07	1.6	0.125	0.067	0.086	0.106	0.41	0.114	0.23	0.96
La	3.78	0.599	1.631	2.26	0.777	8.46	18.61	2.4	0.569	2.24	0.659	1.71	3.75	13.19	2.251
Ce	16.94	3.852	8.42	13.74	4.86	32.51	73.4	13.18	4.61	11.05	4.21	9.98	17.48	59	13.26
Pr	3.51	0.921	1.91	3.04	1.116	5.6	11.51	2.13	1.211	2.495	1.098	2.412	4.26	10.03	2.951
Nd	22.89	8.34	14.59	25.4	10.35	32.24	65.3	14.86	11.8	19.2	10.54	18.42	32.41	58.5	23.2
Sm	13.14	8.2	10.47	20.02	10.13	13.65	20.05	9.74	10.34	12.99	10.99	13.42	23.39	20.56	13.94
Eu	4.56	3.97	4.35	7.49	5	4.14	6.27	3.98	4.82	5.4	5.19	5.1	9.68	5.8	5.48
Gd	27.2	27.05	27.73	47.9	33.8	22.86	34	23.31	32.56	34.53	35.72	27.82	55.5	34.3	30.22
Tb	6.12	7.81	5.62	7.79	9.35	4.36	5.41	5.14	8.1	7.47	10.24	5.9	8.46	6.17	6.05
Dy	49.8	70.4	32.5	30.83	85.2	33.21	37.41	37.1	73.3	47.9	97.2	45	30.27	40.2	43.47
Ho	12.7	16.29	4.29	2.91	19.28	7.91	8.31	6.64	18.88	7.13	22.68	10.68	2.726	8.25	10.34
Er	44.8	45.27	6.79	3.74	53.4	26.33	25.07	15.16	66.5	13.16	67.1	34.54	3.28	22.1	34.12
Tm	6.45	5.04	0.405	0.218	5.65	3.6	2.953	1.384	9.07	0.879	7.44	4.64	0.179	2.39	4.5
Yb	44	23.81	1.4	0.793	26.1	23.78	18.2	5.94	55.1	2.95	35.37	29.23	0.557	13.84	29.26
Lu	7.14	2.406	0.173	0.092	2.38	3.749	3.083	0.61	7.1	0.295	3.29	4.58	0.06	1.95	4.59
Pb	20.89	17.39	25.56	30.94	19.28	8.57	12.74	26.93	14.14	28.11	19.43	24.49	32.09	26.47	23.5
Th	0.004	bdl	0.002	bdl	bdl	0.0093	0.043	0.071	0.0024	0.0069	bdl	bdl	0.0032	0.018	0.001
U	0.068	0.0219	0.123	0.153	0.031	0.039	0.047	0.117	0.027	0.147	0.0367	0.07	0.173	0.076	0.071

**Table A4-1. Apatite trace-element composition determined by La-ICP-MS. c: core, m: mantle, r:rim**

sample	SHS44B	SHB45	SHB45	SHB45	SHB45	SHB45	SHB45	SHB45	SHB45	SHB45	SHB45	SHB45	SHB45	SHB45	SHB45
Analysis#	155	173	176	8	175	9	177	10	178	168	174	171	170	172	169
SHRIMP		SHB45-1	SHB45-10	SHB45-11	SHB45-12	SHB45-13	SHB45-14	SHB45-15	SHB45-16	SHB45-17	SHB45-2	SHB45-3	SHB45-4	SHB45-5	SHB45-6
zone							c				r	c	r	bc	c
EMPA		4						7			5				2
Element ( $\mu\text{g}$ )															
Li	1.2	bdl		1.14	bdl	0.92	bdl	0.83	0.11	bdl	0.5	bdl	bdl	0.8	0.7
Mg	446	323.3			331.7		345		351.7	346.7	341.5	324.6	293	315	342.8
Al	0.59	5.13		1.83	0.29	0.03	0.63	0.14	0.49	63	0.18	0.26	20	254	50.1
Si	1140	1106		1284	905	1280	1003	1288	1107	1370	940	1110	1240	2760	1286
Sc	0.056	0.17		0.128	0.115	0.171	0.11	0.139	0.063	0.262	0.133	0.122	0.29	0.44	0.248
Ti	0.13	0.63		0.33	-0.01	0.55	0.1	0.04	-0.07	59	0.4	4.8	0.48	2.9	0.18
V	0.016	0.2		0.146	0.038	0.07	0.08	0.051	0.135	0.41	0.026	0.057	0.16	2.65	0.46
Cr	0.21	0.99		1.22	0.44	0.78	0.38	1.12	0.43	1.2	0.67	0.76	1.53	5.3	0.78
Mn	593	125.6		98.2	149.9	70.32	127	77.4	138.2	87.6	82.2	103	60.7	140	138.7
Fe	309	404		411.4	280	536	388	400	383	513	322	367	403	810	450
Rb	0.055	0.014		bdl	0.036	bdl	0.022	0.004	0.028	0.023	0.018	0.047	0.11	0.011	0.08
Sr	1027	4720		1817	645	3982	4801	1655	3989	3931	1606	3801	2460	1588	3606
Y	222.1	49.6		28.57	12.19	40.58	50.4	33.2	39.3	49.1	28.8	52.6	34	38.9	36.87
Zr	0.0031	bdl	bdl	bdl	0.0025	0.01	0.0012	bdl	0.009	0.071	bdl	0.0001	0.101	109	bdl
Cs	0.013	0.251		0.0123	0.02	bdl	0.009	bdl	bdl	0.006	0.011	0.014	1.18	1.68	2.95
Ba	0.75	0.78		0.65	0.047	0.81	0.49	0.169	0.4	0.54	0.33	0.88	0.28	0.46	0.53
La	1.329	5.41		0.869	0.052	3.01	5	0.492	2.95	3.53	0.277	4.64	2.3	31.1	4.21
Ce	8.01	19.76		3.54	0.314	11.47	20.09	2.12	11.99	11.52	1.24	18.3	8.79	80.9	11.89
Pr	1.897	3.66		0.739	0.072	2.198	3.53	0.442	2.25	1.99	0.219	3.4	1.88	9.93	2.35
Nd	14.46	26.35		5.66	0.59	16.26	24.2	3.07	15.64	12.56	1.58	20.77	13.4	51.6	15.92
Sm	9.29	13		3.48	0.43	8.38	12.47	1.77	8.46	6.31	0.89	10.66	8.7	10.3	7.56
Eu	4.16	5.92		1.533	0.137	4.05	5.89	0.855	4.03	3	0.571	5.43	4.32	3.42	3.53
Gd	21.46	27.6		8.93	1.48	20.14	25.28	5.2	17.43	13.26	3.11	23.33	21.1	12.9	16.83
Tb	4.38	4.31		1.705	0.346	3.529	4.06	1.26	2.94	2.61	0.717	3.72	4.14	1.89	2.69
Dy	32.86	19.7		9.54	2.09	16.37	18.59	8.44	14.72	14.73	6.15	16.49	18.5	11.04	13.01
Ho	7.69	2.07		1.147	0.474	1.704	2.06	1.286	1.746	1.93	1.106	2.2	1.5	1.47	1.533
Er	24.23	3.16		1.819	1.21	2.4	3.42	1.7	2.33	3.32	1.74	4.37	1.56	3.06	2.23
Tm	3.11	0.212		0.152	0.143	0.152	0.276	0.102	0.167	0.295	0.094	0.399	0.097	0.324	0.198
Yb	20.32	1.28		0.711	1	0.809	1.49	0.305	0.92	1.48	0.403	1.86	0.29	2.22	0.938
Lu	3.14	0.221		0.11	0.149	0.122	0.186	0.0236	0.134	0.184	0.051	0.218	0.029	0.326	0.198
Pb	20.84	9.36		14.96	3.58	31.86	8.43	10.74	6.98	14.06	10.18	15.38	20.2	4.75	5.78
Th	0.0026	0.0152		0.0016	bdl	0.013	0.0044	bdl	0.0017	0.13	bdl	0.0145	0.018	2.27	0.0043
U	0.031	0.344		0.0436	bdl	0.124	0.191	0.0093	0.194	0.082	0.0004	0.192	0.03	0.569	0.242

**Table A4-1. Apatite trace-element composition determined by La-ICP-MS. c: core, m: mantle, r:rim**

sample	SHB45	SHB45	SHB53ecl	SHB53ecl	SHB53ecl	SHB53ecl	SHB53ecl	SHB53ecl	SHB53ecl	SHB53ecl	SHB53ecl	SHB53ecl	SHB53ecl	SHB53ep	SHB53ep	SHB53ep
Analysis#	12	11	63	55	53	52	62	60	59	61	56	58	67	66	65	
SHRIMP	SHB45-7	SHB45-9	SHB53ecl-1	SHB53ecl-11	SHB53ecl-12	SHB53ecl-14	SHB53ecl-2	SHB53ecl-3	SHB53ecl-4	SHB53ecl-5	SHB53ecl-7	SHB53ecl-8	SHB53ep-11	SHB53ep-12	SHB53ep-13	
zone																
EMPA		6						4	3			2				
Element (ppm)																
Li	0.72	0.1	bdl	0.61	0.4	bdl	0.5	0.67	bdl	0.59	1.18	0.72	bdl	1.01	bdl	
Mg																
Al	0.18	0.25	bdl	bdl	bdl	0.01	bdl	0.2	bdl	bdl	0.06	bdl	bdl	bdl	bdl	
Si	1356	1266	982	1101	1003	910	1002	1003	1039	1034	1030	1009	919	862	916	
Sc	0.131	0.155	0.109	0.096	0.111	0.12	0.042	0.076	0.086	0.104	0.097	0.112	0.075	0.101	0.094	
Ti	0.19	0.4	0.31	0.53	0.49	0.56	0.53	0.39	0.35	0.28	0.51	0.2	0.38	0.38	0.02	
V	0.035	0.06	0.099	0.082	0.062	0.054	0.05	0.05	0.048	0.084	bdl	0.06	0.059	0.035	0.026	
Cr	0.7	0.68	0.43	0.36	0.34	0.08	0.25	0.19	0.32	0.33	0.29	0.6	-0.04	0.41	0.72	
Mn	33.3	62.27	318.1	331.7	325.6	338.1	236.5	299.3	332.9	319.9	265.1	304.2	297.4	301	314.2	
Fe	422	522	383	421	397	417	386	412	409	403	397	418	388	391	401	
Rb	0.014	0.007	0.028	bdl	bdl	0.049	0.009	bdl	bdl	bdl	0.009	0.044	-0.032	0.02	0.011	
Sr	2372	3058	1431	1123	1252	1468	1186	840	933	1115	1023	1617	673	1056	803	
Y	42.66	41.3	298.1	48.8	65	267.7	140.3	41.9	71.8	82.5	63.1	231	23.54	92.5	23.43	
Zr	bdl	bdl	0.021	0.022	bdl	0.012	bdl	bdl	bdl	0.013	bdl	0.026	bdl	bdl	0.0021	
Cs	bdl	bdl	bdl	bdl	0.01	0.0017	0.02	0.008	bdl	0.0021	bdl	0.028	0.0015	0.0097	bdl	
Ba	0.059	1.46	0.21	0.277	0.269	0.236	0.161	0.259	0.29	0.36	0.132	0.39	0.29	0.137	0.173	
La	1.84	3.12	2.17	0.321	0.387	1.835	0.91	0.169	0.347	0.562	0.183	1.343	0.207	0.22	0.168	
Ce	7.74	9.39	8.62	1.045	1.41	7.67	3.89	0.645	1.456	2.35	0.868	5.69	0.719	0.888	0.731	
Pr	1.58	1.519	1.855	0.168	0.233	1.67	0.777	0.112	0.312	0.449	0.175	1.214	0.141	0.148	0.134	
Nd	10.88	9.34	13.14	1.14	1.5	12.39	6.1	1.03	2.12	2.78	1.3	8.58	0.91	1.09	0.84	
Sm	6.49	4.57	8.55	0.45	0.85	8.13	4.05	0.66	1.38	1.79	0.85	6.09	0.53	0.8	0.368	
Eu	3.53	2.218	4.98	0.335	0.409	4.47	2.29	0.377	0.892	0.952	0.421	3.36	0.243	0.353	0.228	
Gd	19.7	10.86	26.92	1.83	2.51	24.51	12.88	2.8	4.64	5.21	2.69	18.31	1.2	2.58	1.35	
Tb	4.13	2.275	6.35	0.501	0.754	5.66	2.99	0.752	1.201	1.312	0.727	4.46	0.341	0.688	0.332	
Dy	20.59	12.87	51.6	5.32	7.68	46.7	24.53	6.32	10.71	11.3	7.65	37.38	3.2	8.44	2.99	
Ho	1.747	1.597	11.32	1.477	1.989	9.96	5.27	1.536	2.461	2.77	2.049	8.2	0.768	2.646	0.713	
Er	2.1	2.71	28.2	4.82	6.82	25.69	13.54	4.51	7.13	8.38	6.16	22.36	2.47	10.85	2.47	
Tm	0.105	0.224	2.85	0.655	0.751	2.45	1.249	0.568	0.798	1.018	0.667	2.259	0.342	1.385	0.334	
Yb	0.375	1.076	13.05	3.73	4.59	11.8	5.78	3.04	4.43	5.98	3.46	10.7	2.35	8.22	2.32	
Lu	0.0306	0.122	1.507	0.486	0.552	1.363	0.665	0.405	0.553	0.784	0.324	1.226	0.436	0.886	0.381	
Pb	19.99	39.63	8.59	13.41	12.12	9.52	12.08	13.49	12.07	12.55	16.16	13.31	11.31	18.96	13.63	
Th	0.0037	0.0182	0.0118	0.0048	0.0013	0.0058	0.0121	bdl	0.0014	0.0023	bdl	bdl	bdl	bdl	bdl	
U	0.0216	0.053	0.585	0.115	0.125	0.584	0.302	0.107	0.062	0.076	0.0149	0.393	0.0156	0.03	0.0106	

**Table A4-1. Apatite trace-element composition determined by La-ICP-MS. c: core, m: mantle, r:rim**

sample	SHB53ep	SHB53ep	SHB53ep	SHB53ep	SHM23B	SHM23B	SHM23B	SHM23B	SHM23B	SHM23B	SHM23B	SHM23B	SHM23B	SHM23B	SHS27
Analysis#	64	70	69	68	213	36	39	37	212	214	38	211	40	215	208
SHRIMP	SHB53ep-15	SHB53ep-3	SHB53ep-6	SHB53ep-7	SHM23B-1	SHM23B-10	SHM23B-2	SHM23B-3	SHM23B-4	SHM23B-5	SHM23B-6	SHM23B-7	SHM23B-8	SHM23B-9	SHS27-1
zone															c
EMPA			1		6	7	3		4	8	5	1	2		1
Element (ppm)															
Li	bdl	0.74	bdl	1.2	0.7	0.39	0.28	0.27	bdl	0.7	0.4	0.1	bdl	bdl	bdl
Mg					353				344	372		376.6		353.2	354
Al	bdl	bdl	bdl	bdl	1060	bdl	0.11	bdl	0.41	211	0.09	0.01	0.12	0.17	0.29
Si	1058	1017	1041	1022	2790	1129	983	1060	920	1470	1045	981	1051	914	920
Sc	0.105	0.082	0.104	0.055	0.39	0.128	0.107	0.115	0.15	0.154	0.069	0.1	0.106	0.111	0.21
Ti	0.54	0.32	0.36	0.28	3.7	0.47	0.36	0.44	0.8	1.16	0.53	0.25	0.23	0.19	670
V	0.017	0.018	0.035	0.016	1.17	0.0019	0.019	bdl	0.023	0.425	0.005	0.006	0.023	0.037	0.49
Cr	0.42	0.34	0.74	0.35	0.78	0.43	0.21	0.39	0.41	0.7	0.65	0.64	0.55	0.61	0.3
Mn	289.4	279.8	341.5	261.7	131	196.4	27.18	54.8	53.2	23.5	13.3	33.8	35.41	35.1	519
Fe	395	390	372	386	269	367	284	300	249	512	269	221	278	216	286
Rb	-0.024	0.031	-0.01	0.001	3.48	0.064	0.062	0.074	0.085	0.467	0.26	0.096	0.063	0.115	0.091
Sr	1108	972	688	1060	1736	1406	543	444	532	697	605	447	443.3	497	128.6
Y	118.7	91.6	14	65.5	704	784	711	653.1	588	964	2607	550	560.7	644	200
Zr	bdl	bdl	bdl	bdl	bdl	bdl	0.0055	bdl	0.008	0.057	0.05	bdl	bdl	bdl	3.8
Cs	bdl	0.012	bdl	bdl	0.183	0.005	0.0021	bdl	bdl	0.014	0.105	bdl	0.0032	bdl	-0.014
Ba	0.213	0.274	0.35	0.237	8.3	0.185	0.109	0.122	0.23	1.89	0.11	0.095	0.07	0.216	0.42
La	0.304	0.22	0.2	0.186	9.25	51.64	83.9	67.5	44.2	91.2	67.1	77	102.4	114.9	10
Ce	1.393	0.863	0.705	0.663	34.2	193.2	248.4	161.6	131.5	264.7	225.7	212.5	264.2	303.7	38.4
Pr	0.278	0.199	0.136	0.148	6.51	37.45	44.1	26.34	23.5	40.1	50.4	35.2	43.07	51.1	8.9
Nd	1.96	1.2	0.8	1	46.5	251.8	234.1	131.9	119.8	183	351.4	173.4	204.8	250.6	50
Sm	1.33	0.84	0.361	0.66	31.5	153.1	80.8	45.87	41.2	56.1	202.6	54.5	63.4	78	19.1
Eu	0.641	0.469	0.186	0.328	11.39	51.7	20.87	14.1	12.61	19.64	64.1	14.2	15.98	19.73	4.31
Gd	4.36	3.15	0.89	2.36	100.4	300.1	119.3	76	63.9	78.3	490	77.7	85.7	111.5	29.4
Tb	1.196	0.869	0.178	0.61	21.42	43.46	19.73	14.64	12.18	16.11	82.3	13.71	14.65	18.51	3.69
Dy	12.71	9.38	1.66	6.36	161.6	224.3	133	104.6	92.4	126.9	526	91.6	95.2	120.2	25.6
Ho	3.65	2.87	0.449	1.967	28.8	32.8	25.87	22.61	20.4	29.89	95.3	18.21	19.1	23.76	5.87
Er	12.65	10.46	1.65	7.66	62.9	75.7	67.8	64.7	61.1	103	228.7	52.1	52.8	63.1	17.7
Tm	1.411	1.299	0.269	1.008	6.5	8.07	7.2	7.88	7.78	13.78	21.2	6.37	6.14	6.88	2.28
Yb	6.45	6.35	2.28	5.42	31.1	42.12	34.8	41.36	42.8	80	94.7	34.1	32.88	35.94	14.8
Lu	0.733	0.723	0.436	0.649	3.15	4.76	3.77	4.93	4.85	8.46	9.15	3.73	3.65	3.78	1.48
Pb	19.95	17.06	11.64	16.22	29.3	26.97	13.46	33.82	44	10.76	3.44	23.7	22.2	20.61	11.91
Th	bdl	bdl	bdl	bdl	0.17	0.668	0.253	1.459	1.3	4.61	4.02	0.629	1.115	1.098	0.97
U	0.0284	0.0251	0.0031	0.0184	0.074	0.996	0.502	2.603	1.65	0.25	0.408	0.834	0.976	0.7	0.073



**Table A4-1. Apatite trace-element composition determined by La-ICP-MS. c: core, m: mantle, r:rim**

sample	SHS27	SHS27	SHS27	SHS27	SHS27	SHS27	SHS27	SHS27	SHS27	SHS27	SHS27	SHS3	SHS3	SHS3	SHS3	SHS3
Analysis#	34	206	207	35	31	205	209	33	210	32	216	220	44	221	45	
SHRIMP	SHS27-11	SHS27-14	SHS27-15	SHS27-19	SHS27-2	SHS27-5	SHS27-6	SHS27-7	SHS27-8	SHS27-9	SHS3-1	SHS3-10	SHS3-12	SHS3-13	SHS3-15	
zone							r			r	c	r				
EMPA	10						3	5	7							10
Element (ppm)																
Li	0.12	0.8	0.6	0.22	bdl	0.4	bdl	bdl	bdl	bdl	0.1	0.8	0.39	bdl	1.09	
Mg		372	358.6			342.5	343		372.2		353.2	318.4		367.6		
Al	4.5	bdl	0.34	0.1	bdl	0.34	0.64	1710	2.16	2.03	bdl	0.01	0.14	0.51	bdl	
Si	1247	936	950	1181	1250	1016	980	3970	1212	988	907	1037	986	1066	1000	
Sc	0.165	0.151	0.107	0.103	0.113	0.048	0.105	0.217	0.112	0.138	0.141	0.144	0.156	0.147	0.218	
Ti	40	0.46	bdl	22	2.4	bdl	2.39	25	0.6	5710	0.52	bdl	0.25	290	0.4	
V	0.111	0.1	0.135	0.145	0.126	0.105	0.099	1.26	0.045	3.56	0.053	0.008	0.047	0.38	0.055	
Cr	0.7	1.21	0.83	0.42	0.67	1	0.5	5.6	1.51	4.1	0.42	0.75	0.55	0.96	0.3	
Mn	379	774	787	595	673	532	523	299.7	332.1	524	1370	782	1049	1187	1461	
Fe	285	262	254	293	302	204	296	792	268	424	339	306	405	361	399	
Rb	0.067	0.045	0.042	0.021	0.015	0.022	0.066	4.76	0.061	0.063	0.141	0.026	0.141	0.169	0.192	
Sr	163.7	298	289.4	267	302	190.9	255	190	198.5	207.6	693	1026	1235	1215	612	
Y	263	129.4	113.6	113.9	122.6	159.1	125.1	233.6	232	217.6	1226	268	1138	1088	1378	
Zr	0.16	bdl	bdl	0.108	bdl	0.007	1.7	bdl	0.07	0.22	bdl	bdl	bdl	0.001	bdl	
Cs	0.074	bdl	bdl	bdl	bdl	bdl	0.026	0.254	0.157	0.063	bdl	0.003	bdl	0.128	bdl	
Ba	0.1	0.42	0.5	0.086	0.281	0.134	0.43	20.4	0.093	0.14	0.022	0.13	0.03	0.009	bdl	
La	10.7	7.98	6.19	3.78	5.21	5.16	8.66	0.703	0.918	2.42	27.83	12.89	14.12	16.07	32.34	
Ce	34.2	21.95	16.37	11.6	14.64	14.5	28.4	3.33	4.45	6.59	124.9	57.1	99.8	96.6	124.8	
Pr	9.4	3.43	2.51	1.976	2.58	2.87	4.15	0.657	0.885	1.64	22.21	9.96	29.29	24.7	24.07	
Nd	55	18.1	14.05	10.82	13.76	20.1	19.6	4.72	6.01	10.5	147.4	62.4	265.9	198	149.9	
Sm	21.2	6.62	4.94	4.58	5.27	9.97	5.94	3.38	3.64	5.62	80.9	26.4	285	193	70.8	
Eu	4.87	1.92	1.42	1.492	1.67	3.22	1.89	1.449	1.43	2.02	26.01	7.7	99.6	63.7	23.53	
Gd	29.9	9.49	7.53	7.72	9.4	18.9	9.12	9.94	10.4	14.2	157.5	41.3	494.8	316	138.2	
Tb	4.89	1.8	1.494	1.556	1.96	2.99	2	2.61	2.327	3.32	30.59	8.44	73.5	48.5	28.19	
Dy	34.5	14.48	12.7	12.97	16.25	19.54	16.2	24.24	22.99	27.1	218.3	57.4	354.4	251	219	
Ho	7.65	3.85	3.1	3.23	4.06	4.61	3.76	7.27	6.9	7.11	44.5	9.35	48.53	42.3	47.25	
Er	23.8	14.33	12.68	12.98	14.42	15.57	13.96	26.77	27.84	26.1	116.1	19.2	105.6	113.9	138.1	
Tm	3.42	2.63	2.27	2.267	2.28	2.06	2.49	3.98	4.29	4.2	12.62	1.67	11.14	14	16.49	
Yb	21.42	21.49	18.64	17.48	16.75	12.76	18.6	27	29.45	28.6	63.4	7.6	63.5	83.2	93.1	
Lu	2.66	3.52	3.02	2.641	2.35	1.62	2.6	3.78	4.3	3.77	6.87	0.85	7.37	10.2	11.1	
Pb	15.91	34.44	31.29	24.26	28.9	25.8	23.6	11.82	13.32	18.32	43.9	25.1	56.9	48.1	42.87	
Th	0.79	0.248	0.195	0.0285	0.053	0.101	0.38	0.0077	0.0082	0.307	0.237	0.362	2.154	4	0.231	
U	0.0278	0.217	0.125	0.077	0.098	0.021	0.178	0.025	0.036	0.278	0.816	0.32	2.097	2.16	0.683	

**Table A4-1. Apatite trace-element composition determined by La-ICP-MS. c: core, m: mantle, r:rim**

sample	SHS3	SHS3	SHS3	SHS3	SHS3	SHS3	SHS3	SHS3	SHS3	SHS3	SHS3	SHS3	SIB32	SIB32	SIB32
Analysis#	46	227	41	224	225	43	217	223	222	218	42	226	a1	99	97
SHRIMP	SHS3-16	SHS3-17	SHS3-2	SHS3-21	SHS3-22	SHS3-23	SHS3-3	SHS3-4	SHS3-6	SHS3-7	SHS3-8		SIB32-1	SIB32-1	SIB32-10
zone							r	r	c		c				
EMPA			5					7	8	4	13		1		
Element (ppm)															
Li	0.54	bdl	0.16	bdl	1.3	0.62	1.4	bdl	1.1	bdl	bdl	1.3	1.44	-0.03	1.09
Mg		382.4		352	369		335.4	352	371.5	353.9		359.1	307.7	300.6	300.1
Al	0.1	0.06	bdl	0.16	0.52	20.6	1	0.42	140	18.1	bdl	0.09	4.5	0.33	0.21
Si	1010	838	1070	1034	994	1173	900	1070	1900	994	1148	667	1068	1051	1179
Sc	0.175	0.267	0.257	0.168	0.133	0.169	0.152	0.058	0.64	0.226	0.249	0.248	0.109	0.111	0.09
Ti	0.28	0.73	0.09	0.07	0.24	0.66	0.13	-0.08	0.53	0.04	0.22	0.15	0.3	0.048	0.3
V	0.06	0.023	0.032	0.023	0.045	0.064	0.001	0.002	0.73	0.036	0.025	0.045	0.123	0.04	0.116
Cr	0.59	1.19	0.06	1.13	0.8	0.59	1.18	0.45	1.24	0.67	0.37	0.78	0.65	0.45	0.47
Mn	1285	1399	1506	654	1480	1209	632	802	1345	1008	1545	1550	367.9	315.8	383.3
Fe	378	341	408	294	350	373	275	311	630	344	402	336	278.6	249	299
Rb	0.109	0.18	0.207	0.035	0.2	0.175	0.005	0.047	0.221	0.155	0.249	0.258	bdl	bdl	bdl
Sr	457.9	750	657	1032	673	419.6	877	1053	752	1027	701	686	654.5	465.7	236
Y	1086	1118	1502	244.7	1389	1204	160.1	486	1302	651	1477	1887	31.51	18.75	12.11
Zr	0.0019	0	0.0112	bdl	0.003	0.005	0.013	0.002	0	bdl	0.024	0.004	0.0044	0.0019	bdl
Cs	bdl	bdl	0.0094	0.359	0.221	0.0049	0.168	0.006	bdl	0.017	0.0027	bdl	0.252	0.0066	0.0069
Ba	bdl	bdl	0.002	0.001	0.014	0.29	0.017	bdl	0.01	0.045	bdl	0.079	1.29	bdl	0.073
La	15.08	30.2	31.91	11.56	32.27	15.54	6.03	11.55	36.4	15.69	38.82	49.5	2.86	0.386	0.126
Ce	60.6	121.5	134.6	51.7	134	63.5	28.6	57	148.6	64	151.7	197.2	5.09	1.431	0.412
Pr	13.57	23	24	9.7	23.53	12.33	5.09	12.19	28.16	11.45	27.58	34.8	1.042	0.233	0.0382
Nd	94.9	142.3	157.4	63.4	143.2	84.3	33.7	80.9	182.4	70.7	175.9	220.1	5.06	1.07	0.184
Sm	53.7	72.3	80.3	30.8	68.6	46.9	16.3	45.3	92.4	32.6	86	106.4	1.53	0.398	0.06
Eu	17.48	22.8	25.37	9.55	21.52	16.86	5.05	14.35	29.27	10.8	28.37	34.15	0.547	0.215	0.051
Gd	111.8	134.6	161.8	55.8	124.6	115.4	29.2	75.4	168.3	61.2	169.7	205.9	2.42	0.661	0.329
Tb	22.49	26.2	33.44	11.08	25.79	24.53	6.18	13.75	31.61	13.05	33.53	41.2	0.459	0.198	0.07
Dy	177.8	190.3	250.4	66.2	203.7	198.9	39.9	93.4	225.9	103.9	249.9	316.9	4.01	2.08	0.997
Ho	36.25	40.2	52.18	8.85	47.6	40.01	5.56	17.3	47.7	21.39	53.6	65.6	0.952	0.601	0.341
Er	87.2	121.1	142.6	13.48	154.7	99	9.12	47.5	136.4	57.5	157.7	175.5	3.67	2.54	1.67
Tm	8	15.5	15.81	0.872	20.79	9.35	0.621	4.96	16.49	5.74	19.83	19.72	0.548	0.501	0.293
Yb	33.2	92.7	82.8	3.04	128.4	43.7	2.52	28.9	98.5	27.8	117.4	102.3	4.16	4.01	2.25
Lu	3.21	11.4	9.09	0.314	15.68	4.49	0.264	3.13	11.66	3.14	14.27	11.6	0.67	0.643	0.381
Pb	42.4	41.7	44.27	24.57	43	43.1	19.3	36.1	47.2	32.05	43.72	49	51.63	23.41	13.99
Th	0.046	0.12	0.146	0.046	0.223	0.167	0.042	0.314	0.618	0.112	0.395	0.288	0.105	0.002	0.001
U	0.31	0.528	0.685	0.204	0.691	0.299	0.127	0.538	0.873	0.426	0.747	1.116	0.0227	0.0019	0.0001

**Table A4-1. Apatite trace-element composition determined by La-ICP-MS. c: core, m: mantle, r:rim**

sample	SIB32	SIB32	SIB32	SIB32	SIB32	SIB32	SIB32	SIB32	SIB32	SIB32	SIB50B	SIB50B	SIB50B	SIB50B	SIB50B	SIB50B
Analysis#	96	94	123	91	93	92	100	98	101	134	77	76	132	135	133	
SHRIMP	SIB32-11	SIB32-14	SIB32-15	SIB32-2	SIB32-3	SIB32-4	SIB32-5	SIB32-8	SIB32-9	SIB50B-1	SIB50B-12	SIB50B-14	SIB50B-2	SIB50B-3	SIB50B-4	
zone										c			c	r	r	
EMPA		5			2	3				2			1	6	8	
Element (ppm)																
Li	bdl	bdl	bdl	0.22	0.2	1.26	0.66	0.88	0.71	2.2	1.54	1.84	bdl	2.4	1.4	
Mg	299.2	305.4	444.2	295.1	299.5	306.9	300.6	297	283.9	455	315.4	314.1	456.1	472	479	
Al	0.16	0.04	0.03	0.26	bdl	0.21	0.19	0.16	3	156	-0.08	bdl	25	15.5	0.33	
Si	1218	1096	1066	1170	1162	1094	1047	1116	1153	3460	1288	1226	2060	1170	1247	
Sc	0.09	0.171	0.085	0.145	0.095	0.106	0.104	0.093	0.212	1.41	0.087	0.107	0.79	0.18	0.1	
Ti	0.07	0.34	0.13	0.29	0.09	0.11	0.32	0.22	0.75	370	0.25	0.16	1840	0.22	0.32	
V	0.026	0.14	0.113	0.085	0.034	0.069	0.036	0.093	0.038	16.61	0.087	0.058	12.4	0.147	0.046	
Cr	0.61	0.42	-0.3	0.5	0.55	0.56	0.49	0.3	1.11	1.39	1.02	0.77	3.71	-0.25	0.73	
Mn	317.8	433.1	296	352.9	291.9	455.4	327.2	408.8	280.1	1269	1041.5	1043.4	795	1211	1007	
Fe	260.9	317	272	271	256.7	314	256	309	244	3020	322.8	333	1106	364	306	
Rb	bdl	bdl	bdl	bdl	bdl	bdl	bdl	0.012	0.03	0.13	0.026	0.043	0.092	0.054	0.006	
Sr	512.5	199.3	120	576.9	525.8	389.7	480.9	221.3	514.5	312	334	333.1	1866	446	268.3	
Y	20.49	7.72	7.33	35.5	20.58	25.12	22.87	21.57	23.79	492	375.5	462.7	321.8	212	254.1	
Zr	bdl	bdl	bdl	bdl	0.0007	bdl	0.0007	0.0007	11	17.3	bdl	bdl	86	0.72	0.006	
Cs	0.0094	0.0057	0.009	0.0055	0.0302	0.0064	0.0091	0.0111	0.094	0.006	0.0149	0.0009	bdl	0.003	0.004	
Ba	-0.0049	0.072	-0.01572	0.84	0.006	0.195	bdl	0.064	0.134	0.44	bdl	0.009	21.4	bdl	0.074	
La	0.634	0.057	0.028	1.729	0.545	0.248	0.448	0.161	1.08	177.1	3.213	3.121	765	11.95	1.25	
Ce	2.315	0.161	0.069	4.47	2.013	0.948	1.806	0.605	2.55	579	14.38	14.56	1739	44.6	5.79	
Pr	0.325	0.0266	0.0022	0.617	0.314	0.14	0.314	0.114	0.5	106.1	2.652	2.84	195.1	8.15	1.044	
Nd	1.78	0.087	0.048	3.19	1.54	1	1.49	0.728	2.49	642	19.57	20.02	781	48	7.81	
Sm	0.604	0.01	0.014	0.99	0.593	0.473	0.536	0.321	0.98	154.8	11.97	13.32	130.8	20.3	5.19	
Eu	0.267	0.0234	0.027	0.479	0.321	0.244	0.261	0.175	0.351	32.58	5.18	5.77	33.7	7.41	2.3	
Gd	0.95	0.125	0.059	2.43	0.911	1.23	1.009	1.01	1.3	179	32.68	38.9	111.3	37.5	16.62	
Tb	0.236	0.0458	0.031	0.475	0.241	0.254	0.257	0.203	0.307	20.84	7.81	9.31	13.84	7.21	4.05	
Dy	2.3	0.46	0.57	4.5	2.23	2.57	2.5	1.97	2.98	108.3	66.34	80.45	73.5	45.3	36.3	
Ho	0.668	0.229	0.165	1.147	0.627	0.724	0.723	0.647	0.729	18.31	13.82	16.89	12.07	7.47	8.16	
Er	2.68	1.071	0.96	4.19	2.84	3.25	3.15	2.86	3.25	41.3	32.1	39.03	26.41	14.1	16.87	
Tm	0.524	0.219	0.261	0.581	0.543	0.55	0.557	0.401	0.58	3.97	2.822	3.324	2.51	0.941	1.145	
Yb	4.48	1.7	2.06	4.13	4.6	4.18	4.82	3.18	4.81	20.2	11	13.82	12.5	3.35	4.47	
Lu	0.705	0.315	0.379	0.667	0.71	0.828	0.771	0.546	0.676	2.82	1.073	1.334	1.69	0.371	0.388	
Pb	25.31	10.38	1.81	43.08	25.69	19.85	24.3	10.66	27.14	40.6	34.69	39.31	25.8	55.7	33.46	
Th	0.0012	bdl	0.001	0.0289	0.0021	0.0104	0.0009	0.0016	0.03	58.5	0.0354	0.0316	14.43	0.09	0.0127	
U	0.0104	bdl	bdl	0.0149	0.0094	bdl	0.007	0.005	0.027	0.76	0.092	0.138	3.57	0.286	0.058	

**Table A4-1. Apatite trace-element composition determined by La-ICP-MS. c: core, m: mantle, r:rim**

sample	SIB50B	SIB50B	SIB50B	SIS52	SIS52	SIS52	SIS52	SIS52	SIS52	SIS52	SIS52	SIS52	SIS52	SIS52	SIS52
Analysis#	79	131	130	120	111	109	107	108	116	104	105	119	115	106	110
SHRIMP	SIB50B-5	SIB50B-8	SIB50B-9	SIS52-1	SIS52-10	SIS52-13	SIS52-14	SIS52-15	SIS52-17	SIS52-18	SIS52-19	SIS52-2	SIS52-20	SIS52-21	SIS52-23
zone				c			r						r		
EMPA	7			4									3		
Element ( $\mu\text{g}$ )															
Li	2.07	bdl	1.7	0.1	0.8	0.19	0.7	0.08	1	0.02	0.12	0.8	bdl	1.27	0.56
Mg	294.3	525	461	465	467	282	278	294.9	482	292.8	287.9	494	506	276.8	291.5
Al	bdl	6000	0.37	4.5	600	0.15	1.84	0.49	0.19	0.24	bdl	0.44	208	2.1	0.18
Si	1530	12500	1460	1120	2740	992	1010	912	905	1113	1156	607	930	1096	1011
Sc	0.08	5.57	2.7	1.46	0.12	0.155	0.096	0.108	0.054	0.1	0.126	0.068	0.073	0.08	0.142
Ti	0.17	74	0.4	3.9	620	0.42	4.2	0.73	0.31	0.16	0.17	0.33	4.3	0.6	0.47
V	0.081	119	0.088	30.1	78.7	27.28	29.8	34.1	25.2	27.52	19.09	30.27	38	31.25	28.4
Cr	0.89	6.7	1.13	bdl	1.6	0.28	1.15	0.38	0.32	0.39	0.99	0.53	0.29	0.58	0.39
Mn	1103	1810	1200	673	85	21.43	68	14.95	17.28	20.57	18.64	14.25	14.8	13.79	20.13
Fe	330	7400	286	2550	2310	245	6300	248	228	240.7	244.7	230	329	237	241.2
Rb	0.025	0.055	bdl	bdl	1.18	0.035	bdl	bdl	-0.031	0.01	-0.005	0.047	bdl	0.025	0.003
Sr	431.2	1820	333	389	99.1	245.6	240.9	215.2	222.1	220.9	230.7	232.2	229.1	238.4	233.1
Y	482	197	249.7	409	87.7	42.2	52.6	72.2	56.6	68	24.29	51.8	32.6	58.7	46.21
Zr	0.43	3.71	550	2.06	7.3	bdl	28	0.17	0.0057	bdl	bdl	bdl	6.5	0.0045	0.0017
Cs	bdl	0.087	0.013	bdl	0.057	0.0019	0.003	0.0056	0.028	0.0067	0.0081	0.009	bdl	0.0082	0.0061
Ba	0.096	2.9	bdl	3.05	2.9	0.004	bdl	bdl	0.026	0.003	0.003	bdl	0.035	0.06	bdl
La	4.12	4400	11.06	275	47.6	0.035	0.248	0.049	0.035	0.109	0.037	0.089	0.24	0.75	0.138
Ce	18.21	7300	41.8	662	8.8	0.468	1.57	0.789	0.662	1.396	0.374	1.154	0.46	1.77	1.329
Pr	3.6	593	7.16	127	59.3	0.0294	0.173	0.091	0.059	0.083	0.0229	0.074	0.24	0.36	0.112
Nd	24.6	1660	42	647	291	0.242	1.02	0.673	0.53	0.626	0.075	0.63	1.3	2.56	0.8
Sm	16.72	148	19	159	68.9	0.145	0.53	0.482	0.297	0.394	0.086	0.296	0.51	1.15	0.529
Eu	8.31	32.8	6.82	27.9	14.1	0.109	0.25	0.213	0.157	0.205	0.063	0.138	0.141	0.351	0.186
Gd	51.8	87	36.9	149	50.3	0.89	2.03	1.65	1.29	1.61	0.326	1.26	1.14	2.11	1.48
Tb	11.36	9.32	7.73	15.6	4.88	0.25	0.396	0.421	0.349	0.472	0.145	0.368	0.235	0.501	0.36
Dy	92.2	46.1	50	85.6	19	2.89	4.85	5.27	4.29	5.51	1.49	4.34	2.39	5.42	3.75
Ho	17.58	7.5	8.27	15	2.56	1.038	1.47	2.056	1.608	2.005	0.608	1.571	0.907	1.713	1.329
Er	35.6	16.5	16.8	34.8	5.3	5.49	7.6	10.52	8.73	10.43	3.29	7.94	4.57	8.74	6.46
Tm	2.67	1.68	1.3	4.04	0.41	1.207	1.39	2.059	1.73	2.025	0.698	1.578	0.9	1.678	1.268
Yb	10.6	9.4	5.72	24.1	1.57	10.52	12.9	15.33	14.23	17.64	6.78	12.43	6.88	14.39	11.55
Lu	1.011	1.15	0.65	2.8	0.257	1.93	2.29	2.19	2.28	2.977	1.078	1.85	1.046	2.327	1.982
Pb	60.9	119.6	35.2	0.99	0.54	0.53	0.61	0.603	1	0.837	1.131	0.666	0.265	0.41	0.57
Th	0.048	163	0.94	8.86	1.65	bdl	0.0373	0.001	bdl	bdl	bdl	0.0022	0.028	0.58	0.055
U	0.281	10.4	4.1	3.11	0.018	bdl	0.0041	bdl	bdl	bdl	bdl	0.0031	bdl	bdl	bdl

**Table A4-1. Apatite trace-element composition determined by La-ICP-MS. c: core, m: mantle, r:rim**

sample	SIS52	SIS52	SIS53	SIS53	SIS53	SIS53	SIS53	SIS53	SIS53	SIS53	SIS53	SIS53	SIS53	SIS53	SIS53
Analysis#	121	118	a2	126	128	a3	a4	a5	124	80	a6	125	a7	129	a8
SHRIMP	SIS52-3	SIS52-4	SIS53-1	SIS53-10	SIS53-11	SIS53-13	SIS53-14	SIS53-15	SIS53-16	SIS53-17	SIS53-18	SIS53-3	SIS53-4	SIS53-5	SIS53-6
zone	r	c			c	r		r				c			
EMPA	5	2	3		1							2	5		
Element ( $\mu\text{g}$ )															
Li	0.6	1.3	0.89	0.3	0.8	1.05	0.92	1.09	1.2	1.5	0.23	0.6	0.75	0.8	0.38
Mg	454	463	304.3	466	456	321.6	323.2	320	478	321.1	325.1	434	315.6	476	294.1
Al	0.57	560	0.04	0.72	556	1.2	-0.07	0.2	130	0.45	0.08	1350	-0.15	bdl	0.11
Si	953	4000	1306	957	3040	1043	1134	1217	3930	1319	1138	5190	1191	1283	1141
Sc	0.21	0.5	0.103	0.2	0.47	0.146	0.129	0.094	0.69	0.197	0.206	0.42	0.104	0.099	0.092
Ti	bdl	19.8	0.073	1.6	293	0.34	0.27	0.1	15.4	11700	0.036	325	0.13	0.3	0.28
V	39.9	79.6	0.037	0.065	14.7	0.072	0.032	0.036	4.71	3.7	0.02	85	0.022	0.054	0.042
Cr	0.38	1.13	0.85	0.18	1.8	0.78	0.37	0.82	bdl	4.6	0.93	1.77	0.55	0.9	0.68
Mn	10.84	195	752	714	779	927	817	758	791	525.4	813	594	703	816	931
Fe	238	1860	317.8	331	1710	296.7	321.1	314.8	528	532	319.3	6000	342.2	258	310
Rb	0.013	1.68	0.017	0.061	1.18	0.032	0.032	0.012	0.13	0.029	0.004	2.56	0.009	0.045	0.037
Sr	223.2	934	532	764	1800	495.4	670.3	619.6	551	678.4	734.2	780	720	494	517
Y	54.6	314	202.2	348	288.6	277	298.7	228.4	267	245.4	296.1	229	303.8	331.4	298.9
Zr	bdl	7.75	0.003	bdl	12.8	bdl	bdl	bdl	54	0.163	23	18.8	bdl	bdl	bdl
Cs	bdl	0.084	0.0102	0.01	0.042	0.0084	0.0067	0.0081	0.017	0.0084	0.0032	0.125	0.0075	0.013	bdl
Ba	bdl	7.1	0.058	0.004	9.9	0.036	0.058	0.06	3.13	0.275	0.072	14.2	0.114	bdl	0.083
La	0.072	813	1.41	4.21	481	1.569	2.886	2.097	189	3.04	3.291	261	4	1.464	1.85
Ce	1.245	1814	6.72	19.27	1179	6.81	11.54	9.69	499	13.6	14.64	579	17.69	6.72	8.2
Pr	0.117	317	1.334	3.55	144	1.262	2.268	1.756	64.1	2.57	2.923	129	3.375	1.278	1.693
Nd	0.75	1446	9.11	26.7	628	8.63	15.35	12.38	287	18.66	20.82	652	23.89	9.9	12.09
Sm	0.54	286	5.71	16.41	100	5.42	9.63	7.54	60.7	12.11	13.75	137.4	14.91	6.49	8.12
Eu	0.165	58.7	2.17	6.25	26.4	2.021	3.62	2.68	14	4.73	5.02	28.2	5.55	2.47	3.26
Gd	1.85	204	14.57	42	102.7	14.42	24.14	19.18	60.3	31.91	34.01	100.2	37.07	17.93	23.07
Tb	0.488	19.99	3.56	9.51	11.05	3.612	5.98	4.5	7.3	7.77	8.02	10.83	8.65	4.65	5.66
Dy	4.86	83	32.5	76.9	56.5	35.53	53.21	39.46	48.3	59.71	64.93	51.4	68.64	45.7	53.5
Ho	1.63	11.52	6.89	12.33	10.02	9	10.29	7.81	9.06	9.08	10.71	7.59	11.24	10.83	10.66
Er	8.84	24.5	13.99	20.23	21.3	21.02	18.13	14.95	20.6	13.41	16	16.3	18.08	21.66	16.87
Tm	1.65	2.56	0.958	1.224	2.04	1.48	1.21	0.93	1.95	0.87	0.966	1.42	1.192	1.319	0.909
Yb	12.24	14	3.4	4.44	10.93	5.39	4.14	3.01	8.63	2.79	3.04	5.5	4.24	4.02	2.74
Lu	1.62	1.58	0.298	0.382	1.29	0.465	0.354	0.275	0.78	0.277	0.314	0.65	0.392	0.331	0.241
Pb	0.49	2.2	12.76	17.53	8.8	6.08	14.82	14.84	9.55	15.47	17.39	9.7	17.12	10.63	12.17
Th	bdl	59.5	0.0155	0.055	14.9	0.0133	0.92	0.0138	9.5	0.061	0.057	8.37	0.0204	bdl	0.029
U	bdl	6.26	0.062	0.156	1.99	0.04	0.117	0.105	1.35	0.311	0.33	0.64	0.181	0.038	0.052

**Table A4-1. Apatite trace-element composition determined by La-ICP-MS. c: core, m: mantle, r:rim**

sample	SIS53	SIS53	SIS52	SIS52	SIS52	SIS52	SIS52
Analysis#	127	a9	112	102	103	113	114
SHRIMP	SIS53-7	SIS53-8					
zone							
EMPA							
Element (ppm)							
Li	0.7	0.79	0.4	0.22	1.2	0.8	0.2
Mg	447	292	483.6	271.3	274	481	491
Al	4.8	0.41	52	0.12	33	bdl	11.1
Si	1040	1194	895	986	1140	570	752
Sc	0.028	0.193	0.065	0.155	0.076	0.088	0.121
Ti	13.7	890	0.41	0.61	0.21	0.08	0.68
V	0.25	1.6	25.91	30.6	28.2	28.2	20.28
Cr	0.07	1.31	0.32	0.24	0.17	0.54	0.67
Mn	1099	854	26.89	17.26	20	8.98	18.76
Fe	438	2500	236	239	262	215	232
Rb	0.067	0.035	0.003	-0.002	0.17	0.007	0.013
Sr	406	658	243	235.4	219	194.8	226.3
Y	171.3	298.2	41.4	66.6	62.9	16.52	32.41
Zr	15.9	0.009	0.97	0.002	bdl	bdl	0.0053
Cs	0.007	0.0052	0.007	0.003	0.034	0.022	0.02
Ba	0.32	0.118	0.01	0.024	0.21	0.101	0.006
La	0.737	2.38	0.053	0.101	0.069	0.078	0.192
Ce	2.91	10.61	0.919	1.55	1.163	0.291	0.596
Pr	0.533	2.08	0.06	0.076	0.04	0.049	0.123
Nd	3.44	14.5	0.48	0.66	0.52	0.22	0.8
Sm	2.52	8.5	0.36	0.54	0.41	0.134	0.37
Eu	1.04	3.17	0.139	0.202	0.153	0.043	0.158
Gd	8.2	21.54	0.99	1.57	1.69	0.32	1.19
Tb	2.2	5.39	0.278	0.455	0.401	0.068	0.255
Dy	22.8	48.3	3.36	4.77	4.67	1.02	2.6
Ho	5.37	9.97	1.228	1.79	1.77	0.411	0.914
Er	12.29	18.78	6	8.74	10.2	2.46	4.67
Tm	0.921	1.21	1.232	1.85	2	0.514	0.915
Yb	3.58	4.07	10.23	14.26	16.64	4.57	7.57
Lu	0.31	0.333	1.668	2.36	2.73	0.673	1.351
Pb	11.19	13.72	0.901	0.61	0.914	0.76	1.262
Th	0.79	0.18	bdl	0.021	bdl	0.066	0.019
U	0.206	0.131	bdl	0.0006	bdl	bdl	bdl

Table A4 - 2: EMPA data for clinpyroxene

SAMPLE	SHB45	SHB45	SHB45	SHB45	SHB45	SHB45	SHB45	SHB45	SHB45	SHB45	SHB45	SHB45
Analysis #	Cpx5	Cpx5	Cpx5	cpx1	Cpx5	Cpx4	cpx1	Cpx4	Cpx2	Cpx2	Cpx4	Cpx5
zone	142	146	148	89	143	120	88	129	113	118	121	140
	core	core	core	core	core	core	core	core	core	core	core	core
SiO <sub>2</sub>	55.47	55.22	55.29	55.24	55.55	54.99	55.65	55.35	55.29	55.42	55.69	55.05
TiO <sub>2</sub>	0.10	0.11	0.06	0.09	0.16	0.07	0.12	0.11	0.20	0.14	0.05	0.04
Al <sub>2</sub> O <sub>3</sub>	10.94	9.57	9.73	9.87	10.52	9.96	10.45	9.74	10.89	10.91	10.49	9.26
Cr <sub>2</sub> O <sub>3</sub>	0.07	0.18	0.04	0.00	0.02	0.00	0.02	0.11	0.06	0.01	0.19	0.10
FeO	7.74	7.96	7.97	7.98	8.01	8.01	8.08	8.10	8.11	8.13	8.16	8.22
MnO	0.13	0.01	0.03	0.16	0.14	0.10	0.09	0.04	0.06	0.11	0.14	0.02
MgO	6.52	7.36	7.20	7.17	6.92	6.92	6.66	7.28	6.55	6.64	6.73	7.60
CaO	11.78	13.04	13.15	13.26	12.61	12.67	12.14	13.12	11.85	12.16	12.41	13.64
Na <sub>2</sub> O	7.50	6.66	6.77	6.74	7.18	7.12	7.05	7.20	7.60	7.35	7.10	6.42
<b>TOTAL</b>	<b>100.24</b>	<b>100.10</b>	<b>100.25</b>	<b>100.55</b>	<b>101.14</b>	<b>99.85</b>	<b>100.32</b>	<b>101.05</b>	<b>100.61</b>	<b>100.87</b>	<b>100.98</b>	<b>100.35</b>
<b>Cations - 6 oxygen formula</b>												
Si	1.98	1.99	1.98	1.98	1.97	1.98	2.00	1.96	1.97	1.97	1.98	1.98
Ti	0.00	0.00	0.00	0.00	0.00	0.00	0.00	0.00	0.01	0.00	0.00	0.00
Al	0.46	0.41	0.41	0.42	0.44	0.42	0.44	0.41	0.46	0.46	0.44	0.39
Fe <sup>3+</sup>	0.09	0.08	0.09	0.09	0.10	0.12	0.05	0.15	0.12	0.10	0.08	0.10
Cr <sup>3+</sup>	0.00	0.00	0.00	0.00	0.00	0.00	0.00	0.00	0.00	0.00	0.01	0.00
Fe <sup>2+</sup>	0.14	0.16	0.15	0.15	0.13	0.12	0.19	0.09	0.12	0.14	0.17	0.15
Mn	0.00	0.00	0.00	0.00	0.00	0.00	0.00	0.00	0.00	0.00	0.00	0.00
Mg	0.35	0.39	0.39	0.38	0.37	0.37	0.36	0.39	0.35	0.35	0.36	0.41
Ca	0.45	0.50	0.51	0.51	0.48	0.49	0.47	0.50	0.45	0.46	0.47	0.52
Na	0.52	0.46	0.47	0.47	0.49	0.50	0.49	0.50	0.52	0.51	0.49	0.45
<b>Mol%</b>												
Aegerine	9	8	9	9	11	12	5	15	12	10	8	10
Jadeite	44	40	39	39	40	39	46	35	42	42	43	36
Diopside	46	52	52	52	49	50	49	50	46	48	49	54

Table A4 - 2: EMPA data for clinpyroxene

SAMPLE	SHB45	SHB45	SHB45	SHB45	SHB45	SHB45	SHB45	SHB45	SHB45	SHB45	SHB45
Analysis #	Cpx2	cpx1	Cpx4	Cpx2	Cpx2	Cpx2	cpx1	Cpx2	Cpx2	Cpx4	Cpx2
zone	107	90	123	112	106	116	91	111	114	119	110
	core	core	core	core	core	core	core	core	core	core	core
SiO <sub>2</sub>	55.06	55.55	55.30	55.01	55.25	55.29	55.28	55.61	55.36	55.24	55.27
TiO <sub>2</sub>	0.13	0.03	0.15	bdl	0.11	bdl	0.13	0.05	0.10	bdl	0.21
Al <sub>2</sub> O <sub>3</sub>	9.43	9.21	9.56	8.83	9.51	9.29	9.11	9.46	9.11	8.63	9.51
Cr <sub>2</sub> O <sub>3</sub>	0.05	0.06	0.02	0.07	0.03	0.09	0.05	0.01	0.02	0.08	0.02
FeO	8.24	8.31	8.36	8.38	8.38	8.40	8.40	8.42	8.48	8.49	8.49
MnO	0.03	0.16	0.05	0.18	0.07	0.13	0.15	0.02	0.06	0.17	0.01
MgO	7.44	7.24	7.31	7.38	7.21	7.28	7.18	7.41	7.60	7.65	7.31
CaO	13.54	13.32	13.03	13.86	13.12	13.13	13.41	13.37	13.82	14.02	13.18
Na <sub>2</sub> O	6.41	6.71	6.65	6.38	6.81	6.63	6.78	6.78	6.40	6.27	6.73
<b>TOTAL</b>	100.35	100.59	100.44	100.11	100.51	100.24	100.51	101.12	100.97	100.54	100.74
<b>Cations - 6 oxy<sub>i</sub></b>											
Si	1.98	1.99	1.98	1.98	1.98	1.99	1.98	1.98	1.98	1.99	1.98
Ti	0.00	0.00	0.00	0.00	0.00	0.00	0.00	0.00	0.00	0.00	0.01
Al	0.40	0.39	0.40	0.38	0.40	0.39	0.39	0.40	0.38	0.37	0.40
Fe <sup>3+</sup>	0.08	0.09	0.08	0.10	0.11	0.09	0.11	0.11	0.10	0.10	0.10
Cr <sup>3+</sup>	0.00	0.00	0.00	0.00	0.00	0.00	0.00	0.00	0.00	0.00	0.00
Fe <sup>2+</sup>	0.17	0.16	0.17	0.15	0.14	0.16	0.14	0.14	0.16	0.16	0.15
Mn	0.00	0.00	0.00	0.01	0.00	0.00	0.00	0.00	0.00	0.01	0.00
Mg	0.40	0.39	0.39	0.40	0.39	0.39	0.38	0.39	0.41	0.41	0.39
Ca	0.52	0.51	0.50	0.54	0.50	0.51	0.52	0.51	0.53	0.54	0.51
Na	0.45	0.47	0.46	0.45	0.47	0.46	0.47	0.47	0.44	0.44	0.47
<b>Mol%</b>											
Aegerine	8	10	9	10	11	9	11	11	10	10	10
Jadeite	38	38	39	35	37	39	36	37	36	35	38
Diopside	54	52	52	55	52	52	52	52	54	55	52



Table A4 - 2: EMPA data for clinpyroxene

SAMPLE	SHB45	SHB45	SHB45	SHB45	SHB45	SHB45	SHB45	SHB45	SHB45	SHB45	SHB45
Analysis #	Cpx4	Cpx4	Cpx4	cpx1	Cpx5	Cpx2	Cpx4	Cpx2	Cpx4	Cpx5	Cpx4
zone	127	126	124	87	149	109	122	108	125	141	128
	rim	rim	rim	rim	rim	rim	rim	rim	rim	rim	rim
SiO <sub>2</sub>	54.90	55.15	55.83	55.00	54.90	55.04	54.91	54.80	54.70	54.85	54.64
TiO <sub>2</sub>	0.07	0.05	0.06	0.08	bdl	0.05	0.00	0.08	0.12	0.04	0.04
Al <sub>2</sub> O <sub>3</sub>	4.64	7.03	7.18	6.42	5.49	5.24	6.41	6.08	6.09	6.13	6.92
Cr <sub>2</sub> O <sub>3</sub>	0.06	0.10	0.02	0.05	0.03	0.00	0.06	0.10	0.16	0.01	bdl
FeO	10.00	10.08	10.44	10.54	10.55	10.61	10.30	10.38	10.44	10.44	10.46
MnO	0.12	0.05	0.13	0.03	0.07	0.11	0.11	0.06	0.05	0.01	0.05
MgO	9.21	7.70	7.29	7.63	8.35	8.63	7.98	8.23	8.16	8.21	7.43
CaO	16.18	13.26	13.28	13.67	15.04	15.47	14.40	14.62	14.81	14.43	13.67
Na <sub>2</sub> O	5.01	6.33	6.66	6.44	5.68	5.28	6.16	5.77	5.97	5.91	6.44
<b>TOTAL</b>	100.20	99.76	100.90	99.85	100.12	100.44	100.32	100.11	100.50	100.06	99.67
<b>Cations - 6 oxy<sub>i</sub></b>											
Si	2.00	2.01	2.01	2.00	2.00	2.00	1.99	1.99	1.98	1.99	1.99
Ti	0.00	0.00	0.00	0.00	0.00	0.00	0.00	0.00	0.00	0.00	0.00
Al	0.20	0.30	0.30	0.28	0.24	0.22	0.27	0.26	0.26	0.26	0.30
Fe <sup>3+</sup>	0.15	0.13	0.14	0.17	0.17	0.14	0.18	0.15	0.19	0.17	0.18
Cr <sup>3+</sup>	0.00	0.00	0.00	0.00	0.00	0.00	0.00	0.00	0.00	0.00	0.00
Fe <sup>2+</sup>	0.16	0.18	0.17	0.15	0.15	0.18	0.13	0.16	0.13	0.15	0.14
Mn	0.00	0.00	0.00	0.00	0.00	0.00	0.00	0.00	0.00	0.00	0.00
Mg	0.50	0.42	0.39	0.41	0.45	0.47	0.43	0.45	0.44	0.45	0.40
Ca	0.63	0.52	0.51	0.53	0.59	0.60	0.56	0.57	0.57	0.56	0.53
Na	0.35	0.45	0.46	0.45	0.40	0.37	0.43	0.41	0.42	0.42	0.45
<b>Mol%</b>											
Aegerine	15	13	14	18	17	14	18	16	19	17	18
Jadeite	21	33	33	28	24	24	25	26	23	26	28
Diopside	64	54	52	54	59	62	56	58	58	57	54

Table A4 - 2: EMPA data for clinpyroxene

SAMPLE	SHB45	SHB45	SHB45	SHB45	SHB45	SHB45	SHB45	SHB12A	SHB12A	SHB12A	SHB12A
Analysis #	cpx1	Cpx2	Cpx5	Cpx5	Cpx5	Cpx2	Cpx4	cpx1	cpx1b	cpx1	cpx1
zone	86	115	147	145	144	117	130	424	429	427	428
	rim	rim	rim	rim	rim	rim	rim	core	core	core	core
SiO <sub>2</sub>	53.94	55.02	54.85	54.68	54.73	55.06	53.71	54.47	55.16	55.84	54.51
TiO <sub>2</sub>	0.01	0.06	0.01	0.04	bdl	0.11	0.01	0.12	bdl	0.16	0.11
Al <sub>2</sub> O <sub>3</sub>	5.33	6.08	6.52	5.99	6.54	7.05	5.97	10.62	10.89	11.18	10.54
Cr <sub>2</sub> O <sub>3</sub>	0.00	0.08	0.00	0.01	0.00	0.09	0.19	0.03	0.03	0.03	0.09
FeO	10.55	10.62	10.77	10.79	10.80	10.81	10.95	5.93	6.13	5.98	6.05
MnO	0.14	0.02	0.05	0.04	0.03	0.06	0.11	0.10	0.12	0.14	0.10
MgO	8.34	8.09	7.63	8.14	7.68	7.49	7.50	8.05	7.96	7.98	7.83
CaO	14.87	14.65	14.12	14.28	13.67	13.27	13.98	13.82	13.87	13.41	14.03
Na <sub>2</sub> O	5.82	5.92	6.20	6.12	6.19	6.57	5.77	6.34	6.52	6.81	6.27
<b>TOTAL</b>	<b>99.00</b>	<b>100.54</b>	<b>100.15</b>	<b>100.11</b>	<b>99.63</b>	<b>100.50</b>	<b>98.24</b>	<b>99.49</b>	<b>100.67</b>	<b>101.53</b>	<b>99.55</b>
<b>Cations - 6 oxy<sub>i</sub></b>											
Si	1.98	1.99	1.99	1.99	2.00	1.99	2.00	1.96	1.96	1.96	1.96
Ti	0.00	0.00	0.00	0.00	0.00	0.00	0.00	0.00	0.00	0.00	0.00
Al	0.23	0.26	0.28	0.26	0.28	0.30	0.26	0.45	0.46	0.46	0.45
Fe <sup>3+</sup>	0.22	0.16	0.17	0.20	0.16	0.17	0.16	0.07	0.07	0.06	0.06
Cr <sup>3+</sup>	0.00	0.00	0.00	0.00	0.00	0.00	0.01	0.00	0.00	0.00	0.00
Fe <sup>2+</sup>	0.11	0.16	0.16	0.12	0.17	0.15	0.18	0.11	0.11	0.11	0.13
Mn	0.00	0.00	0.00	0.00	0.00	0.00	0.00	0.00	0.00	0.00	0.00
Mg	0.46	0.44	0.41	0.44	0.42	0.40	0.42	0.43	0.42	0.42	0.42
Ca	0.59	0.57	0.55	0.56	0.53	0.51	0.56	0.53	0.53	0.51	0.54
Na	0.41	0.42	0.44	0.43	0.44	0.46	0.42	0.44	0.45	0.46	0.44
<b>Mol%</b>											
Aegerine	22	17	17	21	17	18	16	7	8	7	6
Jadeite	20	26	27	23	28	29	27	38	38	41	39
Diopside	59	58	56	56	55	53	57	55	54	52	55

Table A4 - 2: EMPA data for clinpyroxene

SAMPLE	SHB12A	SHB12A	SHB12A	SHB12A	SHB12A	SHB12B	SHB12B	SHB12B	SHB12A	SHB12B	SHB12B	SHB12A
Analysis #	cpx1	cpx1	cpx1b	cpx1	cpx1	cpx1	cpx1b	cpx1	cpx1	cpx1	cpx1b	cpx1
zone	413	414	438	412	425	220	238	221	420	222	231	415
	core	core	core	core	core	core	core	core	core	core	core	core
SiO <sub>2</sub>	55.00	55.37	55.33	55.47	55.16	55.32	55.70	55.64	55.51	55.77	55.65	55.68
TiO <sub>2</sub>	0.17	0.02	0.09	0.05	bdl	0.11	0.05	0.18	0.08	0.04	0.04	0.11
Al <sub>2</sub> O <sub>3</sub>	10.91	10.93	10.89	10.74	10.72	10.58	10.90	10.86	10.81	10.68	11.04	10.56
Cr <sub>2</sub> O <sub>3</sub>	0.06	0.01	0.06	0.10	0.07	0.08	0.14	bdl	0.02	bdl	0.09	0.14
FeO	5.87	6.02	5.83	6.08	5.98	6.25	5.91	6.19	5.82	5.89	6.00	6.12
MnO	0.15	0.13	0.22	0.14	0.11	0.08	0.06	0.10	0.18	0.10	0.08	0.13
MgO	7.87	7.90	7.96	8.10	8.10	7.93	7.70	7.83	7.96	7.81	7.81	8.07
CaO	13.70	13.72	13.45	13.88	13.83	13.58	13.25	13.50	13.69	13.68	13.64	14.10
Na <sub>2</sub> O	6.45	6.53	6.54	6.41	6.28	6.48	6.77	6.64	6.44	6.57	6.52	6.25
<b>TOTAL</b>	100.17	100.63	100.39	100.97	100.25	100.45	100.48	100.99	100.52	100.55	100.88	101.17
<b>Cations - 6 oxy<sub>i</sub></b>												
Si	1.96	1.97	1.97	1.97	1.97	1.97	1.98	1.97	1.98	1.98	1.97	1.97
Ti	0.00	0.00	0.00	0.00	0.00	0.00	0.00	0.00	0.00	0.00	0.00	0.00
Al	0.46	0.46	0.46	0.45	0.45	0.44	0.46	0.45	0.45	0.45	0.46	0.44
Fe <sup>3+</sup>	0.05	0.06	0.05	0.05	0.04	0.05	0.04	0.05	0.03	0.04	0.03	0.03
Cr <sup>3+</sup>	0.00	0.00	0.00	0.00	0.00	0.00	0.00	0.00	0.00	0.00	0.00	0.00
Fe <sup>2+</sup>	0.13	0.12	0.13	0.13	0.14	0.14	0.13	0.13	0.14	0.14	0.14	0.15
Mn	0.00	0.00	0.01	0.00	0.00	0.00	0.00	0.00	0.01	0.00	0.00	0.00
Mg	0.42	0.42	0.42	0.43	0.43	0.42	0.41	0.41	0.42	0.41	0.41	0.43
Ca	0.52	0.52	0.51	0.53	0.53	0.52	0.50	0.51	0.52	0.52	0.52	0.54
Na	0.45	0.45	0.45	0.44	0.43	0.45	0.47	0.46	0.44	0.45	0.45	0.43
<b>Mol%</b>												
Aegerine	5	6	5	5	4	5	4	5	4	4	3	3
Jadeite	41	41	42	40	41	41	44	42	42	43	43	41
Diopside	54	54	53	54	55	54	52	53	54	54	54	55

Table A4 - 2: EMPA data for clinpyroxene

SAMPLE	SHB12A	SHB12B	SHB12A	SHB12B	SHB12A	SHB12A	SHB12A	SHB12A	SHB12A	SHB12A	SHB12B
Analysis #	cpx1b	cpx1b	cpx1b	cpx1b	cpx1	cpx1	cpx1b	cpx1b	cpx1b	cpx1b	cpx1b
zone	430	235	432	233	417	423	440	433	439	431	234
	rim	rim	rim	rim	rim	rim	rim	rim	rim	rim	rim
SiO <sub>2</sub>	56.12	55.55	55.55	55.29	55.26	55.31	54.79	54.11	54.95	54.94	54.72
TiO <sub>2</sub>	0.03	bdl	0.03	0.03	0.05	0.05	0.02	bdl	bdl	bdl	0.03
Al <sub>2</sub> O <sub>3</sub>	8.89	9.76	8.94	7.57	7.28	7.85	6.74	5.37	6.33	5.39	6.41
Cr <sub>2</sub> O <sub>3</sub>	0.14	0.05	bdl	0.06	0.02	bdl	bdl	0.02	0.08	0.03	0.08
FeO	6.87	7.42	7.98	8.13	8.86	9.42	9.48	9.76	9.90	10.29	10.30
MnO	0.11	0.10	0.13	0.19	0.15	0.08	0.24	0.20	0.21	0.18	0.10
MgO	8.53	7.14	7.76	8.35	8.32	7.46	7.99	8.81	8.34	8.90	7.86
CaO	14.52	12.45	13.45	14.79	14.40	12.91	13.80	15.13	14.25	15.19	13.83
Na <sub>2</sub> O	6.34	7.22	6.82	5.90	6.37	6.98	6.33	5.60	6.10	5.59	6.32
<b>TOTAL</b>	101.56	99.71	100.66	100.32	100.73	100.08	99.40	98.98	100.18	100.51	99.68
<b>Cations - 6 oxy</b>											
Si	1.98	2.00	1.98	1.99	1.98	1.99	1.99	1.99	1.99	1.99	1.99
Ti	0.00	0.00	0.00	0.00	0.00	0.00	0.00	0.00	0.00	0.00	0.00
Al	0.37	0.41	0.38	0.32	0.31	0.33	0.29	0.23	0.27	0.23	0.27
Fe <sup>3+</sup>	0.09	0.10	0.13	0.10	0.17	0.17	0.17	0.19	0.18	0.18	0.18
Cr <sup>3+</sup>	0.00	0.00	0.00	0.00	0.00	0.00	0.00	0.00	0.00	0.00	0.00
Fe <sup>2+</sup>	0.11	0.12	0.11	0.14	0.09	0.12	0.12	0.11	0.12	0.13	0.13
Mn	0.00	0.00	0.00	0.01	0.00	0.00	0.01	0.01	0.01	0.01	0.00
Mg	0.45	0.38	0.41	0.45	0.44	0.40	0.43	0.48	0.45	0.48	0.43
Ca	0.55	0.48	0.51	0.57	0.55	0.50	0.54	0.59	0.55	0.59	0.54
Na	0.43	0.50	0.47	0.41	0.44	0.49	0.45	0.40	0.43	0.39	0.45
<b>Mol%</b>											
Aegerine	9	10	13	10	17	17	17	19	18	19	19
Jadeite	35	41	35	31	27	33	28	21	25	21	27
Diopside	56	49	52	58	56	51	55	60	56	60	55

Table A4 - 2: EMPA data for clinpyroxene

SAMPLE	SHB12A	SHB12B	SHB12B	SHB12B	SHB12A	SHB12A	SHB12B	SHB12A	SHB05	SHB05
Analysis #	cpx1	cpx1	cpx1b	cpx1	cpx1	cpx1	cpx1	cpx1b	cpx4	cpx2
zone	rim	rim	rim	rim	rim	rim	rim	l.rim		
SiO <sub>2</sub>	54.11	55.28	55.18	54.99	54.43	54.79	54.66	51.64	52.54	52.67
TiO <sub>2</sub>	0.01	0.05	0.02	0.03	bdl	0.12	0.03	0.05	0.11	bdl
Al <sub>2</sub> O <sub>3</sub>	4.99	6.48	7.24	5.64	3.26	4.80	5.32	6.48	5.40	4.91
Cr <sub>2</sub> O <sub>3</sub>	0.03	0.01	0.08	0.03	bdl	0.04	0.05	0.02	bdl	0.25
FeO	10.48	10.53	10.70	10.81	11.87	11.97	12.31	10.41	12.63	12.61
MnO	0.22	0.05	0.14	0.15	0.11	0.09	0.06	0.14	0.05	0.02
MgO	8.69	7.97	7.17	8.28	9.30	8.10	7.76	7.57	7.28	7.68
CaO	15.03	13.73	12.31	14.16	15.82	14.06	13.54	13.70	13.82	14.25
Na <sub>2</sub> O	5.54	6.49	6.96	6.17	5.08	6.15	6.37	6.46	6.24	5.93
<b>TOTAL</b>	<b>99.12</b>	<b>100.61</b>	<b>99.80</b>	<b>100.27</b>	<b>99.88</b>	<b>100.14</b>	<b>100.11</b>	<b>96.51</b>	<b>98.08</b>	<b>98.32</b>
<b>Cations - 6 oxy<sub>i</sub></b>										
Si	1.99	1.99	2.00	1.99	2.00	2.00	1.99	1.94	1.96	1.96
Ti	0.00	0.00	0.00	0.00	0.00	0.00	0.00	0.00	0.00	0.00
Al	0.22	0.28	0.31	0.24	0.14	0.21	0.23	0.29	0.24	0.22
Fe <sup>3+</sup>	0.20	0.19	0.17	0.20	0.23	0.23	0.23	0.31	0.29	0.28
Cr <sup>3+</sup>	0.00	0.00	0.00	0.00	0.00	0.00	0.00	0.00	0.00	0.01
Fe <sup>2+</sup>	0.12	0.13	0.15	0.12	0.14	0.14	0.14	0.02	0.10	0.11
Mn	0.01	0.00	0.00	0.00	0.00	0.00	0.00	0.00	0.00	0.00
Mg	0.48	0.43	0.39	0.45	0.51	0.44	0.42	0.42	0.40	0.43
Ca	0.59	0.53	0.48	0.55	0.62	0.55	0.53	0.55	0.55	0.57
Na	0.39	0.45	0.49	0.43	0.36	0.43	0.45	0.47	0.45	0.43
<b>Mol%</b>										
Aegerine	20	20	18	21	23	23	24	30	29	28
Jadeite	20	27	33	23	14	21	22	16	16	15
Diopside	60	54	49	56	63	56	54	54	55	57

Table A4 - 2: EMPA data for clinpyroxene

SAMPLE	SHB05	SHB05	SHB05	SHB05	SHB05	SHB05	SHB05	SHB05	SHB05	SHB05	SHB05	SHB05
Analysis #	cpx3	cpx4	cpx3	cpx2	cpx4	cpx3	cpx3	cpx2	cpx3	cpx2	cpx2	cpx4
zone	479	493	483	465	495	480	481	469	478	467	468	490
SiO <sub>2</sub>	52.99	53.62	52.53	53.55	53.56	53.98	53.70	53.95	53.44	54.18	53.64	54.32
TiO <sub>2</sub>	0.15	0.07	bdl	0.18	0.02	0.13	0.02	0.02	0.02	0.04	bdl	0.03
Al <sub>2</sub> O <sub>3</sub>	5.20	5.57	4.97	4.82	3.73	5.36	4.57	5.10	4.72	4.96	4.14	4.53
Cr <sub>2</sub> O <sub>3</sub>	0.11	0.01	0.02	0.18	0.32	0.08	0.03	0.11	0.07	0.18	0.12	0.50
FeO	12.83	13.16	12.42	12.86	12.81	12.28	12.97	12.74	13.28	12.66	12.35	11.92
MnO	0.04	0.08	0.07	0.18	0.07	0.02	0.06	0.12	0.07	0.04	0.10	0.07
MgO	7.22	7.25	7.58	7.39	8.36	7.42	7.95	7.41	7.35	7.63	8.00	7.99
CaO	14.25	13.63	14.27	14.29	15.70	14.30	14.46	14.17	14.08	14.18	15.70	15.22
Na <sub>2</sub> O	6.12	6.36	5.62	5.84	4.99	5.85	5.61	6.00	6.01	6.10	5.13	5.53
<b>TOTAL</b>	<b>98.94</b>	<b>99.78</b>	<b>97.47</b>	<b>99.29</b>	<b>99.57</b>	<b>99.44</b>	<b>99.40</b>	<b>99.64</b>	<b>99.04</b>	<b>99.99</b>	<b>99.20</b>	<b>100.11</b>
<b>Cations - 6 oxy<sub>i</sub></b>												
Si	1.96	1.97	1.98	1.98	1.98	1.99	1.98	1.99	1.98	1.98	1.99	1.99
Ti	0.00	0.00	0.00	0.01	0.00	0.00	0.00	0.00	0.00	0.00	0.00	0.00
Al	0.23	0.24	0.22	0.21	0.16	0.23	0.20	0.22	0.21	0.21	0.18	0.20
Fe <sup>3+</sup>	0.28	0.28	0.24	0.23	0.22	0.20	0.23	0.23	0.26	0.25	0.20	0.20
Cr <sup>3+</sup>	0.00	0.00	0.00	0.01	0.01	0.00	0.00	0.00	0.00	0.01	0.00	0.01
Fe <sup>2+</sup>	0.12	0.13	0.15	0.17	0.18	0.18	0.17	0.16	0.15	0.14	0.18	0.17
Mn	0.00	0.00	0.00	0.01	0.00	0.00	0.00	0.00	0.00	0.00	0.00	0.00
Mg	0.40	0.40	0.42	0.41	0.46	0.41	0.44	0.41	0.41	0.42	0.44	0.44
Ca	0.57	0.54	0.58	0.57	0.62	0.56	0.57	0.56	0.56	0.56	0.62	0.60
Na	0.44	0.45	0.41	0.42	0.36	0.42	0.40	0.43	0.43	0.43	0.37	0.39
<b>Mol%</b>												
Aegerine	28	28	24	23	22	20	24	24	26	25	20	20
Jadeite	16	18	18	19	14	23	17	20	17	19	17	20
Diopside	56	54	58	57	63	57	59	57	56	56	63	60

Table A4 - 2: EMPA data for clinpyroxene

SAMPLE	SHB05	SHB05	SHB05	SHB05	SHB05	SHB05	SHB05	SHB05	SHB05	SHB05	SHB05
Analysis #	cpx1	cpx1	cpx1	cpx3	cpx4	cpx2	cpx2	cpx4	cpx2	cpx2	cpx3
zone	459	457	458	482	496	461	462	492	463	464	484
SiO <sub>2</sub>	54.18	54.31	54.26	52.85	54.12	54.24	54.38	53.66	54.40	54.54	53.68
TiO <sub>2</sub>	0.05	0.07	0.08	0.12	0.03	0.05	bdl	0.06	bdl	bdl	0.01
Al <sub>2</sub> O <sub>3</sub>	5.21	5.18	4.97	6.83	5.14	3.56	3.89	5.06	5.30	5.72	3.30
Cr <sub>2</sub> O <sub>3</sub>	0.03	bdl	0.03	0.02	0.19	0.09	0.16	0.02	0.22	0.34	0.05
FeO	12.55	12.42	13.01	16.40	12.55	12.92	12.66	12.89	12.75	12.40	14.27
MnO	0.11	0.05	0.07	0.20	0.07	0.07	0.09	0.32	0.04	0.03	0.23
MgO	7.49	7.43	7.50	4.74	7.37	8.37	8.26	7.19	7.31	6.95	7.72
CaO	14.34	14.49	14.33	8.57	13.97	16.10	15.76	13.46	13.70	13.38	14.14
Na <sub>2</sub> O	5.81	6.08	5.77	8.45	6.13	4.93	5.19	6.21	6.17	6.35	6.02
<b>TOTAL</b>	<b>99.79</b>	<b>100.03</b>	<b>100.02</b>	<b>98.20</b>	<b>99.57</b>	<b>100.34</b>	<b>100.41</b>	<b>98.87</b>	<b>99.89</b>	<b>99.71</b>	<b>99.41</b>
<b>Cations - 6 oxy<sub>i</sub></b>											
Si	1.99	1.99	1.99	1.97	1.99	2.00	1.99	1.99	2.00	2.00	1.99
Ti	0.00	0.00	0.00	0.00	0.00	0.00	0.00	0.00	0.00	0.00	0.00
Al	0.23	0.22	0.22	0.30	0.22	0.15	0.17	0.22	0.23	0.25	0.14
Fe <sup>3+</sup>	0.20	0.23	0.20	0.37	0.23	0.20	0.21	0.24	0.21	0.19	0.31
Cr <sup>3+</sup>	0.00	0.00	0.00	0.00	0.01	0.00	0.00	0.00	0.01	0.01	0.00
Fe <sup>2+</sup>	0.19	0.15	0.20	0.14	0.16	0.20	0.18	0.16	0.18	0.19	0.13
Mn	0.00	0.00	0.00	0.01	0.00	0.00	0.00	0.01	0.00	0.00	0.01
Mg	0.41	0.41	0.41	0.26	0.40	0.46	0.45	0.40	0.40	0.38	0.43
Ca	0.57	0.57	0.56	0.34	0.55	0.63	0.62	0.53	0.54	0.53	0.56
Na	0.41	0.43	0.41	0.61	0.44	0.35	0.37	0.45	0.44	0.45	0.43
<b>Mol%</b>											
Aegerine	20	23	21	39	23	20	21	25	22	19	32
Jadeite	22	20	21	25	21	15	16	21	23	27	12
Diopside	58	57	58	36	56	64	63	54	55	54	56

Table A4 - 2: EMPA data for clinpyroxene

SAMPLE	SIB50B	SIB50B	SIB50B	SIB50B	SIB50B	SIB50B	SIB50B	SIB50B	SIB50B	SIB50B	SIB50B	SIB50B
Analysis #	Cpx5	Cpx4	Cpx5	Cpx4	Cpx5	Cpx4	Cpx4	Cpx4	Cpx2	Cpx4	Cpx4	Cpx4
zone	670	668	671	661	672	667	657	662	636	663	656	658
SiO <sub>2</sub>	51.79	53.24	51.44	53.24	52.17	52.04	54.53	54.02	54.19	54.03	54.22	53.81
TiO <sub>2</sub>	0.01	0.19	bdl	bdl	0.05	0.01	0.07	0.09	0.00	0.08	0.06	0.03
Al <sub>2</sub> O <sub>3</sub>	3.35	7.20	3.07	7.13	4.65	5.21	7.01	7.06	6.92	4.04	7.17	4.05
Cr <sub>2</sub> O <sub>3</sub>	0.05	bdl	bdl	bdl	bdl	0.07	0.07	bdl	0.08	0.02	0.01	bdl
FeO	12.65	12.83	12.75	12.81	13.74	12.71	12.35	12.20	12.12	12.00	12.92	11.88
MnO	0.53	0.39	0.47	0.35	0.43	0.38	0.37	0.35	0.36	0.41	0.37	0.38
MgO	8.29	5.72	8.08	5.89	6.75	7.15	6.28	6.21	6.44	8.46	5.78	8.28
CaO	13.60	9.51	13.72	9.55	11.52	10.89	10.50	10.25	10.49	13.80	9.53	13.82
Na <sub>2</sub> O	6.07	8.32	6.00	8.37	7.17	7.03	8.09	7.99	7.81	6.10	8.34	5.96
<b>TOTAL</b>	<b>96.33</b>	<b>97.39</b>	<b>95.53</b>	<b>97.33</b>	<b>96.52</b>	<b>95.50</b>	<b>99.28</b>	<b>98.16</b>	<b>98.40</b>	<b>98.98</b>	<b>98.40</b>	<b>98.24</b>
<b>Cations - 6 oxy<sub>i</sub></b>												
Si	1.96	1.98	1.97	1.97	1.97	1.98	1.99	1.99	1.99	1.99	1.99	2.00
Ti	0.00	0.01	0.00	0.00	0.00	0.00	0.00	0.00	0.00	0.00	0.00	0.00
Al	0.15	0.31	0.14	0.31	0.21	0.23	0.30	0.31	0.30	0.18	0.31	0.18
Fe <sup>3+</sup>	0.37	0.32	0.37	0.34	0.38	0.33	0.29	0.28	0.27	0.27	0.30	0.25
Cr <sup>3+</sup>	0.00	0.00	0.00	0.00	0.00	0.00	0.00	0.00	0.00	0.00	0.00	0.00
Fe <sup>2+</sup>	0.03	0.08	0.04	0.06	0.06	0.08	0.08	0.10	0.10	0.10	0.10	0.12
Mn	0.02	0.01	0.02	0.01	0.01	0.01	0.01	0.01	0.01	0.01	0.01	0.01
Mg	0.47	0.32	0.46	0.33	0.38	0.41	0.34	0.34	0.35	0.46	0.32	0.46
Ca	0.55	0.38	0.56	0.38	0.47	0.44	0.41	0.40	0.41	0.54	0.38	0.55
Na	0.45	0.60	0.45	0.60	0.53	0.52	0.57	0.57	0.56	0.44	0.59	0.43
<b>Mol%</b>												
Aegerine	37	33	37	35	38	34	30	29	28	28	30	26
Jadeite	8	28	8	27	15	20	28	30	29	16	31	18
Diopside	55	39	56	39	47	46	42	41	43	56	39	56



Table A4 - 2: EMPA data for clinpyroxene

SAMPLE	SIB50B	SIB50B	SIB50B	SIB50B	SIB50B	SIB50B	SIB50B	SIB50B	SIB50B	SIB50B	SIB50B	SIB50B
Analysis #	Cpx4	Cpx2	Cpx4	Cpx1	Cpx2	Cpx3	Cpx5	Cpx5	Cpx2	Cpx1	Cpx5	Cpx1
zone	664	635	659	627	637	647	673	669	641	628	674	629
SiO <sub>2</sub>	53.56	54.34	53.66	54.02	53.18	54.02	53.33	53.08	53.17	53.96	52.76	53.76
TiO <sub>2</sub>	0.08	0.05	0.09	0.08	bdl	0.06	0.03	0.09	0.03	0.01	0.15	bdl
Al <sub>2</sub> O <sub>3</sub>	4.63	6.05	4.71	6.72	3.80	8.05	6.09	7.26	5.94	6.47	6.97	6.35
Cr <sub>2</sub> O <sub>3</sub>	0.05	bdl	bdl	0.02	0.05	0.01	0.05	0.02	bdl	bdl	0.04	0.03
FeO	13.67	12.17	13.53	14.68	13.43	15.25	14.39	14.83	14.80	14.55	15.81	14.73
MnO	0.48	0.31	0.45	0.36	0.39	0.31	0.41	0.28	0.35	0.28	0.34	0.25
MgO	6.94	6.93	6.85	5.23	7.55	4.11	5.45	4.35	5.34	5.50	4.00	5.23
CaO	11.75	11.38	11.91	8.45	12.39	6.50	8.80	6.96	8.68	8.36	6.47	8.21
Na <sub>2</sub> O	7.15	7.25	7.19	8.97	6.62	9.87	8.62	9.50	8.66	8.66	9.53	8.94
<b>TOTAL</b>	<b>98.32</b>	<b>98.49</b>	<b>98.39</b>	<b>98.53</b>	<b>97.41</b>	<b>98.18</b>	<b>97.17</b>	<b>96.40</b>	<b>96.97</b>	<b>97.81</b>	<b>96.09</b>	<b>97.51</b>
<b>Cations - 6 oxy<sub>i</sub></b>												
Si	1.99	2.00	1.99	1.99	2.00	1.99	1.99	1.99	1.99	2.00	1.99	2.00
Ti	0.00	0.00	0.00	0.00	0.00	0.00	0.00	0.00	0.00	0.00	0.00	0.00
Al	0.20	0.26	0.21	0.29	0.17	0.35	0.27	0.32	0.26	0.28	0.31	0.28
Fe <sup>3+</sup>	0.33	0.25	0.33	0.37	0.32	0.38	0.37	0.39	0.39	0.34	0.40	0.37
Cr <sup>3+</sup>	0.00	0.00	0.00	0.00	0.00	0.00	0.00	0.00	0.00	0.00	0.00	0.00
Fe <sup>2+</sup>	0.09	0.13	0.09	0.08	0.10	0.09	0.08	0.08	0.08	0.11	0.10	0.08
Mn	0.02	0.01	0.01	0.01	0.01	0.01	0.01	0.01	0.01	0.01	0.01	0.01
Mg	0.38	0.38	0.38	0.29	0.42	0.23	0.30	0.24	0.30	0.30	0.23	0.29
Ca	0.47	0.45	0.47	0.33	0.50	0.26	0.35	0.28	0.35	0.33	0.26	0.33
Na	0.51	0.52	0.52	0.64	0.48	0.70	0.62	0.69	0.63	0.62	0.70	0.64
<b>Mol%</b>												
Aegerine	34	26	33	38	33	40	38	40	40	36	41	38
Jadeite	19	28	19	27	16	34	26	31	25	29	31	28
Diopside	48	46	48	34	51	27	36	29	36	35	27	34

Table A4 - 2: EMPA data for clinpyroxene

SAMPLE	SIB50B	SIB50B	SIB50B	SIB50B	SIB50B	SIB50B	SIB50B	SIB50B	SIB50B	SIB50B	SIB50B	SIB50B
Analysis #	Cpx1	Cpx4	Cpx4	Cpx4	Cpx1	Cpx1	Cpx1	Cpx1	Cpx2	Cpx2	Cpx2	Cpx1
zone	634	665	660	666	632	633	631	640	639	638	630	630
				rim	rim	rim	rim	rim	rim	rim	rim	rim
SiO <sub>2</sub>	54.66	53.30	53.86	52.25	52.60	52.73	52.50	52.15	52.70	52.51	52.33	
TiO <sub>2</sub>	0.01	0.01	0.03	0.05	0.16	0.03	0.08	0.18	0.23	0.27	0.02	
Al <sub>2</sub> O <sub>3</sub>	6.28	7.50	7.82	4.92	3.34	4.06	4.33	4.08	4.33	3.95	3.77	
Cr <sub>2</sub> O <sub>3</sub>	0.01	0.05	0.01	bdl	0.04	bdl	bdl	bdl	0.08	0.04	bdl	
FeO	14.55	15.58	15.86	19.08	21.45	23.39	23.21	23.77	23.98	23.90	24.59	
MnO	0.37	0.32	0.29	0.27	0.24	0.20	0.10	0.07	0.11	0.07	0.11	
MgO	5.58	3.68	3.70	3.28	3.54	1.94	1.76	1.55	1.31	1.37	1.12	
CaO	8.86	5.99	5.99	5.40	4.24	3.20	2.73	2.25	2.05	2.17	1.80	
Na <sub>2</sub> O	8.41	9.92	9.62	10.25	10.57	11.30	11.55	11.70	11.90	11.85	11.84	
<b>TOTAL</b>	<b>98.73</b>	<b>96.38</b>	<b>97.17</b>	<b>95.51</b>	<b>96.20</b>	<b>96.87</b>	<b>96.30</b>	<b>95.78</b>	<b>96.70</b>	<b>96.17</b>	<b>95.59</b>	
<b>Cations - 6 oxy</b>												
Si	2.01	2.00	2.01	1.99	2.00	2.00	2.00	2.00	2.00	2.00	2.01	2.01
Ti	0.00	0.00	0.00	0.00	0.00	0.00	0.00	0.01	0.01	0.01	0.00	0.00
Al	0.27	0.33	0.34	0.22	0.15	0.18	0.19	0.18	0.19	0.18	0.17	0.17
Fe <sup>3+</sup>	0.30	0.39	0.33	0.55	0.62	0.65	0.66	0.68	0.67	0.68	0.69	0.69
Cr <sup>3+</sup>	0.00	0.00	0.00	0.00	0.00	0.00	0.00	0.00	0.00	0.00	0.00	0.00
Fe <sup>2+</sup>	0.14	0.10	0.16	0.06	0.06	0.09	0.08	0.08	0.09	0.08	0.10	0.10
Mn	0.01	0.01	0.01	0.01	0.01	0.01	0.00	0.00	0.00	0.00	0.00	0.00
Mg	0.31	0.21	0.21	0.19	0.20	0.11	0.10	0.09	0.07	0.08	0.06	0.06
Ca	0.35	0.24	0.24	0.22	0.17	0.13	0.11	0.09	0.08	0.09	0.07	0.07
Na	0.60	0.72	0.70	0.76	0.78	0.83	0.85	0.87	0.88	0.88	0.88	0.88
<b>Mol%</b>												
Aegerine	32	41	35	56	65	68	69	71	70	70	72	72
Jadeite	31	34	39	22	17	19	20	20	22	21	20	20
Diopside	37	25	26	23	18	14	12	10	9	9	8	8

Table A4 - 3: EMPA data for garnet.

SAMPLE	SHB45	SHB45	SHB45	SHB45	SHB45	SHB45	SHB45	SHB45	SHB45	SHB45	SHB45	SHB45	SHB45	SHB45	SHB45	SHB45	SHB45
	Grt5	Grt5	Grt6	Grt4	Grt3	Grt5	grt1	Grt3	Grt4	Grt5	grt1	Grt5	Grt4	Grt3	Grt6	grt1	Grt6
Analysis #	138	135	152	100	92	136	85	97	99	139	84	137	101	93	153	82	154
zone	rim	rim	rim	rim	rim	rim	rim	rim	rim	rim	rim	rim	rim	rim	rim	core	core
SiO <sub>2</sub>	37.37	37.12	37.72	37.08	36.12	36.99	37.57	37.25	37.06	37.21	37.76	36.77	37.22	36.83	38.00	37.29	37.21
TiO <sub>2</sub>	0.02	0.00	0.00	0.00	0.04	0.04	0.13	0.11	0.17	0.04	0.06	0.07	0.09	0.20	0.02	0.33	0.22
Al <sub>2</sub> O <sub>3</sub>	20.92	20.74	21.06	20.59	20.33	21.10	21.16	21.00	20.97	21.23	21.08	20.93	21.05	20.49	21.43	21.13	21.00
Cr <sub>2</sub> O <sub>3</sub>	bdl	0.06	0.02	0.01	0.07	0.04	0.04	0.06	bdl	0.04	0.05	0.13	bdl	0.07	0.02	0.04	0.06
FeO	26.13	26.74	27.46	27.97	28.37	28.65	28.92	28.86	28.79	29.26	28.99	29.71	29.31	29.91	29.59	26.06	25.73
NiO	bdl	0.02	0.01	bdl	bdl	bdl	bdl	0.14	0.03	bdl	bdl	bdl	bdl	bdl	bdl	bdl	0.04
MnO	3.33	3.03	2.35	1.84	2.56	0.48	0.89	0.64	0.63	0.45	0.56	0.52	0.42	0.50	0.52	2.70	3.04
MgO	1.46	1.49	1.68	1.77	1.80	1.92	1.95	2.01	2.03	2.03	2.04	2.10	2.11	2.11	2.11	2.40	2.44
CaO	10.24	10.05	10.00	10.07	8.46	9.84	9.22	9.77	9.44	9.33	9.26	8.97	8.94	8.24	8.75	9.31	9.26
TOTAL	99.50	99.25	100.32	99.34	97.77	99.11	99.91	99.87	99.12	99.59	99.83	99.25	99.18	98.38	100.44	99.30	99.00
<b>Cations - 12 oxygen formula</b>																	
Si	3.00	2.99	3.00	2.99	2.97	2.98	2.99	2.98	2.98	2.98	3.01	2.96	2.99	2.99	3.01	2.98	2.98
Ti	0.00	0.00	0.00	0.00	0.00	0.00	0.01	0.01	0.01	0.00	0.00	0.00	0.01	0.01	0.00	0.02	0.01
Al	1.98	1.97	1.97	1.95	1.97	2.00	1.99	1.98	1.99	2.00	1.98	1.99	1.99	1.96	2.00	1.99	1.98
Cr	0.00	0.00	0.00	0.00	0.00	0.00	0.00	0.00	0.00	0.00	0.00	0.01	0.00	0.00	0.00	0.00	0.00
Fe	1.75	1.80	1.83	1.88	1.95	1.93	1.93	1.93	1.94	1.96	1.93	2.00	1.97	2.03	1.96	1.74	1.73
Ni	0.00	0.00	0.00	0.00	0.00	0.00	0.00	0.01	0.00	0.00	0.00	0.00	0.00	0.00	0.00	0.00	0.00
Mn	0.23	0.21	0.16	0.13	0.18	0.03	0.06	0.04	0.04	0.03	0.04	0.04	0.03	0.03	0.03	0.18	0.21
Mg	0.17	0.18	0.20	0.21	0.22	0.23	0.23	0.24	0.24	0.24	0.24	0.25	0.25	0.26	0.25	0.29	0.29
Ca	0.88	0.87	0.85	0.87	0.75	0.85	0.79	0.84	0.81	0.80	0.79	0.77	0.77	0.72	0.74	0.80	0.80
Na	0.00	0.00	0.00	0.00	0.00	0.00	0.00	0.00	0.00	0.00	0.00	0.00	0.00	0.00	0.00	0.00	0.00
K	0.00	0.00	0.00	0.00	0.00	0.00	0.00	0.00	0.00	0.00	0.00	0.00	0.00	0.00	0.00	0.00	0.00
<b>Mol%</b>																	
Grs	29	28	28	28	24	28	26	27	27	26	26	25	25	24	25	27	26
Pyr	6	6	7	7	7	8	8	8	8	8	8	8	8	8	8	10	10
Alm	58	59	60	61	63	63	64	63	64	65	64	65	65	67	66	58	57
Sps	7	7	5	4	6	1	2	1	1	1	1	1	1	1	1	6	7

Table A4 - 3: EMPA data for garnet.

SAMPLE	SHB45	SHB45	SHB45	SHB45	SHB45	SHB45	SHB45	SHB45	SHB45	SHB45	SHB45	SHB45	SHB45	SHB12B	SHB12A	SHB12B	SHB12B
	Grt4	Grt6	grt1	Grt4	Grt5	Grt3	Grt5	Grt5	Grt4	Grt3	Grt4	Grt6	Grt3	grt1	grt1	grt1b	grt1
Analysis #	103	150	83	104	132	96	133	131	105	94	102	151	98	218	393	229	213
zone	core	core	core	core	core	core	core	core	core	core	core	core	core	rim	rim	rim	rim
SiO <sub>2</sub>	37.13	37.73	37.49	37.60	37.72	37.30	37.56	37.59	37.85	37.04	37.70	37.55	37.71	36.72	37.40	37.29	37.14
TiO <sub>2</sub>	0.07	0.09	0.04	0.18	0.10	0.14	0.07	0.24	0.13	0.10	0.03	0.05	0.13	0.02	0.07	0.00	0.11
Al <sub>2</sub> O <sub>3</sub>	21.12	21.14	21.41	21.34	21.52	21.29	21.32	21.33	21.40	20.92	21.21	20.96	21.43	21.00	21.19	21.21	21.07
Cr <sub>2</sub> O <sub>3</sub>	0.06	0.11	0.12	0.06	0.04	0.02	0.08	0.07	0.12	0.02	0.09	0.12	0.00	bdl	0.02	0.01	bdl
FeO	25.93	24.92	26.24	25.87	26.47	26.54	27.03	25.93	25.94	26.60	26.88	26.76	27.25	24.06	22.74	24.45	25.18
NiO	bdl	0.04	0.00	0.05	0.03	bdl	bdl	bdl	0.04	bdl	0.08	bdl	0.01	bdl	bdl	0.02	0.07
MnO	3.60	3.41	2.89	3.09	2.77	2.28	1.83	3.45	2.32	2.56	1.72	1.74	1.11	6.93	8.12	7.00	5.02
MgO	2.47	2.48	2.51	2.58	2.60	2.64	2.64	2.66	2.69	2.71	2.75	2.88	3.16	1.49	1.51	1.70	1.84
CaO	8.68	9.71	9.05	9.14	8.72	8.98	9.22	8.63	9.28	8.33	9.51	9.21	8.91	8.44	7.96	7.80	9.11
<b>TOTAL</b>	<b>99.09</b>	<b>99.66</b>	<b>99.79</b>	<b>99.95</b>	<b>99.98</b>	<b>99.21</b>	<b>99.77</b>	<b>99.92</b>	<b>99.80</b>	<b>98.32</b>	<b>100.00</b>	<b>99.30</b>	<b>99.76</b>	<b>98.69</b>	<b>99.02</b>	<b>99.57</b>	<b>99.55</b>
<b>Cations - 12</b>																	
Si	2.98	3.00	2.98	2.98	2.99	2.98	2.98	2.98	3.00	2.99	2.99	3.00	2.99	2.98	3.01	2.99	2.98
Ti	0.00	0.01	0.00	0.01	0.01	0.01	0.00	0.01	0.01	0.01	0.00	0.00	0.01	0.00	0.00	0.00	0.01
Al	2.00	1.98	2.01	2.00	2.01	2.00	2.00	2.00	2.00	1.99	1.98	1.97	2.00	2.01	2.01	2.01	1.99
Cr	0.00	0.01	0.01	0.00	0.00	0.00	0.00	0.00	0.01	0.00	0.01	0.01	0.00	0.00	0.00	0.00	0.00
Fe	1.74	1.66	1.75	1.72	1.75	1.77	1.80	1.72	1.72	1.80	1.78	1.79	1.80	1.63	1.53	1.64	1.69
Ni	0.00	0.00	0.00	0.00	0.00	0.00	0.00	0.00	0.00	0.00	0.01	0.00	0.00	0.00	0.00	0.00	0.00
Mn	0.24	0.23	0.19	0.21	0.19	0.15	0.12	0.23	0.16	0.18	0.12	0.12	0.07	0.48	0.55	0.48	0.34
Mg	0.29	0.29	0.30	0.30	0.31	0.31	0.31	0.31	0.32	0.33	0.32	0.34	0.37	0.18	0.18	0.20	0.22
Ca	0.75	0.83	0.77	0.78	0.74	0.77	0.78	0.73	0.79	0.72	0.81	0.79	0.76	0.73	0.69	0.67	0.78
Na	0.00	0.00	0.00	0.00	0.00	0.00	0.00	0.00	0.01	0.01	0.00	0.00	0.01	0.00	0.00	0.01	0.00
K	0.00	0.00	0.00	0.00	0.00	0.00	0.00	0.00	0.00	0.00	0.00	0.00	0.00	0.00	0.00	0.00	0.00
<b>Mol%</b>																	
Grs	25	28	26	26	25	26	26	24	26	24	27	26	25	24	23	22	26
Pyr	10	10	10	10	10	10	10	10	11	11	11	11	12	6	6	7	7
Alm	57	55	58	57	59	59	60	57	58	60	59	59	60	54	52	55	56
Sps	8	8	6	7	6	5	4	8	5	6	4	4	2	16	19	16	11

Table A4 - 3: EMPA data for garnet.

SAMPLE	SHB12A	SHB12A	SHB12A	SHB12A	SHB12A	SHB12A	SHB12A	SHB12B	SHB12B	SHB12B	SHB12B	SHB12A	SHB12B	SHB12A	SHB12B
	grt1b	grt1	grt1b	grt1	grt1b	grt1	grt1b	grt1	grt1	grt1b	grt1	grt1	grt1b	grt1	grt1
Analysis #	410	394	407	395	408	399	409	215	216	226	219	401	227	403	212
zone	rim	rim	rim	rim	rim	rim	rim	rim	rim	core	core	core	core	core	core
SiO <sub>2</sub>	38.14	37.06	37.69	36.21	37.10	36.66	37.51	37.25	37.28	37.85	38.12	37.55	38.02	37.78	37.37
TiO <sub>2</sub>	0.03	0.13	0.00	0.16	0.03	0.10	0.00	0.00	0.12	0.07	bdl	0.11	0.14	0.11	0.16
Al <sub>2</sub> O <sub>3</sub>	21.35	20.85	21.39	20.54	20.82	20.80	21.27	21.05	20.93	21.70	21.63	21.48	21.77	21.85	21.49
Cr <sub>2</sub> O <sub>3</sub>	bdl	bdl	0.01	0.02	0.08	bdl	0.08	bdl	bdl	bdl	0.04	0.08	bdl	bdl	0.03
FeO	25.24	23.23	23.49	24.77	23.74	24.17	25.46	25.58	26.11	23.40	23.18	22.61	23.97	23.37	23.86
NiO	0.01	bdl	0.02	bdl	0.02	0.04	bdl	bdl	0.03	0.01	0.09	bdl	bdl	bdl	0.03
MnO	5.49	6.09	7.69	5.68	5.93	6.29	5.36	4.60	4.65	4.28	4.08	4.38	3.41	4.12	3.46
MgO	1.88	1.88	1.89	1.90	1.91	1.92	2.01	2.03	2.03	3.56	3.63	3.78	3.81	3.83	3.86
CaO	8.26	9.49	7.70	8.49	8.78	8.90	8.07	8.33	8.31	8.93	8.97	8.60	8.68	8.63	9.09
TOTAL	100.43	98.75	99.89	97.80	98.42	98.91	99.82	98.88	99.49	99.83	99.78	98.64	99.84	99.71	99.39
<b>Cations - 12</b>															
Si	3.02	2.99	3.01	2.97	3.00	2.97	3.00	3.00	2.99	2.98	3.00	2.99	2.99	2.98	2.96
Ti	0.00	0.01	0.00	0.01	0.00	0.01	0.00	0.00	0.01	0.00	0.00	0.01	0.01	0.01	0.01
Al	1.99	1.98	2.01	1.98	1.99	1.98	2.00	2.00	1.98	2.02	2.01	2.01	2.02	2.03	2.01
Cr	0.00	0.00	0.00	0.00	0.01	0.00	0.01	0.00	0.00	0.00	0.00	0.00	0.00	0.00	0.00
Fe	1.67	1.57	1.57	1.70	1.61	1.64	1.70	1.72	1.75	1.54	1.53	1.50	1.58	1.54	1.58
Ni	0.00	0.00	0.00	0.00	0.00	0.00	0.00	0.00	0.00	0.00	0.01	0.00	0.00	0.00	0.00
Mn	0.37	0.42	0.52	0.39	0.41	0.43	0.36	0.31	0.32	0.29	0.27	0.29	0.23	0.27	0.23
Mg	0.22	0.23	0.22	0.23	0.23	0.23	0.24	0.24	0.24	0.42	0.43	0.45	0.45	0.45	0.46
Ca	0.70	0.82	0.66	0.75	0.76	0.77	0.69	0.72	0.71	0.75	0.76	0.73	0.73	0.73	0.77
Na	0.00	0.00	0.00	0.00	0.00	0.00	0.00	0.00	0.00	0.00	0.01	0.01	0.00	0.00	0.01
K	0.00	0.00	0.00	0.00	0.00	0.00	0.00	0.00	0.00	0.00	0.00	0.00	0.00	0.00	0.00
<b>Mol%</b>															
Grs	24	27	22	24	25	25	23	24	24	25	25	25	25	24	25
Pyr	7	7	8	8	8	8	8	8	8	14	14	15	15	15	15
Alm	56	52	53	55	53	53	57	57	58	51	51	50	53	51	52
Sps	12	14	17	13	14	14	12	10	10	10	9	10	8	9	8

Table A4 - 3: EMPA data for garnet.

SAMPLE	SHB12A	SHB12A	SHB12A	SHB12A	SHB12A	SHB12B	SHB12A	SHB12A	SHB12A	SHB12B	SHB12B	SHB05	SHB05	SHB05	SHB05	SHB05
Analysis #	grt1	grt1	grt1b	grt1	grt1	grt1	grt1b	grt1b	grt1b	grt1	grt1b	grt1	grt1	grt1	grt1	grt1
zone	core	core	core	core	core	core	core	core	core	core	core	core	core	core	core	core
SiO <sub>2</sub>	38.11	38.13	38.15	38.69	37.90	37.79	38.04	38.15	38.18	38.39	38.53	36.94	36.95	36.94	37.32	37.55
TiO <sub>2</sub>	0.12	0.00	0.16	0.19	0.15	0.03	0.04	bdl	0.14	bdl	0.03	0.08	0.19	0.12	0.14	0.13
Al <sub>2</sub> O <sub>3</sub>	21.71	21.49	22.09	22.36	21.43	21.61	21.59	21.71	21.80	21.77	21.96	20.64	20.35	20.29	20.68	20.82
Cr <sub>2</sub> O <sub>3</sub>	0.13	bdl	0.09	0.05	bdl	0.05	0.05	0.07	0.10	bdl	0.01	0.00	0.02	0.02	0.00	0.04
FeO	23.15	23.18	23.57	23.44	23.09	23.81	23.85	23.40	23.76	24.15	24.03	20.39	19.42	20.78	24.78	29.49
NiO	0.05	0.02	0.04	0.04	bdl	bdl	0.01	bdl	0.06	bdl	bdl	0.01	0.00	0.00	0.00	0.00
MnO	4.11	4.04	3.06	3.37	3.67	2.40	3.00	3.09	2.98	2.31	2.22	12.09	12.27	11.64	7.35	2.82
MgO	3.86	3.99	4.20	4.27	4.34	4.35	4.35	4.44	4.54	4.56	4.69	0.69	0.67	0.74	0.97	1.49
CaO	8.45	8.67	8.68	8.56	8.42	8.85	8.73	8.60	8.63	8.57	8.55	9.12	9.37	9.15	8.78	8.16
<b>TOTAL</b>	<b>99.75</b>	<b>99.59</b>	<b>100.12</b>	<b>101.02</b>	<b>99.08</b>	<b>98.93</b>	<b>99.72</b>	<b>99.51</b>	<b>100.26</b>	<b>99.77</b>	<b>100.06</b>	<b>99.99</b>	<b>99.26</b>	<b>99.70</b>	<b>100.06</b>	<b>100.51</b>
<b>Cations - 12</b>																
Si	3.00	3.00	2.98	2.99	2.99	2.99	2.99	3.00	2.98	3.00	3.00	2.98	3.00	2.99	3.00	3.00
Ti	0.01	0.00	0.01	0.01	0.01	0.00	0.00	0.00	0.01	0.00	0.00	0.00	0.01	0.01	0.01	0.01
Al	2.01	1.99	2.03	2.04	1.99	2.01	2.00	2.01	2.00	2.01	2.02	1.96	1.95	1.94	1.96	1.96
Cr	0.01	0.00	0.01	0.00	0.00	0.00	0.00	0.00	0.01	0.00	0.00	0.00	0.00	0.00	0.00	0.00
Fe	1.52	1.53	1.54	1.51	1.53	1.57	1.57	1.54	1.55	1.58	1.56	1.38	1.32	1.41	1.67	1.97
Ni	0.00	0.00	0.00	0.00	0.00	0.00	0.00	0.00	0.00	0.00	0.00	0.00	0.00	0.00	0.00	0.00
Mn	0.27	0.27	0.20	0.22	0.25	0.16	0.20	0.21	0.20	0.15	0.15	0.83	0.84	0.80	0.50	0.19
Mg	0.45	0.47	0.49	0.49	0.51	0.51	0.51	0.52	0.53	0.53	0.54	0.08	0.08	0.09	0.12	0.18
Ca	0.71	0.73	0.73	0.71	0.71	0.75	0.73	0.72	0.72	0.72	0.71	0.79	0.81	0.79	0.76	0.70
Na	0.01	0.01	0.01	0.01	0.01	0.01	0.01	0.00	0.01	0.01	0.01	0.00	0.00	0.00	0.01	0.00
K	0.00	0.00	0.00	0.00	0.00	0.00	0.00	0.00	0.00	0.00	0.00	0.00	0.00	0.00	0.00	0.00
<b>Mol%</b>																
Grs	24	24	25	24	24	25	24	24	24	24	24	26	27	26	25	23
Pyr	15	16	17	17	17	17	17	17	18	18	18	3	3	3	4	6
Alm	51	51	52	52	51	53	52	51	52	53	53	45	43	46	55	65
Sps	9	9	7	8	8	5	7	7	7	5	5	27	28	26	16	6

Table A4 - 3: EMPA data for garnet.

SAMPLE	SHB05	SHB05	SHB05	SHB05	SHB05	SHB05	SHB05	SHB05	SHB05	SHB05	SHB05	SHB05	SHB05	SHB05	SHB05	SHB05	SHB03
Analysis #	grt1	grt1	grt1	grt1	grt2	grt2	grt2	grt2	grt2	grt2	grt2	grt3	grt3	grt3	grt3	grt3	grt1
zone	453	454	455	456	470	471	473	474	475	476	477	485	486	487	488	489	362
SiO <sub>2</sub>	37.29	37.16	37.22	37.03	37.19	37.30	37.14	37.42	37.37	36.96	37.38	36.80	37.33	36.83	37.09	36.83	36.47
TiO <sub>2</sub>	0.11	0.07	0.09	0.15	0.08	0.16	0.09	0.06	0.14	0.10	0.07	0.18	0.14	0.02	0.08	0.05	0.10
Al <sub>2</sub> O <sub>3</sub>	20.99	20.53	20.88	20.90	20.82	20.50	21.00	20.96	21.04	20.87	21.11	20.96	20.69	20.89	21.02	21.09	20.41
Cr <sub>2</sub> O <sub>3</sub>	0.00	0.00	0.01	0.09	0.05	0.02	0.00	0.00	0.05	0.23	0.04	0.00	0.00	0.03	0.04	0.00	0.01
FeO	29.84	26.79	28.41	29.67	26.28	25.23	28.62	29.27	25.35	28.08	29.96	24.44	26.01	26.88	28.65	29.74	21.50
NiO	0.00	0.00	0.00	0.01	0.03	0.00	0.00	0.00	0.05	0.06	0.03	0.00	0.00	0.00	0.00	0.02	0.03
MnO	2.22	5.34	3.27	1.72	6.20	6.69	3.52	2.18	7.74	3.91	1.86	7.95	5.71	5.03	3.26	1.99	14.45
MgO	1.52	1.24	1.37	1.57	1.10	1.02	1.33	1.42	0.95	1.31	1.61	0.93	1.14	1.16	1.29	1.50	1.18
CaO	8.17	8.82	8.21	8.13	7.88	9.09	8.32	8.27	8.33	8.55	8.31	8.80	8.50	8.62	8.72	8.40	4.36
TOTAL	100.16	99.96	99.49	99.29	99.64	100.07	100.02	99.58	101.02	100.09	100.38	100.12	99.52	99.46	100.18	99.61	98.58
<b>Cations - 12</b>																	
Si	2.99	2.99	3.00	2.99	3.00	3.00	2.98	3.01	2.98	2.97	2.99	2.96	3.01	2.98	2.98	2.97	3.00
Ti	0.01	0.00	0.01	0.01	0.00	0.01	0.01	0.00	0.01	0.01	0.00	0.01	0.01	0.00	0.00	0.00	0.01
Al	1.98	1.95	1.98	1.99	1.98	1.94	1.99	1.99	1.98	1.98	1.99	1.99	1.97	1.99	1.99	2.00	1.98
Cr	0.00	0.00	0.00	0.01	0.00	0.00	0.00	0.00	0.00	0.01	0.00	0.00	0.00	0.00	0.00	0.00	0.00
Fe	2.00	1.80	1.91	2.00	1.77	1.70	1.92	1.97	1.69	1.89	2.00	1.65	1.75	1.82	1.92	2.01	1.48
Ni	0.00	0.00	0.00	0.00	0.00	0.00	0.00	0.00	0.00	0.00	0.00	0.00	0.00	0.00	0.00	0.00	0.00
Mn	0.15	0.36	0.22	0.12	0.42	0.46	0.24	0.15	0.52	0.27	0.13	0.54	0.39	0.34	0.22	0.14	1.01
Mg	0.18	0.15	0.16	0.19	0.13	0.12	0.16	0.17	0.11	0.16	0.19	0.11	0.14	0.14	0.15	0.18	0.15
Ca	0.70	0.76	0.71	0.70	0.68	0.78	0.72	0.71	0.71	0.74	0.71	0.76	0.73	0.75	0.75	0.73	0.38
Na	0.00	0.00	0.00	0.00	0.00	0.01	0.00	0.00	0.00	0.00	0.00	0.01	0.00	0.00	0.00	0.00	0.01
K	0.00	0.00	0.00	0.00	0.00	0.00	0.00	0.00	0.00	0.00	0.00	0.00	0.00	0.00	0.00	0.00	0.00
<b>Mol%</b>																	
Grs	23	25	24	23	23	26	24	24	23	24	23	25	24	25	25	24	13
Pyr	6	5	5	6	4	4	5	6	4	5	6	4	5	5	5	6	5
Alm	66	59	64	66	59	55	63	66	56	62	66	54	58	60	63	66	49
Sps	5	12	7	4	14	15	8	5	17	9	4	18	13	11	7	4	33

Table A4 - 3: EMPA data for garnet.

SAMPLE	SHB03	SHB03	SHB03	SHB03	SHB03	SHB03	SHB03	SHB03	SHB03	SHB03	SHB03	SHB03	SHB03	SHB03	SHB03	SHB03	SIB50B	SIB50B
Analysis #	grt1	grt1	grt1	grt1	grt1	grt1	grt2	grt2	grt2	grt2	grt2	grt2	grt2	grt2	grt2	grt2	Grt1	Grt1
zone	363	364	365	367	368	369	372	373	374	375	376	377	378	379	380	381	642	643
SiO <sub>2</sub>	36.50	35.86	36.71	36.52	36.50	36.57	34.96	35.58	35.92	36.18	36.03	35.57	36.07	36.13	36.64	37.02	36.04	36.48
TiO <sub>2</sub>	0.06	0.03	0.05	0.10	0.02	0.07	0.10	0.10	0.03	0.05	0.13	0.14	0.02	0.08	0.06	0.01	0.21	0.31
Al <sub>2</sub> O <sub>3</sub>	20.58	19.77	20.40	20.80	20.50	20.51	19.38	19.73	20.31	20.46	20.14	19.94	20.54	20.14	20.22	21.04	19.51	19.79
Cr <sub>2</sub> O <sub>3</sub>	0.08	0.02	0.03	0.03	0.00	0.06	0.02	0.00	0.05	0.00	0.03	0.04	0.04	0.03	0.03	0.00	0.11	0.00
FeO	21.68	21.43	16.35	22.43	21.63	21.24	21.81	21.98	21.64	16.42	15.28	15.78	15.59	19.31	21.95	21.79	5.82	6.34
NiO	0.01	0.00	0.00	0.00	0.00	0.00	0.00	0.00	0.00	0.02	0.01	0.00	0.09	0.05	0.06	0.02	0.00	0.00
MnO	14.12	15.39	21.03	15.11	15.02	14.60	15.65	14.96	14.94	18.98	20.60	20.07	20.12	16.65	14.54	14.58	29.73	29.50
MgO	1.06	0.69	0.27	0.83	0.93	1.15	0.51	0.79	0.89	1.33	1.31	1.32	1.24	1.17	0.94	0.94	0.36	0.35
CaO	4.13	4.20	4.52	3.93	4.25	4.10	3.89	4.07	3.97	4.18	3.94	3.70	4.17	4.14	4.22	4.16	5.81	6.08
TOTAL	98.29	97.45	99.37	99.75	98.90	98.39	96.37	97.20	97.76	97.70	97.56	96.62	97.94	97.79	98.72	99.59	97.58	98.88
<b>Cations - 12</b>																		
Si	3.01	3.00	3.01	2.98	3.00	3.01	2.98	2.99	2.99	3.00	2.99	2.99	2.98	3.00	3.01	3.01	3.01	3.00
Ti	0.00	0.00	0.00	0.01	0.00	0.00	0.01	0.01	0.00	0.00	0.01	0.01	0.00	0.00	0.00	0.00	0.01	0.02
Al	2.00	1.95	1.97	2.00	1.98	1.99	1.95	1.95	1.99	2.00	1.97	1.97	2.00	1.97	1.96	2.01	1.92	1.92
Cr	0.01	0.00	0.00	0.00	0.00	0.00	0.00	0.00	0.00	0.00	0.00	0.00	0.00	0.00	0.00	0.00	0.01	0.00
Fe	1.49	1.50	1.12	1.53	1.49	1.46	1.55	1.55	1.51	1.14	1.06	1.11	1.08	1.34	1.51	1.48	0.41	0.44
Ni	0.00	0.00	0.00	0.00	0.00	0.00	0.00	0.00	0.00	0.00	0.00	0.00	0.01	0.00	0.00	0.00	0.00	0.00
Mn	0.98	1.09	1.46	1.04	1.04	1.02	1.13	1.07	1.05	1.33	1.45	1.43	1.41	1.17	1.01	1.00	2.10	2.06
Mg	0.13	0.09	0.03	0.10	0.11	0.14	0.06	0.10	0.11	0.16	0.16	0.17	0.15	0.14	0.12	0.11	0.04	0.04
Ca	0.36	0.38	0.40	0.34	0.37	0.36	0.35	0.37	0.35	0.37	0.35	0.33	0.37	0.37	0.37	0.36	0.52	0.54
Na	0.01	0.01	0.00	0.00	0.01	0.01	0.00	0.00	0.00	0.01	0.02	0.01	0.01	0.01	0.01	0.00	0.00	0.00
K	0.00	0.00	0.00	0.00	0.00	0.00	0.00	0.00	0.00	0.00	0.00	0.00	0.00	0.00	0.00	0.00	0.00	0.00
<b>Mol%</b>																		
Grs	12	12	13	11	12	12	11	12	12	12	12	11	12	12	12	12	17	17
Pyr	4	3	1	3	4	5	2	3	4	5	5	5	5	5	4	4	1	1
Alm	50	49	37	51	49	49	50	50	50	38	35	37	36	44	50	50	13	14
Sps	33	36	49	35	35	34	36	35	35	44	48	47	47	39	34	34	68	67



Table A4 - 3: EMPA data for garnet.

SAMPLE	SIB50B	SIB50B	SIB50B	SIB50B	SIB50B	SIB50B	SIB50B	SIB50B	SIB50B	SIB50B	SIB50B	SIB50B	SIB50B	SIB50B	SHB44B	SHB44B	SHB44B
	Grt2	Grt2	Grt2	Grt3	Grt3	Grt4	Grt4	Grt5	Grt5	Grt5	Grt5	Grt5	Grt5	Grt5	grt1	grt1	grt1
Analysis #	644	645	646	652	653	654	655	675	676	677	678	679	680		681	682	683
zone																	
SiO <sub>2</sub>	36.28	36.04	35.17	35.43	36.24	35.67	35.82	34.98	36.90	35.62	35.64	36.83	35.24		36.51	36.65	36.99
TiO <sub>2</sub>	0.22	0.26	0.16	0.27	0.21	0.31	0.26	0.21	0.00	0.13	0.06	0.00	0.22		0.13	0.11	0.17
Al <sub>2</sub> O <sub>3</sub>	19.48	19.19	18.95	18.87	19.53	19.27	19.11	18.56	20.48	19.17	19.87	20.41	19.14		20.65	20.59	20.69
Cr <sub>2</sub> O <sub>3</sub>	0.11	0.05	0.08	0.01	0.07	0.01	0.08	0.06	0.04	0.06	0.00	0.02	0.08		0.00	0.00	0.00
FeO	5.20	6.23	6.00	6.33	6.64	4.93	6.31	6.58	10.97	8.51	13.32	12.65	6.03		32.30	32.94	32.57
NiO	0.05	0.00	0.00	0.04	0.00	0.02	0.04	0.01	0.00	0.00	0.00	0.03	0.02		0.00	0.03	0.03
MnO	30.94	28.21	29.49	28.66	28.10	30.65	28.07	28.23	22.87	24.99	21.01	21.77	29.27		1.24	0.85	0.85
MgO	0.26	0.38	0.37	0.47	0.49	0.23	0.44	0.47	1.16	0.76	1.60	1.37	0.43		1.46	1.55	1.52
CaO	5.45	7.00	6.23	6.58	6.72	6.23	6.78	6.11	6.42	6.81	4.73	5.56	5.84		6.74	6.36	6.27
TOTAL	98.02	97.38	96.46	96.68	98.04	97.34	96.92	95.21	98.85	96.06	96.22	98.67	96.28		99.04	99.08	99.13
<b>Cations - 12</b>																	
Si	3.02	3.01	2.98	2.99	3.00	2.99	3.01	3.00	3.01	3.01	2.99	3.01	2.99		2.98	2.99	3.00
Ti	0.01	0.02	0.01	0.02	0.01	0.02	0.02	0.01	0.00	0.01	0.00	0.00	0.01		0.01	0.01	0.01
Al	1.91	1.89	1.90	1.88	1.91	1.91	1.89	1.88	1.97	1.91	1.97	1.97	1.91		1.98	1.98	1.98
Cr	0.01	0.00	0.01	0.00	0.00	0.00	0.01	0.00	0.00	0.00	0.00	0.00	0.01		0.00	0.00	0.00
Fe	0.36	0.44	0.43	0.45	0.46	0.35	0.44	0.47	0.75	0.60	0.94	0.86	0.43		2.20	2.24	2.21
Ni	0.00	0.00	0.00	0.00	0.00	0.00	0.00	0.00	0.00	0.00	0.00	0.00	0.00		0.00	0.00	0.00
Mn	2.18	2.00	2.12	2.05	1.97	2.18	2.00	2.05	1.58	1.79	1.49	1.51	2.10		0.09	0.06	0.06
Mg	0.03	0.05	0.05	0.06	0.06	0.03	0.06	0.06	0.14	0.10	0.20	0.17	0.05		0.18	0.19	0.18
Ca	0.49	0.63	0.57	0.60	0.60	0.56	0.61	0.56	0.56	0.62	0.43	0.49	0.53		0.59	0.56	0.55
Na	0.00	0.00	0.00	0.00	0.01	0.00	0.00	0.00	0.00	0.00	0.00	0.01	0.00		0.00	0.00	0.00
K	0.00	0.00	0.00	0.00	0.00	0.00	0.00	0.00	0.00	0.00	0.00	0.00	0.00		0.00	0.00	0.00
<b>Mol%</b>																	
Grs	16	20	18	19	19	18	20	18	19	20	14	16	17		19	18	18
Pyr	1	2	1	2	2	1	2	2	5	3	7	6	2		6	6	6
Alm	12	14	13	14	15	11	14	15	25	19	31	29	14		72	74	74
Sps	71	64	67	65	64	70	64	65	52	58	49	50	67		3	2	2

Table A4 - 3: EMPA data for garnet.

SAMPLE	SHB44B	SHB44B	SHB44B	SHB44B	SHB44B	SHB44B	SHB44B	SHB44B	SHB44B	SHB44B	SHB44B
	grt1	grt2	grt2	grt2	grt2	grt3	grt3	grt3	grt3	grt3	grt3
Analysis #	684	685	686	687	688	689	690	691	692	693	694
zone											
SiO <sub>2</sub>	36.59	36.46	36.79	36.79	36.08	36.83	37.15	36.76	36.05	36.52	36.88
TiO <sub>2</sub>	0.10	0.10	0.04	0.07	0.02	0.04	0.03	0.05	0.00	0.07	0.00
Al <sub>2</sub> O <sub>3</sub>	20.50	20.47	20.40	20.34	19.76	20.49	21.09	19.99	19.89	20.32	20.83
Cr <sub>2</sub> O <sub>3</sub>	0.00	0.00	0.00	0.00	0.00	0.07	0.03	0.03	0.02	0.00	0.00
FeO	32.35	31.92	32.63	32.18	32.01	31.67	33.29	31.43	31.92	32.54	32.48
NiO	0.00	0.07	0.01	0.00	0.05	0.00	0.01	0.02	0.04	0.00	0.00
MnO	0.63	1.01	0.84	0.86	0.69	1.46	0.81	0.76	0.87	0.60	0.79
MgO	1.49	1.51	1.57	1.64	1.42	1.43	1.57	1.29	1.52	1.50	1.57
CaO	6.66	6.68	6.34	6.63	6.92	6.59	5.87	7.61	7.07	6.73	6.55
TOTAL	98.32	98.23	98.62	98.52	96.98	98.63	99.86	97.95	97.42	98.28	99.10
<b>Cations - 12</b>											
Si	3.00	2.99	3.01	3.01	3.01	3.01	3.00	3.02	2.99	3.00	2.99
Ti	0.01	0.01	0.00	0.00	0.00	0.00	0.00	0.00	0.00	0.00	0.00
Al	1.98	1.98	1.97	1.96	1.94	1.97	2.00	1.94	1.95	1.97	1.99
Cr	0.00	0.00	0.00	0.00	0.00	0.00	0.00	0.00	0.00	0.00	0.00
Fe	2.22	2.19	2.23	2.20	2.23	2.16	2.24	2.16	2.21	2.23	2.21
Ni	0.00	0.00	0.00	0.00	0.00	0.00	0.00	0.00	0.00	0.00	0.00
Mn	0.04	0.07	0.06	0.06	0.05	0.10	0.06	0.05	0.06	0.04	0.05
Mg	0.18	0.18	0.19	0.20	0.18	0.17	0.19	0.16	0.19	0.18	0.19
Ca	0.58	0.59	0.56	0.58	0.62	0.58	0.51	0.67	0.63	0.59	0.57
Na	0.00	0.00	0.00	0.00	0.00	0.00	0.00	0.00	0.00	0.00	0.00
K	0.00	0.00	0.00	0.00	0.00	0.00	0.00	0.00	0.00	0.00	0.00
<b>Mol%</b>											
Grs	19	19	18	19	20	19	17	22	20	19	19
Pyr	6	6	6	7	6	6	6	5	6	6	6
Alm	73	72	73	72	73	72	75	71	72	73	73
Sps	1	2	2	2	2	3	2	2	2	1	2

Table A4 - 4: Antigorite oxygen isotope composition determined by SHRIMP.

Spot	$^{18}\text{O}/^{16}\text{O}$	$\pm\text{SE}$	$\delta^{18}\text{O}$ (‰)	$\pm\text{SE}$
SHS26-1	0.00204463	2.57E-07	13.15	0.13
SHS26-2	0.00204404	2.34E-07	12.86	0.11
SHS26-3	0.00204574	2.64E-07	13.69	0.13
SHS26-4	0.00204464	3.13E-07	13.15	0.15
SHS26-5	0.00204477	2.88E-07	13.22	0.14
SHS26-6	0.00204567	2.60E-07	13.66	0.13
SHS26-7	0.00204564	2.45E-07	13.64	0.12
SHS26-8	0.00204544	3.23E-07	13.55	0.16
SHS26-9	0.00204445	3.54E-07	13.06	0.17
SHS26-10*	0.00204276	2.87E-07	12.23	0.14
SHS26-11	0.00204605	3.96E-07	13.85	0.19
SHS26-12	0.00204599	3.74E-07	13.82	0.18
SHS26-13	0.00204492	3.11E-07	13.29	0.15
SHS26-14	0.00204512	2.66E-07	13.39	0.13
SHS26-15	0.00204442	2.69E-07	13.05	0.13
SHS26-16	0.00204475	2.32E-07	13.21	0.11
*rejected outliers		<b>average</b>	13.37	
		<b>std. dev.</b>	0.31	

Spot	$^{18}\text{O}/^{16}\text{O}$	$\pm\text{SE}$	$\delta^{18}\text{O}$ (‰)	$\pm\text{SE}$
SHS26M-1	0.00204447	2.70E-07	13.07	0.13
SHS26M-2*	0.00204400	2.71E-07	12.84	0.13
SHS26M-3	0.00204446	3.18E-07	13.07	0.16
SHS26M-4	0.00204471	3.51E-07	13.19	0.17
SHS26M-5	0.00204554	3.10E-07	13.60	0.15
SHS26M-6	0.00204577	2.42E-07	13.71	0.12
SHS26M-7	0.00204496	2.84E-07	13.31	0.14
SHS26M-8	0.00204454	3.60E-07	13.11	0.18
SHS26M-9	0.00204479	3.15E-07	13.23	0.15
SHS26M-10	0.00204539	3.01E-07	13.53	0.15
SHS26M-11	0.00204565	3.11E-07	13.65	0.15
SHS26M-12	0.00204608	3.05E-07	13.86	0.15
SHS26M-13	0.00204575	2.87E-07	13.70	0.14
		<b>average</b>	13.42	
		<b>std. dev.</b>	0.29	

<b>Instrument:</b>	SHRIMP II
<b>Session:</b>	18/06/2013
<b>AL44 repeatability:</b>	0.30‰ (1 $\sigma$ )

**Table A4 - 5: Zircon oxygen isotope composition determined by SHRIMP.**

Spot	$^{18}\text{O}/^{16}\text{O}$	$\pm 2\text{SE}$	$\delta^{18}\text{O}$ (‰)	$\pm \text{SE}$
SHS44A-1C	0.00204418	7.80E-08	5.49	0.04
SHS44A-2R B2	0.00205132	1.23E-07	8.98	0.06
SHS44A-3R B1	0.00205657	1.17E-07	11.54	0.06
SHS44A-4C	0.00204284	2.74E-07	4.84	0.13
SHS44A-5R B2	0.00204994	1.43E-07	8.30	0.07
SHS44A-6R A	0.00204374	1.79E-07	5.28	0.09
SHS44A-7C	0.00204464	1.32E-07	5.71	0.06
SHS44A-8C	0.00204369	8.30E-08	5.25	0.04
SHS44A-9C	0.00204358	1.32E-07	5.20	0.06
SHS44A-10R A	0.00204656	1.00E-07	6.65	0.05
SHS44A-11R A	0.00204235	2.76E-07	4.60	0.14
SHS44A-12C	0.00204383	1.27E-07	5.32	0.06
SHS44A-13C	0.00204387	6.20E-08	5.34	0.03
SHS44A-14R	0.00204792	5.90E-08	7.32	0.03
SHS44A-15R	0.00205602	1.06E-07	11.27	0.05
SHS44A-16C	0.00204267	1.56E-07	4.76	0.08
SHA44A-17C	0.00204382	7.50E-08	5.32	0.04
SHS44A-18R A	0.00205001	9.70E-08	8.33	0.05
SHS44A-19R	0.00205891	5.10E-08	12.68	0.02
SHS44A-20C	0.00204164	8.50E-08	4.25	0.04
SHS44A-21R	0.00205182	8.80E-08	9.22	0.04
SHS44A-22C	0.00204419	7.70E-08	5.50	0.04
SHS44A-23R B1	0.00205686	2.18E-07	11.68	0.11
SHS44A-24C	0.00204328	1.81E-07	5.05	0.09
SHS44A-25R B2	0.00205125	7.10E-08	8.94	0.03
SHS44A-26R	0.00204547	2.53E-07	6.12	0.12
SHS44A-27R	0.00204780	1.31E-07	7.26	0.06
SHS44A-28R B2	0.00204789	2.53E-07	7.30	0.12
SHS44A-29R	0.00205351	1.21E-07	10.04	0.06
SHS44A-30R	0.00205114	1.92E-07	8.89	0.09
SHS44A-31C	0.00204337	2.00E-07	5.24	0.10
SHS44A-32R	0.00205164	5.61E-07	9.28	0.27
SHS44A-33C	0.00204305	2.90E-08	5.09	0.01
SHS44A-34C	0.00204473	1.68E-07	5.91	0.08
SHS44A-35R B1	0.00205862	1.44E-07	12.68	0.07
SHS44A-36C	0.00204362	2.88E-07	5.37	0.14
SHS44A-37C	0.00204449	1.37E-07	5.79	0.07
SHS44A-38C	0.00204342	1.92E-07	5.27	0.09
SHS44A-39C	0.00204321	1.42E-07	5.17	0.07
SHS44A-40C	0.00204405	1.45E-07	5.57	0.07
SHS44A-41R	0.00204699	1.53E-07	7.01	0.07
SHS44A-42R	0.00205431	2.46E-07	10.58	0.12
SHS44A-43R	0.00204254	4.90E-08	4.84	0.02
SHS44A-44R	0.00204608	2.17E-07	6.57	0.11
SHS44A-45R	0.00205400	7.80E-08	10.43	0.04
SHS44A-46R	0.00205008	1.52E-07	8.52	0.07
SHS44A-47C	0.00204346	1.51E-07	5.29	0.07
SHS44A-48R	0.00204758	1.05E-07	7.30	0.05
SHS44A-49C	0.00204352	1.70E-07	5.32	0.08
SHS44A-50R	0.00204265	1.48E-07	4.89	0.07
		Cores average	5.24	
		Cores std.dev.	0.36	

<b>Instrument:</b>	SHRIMP II
<b>Session:</b>	17/03/2014
<b>TEM repeatability:</b>	0.33‰ (1σ)

C : core  
R : rim  
R A: rim A  
R B1: rim B1  
R B2: rim B2

**Table A4 - 5: Zircon oxygen isotope composition determined by SHRIMP.**

Spot	$^{18}\text{O}/^{16}\text{O}$	$\pm 2\text{SE}$	$\delta^{18}\text{O}$ (‰)	$\pm \text{SE}$
SHB45-1 CW	0.00204247	2.11E-07	4.66	0.10
SHB45-3 C	0.00204732	1.07E-07	7.02	0.05
SHB45-5 C	0.00204266	1.02E-07	4.75	0.05
SHB45-6 R	0.00205772	1.36E-07	12.10	0.07
SHB45-7 CW	0.00204514	7.70E-08	5.96	0.04

<b>Instrument:</b>	SHRIMP II
<b>Session:</b>	17/03/2014
<b>TEM repeatability:</b>	0.33‰ (1 $\sigma$ )

C : core

R : rim

CW: white zone in core

**Table A4 - 6: Garnet isotope composition determined by SHRIMP. Error propagation follows Martin et al. (2014b).**

Spot	zone	$^{18}\text{O}/^{16}\text{O}$	$\pm\text{SE}$	meas. $\delta^{18}\text{O}$ (‰)	$\pm\text{SE}$	Xgrs	Xpyr	Xspess	Xalm	BIAS grs	BIAS spess	corr. $\delta^{18}\text{O}$ (‰)	$\pm\text{SE}$
SV0175-1	c	0.00205345	4.31E-07	11.41	0.21	0.25	0.08	0.11	0.56	0.33	0.12	<b>10.96</b>	<b>0.34</b>
SV0175-2	c	0.00205313	3.85E-07	11.26	0.19	0.25	0.08	0.11	0.56	0.33	0.12	<b>10.80</b>	<b>0.32</b>
SV0175-3	c	0.00205321	3.64E-07	11.29	0.18	0.25	0.08	0.11	0.56	0.33	0.12	<b>10.84</b>	<b>0.32</b>
SV0175-20	c	0.00205351	4.38E-07	11.44	0.21	0.25	0.08	0.11	0.56	0.33	0.12	<b>10.99</b>	<b>0.34</b>
SV0175-18	c	0.00205261	4.59E-07	11.00	0.22	0.25	0.08	0.11	0.56	0.33	0.12	<b>10.55</b>	<b>0.35</b>
SV0175-7	c	0.00205332	2.30E-07	11.35	0.11	0.27	0.10	0.06	0.57	0.34	0.11	<b>10.89</b>	<b>0.29</b>
SV0175-8	c	0.00205383	2.92E-07	11.59	0.14	0.27	0.10	0.06	0.57	0.34	0.11	<b>11.14</b>	<b>0.30</b>
SV0175-15	c	0.00205421	1.58E-07	11.78	0.08	0.29	0.11	0.02	0.58	0.35	0.11	<b>11.33</b>	<b>0.28</b>
SV0175-9	c	0.00205345	5.20E-07	11.41	0.25	0.29	0.11	0.02	0.58	0.35	0.11	<b>10.95</b>	<b>0.37</b>
											Average:	<b>10.94</b>	
											Std. dev:	<b>0.22</b>	
SV0175-10	m	0.00205341	5.42E-07	11.39	0.26	0.31	0.12	0.01	0.56	0.35	0.11	<b>10.93</b>	<b>0.37</b>
SV0175-11	m	0.00205416	5.53E-07	11.76	0.27	0.31	0.12	0.01	0.56	0.35	0.11	<b>11.30</b>	<b>0.38</b>
SV0175-12	m	0.00205449	6.38E-07	11.92	0.31	0.31	0.12	0.01	0.56	0.35	0.11	<b>11.46</b>	<b>0.41</b>
											Average:	<b>11.23</b>	
											Std. dev:	<b>0.27</b>	
SV0175-4	r	0.00205573	4.29E-07	12.53	0.21	0.28	0.06	0.08	0.58	0.34	0.12	<b>12.07</b>	<b>0.34</b>
SV0175-5	r	0.00205594	5.73E-07	12.63	0.28	0.28	0.06	0.08	0.58	0.34	0.12	<b>12.17</b>	<b>0.38</b>
SV0175-6	r	0.00205545	2.51E-07	12.39	0.12	0.28	0.06	0.08	0.58	0.34	0.12	<b>11.93</b>	<b>0.29</b>
SV0175-19	r	0.00205698	3.10E-07	13.14	0.15	0.28	0.06	0.08	0.58	0.34	0.12	<b>12.68</b>	<b>0.30</b>
SV0175-16	r	0.00205718	2.89E-07	13.24	0.14	0.28	0.06	0.08	0.58	0.34	0.12	<b>12.78</b>	<b>0.30</b>
SV0175-17	r	0.00205638	2.88E-07	12.84	0.14	0.28	0.06	0.08	0.58	0.34	0.12	<b>12.39</b>	<b>0.30</b>
SV0175-13	r	0.00206125	2.47E-07	15.23	0.12	0.25	0.06	0.12	0.57	0.33	0.12	<b>14.78</b>	<b>0.29</b>
SV0175-14	r	0.00205894	5.19E-07	14.10	0.25	0.25	0.06	0.12	0.57	0.33	0.12	<b>13.64</b>	<b>0.36</b>
											Average:	<b>12.81</b>	
											Std. dev:	<b>0.96</b>	

c: core  
m: mantle  
r: rim

Instrument:	SHRIMP SI
Session:	04/08/2014
UWG2 repeatability:	0.23

**Table A4 - 6: Garnet isotope composition determined by SHRIMP. Error propagation follows Martin et al. (2014b).**

Spot	zone	$^{18}\text{O}/^{16}\text{O}$	$\pm\text{SE}$	meas. $\delta^{18}\text{O}$ (‰)	$\pm\text{SE}$	Xgrs	Xpyr	Xspess	Xalm	BIAS grs	BIAS spess	corr. $\delta^{18}\text{O}$ (‰)	$\pm\text{SE}$
SV1213-3	c	0.00206159	4.65E-07	15.40	0.23	0.30	0.06	0.05	0.59	0.35	0.11	<b>14.93</b>	<b>0.35</b>
SV1213-5	c	0.00206102	3.20E-07	15.12	0.16	0.30	0.06	0.05	0.59	0.35	0.11	<b>14.65</b>	<b>0.31</b>
SV1213-9	c	0.00206168	3.84E-07	15.44	0.19	0.30	0.06	0.05	0.59	0.35	0.11	<b>14.98</b>	<b>0.32</b>
SV1213-13	c	0.00206147	4.75E-07	15.34	0.23	0.30	0.06	0.05	0.59	0.35	0.11	<b>14.87</b>	<b>0.35</b>
SV1213-14	c	0.00206082	2.07E-07	15.02	0.10	0.30	0.06	0.05	0.59	0.35	0.11	<b>14.56</b>	<b>0.28</b>
SV1213-15	c	0.00206004	3.09E-07	14.64	0.15	0.30	0.06	0.05	0.59	0.35	0.11	<b>14.17</b>	<b>0.30</b>
SV1213-16	c	0.00206141	5.50E-07	15.31	0.27	0.30	0.06	0.05	0.59	0.35	0.11	<b>14.84</b>	<b>0.38</b>
												Average:	<b>14.72</b>
												Std. dev:	<b>0.28</b>
SV1213-6	m	0.00205556	4.69E-07	12.44	0.23	0.29	0.16	0.07	0.48	0.35	0.12	<b>11.98</b>	<b>0.35</b>
SV1213-2	m	0.00205433	5.48E-07	11.84	0.27	0.29	0.16	0.07	0.48	0.35	0.12	<b>11.38</b>	<b>0.38</b>
SV1213-17	m	0.00205589	4.15E-07	12.60	0.20	0.29	0.16	0.07	0.48	0.35	0.12	<b>12.14</b>	<b>0.33</b>
SV1213-11	m	0.00205500	2.08E-07	12.17	0.10	0.29	0.16	0.07	0.48	0.35	0.12	<b>11.71</b>	<b>0.28</b>
												Average:	<b>11.80</b>
												Std. dev:	<b>0.33</b>
SV1213-4	r	0.00205527	2.19E-07	12.30	0.11	0.26	0.08	0.10	0.56	0.33	0.12	<b>11.85</b>	<b>0.28</b>
SV1213-1	r	0.00205569	1.86E-07	12.51	0.09	0.26	0.08	0.10	0.56	0.33	0.12	<b>12.06</b>	<b>0.28</b>
SV1213-8	r	0.00205668	5.28E-07	12.99	0.26	0.26	0.08	0.10	0.56	0.33	0.12	<b>12.54</b>	<b>0.37</b>
SV1213-12	r	0.00205555	6.83E-07	12.44	0.33	0.26	0.08	0.10	0.56	0.33	0.12	<b>11.98</b>	<b>0.42</b>
SV1213-10	r	0.00205707	2.15E-07	13.19	0.10	0.26	0.08	0.10	0.56	0.33	0.12	<b>12.73</b>	<b>0.28</b>
SV1213-7	r	0.00205540	1.68E-07	12.37	0.08	0.26	0.08	0.10	0.56	0.33	0.12	<b>11.91</b>	<b>0.28</b>
SV1213-20	r	0.00205688	3.14E-07	13.09	0.15	0.26	0.08	0.10	0.56	0.33	0.12	<b>12.64</b>	<b>0.30</b>
SV1213-18	r	0.00205600	4.13E-07	12.66	0.20	0.26	0.08	0.10	0.56	0.33	0.12	<b>12.21</b>	<b>0.33</b>
SV1213-19	r	0.00205566	2.03E-07	12.49	0.10	0.26	0.08	0.10	0.56	0.33	0.12	<b>12.04</b>	<b>0.28</b>
												Average:	<b>12.22</b>
												Std. dev:	<b>0.33</b>

<b>Instrument:</b>	SHRIMP SI
<b>Session:</b>	04/08/2014
<b>UWG2 repeatability:</b>	0.23

**Table A4 - 6: Garnet isotope composition determined by SHRIMP.** Error propagation follows Martin et al. (2014b).

Spot	zone	$^{18}\text{O}/^{16}\text{O}$	$\pm\text{SE}$	meas. $\delta^{18}\text{O}$ (‰)	$\pm\text{SE}$	Xgrs	Xpyr	Xspess	Xalm	BIAS grs	BIAS spess	corr. $\delta^{18}\text{O}$ (‰)	$\pm\text{SE}$
SHS3-1		0.00206648	3.11E-07	15.80	0.15	0.14	0.03	0.32	0.50	0.29	0.15	<b>15.36</b>	<b>0.30</b>
SHS3-10		0.00206729	1.31E-07	16.22	0.06	0.13	0.05	0.27	0.56	0.29	0.14	<b>15.78</b>	<b>0.27</b>
SHS3-11		0.00206690	2.53E-07	16.02	0.12	0.13	0.04	0.30	0.53	0.29	0.15	<b>15.58</b>	<b>0.29</b>
SHS3-12		0.00206740	1.05E-07	16.27	0.05	0.13	0.03	0.33	0.51	0.29	0.15	<b>15.83</b>	<b>0.27</b>
SHS3-2		0.00206788	1.47E-07	16.48	0.07	0.13	0.05	0.31	0.51	0.29	0.15	<b>16.04</b>	<b>0.27</b>
SHS3-3		0.00206674	2.91E-07	15.93	0.14	0.12	0.03	0.34	0.51	0.29	0.16	<b>15.49</b>	<b>0.30</b>
SHS3-4		0.00206761	1.96E-07	16.35	0.09	0.12	0.03	0.34	0.51	0.28	0.16	<b>15.91</b>	<b>0.28</b>
SHS3-5		0.00206739	1.20E-07	16.25	0.06	0.13	0.05	0.28	0.55	0.29	0.14	<b>15.81</b>	<b>0.27</b>
SHS3-6		0.00206720	1.55E-07	16.16	0.08	0.15	0.04	0.24	0.56	0.30	0.14	<b>15.73</b>	<b>0.27</b>
SHS3-7		0.00206776	1.58E-07	16.44	0.08	0.11	0.04	0.30	0.54	0.28	0.15	<b>16.01</b>	<b>0.27</b>
SHS3-8		0.00206775	2.16E-07	16.44	0.10	0.13	0.05	0.27	0.55	0.29	0.14	<b>16.01</b>	<b>0.28</b>
SHS3-9		0.00206738	2.90E-08	16.25	0.01	0.14	0.03	0.34	0.49	0.29	0.16	<b>15.81</b>	<b>0.26</b>
Average:												<b>15.78</b>	
Std. dev:												<b>0.21</b>	
SHB51B-1		0.00206322	9.20E-08	13.81	0.04	0.16	0.01	0.69	0.14 si	0.30	0.23	<b>13.28</b>	<b>0.26</b>
SIB50B-10		0.00206365	5.50E-08	14.02	0.03	0.17	0.07	0.42	0.34 si	0.30	0.17	<b>13.55</b>	<b>0.26</b>
SIB50B-2		0.00206356	1.32E-07	13.97	0.06	0.16	0.02	0.69	0.14 si	0.30	0.23	<b>13.44</b>	<b>0.27</b>
SIB50B-3		0.00206379	7.40E-08	14.09	0.04	0.20	0.06	0.40	0.33 si	0.31	0.17	<b>13.61</b>	<b>0.26</b>
SIB50B-4		0.00206334	1.74E-07	13.87	0.08	0.15	0.06	0.48	0.31 si	0.29	0.18	<b>13.39</b>	<b>0.27</b>
SIB50B-5		0.00206439	7.80E-08	14.38	0.04	0.17	0.02	0.67	0.14 si	0.30	0.23	<b>13.85</b>	<b>0.26</b>
Average:												<b>13.52</b>	
Std. dev:												<b>0.20</b>	

<b>Instrument:</b>	SHRIMP SI
<b>Session:</b>	12/07/2013
<b>UWG2 repeatability:</b>	0.22



**Table A4 - 6: Garnet isotope composition determined by SHRIMP. Error propagation follows Martin et al. (2014b).**

Spot	zone	$^{18}\text{O}/^{16}\text{O}$	$\pm\text{SE}$	meas. $\delta^{18}\text{O}$ (‰)	$\pm\text{SE}$	Xgrs	Xpyr	Xspess	Xalm	BIAS grs	BIAS spess	corr. $\delta^{18}\text{O}$ (‰)	$\pm\text{SE}$
SHB05-1		0.00206291	1.78E-07	13.87	0.09	0.22	0.06	0.06	0.66	0.32	0.11	<b>13.44</b>	<b>0.28</b>
SHB05-10		0.00206470	1.04E-07	14.76	0.05	0.23	0.06	0.07	0.65	0.32	0.11	<b>14.32</b>	<b>0.27</b>
SHB05-11		0.00206333	5.00E-08	14.10	0.02	0.24	0.06	0.09	0.62	0.33	0.12	<b>13.66</b>	<b>0.27</b>
SHB05-12		0.00206361	1.63E-07	14.24	0.08	0.23	0.06	0.06	0.64	0.32	0.11	<b>13.80</b>	<b>0.28</b>
SHB05-13		0.00206400	1.96E-07	14.43	0.09	0.24	0.06	0.08	0.63	0.33	0.12	<b>13.99</b>	<b>0.28</b>
SHB05-14		0.00206357	1.83E-07	14.22	0.09	0.23	0.05	0.13	0.59	0.32	0.12	<b>13.77</b>	<b>0.28</b>
SHB05-15		0.00206452	1.73E-07	14.69	0.08	0.25	0.06	0.08	0.62	0.33	0.12	<b>14.24</b>	<b>0.28</b>
SHB05-16		0.00206269	1.10E-07	13.80	0.05	0.23	0.07	0.05	0.66	0.32	0.11	<b>13.36</b>	<b>0.27</b>
SHB05-17		0.00206374	6.40E-08	14.31	0.03	0.23	0.07	0.05	0.65	0.32	0.11	<b>13.87</b>	<b>0.27</b>
SHB05-18		0.00206401	1.24E-07	14.44	0.06	0.24	0.06	0.09	0.62	0.33	0.12	<b>14.00</b>	<b>0.27</b>
SHB05-19		0.00206335	8.20E-08	14.12	0.04	0.23	0.06	0.06	0.65	0.32	0.11	<b>13.69</b>	<b>0.27</b>
SHB05-2		0.00206384	7.40E-08	14.33	0.04	0.24	0.05	0.10	0.61	0.33	0.12	<b>13.88</b>	<b>0.27</b>
SHB05-20		0.00206357	2.18E-07	14.23	0.11	0.23	0.06	0.07	0.64	0.32	0.12	<b>13.79</b>	<b>0.28</b>
SHB05-3		0.00206392	7.30E-08	14.37	0.04	0.23	0.05	0.10	0.61	0.32	0.12	<b>13.93</b>	<b>0.27</b>
SHB05-4		0.00206392	8.90E-08	14.37	0.04	0.22	0.06	0.10	0.62	0.32	0.12	<b>13.93</b>	<b>0.27</b>
SHB05-5		0.00206497	5.80E-08	14.88	0.03	0.21	0.03	0.26	0.50	0.32	0.14	<b>14.42</b>	<b>0.26</b>
SHB05-6		0.00206355	1.86E-07	14.19	0.09	0.23	0.06	0.07	0.65	0.32	0.12	<b>13.75</b>	<b>0.28</b>
SHB05-7		0.00206355	3.70E-08	14.19	0.02	0.23	0.06	0.05	0.65	0.32	0.11	<b>13.75</b>	<b>0.26</b>
SHB05-8		0.00206376	9.70E-08	14.30	0.05	0.24	0.05	0.11	0.60	0.33	0.12	<b>13.85</b>	<b>0.27</b>
SHB05-9		0.00206377	1.51E-07	14.30	0.07	0.23	0.05	0.09	0.63	0.32	0.12	<b>13.86</b>	<b>0.27</b>
												<b>13.87</b>	
												<b>0.26</b>	

<b>Instrument:</b>	SHRIMP SI
<b>Session:</b>	12/07/2013
<b>UWG2 repeatability:</b>	0.22

**Table A4 - 6: Garnet isotope composition determined by SHRIMP. Error propagation follows Martin et al. (2014b).**

Spot	zone	$^{18}\text{O}/^{16}\text{O}$	$\pm\text{SE}$	meas. $\delta^{18}\text{O}$ (‰)	$\pm\text{SE}$	Xgrs	Xpyr	Xspess	Xalm	BIAS grs	BIAS spess	corr. $\delta^{18}\text{O}$ (‰)	$\pm\text{SE}$
SHB12B-9C	c	0.00204948	1.62E-07	7.43	0.08	0.24	0.15	0.11	0.51	0.33	0.12	<b>6.98</b>	<b>0.28</b>
SHB12B-2C	c	0.00204908	3.13E-07	7.21	0.15	0.23	0.18	0.07	0.51	0.32	0.12	<b>6.77</b>	<b>0.31</b>
SHB12B-12C	c	0.00204939	3.29E-07	7.40	0.16	0.23	0.18	0.08	0.51	0.32	0.12	<b>6.96</b>	<b>0.31</b>
SHB12B-1C	c	0.00204961	1.69E-07	7.46	0.08	0.23	0.18	0.07	0.52	0.32	0.12	<b>7.03</b>	<b>0.28</b>
SHB12B-3R	c	0.00204976	1.52E-07	7.55	0.07	0.23	0.18	0.07	0.51	0.32	0.12	<b>7.11</b>	<b>0.27</b>
SHB12B-10C	c	0.00204979	2.45E-07	7.58	0.12	0.22	0.19	0.07	0.51	0.32	0.12	<b>7.15</b>	<b>0.29</b>
SHB12B-11C	c	0.00205006	1.94E-07	7.73	0.09	0.23	0.19	0.07	0.51	0.32	0.12	<b>7.29</b>	<b>0.28</b>
SHB12B-8C	c	0.00205009	2.24E-07	7.72	0.11	0.23	0.19	0.07	0.52	0.32	0.11	<b>7.29</b>	<b>0.29</b>
SHB12B-13C	c	0.00205040	5.30E-08	7.90	0.03	0.24	0.19	0.07	0.51	0.33	0.11	<b>7.46</b>	<b>0.27</b>
SHB12B-5C	c	0.00205053	2.09E-07	7.93	0.10	0.23	0.20	0.07	0.51	0.32	0.11	<b>7.49</b>	<b>0.28</b>
SHB12B-6C	c	0.00205085	3.60E-08	8.10	0.02	0.23	0.19	0.07	0.52	0.32	0.11	<b>7.66</b>	<b>0.26</b>
SHB12B-4C	c	0.00205104	9.60E-08	8.17	0.05	0.22	0.20	0.07	0.51	0.32	0.11	<b>7.73</b>	<b>0.27</b>
*shb12b-2	c	0.00204316	1.42E-07	7.35	0.08	0.23	0.18	0.06	0.53	0.32	0.11	<b>6.91</b>	<b>0.28</b>
*shb12b-3	c	0.00204333	8.05E-08	7.63	0.10	0.24	0.18	0.06	0.52	0.33	0.11	<b>7.19</b>	<b>0.28</b>
*shb12b-4	c	0.00204303	1.35E-07	7.25	0.12	0.23	0.18	0.06	0.53	0.33	0.11	<b>6.81</b>	<b>0.29</b>
*shb12b-6	c	0.00204307	1.94E-07	7.55	0.08	0.25	0.18	0.06	0.52	0.33	0.11	<b>7.11</b>	<b>0.28</b>
*shb12b-8	c	0.00204326	1.20E-07	7.46	0.03	0.24	0.16	0.08	0.52	0.33	0.12	<b>7.02</b>	<b>0.27</b>
*shb12b-9	c	0.00204294	1.22E-07	7.45	0.05	0.23	0.15	0.09	0.52	0.32	0.12	<b>7.00</b>	<b>0.27</b>
*shb12b-13	c	0.00204397	1.33E-07	7.81	0.11	0.24	0.18	0.05	0.52	0.33	0.11	<b>7.37</b>	<b>0.29</b>
*shb12b-14	c	0.00204267	1.21E-07	7.39	0.09	0.24	0.17	0.07	0.53	0.33	0.12	<b>6.95</b>	<b>0.28</b>
*shb12b-21	c	0.00204342	8.70E-08	7.58	0.02	0.24	0.18	0.06	0.53	0.33	0.11	<b>7.14</b>	<b>0.26</b>
*shb12b-22	c	0.00204331	9.40E-08	7.52	0.05	0.23	0.16	0.08	0.52	0.32	0.12	<b>7.08</b>	<b>0.27</b>
*shb12b-24	c	0.00204350	1.16E-07	7.50	0.02	0.25	0.15	0.09	0.51	0.33	0.12	<b>7.05</b>	<b>0.26</b>
*shb12b-25	c	0.00204376	1.13E-07	7.57	0.08	0.24	0.16	0.08	0.53	0.33	0.12	<b>7.13</b>	<b>0.28</b>
Average:												<b>7.15</b>	
Std. dev:												<b>0.25</b>	

c: core

\*

Instrument:	SHRIMP SI
Session:	12/07/2013
UWG2 repeatability:	0.22

Instrument:	SHRIMP SI
Session:	29/07/2013
UWG2 repeatability:	0.27

**Table A4 - 6: Garnet isotope composition determined by SHRIMP. Error propagation follows Martin et al. (2014b).**

Spot	zone	$^{18}\text{O}/^{16}\text{O}$	$\pm\text{SE}$	meas. $\delta^{18}\text{O}$ (‰)	$\pm\text{SE}$	Xgrs	Xpyr	Xspess	Xalm	BIAS grs	BIAS spess	corr. $\delta^{18}\text{O}$ (‰)	$\pm\text{SE}$
SHB12B-4R.2	r	0.00205403	1.47E-07	9.66	0.07	0.21	0.09	0.13	0.58	0.31	0.12	<b>9.22</b>	<b>0.27</b>
SHB12B-7R	r	0.00205744	1.25E-07	11.31	0.06	0.20	0.07	0.19	0.54	0.31	0.13	<b>10.87</b>	<b>0.27</b>
SHB12B-7R.2	r	0.00205842	1.54E-07	11.79	0.07	0.22	0.08	0.16	0.54	0.32	0.13	<b>11.35</b>	<b>0.27</b>
SHB12B-1R	r	0.00205916	1.71E-07	12.14	0.08	0.24	0.08	0.15	0.53	0.33	0.13	<b>11.69</b>	<b>0.28</b>
SHB12B-3R	r	0.00206169	5.30E-08	13.37	0.03	0.25	0.07	0.17	0.51	0.33	0.13	<b>12.91</b>	<b>0.26</b>
SHB12B-2R	r	0.00206258	1.00E-07	13.80	0.05	0.25	0.08	0.13	0.53	0.33	0.12	<b>13.35</b>	<b>0.27</b>
SHB12B-5R	r	0.00206270	1.86E-07	13.87	0.09	0.25	0.08	0.14	0.53	0.33	0.12	<b>13.41</b>	<b>0.28</b>
SHB12B-6R.2	r	0.00206292	8.00E-08	14.01	0.04	0.25	0.08	0.13	0.54	0.33	0.12	<b>13.56</b>	<b>0.27</b>
SHB12B-6R	r	0.00206411	1.92E-07	14.57	0.09	0.23	0.08	0.13	0.56	0.32	0.12	<b>14.12</b>	<b>0.28</b>
SHB12B-4R.2	r	0.00206414	1.09E-07	14.59	0.05	0.21	0.09	0.13	0.58	0.31	0.12	<b>14.16</b>	<b>0.27</b>
SHB12B-4R	r	0.00206461	8.10E-08	14.81	0.04	0.21	0.08	0.13	0.57	0.32	0.12	<b>14.37</b>	<b>0.27</b>
*shb12b-1	r	0.00205531	1.29E-07	13.72	0.14	0.23	0.07	0.15	0.55	0.33	0.12	<b>13.27</b>	<b>0.30</b>
*shb12b-7	r	0.00205476	1.17E-07	13.07	0.05	0.26	0.08	0.11	0.55	0.33	0.12	<b>12.62</b>	<b>0.27</b>
*shb12b-10	r	0.00205396	1.10E-07	12.79	0.09	0.26	0.08	0.10	0.56	0.34	0.12	<b>12.33</b>	<b>0.28</b>
*shb12b-11	r	0.00205383	1.72E-07	12.78	0.08	0.26	0.08	0.11	0.55	0.34	0.12	<b>12.32</b>	<b>0.27</b>
*shb12b-12	r	0.00205696	1.59E-07	14.41	0.08	0.24	0.08	0.10	0.57	0.33	0.12	<b>13.96</b>	<b>0.28</b>
*shb12b-15	r	0.00205297	9.65E-08	12.23	0.07	0.26	0.08	0.11	0.55	0.34	0.12	<b>11.78</b>	<b>0.27</b>
*shb12b-17	r	0.00205642	1.59E-07	13.93	0.01	0.27	0.08	0.10	0.55	0.34	0.12	<b>13.48</b>	<b>0.26</b>
*shb12b-20	r	0.00205313	1.47E-07	12.25	0.18	0.22	0.07	0.15	0.56	0.32	0.13	<b>11.80</b>	<b>0.32</b>
*shb12b-23	r	0.00205426	1.16E-07	12.98	0.11	0.24	0.08	0.10	0.58	0.33	0.12	<b>12.53</b>	<b>0.28</b>
											Average:	<b>12.65</b>	
											Std. dev:	<b>1.29</b>	

r: rim

\* thin-section mount

Instrument:	SHRIMP SI
Session:	12/07/2013
UWG2 repeatability:	0.22

Instrument:	SHRIMP SI
Session:	29/07/2013
UWG2 repeatability:	0.27

**Table A4 - 6: Garnet isotope composition determined by SHRIMP. Error propagation follows Martin et al. (2014b).**

Spot	zone	$^{18}\text{O}/^{16}\text{O}$	$\pm\text{SE}$	meas. $\delta^{18}\text{O}$ (‰)	$\pm\text{SE}$	Xgrs	Xpyr	Xspess	Xalm	BIAS grs	BIAS spess	corr. $\delta^{18}\text{O}$ (‰)	$\pm\text{SE}$
SHS44A-1		0.00206496	1.54E-07	14.93	0.07	0.18	0.07	0.01	0.74	0.30	0.11	<b>14.52</b>	<b>0.27</b>
SHS44A-10		0.00206486	1.94E-07	14.91	0.09	0.20	0.05	0.04	0.71	0.31	0.11	<b>14.48</b>	<b>0.28</b>
SHS44A-2		0.00206567	1.15E-07	15.28	0.06	0.19	0.06	0.02	0.73	0.31	0.11	<b>14.86</b>	<b>0.27</b>
SHS44A-3		0.00206607	2.69E-07	15.48	0.13	0.17	0.07	0.02	0.75	0.30	0.11	<b>15.07</b>	<b>0.29</b>
SHS44A-4		0.00206554	3.90E-08	15.22	0.02	0.19	0.06	0.02	0.73	0.31	0.11	<b>14.80</b>	<b>0.26</b>
SHS44A-6		0.00206572	1.54E-07	15.32	0.07	0.19	0.06	0.02	0.72	0.31	0.11	<b>14.90</b>	<b>0.27</b>
SHS44A-7		0.00206599	1.53E-07	15.45	0.07	0.18	0.07	0.02	0.73	0.31	0.11	<b>15.04</b>	<b>0.27</b>
SHS44A-8		0.00206515	8.20E-08	15.05	0.04	0.17	0.07	0.02	0.74	0.30	0.11	<b>14.63</b>	<b>0.27</b>
SHS44A-9		0.00206484	2.68E-07	14.90	0.13	0.17	0.07	0.02	0.75	0.30	0.11	<b>14.49</b>	<b>0.29</b>
											Average:	<b>14.75</b>	
											Std. dev:	<b>0.23</b>	
SHS44B-1		0.00206542	1.71E-07	15.15	0.08	0.18	0.07	0.01	0.74	0.30	0.11	<b>14.73</b>	<b>0.28</b>
SHS44B-10		0.00206556	2.02E-07	15.24	0.10	0.18	0.07	0.02	0.73	0.31	0.11	<b>14.83</b>	<b>0.28</b>
SHS44B-2		0.00206666	1.18E-07	15.75	0.06	0.18	0.07	0.03	0.71	0.31	0.11	<b>15.33</b>	<b>0.27</b>
SHS44B-3		0.00206590	6.80E-08	15.38	0.03	0.18	0.07	0.02	0.73	0.31	0.11	<b>14.97</b>	<b>0.27</b>
SHS44B-4		0.00206610	1.42E-07	15.48	0.07	0.20	0.05	0.04	0.70	0.31	0.11	<b>15.06</b>	<b>0.27</b>
SHS44B-5		0.00206560	1.30E-07	15.24	0.06	0.19	0.07	0.01	0.73	0.31	0.11	<b>14.82</b>	<b>0.27</b>
SHS44B-6		0.00206562	2.09E-07	15.25	0.10	0.19	0.05	0.08	0.69	0.31	0.12	<b>14.82</b>	<b>0.28</b>
SHS44B-7		0.00206518	2.91E-07	15.05	0.14	0.18	0.07	0.02	0.74	0.31	0.11	<b>14.64</b>	<b>0.30</b>
SHS44B-8		0.00206604	2.09E-07	15.48	0.10	0.19	0.05	0.04	0.71	0.31	0.11	<b>15.06</b>	<b>0.28</b>
SHS44B-9		0.00206488	2.07E-07	14.91	0.10	0.17	0.07	0.01	0.75	0.30	0.11	<b>14.50</b>	<b>0.28</b>
											Average:	<b>14.88</b>	
											Std. dev:	<b>0.24</b>	

Instrument: SHRIMP SI  
 Session: #####  
 UWG2 repeatability: 0.22

**Table A4 - 6: Garnet isotope composition determined by SHRIMP. Error propagation follows Martin et al. (2014b).**

Spot	zone	$^{18}\text{O}/^{16}\text{O}$	$\pm\text{SE}$	meas. $\delta^{18}\text{O}$ (‰)	$\pm\text{SE}$	Xgrs	Xpyr	Xspess	Xalm	BIAS grs	BIAS spess	corr. $\delta^{18}\text{O}$ (‰)	$\pm\text{SE}$
SHB45-4C	c	0.00206028	7.20E-08	12.74	0.04	0.25	0.13	0.03	0.59	0.33	0.11	<b>12.30</b>	<b>0.27</b>
SHB45-6C	c	0.00206092	1.19E-07	13.06	0.06	0.27	0.12	0.03	0.58	0.34	0.11	<b>12.61</b>	<b>0.27</b>
SHB45-3C	c	0.00206152	9.30E-08	13.34	0.04	0.27	0.12	0.03	0.58	0.34	0.11	<b>12.89</b>	<b>0.27</b>
SHB45-12C	c	0.00206127	1.63E-07	13.25	0.08	0.25	0.12	0.04	0.60	0.33	0.11	<b>12.81</b>	<b>0.28</b>
SHB45-8	c	0.00206164	1.59E-07	13.41	0.08	0.25	0.12	0.03	0.59	0.33	0.11	<b>12.97</b>	<b>0.28</b>
SHB45-1C	c	0.00206173	2.22E-07	13.44	0.11	0.25	0.12	0.04	0.60	0.33	0.11	<b>12.99</b>	<b>0.29</b>
SHB45-9C	c	0.00206192	1.41E-07	13.56	0.07	0.25	0.12	0.04	0.59	0.33	0.11	<b>13.11</b>	<b>0.27</b>
SHB45-7C	c	0.00206230	2.20E-07	13.74	0.11	0.26	0.10	0.05	0.58	0.34	0.11	<b>13.29</b>	<b>0.29</b>
SHB45-10C	c	0.00206180	2.06E-07	13.50	0.10	0.24	0.12	0.04	0.60	0.33	0.11	<b>13.07</b>	<b>0.28</b>
SHB45-5C	c	0.00206201	7.40E-08	13.59	0.04	0.25	0.13	0.03	0.60	0.33	0.11	<b>13.15</b>	<b>0.27</b>
Average:												<b>12.92</b>	
Std. dev:												<b>0.29</b>	
SHB45-4R	r	0.00206438	1.86E-07	14.74	0.09	0.25	0.08	0.04	0.64	0.33	0.11	<b>14.30</b>	<b>0.28</b>
SHB45-9R	r	0.00206507	1.19E-07	15.09	0.06	0.27	0.07	0.05	0.60	0.34	0.11	<b>14.64</b>	<b>0.27</b>
SHB45-1R	r	0.00206526	1.83E-07	15.16	0.09	0.27	0.07	0.05	0.61	0.34	0.11	<b>14.71</b>	<b>0.28</b>
SHB45-12R	r	0.00206490	1.25E-07	15.02	0.06	0.27	0.08	0.02	0.63	0.34	0.11	<b>14.57</b>	<b>0.27</b>
SHB45-2	r	0.00206459	6.60E-08	14.83	0.03	0.25	0.09	0.01	0.65	0.33	0.11	<b>14.40</b>	<b>0.27</b>
SHB45-7R	r	0.00206465	2.43E-07	14.88	0.12	0.24	0.09	0.01	0.65	0.33	0.11	<b>14.45</b>	<b>0.29</b>
SHB45-3R	r	0.00206528	1.52E-07	15.17	0.07	0.27	0.08	0.01	0.63	0.34	0.11	<b>14.73</b>	<b>0.27</b>
SHB45-11R	r	0.00206503	4.40E-08	15.08	0.02	0.26	0.08	0.01	0.65	0.33	0.11	<b>14.64</b>	<b>0.27</b>
SHB45-6R	r	0.00206608	7.70E-08	15.58	0.04	0.28	0.08	0.02	0.62	0.34	0.11	<b>15.12</b>	<b>0.27</b>
SHB45-5R	r	0.00207086	2.25E-07	17.91	0.11	0.26	0.08	0.03	0.64	0.33	0.11	<b>17.47</b>	<b>0.29</b>
Average:												<b>14.62</b>	
Std. dev:												<b>0.24</b>	

c: core

r: rim

<b>Instrument:</b>	SHRIMP SI
<b>Session:</b>	12/07/2013
<b>UWG2 repeatability:</b>	0.22

**Table A4 - 7: Garnet trace element composition determined by LA-ICP-MS. c: core, m: mantle, r: rim**

Spot #	SHB45-01	SHB45-02	SHB45-03	SHB45-04	SHB45-05	SHB45-06	SHB45-07	SHB45-08	SHB45-09	SHB45-10	SHB12B-01	SHB12B-02
Sample	SHB45	SHB45	SHB45	SHB45	SHB45	SHB45	SHB45	SHB45	SHB45	SHB45	SHB12B	SHB12B
	r	r	c	c	c	r	r	r	c	c	c	c
(ppm)												
<b>Mg (wt%)</b>	1.14	1.03	1.63	1.51	1.41	1.18	1.15	1.12	1.40	1.63	2.29	2.12
<b>P</b>	38.6	34.1	37.6	40.7	45.5	29.7	28.3	30.3	43	38.4	45.6	46.2
<b>Ca (wt%)</b>	5.318	5.796	5.419	5.394	5.524	5.611	5.51	5.755	5.546	5.264	5.026	5.083
<b>Sc</b>												
<b>Ti</b>	332.2	300	438.4	549	841	300.6	308.6	332.6	720	399.5	5500	3610
<b>Cr</b>	240.5	263.7	353.2	351.4	276.7	229.8	180.1	182.7	268.5	276.3	338.2	267.1
<b>Mn (wt%)</b>	0.33	0.78	0.81	1.20	2.21	0.36	0.32	0.46	1.59	0.81	2.44	2.73
<b>Ni</b>	bdl	0.28	0.53	0.75	0.96	0.88	bdl	0.31	0.38	0.63	1.68	2.00
<b>Zn</b>	25.50	20.00	28.07	27.30	26.30	25.70	26.10	23.10	23.31	28.00	20.33	18.30
<b>Rb</b>	bdl	bdl	bdl	bdl	0.07	bdl	bdl	bdl	bdl	bdl	0.18	0.26
<b>Sr</b>	0.0224	0.0198	0.0556	0.0504	0.089	0.0356	0.0188	0.0139	0.058	0.0607	0.164	0.25
<b>Y</b>	148.8	140	162.6	149.5	300.3	154.2	130.4	167.6	200.6	180.2	849.2	915
<b>Zr</b>	0.4	0.15	3.9	2.77	260	0.39	0.301	0.179	2.13	2.64	2.87	2.95
<b>Nb</b>	bdl	bdl	bdl	bdl	bdl	bdl	bdl	bdl	bdl	bdl	6	4
<b>Ba</b>	bdl	bdl	bdl	bdl	bdl	bdl	bdl	bdl	bdl	bdl	bdl	bdl
<b>La</b>	bdl	bdl	bdl	bdl	bdl	bdl	bdl	bdl	bdl	bdl	bdl	bdl
<b>Ce</b>	bdl	bdl	bdl	bdl	bdl	bdl	bdl	bdl	bdl	bdl	bdl	bdl
<b>Pr</b>	bdl	bdl	bdl	bdl	bdl	bdl	bdl	bdl	bdl	bdl	bdl	bdl
<b>Nd</b>	bdl	bdl	bdl	bdl	0.035	bdl	0.026	bdl	0.033	0.027	0.04	0.036
<b>Sm</b>	0.122	0.036	0.198	0.201	0.235	0.165	0.183	0.1	0.168	0.241	0.577	0.343
<b>Eu</b>	0.283	0.077	0.353	0.313	0.342	0.314	0.338	0.153	0.363	0.371	0.826	0.502
<b>Gd</b>	3.6	0.98	3.54	3.04	3.65	3.69	3.65	1.65	3.4	3.62	9.82	6.01
<b>Tb</b>	2.886	1.033	2.092	1.906	2.167	2.724	2.85	1.742	2.102	2.135	5.72	4.18
<b>Dy</b>	34.35	19.4	25.71	24.42	31.82	34.6	33.02	28.41	29.2	28.15	87.1	77.6
<b>Ho</b>	6.18	5.41	6.51	5.76	10.28	6.45	5.43	6.72	8.04	7.24	29.53	31.38
<b>Er</b>	14.52	14.49	19.38	16.87	37.47	14.88	10.89	17.22	26.56	23.06	124.1	158.7
<b>Tm</b>	1.624	1.565	2.534	1.996	5.28	1.632	1.089	1.954	3.64	3.14	20.8	30.88
<b>Yb</b>	9.67	8.29	15.88	12.03	35.39	8.92	5.55	11.38	24.28	20.87	166.6	276.5
<b>Lu</b>	1.202	0.921	2.118	1.482	4.69	1.055	0.631	1.296	3.29	2.65	25.97	48.6
<b>Hf</b>	bdl	bdl	0.094	0.042	6.5	bdl	bdl	bdl	bdl	0.041	0.062	0.088
<b>Ta</b>	bdl	bdl	bdl	bdl	bdl	bdl	bdl	bdl	bdl	bdl	0.31	0.174
<b>Pb</b>	0.026	0.023	bdl	bdl	bdl	bdl	bdl	bdl	bdl	bdl	0.026	bdl
<b>Th</b>	bdl	bdl	bdl	bdl	0.02	bdl	bdl	bdl	bdl	bdl	bdl	bdl
<b>U</b>	bdl	bdl	bdl	bdl	0.098	bdl	bdl	bdl	bdl	0.0062	bdl	bdl

Table A4 - 7: Garnet trace element composition determined by LA-ICP-MS. c: core, m: mantle, r: rim

Spot #	SHB12B-03	SHB12B-04	SHB12B-05	SHB12B-06	SHB12B-07	SHB12B-08	SHB12B-09	SHB12B-10	SHB44B-01	SHB44B-02	SHB44B-03
Sample	SHB12B	SHB12B	SHB12B	SHB12B	SHB12B	SHB12B	SHB12B	SHB12B	SHB44B	SHB44B	SHB44B
	r	r	r	c	r	c	c	c			
(ppm)											
Mg (wt%)	1.07	1.08	1.05	2.36	1.09	2.46	2.36	2.31	0.88	0.90	0.84
P	30.9	32.3	30.8	52	31.4	47.8	46.6	74.6	51.5	48.6	43.2
Ca (wt%)	5.481	5.193	5.763	4.821	5.481	4.941	4.977	5.011	4.004	3.647	4.186
Sc											
Ti	340	303.3	314.3	443	9200	32100	390	337	334.1	282.6	295.1
Cr	165.1	337.3	230.1	304.5	520.7	359.7	334.3	284	2.33	3.12	1.79
Mn (wt%)	4.34	3.85	4.29	2.20	4.46	1.97	2.17	2.40	0.75	0.57	0.46
Ni	0.59	0.28	0.64	1.24	2.34	0.79	1.24	1.11	0.54	0.55	0.34
Zn	11.90	12.26	12.61	20.30	13.09	20.90	20.71	19.65	33.40	34.00	31.80
Rb	0.28	0.09	0.18	0.12	0.47	0.13	0.16	0.19	0.06	0.08	bdl
Sr	0.193	0.0587	0.105	0.087	0.508	0.191	0.084	0.282	0.0332	0.051	0.044
Y	1020.9	267.9	845	566	1233	609.3	674.8	802.7	410	297.7	137.4
Zr	0.228	0.217	0.185	3.53	0.4	71	3.36	2.13	0.67	0.42	0.41
Nb	0.053	bdl	bdl	0.0142	6.7	42.5	bdl	bdl	bdl	bdl	bdl
Ba	bdl	bdl	bdl	bdl	0.146	bdl	bdl	bdl	bdl	bdl	bdl
La	bdl	bdl	bdl	bdl	bdl	bdl	bdl	bdl	bdl	bdl	0.0087
Ce	bdl	bdl	bdl	bdl	bdl	bdl	bdl	bdl	0.047	0.0126	0.091
Pr	bdl	bdl	bdl	bdl	bdl	bdl	bdl	bdl	bdl	bdl	0.019
Nd	bdl	bdl	bdl	0.045	bdl	0.074	0.067	0.055	0.07	0.051	0.094
Sm	0.068	0.035	0.051	0.545	0.032	0.578	0.489	0.515	0.594	0.583	0.297
Eu	0.126	0.052	0.075	0.748	0.082	0.954	0.727	0.818	0.692	0.616	0.303
Gd	2.54	0.97	1.88	8.56	1.53	10.08	8.47	9.44	11.44	9.65	4.99
Tb	3.025	0.972	2.239	4.65	2.23	5.1	4.93	5.29	6.86	5.63	2.947
Dy	70.2	22.68	57.6	63.8	70.2	69.4	72.6	80.9	74.2	58.8	27.49
Ho	32.48	10.44	26.58	20.29	42.59	21.44	23.85	28.26	15.98	12.42	5.46
Er	168.3	52.9	124.1	79.6	270.5	81.9	96.3	122.3	40	30.1	12.56
Tm	32.35	9.98	20.3	12.86	57.04	12.57	15.52	21.67	4.22	3.31	1.31
Yb	271.9	80.9	140	99	502.1	93.9	119.7	182	24.07	17.86	7.73
Lu	40.12	11.87	18.1	15.2	77	14.22	18.01	29.86	3.16	2.26	1.073
Hf	bdl	bdl	bdl	bdl	bdl	1.9	0.063	0.053	0.039	bdl	bdl
Ta	0.0121	bdl	bdl	bdl	0.51	2.7	bdl	bdl	bdl	bdl	bdl
Pb	0.018	bdl	bdl	bdl	0.452	0.065	bdl	bdl	bdl	0.043	bdl
Th	bdl	bdl	bdl	bdl	bdl	0.0064	bdl	bdl	bdl	bdl	bdl
U	bdl	bdl	bdl	bdl	bdl	0.023	bdl	bdl	bdl	bdl	bdl

Table A4 - 7: Garnet trace element composition determined by LA-ICP-MS. c: core, m: mantle, r: rim

Spot #	SHB44B-04	SHB44B-05	SHB44B-06	SHB44B-07	SHB44B-08	SHB44B-09	SHB44B-10	grt47_47	grt47_48	grt47_49	grt47_50	grt47_51
Sample	SHB44B	SHB44B	SHB44B	SHB44B	SHB44B	SHB44B	SHB44B	SV01-75	SV01-75	SV01-75	SV01-75	SV01-75
										c	m	m
(ppm)												
Mg (wt%)	0.81	0.98	0.94	1.01	1.00	0.42	1.03					
P	44.5	47.7	38.4	39.1	37.4	34.1	39.7	42.7	35.2	39.6	31.8	36.1
Ca (wt%)	4.222	3.761	4.056	3.895	4.173	4.453	3.99	6.98	7.12	6.43	6.57	7.175
Sc								30.03	37.3	33.6	26.04	31.43
Ti	373.3	275.8	294.5	231.8	264.5	754	234.8	777	825	679	264	457
Cr	2.52	2.03	2.6	11.2	8.6	5.8	6.9	bdl	118.4	69.2	34.8	97.1
Mn (wt%)	1.07	0.61	0.48	0.70	0.55	8.43	0.56	1.89	1.32	0.67	0.21	0.19
Ni	0.29	0.59	0.34	0.25	bdl	0.71	0.24					
Zn	31.00	36.90	32.40	28.40	26.10	15.75	29.20					
Rb	0.07	0.05	bdl	bdl	bdl	0.87	bdl	bdl	bdl	bdl	bdl	bdl
Sr	0.0316	0.0221	0.0105	0.0102	0.0146	0.584	bdl	0.017	0.0199	bdl	0.0205	0.059
Y	534.4	363.7	184.1	238.9	207.1	2481	190.1	29.13	45.2	30.63	98.5	40.51
Zr	0.6	0.45	0.24	0.32	0.3	0.25	0.3	2.05	1.94	2.38	0.85	1.09
Nb	bdl	bdl	bdl	bdl	bdl	0.212	bdl	bdl	bdl	bdl	bdl	bdl
Ba	bdl	bdl	bdl	bdl	bdl	0.193	bdl					
La	bdl	bdl	bdl	bdl	bdl	bdl	bdl	bdl	bdl	bdl	bdl	bdl
Ce	bdl	bdl	bdl	bdl	bdl	0.0042	bdl	bdl	bdl	bdl	bdl	bdl
Pr	bdl	bdl	bdl	bdl	bdl	bdl	bdl	bdl	bdl	bdl	bdl	bdl
Nd	0.032	0.045	0.049	bdl	bdl	0.044	bdl	bdl	bdl	bdl	bdl	bdl
Sm	0.535	0.584	0.298	0.405	0.311	0.279	0.472	bdl	0.216	0.145	0.113	0.099
Eu	0.654	0.654	0.458	0.526	0.376	0.434	0.596	0.069	0.227	0.16	0.16	0.1
Gd	11.25	10.03	5.68	7.05	5.47	7.22	7.21	0.74	1.63	1.9	1.86	1.31
Tb	7.43	6.19	3.63	4.63	3.71	7.37	4.5	0.311	0.613	0.523	1.232	0.675
Dy	89.4	65.9	36.8	46.8	39.2	172.3	39.41	3.58	6.07	5.13	15.91	7.47
Ho	22.23	15.5	7.89	9.7	8.2	92.3	7.41	0.874	1.343	0.935	3.59	1.48
Er	61.5	42.2	19.61	22.21	18.87	506.6	16.79	2.8	3.74	2.34	8.68	3.09
Tm	7.64	4.92	2.25	2.28	2.141	109.9	1.809	0.382	0.416	0.268	0.918	0.279
Yb	46.7	29.72	13.86	14.35	13.31	937	10.75	2.64	2.65	1.67	4.29	1.59
Lu	6.01	4.02	2.03	1.89	1.94	119.7	1.524	0.435	0.388	0.174	0.35	0.16
Hf	bdl	bdl	bdl	bdl	bdl	bdl	bdl	bdl	bdl	bdl	bdl	bdl
Ta	bdl	bdl	bdl	bdl	bdl	0.034	bdl	bdl	bdl	bdl	bdl	bdl
Pb	bdl	bdl	bdl	bdl	bdl	0.041	bdl	bdl	0.341	bdl	bdl	0.209
Th	bdl	bdl	bdl	bdl	bdl	bdl	bdl	bdl	0.082	bdl	bdl	0.022
U	bdl	bdl	bdl	bdl	bdl	bdl	bdl	bdl	bdl	bdl	bdl	bdl



Table A4 - 7: Garnet trace element composition determined by LA-ICP-MS. c: core, m: mantle, r: rim

Spot #	grt47_52	grt47_53	grt47_54	grt47_55	grt47_56	grt47_57	grt47_58	grt47_60	grt37-63	grt37-67	grt37-62	grt37-64
Sample	SV01-75	SV01-75	SV01-75	SV01-75	SV01-75	SV01-75	SV01-75	SV12-05F	SV12-05F	SV12-05F	SV12-05F	SV12-05F
	m		r	c	c	c		c	c	c	m	m
(ppm)												
Mg (wt%)												
P	34.5	42.8	28.4	36.7	46.7	46.2	36.9	41	45.4	35.7	38.2	42.3
Ca (wt%)	7.05	6.74	6.14	6.41	6.47	6.522	6.27	7.57	7.13	7.31	6.95	6.54
Sc	32.28	38.91	115.5	57	59.2	56.8	135.6	32.13	61.3	21.89	24.85	26.67
Ti	437.2	732	326	811	1154	1020	339.1	943	1064	822	346	215.5
Cr	176.1	187	180	227.9	245.4	188.2	358.9	181.3	128.3	104.3	71.5	57.1
Mn (wt%)	0.19	0.67	2.70	2.65	3.14	3.53	2.40	2.03	3.13	0.62	1.58	1.66
Ni												
Zn												
Rb	bdl	bdl	bdl	bdl	bdl	bdl	bdl	bdl	bdl	bdl	bdl	bdl
Sr	0.0176	bdl	0.024	0.028	0.192	0.032	bdl	bdl	bdl	bdl	0.03	0.065
Y	78	43.93	84.7	120	138.1	129.7	80.6	38.88	45.6	8.89	17.98	17.02
Zr	0.8	2.31	bdl	1.9	140	3	0.31	1.82	1.59	1.98	0.61	0.154
Nb	bdl	bdl	0.09	0.011	1.21	0.029	bdl	0.064	0.218	0.017	bdl	bdl
Ba												
La	bdl	bdl	bdl	bdl	bdl	bdl	bdl	bdl	bdl	bdl	bdl	bdl
Ce	bdl	bdl	bdl	bdl	0.016	bdl	bdl	bdl	bdl	bdl	bdl	bdl
Pr	bdl	bdl	bdl	bdl	bdl	bdl	bdl	bdl	bdl	bdl	bdl	bdl
Nd	bdl	bdl	bdl	bdl	bdl	bdl	bdl	bdl	bdl	bdl	bdl	bdl
Sm	bdl	0.197	bdl	bdl	0.106	bdl	bdl	bdl	bdl	bdl	bdl	bdl
Eu	0.143	0.218	bdl	0.147	0.141	0.149	bdl	bdl	bdl	bdl	bdl	bdl
Gd	1.89	1.98	bdl	1.12	1.05	1.02	bdl	bdl	bdl	bdl	bdl	bdl
Tb	1.11	0.689	0.205	0.63	0.727	0.581	0.163	0.115	0.1	bdl	bdl	bdl
Dy	13.43	6.35	4.62	11.54	11.67	9.92	4.22	2.02	2.36	0.86	0.74	bdl
Ho	2.92	1.41	2.67	3.92	4.73	4.14	2.44	1.065	1.2	0.26	0.46	0.433
Er	7.28	4.53	15.48	17.1	21.2	19.09	14.42	6.98	8.57	0.94	4.42	4.47
Tm	0.83	0.638	2.74	2.7	3.69	3.56	2.44	1.9	2.58	0.139	1.41	1.554
Yb	4.58	4.01	20.16	19.9	29.7	29.99	17.1	19.25	32.7	1.02	18.39	19.56
Lu	0.469	0.455	2.9	2.97	5.15	4.98	2.24	3.88	6.79	0.147	3.82	4.25
Hf	bdl	bdl	bdl	bdl	2.6	bdl	bdl	bdl	bdl	bdl	bdl	bdl
Ta	bdl	bdl	0.0053	bdl	0.077	bdl	bdl	bdl	bdl	bdl	bdl	bdl
Pb	bdl	bdl	0.022	bdl	0.026	bdl	bdl	bdl	bdl	bdl	bdl	0.127
Th	bdl	bdl	bdl	bdl	0.117	bdl	bdl	bdl	bdl	bdl	bdl	bdl
U	bdl	bdl	bdl	bdl	0.09	bdl	bdl	bdl	bdl	bdl	bdl	bdl

**Table A4 - 7: Garnet trace element composition determined by LA-ICP-MS. c: core, m: mantle, r: rim**

Spot #	grt37-66	grt37-65	grt47_59	grt37-68	grt37-69	grt37-70	grt37-71	grt37-73	grt37-74	grt37-75	grt37-76	grt37-77	grt37-78
Sample	SV12-05F	SV12-05F	SV12-05F	SV12-05F	SV12-05F	SV12-05F	SV12-05F	SIB50B	SIB50B	SIB50B	SHS03	SHS03	SHS03
	m	r	r	c	c	m	r						
(ppm)													
<b>Mg (wt%)</b>													
<b>P</b>	36.3	33.1	37.2	40.4	39.8	34.6	44.5	39.2	31.9	28.8	40	41.4	38.7
<b>Ca (wt%)</b>	6.82	5.6	6.74	7.029	6.25	7.64	6.36	4.15	3.89	3.443	2.686	2.679	2.714
<b>Sc</b>	15.59	55.5	40.2	79.3	35.86	37.5	51.6	518	394.7	323.9	257.4	139.7	294.1
<b>Ti</b>	252.1	322.8	320	1037	742	339	267	3900	1327	1710	274.9	279.8	263.2
<b>Cr</b>	46.6	101.3	68.4	146.1	109.3	77.6	29.6	83	36.1	156.1	33.6	32.7	bdl
<b>Mn (wt%)</b>	2.77	3.51	3.21	3.43	1.42	1.67	3.77	21.65	21.05	17.74	8.92	9.18	9.46
<b>Ni</b>													
<b>Zn</b>													
<b>Rb</b>	bdl	0.296	0.11	0.078	bdl	bdl	0.081	0.21	0.408	0.199	0.125	1.61	0.144
<b>Sr</b>	0.025	0.132	0.06	0.048	bdl	bdl	37.5	0.306	0.33	0.89	0.027	1.392	0.035
<b>Y</b>	36	674	380	33.49	28.61	20.01	138.1	1151	1020	764.2	505.1	2914	464
<b>Zr</b>	0.48	bdl	0.17	1.31	1.51	0.45	bdl	45.9	35	52	bdl	bdl	bdl
<b>Nb</b>	bdl	bdl	bdl	0.114	0.32	bdl	bdl	17.5	1.36	5.45	bdl	bdl	bdl
<b>Ba</b>													
<b>La</b>	bdl	bdl	bdl	bdl	bdl	bdl	0.0177	0.073	0.029	0.127	bdl	bdl	bdl
<b>Ce</b>	bdl	bdl	bdl	bdl	bdl	bdl	0.025	0.052	0.182	0.63	bdl	bdl	bdl
<b>Pr</b>	bdl	bdl	bdl	bdl	bdl	bdl	bdl	bdl	bdl	0.068	bdl	bdl	bdl
<b>Nd</b>	bdl	bdl	bdl	bdl	bdl	bdl	bdl	0.15	0.09	0.37	bdl	bdl	bdl
<b>Sm</b>	bdl	bdl	bdl	bdl	bdl	bdl	bdl	0.88	0.75	0.53	0.205	0.14	0.103
<b>Eu</b>	bdl	0.105	0.042	bdl	bdl	bdl	bdl	0.41	0.78	0.621	0.277	0.135	0.209
<b>Gd</b>	bdl	1.77	0.95	bdl	bdl	bdl	bdl	6.6	8.92	5.64	2.95	3.07	2.58
<b>Tb</b>	bdl	1.685	0.92	bdl	0.119	bdl	0.177	6.03	6.95	4.4	2.31	4.09	2.18
<b>Dy</b>	1.43	42.2	21.7	1.38	1.85	0.87	5.56	104.5	115	75.4	45.3	129.7	43.7
<b>Ho</b>	0.966	22.38	12	0.885	0.83	0.553	3.96	36.2	39.92	25.71	16.3	97.1	16.19
<b>Er</b>	8.26	126.3	57.8	8.06	4.7	4.99	31.2	187.8	162.4	103.1	62.5	763.3	63.8
<b>Tm</b>	2.46	24.3	9.68	2.52	1.04	1.51	7.59	31.7	27.36	15.69	8.75	187.8	9.48
<b>Yb</b>	27.8	185.8	65.1	38.3	10	19.69	72.8	236	200.6	108.8	56.1	1802	67.9
<b>Lu</b>	5.53	24.58	8.06	9.53	1.65	4.13	11.78	33.22	27.01	14.81	7.69	307.5	9.55
<b>Hf</b>	bdl	bdl	bdl	bdl	bdl	bdl	bdl	1.35	0.99	1.15	bdl	bdl	bdl
<b>Ta</b>	bdl	bdl	bdl	bdl	0.014	bdl	bdl	0.573	0.07	0.26	bdl	bdl	bdl
<b>Pb</b>	0.031	bdl	bdl	bdl	bdl	bdl	0.354	2.77	0.8	2.82	bdl	bdl	bdl
<b>Th</b>	bdl	bdl	bdl	bdl	bdl	bdl	0.016	0.375	0.201	0.239	bdl	bdl	bdl
<b>U</b>	bdl	bdl	bdl	bdl	bdl	bdl	bdl	0.63	0.316	0.56	bdl	bdl	bdl

**Table A4 - 7: Garnet trace element composition determined by LA-ICP-MS. c: core, m: mantle, r: rim**

Spot # Sample	grt37-79 SHS03	grt37-80 SHS03	grt37-81 SHS03	grt37-82 SHS03	grt37-83 SHS03	grt37-84 SHS44A	grt37-85 SHS44A	grt37-86 SHS44A	grt37-87 SHS44A	grt37-88 SHS44A	grt37-89 SHS44A	grt37-90 SHS44A	grt37-91 SHS44A	grt37-92 SHS44A
<b>(ppm)</b>														
<b>Mg (wt%)</b>														
<b>P</b>	43.2	47.7	45.7	40.8	40.5	38.5	38	42.4	37.7	45.7	42.1	49.4	51.5	49.9
<b>Ca (wt%)</b>	2.637	3.071	2.606	3.052	3.067	3.998	3.763	3.986	3.902	3.939	4.518	3.883	4.158	3.895
<b>Sc</b>	264.7	294.4	342.3	195.6	394.6	82.2	65.4	138	136.1	109.7	103.3	113.9	97.6	96.7
<b>Ti</b>	284.8	330	290.1	276	321	265.2	249.1	242.9	244	242.7	353.3	301	345	298
<b>Cr</b>	83.3	206.3	49.8	140.2	36.2	bdl	bdl	bdl	bdl	bdl	bdl	bdl	bdl	bdl
<b>Mn (wt%)</b>	10.14	7.51	9.65	8.22	8.64	0.55	0.53	0.49	0.48	0.57	1.16	0.53	0.65	0.62
<b>Ni</b>														
<b>Zn</b>														
<b>Rb</b>	0.199	0.119	0.395	0.379	0.214	bdl	0.068	0.079	0.148	0.123	0.097	bdl	bdl	bdl
<b>Sr</b>	0.066	0.019	0.167	0.053	0.07	bdl	bdl	0.066	0.025	0.042	0.024	bdl	bdl	bdl
<b>Y</b>	965.7	353.7	1196	323.7	847	282.2	317.8	392.3	379.2	389.3	341.9	189.3	230.2	209.1
<b>Zr</b>	bdl	0.24	bdl	bdl	bdl	0.51	0.27	0.2	0.147	0.42	0.38	0.41	0.16	0.44
<b>Nb</b>	bdl	bdl	bdl	bdl	bdl	bdl	bdl	bdl	bdl	bdl	bdl	bdl	bdl	bdl
<b>Ba</b>														
<b>La</b>	bdl	bdl	bdl	bdl	bdl	bdl	bdl	bdl	bdl	bdl	bdl	bdl	bdl	bdl
<b>Ce</b>	bdl	bdl	bdl	0.006	bdl	bdl	bdl	bdl	bdl	bdl	bdl	bdl	bdl	bdl
<b>Pr</b>	bdl	bdl	bdl	bdl	bdl	bdl	bdl	bdl	bdl	bdl	bdl	bdl	bdl	bdl
<b>Nd</b>	bdl	bdl	bdl	bdl	bdl	bdl	bdl	bdl	bdl	bdl	bdl	bdl	bdl	bdl
<b>Sm</b>	0.201	0.191	0.122	0.207	0.257	0.222	0.231	0.218	0.125	0.202	0.39	0.266	0.369	0.197
<b>Eu</b>	0.311	0.285	0.236	0.258	0.279	0.387	0.301	0.263	0.246	0.355	0.437	0.363	0.377	0.333
<b>Gd</b>	4.23	4.03	2.9	3.19	4.49	4.24	4.15	3.51	4.04	3.79	6.2	4.82	4.94	5.08
<b>Tb</b>	3.5	2.86	2.66	2.22	3.46	3.22	3.46	2.85	2.55	2.77	4.04	2.68	3.08	3
<b>Dy</b>	73.2	42.5	67.6	36.5	71.4	41.5	45.5	43.2	41.4	41.7	52.2	31.58	37.37	32.3
<b>Ho</b>	30.27	11.71	36.5	10.9	28.67	9.52	10.63	13.63	13.33	13.41	11.89	6.48	7.7	7.29
<b>Er</b>	125.9	35.77	199.6	37.9	124.1	25.03	27.35	57.7	56.6	53.1	32.99	17.45	22.29	19.27
<b>Tm</b>	18.22	4.68	35.15	5.42	20.01	2.8	2.86	9.3	9.54	8.13	4.42	2.03	2.69	2.29
<b>Yb</b>	120.9	31.8	254.8	37.1	153.1	14.94	14.63	68.7	69.5	55.7	29.1	13.25	15.41	14.7
<b>Lu</b>	16.7	4.65	36.35	5.24	24.07	1.92	1.83	9.96	10.67	7.86	4.45	1.96	2.27	2.02
<b>Hf</b>	bdl	bdl	bdl	bdl	bdl	bdl	bdl	bdl	bdl	bdl	bdl	bdl	bdl	bdl
<b>Ta</b>	bdl	bdl	bdl	bdl	0.0037	bdl	bdl	bdl	bdl	bdl	bdl	bdl	bdl	bdl
<b>Pb</b>	bdl	bdl	bdl	bdl	bdl	bdl	bdl	bdl	0.061	0.032	bdl	bdl	bdl	bdl
<b>Th</b>	bdl	bdl	bdl	bdl	bdl	bdl	bdl	bdl	0.033	bdl	bdl	bdl	bdl	bdl
<b>U</b>	bdl	bdl	bdl	bdl	bdl	bdl	bdl	bdl	bdl	bdl	bdl	bdl	bdl	bdl

**Table A4 - 7: Garnet trace element composition determined by LA-ICP-MS. c: core, m: mantle, r: rim**

Spot # Sample	grt37-93 SHS44A	grt37-94 SHB05	grt37-95 SHB05	grt37-96 SHB05	grt37-97 SHB05	grt37-98 SHB05	grt37-99 SHB05	grt37-100 SHB05
<b>(ppm)</b>								
<b>Mg (wt%)</b>								
P	38.9	36.8	38.4	37.1	46.9	47.5	40.2	42.4
Ca (wt%)	3.88	5.137	5.201	4.768	5.56	5.188	5.01	5.162
Sc	29	67.1	74.2	113	147.8	113.9	91.7	122.9
Ti	234	485	506	594	827	618	539	642
Cr	bdl	115.1	71.2	bdl	43.3	38.2	bdl	187.8
Mn (wt%)	0.55	1.74	1.88	4.48	5.72	2.33	2.08	2.46
Ni								
Zn								
Rb	bdl	0.117	0.109	bdl	bdl	0.118	0.078	0.099
Sr	bdl	bdl	0.032	bdl	bdl	0.033	0.027	0.037
Y	262.3	419.5	430.4	113.3	191.9	408.5	363.5	355.7
Zr	0.43	0.35	0.34	bdl	0.43	0.22	0.19	0.37
Nb	0.074	bdl	bdl	bdl	bdl	bdl	bdl	bdl
Ba								
La	bdl	bdl	bdl	bdl	bdl	bdl	bdl	bdl
Ce	bdl	bdl	bdl	bdl	bdl	bdl	bdl	bdl
Pr	bdl	bdl	bdl	bdl	bdl	bdl	bdl	bdl
Nd	bdl	bdl	bdl	bdl	bdl	bdl	bdl	bdl
Sm	0.45	0.4	0.549	bdl	0.248	0.245	0.144	0.209
Eu	0.51	0.922	0.827	0.113	0.235	0.453	0.409	0.412
Gd	6.4	8.82	9.09	1.6	2.37	5.33	4.5	4.57
Tb	3.91	5.97	5.73	0.73	1.32	3.19	3.17	2.7
Dy	42.5	69.8	69.2	11.63	19.54	48.5	45.5	43.1
Ho	8.42	16.27	17.49	4.16	7.01	16.1	14.05	13.68
Er	19.7	49.4	55.6	14.99	27.32	64.8	50.8	53.9
Tm	1.93	7.16	7.96	2.39	4.5	10.82	7.39	8.96
Yb	7.7	46.6	52	18.18	35.7	83.5	55.2	65.7
Lu	0.61	5.24	5.88	2.55	5.31	11.19	6.51	8.38
Hf	bdl	bdl	bdl	bdl	bdl	bdl	bdl	bdl
Ta	bdl	bdl	bdl	bdl	bdl	bdl	bdl	bdl
Pb	0.174	bdl	bdl	bdl	bdl	bdl	bdl	bdl
Th	bdl	bdl	bdl	bdl	bdl	bdl	bdl	bdl
U	bdl	bdl	bdl	bdl	bdl	bdl	bdl	bdl

**Figure A4 - 8. Garnet trace-element LA-ICP-MS slit profile for sample SHB12B.** The gray band indicates the wash-off tail of the signal (significant for Mn, Yb, Er, Tm, Lu)

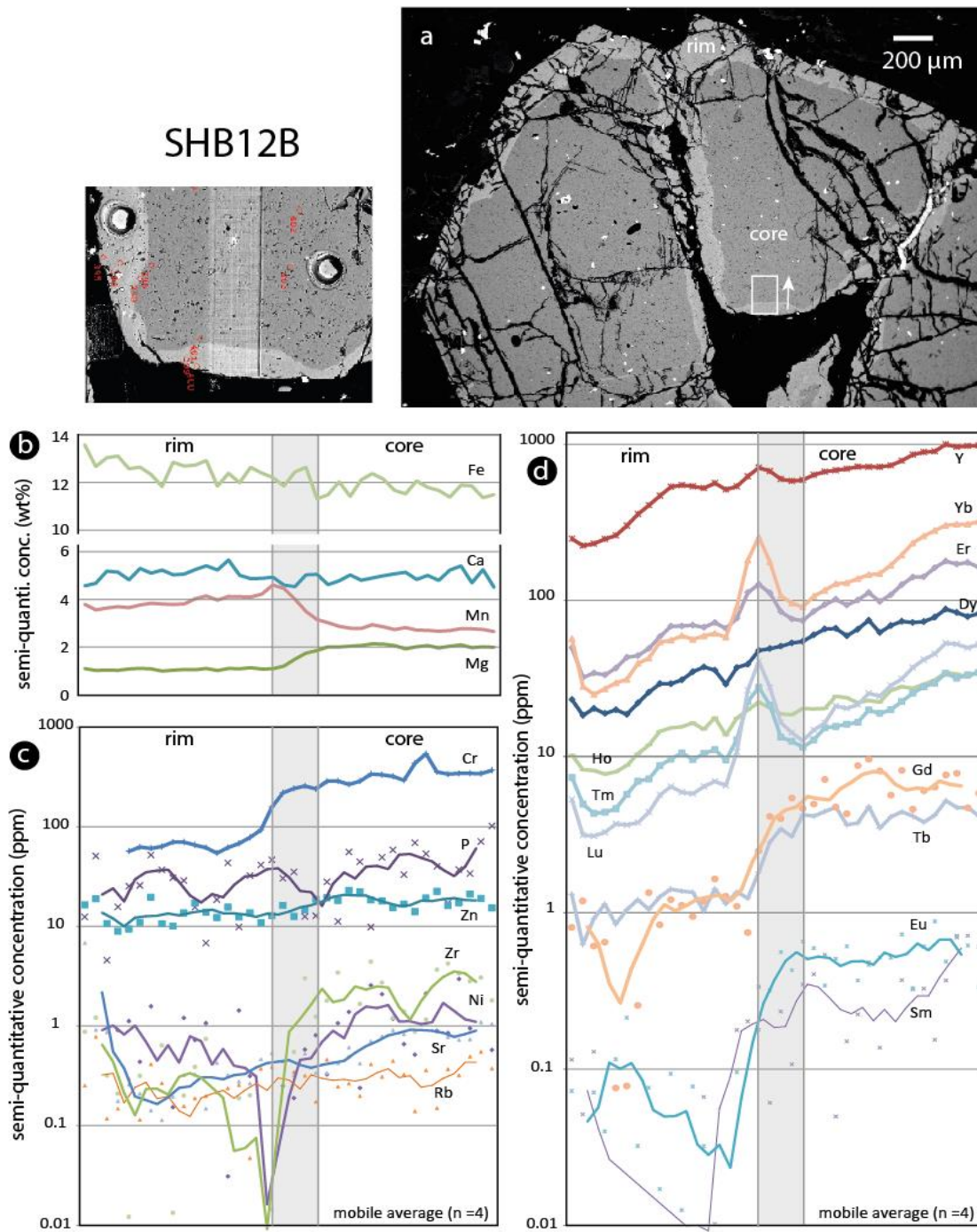


**Figure A4 - 9: Garnet trace-element LA-ICP-MS slit profile for sample SHB45.** The gray band indicates the wash-off tail of the signal (significant for Mn).

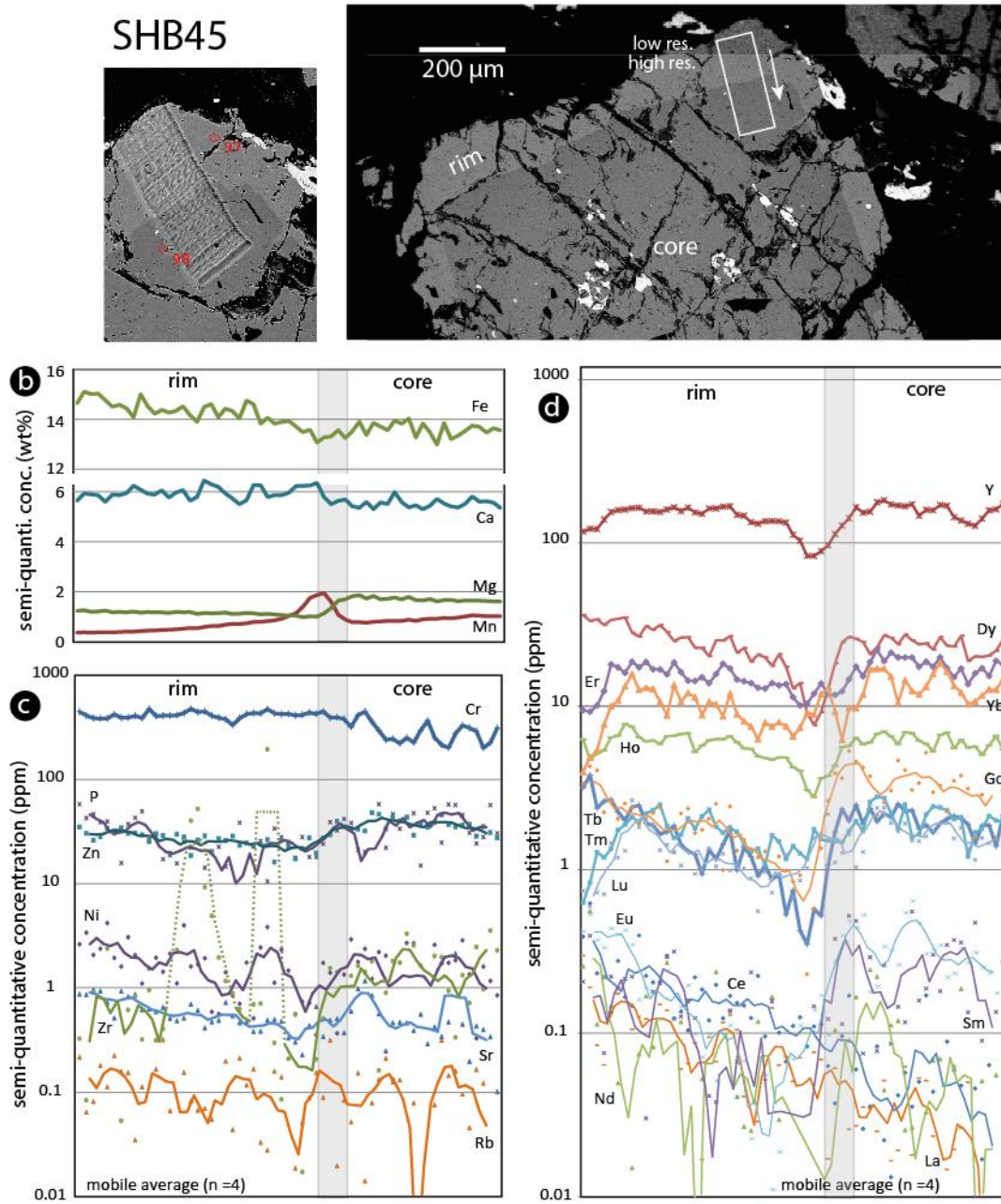


**Figure A4-10: Apatite rare-earth element concentrations normalised to chondrite.** Data normalized to CI chondrite of Sun and Mc Donough (1989).

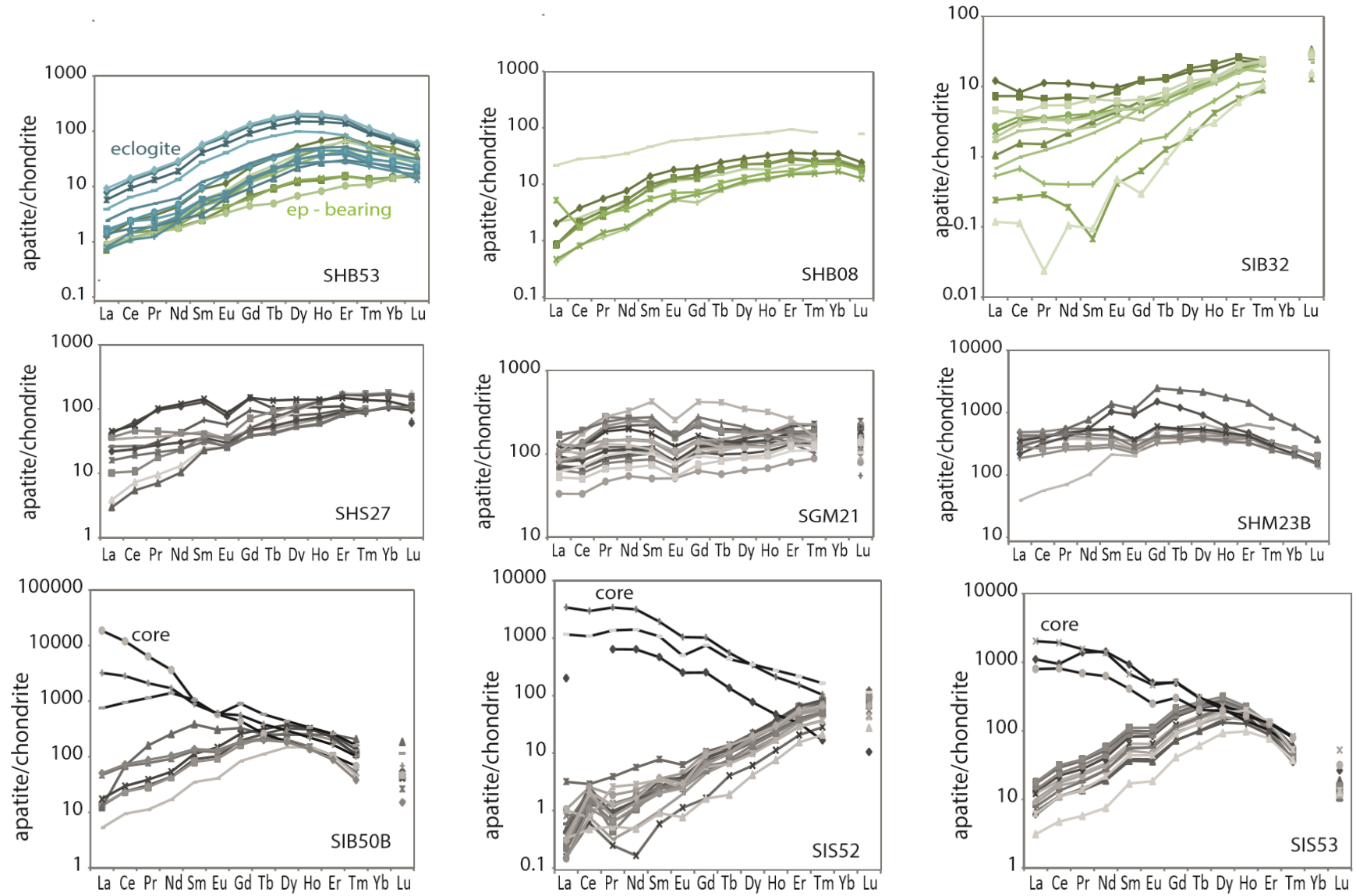


**Table A4 - 11: Lawsonite trace-element composition determined by LA-ICP-MS. Concentrations in ppm. c: core, r:rim, m:mantle.**

Sample	SHB05	SHB05	SHB05	SHB05	SHB05	SHB05	SHB05	SHB05	SHB05	SHB05	SHB05	SHB05	SHB05	SHB05	SHB05	SHB05	SHB05
Analysis ID	119	120	125	121	122	123	124	126	127	128	134	133	131	130	129	135	
SHRIMP #	SHB5@1	SHB5@2	SHB5@3	SHB5@4	SHB5@5	SHB5@6	SHB5@7	SHB5@8	SHB5@9	SHB5@10	SHB5@11	SHB5@12	SHB5@13	SHB5@14	SHB5@15	SHB5@16	
zone																	
Li	bdl	bdl	bdl	bdl	bdl	9.7	bdl	bdl	bdl	bdl	bdl	bdl	bdl	bdl	bdl	bdl	bdl
Na	bdl	bdl	84	bdl	bdl	388	29	29	74	34	95	bdl	bdl	bdl	bdl	bdl	99
Mg	25.1	37.4	25	17.2	31	28	63	32	88	42	17.7	21.9	33.7	12.7	24.7	111	
Al (wt%)	16.54	17.54	15.9	17.46	17.97	18.79	18.32	18.65	17.08	15.81	16.03	17.42	17.05	17.55	17.02	17.79	
P	36	60	41	43	bdl	42	bdl	bdl	41	bdl	bdl	45	53	53	40	60	
Ca (wt%)	11.94	12.24	11.27	12.16	12.59	12.46	12.93	13.76	12.5	11.52	11.21	12.33	12.44	12.53	12.25	12.17	
Sc	2.21	2.29	2.24	2.32	1.51	2.9	1.95	2.36	1.87	1.83	1.62	1.6	2.04	1.8	2.32	2.59	
Ti	352	169	720	603	304	2310	391	3570	324	163	427	220	210	1493	209	975	
V	610.7	496.3	59.4	558	246	142	255.8	167.9	336.5	416	265	243	455.1	349.5	433.6	460	
Cr	110.6	27.7	bdl	18.9	9	3.1	5.2	bdl	6.3	17.3	bdl	6.1	67.1	4.1	30.7	7.9	
Mn	32.2	25.6	28.8	37.8	18.5	18.8	9.5	45.4	24.5	35.9	25.7	23.5	48.1	31.5	45.3	23.6	
Fe (wt%)	1.016	0.632	0.539	0.853	0.482	0.474	0.563	0.648	0.458	0.796	0.616	0.514	0.868	0.509	0.879	0.452	
Sr	326.2	157.9	79.9	229	232.1	93.4	324.6	166	204	135.7	121.5	171	170.8	128.7	168.7	130	
Y	13.33	27.4	21.5	22.4	48.9	26.3	18.8	103.1	45.1	24.2	16.1	21.9	36.7	25.1	41.7	74.9	
Zr	bdl	2	0.07	bdl	bdl	0.58	bdl	0.24	bdl	bdl	0.72	bdl	bdl	0.71	1.42	0.36	
Nb	bdl	bdl	bdl	bdl	bdl	0.36	bdl	bdl	bdl	bdl	bdl	bdl	bdl	bdl	bdl	bdl	
Cs	bdl	0.91	bdl	bdl	1.15	8	bdl	3.1	bdl	bdl	bdl	bdl	bdl	bdl	bdl	bdl	
Ba	bdl	bdl	bdl	bdl	bdl	bdl	bdl	bdl	bdl	bdl	bdl	bdl	bdl	bdl	bdl	bdl	
La	8.02	2.73	3.71	7.34	6.27	14.7	3.82	17.6	6.99	1.06	1.15	2.77	2.19	8.04	1.09	19.29	
Ce	23.3	7.99	9.1	22	16.54	35.4	8.7	40.9	16.6	3.23	2.54	6.75	6.17	18.36	3.61	46.5	
Pr	3.47	1.17	1.02	3.72	2.04	4.13	1.11	5.72	2.1	0.42	0.37	1.05	0.95	2.39	0.564	5.72	
Nd	19	7.07	5.9	20.9	8.5	20.3	4.58	31.8	9.31	2.66	1.8	4.92	5.87	11.74	3.19	26.1	
Sm	5.04	1.93	1.48	7.2	2.44	6.7	1.18	10	2.09	1.25	0.79	1.84	1.89	2.46	1.16	8.12	
Eu	1.52	0.72	0.85	2.63	0.65	1.31	0.54	4.42	0.65	0.35	0.42	0.74	0.67	1.04	0.51	2.59	
Gd	6.81	1.96	2.58	9.9	2.73	6.6	2.05	14.4	3.49	0.94	0.3	2.5	3.04	3.51	2.99	9.9	
Tb	0.77	0.51	0.41	1.13	0.56	0.94	0.169	2.7	0.68	0.23	0.22	0.411	0.533	0.64	0.472	1.75	
Dy	3.34	2.69	3.39	5.05	6.16	6.1	2.47	18.1	5.51	3.36	1.76	3.24	4.26	3.79	4.38	13.3	
Ho	0.453	0.77	0.72	0.76	1.89	0.67	0.58	3.21	1.55	0.84	0.55	0.8	1.21	0.78	1.45	2.52	
Er	0.89	3.56	1.46	1.59	8.5	2.4	2.82	7.8	6.5	4.01	1.49	3.17	5.63	2.3	6.99	7.96	
Tm	0.129	0.52	0.188	0.349	1.35	0.091	0.42	0.68	1.17	0.65	0.16	0.415	1.04	0.255	1.27	0.99	
Yb	1.23	4.14	1.24	1.84	10.6	0.87	3.84	3.6	10.2	6.33	0.9	3.66	9.29	2.18	12.37	4.89	
Lu	0.199	0.75	0.106	0.3	2.16	bdl	0.57	0.4	1.73	0.98	0.091	0.64	2.14	0.211	2.51	0.82	
Hf	bdl	bdl	bdl	bdl	bdl	bdl	bdl	bdl	bdl	bdl	bdl	bdl	bdl	bdl	bdl	0.031	
Ta	bdl	bdl	bdl	bdl	bdl	bdl	bdl	bdl	bdl	bdl	bdl	bdl	bdl	bdl	bdl	bdl	
Pb	22.82	11.59	3.69	14.07	10.55	2.74	4.05	4.16	9.46	16.48	6.32	9.73	18.04	6.1	19.46	3.85	
Th	2.87	0.026	0.037	0.203	0.056	0.6	0.059	0.69	0.116	bdl	0.224	0.012	bdl	0.44	0.012	1.51	
U	0.062	bdl	0.021	0.013	bdl	bdl	0.017	0.114	0.01	bdl	0.049	bdl	bdl	0.017	bdl	0.156	



**Table A4 - 11: Lawsonite trace-element composition determined by LA-ICP-MS. Concentrations in ppm. c: core, r:rim, m:mantle.**

Sample	SHB05	SHB05	SHB05	SHB05	SHB05	SHB12B	SHB12B	SHB12B	SHB12B	SHB12B	SHB12B	SHB12B	SHB12B	SHB12B
Analysis ID	137	136	138	139	132	81	87	86	83	79	75	85	73	76
SHRIMP #	SHB5@17	SHB5@18	SHB5@19	SHB5@20	SHB5@21	SHB12B@17	SHB12B@7	SHB12B@5	SHB12B@18		SHB12B@11	SHB12B@6	SHB12B@9	SHB12B@2
zone	c					r								
Li	bdl	8.2	bdl	bdl	bdl	bdl	bdl	bdl	bdl	bdl	bdl	bdl	bdl	bdl
Na	69	103	38	bdl	bdl	bdl	bdl	bdl	bdl	bdl	bdl	bdl	bdl	bdl
Mg	61	121	60	24	41.5	56	37.6	115	42	59.8	57.5	488	59.3	46.4
Al (wt%)	18.93	17.96	17.45	18.8	17.5	16.59	16.5	16.43	16.65	16.51	16.42	16.49	16.57	15.9
P	bdl	43	37	35	33	43	41	37	bdl	bdl	bdl	38	42	42
Ca (wt%)	13.04	12.43	12.13	13.6	12.56	12.5	12.28	12.48	12.29	12.24	11.82	11.88	12.15	11.27
Sc	1.74	1.67	1.56	3.28	1.47	3.77	2.79	3.4	3.07	5.48	3.71	5.17	4.15	4.28
Ti	362	356	194	529	335	2973	1667	2473	2200	2951	2800	2270	2831	1713
V	519	282.6	230	669	187.6	429.3	436.3	419.5	383.3	447.7	386.1	469.8	481	357.3
Cr	22.2	9.7	10.8	87.4	5.41	1260	708	576.4	1234	1556	920	779.3	1072	436
Mn	35	26.5	18.4	24.5	26.3	23.1	22.7	23.8	21.8	25.5	27.1	32	24	29
Fe (wt%)	0.794	0.444	0.438	1.121	0.452	1.412	1.34	1.392	1.249	1.241	1.209	1.123	1.071	0.987
Sr	160.4	175.1	223	440	163	834	861	901	707	783	725	635	527.1	483
Y	32.6	41.1	28.3	16.6	33.4	19.3	25.74	20.62	16.88	17.51	18.25	23.5	34.4	53.3
Zr	bdl	bdl	bdl	bdl	0.055	bdl	bdl	bdl	bdl	bdl	bdl	bdl	bdl	bdl
Nb	bdl	bdl	bdl	bdl	bdl	bdl	0.118	bdl	bdl	bdl	bdl	bdl	bdl	bdl
Cs	bdl	bdl	bdl	3.1	bdl	bdl	bdl	bdl	1.08	bdl	bdl	3.3	bdl	bdl
Ba	bdl	bdl	bdl	bdl	bdl	bdl	bdl	bdl	bdl	bdl	bdl	0.23	bdl	bdl
La	2.5	8.16	5.86	8.5	6.41	1.35	3.01	1.79	0.6	0.82	0.36	0.719	0.61	0.271
Ce	6.54	18.48	14.3	27.2	15.56	3.59	9.1	5.29	1.55	1.93	1.11	2.18	1.92	0.57
Pr	0.98	2.4	1.86	4.07	1.95	0.54	1.31	0.675	0.25	0.383	0.218	0.303	0.318	0.177
Nd	6	10.5	7.4	29.9	8.88	3.75	7.86	3.86	1.62	2.17	1.33	2.05	2.4	1.37
Sm	2.16	2.33	1.55	6	2.65	1.68	2.93	1.68	0.54	1.05	0.73	0.91	1.3	1.07
Eu	0.88	1	0.58	2.57	1.01	0.67	1.21	0.92	0.387	0.47	0.363	0.74	0.56	0.77
Gd	3.4	4.08	2.69	9.7	3.31	2.34	3.57	2.53	1.59	2.1	1.42	2.03	2.36	2.68
Tb	0.57	0.592	0.458	1.29	0.65	0.63	0.9	0.7	0.367	0.47	0.301	0.38	0.519	0.6
Dy	4.3	5.09	3.4	5.5	4.41	4.68	6	4.55	2.41	3.6	2.56	4.52	4.89	7.54
Ho	1.05	1.6	0.98	0.31	1.38	0.8	1.14	0.78	0.47	0.6	0.61	0.883	1.17	1.73
Er	4.4	5.93	3.69	2.02	4.44	1.72	2.53	1.87	1.48	1.69	1.57	2.12	3.8	7.07
Tm	0.42	0.73	0.66	0.039	0.61	0.181	0.191	0.143	0.084	0.078	0.182	0.223	0.384	0.81
Yb	5.27	7.81	6.4	0.36	5.18	0.94	1	0.79	0.71	0.61	1.02	0.98	2.37	5.58
Lu	0.84	1.18	0.96	bdl	1.06	0.053	0.09	0.074	0.076	0.015	0.091	0.064	0.209	0.51
Hf	bdl	bdl	bdl	bdl	bdl	bdl	bdl	bdl	bdl	bdl	bdl	bdl	bdl	bdl
Ta	bdl	bdl	bdl	bdl	bdl	bdl	bdl	bdl	bdl	bdl	bdl	bdl	bdl	bdl
Pb	13.24	9.16	7.25	28.3	8.15	50	49.35	50.4	35.4	38.6	35.18	29.76	20.36	17.69
Th	0.066	0.388	0.089	0.023	0.26	0.013	0.146	bdl	0.023	bdl	bdl	bdl	bdl	bdl
U	0.033	0.022	bdl	bdl	0.033	bdl	bdl	bdl	bdl	bdl	bdl	bdl	bdl	bdl

**Table A4 - 11: Lawsonite trace-element composition determined by LA-ICP-MS. Concentrations in ppm. c: core, r:rim, m:mantle.**

Sample	SHB12B	SHB12B	SHB12B	SHB12B	SHB12B	SHB12B	SHB12B	SHS3	SHS3	SHS3	SHS3	SHS3	SHS3
Analysis ID	80	78	88	77	82	74	84	71	68	95	70	72	91
SHRIMP #	SHB12B@13	SHB12B@12	SHB12B@8	SHB12B@1	SHB12B@20	SHB12B@10	SHB12B@19	SHB3@9	SHB3@5	SHB3@10	SHS3@4	SHB3@10	SHB3@5
zone	r				c			c	m	c	c	m	c
Li	bdl	bdl	bdl	bdl	bdl	bdl	bdl	bdl	bdl	bdl	bdl	bdl	bdl
Na	bdl	bdl	bdl	bdl	bdl	bdl	bdl	52	50	bdl	143	48	bdl
Mg	36.9	41.7	32.8	37	50	30	56	164	115	139	323	70.5	40.6
Al (wt%)	17.37	16.32	17.78	18.48	17.45	17.98	17.37	16.47	17.62	17.32	17.46	16.58	17.08
P	102	bdl	72	72	85	58	41	59	440	51	bdl	bdl	70
Ca (wt%)	12.66	11.67	13.2	14	12.56	13.14	12.67	11.44	12.84	12.38	11.78	11.88	12.2
Sc	2.94	5.4	2.4	4	2.52	5.1	2.52	3.27	4.71	2.51	3.9	2.76	6.09
Ti	292	1662	303	370	277	463	414	7040	12290	3090	6570	550	844
V	330.5	378.8	289.3	323	270.7	391.9	334.4	352.2	358.5	359	372	310.3	318.1
Cr	676	677	741	386	1203	329.4	1630	251.6	269.8	110.8	309	215.7	41.4
Mn	26.2	32.1	24.5	29.7	29.7	28.7	26.9	180.5	382	118.2	225	138	132.3
Fe (wt%)	0.911	0.932	0.932	0.932	0.829	0.891	0.815	1.436	2.23	1.374	1.85	0.843	0.856
Sr	853	562	784	774	694	761	844	234.4	353	554	341	547	373.9
Y	192	73.4	222	222	233.5	419	946	7120	1185	978	4150	516	322
Zr	bdl	bdl	bdl	bdl	0.057	bdl	bdl	69	170	62.4	60	4.7	0.11
Nb	bdl	bdl	bdl	0.6	bdl	bdl	bdl	24.3	37.3	6	20.4	1.3	bdl
Cs	bdl	bdl	bdl	14	1.6	0.92	bdl	2.52	bdl	1.17	6.28	bdl	1.87
Ba	bdl	bdl	bdl	bdl	bdl	bdl	bdl	0.2	0.66	0.25	0.72	bdl	bdl
La	2.68	0.127	0.7	0.18	1.16	0.48	3.41	279.1	24.72	19.2	125	153.5	170.2
Ce	7.8	0.267	2.12	1.71	4.33	4.07	11.19	739	57.9	54.8	290	388.7	418.4
Pr	1.27	0.036	0.59	0.35	0.76	0.76	2.87	144.2	9.04	11.39	43.7	59.2	52.8
Nd	8.7	0.49	2.45	0.78	4.4	4.8	21.9	1017	55.9	88.3	311	309.6	244.2
Sm	4.61	0.4	3.39	2.4	3.23	4.4	20	534	29.4	53.8	135	87.5	58.9
Eu	3.21	0.58	2.9	1.6	3.02	6.33	15.6	147.1	11.31	14.9	47	22.74	15.42
Gd	13.5	2.42	9.8	9.6	10.7	21.5	76.3	981	60.4	84.2	440	120.8	61.6
Tb	3.6	0.7	3.12	2.6	3.09	5.37	17.5	175	14.9	16.9	88	19.35	10.01
Dy	31.1	7.36	28.2	24.1	28.9	48	148.3	1261	140.6	131.7	710	115.3	60.9
Ho	7.01	2.43	7.45	8.3	7.37	12.9	32.6	253.2	38.1	34.6	137	18.24	9.93
Er	20.9	8.67	26.5	28.4	26.5	39.3	86.3	585	118.7	118.3	293	35.5	18.7
Tm	2.46	1.05	3.61	4.42	3.43	4.21	7.25	46	12.4	17.7	20.7	2.56	1.24
Yb	12.1	6.88	23.9	26.4	25.4	21.7	30.4	153	66.6	106	82.2	10.03	4.14
Lu	1.47	0.707	3.18	3.5	2.98	2.03	2.77	10.38	8.13	12.34	7.7	0.73	0.264
Hf	bdl	bdl	bdl	bdl	bdl	bdl	bdl	2.13	4.58	1.75	2.5	0.115	bdl
Ta	bdl	bdl	bdl	bdl	bdl	bdl	bdl	1.9	3.15	0.54	1.48	0.098	bdl
Pb	30.57	17.93	22.92	22.1	19.8	20.9	22.11	79.3	104.5	162.3	97	134.7	91.6
Th	bdl	bdl	bdl	bdl	bdl	bdl	bdl	141.9	17.1	3.27	570	13.18	14.51
U	bdl	bdl	bdl	bdl	bdl	0.214	0.63	133.4	7.58	1.48	43	1.18	2.13

**Table A4 - 11: Lawsonite trace-element composition determined by LA-ICP-MS. Concentrations in ppm. c: core, r:rim, m:mantle.**

Sample	SHS3	SHS3	SHS3	SHS3	SHS3	SHS3	SHS3	SHS3	SHS3	SHS3	SIB32	SIB32	SIB32	SIB32	SIB32	SIB32
Analysis ID	92	96	65	90	93	67	94	89	66	21	22	24	96	97	98	
SHRIMP #	SHB3@3	SHB3@11	SHS3@1	SHB3@6	SHB3@2	SHB3@6	SHB3@1	SHB3@7	SHS3@3	SIB32@1	SIB32@2	SIB32@5	SIB32@6	SIB32@7	SIB32@8	
zone	m	m	c	m	m		r	r	r							
Li	bdl	bdl	bdl	bdl	bdl	bdl	bdl	bdl	bdl	bdl	bdl	bdl	bdl	bdl	bdl	bdl
Na	45	bdl	33	bdl	52	42	bdl	bdl	bdl	bdl	bdl	bdl	bdl	64.5	bdl	
Mg	43.6	37.2	51	67.8	71	75.1	28.2	23.3	25.8	26.8	152	31.3	21	27.5	34.4	
Al (wt%)	17	17.26	17.99	17.43	15.79	17.91	17.62	16.45	16.97	16.68	16.75	16.73	17.45	16.38	16.99	
P	41	45	64	40	44	49	39	bdl	48	bdl	bdl	bdl	50	bdl	bdl	
Ca (wt%)	12.25	12.71	13.27	12.64	11.39	12.57	12.77	12.22	12	12.44	12.22	12.33	12.83	11.74	12.21	
Sc	3.49	7.06	3.7	3.52	3.02	1.98	3.67	2.81	2.7	3.2	2.69	3.22	4.54	3.64	5.18	
Ti	230	1381	279	321	275	313	1211	852	312	1552	242.2	1713	632	261	709	
V	280.6	294	307.7	249.9	221.1	242.7	317.5	253.2	328.7	211.2	202.5	211	200.1	126.1	232	
Cr	225.8	103.8	101.2	56.1	165	173	393	13.9	126.1	42.8	73.5	46.6	38.4	244	262.7	
Mn	123.5	311	142.8	157.6	138.1	100.5	94.3	86.1	53.9	26.5	17.16	22.88	34.6	35.2	38.7	
Fe (wt%)	0.803	0.947	0.82	0.819	0.744	0.849	1.016	0.973	1.045	1.689	1.561	1.72	1.949	1.314	1.28	
Sr	533	448	605	741	728	1241	1160	958	1208	522.5	691	517.4	753	437	406.8	
Y	250.5	166.1	519	598	522	593	252	125.2	150.3	8.38	633	8.41	56.6	6	16.8	
Zr	15.4	2.2	bdl	bdl	0.054	bdl	bdl	bdl	0.054	bdl	bdl	bdl	bdl	0.21	6.8	
Nb	bdl	0.52	bdl	bdl	bdl	bdl	2.81	bdl	bdl	bdl	bdl	0.068	0.058	0.77	bdl	
Cs	1.49	1.54	bdl	1.27	1.43	bdl	2.79	2.2	1.46	bdl	bdl	bdl	7.2	bdl	bdl	
Ba	bdl	bdl	bdl	bdl	bdl	0.17	bdl	0.14	bdl	bdl	1.16	bdl	0.9	0.84	0.74	
La	196.8	151.4	235.5	276	194	100.6	82.6	84.5	131.5	8.08	792	9.65	71.6	2.88	5.56	
Ce	484.2	331	605	839	741	516	193	207.5	349.3	18.8	1742	22.2	136.5	7.85	16.8	
Pr	60.2	40.3	79.7	118.8	118.9	112.8	24.73	28.1	45.2	1.716	200.7	2.193	13.18	0.614	1.15	
Nd	280.3	189	380	567.2	599	756	107.3	122.2	223	6.11	876	7.08	49.1	2.39	5.94	
Sm	61.8	47.9	103.3	150.3	175.1	361	23.1	27.5	51.3	1.01	168.2	1.19	8.9	0.4	1.7	
Eu	15.78	10.53	24.5	39.05	45.4	87.8	5.73	7.16	12.21	0.454	47.6	0.538	2.72	0.161	0.56	
Gd	63.1	44.8	124.7	146.8	166.4	349	26	29.9	61.2	0.82	170.8	1.04	8.6	0.27	2.32	
Tb	9.23	6.42	17.9	21.63	21.3	41.3	5.1	4.5	8.58	0.15	21.4	0.164	1.21	0.075	0.258	
Dy	55.2	36.3	110.8	125.9	113.4	185.4	34.6	27.1	44.4	1.06	117.6	1.23	9.22	0.77	2.35	
Ho	7.94	5.45	18.2	21.92	19.3	23.7	8.12	4.18	5.68	0.293	21.2	0.245	1.62	0.132	0.51	
Er	14.01	8.36	38.1	58	53.4	50.4	23.7	7.29	7.53	0.88	49.5	0.76	5.45	0.74	1.35	
Tm	0.93	0.56	3.35	7.27	6.13	5	2.28	0.441	0.37	0.134	4.07	0.108	0.67	0.128	0.156	
Yb	3.01	2.6	13.7	39.8	34.8	25.8	12.1	1.96	1.1	0.91	16.91	0.73	4.64	0.88	1.19	
Lu	0.31	0.225	1.37	4.71	3.8	2.34	1.05	0.166	0.032	0.103	1.88	0.093	0.48	0.081	0.094	
Hf	0.62	0.17	bdl	bdl	bdl	bdl	bdl	bdl	bdl	bdl	bdl	bdl	bdl	bdl	0.136	
Ta	bdl	0.064	bdl	bdl	0.008	bdl	0.192	bdl	bdl	bdl	bdl	bdl	bdl	bdl	bdl	
Pb	128.3	92.4	105.4	96	92.3	125.1	71.5	58.7	70	60.84	76.75	62.36	74.4	18.65	35.4	
Th	8.68	46.9	8.13	31	52	51.6	2.14	5.57	53.3	bdl	84.2	0.138	2.38	1.75	5.63	
U	0.99	2.28	1.03	2.37	2.64	3.64	0.48	0.458	2.04	bdl	27.51	0.024	1.06	0.057	0.097	

**Table A4 - 11: Lawsonite trace-element composition determined by LA-ICP-MS. Concentrations in ppm. c: core, r:rim, m:mantle.**

Sample	SIB32	SIB32	SIB32	SIB32	SIB32	SIB32	SIB32	SIB32	SIB32	SIB32	SIB32	SIB32	SIB32	SIB32	SIB32	SIB32	SIB32	SIB32	SIB32	SIB50B
Analysis ID	99	100	101	101	17	102	103	104	18	92	91	19	93	94	95	114				
SHRIMP #	SIB32@10	SIB32@11	SIB32@12	SIB32@13	SIB32@14	SIB32@15	SIB32@17	SIB32@18	SIB32@19	SIB32@20	SIB32@27									
zone																				
Li	bdl	bdl	11	bdl	bdl	bdl	bdl	bdl	bdl	bdl	bdl	bdl	bdl	bdl	bdl	bdl	bdl	bdl	bdl	bdl
Na	96	46	5690	bdl	bdl	bdl	30	40	bdl	bdl	bdl	bdl	bdl	bdl	34	bdl				
Mg	41.2	41.1	11100	18.9	40	58	43.4	45	74	28.1	28	20.4	34.9	60	93.4					
Al (wt%)	16.32	16.69	13.38	17.44	17.77	17.78	17.87	18.28	17.89	16.2	16.94	18.12	16.26	17.3	16.98					
P	48	39	41	bdl	43	41	bdl	bdl	67	33	34.7	42	bdl	bdl	42					
Ca (wt%)	12.12	12.32	12.1	12.72	12.94	12.84	13.18	14	12.26	11.91	12.33	13.44	11.82	12.22	12.17					
Sc	8.28	5.09	153	7.74	5.98	20.1	3.64	6.4	2.96	2.18	5.28	3.03	3.7	4.12	2.31					
Ti	2071	488	462	407	754	3694	3240	1313	488	1682	276	1980	1557	1041	1744					
V	236.1	155.7	210	304.6	253.9	102.8	176.9	267.7	204.7	201.5	226.7	207.3	198	204.9	258.1					
Cr	209.9	205.2	255	489.4	205.5	228	331.4	193.5	50.9	28.6	205.4	53.6	48.8	4.2	1102					
Mn	24.5	66.8	329	34.3	43.2	87.5	37.1	45	39.9	22.1	34.5	23.5	24.8	30.8	108.6					
Fe (wt%)	1.925	1.193	2	1.327	1.412	5.29	2.687	1.489	1.779	1.745	1.326	1.887	1.807	1.793	1.234					
Sr	482	387.1	332	453	519	209.5	186.3	605	684	518	835	557	545	566	672					
Y	6.51	19.3	7.7	11.85	23.9	6.47	2.34	64.2	280	8.59	17.95	18.4	9.09	49.1	73.8					
Zr	bdl	0.88	bdl	bdl	bdl	2.17	0.4	bdl	bdl	bdl	bdl	bdl	bdl	bdl	bdl					
Nb	0.149	2.2	bdl	bdl	bdl	3.47	1.18	bdl	0.11	0.027	bdl	bdl	0.154	0.29	0.32					
Cs	bdl	1.56	8.8	bdl	7.2	2.2	3.9	3.52	12.9	bdl	bdl	5.1	0.99	9.2	bdl					
Ba	bdl	0.35	0.8	bdl	bdl	1.75	0.19	0.81	0.48	bdl	bdl	bdl	bdl	0.23	bdl					
La	2.99	4.14	1.37	5.1	6.53	10.09	1.82	19.42	436	9.06	8.49	20.7	9.11	88.1	94.5					
Ce	7.73	16.02	5.54	20.6	17.8	22.5	4.23	58.8	818	18.98	25.51	42.8	20.86	149.9	268.7					
Pr	0.699	0.97	0.38	1.44	1.42	2.07	0.34	4.95	82.5	1.76	1.85	4.69	2.12	14.77	34.36					
Nd	2.64	4.05	2.4	6.79	7.1	9.3	1.4	24.3	333	5.87	8.39	17.4	7.65	49.9	171.2					
Sm	0.57	1.25	0.54	1.45	1.86	1.32	0.22	7.4	56.9	1.23	1.5	3.77	1.37	9.1	47.9					
Eu	0.252	0.389	0.37	0.51	0.58	0.41	0.134	2.37	20	0.349	0.668	0.91	0.471	3.11	13.26					
Gd	0.58	1.39	0.39	1.98	3.14	1.51	0.35	9.3	62.3	0.61	2.17	2.12	1.27	9.9	57.5					
Tb	0.145	0.345	0.107	0.233	0.53	0.119	0.015	1.38	8.25	0.129	0.393	0.48	0.195	1.27	7.39					
Dy	0.78	2.35	0.65	2.17	2.66	1.14	0.26	8.8	47.1	1.33	2.46	3.46	1.19	7.2	31.4					
Ho	0.165	0.576	0.28	0.402	0.8	0.154	0.028	2.15	8.83	0.166	0.557	0.44	0.303	1.43	2.57					
Er	0.71	1.74	0.16	1.25	1.98	0.54	0.19	4.7	26.4	0.79	1.53	1.79	1.04	4.03	2.49					
Tm	0.062	0.184	0.22	0.098	0.197	0.02	bdl	0.7	2.5	0.081	0.234	0.173	0.126	0.53	0.063					
Yb	0.57	0.98	0.63	0.79	1.74	0.23	0.2	3.44	13.4	0.55	1.42	1.06	0.92	2.88	0.27					
Lu	0.079	0.174	0.043	0.131	0.217	bdl	0.011	0.4	1.8	0.087	0.182	0.138	0.087	0.42	bdl					
Hf	bdl	0.028	bdl	bdl	bdl	0.04	bdl	bdl	bdl	bdl	bdl	bdl	bdl	bdl	bdl					
Ta	0.0067	bdl	bdl	bdl	bdl	0.052	bdl	bdl	bdl	bdl	bdl	bdl	bdl	bdl	bdl					
Pb	59.4	20.3	27.6	41.8	53.1	15.1	7.91	66.8	73.2	70.6	98.2	57.5	62.6	62.4	204.7					
Th	0.119	9.46	0.38	20.2	3.9	2.16	0.85	42	29.4	bdl	0.057	0.97	0.089	1.78	83.9					
U	bdl	0.228	0.1	bdl	0.144	0.108	0.019	0.62	8.88	bdl	bdl	0.33	bdl	0.99	2.5					

**Table A4 - 11: Lawsonite trace-element composition determined by LA-ICP-MS. Concentrations in ppm. c: core, r:rim, m:mantle.**

Sample	SIB50B	SIB50B	SIB50B	SIB50B	SIB50B	SIB50B	SIB50B	SIB50B	SIB50B	SIB50B	SIB50B	SIB50B	SIB50B	SIB50B	SV10-75
Analysis ID	116	110	117	106	105	107	115	111	118	109	112	108	113	40	
SHRIMP #	SIB50B@12	SIB50B@6	SIB50B@10	SIB50B@2	SIB50B@1	SIB50B@3	SIB50B@7		SIB50B@11	SIB50B@5	SIB50B@8	SIB50B@4	SIB50B@9	SV1075@1	
zone	c	r	c		r	c			r	m		m	c	r	
Li	bdl	bdl	bdl	bdl	bdl	bdl	bdl	bdl	bdl	bdl	bdl	bdl	bdl	bdl	
Na	bdl	bdl	bdl	bdl	bdl	bdl	bdl	bdl	231	bdl	44	bdl	56	bdl	
Mg	75	65.8	83.5	83	52.5	50.4	64	63	96	21.9	65.8	34.4	50.5	31.6	
Al (wt%)	17.09	16.45	17.16	17.68	17.67	17.44	18.03	18.41	17.89	17.73	16.68	16.59	16.85	17.5	
P	bdl	42	33	47	60	41	44	bdl	bdl	65	41	41	62	43	
Ca (wt%)	11.95	11.83	12.32	12.91	12.49	12.86	12.85	13.25	12.66	12.88	12.5	11.98	12.14	12.78	
Sc	2.28	2.99	2.26	2.22	2.25	1.84	1.67	1.74	3.32	2.29	1.75	2.52	1.87	2.59	
Ti	366	2780	407	389	263	1340	750	216	857	751	2466	972	376	2377	
V	332.1	349.7	393.5	343.6	303	307.3	380	272.4	370	402	194	331	184.5	680.9	
Cr	834.8	362	385	979	681	678	316	543	553	225	103.3	201.4	157.9	753	
Mn	97.5	97.6	90.8	104.6	92.8	113	156.7	120.2	95.6	34.9	77.6	24.4	70.6	23.7	
Fe (wt%)	1.174	1.305	1.201	1.18	1.124	1.2	1.301	1.103	1.133	1.185	1.184	1.17	1.136	0.66	
Sr	723	635	750	844	981	667	770	1072	653	400	304.6	298.7	458	388.4	
Y	198.5	29.5	220.7	120.5	54.3	46.6	177.5	64.9	40.1	28.5	18.28	128.8	17.43	27.8	
Zr	bdl	bdl	bdl	0.22	0.13	bdl	bdl	2.1	bdl	bdl	0.47	bdl	bdl	bdl	
Nb	bdl	2.6	bdl	bdl	bdl	bdl	0.23	bdl	bdl	bdl	bdl	0.031	bdl	bdl	
Cs	bdl	bdl	bdl	bdl	1.21	bdl	bdl	bdl	1	bdl	bdl	bdl	bdl	bdl	
Ba	bdl	bdl	bdl	bdl	bdl	bdl	bdl	bdl	bdl	bdl	bdl	bdl	bdl	bdl	
La	650.7	53.66	820.8	397	225.3	78.3	567	276	52.3	92.2	3.4	280	2.37	11.3	
Ce	1538	128.9	1826	964	474	195.2	1255	569	134	256.5	10.88	767	6.67	29.01	
Pr	177.2	12.99	209	113.8	47.2	21.22	143.4	59	14.03	30.9	1.36	106.6	0.692	3.92	
Nd	793	49.9	923	523	179	81.8	623	220	60.4	148.7	6.81	557	3.64	20.7	
Sm	163.2	10.28	201.2	112.4	34.2	16.2	139.4	41.1	13.1	16.8	1.88	79.5	0.98	6.44	
Eu	41.6	3.36	49.03	27.4	8.49	5.76	34.9	11.48	3.97	3.13	0.61	16	0.408	1.74	
Gd	153.4	8.94	195	99.5	25.4	15.4	133.5	30.1	13.4	13.2	2.69	71.8	1.22	6.99	
Tb	17.65	1.52	21.97	12.04	3.74	2.73	15.87	4.88	2.4	0.97	0.46	4.1	0.261	0.97	
Dy	72.4	7.75	90.7	44	18.6	13.6	66.8	23.7	10.6	4.76	2.83	18	1.54	5.01	
Ho	7.14	0.877	8.39	4.26	1.94	1.39	6.51	2.41	1.18	0.77	0.61	3.47	0.489	0.888	
Er	6.67	1.18	7.13	4.32	2.64	1.67	6.32	2.69	1.58	1.67	1.65	7.86	1.53	2.35	
Tm	0.177	0.072	0.171	0.226	0.098	0.115	0.156	0.08	0.019	0.1	0.181	0.599	0.146	0.176	
Yb	0.302	0.178	0.286	0.39	0.25	0.22	0.041	0.38	0.22	0.53	0.82	3.27	1.13	0.9	
Lu	bdl	bdl	0.011	bdl	bdl	bdl	0.03	bdl	bdl	0.149	0.063	0.81	0.146	0.163	
Hf	bdl	bdl	bdl	bdl	bdl	bdl	bdl	bdl	bdl	bdl	bdl	bdl	bdl	bdl	
Ta	bdl	0.25	bdl	bdl	bdl	bdl	bdl	bdl	bdl	bdl	bdl	bdl	bdl	bdl	
Pb	190.8	166.2	195.1	212.8	246.9	167.5	189.8	243.3	146.4	60.4	43.42	36.08	53.8	4.28	
Th	206.6	0.396	69	712	1.53	0.383	119	1.26	0.92	18.6	0.422	149	0.575	0.621	
U	127.9	0.307	167.4	44.7	0.61	0.441	115.3	0.8	2.02	0.091	bdl	1.37	0.088	0.118	

**Table A4 - 11: Lawsonite trace-element composition determined by LA-ICP-MS. Concentrations in ppm. c: core, r:rim, m:mantle.**

Sample	SV10-75	SV10-75	SV10-75	SV10-75	SV10-75	SV10-75	SV10-75	SV10-75	SV10-75	SV10-75	SV10-75	SV10-75	SV10-75
Analysis ID	39	38	81	82	33	85	34	35	36	83	40	38	37
SHRIMP #	SV1075@2	SV1075@3	SV1075@4	SV1075@5	SV1075@6	SV1075@7	SV1075@8		SV1075@10	SV1075@11	SV1075@12	SV1075@14	SV1075@15
zone													
Li	bdl	bdl	bdl	bdl	bdl	bdl	bdl	bdl	bdl	9.2	bdl	bdl	bdl
Na	bdl	bdl	33	211	bdl	bdl	73.5	bdl	bdl	bdl	bdl	bdl	bdl
Mg	31.4	50.3	15.7	1730	75.5	52	64.7	121	210	348	31.6	50.3	103
Al (wt%)	17.06	17.47	17.64	17.45	17.09	17.31	16.41	16.93	17.84	19.44	17.5	17.47	16.57
P	33	54	33	bdl	44	53	bdl	bdl	bdl	71	43	54	bdl
Ca (wt%)	12.24	12.47	12.56	11.7	12.07	12.33	11.83	12.31	13.03	14.3	12.78	12.47	11.91
Sc	2.85	2.77	3.06	3.1	2.68	3.77	6.8	7.31	4.1	6.2	2.59	2.77	13.28
Ti	280	271	775	844	241	5070	2041	2471	331	1000	2377	271	601
V	552.4	581.3	529	437	654.9	744	1172	1216	947	515	680.9	581.3	554.9
Cr	424	645.5	705	1875	427	174.8	486	873	772	4240	753	645.5	1108
Mn	17.9	17.61	28.6	35.7	37.3	40.1	29.7	29.1	23.7	48.5	23.7	17.61	31.2
Fe (wt%)	0.699	0.695	0.832	1.236	0.752	1.015	0.899	0.97	0.928	1.318	0.66	0.695	0.9
Sr	551.9	611	841	669	731	600	1060	1218	2056	292	388.4	611	747
Y	21.66	21.81	42.9	34.7	15.79	6.21	10.5	9.19	16	23.8	27.8	21.81	27.4
Zr	bdl	bdl	bdl	bdl	bdl	bdl	0.08	bdl	bdl	bdl	bdl	bdl	0.074
Nb	bdl	bdl	bdl	bdl	bdl	bdl	bdl	0.063	bdl	bdl	bdl	bdl	0.161
Cs	1.16	bdl	bdl	0.87	bdl	1.33	bdl	1.01	bdl	14	bdl	bdl	bdl
Ba	bdl	bdl	0.25	51.7	bdl	bdl	bdl	bdl	bdl	3.9	bdl	bdl	1.02
La	10.23	10.58	13.52	8.09	3.1	2.87	22.81	13.72	31.7	5.92	11.3	10.58	24.93
Ce	23.82	22.95	34.5	22	8.14	8.58	57.1	38.61	86.4	18.9	29.01	22.95	62
Pr	2.83	2.8	5.02	3.08	1.185	1.24	7.9	5.56	12.55	1.85	3.92	2.8	8.42
Nd	13.34	12.21	25.2	15.6	6.91	7.98	39.7	28.7	56.6	10.8	20.7	12.21	39.5
Sm	2.95	2.86	7.7	4.66	2.57	1.92	9.7	6.45	11.4	1.4	6.44	2.86	8.8
Eu	1.62	1.124	2.22	1.81	1.14	0.74	2.38	1.8	2.87	0.83	1.74	1.124	2.6
Gd	4.15	3.2	10	5.3	3.87	2.55	7.8	5.24	9.7	6.3	6.99	3.2	9.6
Tb	0.572	0.6	1.41	0.99	0.544	0.275	0.63	0.455	0.77	0.35	0.97	0.6	1.2
Dy	3.45	3.75	8.11	7.8	2.72	1.47	2.53	2.06	3.15	5.24	5.01	3.75	5.32
Ho	0.551	0.78	1.21	1.16	0.601	0.213	0.347	0.271	0.64	1.11	0.888	0.78	0.79
Er	1.9	2.43	3.86	2.49	1.27	0.63	0.89	0.6	0.98	2.1	2.35	2.43	2.4
Tm	0.19	0.223	0.315	0.147	0.099	bdl	0.045	0.031	0.065	0.31	0.176	0.223	0.203
Yb	1.17	1.58	1.57	0.52	0.63	0.061	0.23	0.187	0.4	1.55	0.9	1.58	0.96
Lu	0.24	0.378	0.203	0.068	0.083	0.021	0.053	0.03	0.041	0.28	0.163	0.378	0.186
Hf	bdl	bdl	bdl	bdl	bdl	bdl	bdl	bdl	bdl	bdl	bdl	bdl	bdl
Ta	bdl	bdl	bdl	bdl	bdl	bdl	bdl	bdl	bdl	bdl	bdl	bdl	bdl
Pb	5.78	7.2	9.04	17.74	14.4	9.9	15.74	18.34	29.48	16.6	4.28	7.2	12.08
Th	0.294	0.119	3.15	0.63	0.018	0.055	1.21	0.413	1.91	1.28	0.621	0.119	7.51
U	0.069	0.025	0.64	0.163	bdl	bdl	0.064	0.029	0.174	0.32	0.118	0.025	1.45

**Table A4 - 11: Lawsonite trace-element composition determined by LA-ICP-MS. Concentrations in ppm. c: core, r:rim, m:mantle.**

Sample	SV10-75	SV10-75	SV10-75	SV10-75	SV10-75	SV12-13C	SV12-13C	SV12-13C	SV12-13C	SV12-13C	SV12-13C	SV12-13C
Analysis ID	31	84	32	35	36	25	87	86	88	28	27	89
SHRIMP #	SV1075@16	SV1075@17	SV1075@18	SV1075@20	SV1075@21	SV1213C@1	SV1213C@3	SV1213C@4	SV1213C@5	SV1213C@6	SV1213C@8	SV1213C@9
zone												
Li	bdl	bdl	bdl	bdl	bdl	bdl	bdl	bdl	bdl	bdl	bdl	bdl
Na	110	bdl	bdl	bdl	bdl	bdl	bdl	bdl	bdl	bdl	bdl	bdl
Mg	120	33.5	48.6	121	210	30.7	25.2	114	22	63.3	19.2	18
Al (wt%)	18	17.04	17	16.93	17.84	16.87	17.19	17.64	18.06	17.23	17.02	16.94
P	51	54	33.5	bdl	bdl	47	73	190	bdl	41	37	bdl
Ca (wt%)	13	12.03	12.48	12.31	13.03	12.23	12.06	12.52	12.65	12.72	12.31	12.06
Sc	3.9	4.12	13.01	7.31	4.1	3.45	2.14	2.7	2.05	2.77	2.43	2.19
Ti	6000	3926	2738	2471	331	2814	527	598	1000	2186	1168	958
V	770	709	1286	1216	947	332.3	253.8	276	329	278.6	260.5	248.3
Cr	540	316.3	616	873	772	155.9	99	203.1	213	181.6	73.8	65.8
Mn	56	33.8	30.4	29.1	23.7	37.4	26.7	24.1	20.4	31.2	33.3	21
Fe (wt%)	0.9	0.982	0.985	0.97	0.928	0.964	0.85	0.801	0.753	0.953	0.762	0.833
Sr	490	911	1302	1218	2056	561.8	640	848	663	924	698.9	965
Y	14	7.34	9.45	9.19	16	18.16	16.94	12.6	32.1	167.8	19.88	12.69
Zr	0.38	bdl	bdl	bdl	bdl	bdl	bdl	bdl	bdl	0.115	bdl	bdl
Nb	5.7	bdl	1.02	0.063	bdl	0.179	bdl	bdl	bdl	bdl	0.151	bdl
Cs	bdl	1.19	bdl	1.01	bdl	bdl	bdl	bdl	6	1.54	bdl	bdl
Ba	bdl	bdl	bdl	bdl	bdl	2.15	0.63	0.4	bdl	bdl	2.18	bdl
La	4.5	8.97	10.68	13.72	31.7	2.8	10.6	2.03	12.02	36.4	2.55	1.26
Ce	15	23	30.5	38.61	86.4	6.12	20.3	4.81	24.7	75.9	5.93	3.18
Pr	1.9	3.09	4.02	5.56	12.55	0.899	2.92	0.67	3.75	11.21	0.94	0.475
Nd	12	15.3	21.1	28.7	56.6	3.98	13.18	3.52	16.4	53.2	4.86	2.74
Sm	2.1	3.76	4.79	6.45	11.4	1.13	2.49	0.67	6	17.8	1.49	0.74
Eu	1.1	1.03	1.7	1.8	2.87	0.294	0.475	0.216	1.22	5.67	0.462	0.137
Gd	5.9	3.49	4.99	5.24	9.7	1.67	2.96	0.87	5.9	27.2	2.66	1.27
Tb	0.83	0.28	0.515	0.455	0.77	0.272	0.354	0.179	0.8	4.77	0.381	0.218
Dy	4	1.37	1.99	2.06	3.15	2.31	2.27	1.53	5.4	32.3	3.42	1.42
Ho	0.088	0.216	0.275	0.271	0.64	0.56	0.537	0.321	1.13	5.84	0.64	0.394
Er	1.3	0.5	0.76	0.6	0.98	1.85	1.58	1.07	2.6	12.81	1.78	1.21
Tm	bdl	0.025	0.066	0.031	0.065	0.206	0.144	0.231	0.248	0.986	0.153	0.105
Yb	0.77	0.031	0.306	0.187	0.4	1.35	1.13	0.7	1.13	4.34	1.28	0.5
Lu	0.16	bdl	0.036	0.03	0.041	0.251	0.115	0.115	0.21	0.36	0.139	0.077
Hf	bdl	bdl	bdl	bdl	bdl	bdl	bdl	bdl	bdl	bdl	bdl	bdl
Ta	0.94	bdl	0.04	bdl	bdl	0.042	bdl	bdl	bdl	0.0067	bdl	bdl
Pb	12	12.4	17.66	18.34	29.48	17.52	14.66	19.19	13.3	31.46	19.73	23.69
Th	0.35	0.475	0.15	0.413	1.91	0.637	5.3	2.36	1.4	6.68	0.465	0.239
U	bdl	bdl	0.039	0.029	0.174	0.311	0.268	0.073	0.29	5.94	0.279	0.0092

**Table A4 - 11: Lawsonite trace-element composition determined by LA-ICP-MS. Concentrations in ppm. c: core, r:rim, m:mantle.**

Sample	SV12-13C	SV12-13C
Analysis ID	90	30
SHRIMP #	SV1213C@10	SV1213C@11
zone		
Li	bdl	bdl
Na	31	bdl
Mg	14	36
Al (wt%)	16.99	17.37
P	45	42
Ca (wt%)	12	12.53
Sc	2.61	3.12
Ti	1087	963
V	296.5	287.8
Cr	84.7	222.6
Mn	23.3	40.6
Fe (wt%)	0.804	0.876
Sr	634.7	1080
Y	18.9	59.2
Zr	0.054	bdl
Nb	bdl	bdl
Cs	bdl	bdl
Ba	0.32	0.48
La	1.56	18.6
Ce	3.36	38
Pr	0.498	5.54
Nd	2.7	28.3
Sm	0.83	7.89
Eu	0.187	2.15
Gd	1.61	10.44
Tb	0.274	1.89
Dy	1.78	12.2
Ho	0.612	2.01
Er	1.81	4.79
Tm	0.151	0.358
Yb	1.17	1.36
Lu	0.118	0.146
Hf	bdl	bdl
Ta	bdl	bdl
Pb	17.05	30.18
Th	0.229	4.12
U	0.143	1.29



Table A4 - 12: Lawsonite oxygen isotope composition determined by SIMS.

Spot	$^{18}\text{O}/^{16}\text{O}$	$\pm 2\text{SE}$	$\delta^{18}\text{O}$ (‰)	$\pm 2\text{SE}$
SHB12B@1	0.00203180	6.14E-07	13.26	0.61
SHB12B@2	0.00203413	6.00E-07	14.43	0.60
SHB12B@3	0.00203416	6.17E-07	14.44	0.62
SHB12B@4	0.00203354	5.85E-07	14.13	0.58
SHB12B@5	0.00203373	6.07E-07	14.23	0.61
SHB12B@6	0.00203362	6.16E-07	14.17	0.61
SHB12B@7	0.00203465	5.98E-07	14.69	0.60
SHB12B@8	0.00203130	5.95E-07	13.01	0.59
SHB12B@9	0.00203440	6.20E-07	14.56	0.62
SHB12B@10	0.00203179	6.04E-07	13.26	0.60
SHB12B@11	0.00203410	6.13E-07	14.41	0.61
SHB12B@12	0.00203190	5.94E-07	13.31	0.59
SHB12B@13	0.00203428	6.10E-07	14.50	0.61
SHB12B@14	0.00203514	5.98E-07	14.93	0.60
SHB12B@15	0.00203521	6.23E-07	14.97	0.62
SHB12B@16R	0.00203597	6.01E-07	15.34	0.60
SHB12B@17M	0.00203417	6.01E-07	14.45	0.60
SHB12B@18C	0.00203485	5.98E-07	14.79	0.60
SHB12B@19	0.00203189	6.50E-07	13.31	0.65
SHB12B@20	0.00203286	5.90E-07	13.79	0.59
		<b>average</b>	14.2	
		<b>std. dev.</b>	0.66	

Spot	$^{18}\text{O}/^{16}\text{O}$	$\pm 2\text{SE}$	$\delta^{18}\text{O}$ (‰)	$\pm 2\text{SE}$
SHS3@1C	0.00204277	5.99E-07	18.74	0.60
SHS3@2M	0.00204203	6.02E-07	18.37	0.60
SHS3@3R	0.00203713	6.08E-07	15.92	0.61
SHS3@4C	0.00203970	5.97E-07	17.20	0.60
SHB3@5C	0.00203865	6.04E-07	16.68	0.60
SHB3@6M	0.00204201	6.13E-07	18.36	0.61
SHB3@7	0.00203870	6.04E-07	16.70	0.60
SHB3@8	0.00203869	6.01E-07	16.70	0.60
SHB3@9C	0.00203935	6.13E-07	17.03	0.61
SHB3@10M	0.00204081	6.05E-07	17.76	0.60
SHB3@11	0.00204028	6.02E-07	17.50	0.60
SHB3@12R	0.00203813	5.95E-07	16.42	0.59
SHB3@13C	0.00204135	6.06E-07	18.03	0.60
SHB3@14M	0.00204143	6.21E-07	18.07	0.62
SHB3@15R	0.00203752	6.37E-07	16.12	0.64
SHB3@16R	0.00203811	6.14E-07	16.41	0.61
SHB3@17	0.00203817	5.98E-07	16.44	0.60
SHB3@18	0.00203789	6.05E-07	16.30	0.60
SHB3@19	0.00203791	6.05E-07	16.31	0.60
SHB3@20	0.00204151	6.15E-07	18.11	0.61
		<b>average</b>	17.2	
		<b>std. dev.</b>	0.88	

<b>Instrument:</b>	Cameca 1280
<b>Mount:</b>	Grain mount
<b>Session:</b>	08.12.2014
<b>CAL repeatability:</b>	0.26‰ (1 $\sigma$ )

Table A4 - 12: Lawsonite oxygen isotope composition determined by SIMS.

Spot	$^{18}\text{O}/^{16}\text{O}$	$\pm 2\text{SE}$	$\delta^{18}\text{O}$ (‰)	$\pm 2\text{SE}$
SHB5@1	0.00203363	6.27E-07	14.18	0.63
SHB5@2	0.00203303	6.10E-07	13.88	0.61
SHB5@3	0.00203266	5.97E-07	13.69	0.60
SHB5@4	0.00203362	6.19E-07	14.17	0.62
SHB5@5	0.00203390	6.05E-07	14.31	0.60
SHB5@6	0.00203216	6.00E-07	13.44	0.60
SHB5@7	0.00203311	6.97E-07	13.92	0.70
SHB5@8	0.00203663	6.21E-07	15.67	0.62
SHB5@9	0.00203412	6.21E-07	14.42	0.62
SHB5@10	0.00203410	6.16E-07	14.41	0.61
SHB5@11	0.00203320	6.17E-07	13.97	0.62
SHB5@12	0.00203348	6.37E-07	14.10	0.64
SHB5@13	0.00203454	6.67E-07	14.63	0.67
SHB5@14	0.00203399	6.49E-07	14.36	0.65
SHB5@15	0.00203515	6.20E-07	14.94	0.62
SHB5@16	0.00203342	6.23E-07	14.08	0.62
SHB5@17	0.00203445	6.92E-07	14.59	0.69
SHB5@18	0.00203434	6.01E-07	14.53	0.60
SHB5@19	0.00203479	6.70E-07	14.76	0.67
SHB5@20	0.00203353	6.12E-07	14.13	0.61
SHB5@21	0.00203449	6.02E-07	14.61	0.60
		<b>average</b>	14.3	
		<b>std. dev.</b>	0.48	

Spot	$^{18}\text{O}/^{16}\text{O}$	$\pm 2\text{SE}$	$\delta^{18}\text{O}$ (‰)	$\pm 2\text{SE}$
SIB50B@1R	0.00203299	6.19E-07	13.86	0.62
SIB50B@2C	0.00203152	6.09E-07	13.12	0.61
SIB50B@3	0.00203246	6.08E-07	13.59	0.61
SIB50B@4C	0.00203145	6.99E-07	13.09	0.70
SIB50B@5	0.00203277	6.23E-07	13.75	0.62
SIB50B@6R	0.00203342	6.11E-07	14.07	0.61
SIB50B@7	0.00203144	6.06E-07	13.09	0.60
SIB50B@8	0.00203117	6.02E-07	12.95	0.60
SIB50B@9	0.00203171	6.11E-07	13.22	0.61
SIB50B@10C	0.00203082	6.08E-07	12.78	0.61
SIB50B@11R	0.00203096	6.12E-07	12.85	0.61
SIB50B@12C	0.00203075	6.47E-07	12.74	0.65
		<b>average</b>	13.3	
		<b>std. dev.</b>	0.45	

<b>Instrument:</b>	Cameca 1280
<b>Mount:</b>	Grain mount
<b>Session:</b>	08.12.2014
<b>CAL repeatability:</b>	0.26‰ (1 $\sigma$ )

Table A4 - 12: Lawsonite oxygen isotope composition determined by SIMS.

Spot	$^{18}\text{O}/^{16}\text{O}$	$\pm 2\text{SE}$	$\delta^{18}\text{O}$ (‰)	$\pm 2\text{SE}$
SHB05@1	0.00203476	6.97E-07	14.74	0.69
SHB05@2	0.00203450	6.89E-07	14.61	0.69
SHB05@3	0.00203503	6.95E-07	14.88	0.69
SHB05@4	0.00203492	7.03E-07	14.82	0.70
SHB05@5	0.00203554	6.98E-07	15.13	0.70
SHB05@6	0.00203387	6.97E-07	14.30	0.69
SHB05@7	0.00203426	7.00E-07	14.49	0.70
SHB05@8	0.00203464	6.95E-07	14.68	0.69
SHB05@9	0.00203483	6.99E-07	14.77	0.70
SHB05@10	0.00203425	7.14E-07	14.49	0.71
SHB05@11	0.00203463	6.93E-07	14.68	0.69
SHB05@12	0.00203517	6.94E-07	14.95	0.69
SHB05@13	0.00203550	7.07E-07	15.11	0.71
SHB05@14	0.00203434	7.06E-07	14.53	0.70
			<b>average</b>	14.7
			<b>std. dev.</b>	0.24

Spot	$^{18}\text{O}/^{16}\text{O}$	$\pm 2\text{SE}$	$\delta^{18}\text{O}$ (‰)	$\pm 2\text{SE}$
SHB3@1R	0.00203915	6.98E-07	16.93	0.70
SHB3@2M	0.00204360	7.03E-07	19.15	0.70
SHB3@3M	0.00204317	6.88E-07	18.94	0.69
SHB3@4M	0.00204362	6.89E-07	19.16	0.69
SHB3@5M	0.00204398	6.93E-07	19.34	0.69
SHB3@6M	0.00204479	7.15E-07	19.74	0.71
SHB3@7R	0.00204063	6.95E-07	17.67	0.69
SHB3@8M	0.00204317	6.97E-07	18.94	0.69
SHB3@9M	0.00204206	7.15E-07	18.38	0.71
SHB3@10C	0.00204172	6.99E-07	18.21	0.70
SHB3@11M	0.00204225	7.00E-07	18.48	0.70
SHB3@12M	0.00204249	7.08E-07	18.60	0.71
			<b>average</b>	18.6
			<b>std. dev.</b>	0.77

Spot	$^{18}\text{O}/^{16}\text{O}$	$\pm 2\text{SE}$	$\delta^{18}\text{O}$ (‰)	$\pm 2\text{SE}$
SHB12B@1R	0.00203550	7.07E-07	15.11	0.70
SHB12B@2C	0.00203657	7.04E-07	15.65	0.70
SHB12B@3	0.00203591	6.99E-07	15.32	0.70
SHB12B@4	0.00203596	7.00E-07	15.34	0.70
SHB12B@5	0.00203775	6.91E-07	16.23	0.69
			<b>average</b>	15.5
			<b>std. dev.</b>	0.44

<b>Instrument:</b>	Cameca 1280
<b>Mount:</b>	Thin section cuts
<b>Session:</b>	11.12.2014
<b>CAL repeatability:</b>	0.38‰ (1 $\sigma$ )

Table A4 - 12: Lawsonite oxygen isotope composition determined by SIMS.

Spot	$^{18}\text{O}/^{16}\text{O}$	$\pm 2\text{SE}$	$\delta^{18}\text{O}$ (‰)	$\pm 2\text{SE}$
SV0175@1	0.00203063	4.51E-07	12.68	0.45
SV0175@2	0.00203084	4.55E-07	12.79	0.45
SV0175@3	0.00203101	4.45E-07	12.87	0.44
SV0175@4	0.00203207	4.42E-07	13.40	0.44
SV0175@5	0.00203041	4.31E-07	12.57	0.43
SV0175@6	0.00203261	4.62E-07	13.67	0.46
SV0175@7	0.00203241	4.70E-07	13.57	0.47
SV0175@8	0.00203325	4.34E-07	13.99	0.43
SV0175@10	0.00203378	4.46E-07	14.26	0.45
SV0175@11	0.00203150	4.44E-07	13.11	0.44
SV0175@12	0.00203341	4.26E-07	14.07	0.42
SV0175@13	0.00203257	6.13E-07	13.65	0.61
SV0175@14	0.00203159	6.12E-07	13.16	0.61
SV0175@15	0.00203202	6.28E-07	13.37	0.63
SV0175@16	0.00203266	6.21E-07	13.70	0.62
SV0175@17	0.00203428	6.10E-07	14.50	0.61
SV0175@18	0.00203371	6.08E-07	14.22	0.61
SV0175@19	0.00203424	6.21E-07	14.48	0.62
SV0175@20	0.00203356	6.14E-07	14.14	0.61
SV0175@21	0.00203484	6.41E-07	14.78	0.64
		<b>average</b>	13.6	
		<b>std. dev.</b>	0.65	

Spot	$^{18}\text{O}/^{16}\text{O}$	$\pm 2\text{SE}$	$\delta^{18}\text{O}$ (‰)	$\pm 2\text{SE}$
SV1213C@1	0.00203100	4.40E-07	12.87	0.44
SV1213C@2	0.00203202	4.41E-07	13.38	0.44
SV1213C@3	0.00203156	4.46E-07	13.14	0.44
SV1213C@4	0.00203070	4.41E-07	12.71	0.44
SV1213C@5	0.00203076	4.37E-07	12.74	0.44
SV1213C@6	0.00203059	4.34E-07	12.66	0.43
SV1213C@7	0.00203168	4.49E-07	13.21	0.45
SV1213C@8	0.00203218	4.51E-07	13.46	0.45
SV1213C@9	0.00203097	4.62E-07	12.85	0.46
SV1213C@10	0.00203137	4.36E-07	13.05	0.43
SV1213C@11	0.00203214	4.67E-07	13.44	0.47
SV1213C@12	0.00203083	4.52E-07	12.78	0.45
		<b>average</b>	13.0	
		<b>std. dev.</b>	0.29	

<b>Instrument:</b>	Cameca 1280
<b>Mount:</b>	Rock chips
<b>Session:</b>	09.12.2014
<b>CAL repeatability:</b>	0.27‰ (1 $\sigma$ )

Table A4 - 12: Lawsonite oxygen isotope composition determined by SIMS.

Spot	$^{18}\text{O}/^{16}\text{O}$	$\pm 2\text{SE}$	$\delta^{18}\text{O}$ (‰)	$\pm 2\text{SE}$
SIB32@1	0.00203153	6.03E-07	13.13	0.60
SIB32@2	0.00203180	6.23E-07	13.27	0.62
SIB32@3	0.00203182	6.42E-07	13.27	0.64
SIB32@4	0.00203227	6.14E-07	13.50	0.61
SIB32@5	0.00203128	6.35E-07	13.01	0.63
SIB32@6	0.00203130	6.40E-07	13.01	0.64
SIB32@7	0.00203094	6.13E-07	12.83	0.61
SIB32@8	0.00203114	6.07E-07	12.94	0.61
SIB32@9	0.00203116	6.09E-07	12.95	0.61
SIB32@10	0.00203209	6.45E-07	13.41	0.64
SIB32@11	0.00203093	6.17E-07	12.83	0.62
SIB32@12	0.00203243	6.50E-07	13.58	0.65
SIB32@13	0.00203177	6.37E-07	13.25	0.63
SIB32@14	0.00203183	6.16E-07	13.28	0.61
SIB32@15	0.00202954	6.40E-07	12.14	0.64
SIB32@16	0.00203068	6.54E-07	12.71	0.65
SIB32@17	0.00203077	6.09E-07	12.75	0.61
SIB32@18	0.00203117	6.32E-07	12.95	0.63
SIB32@19	0.00203181	6.21E-07	13.27	0.62
SIB32@20	0.00203164	6.18E-07	13.18	0.62
SIB32@21	0.00203159	6.19E-07	13.16	0.62
SIB32@22	0.00203067	6.31E-07	12.70	0.63
SIB32@23	0.00203109	6.25E-07	12.91	0.62
SIB32@24	0.00203175	6.46E-07	13.24	0.64
SIB32@25	0.00203044	6.17E-07	12.59	0.62
SIB32@26	0.00202948	6.22E-07	12.11	0.62
SIB32@27	0.00203237	6.17E-07	13.55	0.62
		<b>average</b>	13.0	
		<b>std. dev.</b>	0.37	

Spot	$^{18}\text{O}/^{16}\text{O}$	$\pm 2\text{SE}$	$\delta^{18}\text{O}$ (‰)	$\pm 2\text{SE}$
------	-------------------------------	------------------	---------------------------	------------------

<b>Instrument:</b>	Cameca 1280
<b>Mount:</b>	Rock chips
<b>Session:</b>	09.12.2014
<b>CAL repeatability:</b>	0.27‰ (1 $\sigma$ )

**Figure A4 - 13: Lawsonite rare-earth element concentrations normalised to chondrite.** Data normalized to CI chondrite of Sun and Mc Donough (1989).

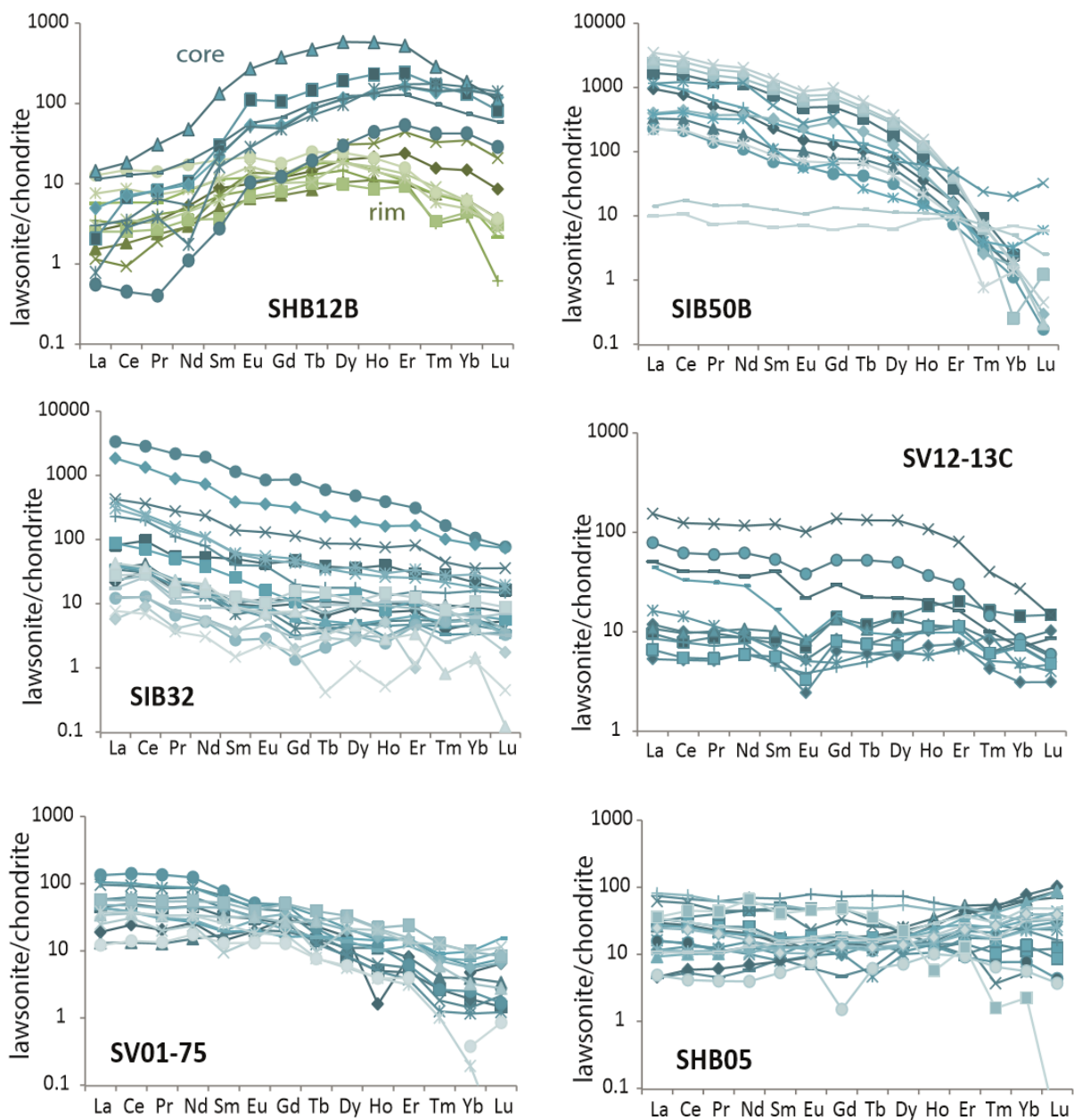


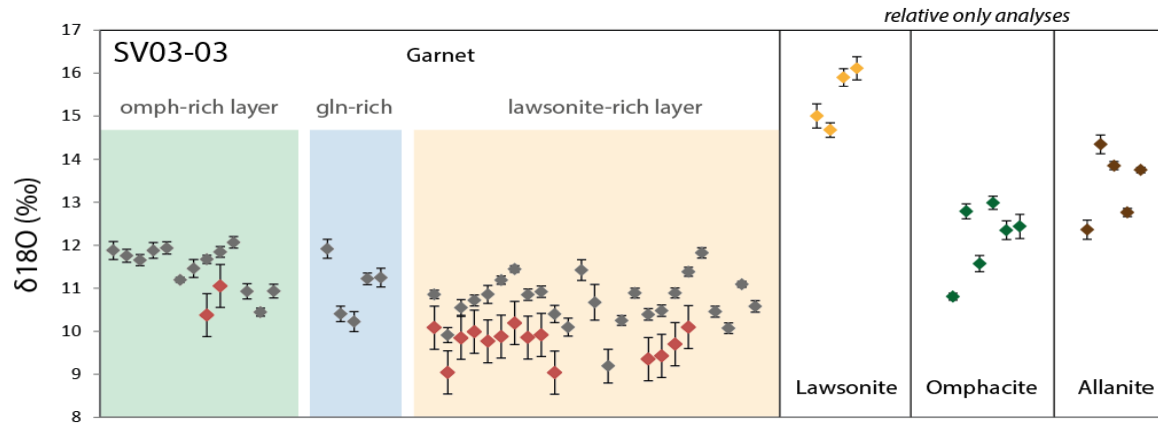
**Figure A4 - 13: Lawsonite rare-earth element concentrations normalised to chondrite.** Data normalized to CI chondrite of Sun and Mc Donough (1989).

**Table A4 - 14: Mineral modes observed in thin section.**

sample	qz	ph	omph	gln	ep	lws	grt	cc	ox	total
SGM21	45	10						35	10	100
SHB05			15	35		35	15			100
SHB08				60		40				100
SHB12B		30	60				5		5	100
SHB45		10	40	30		5	10		5	100
SHB53		20	20	20		20	20			100
SHM23B	65	5						30		100
SHS27	30	20			10	10		30		100
SHS3	70	15		5		5	5			100
SHS44A	10	30	20		5	30	5			100
SHS44B	5		20	40		20	15			100
SIB32			20		10	70				100
SIB50B		30	15	40		10	5			100
SIS52	85	5			5				5	100
SIS53	50	20			15	15				100



Figure A4 - 15: Preliminary SHRIMP oxygen isotope data for sample SV03-103.



Grey symbols are uncorrected analyses with measurement 2σ error, red symbols show garnet analyses with 2σ error propagated as per Martin et al. (2014b).

## **A5 – Appendix to Chapter 5**

Table A5 - 1: Garnet trace-element composition determined by LA-ICP-MS.

Sample	grt47_1	grt47_2	grt47_3	grt47_4	grt47_5	grt47_6	grt47_7	grt47_8	grt47_9	grt47_10	grt47_11	grt47_12
Zone	G12-113	G12-113	G12-113	G12-113	G12-113	G12-113	G12-113	G12-113	G12-113	G12-113	G12-113	G12-113
	I	I	I	I	I	II	II	III	III	III	III	III
(ppm)												
P	61.8	70.1	61	71.9	57.1	24.6	32.9	30.8	32.4	34.7	43.1	39.1
Ca (wt%)	1.366	1.328	1.309	1.345	1.207	2.492	2.834	3.47	3.289	2.488	2.637	2.35
Sc	124.2	152.5	178.1	144.4	111.7	107.3	167.3	197.4	199.9	218.2	163.4	124.6
Ti	229	293	258.5	316	167.5	57.8	135.3	232.1	190.1	204	207	130
Cr	1402	1676	2114	1829	1131	1536	2081	1871	1240	1357	1439	1628
Mn	47770	52390	43360	36510	25790	17280	12630	10462	8214	6553	5585	4337
Rb	0.774	0.428	bdl	bdl	bdl	0.085	bdl	0.316	bdl	0.088	0.224	bdl
Sr	0.287	0.142	0.032	bdl	bdl	bdl	bdl	bdl	bdl	0.044	0.027	bdl
Y	2699	1833	625.1	71.7	31.85	229.8	15.82	26.64	31.85	29.52	25.52	52.6
Zr	3.04	3.34	3.34	3.6	3.41	1.6	1.01	1.55	1.13	2.11	1.83	1.72
Nb	0.035	0.0091	0.028	bdl	0.022	bdl	bdl	0.0073	bdl	0.022	0.024	bdl
La	bdl	bdl	bdl	bdl	bdl	bdl	bdl	bdl	bdl	bdl	0.0168	bdl
Ce	bdl	bdl	0.0119	0.0148	bdl	bdl	bdl	bdl	bdl	bdl	0.073	bdl
Pr	0.0057	0.0074	0.007	0.0076	bdl	bdl	bdl	bdl	bdl	bdl	0.0078	bdl
Nd	0.168	0.197	0.235	0.379	0.23	bdl	bdl	0.052	bdl	bdl	0.064	0.054
Sm	2.56	3.65	4.96	3.96	2.69	0.156	0.303	0.324	0.385	0.331	0.525	0.75
Eu	0.306	0.383	0.463	0.584	0.485	0.581	0.687	0.836	0.81	0.588	0.779	0.617
Gd	53	68.5	59	16.66	9.21	3.6	3.57	3.51	3.66	3.12	3.93	4.81
Tb	24.59	24.43	13.58	2.26	1.289	2.19	0.775	0.75	0.722	0.714	0.757	1.076
Dy	298.7	233.3	93.9	12.7	6.64	27.64	3.38	4.73	5.44	5.41	5.21	8.53
Ho	92.32	60.78	17.84	2.25	0.992	6.72	0.411	0.861	1.225	1.199	0.992	1.84
Er	362.3	213.8	49.7	5.93	2.75	20.33	1.11	2.67	4.11	3.77	3.03	6.4
Tm	55.68	30.37	6.22	0.717	0.383	2.74	0.125	0.372	0.721	0.557	0.479	1.03
Yb	402.5	208.8	37.82	4.23	2.92	20.2	0.9	3.43	6.42	5.07	4.02	8.1
Lu	59.37	29.04	4.77	0.622	0.486	2.83	0.123	0.531	1.234	0.964	0.685	1.6
Hf	0.066	bdl	bdl	0.076	0.026	0.05	bdl	bdl	bdl	bdl	bdl	bdl
Ta	0.024	0.0229	0.0051	0.004	bdl	bdl	bdl	bdl	bdl	0.0051	bdl	bdl
Pb	bdl	0.035	bdl	bdl	bdl	0.082	bdl	0.88	0.089	0.81	0.86	0.037
Th	bdl	bdl	bdl	bdl	bdl	bdl	bdl	bdl	bdl	bdl	bdl	bdl
U	0.036	0.031	0.057	0.0176	bdl	bdl	bdl	bdl	bdl	bdl	bdl	bdl

Table A5 - 1: Garnet trace-element composition determined by LA-ICP-MS.

Sample	grt47_13	grt47_14	grt47_15	grt47_16	grt47_18	grt47_19	grt47_20	grt47_21	grt47_22	grt47_23	grt47_24	grt47_25
Zone	G12-113	G12-113	G12-113	G12-113	G12-165	G12-165	G12-165	G12-165	G12-165	G12-165	G12-165	G12-165
	IV	IV	IV	IV	core	core	core	core	rim 2a	rim 2a	rim 2a	rim 2a
(ppm)												
P	50.9	69.7	84.2	116.6	46.6	54.8	42.8	43.7	53.2	61.6	59.3	65.6
Ca (wt%)	1.627	1.401	1.234	0.984	4.107	4.284	4.246	4.025	2.858	3.08	3.007	3.29
Sc	85.3	76.7	69.9	64.7	89.2	82	96.1	103	129.8	138.7	156.7	152.3
Ti	103.7	176.4	152.9	145.8	94.8	130	178.1	135.1	100.5	230	103.3	133
Cr	1997	1983	1749	1260	103.9	96.4	99	99.8	89.2	89	98.5	94.7
Mn	3250	1604	bdl	bdl	32400	31750	31090	31660	2466	2496	2637	2734
Rb	bdl	bdl	bdl	bdl	bdl	bdl	bdl	bdl	bdl	bdl	bdl	bdl
Sr	bdl	bdl	bdl	bdl	bdl	bdl	bdl	bdl	bdl	bdl	bdl	bdl
Y	bdl	bdl	bdl	bdl	20.5	10.62	25.09	15.72	34.1	32.68	46.68	40.6
Zr	2.03	4.28	7.5	6.51	1.49	1.57	2.45	1.55	2.71	4	2.54	1.74
Nb	bdl	bdl	bdl	bdl	bdl	bdl	bdl	bdl	bdl	bdl	bdl	bdl
La	bdl	bdl	bdl	bdl	bdl	bdl	bdl	bdl	bdl	bdl	bdl	bdl
Ce	bdl	bdl	bdl	bdl	bdl	bdl	0.0181	bdl	0.0122	bdl	0.0127	0.008
Pr	bdl	bdl	0.0056	bdl	0.006	0.015	0.0222	0.0162	0.0146	0.0159	0.0153	bdl
Nd	0.086	0.266	0.34	0.263	0.563	1.1	1.15	0.94	0.83	0.8	0.59	0.63
Sm	1.03	1.65	1.29	1.91	1.13	1.59	1.3	1.42	1.45	1.64	1.76	1.25
Eu	0.537	0.562	0.343	0.813	0.289	0.31	0.311	0.372	0.502	0.64	0.595	0.56
Gd	2.68	1.88	0.9	4.67	1.55	1.26	1.82	2.23	4.4	4.62	6.72	5.48
Tb	0.226	0.146	bdl	0.498	0.375	0.378	0.493	0.428	0.975	1.09	1.359	1.17
Dy	1.17	0.77	bdl	2.15	3.04	2.2	4.1	3.37	6.8	7.17	9.37	9.68
Ho	0.2	bdl	bdl	0.226	0.757	0.342	0.974	0.561	1.299	1.35	1.895	1.67
Er	bdl	bdl	bdl	bdl	2.47	0.85	2.78	1.303	3.6	3.69	4.96	4.43
Tm	bdl	bdl	bdl	bdl	0.324	0.092	0.439	0.158	0.427	0.479	0.583	0.533
Yb	bdl	bdl	bdl	bdl	2.14	0.59	2.92	0.97	2.69	2.39	4.03	3.67
Lu	bdl	bdl	0.088	bdl	0.334	0.136	0.408	0.18	0.3	0.375	0.512	0.423
Hf	bdl	bdl	0.035	0.084	bdl	bdl	0.023	bdl	bdl	0.028	0.051	bdl
Ta	bdl	bdl	bdl	bdl	bdl	bdl	bdl	bdl	bdl	bdl	bdl	bdl
Pb	bdl	bdl	bdl	bdl	bdl	bdl	bdl	0.026	bdl	bdl	bdl	bdl
Th	bdl	bdl	bdl	bdl	bdl	bdl	bdl	bdl	bdl	bdl	bdl	bdl
U	bdl	bdl	0.042	bdl	bdl	bdl	bdl	bdl	bdl	0.026	bdl	bdl

Table A5 - 1: Garnet trace-element composition determined by LA-ICP-MS.

Sample	grt47_26	grt47_27	grt47_28	grt47_29	grt47_30	grt47_31	grt47_32	grt47_33	grt47_34	grt47_35	grt47_36	grt47_37
Zone	G12-165	G12-165	G12-165	G12-165	G12-165	G12-165	G12-165	G12-101	G12-101	G12-101	G12-101	G12-101
	rim 2a	rim 1	rim 1	rim 1	rim 2b	rim 2b	rim 2b	I	I	I	I	II
(ppm)												
P	68.1	88.1	46.4	48.2	62	67.9	75.5	62.8	57.7	67.2	50	28.1
Ca (wt%)	2.732	2.158	1.947	2.081	1.786	1.945	1.988	1.788	1.803	1.697	1.776	4.396
Sc	145	186.1	185.7	187.5	157.4	244.8	189.9	305.4	229.8	309	166.6	152.6
Ti	190	83.8	286	37.5	52.1	56	65.2	345	300.7	346.4	232.1	304.8
Cr	87.7	92.6	78.1	124.3	77.5	92.8	93.6	539	420.1	411.9	239.3	347.6
Mn	3311	7551	14560	8390	6577	7041	6235	58160	50470	56520	46140	40790
Rb	bdl	bdl	29.3	0.262	bdl	0.08	bdl	0.117	bdl	bdl	bdl	bdl
Sr	bdl	bdl	0.025	bdl	bdl	bdl	bdl	0.039	bdl	bdl	bdl	bdl
Y	33.33	75.6	85.2	88.67	69.27	71.6	67.31	591.5	238	184.8	305.1	109.6
Zr	3.98	2.13	2.55	1.52	2.14	1.67	1.71	4.03	3.08	3.97	2.65	0.95
Nb	0.04	0.03	0.148	bdl	bdl	bdl	bdl	0.0115	0.0104	0.019	0.007	bdl
La	bdl	0.0134	0.097	bdl	bdl	bdl	bdl	bdl	bdl	bdl	bdl	bdl
Ce	0.0187	0.107	0.298	0.0071	bdl	bdl	bdl	bdl	bdl	0.0055	bdl	bdl
Pr	0.0219	0.036	0.064	bdl	0.0115	0.0124	0.0092	0.011	bdl	0.0076	bdl	bdl
Nd	0.7	0.79	0.73	0.282	0.429	0.29	0.324	0.189	0.172	0.25	0.111	bdl
Sm	1.83	1.93	1.28	1.5	1.81	1.61	1.54	1.58	1.95	2.13	1.75	bdl
Eu	0.391	0.136	0.105	0.106	0.116	0.153	0.135	0.378	0.35	0.432	0.339	0.228
Gd	5.12	4.34	3.71	3.53	5.81	4.71	4.67	25.6	18.3	18.95	21.32	1.91
Tb	1.164	1.297	0.996	1.058	1.208	1.19	1.185	9.09	4.18	4.02	5.6	1.042
Dy	7.49	13.07	10.71	11.05	11.16	10.88	10.63	82.1	33.22	28.5	43.7	12.44
Ho	1.33	2.85	3.5	3.51	2.344	2.78	2.5	18.55	7.5	5.77	9.88	3.41
Er	3.53	7.75	11.56	12.9	7.24	8.26	7.36	61.4	24.53	17.46	30.76	12.6
Tm	0.486	0.881	1.641	1.905	0.887	0.893	0.91	8.74	3.4	2.38	4.06	2.02
Yb	2.75	5.14	11.8	14.61	6.3	5.94	5.51	61.74	21.64	16.29	24.37	17.74
Lu	0.358	0.624	1.569	2.305	0.82	0.75	0.723	9.35	2.93	2.22	3.07	3.16
Hf	0.107	bdl	bdl	bdl	bdl	0.097	bdl	0.032	bdl	bdl	0.071	bdl
Ta	bdl	0.0072	0.0056	bdl	bdl	bdl	bdl	0.0128	0.0044	0.023	0.0065	bdl
Pb	bdl	bdl	0.181	bdl	bdl	bdl	0.0176	bdl	bdl	bdl	bdl	bdl
Th	bdl	bdl	0.042	bdl	bdl	bdl	bdl	bdl	bdl	bdl	bdl	bdl
U	bdl	bdl	bdl	bdl	bdl	bdl	bdl	0.03	0.038	0.044	0.031	bdl

Table A5 - 1: Garnet trace-element composition determined by LA-ICP-MS.

Sample	grt47_38	grt47_39	grt47_40	grt47_41	grt47_42	grt47_43	grt47_44	grt47_45	grt47_46
Zone	G12-101	G12-101	G12-101	G12-101	G12-101	G12-101	G12-101	G12-101	G12-101
	II	II	III	III	IV	IV	IV	IV	IV
(ppm)									
P	29.7	30.4	37.5	40	51.6	57.3	66.1	59.2	75
Ca (wt%)	3.973	2.962	4.252	4.455	2.638	1.846	1.589	1.684	1.368
Sc	209.3	137.1	111.6	172.1	163.3	158.2	145.9	162	162.7
Ti	289	155.7	278.7	294	181.8	143	138.8	140.7	150.1
Cr	555.1	566	633	880	1603	786.9	710	700	577.2
Mn	35610	23750	11890	6963	6943	1952	2190	2772	3494
Rb	bdl	bdl	bdl	bdl	0.249	bdl	bdl	bdl	bdl
Sr	bdl	bdl	bdl	bdl	bdl	bdl	bdl	bdl	bdl
Y	59.47	76.8	13.34	17.3	70.9	61.2	78.4	79.3	53.79
Zr	1.01	0.94	3.52	1.26	1.63	2.78	3.22	3.77	3.85
Nb	bdl	bdl	bdl	bdl	bdl	bdl	bdl	bdl	bdl
La	bdl	bdl	bdl	bdl	bdl	bdl	bdl	bdl	bdl
Ce	bdl	bdl	bdl	bdl	bdl	bdl	bdl	bdl	bdl
Pr	bdl	bdl	bdl	bdl	bdl	bdl	0.0071	bdl	bdl
Nd	bdl	bdl	bdl	bdl	0.052	0.105	0.205	0.106	0.073
Sm	0.247	0.248	bdl	0.13	0.99	1.43	2.52	2.07	1.79
Eu	0.438	0.381	0.342	0.464	0.468	0.326	0.314	0.35	0.218
Gd	3.01	5.35	1.4	1.51	9.19	6.87	10.5	8.32	7.05
Tb	0.953	1.467	0.242	0.342	1.759	1.287	1.75	1.46	1.414
Dy	8.31	10.71	2.07	2.42	11.89	9.51	12.25	12.62	8.34
Ho	2.002	2.57	0.436	0.539	2.3	2	2.56	2.61	1.78
Er	6.37	8.39	1.22	1.94	6.06	6.03	7.57	8.58	4.26
Tm	0.992	1.257	0.173	0.312	0.697	0.658	0.882	1.085	0.476
Yb	7.53	8.58	1.28	2.63	3.63	3.99	5.08	6.53	2.45
Lu	1.104	1.229	0.178	0.4	0.351	0.367	0.536	0.661	0.185
Hf	bdl	0.032	0.064	bdl	bdl	bdl	0.041	0.026	bdl
Ta	0.0036	bdl	bdl	bdl	bdl	bdl	bdl	bdl	bdl
Pb	bdl	0.027	0.023	0.045	0.034	bdl	bdl	bdl	bdl
Th	bdl	bdl	bdl	bdl	bdl	bdl	bdl	bdl	bdl
U	bdl	0.0092	bdl	bdl	bdl	0.02	bdl	bdl	bdl

Table A5 - 2: SHRIMP U-Pb analyses of zircon for Isua samples.

Spot Nam	CL	ppm U	ppm Th	$^{232}\text{Th}$ $/^{238}\text{U}$	%c. $^{206}\text{Pb}$	$^{238}\text{U}$ $/^{206}\text{Pb}^*$	% err	$^{207}\text{Pb}^*$ $/^{206}\text{Pb}^*$	% err	$^{204}\text{Pb}$ corrected data							err corr
										$^{207}\text{Pb}$ date	$1\sigma$ err	% disc.	$^{207}\text{Pb}^*$ $/^{235}\text{U}$	% err	$^{206}\text{Pb}^*$ $/^{238}\text{U}$	% err	
G0446-1	osc	246	145	0.61	0.01	1.289	3.0	0.3511	0.24	<b>3712</b>	<b>4</b>	+0	37.57	3.0	0.7760	3.0	0.997
G0446-3	osc	484	530	1.13	0.08	1.298	3.2	0.3495	0.18	<b>3705</b>	<b>3</b>	+1	37.13	3.2	0.7705	3.2	0.998
G0446-4	osc	227	169	0.77	0.03	1.274	2.9	0.3494	0.26	<b>3704</b>	<b>4</b>	-1	37.82	2.9	0.7851	2.9	0.996
G0446-6	osc	152	102	0.70	0.01	1.266	2.9	0.3519	0.32	<b>3715</b>	<b>5</b>	-1	38.33	2.9	0.7902	2.9	0.994
G0446-7	osc	490	494	1.04	0.05	1.320	2.7	0.3549	1.39	<b>3728</b>	<b>21</b>	+3	37.06	3.0	0.7574	2.7	0.889
G0446-8	osc	233	164	0.73	0.03	1.303	3.2	0.3504	0.27	<b>3709</b>	<b>4</b>	+1	37.06	3.2	0.7672	3.2	0.996
G0446-9	osc	119	86	0.75	0.26	1.270	1.1	0.3483	0.38	<b>3700</b>	<b>6</b>	-2	37.81	1.2	0.7873	1.1	0.946
G0446-10	osc	235	159	0.70	0.01	1.275	3.3	0.3530	0.25	<b>3720</b>	<b>4</b>	-0	38.16	3.3	0.7840	3.3	0.997
G0446-11	osc	291	263	0.93	0.00	1.289	2.9	0.3505	0.23	<b>3709</b>	<b>4</b>	+0	37.48	2.9	0.7757	2.9	0.997

*Rejected discordant analyses*

G0446-2	w	87	58	0.69	8.48	1.443	8.1	0.3406	4.59	<b>3666</b>	<b>70</b>	+10	32.54	9.3	0.6930	8.1	0.869
G0446-5	w	53	31	0.61	0.19	1.425	2.7	0.3377	0.55	<b>3652</b>	<b>8</b>	+8	32.67	2.8	0.7017	2.7	0.981

osc: oscillatory zone

w: white rim/zone

c.: common

disc.: discordant

err are  $1\sigma$

Table A5 - 3: Zircon trace-element composition for sample G04-46 determined by LA-ICP-MS.

spot #	zirc28-02	zirc28-03	zirc28-05	zirc28-07	zirc28-08	zirc28-09	zirc28-10	zirc22-25	zirc22-27	zirc22-24	zirc22-29	zirc22-30
CL	osc	osc	osc	osc	osc	osc	osc	osc	osc	osc	osc	osc
(ppm)												
P	322	550	124	259	271	368	453	426	232	226	297	556
Ca	78	630	47	bdl	13	320	43	270	247	41	108	97
Sc	449	454	422	442	472	460	546	456	420	502	552	453
Ti	4	4	6	3	10	25	8	4	5	8	8	14
Fe	110	109	403	62	157	614	166	113	148	168	81	37
Y	1051	1568	900	972	2326	2182	4300	1542	1796	1224	1777	2556
Zr (wt%)	40.95	41.09	43.39	40.79	42.63	41.29	42.8	43.67	38.91	41.9	42.8	46.79
Nb	2.26	1.61	1.01	2.39	2.02	4.05	4.33	2.9	1.98	2.59	3	3.67
La	0.082	0.195	1.19	0.144	0.656	0.179	1.43	0.35	0.334	0.386	0.169	bdl
Ce	11.56	13.37	8.82	16.12	19.19	8.27	40.32	16.76	10.01	9.56	8.41	9.03
Pr	0.117	0.323	0.542	0.08	0.686	0.473	1.34	0.305	0.436	0.23	0.197	0.076
Nd	1.99	5.08	5.06	1.66	8.84	7.51	18.61	4.15	5.78	2.48	3.42	2.36
Sm	4.25	8.95	5.57	3.48	15.68	13.9	33.8	8.25	11.18	3.94	6.93	5.94
Eu	0.546	1.34	1.92	0.435	3.42	3.19	6.32	0.86	2.19	1.42	1.52	1.29
Gd	25.31	47.7	25.5	23.55	76.9	77.7	166.2	40.9	58.2	24.3	42.2	47.7
Tb	7.92	13.6	7.19	7.68	22.08	21.47	46.2	12.56	16.86	7.93	13.68	17.83
Dy	99.6	158.7	82	92.6	243.5	238.6	504	153.2	189.7	104.1	168.8	233.3
Ho	36.05	54.42	28.1	33.16	80.5	76.9	156.4	53.2	63	40.2	62	87.3
Er	172	244.1	134	155	355.4	342.9	677	246	275.7	201.7	283.7	416
Tm	33.01	45.25	27.9	30.21	67.3	62.3	119.3	47.6	51	41.4	54.04	83.3
Yb	313.5	408.6	270	271.6	580	543	1035	444	439	387	490.6	754
Lu	56.4	70.1	47.9	48.71	97.5	94.2	169.7	74.2	78.7	73.2	86.6	124.9
Hf	8830	8730	7970	9010	8110	7250	7680	9150	7355	7410	6620	8700
Ta	0.72	0.52	0.24	0.85	0.57	1.06	0.93	0.88	0.65	0.59	0.75	1.30
Pb	30	44	27	50	79	52	158	47	46	21	47	1.5
Th	75	108	66	122	194	124	408	121	107	56	125	77
U	130	142	74	175	199	168	318	181	141	115	173	71



**Table A5 - 4. Garnet oxygen isotope composition determined by SHRIMP. Error propagation following Martin et al. (2014b).**

Spot	zone	$^{18}\text{O}/^{16}\text{O}$	$\pm\text{SE}$	meas. $\delta^{18}\text{O}$ (‰)	$\pm\text{SE}$	Xgrs	Xpyr	Xspess	Xalm	BIASgrs	BIASsps	corr. $\delta^{18}\text{O}$ (‰)	$\pm\text{SE}$
g12-113-6b	I	0.00203830	1.85E-07	8.95	0.09	0.05	0.05	0.09	0.81	-0.76	0.51	<b>8.91</b>	<b>0.28</b>
g12-113-19	I	0.00203848	2.09E-07	9.04	0.10	0.06	0.05	0.10	0.80	-0.70	0.57	<b>9.00</b>	<b>0.28</b>
g12-113-44	I	0.00204687	1.01E-07	9.32	0.02	0.06	0.05	0.12	0.77	-0.69	0.70	<b>9.27</b>	<b>0.26</b>
g12-113-20	I	0.00203895	1.90E-07	9.27	0.09	0.06	0.05	0.12	0.77	-0.66	0.72	<b>9.23</b>	<b>0.27</b>
g12-113-21	I	0.00203899	2.25E-07	9.30	0.11	0.06	0.04	0.13	0.76	-0.64	0.77	<b>9.26</b>	<b>0.28</b>
g12-113-7b	I	0.00203919	5.40E-08	9.40	0.03	0.06	0.04	0.14	0.76	-0.69	0.80	<b>9.35</b>	<b>0.26</b>
g12-113-45x	I	0.00204693	1.25E-07	9.48	0.09	0.07	0.04	0.14	0.75	-0.63	0.85	<b>9.43</b>	<b>0.27</b>
g12-113-7.5	I	0.00203921	2.02E-07	9.40	0.10	0.06	0.04	0.15	0.75	-0.65	0.87	<b>9.36</b>	<b>0.27</b>
g12-113-22	I	0.00203896	1.13E-07	9.28	0.06	0.06	0.04	0.16	0.73	-0.64	0.96	<b>9.24</b>	<b>0.26</b>
g12-113-8b	I	0.00203978	2.06E-07	9.69	0.10	0.06	0.04	0.18	0.72	-0.69	1.04	<b>9.64</b>	<b>0.27</b>
										Average:		<b>9.27</b>	
										Std. dev.:		<b>0.21</b>	
g12-113-5.5	II	0.00203985	1.19E-07	9.72	0.06	0.11	0.04	0.06	0.79	-0.16	0.31	<b>9.67</b>	<b>0.26</b>
g12-113-26	II	0.00203881	9.10E-08	9.21	0.04	0.09	0.05	0.06	0.81	-0.42	0.33	<b>9.16</b>	<b>0.26</b>
g12-113-17	II	0.00203853	4.80E-08	9.07	0.02	0.08	0.05	0.06	0.81	-0.43	0.34	<b>9.03</b>	<b>0.26</b>
g12-113-43	II	0.00204707	1.55E-07	9.42	0.11	0.08	0.05	0.07	0.81	-0.45	0.37	<b>9.37</b>	<b>0.28</b>
g12-113-18	II	0.00203911	2.04E-07	9.36	0.10	0.08	0.05	0.08	0.79	-0.43	0.45	<b>9.31</b>	<b>0.28</b>
										Average:		<b>9.31</b>	
										Std. dev.:		<b>0.24</b>	
g12-113-23	III	0.00203800	1.50E-07	8.81	0.07	0.10	0.06	0.02	0.83	-0.32	0.06	<b>8.76</b>	<b>0.28</b>
g12-113-38	III	0.00204642	2.65E-07	9.05	0.14	0.07	0.06	0.02	0.85	-0.57	0.06	<b>9.01</b>	<b>0.30</b>
g12-113-24	III	0.00203903	1.22E-07	9.31	0.06	0.12	0.05	0.03	0.80	-0.10	0.12	<b>9.27</b>	<b>0.26</b>
g12-113-3b	III	0.00203962	1.58E-07	9.60	0.08	0.11	0.05	0.01	0.83	-0.16	0.01	<b>9.56</b>	<b>0.28</b>
g12-113-28	III	0.00203985	5.80E-08	9.72	0.03	0.11	0.05	0.01	0.83	-0.20	0.02	<b>9.68</b>	<b>0.27</b>
g12-113-39	III	0.00204682	1.47E-07	9.11	0.04	0.07	0.06	0.02	0.85	-0.54	0.04	<b>9.07</b>	<b>0.27</b>
g12-113-42	III	0.00204667	1.92E-07	9.23	0.07	0.07	0.06	0.02	0.85	-0.59	0.05	<b>9.19</b>	<b>0.28</b>
g12-113-4b	III	0.00204028	7.80E-08	9.93	0.04	0.10	0.05	0.02	0.82	-0.24	0.07	<b>9.89</b>	<b>0.27</b>
g12-113-35	III	0.00204806	1.70E-07	9.97	0.15	0.13	0.05	0.02	0.79	0.04	0.09	<b>9.92</b>	<b>0.29</b>
g12-113-15	III	0.00204005	7.30E-08	9.81	0.04	0.10	0.05	0.03	0.82	-0.31	0.12	<b>9.77</b>	<b>0.27</b>
g12-113-36	III	0.00204803	1.52E-07	10.18	0.04	0.16	0.04	0.03	0.77	0.27	0.14	<b>10.13</b>	<b>0.27</b>
g12-113-29	III	0.00204071	1.58E-07	10.14	0.08	0.16	0.04	0.03	0.76	0.31	0.14	<b>10.09</b>	<b>0.27</b>
g12-113-5b	III	0.00204086	9.60E-08	10.22	0.05	0.14	0.04	0.04	0.78	0.10	0.17	<b>10.17</b>	<b>0.26</b>
g12-113-25	III	0.00204029	2.44E-07	9.94	0.12	0.14	0.04	0.04	0.78	0.08	0.20	<b>9.89</b>	<b>0.28</b>
g12-113-37	III	0.00204754	1.23E-07	9.76	0.06	0.13	0.04	0.04	0.79	0.00	0.21	<b>9.71</b>	<b>0.25</b>
g12-113-16	III	0.00204006	2.02E-07	9.82	0.10	0.14	0.04	0.05	0.77	0.07	0.24	<b>9.77</b>	<b>0.27</b>
										Average:		<b>9.62</b>	
										Std. dev.:		<b>0.43</b>	

**Table A5 - 4. Garnet oxygen isotope composition determined by SHRIMP. Error propagation following Martin et al. (2014b).**

Spot	zone	$^{18}\text{O}/^{16}\text{O}$	$\pm\text{SE}$	meas. $\delta^{18}\text{O}$ (‰)	$\pm\text{SE}$	Xgrs	Xpyr	Xspess	Xalm	BIASgrs	BIASsps	corr. $\delta^{18}\text{O}$ (‰)	$\pm\text{SE}$
g12-113-10	IV	0.00203603	2.00E-07	7.84	0.10	0.03	0.10	0.00	0.87	-0.99	-0.08		<b>7.80 0.29</b>
g12-113-11	IV	0.00203637	6.50E-08	8.01	0.03	0.05	0.09	0.00	0.87	-0.82	-0.08		<b>7.97 0.27</b>
g12-113-12	IV	0.00203639	6.80E-08	8.02	0.03	0.06	0.06	0.00	0.88	-0.74	-0.07		<b>7.98 0.27</b>
g12-113-32	IV	0.00204446	1.85E-07	7.95	0.04	0.06	0.07	0.00	0.87	-0.73	-0.06		<b>7.91 0.27</b>
g12-113-31	IV	0.00204497	1.38E-07	8.15	0.13	0.05	0.07	0.00	0.87	-0.76	-0.06		<b>8.11 0.30</b>
g12-113-33	IV	0.00204463	1.59E-07	8.04	0.04	0.07	0.07	0.00	0.86	-0.61	-0.05		<b>8.00 0.27</b>
g12-113-27	IV	0.00203607	1.28E-07	7.86	0.06	0.07	0.06	0.01	0.86	-0.61	-0.03		<b>7.82 0.28</b>
g12-113-2b	IV	0.00203659	2.43E-07	8.11	0.12	0.05	0.07	0.01	0.87	-0.84	-0.02		<b>8.07 0.30</b>
g12-113-41	IV	0.00204493	1.88E-07	8.13	0.09	0.06	0.06	0.01	0.86	-0.64	-0.02		<b>8.09 0.29</b>
g12-113-13	IV	0.00203655	1.99E-07	8.10	0.10	0.06	0.07	0.01	0.86	-0.65	0.00		<b>8.05 0.29</b>
g12-113-14	IV	0.00203662	1.68E-07	8.13	0.08	0.07	0.06	0.01	0.86	-0.63	0.00		<b>8.09 0.28</b>
g12-113-30	IV	0.00204445	1.39E-07	7.90	0.05	0.04	0.07	0.01	0.88	-0.90	0.00		<b>7.86 0.28</b>
g12-113-34	IV	0.00204390	1.96E-07	7.67	0.11	0.08	0.06	0.01	0.85	-0.48	0.00		<b>7.63 0.29</b>
g12-113-40	IV	0.00204393	1.60E-07	7.85	0.05	0.08	0.06	0.01	0.85	-0.47	0.01		<b>7.80 0.27</b>
g12-113-1b	outer	0.00203653	1.48E-07	8.08	0.07	0.03	0.10	0.01	0.86	-1.02	-0.03		<b>8.04 0.28</b>
												<b>7.95</b>	
												<b>0.14</b>	

Instrument:	SHRIMP SI
Session:	29/07/2013
UWG repeatability:	0.27

**Table A5 - 4. Garnet oxygen isotope composition determined by SHRIMP. Error propagation following Martin et al. (2014b).**

Spot	zone	$^{18}\text{O}/^{16}\text{O}$	$\pm\text{SE}$	meas. $\delta^{18}\text{O}$ (‰)	$\pm\text{SE}$	Xgrs	Xpyr	Xspess	Xalm	BIASgrs	BIASsps	corr. $\delta^{18}\text{O}$ (‰)	$\pm\text{SE}$	
g12-101-3b	I	0.00203998	2.00E-07	9.78	0.10	0.08	0.05	0.13	0.73	-0.4416	0.7698		<b>9.74</b>	<b>0.27</b>
g12-101-21	I	0.00204060	6.30E-08	10.09	0.03	0.09	0.04	0.14	0.73	-0.3973	0.82153		<b>10.04</b>	<b>0.25</b>
g12-101-19	I	0.00203955	1.20E-07	9.57	0.06	0.08	0.05	0.16	0.71	-0.4611	0.92234		<b>9.53</b>	<b>0.26</b>
g12-101-20	I	0.00203951	7.50E-08	9.55	0.04	0.08	0.05	0.17	0.69	-0.4411	1.00221		<b>9.51</b>	<b>0.25</b>
g12-101-2b	I	0.00204021	2.08E-07	9.90	0.10	0.08	0.05	0.17	0.70	-0.4818	1.00907		<b>9.85</b>	<b>0.27</b>
g12-101-22	I	0.00204019	1.86E-07	9.88	0.09	0.08	0.05	0.18	0.70	-0.5062	1.03989		<b>9.84</b>	<b>0.27</b>
g12-101-23	I	0.00204783	1.06E-07	10.00	0.13	0.08	0.05	0.19	0.69	-0.5023	1.08796		<b>9.95</b>	<b>0.28</b>
g12-101-1b	I	0.00204084	1.29E-07	10.21	0.06	0.08	0.05	0.19	0.68	-0.4861	1.12007		<b>10.16</b>	<b>0.26</b>
													<b>9.83</b>	
													<b>0.23</b>	
g12-101-16	II	0.00204055	1.00E-08	10.06	0.00	0.15	0.05	0.08	0.72	0.16344	0.46536		<b>10.01</b>	<b>0.25</b>
g12-101-6b	II	0.00204146	2.53E-07	10.51	0.12	0.21	0.04	0.08	0.67	0.6865	0.46594		<b>10.46</b>	<b>0.29</b>
g12-101-5b	II	0.00204135	1.99E-07	10.46	0.10	0.15	0.05	0.10	0.70	0.22167	0.56675		<b>10.41</b>	<b>0.27</b>
g12-101-17	II	0.00204128	1.66E-07	10.42	0.08	0.17	0.04	0.11	0.68	0.37394	0.67691		<b>10.37</b>	<b>0.27</b>
g12-101-18	II	0.00204123	1.25E-07	10.40	0.06	0.19	0.04	0.14	0.64	0.52358	0.79861		<b>10.34</b>	<b>0.26</b>
g12-101-4b	II	0.00204156	2.00E-07	10.56	0.10	0.18	0.04	0.14	0.65	0.41034	0.81314		<b>10.51</b>	<b>0.27</b>
													<b>9.42</b>	
													<b>2.47</b>	
g12-101-8b	III	0.00204162	7.20E-08	10.59	0.04	0.22	0.05	0.01	0.72	0.78715	-0.00294		<b>10.54</b>	<b>0.27</b>
g12-101-14	III	0.00204138	2.28E-07	10.47	0.11	0.20	0.06	0.02	0.73	0.58473	0.05652		<b>10.42</b>	<b>0.29</b>
g12-101-13	III	0.00203920	3.07E-07	9.40	0.15	0.11	0.07	0.02	0.80	-0.16	0.05682		<b>9.35</b>	<b>0.30</b>
g12-101-9b	III	0.00203921	1.05E-07	9.40	0.05	0.12	0.06	0.04	0.79	-0.0844	0.16767		<b>9.36</b>	<b>0.26</b>
g12-101-7b	III	0.00204147	6.90E-08	10.52	0.03	0.21	0.04	0.04	0.71	0.69393	0.19146		<b>10.46</b>	<b>0.27</b>
g12-101-15	III	0.00204120	2.68E-07	10.38	0.13	0.19	0.05	0.05	0.71	0.56712	0.25597		<b>10.33</b>	<b>0.29</b>
													<b>10.08</b>	
													<b>0.56</b>	
g12-101-25	IV	0.00204585	1.48E-07	8.76	0.13	0.07	0.09	0.00	0.84	-0.5845	-0.08		<b>8.72</b>	<b>0.30</b>
g12-101-27	IV	0.00204460	1.42E-07	8.24	0.14	0.05	0.09	0.00	0.85	-0.7433	-0.06993		<b>8.20</b>	<b>0.31</b>
g12-101-12	IV	0.00203863	2.07E-07	9.12	0.10	0.08	0.09	0.00	0.82	-0.4898	-0.06308		<b>9.08</b>	<b>0.29</b>
g12-101-24	IV	0.00204553	1.95E-07	8.54	0.04	0.05	0.10	0.00	0.85	-0.7852	-0.05979		<b>8.50</b>	<b>0.27</b>
g12-101-11b	IV	0.00203805	8.00E-08	8.83	0.04	0.07	0.09	0.01	0.84	-0.5976	-0.04217		<b>8.79</b>	<b>0.27</b>
g12-101-26	IV	0.00204666	1.71E-07	9.10	0.06	0.09	0.09	0.01	0.82	-0.3876	-0.02746		<b>9.05</b>	<b>0.28</b>
g12-101-30	IV	0.00204558	1.54E-07	8.63	0.08	0.10	0.07	0.01	0.82	-0.2938	-0.0223		<b>8.58</b>	<b>0.28</b>
g12-101-10b	IV	0.00203775	2.56E-07	8.68	0.13	0.08	0.08	0.01	0.83	-0.4678	-0.01193		<b>8.64</b>	<b>0.30</b>
g12-101-29	IV	0.00204632	1.23E-07	8.67	0.06	0.06	0.07	0.02	0.85	-0.7052	0.06805		<b>8.63</b>	<b>0.28</b>
g12-101-28	IV	0.00204546	1.46E-07	8.33	0.11	0.06	0.07	0.03	0.84	-0.7326	0.14652		<b>8.29</b>	<b>0.29</b>
<b>Instrument:</b>		SHRIMP SI											<b>8.65</b>	
<b>Session:</b>		29/07/2013											<b>0.29</b>	
<b>UWG repeatability:</b>		0.27												

**Table A5 - 4. Garnet oxygen isotope composition determined by SHRIMP. Error propagation following Martin et al. (2014b).**

Spot	zone	$^{18}\text{O}/^{16}\text{O}$	$\pm\text{SE}$	meas. $\delta^{18}\text{O}$ (‰)	$\pm\text{SE}$	Xgrs	Xpyr	Xspess	Xalm	BIASgrs	BIASsps	corr. $\delta^{18}\text{O}$ (‰)	$\pm\text{SE}$
g12-165-1	core	0.00204682	1.43E-07	9.29	0.07	0.07	0.18	0.12	0.62	-0.584	0.73669		<b>9.23</b> <b>0.27</b>
g12-165-2	core	0.00204752	9.95E-08	9.82	0.03	0.06	0.19	0.12	0.63	-0.6544	0.71054		<b>9.77</b> <b>0.26</b>
g12-165-3	core	0.00204789	1.18E-07	9.82	0.05	0.07	0.19	0.11	0.64	-0.6319	0.61917		<b>9.77</b> <b>0.26</b>
g12-165-4	core	0.00204658	1.24E-07	9.49	0.11	0.06	0.20	0.10	0.64	-0.6665	0.61482		<b>9.44</b> <b>0.28</b>
g12-165-5	core	0.00204761	1.26E-07	9.69	0.05	0.07	0.19	0.11	0.63	-0.625	0.67152		<b>9.64</b> <b>0.26</b>
g12-165-6	core	0.00204748	1.10E-07	9.71	0.11	0.07	0.19	0.11	0.64	-0.6266	0.65386		<b>9.66</b> <b>0.28</b>
										Average:			<b>9.59</b>
										Stdev:			<b>0.21</b>
g12-165-11	rim 1	0.00204515	9.65E-08	8.65	0.06	0.09	0.19	0.03	0.69	-0.3415	0.10883		<b>8.60</b> <b>0.27</b>
g12-165-12	rim 1	0.00204533	1.28E-07	8.70	0.07	0.10	0.13	0.03	0.74	-0.3185	0.16271		<b>8.65</b> <b>0.27</b>
g12-165-13	rim 1	0.00204535	1.28E-07	8.58	0.07	0.10	0.18	0.03	0.69	-0.3204	0.13		<b>8.54</b> <b>0.27</b>
g12-165-15	rim 1	0.00204518	1.38E-07	8.62	0.07	0.10	0.19	0.03	0.69	-0.3158	0.10541		<b>8.57</b> <b>0.27</b>
										Average:			<b>8.59</b>
										Stdev:			<b>0.05</b>
g12-165-7	rim 2a	0.00204629	1.20E-07	9.14	0.11	0.13	0.21	0.01	0.65	0.02007	0.00241		<b>9.09</b> <b>0.29</b>
g12-165-8	rim 2a	0.00204722	1.17E-07	9.34	0.18	0.13	0.19	0.01	0.66	0.02898	-0.00207		<b>9.30</b> <b>0.32</b>
g12-165-9	rim 2a	0.00204698	1.36E-07	9.46	0.05	0.13	0.19	0.01	0.67	0.03924	-0.01457		<b>9.41</b> <b>0.27</b>
g12-165-10	rim 2a	0.00204694	1.07E-07	9.41	0.07	0.14	0.19	0.01	0.66	0.06125	-0.00989		<b>9.36</b> <b>0.28</b>
										Average:			<b>9.29</b>
										Stdev:			<b>0.14</b>
g12-165-16	rim 2b	0.00204532	9.20E-08	8.63	0.09	0.08	0.24	0.02	0.65	-0.4695	0.07422		<b>8.59</b> <b>0.28</b>
g12-165-17	rim 2b	0.00204524	1.25E-07	8.65	0.13	0.09	0.25	0.02	0.64	-0.3919	0.04134		<b>8.60</b> <b>0.30</b>
g12-165-18	rim 2b	0.00204422	1.12E-07	7.94	0.08	0.07	0.19	0.02	0.71	-0.5574	0.07271		<b>7.90</b> <b>0.28</b>
g12-165-19	rim 2b	0.00204479	9.05E-08	8.55	0.08	0.08	0.26	0.02	0.65	-0.484	0.03533		<b>8.50</b> <b>0.28</b>
g12-165-20	outer	0.00204503	1.37E-07	8.48	0.06	0.08	0.27	0.02	0.63	-0.4671	0.05769		<b>8.44</b> <b>0.27</b>
										Average:			<b>8.41</b>
										Stdev:			<b>0.29</b>

<b>Instrument:</b>	SHRIMP SI
<b>Session:</b>	29/07/2013
<b>UWG repeatability:</b>	0.27

Table A5 - 5: Zircon oxygen isotope composition determined by SHRIMP.

Spot	zone	$^{18}\text{O}/^{16}\text{O}$	$\pm 2\text{SE}$	$\delta^{18}\text{O}$ (‰)	$\pm \text{SE}$
G0446-9	osc	0.00204431	7.7E-08	5.17	0.04
G0446-4	osc	0.00204523	1.52E-07	5.62	0.07
G0446-1	osc	0.00204432	2.1E-07	5.18	0.10
G0446-2	osc	0.00204476	1.3E-07	5.39	0.06
G0446-3*	osc	0.00204281	2.42E-07	4.45	0.12
G0446-5	osc	0.00204500	1.28E-07	5.51	0.06
G0446-10	osc	0.00204471	1.45E-07	5.37	0.07
Average:				<b>5.38</b>	
Stdev:				<b>0.18</b>	
G0446-7	w	0.00204565	2.1E-07	5.83	0.10
G0446-8	w	0.00204657	1.25E-07	6.28	0.06
G0446-13	w	0.00204483	1.98E-07	5.43	0.10
G0446-12	w	0.00204425	1.2E-07	5.14	0.06
G0446-14	w	0.00204615	1.39E-07	6.07	0.07
G0446-6	w	0.00204384	1.44E-07	4.95	0.07
G0446-15	w	0.00204528	1.01E-07	5.65	0.05
Average:				<b>5.62</b>	
Stdev:				<b>0.48</b>	
G0446-11	w, fr	0.00205445	1.68E-07	10.12	0.08

\* outlier rejected from average

osc: oscillatory zone

w: white rim/zone

fr: fracture

<b>Instrument:</b>	SHRIMP SI
<b>Session:</b>	17/03/2014
<b>TEM repeatability:</b>	0.20